

Structure-property relationships in poly(2-oxazoline)/poly(2-oxazine) based drug formulations



Dissertation zur Erlangung des naturwissenschaftlichen Doktorgrades
an der Fakultät für Chemie und Pharmazie
der Julius-Maximilians-Universität Würzburg

vorgelegt
von

Michael M. Lübtow

aus **Dingolfing**

Würzburg, 2019

eingereicht bei der Fakultät für Chemie und Pharmazie am

19.11.2019

Gutachter der Dissertation

1. Gutachter: Prof. Dr. Robert Luxenhofer

2. Gutachter: Prof. Dr. Jürgen Groll

Prüfer des öffentlichen Promotionskolloquiums

1. Prüfer: Prof. Dr. Anke Krüger

2. Prüfer: Prof. Dr. Jürgen Groll

3. Prüfer: Prof. Dr. Matthias Lehmann

4. Prüfer: Jun.-Prof. Dr. Ann-Christin Pöppler

5. Prüfer: Prof. Dr. Christoph Lambert

Tag des öffentlichen Promotionskolloquiums

17.12.2019

Focus

Für meine Eltern

Acknowledgement

First and foremost, I would like to thank my advisor Prof. Dr. Robert Luxenhofer for giving me the opportunity to investigate this fascinating research topic within the last years. Needless to say, he played a major role in guiding me during this study by providing the best possible working environment. Although I rarely had to give an account on my research progress, I always had the opportunity to discuss the latter and therefore getting inspired by his insights and creativity. At the same time, he constantly challenged me to always dig deeper, in order to understand the root causes of various problems instead of content oneself halfway through. This mixture of trust, skepticism, as well as positive reinforcement made me go that extra mile much more often as I originally planned to.

Many thanks also to my colleagues in Würzburg. I really enjoyed working with you, as well as the activities outside the lab including boßeln, Chemcup (winner 2019!!!), barbecues and stays at the local beer gardens. In this regard I would like to thank Sebastian Halupczok, Jochen Löblein, Mengshi Yang, Chen Hu, Lukas Hahn, Stefan Forster, Daniel Nahm, Thomas Lorson, Juliane Marx, Markus Schäfer, Claudia Stauch, Solomia Borova, Christine Schlutt, Julian Heck, Robin Bissert, Mira Rupp and Anita Luxenhofer for a great time. Special thanks to Malik Salman Haider, with whom I worked closely in the lab, supporting each other with regard to various scientific problems as well as the supervision of students.

Apart from that, I am grateful for the opportunity to exchange with colleagues around the world at conferences in Boston, Philadelphia, Freiburg and Würzburg, being the starting point of multiple, interdisciplinary research cooperation.

The latter also includes a three months research stay at the Innovation Center of Nanomedicine (iCONM) in Tokyo, Japan. In this regard, I would like to thank Prof. Dr. Kazunori Kataoka for giving me a warm welcome and the opportunity to investigate our and their drug delivery platforms from a pharmaceutical point of view. From the first day on, I felt as part of the group, which is largely attributed to the great supervision of Dr. Sabina Quader. Thank you for your patience regarding my work at the clean bench, as well as the nice activities outside the lab.

Furthermore, I would like to thank Dr. Hiroaki Kinoh and Dr. Amit Maity for support regarding 3D cell culture, Dr. Xueying Liu for confocal microscopy studies, Dr. Saed Abbasi for insights regarding cellular uptake, Shigeto Fukushima for insights regarding polymer synthesis, Vinicio Melo for showing me the excellent all you can eat buffet close by, all other group members for a good time and valuable discussions as well as Rie Yamashita and all other members of the administrative office for straightforward organization.

Furthermore, I want to thank all my collaborators, who enabled to study the polymers and polymer based formulations in even greater detail. Thank you for valuable discussions:

Dr. Gudrun Dandekar, Dr. Antje Appelt-Menzel, Dr. Sarah L. Nietzer, Dr. Lena Nelke, Johanna Kühnemundt and Julia Seifert for performing various *in vitro* cell culture studies; *University Hospital Würzburg, Germany*

Prof. Dr. Gaurav Sahay and colleagues for cryo-TEM images; *Department of Pharmaceutical Sciences, College of Pharmacy, Oregon State University, Portland, United States*

Jun.-Prof. Ann-Christin Pöppler, Marvin Grüne and Jonas Schlauersbach for solid state NMR investigations; *Institute of Organic Chemistry, University of Würzburg, Germany*

Prof. Dr. Dr. Lorenz Meinel, Dr. Johannes Wiest and Jonas Schlauersbach for dissolution studies; *Institute for Pharmacy and Food Chemistry, University of Würzburg, Germany*

Dr. Sebastian Jaksch; *Forschungszentrum Jülich GmbH, JCNS at Heinz Maier-Leibnitz Zentrum, Garching, Germany* and Benedikt Sochor, Özgür Düdükçü and Bernhard Schummer for SANS measurements; *Chair of X-Ray Microscopy, Department of Physics and Astronomy, University of Würzburg, Germany*

PD Dr. Tessa Lühmann and Matthias Beudert for *in vitro* cell culture studies; *Institute of Pharmacy and Food Chemistry, University of Würzburg, Germany*

Prof. Dr. Christoph Lambert, Dr. Henning Marciniak, Alexander Schmiedel and Markus Roos for fluorescence-upconversion, -lifetime, and -anisotropy studies; *Institute of Organic Chemistry and Center for Nanosystems Chemistry, University of Würzburg, Germany*

Prof. Dr. Avi Schroeder and colleagues for *in vitro* cell culture and *in vivo* studies; *Laboratory for Targeted Drug Delivery and Personalized Medicine Technologies, Department of Chemical Engineering, Technion–Israel Institute of Technology, Haifa, Israel*

Dr. Florian-Kai Gröber-Becker and Tamara Finger for drug release studies; *Translational Center ‘Regenerative Therapies’ Fraunhofer Institute for Silicate Research (ISC), Würzburg, Germany*

Judith Friedlein for SEM-images; *Department for Functional Materials in Medicine and Dentistry, University Hospital Würzburg, Germany*

I am glad for the opportunity to supervise numerous students. I learned a lot from you, and I hope so did you. Therefore, thank you to my bachelor students Selma Dahms, Marius Kirsch, Laura Meier, Larissa Keßler, Clemens Schulte, Frederik Schmitt, Rafael Worschech, Daniela Lautz, Johannes Schneider, Anna Stegmann and Sven Heilig, my Masters' students Lukas Hahn and Maximilian Rist as well as interns Andreas Sieblist, Tim Görlich, Benedikt Ritschel, Regina Drescher, Korbinian Niedermüller, Thomas Bretschneider and Stefanie Klisch. I wish you all the best in your upcoming (academic) career.

A special thank you to Christian May and Anna Kucharski, who always supported me in various situations regarding the everyday laboratory life. The same is true for Dr. Guntram Schwarz, with whom I could discuss several scientific issues. Furthermore, I would like to thank Sandra Stockmann, Ulrike Midtbö and Diana Stürmer for excellent administrative support.

Furthermore, I would like to thank the Evonik Stiftung for providing a doctoral fellowship. I always enjoyed the exchange with colleagues from Evonik as well as the other fellows. This includes some memorable experiences such as the facility visit in Alabama, USA.

Apart from that, I would like to thank the Deutsche Forschungsgemeinschaft and the Freistaat Bayern for financial support as well as the Jülich Centre for Neutron Science for allocating beamtime and providing excellent equipment and support.

Last but not least, I thank my family and friends for ongoing support!

List of Publications

“Drug Specificity, Synergy and Antagonism in Ultrahigh Capacity Poly(2-oxazoline)/Poly(2-oxazine) based Formulations”

M. M. Lübtow*, L. Hahn, M. S. Haider, R. Luxenhofer†

Journal of American Chemical Society **2017**, *139*, 10980-10983

“Drug induced micellization into ultra-high capacity and stable curcumin nanoformulations: Physico-chemical characterization and evaluation in 2D and 3D *in vitro* models”

M. M. Lübtow*, L. C. Nelke, J. Seifert, J. Kühnemundt, G. Sahay, G. Dandekar, S. L. Nietzer, R. Luxenhofer†

Journal of Controlled Release **2019**, *303*, 162-180

“Ultra-high to ultra-low drug loaded micelles: Probing host-guest interactions by fluorescence spectroscopy”

M. M. Lübtow*, H. Marciniak, A. Schmiedel, M. Roos, C. Lambert, R. Luxenhofer†

Chemistry: A European Journal **2019**, *25*, 12601-12610

“Like Dissolves Like? A Comprehensive Evaluation of Partial Solubility Parameters to Predict Polymer-Drug Compatibility in Ultra-High Drug Loaded Polymer Micelles”

M. M. Lübtow*, M. S. Haider, M. Kirsch, S. Klisch, R. Luxenhofer†

Biomacromolecules **2019**, *20*, 3041-3056

“More is Sometimes Less: Curcumin and Paclitaxel Formulations Using Poly(2-Oxazoline) and Poly(2-Oxazine) Based Amphiphiles Bearing linear and branched C9 Side Chains”

M. M. Lübtow*, L. Keßler, A. Appelt-Menzel, T. Lorson, N. Gangloff, M. Kirsch, S. Dahms, R. Luxenhofer†

Macromolecular Bioscience **2018**, *18*, 1800155

“Poly(2-oxazoline)s based biomaterials: A comprehensive and critical review”

T. Lorson*, M. M. Lübtow*, E. Wegener, M. S. Haider, S. Borova, D. Nahm, R. Jordan, M. Sokolski-Papkov, A. V. Kabanov, R. Luxenhofer†

Biomaterials **2018**, *178*, 204-280

“Temperature-Dependent Rheological and Viscoelastic Investigation of a Poly(2-methyl-2-oxazoline)-b-poly(2-iso-butyl-2-oxazoline)-b-poly(2-methyl-2-oxazoline)-Based Thermogelling Hydrogel”

M. M. Lübtow*, M. Mrlik*, L. Hahn, A. Altmann, M. Beudert, T. Lühmann, R. Luxenhofer†

Journal of Functional Biomaterials **2019**, *10*, 36

“Combining ultra-high drug loaded micelles and injectable hydrogel drug depots for prolonged drug release”

M. M. Lübtow*, T. Lorson, T. Finger, F.-K. Gröber-Becker, R. Luxenhofer†

Macromolecular Chemistry and Physics **2019**, doi.org/10.1002/macp.201900341

“Investigating the influence of aromatic moieties on the formulation of hydrophobic natural products and drugs in poly(2-oxazoline) based amphiphiles”

L. Hahn*, M. M. Lübtow, T. Lorson, F. Schmitt, A. Appelt-Menzel, R. Schobert, R. Luxenhofer†

Biomacromolecules **2018**, *19*, 3119-3128

“Loading dependent Structural Model of Polymeric Micelles Encapsulating Curcumin by Solid-State NMR Spectroscopy”

A.-C. Pöppler*, M. M. Lübtow, J. Schlauersbach, J. Wiest, L. Meinel, R. Luxenhofer†

Angewandte Chemie International Edition **2019**, doi.org/10.1002/anie.201908914

“Collagenase Nanoparticles Enhance the Penetration of Drugs into Pancreatic Tumors”

A Zinger*, L. Koren, O. Adir, M. Poley, M. Alyan, Z. Yaari, N. Noor, N. Krinsky, A. Simon, H. Gibori, M. Krayem, Y. Mumblat, S. Kasten, S. Ofir, E. Fridman, N. Milman, M. M. Lübtow, L. Liba, J. Shklover, J. Shainsky-Roitman, Y. Binenbaum, D. Hershkovitz, Z. Gil, T. Dvir, R. Luxenhofer, R. Satchi-Fainaro, A. Schroeder†

ACS Nano **2019**, *13*, 11008-11021

“A Thermogelling Supramolecular Hydrogel with Sponge-Like Morphology as a Cytocompatible Bioink”

T. Lorson*, S. Jaksch, M. M. Lübtow, T. Jüngst, J. Groll, T. Lühmann, R. Luxenhofer†

Biomacromolecules **2017**, *18*, 2161-2171

Preprints

“*In vitro* blood-brain-barrier permeability and cytotoxicity of atorvastatin-loaded nanoformulation against glioblastoma in 2D and 3D models”

M. M. Lübtow*, S. Oerter, S. Quader, E. Jeanclos, A. Cubukova, M. Krafft, C. Schulte, L. Meier, M. Rist, A. Gohla, H. Kinoh, H. Saya, A. Appelt-Menzel, K. Kataoka, R. Luxenhofer†

ChemRxiv **2019**, doi.org/10.26434/chemrxiv.10067993.v1

“Probing the complex loading dependent structural changes in ultra-high drug loaded polymer micelles by small angle neutron scattering”

B. Sochor*, Ö. Düdükçü*, M. M. Lübtow, S. Jaksch, B. Schummer, R. Luxenhofer†

ChemRxiv **2019**, doi.org/10.26434/chemrxiv.10259552

“Think beyond the core: The impact of the hydrophilic corona on the drug solubilization using polymer micelles”

M. S. Haider*, M. M. Lübtow, V. Aseyev, A.-C. Pöppler, R. Luxenhofer†

ChemRxiv **2019**, doi.org/10.26434/chemrxiv.9710579.v1

Contents

Abbreviations and Symbols	III
1 Introduction.....	1
2 State of Knowledge	3
2.1 Routes of Administration	4
2.2 Nanomedicine	5
2.3 Polymeric Micelles as DDS for Water Insoluble Drugs	8
2.4 Impact of Polymer-Drug Interactions on Drug Loading	9
2.5 Impact of Drug-Drug Interactions on Drug Loading	23
2.6 Prediction of Polymer-Drug Compatibility	27
3 References	37
4 Results	43
4.1 Poly(2-oxazoline) and Poly(2-oxazine) Based Biomaterials – an Overview.....	44
4.2 Polymer-Drug Compatibility.....	56
4.3 Structure of Drug-Loaded Micelles.....	118
4.4 Pharmaceutical Properties of Drug-Loaded Micelles.....	146
4.5 Drug-Loaded Hydrogels.....	178
5 Summary and Outlook.....	221
6 Zusammenfassung und Ausblick	227
Erklärung	235
Eigenanteil.....	237

Abbreviations and Symbols

Abbreviations

17-AAG	17-allylamino-17-demethoxygeldanamycin
Ala	alanine
API	active pharmaceutical ingredient
approx.	approximately
ATV	atorvastatin
AUC	area under the curve
Ce6	chlorin E6
CED	cohesive energy density
CMC	critical micelle concentration
CMT	critical micelle temperature
COMPASS	condensed-phase optimized molecular potentials for atomistic simulations
CPMAS	cross polarized magic angle spinning
CsA	cyclosporin A
CUR	curcumin (extracted from turmeric)
D ₂ O	deuterated water
DDS	drug delivery system
D _h	hydrodynamic diameter (investigated by DLS)
DLS	dynamic light scattering
DMF	dimethylformamide
DMF-d ₇	deuterated DMF
DOX	doxorubicin
DSC	dynamic scanning calorimetry
DTX	docetaxel
etc	et cetera (and so on)
e.g.	exempli gratia (for example)
ELP	ellipticine
EPR	enhanced permeability and retention effect
<i>et al.</i>	et aliae (and others)
FDA	U.S. Food and Drug Administration
FT-IR	Fourier-transform infrared spectroscopy
GAFF	general AMBER force field
GCM	group contribution method
GF	griseofulvin
Gln	glutamine
H ₂ O ₂	hydrogen peroxide
HETCOR	heteronuclear correlation (in 2D NMR spectroscopy)

HPMAm	poly(<i>N</i> -(2-hydroxypropyl) methacrylamide)
HPMAm-Bz	poly(<i>N</i> -(2-benzoyloxypropyl) methacrylamide)
HPMAm-Nt	poly(<i>N</i> -(2-naphthoyloxypropyl) methacrylamide)
HPMCAS	hydroxypropylmethyl cellulose
HSP	Hansen solubility parameter
<i>i.e.</i>	id est (that is)
IV	intravenous
IMC	indomethacin
KETO	ketoconazole
LPC	β-lapachone
LC	loading capacity; ($m_{\text{drug}}/(m_{\text{drug}} + m_{\text{excipient}})$)
LE	loading efficiency; ($m_{\text{drug, solubilized}}/m_{\text{drug, added}}$)
log <i>P</i>	partition coefficient (ratio of concentrations of a compound in a mixture of two immiscible phases, usually between octanol and water)
<i>m</i> -THPC	<i>meta</i> -tetra(hydroxyphenyl)chlorin
MD	molecular dynamics
MPS	mononuclear phagocytic system
nab	nanoparticle albumin-bound
NCE	new chemical entity
NIF	nifedipine
NMR	nuclear magnetic resonance
NP	nanoparticle
IM	intramuscular
IV	intravenous
Ox	2-oxazoline; unspecified substituent at 2-position (according to the Hantzsch-Widmann-Patterson nomenclature for heterocyclic systems) systematic IUPAC name: 4,5-dihydrooxazole
Ozi	2-oxazine; unspecified substituent at 2-position (according to the Hantzsch-Widmann-Patterson nomenclature for heterocyclic systems) systematic IUPAC name: 5,6-dihydro-4 <i>H</i> -1,3-oxazine
PAA	polyacrylic acid
PAP	papaverine
PBS	phosphate buffered saline
PASA	poly(α,β-aspartic acid)
PLA	polylactic acid
Pba	pheophorbide
PBA	phenylboronic acid
PDI	polydispersity index
PEG	polyethylene glycol
PEG-hexPLA	polyethylene glycol- <i>b</i> -poly(hexyl-substituted lactic acid)
PEG-PLA	polyethylene glycol- <i>b</i> -polylactic acid
pH	$-\log_{10}[\text{H}^+]$
Phe	phenylalanine
PHEA	poly[(<i>N</i> -2-hydroxyethyl)-aspartamide]
Phen-Pt	1,10 phenanthroline Pt-complex
PLA	polylactic acid
PLGA	poly(<i>D,L</i> ,-lactic- <i>co</i> -glycolic acid)

PMMA	poly(methacrylic acid)
POx	poly(2-oxazoline)
POzi	poly(2-oxazine)
ppm	parts per million
PRINT	particle replication in non-wetting template
PS	polystyrene
PTX	paclitaxel
PVP	polyvinylpyrrolidone
PVA	polyvinyl acetate
QUER	quercetin
QSPR	quantitative structure-property relationship
RAP	rapamycin
ref	reference
ROS	reactive oxygen species
R_h	hydrodynamic radius (investigated by DLS)
RNA	ribonucleic acid
SC	subcutaneous
Ser	serine
SiRMS	simplex representation of a molecular structure
siRNA	small interfering RNA
SQAd	squalene-adenosine
T2A	tanshinone IIA
TEM	transmission electron microscopy
PVA	polyvinyl acetate

List of symbols

$^{\circ}\text{C}$	degree Celsius
δ	solubility parameter δ_T total solubility parameter (Hildebrand solubility parameter) $\delta_D, \delta_P, \delta_H$ contributions from intermolecular van-der-Waals forces, dipole-dipole interactions and hydrogen bonding, respectively
E_{total}	total energy of a system derived by COMPASS force field
ΔG_{mix}	Gibbs' free energy of mixing
ΔH_M	enthalpy of mixing
h	hour
m	milli, 10^{-3}
ms	milliseconds
M	molar concentration, [mol/L]
M_w	weight average molar mass
ρ	mass concentration (w/v)
ϕ	volume fraction
wt. %	weight percent ($w_{\text{substance}}/w_{\text{mixture}} \cdot 100\%$) e.g. 20 wt.% solution = 200 mg (substance)/0.8 mL (H_2O) = 200 mg (substance)/1000 mg(total)
mol	amount of substance: Avogadro number ($N_A = 6.022 \dots \times 10^{23}$) x substance
χ_{FH}	Flory Huggins interaction parameter

1 Introduction

Parts of this chapter are based on the publication: M. M. Lübtow et al., Drug induced micellization into ultra-high capacity and stable curcumin nanoformulations: Physico-chemical characterization and evaluation in 2D and 3D in vitro models; J. Control. Release, 2019, 303, 162-180

For many years, high-throughput screenings^[1] have been seen as a game changer for the discovery of new lead molecules for active pharmaceutical ingredients (APIs) against various illnesses. However, when it comes to the development of a dosage form, one major challenge, the appropriate formulation of the API, remains. An estimated 40%^[2] - 60%^[3] of all NCEs (new chemical entities) developed in medicinal chemistry and pharmaceutical industry are practically insoluble in water. Naturally, the demand for excipients which increase the water solubility and thus, the bioavailability of such hydrophobic compounds is enormous.^[4, 5]

Polymer micelles are nanoscopic, typically core/shell structures formed by amphiphilic block copolymers. Both, the inherent and modifiable properties of polymer micelles make them particularly well suited for drug-formulation purposes.^[6, 7] Conceptually, a hydrophobic API gets dissolved in the hydrophobic core, whereas the hydrophilic shell acts as a protective layer to prevent premature disintegration and to ensure a sufficient water solubility. Poly(2-oxazoline)s (POx) are currently intensively discussed as promising and highly versatile class of biomaterials^[8-10] due to their high cytocompatibility^[11-14] as well as easy modulation of solubility, size^[15] and architecture^[16-18]. Although selected POx based formulations exhibit extraordinarily high drug loadings > 50 wt.% enabling high anti-tumor efficacies *in vivo*^[19-21], the formulation of other hydrophobic compounds^[22, 23] has failed. This casts doubt on the general understanding in which a hydrophobic API is dissolved rather unspecifically in the hydrophobic core following the fundamental concept of “like dissolves like”.^[23, 24]

Although the challenge of finding a suitable, polymer-based vehicle for a specific API is well known in industry as well as academics, a comprehensive understanding of the solubilization behavior of polymer micelles is still lacking. As a result, the selection is typically based on intuition as well as trial and error, associated with a lot of effort as well as expense.^[25-31]

The scope of such becomes evident by the strongly different solubilization behaviors of POx and structurally related poly(2-oxazine)s (POzi) based vehicles.^[31] Therefore, a closer look at the interactions between all components within a formulation becomes increasingly important, especially when considering the changing perception of excipients which simply act as an inert medium for the drug, towards complex systems which actively enhance the overall safety of the API.^[32]

Having this in mind, the purpose of this thesis was to shed new light on an established and at first sight straightforward system such as drug-loaded micelles. A large vehicle platform^[23] was synthesized, loaded with various hydrophobic drugs of different structure, and subsequently characterized with conventional^[24, 30, 31, 33, 34] and less conventional^[35-37] techniques. The obtained in-depth insights helped to develop a more thorough understanding about the interaction of polymer and incorporated API finally revealing morphologies deviating from a classical core/shell structure. During these studies, the polymer class of POzi, which has never been used for formulation purposes before, was found as promising drug-delivery vehicle for hydrophobic drugs.

Apart from this fundamental research, the anti-tumor efficacy of the two APIs curcumin (CUR) and atorvastatin (ATV) has been studied in more detail. In this regard, highly controversial CUR has been investigated critically to exclude misinterpretation due to e.g. false readouts.^[33] On the other hand, ATV could be identified as promising drug-candidate against various glioblastoma.^[34]

To increase the scope of POx and POzi based formulations designed for intravenous (IV) administration, a CUR-loaded hydrogel was developed as injectable drug-depot.^[38] Within this study, the interactions between a cytocompatible hydrogel and incorporated, CUR-loaded polymer micelles were investigated systematically.

2 State of Knowledge

The following chapters should give (critical) insights into nanomedicine, *i.e.* the treatment or prevention of diseases with materials in the nanoscale. This includes a brief introduction into general concepts (chapters 2.1 – 2.3), followed by an in-depth discussion of state-of-the-art literature about the interaction of polymers and solubilized drug (chapters 2.4 & 2.5). Instead of explaining various measurement techniques from scratch, recent publications will be used to introduce current approaches for characterization from an application point of view. Although not all the discussed techniques were applied in this thesis, knowledge about the latter supports a thorough understanding about the complexity of polymer-drug interactions. The final chapter 2.6 is designed as outlook, giving insights into current approaches to predict polymer-drug compatibilities ranging from (at first sight) straightforward group contribution methods to sophisticated and computationally expensive molecular dynamics simulations. Although the latter are not a topic of this work, the interconnection of chemistry and informatics will become increasingly important as e.g. elucidated in the strongly increased demand on artificial intelligence in the chemical industry. Although some of the discussed simulations are too sophisticated to be widely applied at the moment, ever increasing computational power and simplified interfaces will pave their way as standard tool for prediction and characterization.

2.1 Routes of Administration

The majority of drugs are not administered in pure form in order to reduce side-effects^[39], to prolong their mode of action or due to solubility issues^[40]. Therefore, drug delivery is often approached via a drug's formulation, in which different chemical substances including the API, are combined to produce a final medicinal product. Every system that delivers a drug to its site of action is a drug delivery system (DDS). After administration, the drug is typically released from the DDS via diffusion^[41, 42], swelling^[43], degradation^[44, 45], and/or stimuli-controlled mechanisms^[46]. The kind of administration of a medicine will determine to some extent whether the patient gains clinical benefit and/or suffers any adverse effect.^[47] Common routes of drug administration are topical^[48], oral^[49], inhalation^[50] or injection^[51] (Figure 2.1). The latter includes intramuscular (IM), subcutaneous (SC) and intravenous (IV) administration.





Routes of Administration			
			
topical	oral	inhalation	injection
<ul style="list-style-type: none"> • convenient • little side effects 	<ul style="list-style-type: none"> • convenient • no sterile conditions 	<ul style="list-style-type: none"> • quick adsorption • acts locally and systemically 	<ul style="list-style-type: none"> • 100 % bioavailability • exact dosage control
<ul style="list-style-type: none"> • low systemic concentration 	<ul style="list-style-type: none"> • unpredictable gastro-intestinal absorption 	<ul style="list-style-type: none"> • no sustained release • device necessary 	<ul style="list-style-type: none"> • inconvenient • trained staff necessary

Figure 2.1: Advantages and disadvantages of different routes of administration.

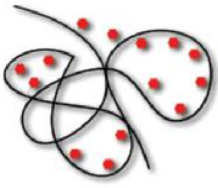


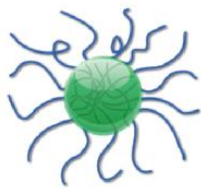
Bioavailability describes the proportion of a drug which enters systemic circulation after administration and is therefore crucial to unfold a drug's therapeutic potential. Although not being the most convenient for the patient, IV injections have by definition a 100% bioavailability.^[52] This is especially important when administering drugs which are poorly absorbed or ineffective when given orally. Unfortunately, as mentioned earlier, an estimated 40% - 60% of all NCEs developed in pharmaceutical industry are poorly water-soluble.^[2, 3] This poses a major challenge for the IV administration of such drugs.

A plethora of methods are used for solubility enhancement of poorly soluble drugs. Physical modifications with solubility-mediating excipients are the preferred way to avoid side-reactions and altered efficacies caused by chemical modification of the respective drug. Ideally, these excipients are non-toxic, non-immunogenic, cheap and widely applicable.^[53] Physical methods include particle size reduction^[54], crystal engineering^[55, 56], salt formation^[57], solid dispersions^[58] or the use of surfactants^[59]. For the latter, physical entrapment of non-water soluble drugs in nanosized drug delivery vehicles has been investigated intensively in the field of “nanomedicine” in the last decades.^[60]

2.2 Nanomedicine

Except a common low aqueous solubility, hydrophobic drugs exhibit different functional groups, geometries and stabilities under ambient conditions. This versatility makes the discovery of suitable drug delivery vehicles as tedious as the search of new APIs and might explain the enormous versatility of carrier systems developed in the field of nanomedicine in recent years. Nano-sized carrier systems, *i.e.* DDS with sizes below 100 nm (systems < 500 nm also described as “nano” in selected literature), have emerged in various pharmaceutical areas including drug delivery, diagnosis and imaging, synthetic vaccine development and miniature medical devices.^[60] This success can be partly explained by the fact that particles with sizes exceeding ≈ 100 nm tend to be cleared fast by the mononuclear phagocytic system (MPS).^[61] Besides their longer circulation time, smaller particles also extravasate and penetrate the surrounding tissue more efficiently and are able to utilize size specific cellular uptake mechanisms.^[61] Non-ionic drug delivery vehicles are generally less toxic, less hemolytic and less irritating to cellular surfaces compared to their anionic, amphoteric or cationic counterparts and tend to maintain near physiological pH in solution.^[62] Examples of commercially available or clinically relatively well-established, non-ionic polymeric nanocarrier materials for IV injections are polymer-drug conjugates (e.g. SMANCS^[63]), dendrimers (e.g. DEPTM ^[64]), polymersomes (e.g. Doxil[®]^[65]), and polymeric micelles (e.g. Genexol[®]^[66]) (Table 2.1). For an extended list, the reader is referred to ref[60].

Table 2.1: Polymer based, non-ionic nanotherapeutic technologies used for cancer therapy (NP = nanoparticle). Table modified with permission from ref[67].

	polymer-drug conjugates	dendrimers	polymersomes	polymeric micelles / NP
non-ionic, nanoscopic drug delivery systems				
size	< 10 nm	2 - 10 nm	100 - 200 nm	10 - 100 nm
structural characteristics	macromolecular structure	macromolecular tree-like structure	spherical, bilayer vesicle structure	spherical, core/shell structure
carrier composition	water-soluble polymer	hyperbranched polymer chain	amphiphilic copolymers	amphiphilic copolymers
drug incorporation strategy	covalent conjugation requiring functional groups on drug and polymer	non-covalent encapsulation compatible with hydrophobic drugs	non-covalent encapsulation compatible with hydrophilic and hydrophobic drugs	non-covalent encapsulation compatible with hydrophobic drugs

Although this intersystem versatility might sound promising at first, a closely related aspect is most often neglected. Reproducibility, *i.e.* intrasystem versatility, is hardly discussed in the field of nanomedicine. This seems somehow surprising, as the impact of small structural changes such as the different biochemical activities of enantiomers or the impact of trace impurities such as copper in enzyme inhibition is well known in biomedical research.^[68, 69] Focusing on the polymer vehicle rather than the drug reveals another source of irreproducibility. Despite increased control over various polymerization techniques, polymers are intrinsically statistical in nature leading to a structural variability.^[70] Such batch-to-batch reproducibility (variation between different syntheses) may strongly affect polymer aggregation^[71-73], leading to significant differences in aggregation of nanoparticles, cellular uptake^[74], toxicity^[75], complement activation or platelet aggregation^[76]. Nevertheless, in the vast majority of publications, only a single polymer batch is investigated for drug-formulation which is among others due to the complexity of (i) certain polymeric systems resulting in high synthetic effort and (ii) the polymer characterization itself requiring sophisticated analytical devices and trained staff.

Critical is also the challenge of scaling-up nanomaterial synthesis and formulation from laboratory (20 g) to larger (1 kg) scale while maintaining control over particle properties such as size, surface charge, or cytotoxicity as shown in the case of squalene-adenosine (SQAd) nanoparticles (Figure 2.2).^[77]

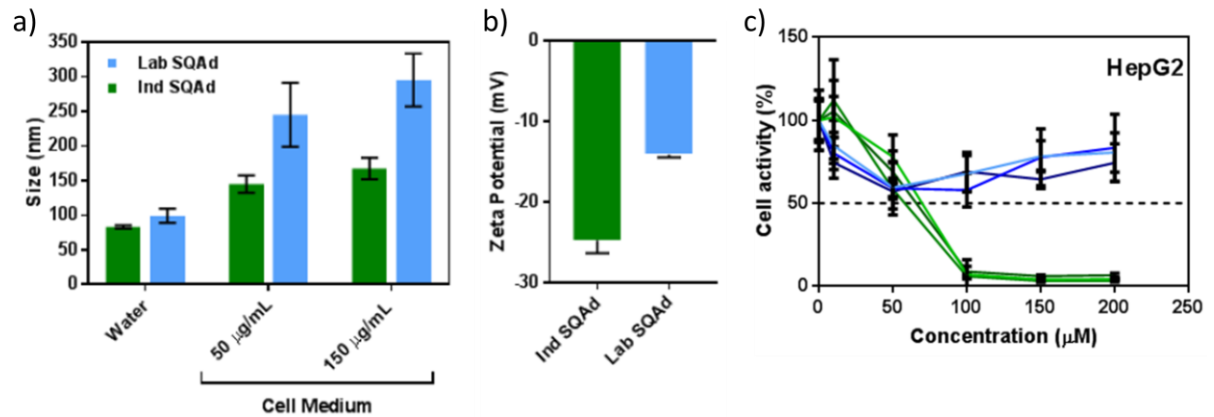


Figure 2.2: Deviations in a) hydrodynamic diameters (investigated by dynamic light scattering (DLS)), b) zeta-potential or c) cytotoxicity (HepG2: human liver cancer cells) between SQAd NPs prepared in laboratory (blue) or industrial (green) scale. Figure modified with permission from ref[77].

Although the challenge of reproducibility and proper characterization remains, numerous polymer-based DDS managed the transition from preclinics to clinical trials and into the clinics^[60], resulting in the first FDA (U.S. Food and Drug Administration) approved liposomal formulation of doxorubicin in 1995, marketed under the trade name Doxil[®]^[65] (Figure 2.3).

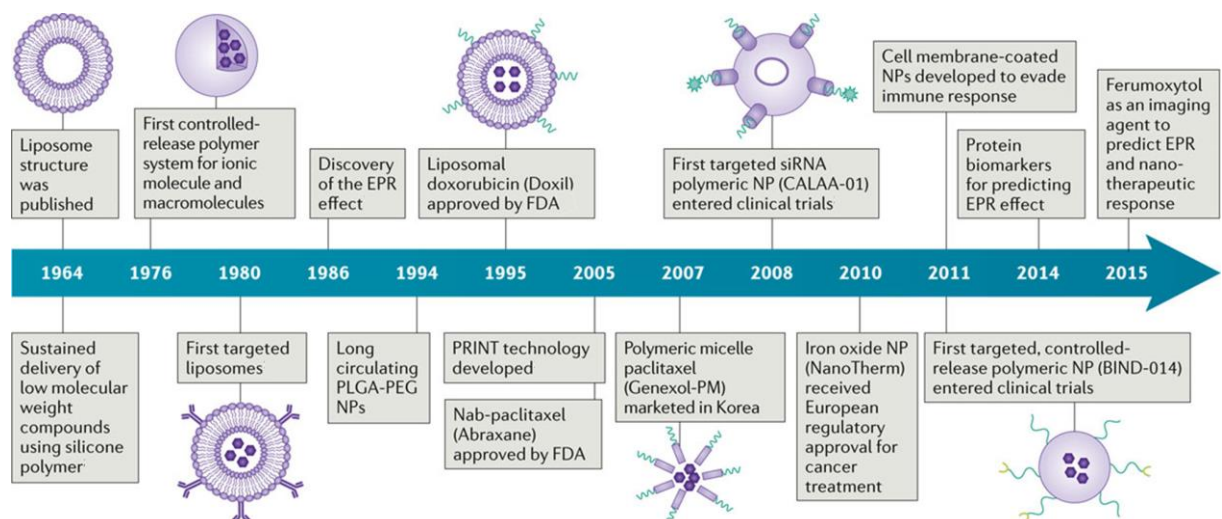


Figure 2.3: Historical timeline of major developments in the field of cancer nanomedicine. EPR: enhanced permeability and retention effect; nab: nanoparticle albumin-bound; PLGA-PEG: poly(*D,L*-lactic-co-glycolic acid)-*b*-polyethylene glycol; PRINT: particle replication in non-wetting template; siRNA: small interfering RNA. Figure modified with permission from ref[60].

The varying chemical and physical properties of chemotherapeutics make it (most likely) impossible to build a universal carrier system for all kind of drugs especially when considering the different types of application. However, the easy preparation, size in the nanoscale and various possibilities of modification make polymeric micelles ideal candidates to overcome the restrictions of numerous water insoluble drugs.^[7]

2.3 Polymeric Micelles as DDS for Water Insoluble Drugs

Polymeric micelles are nanoscopic core/shell structures formed by amphiphilic block copolymers (Figure 2.4). In aqueous solution, the hydrophobic part of an amphiphilic block copolymer self assembles into a semi-solid core, with the hydrophilic segments forming a coronal layer.^[67] The self-assembly is mainly entropy-driven^[78, 79], due to the reduced allowed orientations of water hydrogen-bonds close to the hydrophobic block of the polymer. Micelles are formed once this loss of entropy exceeds the loss of entropy caused by self-assembly. The narrow concentration range in which the process occurs is termed the critical micelle concentration (CMC). Below the CMC, the added amphiphiles enrich at the water-air interface, lowering the surface tension.

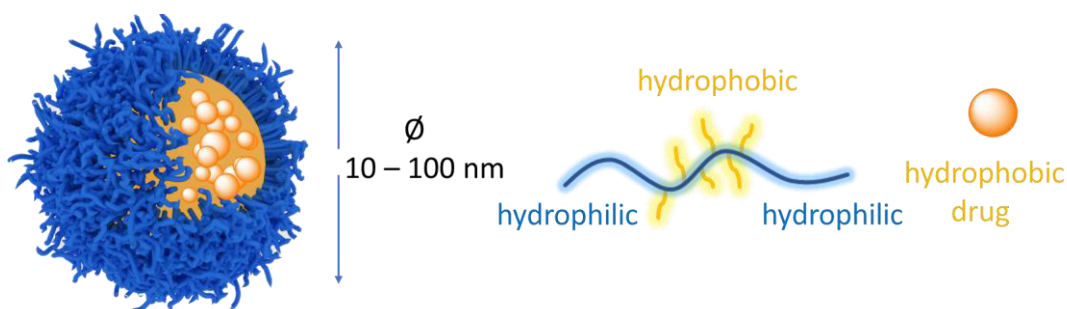


Figure 2.4: Illustration of the core/shell architecture of drug-loaded polymeric micelles comprising an amphiphilic ABA-triblock copolymer. Hydrophobic drugs can be solubilized within the hydrophobic core of the micelle.

Important to note, micelles are highly dynamic, *i.e.* always in equilibrium with non-assembled, single polymer chains (unimers). This distinguishes polymeric micelles from e.g. solid silica^[80] or solid lipid NPs^[81], both having a defined composition and shape in various conditions. In contrast, micellization is affected by various factors including temperature^[82], pressure^[83], or the structure of the surfactant (e.g. hydrophobic volume, chain length, hydrophilic-lipophilic balance^[84]). For nonionic surfactants, the CMC decreases with increasing temperature due to an increase in hydrophobicity caused by the destruction of hydrogen bonds between water molecules and the hydrophilic part of the polymer.^[85] Furthermore, aggregation of polymeric amphiphiles is influenced by the presence of different types of additives such as (non)electrolytes, hydrotopes, as well as low molecular weight surfactants.^[86, 87]

While the hydrophobicity of water insoluble drugs is favorable for drug permeation through cell membranes, IV administration of the latter would result in rapid drug aggregation and formation of capillary embolisms.^[88] Polymer micelles can enable the *in vivo* use of drugs which would otherwise be deemed too hydrophobic or toxic, without the necessity to change the chemical structure of the agent. However, to obtain desired particle properties, a comprehensive understanding of the interactions between polymeric drug carrier and solubilized, hydrophobic drug is necessary.

2.4 Impact of Polymer-Drug Interactions on Drug Loading

Since the first thoughts of using micelles for medicinal applications in the early 1980s by Ringsdorf and coworkers^[89], the properties of drug-loaded polymer micelles have been studied intensively. Intersystem interactions, *i.e.* interactions between drug-loaded micelles and e.g. biological systems, have gained major research attention due to their impact on treatment outcomes. These include among others the understanding and optimization of:

- passive targeting, *i.e.* accumulation of drug at the site of action, mainly based on the so called “enhanced permeability and retention” (EPR) effect^[90-92],
- active targeting, based on specific interactions between selective ligands (e.g. antibodies^[93], peptides, sugars, T-cells^[94]) conjugated onto the polymer surface and e.g. membrane associated cellular uptake transporters^[95],
- stealth properties, *i.e.* the ability of micelles to escape the MPS and therefore increase blood retention times^[96] due to the formation of a biocompatible protein corona^[97, 98].

Naturally, all these characteristics strongly depend on the colloidal properties (size, charge, stability) of the respective drug-loaded micelles. Unfortunately, colloidal properties cannot be simply derived from the initial properties of the neat polymer micelles, but are strongly affected by the kind and amount of incorporated drug. This becomes evident by the drug induced morphology switch of POx based micelles from worm-like, to spherical and raspberry-like structures with increasing loading (0 – 50 wt.%) of the chemotherapeutic agent paclitaxel (PTX) (Figure 2.5).^[99, 100]

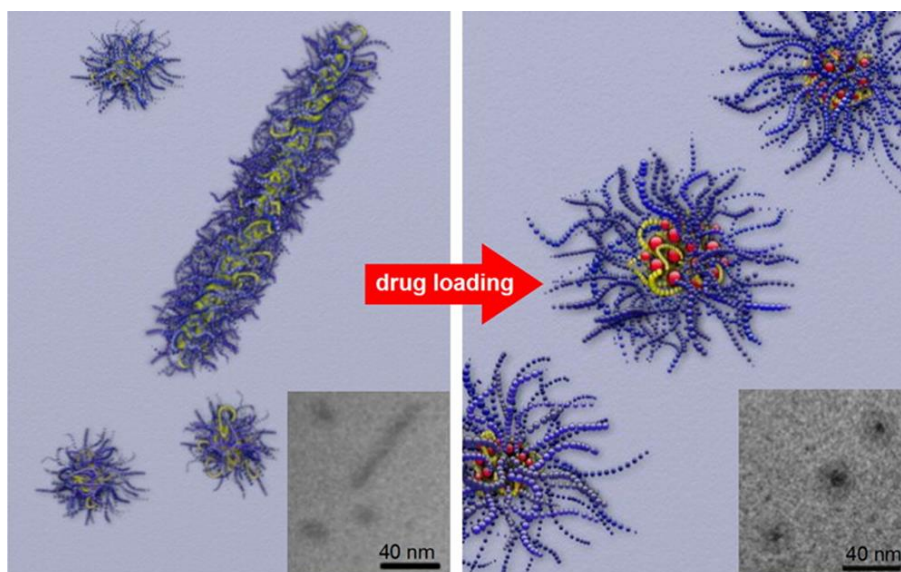


Figure 2.5: Drug-induced morphology switch of PTX-loaded POx micelles from initially worm-like (left) to spherical (right) structures with increasing PTX loading. Cryo-TEM images are shown on the bottom right corners, whereas cartoons are used for visualization. Figure reprinted with permission from ref[99].

Despite their impact, the interactions between polymer vehicle and incorporated drug are little understood. Obsolete perceptions such as “like dissolves like”, *i.e.* hydrophobic drugs are simply dissolved within the hydrophobic core, or the overemphasize of a distinct core/shell structure should be regarded with great care.^[101, 102] In the context of colloidal stability, polymer-drug interactions also determine the drug loading capacity (LC), *i.e.* the amount (%) of drug solubilized within a formulation (equation 1):

$$LC = \frac{m_{drug}}{m_{drug} + m_{polymer}} \quad \begin{array}{l} m_{drug} = \text{mass of solubilized drug} \\ m_{polymer} = \text{mass of polymer added to formulation} \end{array} \quad (1)$$

The LC can strongly effect treatment outcomes, as the higher the LC , the lower the risk of adverse side-effects caused by the excipient, as observed for the vehicle Cremophor EL used for PTX formulation (Taxol®).^[103] Furthermore, increased anti-tumor efficacy of high-dose compared to low-dose PTX treatment has been observed *in vivo*.^[19] Unfortunately, besides their discussed advantages (easy preparation, small sizes, etc.), drug-loaded micelles generally suffer rather low LC below 20 wt%.^[104] Therefore, various strategies have been employed in recent years to increase LC and stability of drug-loaded micelles.

The scope of such effort is displayed by the work of Börner and coworkers, using a combinatorial approach to identify suitable peptide sequences out of 7^7 possible heptamers to efficiently formulate the non-water soluble, anti-Alzheimer compound B4A1.^[105] Raman microscopy was used to select B4A1-binding peptides from large one-bead-one-compound peptide libraries (Figure 2.6a).

This selection approach increased the scope of suitable peptide-selection initially performed by fluorescence microscopy, being applicable only for fluorescent lead molecules.^[106] The sequential space of 7^7 different heptamer peptides was synthesized on ChemMatrix resin by split-and-mix procedures. As the peptide sequences with high affinity were rich in phenylalanine (Phe) and basic residues (Figure 2.6b), it was concluded that π - π stacking and Coulomb interactions dominate B4A1-peptide binding. LC strongly depended on the peptide sequence, as Pep₁-PEG, Pep₂-PEG and Pep₃-PEG exhibited payloads of 0.83 mol, 0.94 mol and 0.65 mol B4A1 per mol carrier, respectively. Important to note, such rather low drug loadings suggest the formation of colloidal aggregates, rather than drug-loaded micelles, which usually incorporate more than one drug molecule per polymer chain. The formation of aggregates was confirmed by dynamic light scattering (DLS) (hydrodynamic radii (R_h) = 105 – 175 nm). Nevertheless, the payloads were five to seven times higher than those achieved with the common solubilizer Chremophor EL. Idealized 1:1 complexes of B4A1 and the peptide domains were simulated showing considerable binding of all three peptide sequences to B4A1 (Figure 2.6c,d). The proposed π - π interactions between the Phe residues and the central pyrimidine ring of B4A1 were clearly visible, despite the dynamic nature of the model complexes (interaction energies between -150 and -200 kJ/mol).

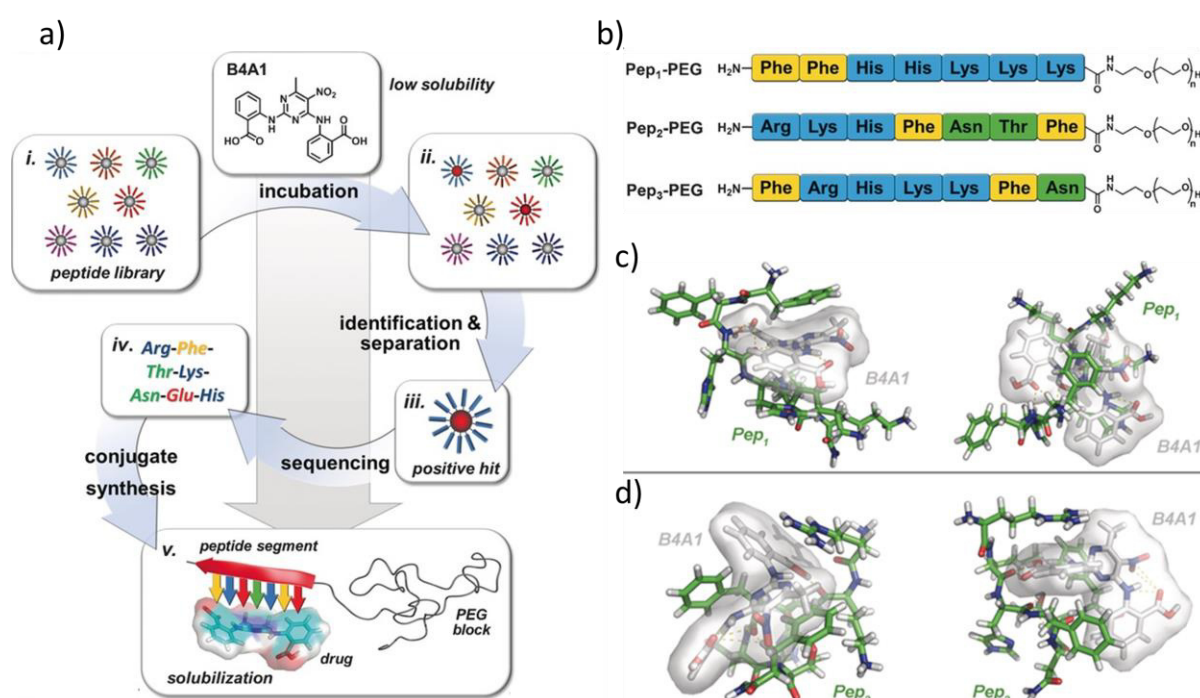


Figure 2.6: a) Selection of suitable peptide sequences for the solubilization of B4A1: (i) incubation of a one-bead-one-compound peptide library with B4A1 followed by (ii) Raman microscopy to identify (iii) compound-enriched beads; (iv) single-bead sequencing revealed b) peptides with high B4A1 binding capacities; c,d) representative snapshots from molecular dynamics (MD) simulations of B4A1 (shown as van-der-Waals surface) bound to tailored peptide sequences (sticks) shown in b). Figure reprinted with permission from ref[105].

Peptide-drug specificities were also apparent when formulating the structurally similar photosensitizers Chlorin E6 (Ce6), *meta*-tetra(hydroxyphenyl)chlorin (*m*-THPC) and Pheophorbide A (Pba) (Figure 2.7a). The peptide sequence most suitable for Ce6 loaded 18 and 5 times more Ce6 than *m*-THPC and Pba, respectively (Figure 2.7b).^[107] On the other hand, the peptide sequence selected for *m*-THPC was more compatible with Ce6 and Pba than with *m*-THPC. Generally, the specificity of the polymers for Ce6 was not very pronounced (1/1.1/1.2). Important to note, the difference in *LC* nicely correlated to drug release kinetics, *i.e.* prolonged drug release kinetics of polymer-drug pairs with higher maximum *LC*.^[26, 28]

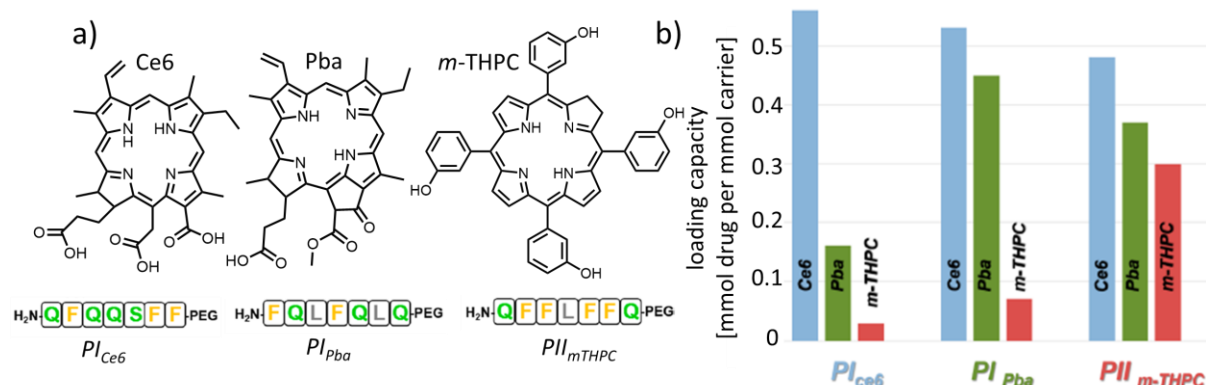


Figure 2.7: a) Chemical structure of photosensitizers Ce6, Pba, *m*-THPC as well as of peptide based drug carriers with the highest affinity for the latter (Q = glutamine; F = phenylalanine; S = serine; L = leucine); b) maximum *LC*s of the three different solubilizers. Figure modified with permission from ref[107].

To evaluate the contribution of amino acid residues at specific sequence positions to the overall *LC*, systematic residue point mutations (alanine (Ala) scan) were investigated.^[107] Again, hydrophobic and π - π stacking interactions were revealed as the main driving forces for solubilization, as replacement of a Phe residue with Ala strongly reduced *LC* (almost 100% decrease) for *m*-THPC, bearing easily accessible phenyl-rings. Although this sounds straightforward at first, replacing glutamine (Gln) or serine (Ser) residues with Ala caused a similar dramatic reduction in *LC*. The authors argued, that this points out the importance of H-bonds for solubilization. However, taking into account the impact of the various point mutations gives a rather random picture and casts doubt on conclusive structure-property relationships.

The combinatorial approach by Börner and coworkers gives first insights into the complexity and at first glance unpredictable nature of polymer-drug interactions. Nevertheless, also a targeted tuning of the polymer-drug compatibility by specific coordination interactions was realized in selected cases.

In 2018, Lv *et al.* prepared polymer micelles with ultrahigh drug loadings up to 50 wt.% of the chemotherapeutic agent doxorubicin (DOX).^[108] This was realized by specific, coordinative interactions between DOX and the polymeric drug carrier PEG-*b*-poly[(*N*-2-hydroxyethyl)-aspartamide] (PEG-PHEA), containing phenylboronic acid (PBA) moieties in the hydrophobic core (PBA was also used due to its sensitivity to reactive oxygen species (ROS) possibly selectively releasing DOX in cancer cells overproducing ROS) (Figure 2.8a,b). After interaction with DOX, a shift to high field (≈ 20 ppm) in the ^{11}B NMR spectra of PBA appeared due to the coordination of the nitrogen atom of DOX to PBA in deuterated dimethylformamide (DMF- d_7) (Figure 2.8c). After addition of deuterated water (D_2O), the shift remained, indicating aqueous stability of the coordination reaction.

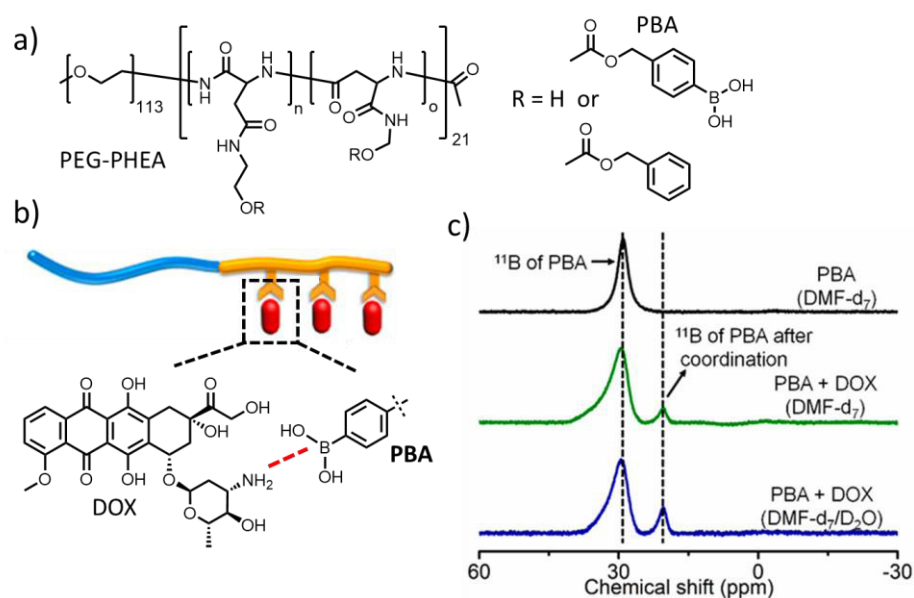


Figure 2.8: a) Chemical structure of the amphiphilic drug carrier PEG-PHEA comprising PBA moieties within the hydrophobic core to enable b) coordination reactions to DOX; c) ^{11}B -NMR spectra of PBA (black, DMF- d_7), PBA + DOX (green, DMF- d_7) and PBA + DOX (blue, DMF- d_7 + D_2O). Figure modified with permission from ref[108].

Whereas the PBA containing polymer enabled extremely high DOX loadings up to 49 wt.% (hydrodynamic diameters (D_h) < 50 nm; investigated by DLS), a polymer containing the same phenyl sidechains, however without boronic acid, achieved drug loadings of only 3.3 wt.% accompanied with the formation of micrometer-sized precipitates. It should be noted that the solubility of DOX is highly dependent on the pH, as a protonation of the primary amine at low pH strongly increases its solubility. However, the addition of hydrogen peroxide (H_2O_2) and the resulting decrease in pH accelerated DOX release from PBA containing micelles somehow suggesting the solubilization of non-protonated DOX.

Concerning the stoichiometry, a *LC* of 49 wt.% corresponds to a molar ratio of polymer/DOX ≈ 1.0 mmol / 18.4 mmol (composition of final polymer was not given; molar mass (M_w) of polymer was therefore calculated using M_w of a precursor polymer ($M_w = 8.4$ kg/mol)). Considering a high degree of substitution of 80% of PBA within the hydrophobic core, this corresponds to approx. one DOX molecule per PBA moiety. Considering the steric demand of rigid DOX, it is hard to imagine specific and well-defined 1:1 complexes between DOX and every PBA moiety of the repeating units of the hydrophobic core. Nevertheless, such high DOX loadings are remarkable, making it a promising DDS for cancer therapy, especially when taking into account the sustained DOX release under various conditions and pronounced cytotoxicity against HeLa cells.

π - π stacking has also been utilized to increase the *LC* of polymeric micelles for the non-water soluble, chemotherapeutic drugs PTX and docetaxel (DTX) ($\log P = 4.7$ and 4.1, respectively).^[109] Hennink and coworkers utilized polymeric drug carriers with a hydrophobic core of poly(*N*-(2-hydroxypropyl) methacrylamide) (HPMAm) comprising either naphthoyl (Nt, =HPMAm-Nt) or benzoyl (Bz, =HPMAm-Bz) residues and a hydrophilic PEG shell (Figure 2.9a). Critical micelle temperature (CMT) and CMC of the respective block copolymers decreased with increasing HPMAm-Bz or HPMAm-Nt content due to increased hydrophobic interactions and π - π stacking (Figure 2.9b; content of respective aromatic repeating units should be < 30 mol% to retain water solubility). In accordance with the latter observation, D_h (investigated by DLS) of empty micelles containing aromatic moieties was smaller than those of corresponding, non-aromatic polymers. The *LC* for PTX or DTX, both containing a substantial amount of aromatic moieties, strongly increased by the introduction of aromatic groups within the polymer side chains (Figure 2.9c). However, at constant PTX or DTX feed concentrations of 4 g/L, the *LC* slightly decreased while increasing the HPMAm-Nt content from 18 – 28 mol%. This was assigned to enhanced interactions between the hydrophobic blocks of the polymers, which would reduce the space available for drug-encapsulation. A similar decrease in *LC* with increasing hydrophobicity was already reported for cholesterol-modified polymers.^[110]

Maximum *LC* for DTX at varying DTX-feed concentrations (4, 5, 7 or 10 g/L) of polymers (10 g/L) containing 0% aromatic moieties, 24% HPMAm-Bz, or 18% HPMAm-Nt were 29.5 ± 0.5 , 33.3 ± 0.9 and 10.5 ± 0.2 wt.%, respectively.^[109] Important to note, these high *LC*s correspond to up to 3 molecules of DTX per aromatic moiety, again contradicting well defined, intermolecular π - π interactions between the naphthoyl or benzoyl moieties and DTX. Although the size of all drug-loaded micelles increased compared to the empty micelles ($D_h = 30$ -50 nm), this increase was strongly attenuated for the polymers containing aromatic moieties ($D_h = 60$ -80 nm) compared to the polymers without such ($D_h = 110$ nm) (Figure 2.9d).

The smaller size of the micelles carrying aromatic comonomers indicated that their cores were more strongly condensed due to π - π stacking and hydrophobic effects of the aromatic groups. The more condensed core also increased particle stability, as PTX was fully released after 240 h from the non-aromatic containing micelles, whereas the corresponding aromatic ones still contained approx. 50% payload (release studies were carried out under non-sink conditions to avoid limit of detection as well as destabilization of the micelles by passing the CMC). The π - π interactions within empty PEG-HPMAM-Nt micelles were investigated in more detail by ^1H solid-state NMR. The chemical shift of hydrogen atoms is strongly influenced by external electrons providing means to study packing of π -electron systems. Upon increasing temperature, the aromatic naphthoyl signals of the block copolymer broadened significantly together with an overall increase in effective molecular size. This is in accordance with an overall reduction in molecular mobility due to micelle formation which involves π - π stacking among aromatic moieties at higher temperatures. Unfortunately, the influence of incorporated PTX or DTX on the aromatic signals of the polymer was not further investigated.

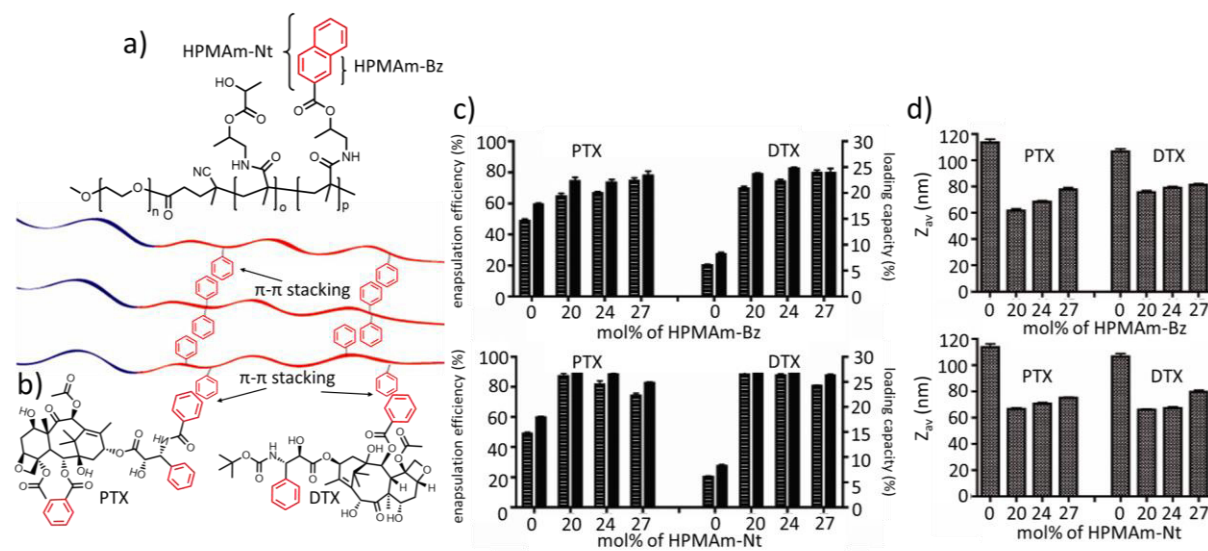


Figure 2.9: a) Chemical structure of the amphiphilic drug carrier PEG-HPMAM comprising either naphthoyl (Nt) or benzoyl (Bz) residues to b) enable π - π stacking with non-water soluble drugs PTX and DTX; c) encapsulation efficiency (striped bars) as well as LC (solid bars) in dependence of the Bz (top) or Nt (bottom) content at feed concentrations of $\rho(\text{polymer/drug}) = 9/4$ g/L as well as d) corresponding D_h , investigated by DLS. Figure modified with permission from ref[109].

Although minor inconsistencies occurred (decreasing LC with increasing Nt content; Figure 2.9c, bottom), the drug loading for PTX or DTX could be enhanced by the introduction of aromatic moieties in all cases. Although this sounds straightforward at first, most polymer-drug compatibilities are much harder to predict and rarely follow such patterns.

Other examples of improving intermolecular polymer-drug interactions through π - π stacking include the well-known PEG-*b*-poly(α,β -aspartic acid) (PEG-PASA) drug carriers designed by Kataoka and co-workers (NK911; currently evaluated in phase II clinical trial against metastatic pancreatic cancer).^[111] The hydrophobic PASA core was partially chemically modified with doxorubicin (DOX) and subsequently DOX was loaded physically. Apart from hydrophobic interactions, strong π - π stacking was most likely responsible for enhanced micellar stability resulting in a 29-fold increase in the area under the curve (AUC) in blood and a 3.4-fold increase in tumor disposition of PEG-PASA/DOX as compared to free DOX. Recently reported PTX-loaded micelles composed of PEG-*b*-poly(*N*-(2-benzoyloxypropyl) methacrylamide) showed a high stability and long circulation kinetics^[112] comparable to those of chemically cross-linked polymer micelles^[113], resulting in complete tumor regression in two different xenograft models (A431 and MDA-MB-231). Again, the long circulation in blood was attributed to π - π stacking between PTX and benzoyl-moieties in the polymer hydrophobic core.

Besides π - π stacking, also hydrogen-bonding has been utilized to increase intermolecular polymer-drug interactions. Although discussed in the context of solid dispersions^[114], the compatibility between polyvinylpyrrolidone (PVP), hydroxypropylmethyl cellulose (HPMCAS) or poly(acrylic acid) (PAA) with the poorly water-soluble (5.8 mg/L^[115]) drug nifedipine (NIF, Adalat®) investigated by Kothari *et al.* are highly relevant for drug-loaded micelles, as all three polymers are widely incorporated in amphiphilic, polymer-based drug carriers (Figure 2.10a).^[25] The molecular mobility in neat NIF and polymer/NIF solid dispersions was investigated by dielectric spectroscopy. As expected, the α -relaxation peak (= glass-transition relaxation) shifted to higher frequencies with increasing temperature, indicating an increased global mobility (*i.e.* shorter relaxation time) of the various NIF formulations during isothermal frequency experiments (Figure 2.10b). However, only in the case of PAA, rapid drug crystallization interfered with the detection of the α -relaxations at $T > 75$ °C. In contrast, PVP and HPMCAS prevented NIF crystallization, attributed to stronger hydrogen bonding between the polymers and the drug. Furthermore, at any given temperature and polymer concentration, the differences in molecular mobility of the various formulations were evident from the peak frequency of dielectric loss. In accordance with the previous observation, the dielectric loss peak in the PVP/NIF dispersions appeared at much lower frequency compared to the PAA/NIF dispersion, indicating a more pronounced lowering in molecular mobility within the former (Figure 2.10c). In line with the temperature dependent dielectric spectroscopy measurements, the vibration of the N-H group of NIF shifted to higher wavenumbers (FT-IR spectroscopy) with increasing temperatures, indicating a decrease in intermolecular polymer-NIF hydrogen bond strength.

Subtracting the NIF spectrum from that of the dispersions revealed new populations in PVP/NIF and HPMCAS/NIF solid dispersions (Figure 2.10d). The peak at lower wavenumber compared to neat NIF indicated stronger intermolecular polymer-NIF than intramolecular NIF-NIF hydrogen-bonding in the case of PVP. In contrast, the higher wavenumber in the HPMCAS/NIF dispersions indicated stronger intra- than intermolecular interactions. Similar effects were already observed in solid dispersions of felodipine, a structural analogue of NIF.^[116] Most interestingly, the subtracted spectrum of PAA/NIF suggested no intermolecular PAA-NIF hydrogen-bonding.^[25] In conclusion, the strength of hydrogen bonding was the same as derived from the relaxation times: PVP > HPMCAS > PAA. These observations were in accordance with the physical stability of the various NIF dispersions. PVP suppressed NIF recrystallization most effectively, whereas PAA was the least effective as observed by dynamic scanning calorimetry (DSC) measurements (Figure 2.10e for further insights into the role of thermodynamics and kinetics for crystallization from the amorphous state the reader is referred to the review by Bhugra *et al.*^[117]). A similar strong suppression of recrystallization was also observed for PVP/indomethacin^[118] as well as PVP/felodipine^[119] solid dispersions. Unfortunately, shelf-life at ambient conditions and maximum LC of the various NIF solid dispersions were not further investigated.

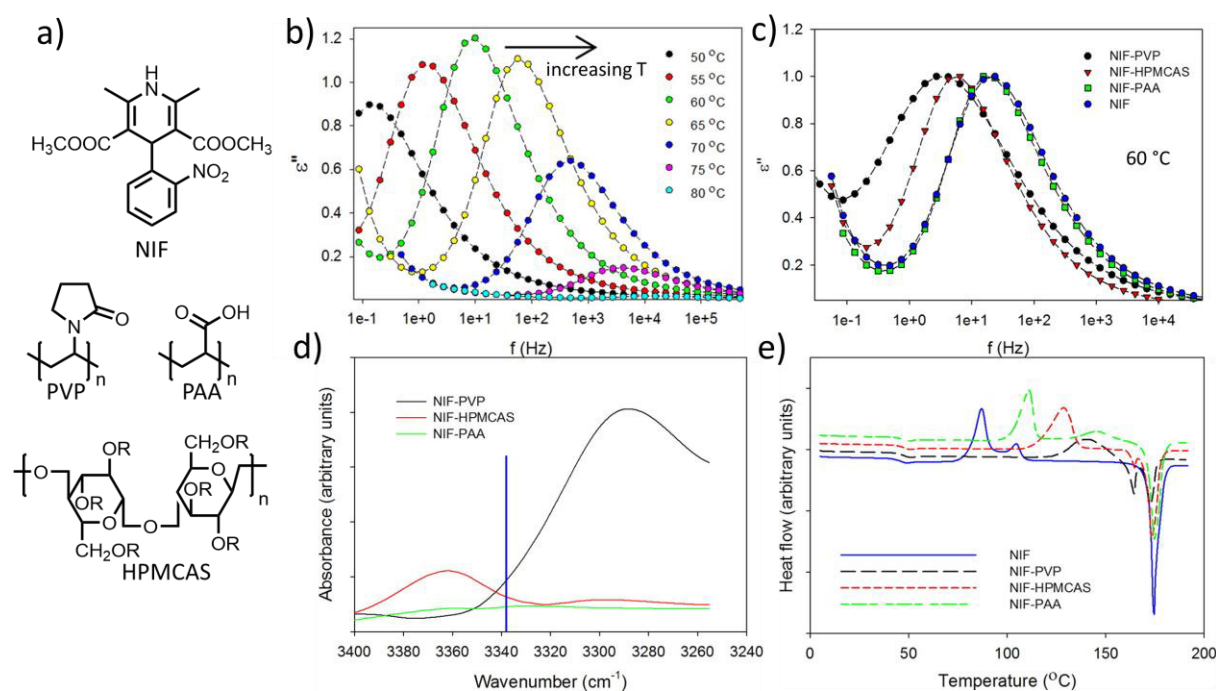


Figure 2.10: a) Chemical structure of non-water soluble drug NIF and the polymers PVP, PAA and HPMCAS (R = H, CH₃, CH₂CH(OH)CH₃, COCH₃, COCH₂CH₂COOH, CH₂CH(CH₃)OCOCH₃, CH₂CH(CH₃)OCOCH₂CH₂COOH) used to prepare solid dispersions; b) dielectric loss behavior of HPMCAS/NIF solid dispersion with increasing temperature (left to right); c) as well as of PVP/NIF (black), PAA/NIF (red), HPMCAS/NIF (green) or neat NIF (blue) at 60 °C. The loss curves were normalized to the maximum loss values; d) FT-IR spectra of polymer/NIF dispersions. The spectrum of neat NIF (maximum at 3342 cm⁻¹; blue line) was subtracted to identify new populations caused by specific polymer-NIF interactions; e) DSC heating curve of NIF and polymer/NIF solid dispersions. Figure modified with permission from ref[25].

However, that polymer-drug hydrogen bonding has indeed a large impact on the *LC* was shown by Lee *et. al.*^[120], using PEG-poly(lactic acid) (PEG-PLA) based block copolymers for the solubilization of hydrophobic papaverine (PAP). To investigate the influence of intermolecular hydrogen bonding, the hydrophobic PLA block was partially substituted with carboxylic acid (Figure 2.11a). Interestingly, the *LC* strongly increased with increasing carboxylic acid content (0% - 20 %) from approx. 4 wt.% up to 14.9 wt.% (Figure 2.11b). Due to the rigid and glassy state of the hydrophobic core investigated by ¹H-NMR spectroscopy (strongly reduced and broadened proton signals of PLA due to limited mobility caused by micellization; in contrast to unaffected signals corresponding to the hydrophilic PEG shell), the authors suggested that the carboxylic acid moieties are much likely non-ionized and the water content within the hydrophobic core is low. Having this in mind, hydrogen bonding between the acid moieties and PAP should occur. However, direct evidence on the existence of such intermolecular hydrogen-bonding was not found by spectroscopic means (not further discussed) which was attributed to the low amount of carboxylic acid moieties within the polymer. Furthermore, the non-ionization of the acid modified PEG-PLA is doubted, especially considering the pyridine base containing PAP. Nevertheless, strong intermolecular interactions were indirectly expressed by the prolonged drug release behavior of the acid modified polymers (Figure 2.11c). Whereas non-functionalized micelles released 90% PAP within 7 days, only 50% PAP were release at the same time from micelles functionalized with 19.5 mol.% acid moieties.

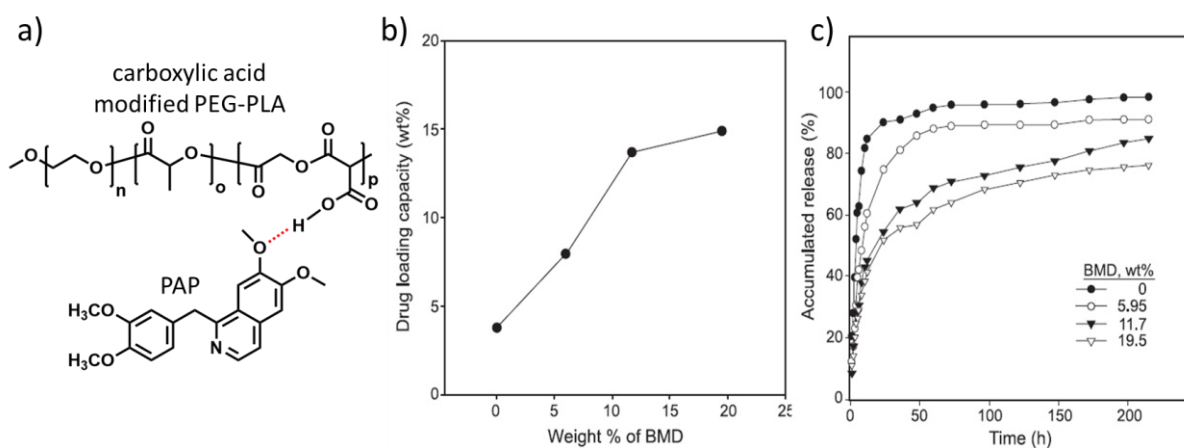


Figure 2.11: a) Intermolecular hydrogen bonding between carboxylic acid modified PEG-PLA and solubilized, hydrophobic PAP; b) *LC* of PEG-PLA micelles for PAP as well as c) PAP release profiles in phosphate buffered saline (PBS) in dependence of the degree of substitution with carboxylic acid. Figure modified with permission from ref[120].

In contrast to the discussed PEG-PLGA/PAP formulations, Yuan *et. al.* could identify distinct hydrogen bonding interactions in solid amorphous dispersions of non-water soluble indomethacin (IMC; water solubility: 0.937mg/L^[121]) and PVP or PVP-co-polyvinyl acetate (PVP-PVA) using ¹³C solid-state NMR spectroscopy (Figure 2.12a).^[122]

Amorphous solid dispersions of IMC were prepared by cryo-milling followed by *in situ* melt quenching at 170°C for 10 min directly inside the spinning NMR rotor. As expected, ^{13}C cross polarized magic angle spinning (CPMAS) spectra of crystalline IMC exhibited narrow peak shapes in contrast to the much broader peaks of amorphous IMC. Subsequently, amorphous IMC was ^{13}C isotopically labeled (5%) selectively at the carboxyl carbon atom to study hydrogen bonding interactions of amorphous indomethacin. After subtracting the unlabeled from the labelled spectrum, (while maintaining same signal intensity for aromatic and aliphatic carbon regions of both spectra), the signals corresponding to carboxyl acid carbons could be isolated. The spectrum of the carboxyl carbon contained two clear peaks, with a potential third peak in the center (Figure 2.12b). The downfield (high ppm) peak with the highest intensity was assigned to the cyclic dimer formed by hydrogen bonding between two carboxyl acid groups (due to the similarity to the same type of hydrogen bond found in crystalline IMC). The upfield (low ppm) peak was assigned to the carboxylic acid carbon hydrogen bonded to the amide carbonyl (same explanation). The middle, lowest intensity peak could be assigned to disordered chains, *i.e.* carboxylic acid chains of various length caused by the formation of rings larger than dimers. A fourth species, corresponding to free carboxylic acid (170.3 ppm) could be identified using solid amorphous dispersions of polystyrene (PS; forming no hydrogen bonds) and IMC at low IMC concentration. In contrast to neat IMC comprising four major carboxylic acid species, five or six carboxylic acid species were present in the PVP/IMC or PVP-PVA/IMC solid dispersions. The new species were assigned to IMC carboxylic acid hydrogen bonded to PVP or PVA carbonyl group. With increasing PVP content, the carboxylic acid dimers were gradually disrupted, whereas carboxylic acid-amide complexes gradually increased (Figure 2.12c). Important to note, due to their similar chemical shifts, IMC carboxylic acid species forming hydrogen bonds with either IMC amide, PVP, or PVP-PVA were treated as one peak in the deconvolution. Although the presence of both polymers strongly interfered with IMC intramolecular hydrogen bonding, the hydrogen bond accepting capability of PVP-PVA was lower than for PVP, as slightly less carboxylic acid – amide complexes were formed in the former (Figure 2.12d). This suggests that PVP-PVA is a weaker hydrogen bond acceptor than PVP.

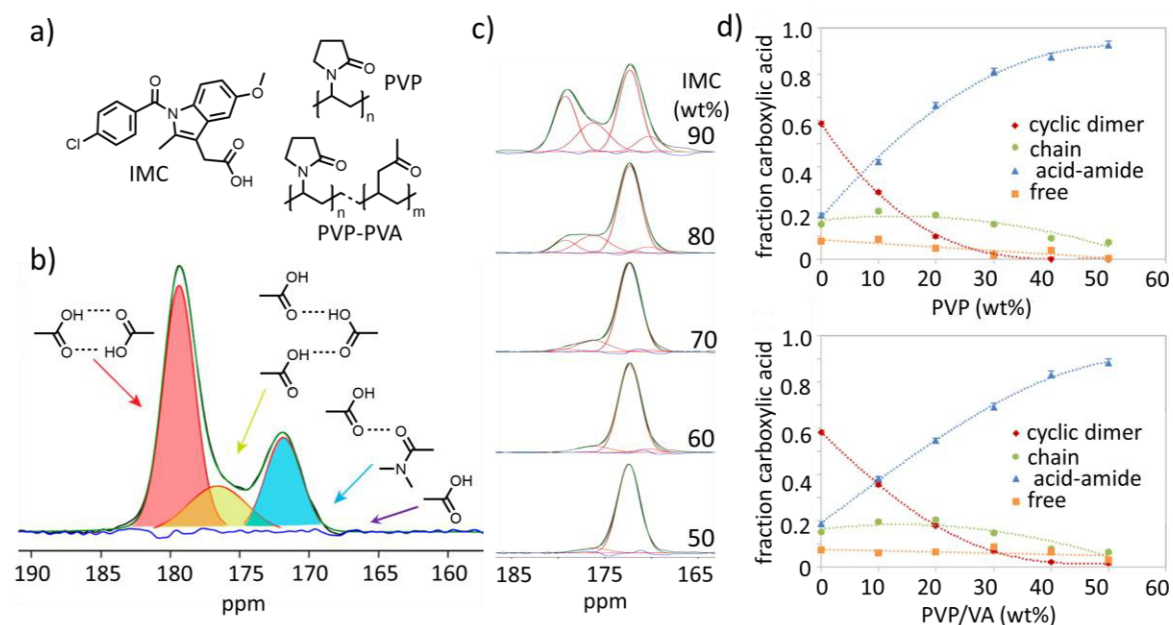


Figure 2.12: a) Chemical structure of non-water soluble drug IMC as well as PVP and PVP-PVA used to prepare solid amorphous dispersions; b) CPMAS ^{13}C NMR spectrum of the carboxylic acid carbon of amorphous IMC. The experimental spectrum is shown in black, the fitting of the individual species is highlighted in red (dimer), green (carboxylic acid chains of various lengths) and blue (carboxylic acid – amide dimer). Occurrence of peak corresponding to free acid is implied in purple. Sum of the species contributions (green spectrum) and residual difference between experimental and fitted peaks (blue spectrum) is given; c) CPMAS ^{13}C spectrum of IMC carboxylic acid carbon in PVP/IMC amorphous solid dispersions with decreasing IMC content (90% - 50%; top to bottom). Color code is same as for b); d) fraction of IMC carboxylic acid participating in various hydrogen bonding interactions in the amorphous solid dispersions with PVP (top) or PVP-PVA (bottom) as a function of polymer concentration. Figure modified with permission from ref[122].

For further discussion about the use of solid-state NMR to identify specific polymer-drug interactions in solid amorphous dispersions of acetaminophen^[123], NIF^[124], nicotinamide^[125], lapatinib^[126], or clofazimine^[127], the reader is referred to given literature.

Apart from specific polymer-drug interactions, solid state NMR can also be used to get insights into the morphology of drug-loaded micelles. Very recently, Callari *et al.* investigated the effect of drug loading on aggregate morphology and internal structure formation of drug-loaded micelles.^[128] The drug-carrier was a block copolymer comprised of a hydrophilic poly fructose shell and a poly(methacrylic acid) (PMAA) core incorporating various amounts of a 1,10 phenanthroline platinum complex (Phen-Pt). The PMAA block provided anchoring points for the complexation of Phen-Pt (Figure 2.13a). At high Phen-Pt loading (50 molecules Phen-Pt per polymer chain), Pt homogeneously distributed within the core, whereas at low loading (7 molecules Phen-Pt per polymer chain), an inner core with a high Pt-concentration surrounded by a region of lower Pt-density occurred (Figure 2.13b). Interestingly, a two-fold higher cellular uptake in breast cancer cells MDA-MB-231 as well as lung cancer cells A594 was observed for low-loaded micelles by flow cytometry and laser scanning confocal microscopy (Figure 2.13c).

This was attributed to an increased interaction of the hydrophilic, fructose-based shell with the fructose receptor GLUT5 associated in the cell membrane. Solid-state NMR experiments were conducted to support this hypothesis. Line-broadening of ^{13}C NMR signals of Phen-Pt after encapsulation showed that the drug was incorporated in amorphous state. Furthermore, 2D $^{13}\text{C}(^1\text{H})$ heteronuclear correlation (HETCOR) experiments revealed a through-space correlation peak from the methyl protons of the PMAA backbone with the aromatic carbons of Phen-Pt (Figure 2.13e). No such correlation peak was found for OCH/COH protons of the hydrophilic shell and Phen-Pt carbon, implying a nanometer scale separation between Phen-Pt and the fructose block in high-loaded micelles. For low-loaded micelles at short mixing time (3 ms for ^1H magnetization exchange), a high signal intensity occurred for the cross-peak from Phen-Pt aromatic ^1H to fructose, water and alkyl ^1H species shown in the horizontal slice extracted from the 2D ^1H - ^1H exchange spectrum (Figure 2.13d, left). Therefore, Phen-Pt seemed to be molecularly dispersed within the polymeric matrix, resulting in a close spatial proximity to the polymer. The cross peak between aromatic Phen-Pt and H_2O was assigned to a zone of intermediate hydrophobicity in between the hydrophobic and hydrophilic regions in which water occurred in sub-nanometer proximity to Phen-Pt (Figure 2.13f, right). This correlated well to the low-density Pt regions observed by TEM (Figure 2.13b, right). Interestingly and in contrast to high-drug loading, the aromatic Phen-Pt ^1H signal did not equilibrate with polymer ^1H signal (even after extended mixing times), attributed to regions within the micellar assembly that are completely free of Phen-Pt at length scales > 30 nm. This was attributed to the outer, hydrophilic corona with high molecular mobility. Furthermore, a fraction of the fructose moieties was also trapped within the hydrophobic core of the high-loaded micelles, as shown by the appearance of cross peaks to both, the polymer backbone and the sugar sidechain at similar time scales.

In contrast, in high-loaded micelles, virtually no cross-peaks to the polymer backbone were found (Figure 2.13d, right), which was assigned to the formation of conjugated Phen-Pt aggregates, reducing the spatial proximity to the polymer backbone (Figure 2.13f, left). Therefore, the higher cellular uptake of low-loaded micelles was assigned to a better interaction of highly mobile fructose moieties in the corona and the GLUT 5 transporters in the cell membrane. Additionally, the slower drug release of highly-loaded micelles was attributed to the formation of segregated Phen-Pt aggregates. However, it should be mentioned that the drug release experiments were only performed once. By including the standard deviation (SD), the rather small difference in release rate might have been negligible, wherefore the claimed higher stability of the high-loaded micelles should be regarded with care.

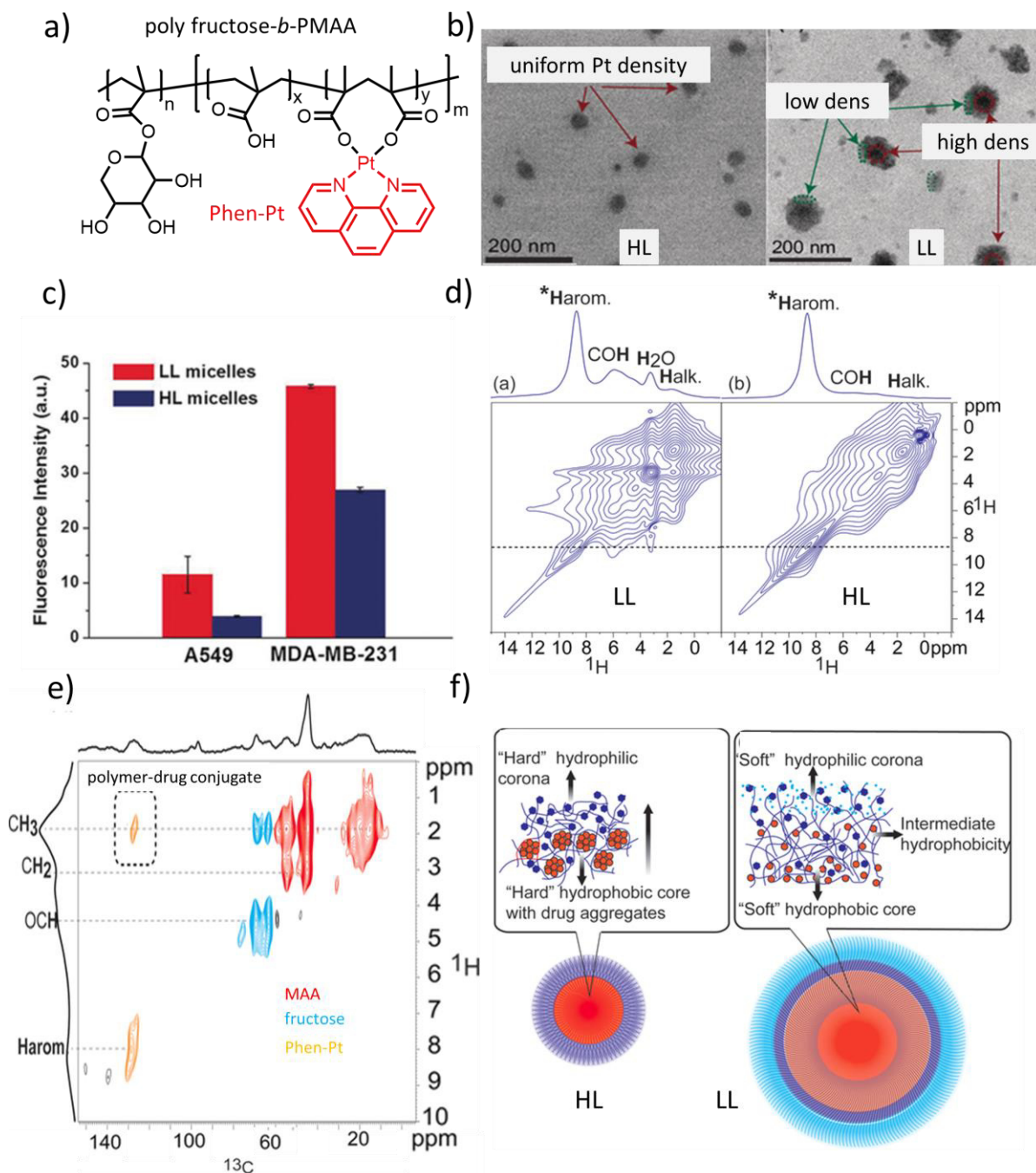


Figure 2.13: a) Formation of low-loaded (LL; Pt/COOH = 0.2/1; $\gamma = 7$) and high-loaded (HL; Pt/COOH = 1/1; $\gamma = 50$) polymer-drug conjugates by coordination of Pt-based drug Phen-Pt to polymeric drug carrier poly fructose-*b*-PMAA; b) TEM images of high-loaded (left) and low-loaded (right) micelles show areas where Pt is located (non-Pt containing corona is non-detectable); c) cellular uptake of Phen-Pt loaded micelles quantified by flow cytometry; d) ultrafast ^1H 2D exchange NMR spectra (3 ms mixing time) of low-loaded (left) and high-loaded (right) micelles. The 1D spectra plotted on top are extracted at 8.5 ppm as indicated by the dashed lines; e) 2D $^{13}\text{C}(^1\text{H})$ HETCOR of high-loaded micelles. Marked signal (dashed square) corresponds to correlation peak between aromatic drug and methyl protons of the polymer backbone confirming the conjugation of Phen-Pt to the polymer. The correlation signals in red, blue, and orange correspond to MAA, fructose, and Phen-Pt, respectively; f) structure of HL (left) and LL (right) micelles. Small orange circles represent individual Pt-Phen molecules, blue lines represent the hydrophilic and red lines the hydrophobic areas of the polymer, dark blue hexagons represent fructose moieties, and light blue circles represent water molecules. Figure modified with permission from ref[128].

Also, the discussed difference in cytotoxicity against MDA-MB-231 as well as A549 was not markedly pronounced. Again, no SD was included, although experiments were performed in triplicates (SD is not visible in the plotted data and it is expected that SD within such *in vitro* study should be larger than the given data points). Therefore, the claimed difference in cytotoxicity based on inhibitory concentrations (IC_{50}) of 11.2 μ M and 11.8 μ M (MDA-MB-231) as well as 5.9 μ M and 2.8 μ M (A549) should be regarded critically, as such minor differences might be due to different amounts of formulated-drug actually added as well as other experimental deviations.

Nevertheless, the different morphologies of Phen-Pt loaded poly fructose-*b*-PMAA micelles demonstrate (i) the effect of drug loading on micellar morphology as well as (ii) the impact of such morphological changes on biological properties such as cellular uptake. Furthermore, the varying interaction of the hydrophilic poly fructose block and encapsulated Phen-Pt in dependence of the drug loading is in accordance with the impact of even the end group of the hydrophilic segment on solubilization properties as observed for poly(*N*-isopropylacrylamide) based micelles.^[27]

Further strategies to increase intermolecular interactions between polymeric drug carrier and (physically) incorporated, hydrophobic drugs are comprehensively reviewed by Hennink and coworkers.^[129] However, not only polymer-drug interactions determine shape and properties of micelles, but also drug-drug interactions in co-formulations can strongly influence particle properties.

2.5 Impact of Drug-Drug Interactions on Drug Loading

Combination drug therapy, *i.e.* co-administration of two or more drugs, is standard clinical practice in the treatment of various disease.^[130] These multidrug regimens are usually designed to achieve therapeutic synergy and therefore a greater medical effect than the sum of each drug alone, *e.g.* by suppressing drug-resistances.^[131] However, the therapeutic efficacy of multiple drug administration is highly susceptible to the concentration and ratios of the respective drugs which can result in synergistic or antagonistic effects of the same drug combinations.^[132] Unfortunately, the translation of synergistic combinations found in conventional *in vitro* cell studies to suitable *in vivo* concentrations is often strongly hampered. This is among others due to different pharmacokinetics and pharmacodynamics of the respective drugs in systemic circulation strongly affecting their concentration at the site of action. This can be particularly challenging for micellar based co-formulations of multiple drugs^[133, 134] due to altered drug release profiles of co-formulated drugs compared to single-formulations as demonstrated in POx based co-formulations of bortezomib and 17-allylamino-17-demethoxygeldanamycin (17-AAG).^[135]

Nevertheless micellar nanoformulations of multiple drugs in a single vehicle can increase *in vivo* anti-tumor efficacy compared to the treatment with both single formulations at same drug concentrations as observed for POx based co-formulations of PTX^[20] or etoposide^[21] and an alkylated cisplatin prodrug.

Although specific properties such as the drug release kinetics of drugs simultaneously solubilized within the hydrophobic core of polymeric micelles are commonly assessed, an understanding about the interactions between both drugs is most often neglected. However, this is of major interest, as the compatibility of both drugs dictates crucial properties such as the *LC*. Very recently, Zhang *et al.* investigated the interaction between poorly water soluble quinone oxidoreductase 1 inhibitors β -lapachone (LPC; water solubility = 38 mg/L) and tanshinone IIA (T2A; water solubility = 0.018 mg/L) co-solubilized with PTX in PEG-PLA micelles (Figure 2.14a).^[136] At $\rho(\text{PEG-PLA}) = 30$ g/L, neither LPC nor T2A could be solubilized at 2 g/L ($LC_{\text{theor}} = 6.25$ wt.%). Interestingly, when combined with 6 g/L PTX ($LC_{\text{theor}}(\text{drug \& PTX}) = 5.3 \& 15.8$ wt.%), the LPC/PTX formulation appeared completely clear, exhibiting micelles with a monodisperse size distribution of $D_h = 60$ -70 nm. In contrast, major precipitation occurred in the T2A/PTX formulation, demonstrating that PTX had little effect on inhibiting the crystallization of T2A. Therefore, the authors concluded that the critical parameters causing these different stabilities are intermolecular drug-drug rather than PLA-drug interactions. However, this assumption should be regarded critically, as illustrated in the discussed interaction of incorporated Phen-Pt with both blocks of a glycopolymer consisting of a hydrophilic poly fructose shell and a PMMA block at low loading (Figure 2.13f).^[128]

Dissolving LPC/PTX or T2A/PTX at 50/50 w/w in methanol and subsequently dispersing the respective solutions in PBS caused different profiles of supersaturation. Whereas the presence of PTX significantly increased the supersaturation of LPC in PBS (supersaturation ratio $S = [\text{drug}_{w/PTX}]/[\text{drug}_{w/o PTX}]$), no detectable supersaturation occurred in the case of T2A/PTX (Figure 2.14b). Stronger intermolecular interactions in LPC/PTX were further apparent by the absence of recrystallization in solid amorphous dispersions of LPC/PTX in contrast to T2A/PTX after 3 months storage (Figure 2.14c). For further physicochemical characterizations of the LPC/PTX formulations, the reader is referred to ref[137]. MD simulations were utilized to get insights into the distribution density of LPC or T2A molecules around a central PTX molecule.^[136] LPC was more evenly distributed around PTX, whereas T2A self-aggregated into a lamellar structure (Figure 2.14d). This again supports the hypothesis of stronger hetero-intermolecular LPC/PTX than T2A/PTX interactions. Direct atomic contact simulations suggested that LPC favorably formed stacking interactions with the benzyl groups of PTX, whereas the hydrophilic part of PTX was still exposed to the solvent (polymer) facilitating aqueous solubility and therefore inhibiting precipitation

(Figure 2.14e). In contrast, no such specific hetero-intermolecular interactions were formed in the case of T2A/PTX, resulting in a more homogeneous distribution of T2A aggregates around PTX interfering with a sufficient solvation of PTX eventually causing precipitation.

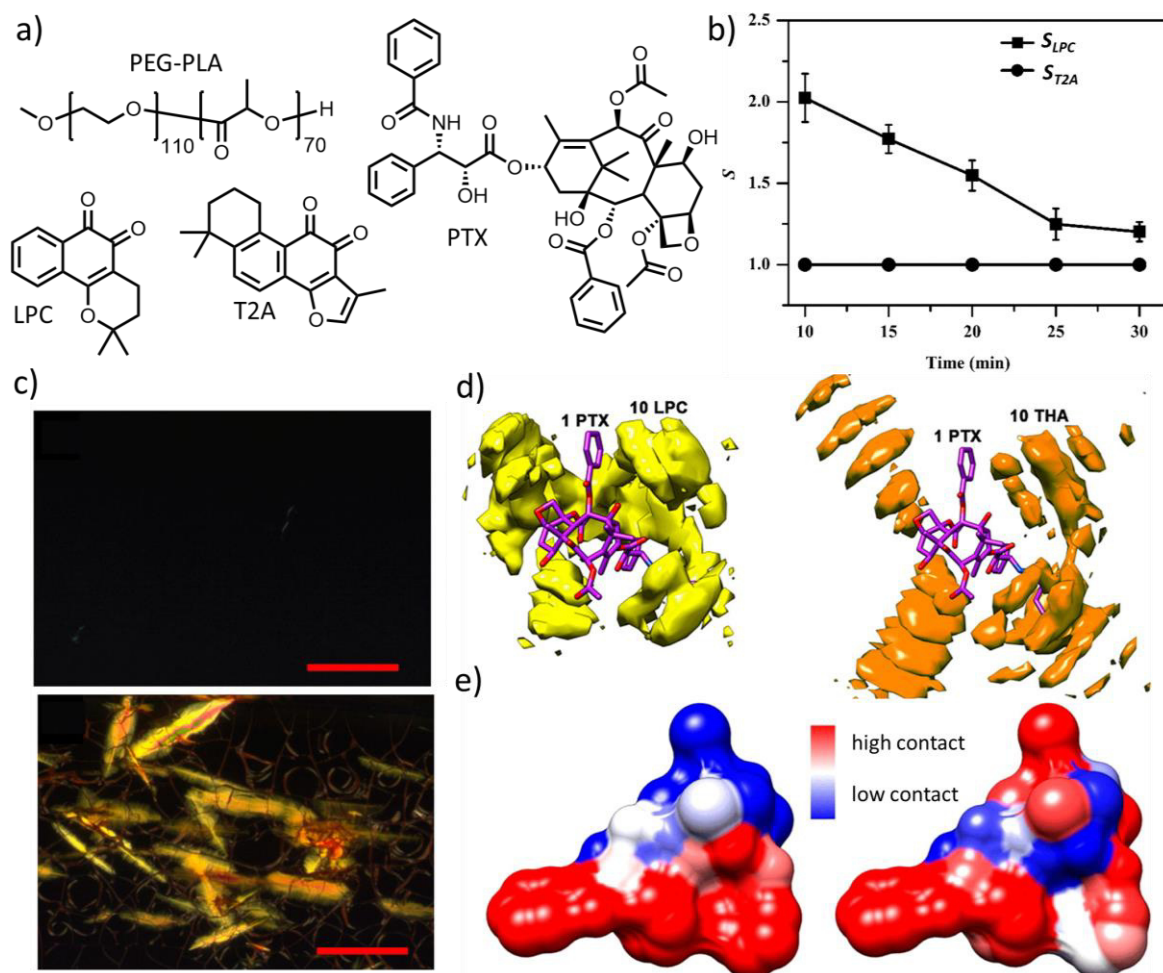


Figure 2.14: a) Chemical structure of hydrophobic drugs LPC, T2A and PTX either single- or co-formulated with polymeric micelles of PEG-PLA; b) supersaturation kinetics of LPC and T2A in the presence of PTX; c) recrystallization of spin-coated films of LPC/PTX (top) or T2A/PTX (bottom) after three months storage observed by polarized optical microscopy; d) density distributions (MD simulations) of 10 molecules of LPC (left) or T2A (right) arranged around a central PTX molecule (density cutoff: $0.0004/\text{\AA}^3$); e) averaged atomic contact of each PTX atom with 10 molecules of LPC (left) or T2A (right) projected on the surface of a PTX molecule with high (red) or low (blue) degree of contact. Figure modified with permission from ref[136].

In contrast and somehow surprising, Kwon and coworkers observed simple additivity of the *LC* when solubilizing the hydrophobic drugs PTX, 17-AAG and rapamycin (RAP; water solubility = $2.6\text{ mg/L}^{[138]}$) in polymeric micelles of PEG-PLA (Figure 2.15a).^[139] However, only a single combination of drug-feed concentrations of PEG-PLA = 30, PTX = 4, 17-AAG = 4, and RAP = 3 g/L was investigated. Nevertheless, the aqueous solubility of PTX, 17-AAG, and RAP in the 3-in-1 PEG-PLA micelles was increased 10^4 -, 700-, and 80-fold, respectively (similar increase in the case of double-loaded micelles).

Interestingly, the size of the respective micelles was more or less unaffected by the kind of incorporated drug(s) with $D_h = 38.8 - 43.8$ nm and narrow polydispersity indices (PDI) < 0.2 . Only in the PTX single formulation, major precipitation occurred after 24 h storage at 25 °C ($LC_{0h} = 11.8$ wt.%; $LC_{24h} = 1.9$ wt.%). In contrast, the triple-loaded system retained 97.9, 96.7, and 97.8 % of initially solubilized PTX, 17-AAG, and RAP in the same time interval.

Apart from that, the drug release kinetics of the single drugs in the 3-in-1 system (Figure 2.15c) were comparable to that of the respective single-formulations (except for PTX, exhibiting fast precipitation in the single formulation; Figure 2.15b). This is somehow surprising, considering pronounced hetero-intermolecular drug-drug interactions elucidated in the prevention of PTX precipitation. Similar drug releases of single- and triple-loaded PEG-PLA micelles have also been observed for PTX, 17-AAG, and etoposide.^[140]

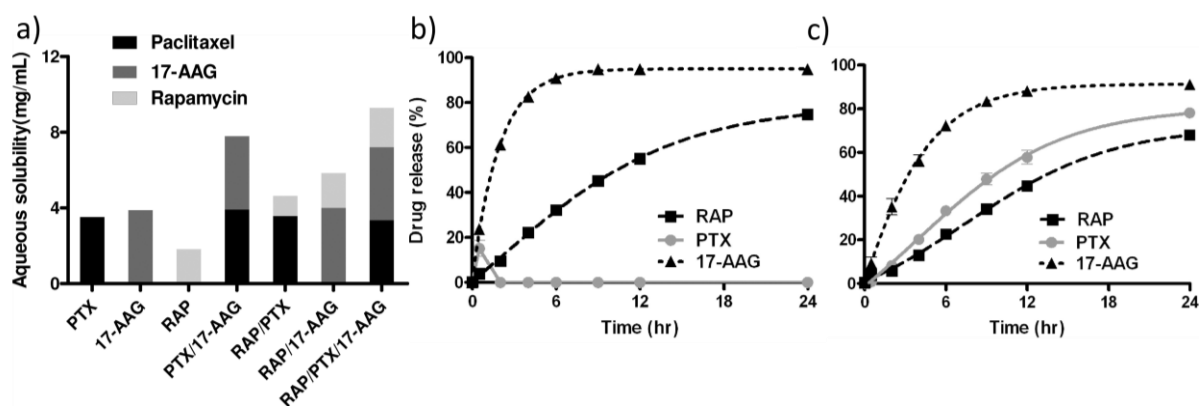


Figure 2.15: a) Aqueous solubility of PTX, 17-AAG and RAP as single-, double-, or triple-loaded PEG-PLA micelles ($n = 3$, mean); *in vitro* drug release profiles of b) single-loaded or c) triple-loaded micelles ($n = 4$, mean). Figure reprinted with permission from ref[139].

The given examples demonstrate the influence of polymer-drug and drug-drug interactions on micellar properties such as size, morphology, LC , stability, cellular uptake and as a consequence thereof their clinical relevance. Although a plethora of drug delivery systems can be found in the literature, it is of great importance to thoroughly characterize the respective formulations to avoid e.g. unnecessary animal studies and to obtain reliable and reproducible structure-property relationships which can be applied for further optimization. Unfortunately, a proper characterization of polymer-based nanoformulations is generally associated with a lot of effort due to the necessity of various characterization techniques, already starting with the characterization of the polymeric drug carrier itself. Therefore, it would be highly beneficial if properties such as the LC could be predicted to a certain extent to exclude non-compatible polymer-drug combinations beforehand.

2.6 Prediction of Polymer-Drug Compatibility

Allen and coworkers tried to predict physicochemical properties of polymer-based formulations of the water insoluble, anticancer agent ellipticine (ELP; water solubility = 0.153 mg/L) using total and partial solubility parameters.^[101] The total solubility parameter δ developed by Hildebrand^[141] provides a numerical estimate of the degree of interaction between materials. Materials with similar δ values are likely to be miscible. It is based on a molecule's cohesive energy density, which needs to be exceeded while vaporizing. The determination of δ of a certain molecule is based on a group contribution method (GCM), *i.e.* each group/moiety within a molecule adds a certain contribution to the final parameter.

However, the predictive power of the Hildebrand solubility parameters is limited to nonpolar and slightly polar systems such as hydrocarbons without hydrogen bonding. Based on this, Hansen developed the more sophisticated three-dimensional partial solubility parameters (Hansen solubility parameters, HSP^[142]), which divide δ into three different kinds of interactions between solvent and solute:

$$\delta_T = \sqrt{\delta_D^2 + \delta_P^2 + \delta_H^2} \quad (2)$$

where δ_D , δ_P and δ_H comprise contributions from intermolecular van-der-Waals forces, dipole-dipole interactions and hydrogen bonding, respectively.

Under consideration of the volume fractions of drug and polymer, the enthalpy of mixing ΔH_M can be calculated.^[101] A lower ΔH_M and therefore higher compatibility of PCL/ELP than PLA/ELP was derived from HSPs (Figure 2.16a).^[101] No obvious shifts in any peaks corresponding to functional groups capable of hydrogen bonding occurred in the FTIR spectra of the physical mixtures of the respective polymers and ELP. In contrast, in the spectra of formulated polymer-ELP films, slight shifts in characteristic peaks occurred, suggesting specific polymer-drug interactions (spectra were discussed, however not shown). Micellar ELP formulations with block copolymers comprising PCL (PEG₁₁₃-*b*-PCL₃₅) or PLA (PEG₁₁₃-*b*-PLA₆₀) as hydrophobic core were prepared by dry down and dialysis method. For both methods, the PCL based formulations exhibited much higher loading efficiencies LE (equation 3) at all investigated polymer/ELP feed concentrations (Figure 2.16b).

$$LE = \frac{m_{drug}}{m_{drug,added}} \quad \begin{array}{l} m_{drug} = \text{mass of solubilized drug} \\ m_{drug,added} = \text{mass of drug initially added to formulation} \end{array} \quad (3)$$

Therefore, the compatibility between polymer and drug predicted with ΔH_M correlated well with the obtained LE s.

Furthermore, drug release kinetics of both formulations differed significantly from each other. Whereas 100% ELP was released from the PLA-based micelles after 36 h (drug/polymer = 1/10 w/w; $R_h = 76$ nm) or 72 h (1/4 w/w), the PCL based micelles only released 30% EPL within 6 days ($R_h = 20$ nm for drug/polymer = 1/10 w/w), again suggesting stronger PCL/ELP than PLA/ELP intermolecular interactions (Figure 2.16c).

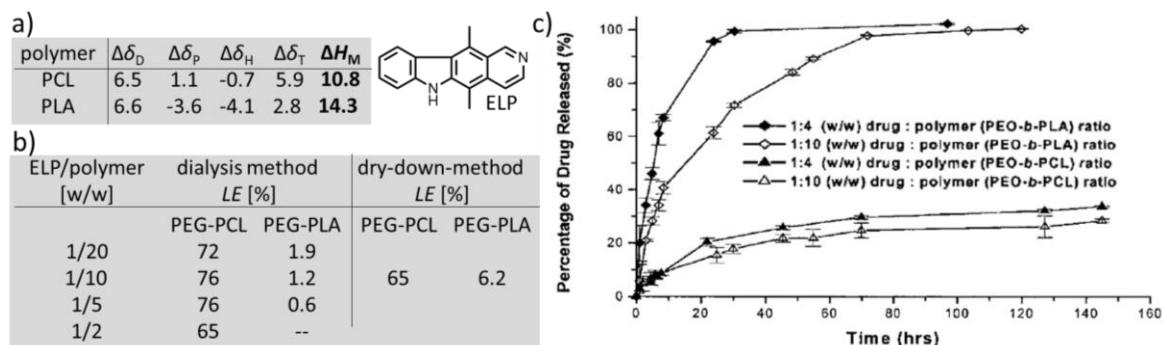


Figure 2.16: a) Difference between total δ_T and partial solubility parameters δ_D , δ_P , δ_H and enthalpy of mixing ΔH_M of ELP and PCL or PLA; b) LE of PEG-PCL and PEG-PLA based ELP formulations prepared by dialysis or dry-down-method at $\rho(\text{polymer}) = 10$ g/L; c) drug release profile of PEG-PLA/ELP (top two graphs) or PEG-PCL/ELP (bottom two graphs). Tables and figure modified with permission from ref[101].

In a more recent study, the same research group predicted the solubility of DTX in five different, small molecule excipients using computational methods (Figure 2.17a).^[143] The solubility parameters δ of DTX and excipients were derived semi-empirically by GCM and C²-Synthia model from Cerius² software as well as by molecular dynamics (MD) simulations. MD takes into account the molecular motions (e.g. simple vibrations, bond stretching and angle bending) that occur within a system. Furthermore, the COMPASS (condensed-phase optimized molecular potentials for atomistic simulations studies) force-field was used to calculate Coulombic and attractive van-der-Waals interactions. For the COMPASS force field, the total energy E_{total} of a system is represented by the sum of the valence interactions, non-bonding interactions and the cross-coupling term. The difference of E_{total} of a molecule in the vacuum state and the amorphous state is directly correlated to a molecule's heat of vaporizing. As discussed above, the Hildebrand solubility parameter δ can be directly derived from the latter. The square root of δ is defined as the cohesive energy density (CED) of a molecule which was employed to calculate the energy of mixing ΔE_{mix} of pure DTX, pure excipient as well as DTX-excipient mixtures. Furthermore, ΔE_{mix} is directly proportional to the Flory-Huggins interaction parameter χ_{FH} which in turn can be used to calculate the Gibbs' free energy of mixing ΔG_{mix} . For a solution to be miscible, ΔG_{mix} needs to be negative. To give a perspective, the MD simulations performed on a supercomputer took an average processing time of approx. four months for simulation of drug, excipient or drug/excipient mixtures. The general methodology for MD simulations includes two stages: equilibration and production (Figure 2.17b,c).

The experimentally determined solubility of DTX in various excipients ranged from 0.4 to 108 g/L with the solubility being highest in tributyrin (Figure 2.17a). According to the authors, the high solubility of DTX in various triglycerides may be correlated to their potential to engage in hydrogen bonding, as the number of carbonyl groups available to form hydrogen bonds with DTX was highest for tributyrin. For each DTX-excipient pair, the difference between δ_{DTX} and δ_{exc} obtained from GCM ($\Delta\delta_{\text{GCM}}$), C²-Synthia module ($\Delta\delta_{\text{Syn}}$), and MD ($\Delta\delta_{\text{MD}}$) was calculated. As discussed previously, the lower $\Delta\delta$, the higher the solubility of DTX in the respective excipient. Calculations using the GCM and C²-Synthia module accurately predicted the relative degree of solubility of DTX in the triglycerides. However, the predicted solubility of DTX in vitamin E and β -caryophyllene disagreed with experimental results. In contrast, MD simulations correctly predicted the order of solubility of DTX in all five excipients (tributyrin > tricaproin > vitamin E > tricaprylin > β -caryophyllene). The MD method accounts for the interactions between atoms (*i.e.* hydrogen-bonding) within a periodic boundary condition and the many conformations of the compounds. In contrast, GCM and C²-Synthia module only consider contributions from the functional groups of a single molecule. Nevertheless, GCM and C²-Synthia module enabled a fast and straightforward prediction of δ of excipients which were similar in structure (tributyrin, tricaproin, tricaprylin). MD simulations further demonstrated that the χ_{FH} values of excipient/DTX mixtures increased with increasing volume fraction of DTX (ϕ_{DTX}). This corresponds to decreasing interactions between DTX and excipient with increasing ϕ_{DTX} (Figure 2.17d). Interestingly, χ_{FH} of all DTX/ β -caryophyllene mixtures were greater than 0.5, indicating complete insolubility of DTX in these mixtures coinciding with the experimentally determined low solubility of this binary mixture. Most interesting, the values of ϕ_{DTX} at $\chi_{\text{FH}} = 0.5$ (highest reliable compatibility) could be utilized to calculate the actual solubility of DTX in each excipient. The solubilities obtained for DTX in tributyrin, tricaproin or vitamin E were within 2 – 6% deviation of the experimental solubilities. However, the predicted solubility in tricaprylin was approx. 15% too high (Figure 2.17a).

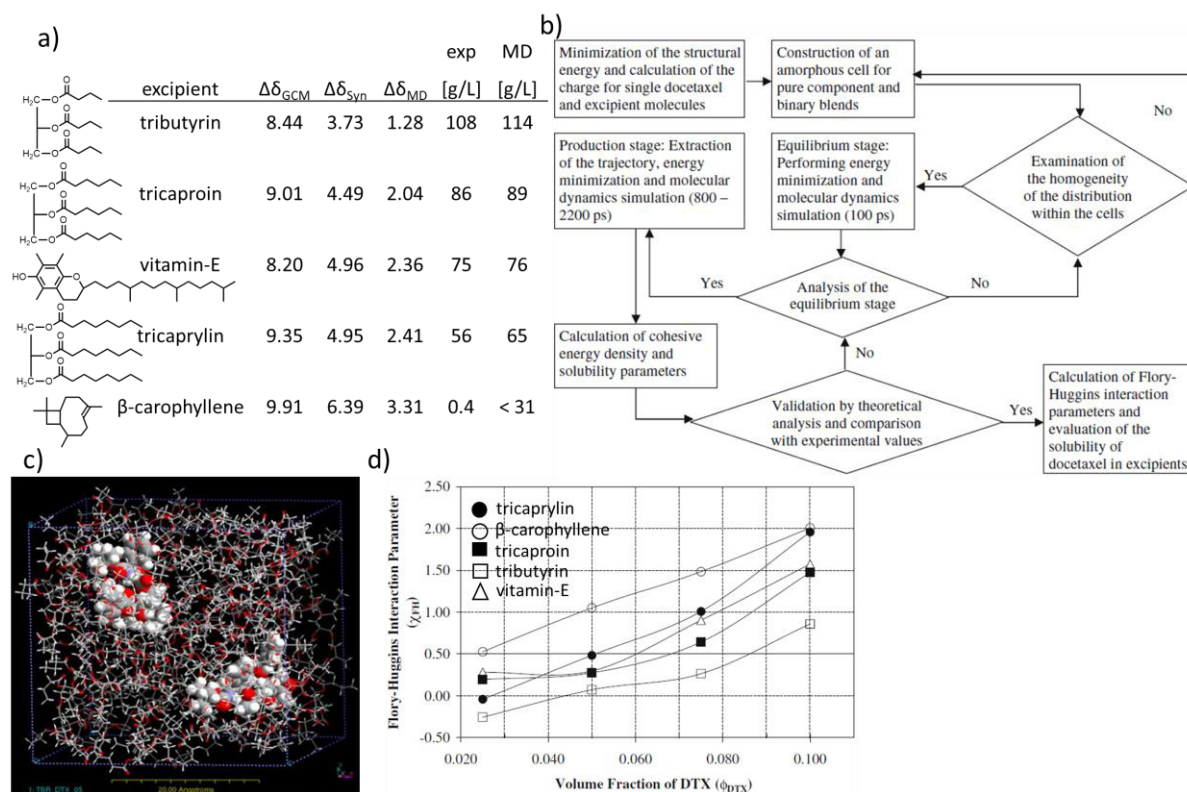


Figure 2.17: a) Difference between Hildebrand solubility parameter δ of DTX and various excipients ($\Delta\delta$ expressed in $(J/cm^3)^{0.5}$). The calculated values of δ were obtained by GCM ($\Delta\delta_{GCM}$), C²-Synthia module ($\Delta\delta_{Syn}$) or MD simulation ($\Delta\delta_{MD}$). Experimentally determined and MD simulated solubilities of DTX in the different excipients at 25 °C are given. The simulated solubility was derived from the volume fraction of DTX ϕ_{DTX} at a Flory-Huggins interaction parameter χ_{FH} of 0.5 (shown in (d)); b) flowchart of the approach used for MD simulations of the pure and binary mixed systems of DTX and excipients; c) amorphous cell containing 2 DTX (space-filling) and 86 tributyrin (stick) molecules; d) χ_{FH} for the binary mixtures of DTX and the different excipients in dependence of ϕ_{DTX} . Table and figures modified with permission from ref[143].

In a similar approach, Möller and coworkers predicted the solubility of the hydrophobic drugs cyclosporin A (CsA, water solubility = 12 mg/L), griseofulvin (GF, 21.2 mg/L), ketoconazole (KETO, 17.0 mg/L) and quercetin dihydrate (QUER dihydrate, 59.9 mg/L) in an amphiphilic diblock copolymer comprising a hydrophilic PEG shell and a hexyl-substituted PLA core (PEG-hexPLA) (Figure 2.18a).^[102] However, in contrast to the approach of Allen and coworkers^[143], the whole diblock copolymer and not only the hydrophobic block was considered for MD simulation of the Flory-Huggins interaction parameter χ_{FH} . Micellization is commonly described as a very uniform process, in which all lipophilic parts of the polymer chains compose the interior of the micelle, while the hydrophilic portions form the micellar surface. However, in the process of micellization, multiple nucleation spots should be present in solution due to the rapid tendency of the flexible polymer to shield the lipophilic zones with PEG chains. These multiple aggregates would aggregate further, eventually forming the whole micelle. Interestingly, the applied simulation accounted for this situation, resulting in a far from uniform structure of the micellar core, exhibiting crowded and compacted ravel of polymer chains and drug molecules.

For further insights into the highly complex dynamics of micellization, the reader is referred to the work of Mohs and coworkers, investigating the time-dependent self-assembly of hydrophobically modified hyaluronic acids^[144] incorporating different kinds of non-water soluble, fluorescent dyes.^[145]

Experimental solubility of the respective drugs in PEG-hexPLA was determined by cosolvent evaporation method (Figure 2.18b).^[102] Whereas the solubility of CsA, GF and KETO increased significantly by formulation with PEG-hexPLA, the solubility of QUER dihydrate remained nearly the same. Subsequently, MD simulations were run using AMBER 10 software and the monomers comprising the linear block copolymer as well as the drugs were parametrized using the “general AMBER force field (GAFF)”. For MD simulations, 16 polymer chains were disposed randomly and uniformly in space. To reproduce the correct polymer/drug stoichiometry inside the micelles, the respective number of drug molecules was chosen in accordance with the experimentally determined drug content. Drug molecules were added randomly and uniformly in the empty cavities between the polymer chains to guarantee an almost equal spacing (Figure 2.18c). After equilibrating the PEG-hexPLA/drug micelles in vacuum to account for compaction that is present in the bulk of the micelles, water molecules were added (Figure 2.18d). After reaching equilibrium with good stability, χ_{FH} was obtained for every polymer/drug combination. The negative values of χ_{FH} in all systems suggested that PEG-hexPLA should be able to solubilize all four drugs which, according to the authors, nicely represents the experimentally determined solubilization behavior. However, as obvious from formulation experiments, the increase in solubility of QUER dihydrate was rather negligible. Nevertheless, the trend in χ_{FH} was in accordance with experimental solubilities with CsA having the highest and QUER dihydrate having the lowest molar solubility after formulation (Figure 2.18e). Unfortunately, the impact of different polymer/drug ratios deviating from the experimentally determined, “optimal” ratios has not been further investigated.

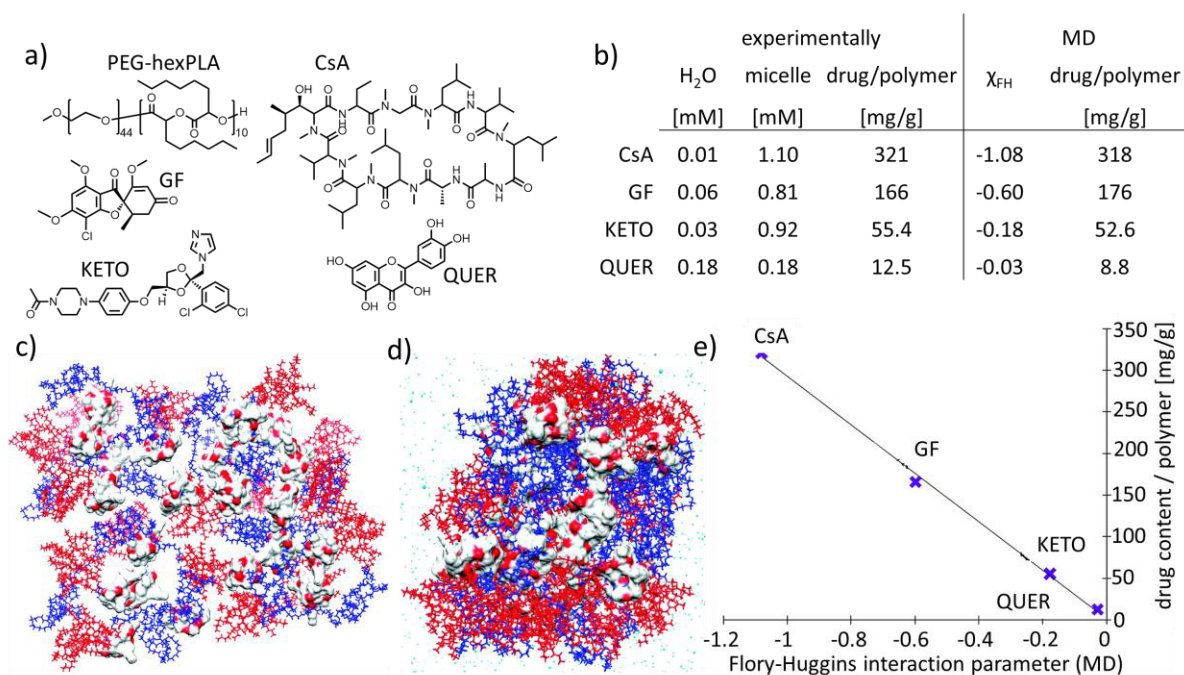


Figure 2.18: a) Chemical structure of polymeric drug carrier PEG-hexPLA as well as hydrophobic drugs; b) experimentally as well as MD determined solubilities of the different drugs in H₂O as well as PEG-hexPLA/drug formulations; c) snapshot of the initial „open configuration“ of the CsA loaded PEG-hexPLA system (blue: PEG; red: hexPLA). The 21 drug molecules are presented as van-der-Waals surface; d) snapshot from the production-phase MD simulation of CsA loaded PEG-hexPLA micelles (same color code than for (c)); e) water molecules are represented in cyan; e) relationship between χ_{FH} (derived from MD simulations) and the experimentally determined maximum drug loading. Table and figures modified with permission from ref[102].

The work by Möller and coworkers gives impressive insights into the complexity of micellization as well as the structure of drug-loaded micelles. In contrast to e.g. well-defined pockets of enzymes being highly selective for specific low molecular weight compounds^[146, 147], the micellar structure is highly flexible, strongly complicating the reliable prediction of polymer/drug compatibilities. This partly explains the widely applied trial-and-error approach in terms of finding a suitable polymeric drug carrier for non-soluble drugs.

Despite their predictive power, the MD simulations are computationally expensive, strongly hampering their routine application in pharmaceuticals. On the other hand, the fast screening of polymer-drug interactions based on GCMs such as Hildebrand or Hansen solubility parameters is many times unreliable. Very recently, Kabanov and coworkers presented a cheminformatics-driven discovery of suitable drug-carriers which requires less computational power than MDs, however is more predictive than GCMs. Both, *LE* and *LC* of POx based formulations of poorly soluble drugs were predicted using novel descriptors of POx/drug complexes.^[148] The workflow included (1) rational selection of 21 poorly soluble and chemically diverse drugs (based on previously collected data on 20 drugs); (2) compilation and integration of experimentally determined *LE* and *LC* of 41 drugs comprising 408 experimental data points including different drug-feed concentrations, structural diversity of POx polymers and experimental conditions;

(3) development of novel chemical descriptors for polymers and polymer/drug complexes; (4) generation and interpretation of quantitative structure-property relationship (QSPR) models; (5) identification (virtual screening) of poorly soluble drugs with either high or low *LE* and *LC*; and (6) validation of model predictions with experimentally determined *LE* and *LC* values of virtual selected hits (Figure 2.19a). The two-dimensional SiRMS (simplex representation of molecular structure) descriptors of tetratomic fragments (consisting of four atoms) with fixed composition and topological structure were generated by HiT QSAR software. At the 2D level, the connectivity of atoms in a simplex includes atom type and bond nature (single, double, triple or aromatic). However, SiRMS descriptors account not only for the type of atom, but also for atomic characteristics such as partial charge, lipophilicity, or ability to form hydrogen-bonds. For the POx based drug-carriers, each block of the polymer was described by the number of its repeating units (Figure 2.19b). In addition, SiRMS descriptors were calculated for simplified polymer representations as pseudo small molecules. For drug/polymer complexes, each complex was represented as a binary mixture consisting of the drug molecule, and the simplified representation of the polymer. The mixed simplexes were able to differentiate if the unbound simplexes belonged to the same or different molecules, wherefore they were specific for each polymer/drug pair. The QSPR models (developed with random forest algorithm^[149]) were used for virtual screening of DrugBank database to identify drugs predicted to have both, high and low *LE* and *LC*. Overall, a 75% experimental hit rate between predicted and experimentally verified polymer/drug compatibility was reached. Thus, three out of four drugs predicted as positive hits (high *LE* and *LC*) displayed moderate to excellent solubilization in POx micelles (e.g. *LC* = 43.2 wt.% for podophyllotoxin, Figure 2.19c). In contrast, highly soluble predicted diosmin was a false positive, *i.e.* insoluble in POx micelles. Besides correctly predicted low *LE* and *LC* for olanzapine, the false negative simvastatin was in fact highly soluble in POx micelles with maximum *LC* = 41.1 wt.%. Although differently interpreted by the authors, the predicted *LC* < 10 wt.% of spironolactone and tamibarotene was also not in good agreement of experimentally determined *LC*s of 17.7 wt.% and 25.9 wt.%, respectively. Therefore, the prediction of negative hits generally seemed to be less reliable than of positive hits.

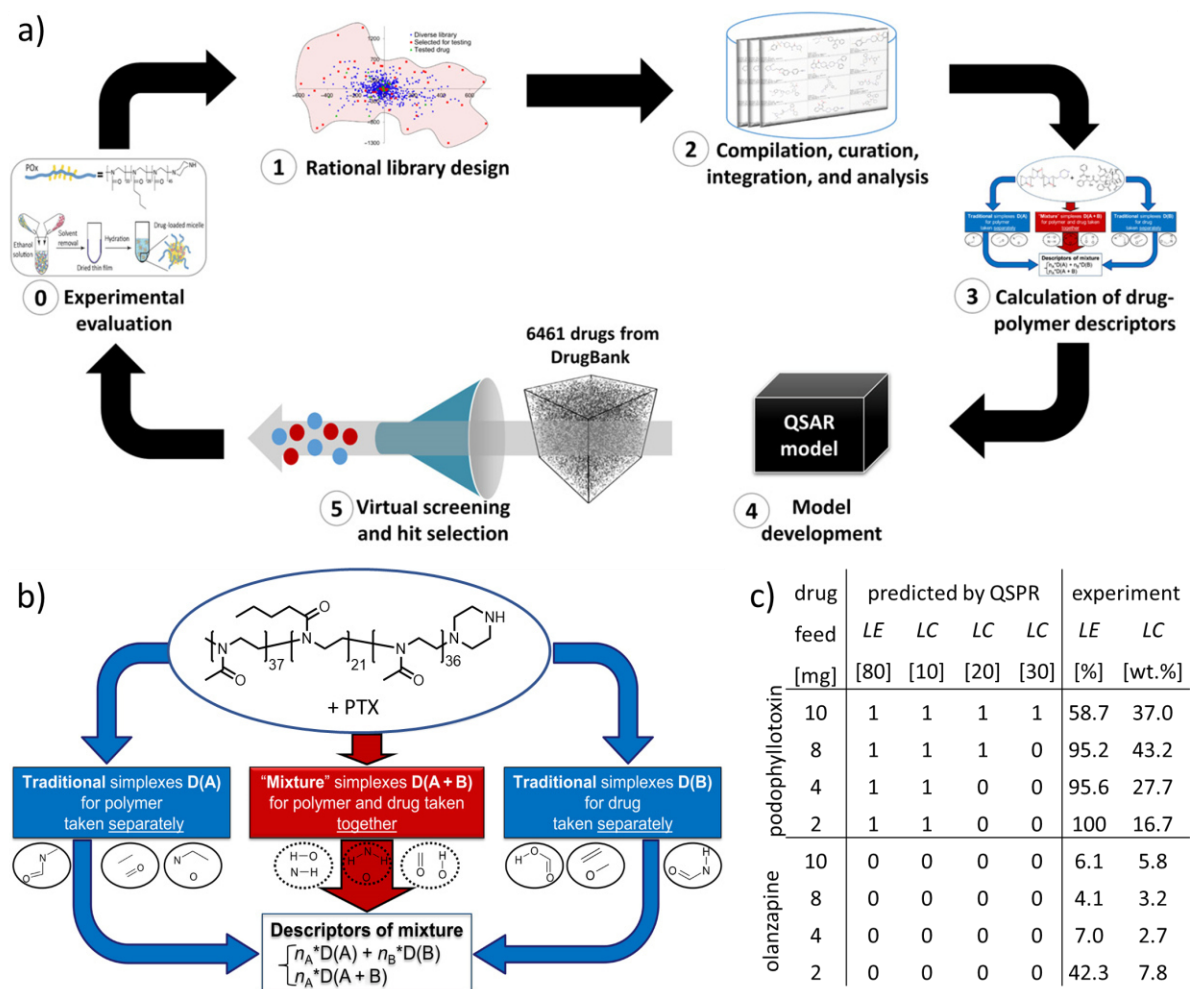


Figure 2.19: a) Study design to identify suitable POx based drug-carriers for the solubilization of poorly-soluble drugs. The process (step 3) to obtain descriptors of polymer, drug, or polymer/drug complexes is shown in b). n_A and n_B are molar fractions of components A and B; c) *LE* and *LC* of POx based formulations of podophyllotoxin (positive hit) or olanzapine (negative hit) either predicted by QSPR or experimentally determined. Predicted values are based on a binary code (0 = false; 1 = true) and the respective units (brackets) correspond to a predicted *LE* > 80 % and a *LC* < 10, 10-20, 20-30 or >30 wt.%. Figure modified with permission from ref[148].

Nevertheless, it is quite remarkable that the variation between experimental and predicted *LE* and *LC* of 6 out of 8 drugs was moderately small. Furthermore, to the best of my knowledge, this is the first study about the prediction of polymer/drug compatibility that considers the impact of experimental formulation conditions such as drug-feed concentration, solvent used for hydration, hydration temperature or total solvent volume before evaporation. Indeed, it was proven multiple times that these conditions have a large impact on formulation properties^[150], wherefore a reliable prediction of polymer/drug compatibility is only possible under consideration of the latter.

The discussed polymer-based formulations of hydrophobic drugs give insights into the complexity of developing a medicine with desired pharmaceutical properties. Although “only” the first steps of the development, namely (i) solubilization of a hydrophobic drug, (ii) morphology of the drug-loaded system, and (iii) drug release kinetics were discussed in more detail, it becomes evident how small changes in the chemical structure of the individual components or their concentrations can have a large impact on crucial formulation characteristics. Although associated with a lot of effort, only an in-depth characterization on a molecular level and preparation of materials in a reproducible manner enables to understand and optimize crucial biological properties such as (i) cellular uptake, (ii) interaction with proteins, (iv) blood circulation kinetics, or (iv) cytotoxicity in a targeted manner.

3 References

- [1] A. Persidis, *Nat. Biotechnol.* **1998**, *16*, 488-489.
- [2] E. M. Merisko-Liversidge, G. G. Liversidge, *Toxicol. Pathol.* **2008**, *36*, 43-48.
- [3] C. Giliyar, D. Fikstad, S. Tyavanagimatt, *Drug Deliv. Technol* **2006**, *6*, 57-63.
- [4] S. Ali, K. Kolter, *A. Pharm. Rev.* **2012**.
- [5] H. D. Williams, N. L. Trevaskis, S. A. Charman, R. M. Shanker, W. N. Charman, C. W. Pouton, C. J. H. Porter, *Pharmacol. Rev.* **2013**, *65*, 315.
- [6] S. R. Croy, G. S. Kwon, *Curr. Pharm. Des.* **2006**, *12*, 4669-4684.
- [7] H. Cabral, K. Miyata, K. Osada, K. Kataoka, *Chem. Rev.* **2018**, *118*, 6844-6892.
- [8] R. Luxenhofer, Y. Han, A. Schulz, J. Tong, Z. He, A. V. Kabanov, R. Jordan, *Macromol. Rapid Commun.* **2012**, *33*, 1613-1631.
- [9] V. R. de la Rosa, *J. Mater. Sci. Mater. Med.* **2014**, *25*, 1211-1225.
- [10] T. Lorson, M. M. Lubtow, E. Wegener, M. S. Haider, S. Borova, D. Nahm, R. Jordan, M. Sokolski-Papkov, A. V. Kabanov, R. Luxenhofer, *Biomaterials* **2018**, *178*, 204-280.
- [11] J. Kronek, Z. Kroneková, J. Lustoň, E. Paulovičová, L. Paulovičová, B. Mendrek, *J. Mater. Sci. Mater. Med.* **2011**, *22*, 1725-1734.
- [12] M. Bauer, S. Schroeder, L. Tauhardt, K. Kempe, U. S. Schubert, D. Fischer, *J. Polym. Sci. A* **2013**, *51*, 1816-1821.
- [13] M. Bauer, C. Lautenschlaeger, K. Kempe, L. Tauhardt, U. S. Schubert, D. Fischer, *Macromol. Biosci.* **2012**, *12*, 986-998.
- [14] R. Luxenhofer, G. Sahay, A. Schulz, D. Alakhova, T. K. Bronich, R. Jordan, A. V. Kabanov, *J. Control. Release* **2011**, *153*, 73-82.
- [15] B. Verbraeken, B. D. Monnery, K. Lava, R. Hoogenboom, *Eur. Polym. J.* **2017**, *88*, 451-469.
- [16] R. Luxenhofer, M. Bezen, R. Jordan, *Macromol. Rapid Commun.* **2008**, *29*, 1509-1513.
- [17] N. Zhang, S. Huber, A. Schulz, R. Luxenhofer, R. Jordan, *Macromolecules* **2009**, *42*, 2215-2221.
- [18] N. Zhang, R. Luxenhofer, R. Jordan, *Macromol. Chem. Phys.* **2012**, *213*, 1963-1969.
- [19] Z. He, X. Wan, A. Schulz, H. Bludau, M. A. Dobrovol'skaia, S. T. Stern, S. A. Montgomery, H. Yuan, Z. Li, D. Alakhova, M. Sokolsky, D. B. Darr, C. M. Perou, R. Jordan, R. Luxenhofer, A. V. Kabanov, *Biomaterials* **2016**, *101*, 296-309.
- [20] X. Wan, J. J. Beaudoin, N. Vinod, Y. Min, N. Makita, H. Bludau, R. Jordan, A. Wang, M. Sokolsky, A. V. Kabanov, *Biomaterials* **2019**, *192*, 1-14.
- [21] X. Wan, Y. Min, H. Bludau, A. Keith, S. S. Sheiko, R. Jordan, A. Z. Wang, M. Sokolsky-Papkov, A. V. Kabanov, *ACS Nano* **2018**, *12*, 2426-2439.
- [22] R. Luxenhofer, A. Schulz, C. Roques, S. Li, T. K. Bronich, E. V. Batrakova, R. Jordan, A. V. Kabanov, *Biomaterials* **2010**, *31*, 4972-4979.
- [23] M. M. Lübtow, M. S. Haider, M. Kirsch, S. Klisch, R. Luxenhofer, *Biomacromolecules* **2019**, *20*, 3041-3056.
- [24] M. M. Lübtow, L. Keßler, A. Appelt-Menzel, T. Lorson, N. Gangloff, M. Kirsch, S. Dahms, R. Luxenhofer, *Macromol. Biosci.* **2018**, *18*, 1800155.
- [25] K. Kothari, V. Ragoonanan, R. Suryanarayanan, *Mol. Pharm.* **2015**, *12*, 162-170.
- [26] S. Wiczorek, T. Schwaar, M. O. Senge, H. G. Börner, *Biomacromolecules* **2015**, *16*, 3308-3312.

- [27] L. M. Johnson, Z. Li, A. J. LaBelle, F. S. Bates, T. P. Lodge, M. A. Hillmyer, *Macromolecules* **2017**, *50*, 1102-1112.
- [28] S. Wieczorek, A. Dallmann, Z. Kochovski, H. G. Börner, *J. Am. Chem. Soc.* **2016**, *138*, 9349-9352.
- [29] M. M. Lübtow, L. Keßler, A. Appelt-Menzel, T. Lorson, N. Gangloff, M. Kirsch, S. Dahms, R. Luxenhofer, *Macromol. Biosci.* **2018**, 1800155.
- [30] L. Hahn, M. M. Lübtow, T. Lorson, F. Schmitt, A. Appelt-Menzel, R. Schobert, R. Luxenhofer, *Biomacromolecules* **2018**, *19*, 3119-3128.
- [31] M. M. Lübtow, L. Hahn, M. S. Haider, R. Luxenhofer, *J. Am. Chem. Soc.* **2017**, *139*, 10980-10983.
- [32] P. Baldrick, *Regul. Toxicol. Pharmacol.* **2000**, *32*, 210-218.
- [33] M. M. Lübtow, L. C. Nelke, J. Seifert, J. Kühnemundt, G. Sahay, G. Dandekar, S. L. Nietzer, R. Luxenhofer, *J. Control. Release* **2019**, *303*, 162-180.
- [34] M. M. Lübtow, S. Oerter, S. Quader, E. Jeanclos, A. Cubukova, M. Krafft, C. Schulte, L. Meier, M. Rist, O. Sampetean, H. Kinoh, A. Gohla, K. Kataoka, A. Appelt-Menzel, R. Luxenhofer, *ChemRxiv* **2019**, doi.org/10.26434/chemrxiv.10067993.
- [35] M. M. Lübtow, H. Marciniak, A. Schmiedel, M. Roos, C. Lambert, R. Luxenhofer, *Chem.: Eur. J.* **2019**, *25*, 12601-12610.
- [36] A.-C. Pöppler, M. M. Lübtow, J. Schlauersbach, J. Wiest, L. Meinel, R. Luxenhofer, *Angew. Chem. Int. Ed.* **2019**, doi:10.1002/anie.201908914.
- [37] B. Sochor, Ö. Düdükçü, M. M. Lübtow, B. Schummer, J. Sebastian, R. Luxenhofer, *ChemRxiv* **2019**, doi.org/10.26434/chemrxiv.10259552.
- [38] M. M. Lübtow, T. Lorson, T. Finger, F.-K. Gröber-Becker, R. Luxenhofer, *Macromol. Chem. Phys.* **2019**, <https://doi.org/10.1002/macp.201900341>.
- [39] H. Wen, H. Jung, X. Li, *AAPS J.* **2015**, *17*, 1327-1340.
- [40] R. Liu, *Water-Insoluble Drug Formulation, 3rd edition*, CRC Press, **2018**.
- [41] B. Amsden, N. Turner, *Biotechnol. and Bioeng.* **1999**, *65*, 605-610.
- [42] D. Y. Arifin, L. Y. Lee, C.-H. Wang, *Adv. Drug Deliv. Rev.* **2006**, *58*, 1274-1325.
- [43] N. X. Wang, H. A. von Recum, *Macromol. Biosci.* **2011**, *11*, 321-332.
- [44] J. Siepman, A. Göpferich, *Adv. Drug Deliv. Rev.* **2001**, *48*, 229-247.
- [45] H. Kimura, Y. Ogura, *Ophthalmologica* **2001**, *215*, 143-155.
- [46] C. d. I. H. Alarcon, S. Pennadam, C. Alexander, *Chem. Soc. Rev.* **2005**, *34*, 276-285.
- [47] R. I. Mahato, A. S. Narang, *Pharmaceutical Dosage Forms and Drug Delivery, 3rd edition*, CRC PR INC, **2017**.
- [48] M. R. Prausnitz, R. Langer, *Nat. Biotechnol.* **2008**, *26*, 1261-1268.
- [49] S. V. Sastry, J. R. Nyshadham, J. A. Fix, *PSTT* **2000**, *3*, 138-145.
- [50] J. Fu, J. Fiegel, E. Krauland, J. Hanes, *Biomaterials* **2002**, *23*, 4425-4433.
- [51] H. S. Chen, J. F. Gross, *Cancer Treat. Rep.* **1980**, *64*, 31-40.
- [52] J. P. Griffin, J. Posner, G. R. Barker, *The Textbook of Pharmaceutical Medicine, 7th edition*, BMJ Books, **2013**.
- [53] D. J. A. Crommelin, A. T. Florence, *Int. J. Pharm.* **2013**, *454*, 496-511.
- [54] J.-i. Jinno, N. Kamada, M. Miyake, K. Yamada, T. Mukai, M. Odomi, H. Toguchi, G. G. Liversidge, K. Higaki, T. Kimura, *J. Control. Release* **2006**, *111*, 56-64.
- [55] G. R. Desiraju, *J. Am. Chem. Soc.* **2013**, *135*, 9952-9967.
- [56] B. Moulton, M. J. Zaworotko, *Chem. Rev.* **2001**, *101*, 1629-1658.
- [57] A. T. M. Serajuddin, *Adv. Drug Deliv. Rev.* **2007**, *59*, 603-616.
- [58] F. Qian, J. Huang, M. A. Hussain, *J. Pharm. Sci.* **2010**, *99*, 2941-2947.
- [59] V. P. Torchilin, *J. Control. Release* **2001**, *73*, 137-172.
- [60] J. Shi, P. W. Kantoff, R. Wooster, O. C. Farokhzad, *Nat. Rev. Cancer* **2017**, *17*, 20-37.
- [61] T. Lammers, *Int. J. Pharm.* **2013**, *454*, 527-529.
- [62] G. P. Kumar, P. Rajeshwarrao, *Acta Pharm. Sin. B* **2011**, *1*, 208-219.

- [63] H. Maeda, M. Ueda, T. Morinaga, T. Matsumoto, *J. Med. Chem.* **1985**, *28*, 455-461.
- [64] V. Leiro, J. P. Garcia, H. Tomás, A. P. Pêgo, *Bioconjug. Chem.* **2015**, *26*, 1182-1197.
- [65] Y. Barenholz, *J. Control. Release* **2012**, *160*, 117-134.
- [66] K. S. Lee, H. C. Chung, S. A. Im, Y. H. Park, C. S. Kim, S.-B. Kim, S. Y. Rha, M. Y. Lee, J. Ro, *Breast Cancer Res. Treat.* **2008**, *108*, 241-250.
- [67] E. Blanco, C. W. Kessinger, B. D. Sumer, J. Gao, *Exp. Biol. Med.* **2009**, *234*, 123-131.
- [68] M. Baker, *Nature* **2017**, *548*, 485.
- [69] R. G. Bergman, R. L. Danheiser, *Angew. Chem. Int. Ed.* **2016**, *55*, 12548-12549.
- [70] R. Luxenhofer, *Nanomedicine* **2015**, *10*, 3109-3119.
- [71] A. Das, K. Petkau-Milroy, G. Klerks, B. van Genabeek, R. P. M. Lafleur, A. R. A. Palmans, E. W. Meijer, *ACS Macro Lett.* **2018**, *7*, 546-550.
- [72] B. Oschmann, J. Lawrence, M. W. Schulze, J. M. Ren, A. Anastasaki, Y. Luo, M. D. Nothling, C. W. Pester, K. T. Delaney, L. A. Connal, A. J. McGrath, P. G. Clark, C. M. Bates, C. J. Hawker, *ACS Macro Lett.* **2017**, *6*, 668-673.
- [73] N. Gangloff, M. Höferth, V. Stepanenko, B. Sochor, B. Schummer, J. Nickel, H. Walles, R. Hanke, F. Würthner, R. N. Zuckermann, R. Luxenhofer, *Biopolymers* **2019**, *110*, e23259.
- [74] N. Hoshyar, S. Gray, H. Han, G. Bao, *Nanomedicine* **2016**, *11*, 673-692.
- [75] P. P. Adiseshiaiah, J. B. Hall, S. E. McNeil, *Wiley Interdiscip. Rev. Nanomed. Nanobiotechnol.* **2010**, *2*, 99-112.
- [76] M. A. Dobrovolskaia, A. K. Patri, J. Simak, J. B. Hall, J. Semberova, S. H. De Paoli Lacerda, S. E. McNeil, *Mol. Pharm.* **2012**, *9*, 382-393.
- [77] F. Dormont, M. Rouquette, C. Mahatsekake, F. Gobeaux, A. Peramo, R. Brusini, S. Calet, F. Testard, S. Lepetre-Mouelhi, D. Desmaële, M. Varna, P. Couvreur, *J. Control. Release* **2019**.
- [78] L. De Maeyer, C. Trachimow, U. Kaatze, *J. Phys. Chem. B* **1998**, *102*, 8480-8491.
- [79] C. Trachimow, L. De Maeyer, U. Kaatze, *J. Phys. Chem. B* **1998**, *102*, 4483-4487.
- [80] Y. Wang, Q. Zhao, N. Han, L. Bai, J. Li, J. Liu, E. Che, L. Hu, Q. Zhang, T. Jiang, S. Wang, *Nanomed-Nanotechnol.* **2015**, *11*, 313-327.
- [81] W. Mehnert, K. Mäder, *Adv. Drug Deliv. Rev.* **2012**, *64*, 83-101.
- [82] S. Hvidt, *Colloids Surf. A* **1996**, *112*, 201-207.
- [83] R. Triolo, A. Triolo, F. Triolo, D. C. Steytler, C. A. Lewis, R. K. Heenan, G. D. Wignall, J. M. DeSimone, *Phys. Rev. E* **2000**, *61*, 4640-4643.
- [84] R. C. Pasquali, M. P. Taurozzi, C. Bregni, *Int. J. Pharm.* **2008**, *356*, 44-51.
- [85] H.-U. Kim, K.-H. Lim, *Colloids Surf. A* **2004**, *235*, 121-128.
- [86] K. Nakashima, P. Bahadur, *Adv. Colloid Interface Sci.* **2006**, *123-126*, 75-96.
- [87] A. Bogomolova, S. K. Filippov, L. Starovoytova, B. Angelov, P. Konarev, O. Sedlacek, M. Hruby, P. Stepanek, *J. Phys. Chem. B* **2014**, *118*, 4940-4950.
- [88] V. P. Torchilin, A. N. Lukyanov, Z. Gao, B. Papahadjopoulos-Sternberg, *PNAS* **2003**, *100*, 6039-6044.
- [89] L. Gros, H. Ringsdorf, H. Schupp, *Angew. Chem. Int. Ed.* **1981**, *20*, 305-325.
- [90] H. Maeda, *Adv. Drug Deliv. Rev.* **2015**, *91*, 3-6.
- [91] F. Danhier, *J. Control. Release* **2016**, *244*, 108-121.
- [92] H. Kobayashi, R. Watanabe, P. L. Choyke, *Theranostics* **2013**, *4*, 81-89.
- [93] S. I. Rudnick, G. P. Adams, *Cancer Biother. Radio.* **2009**, *24*, 155-161.
- [94] B. Huang, W. D. Abraham, Y. Zheng, S. C. Bustamante López, S. S. Luo, D. J. Irvine, *Sci. Transl. Med.* **2015**, *7*, 291ra294.
- [95] J. D. Byrne, T. Betancourt, L. Brannon-Peppas, *Adv. Drug Deliv. Rev.* **2008**, *60*, 1615-1626.
- [96] X. Sun, G. Wang, H. Zhang, S. Hu, X. Liu, J. Tang, Y. Shen, *ACS Nano* **2018**, *12*, 6179-6192.
- [97] J. Müller, J. Simon, P. Rohne, C. Koch-Brandt, V. Mailänder, S. Morsbach, K. Landfester, *Biomacromolecules* **2018**, *19*, 2657-2664.
- [98] Z. Amoozgar, Y. Yeo, *Wiley Interdiscip. Rev. Nanomed. Nanobiotechnol.* **2012**, *4*, 219-233.

- [99] A. Schulz, S. Jaksch, R. Schubel, E. Wegener, Z. Di, Y. Han, A. Meister, J. Kressler, A. V. Kabanov, R. Luxenhofer, C. M. Papadakis, R. Jordan, *ACS Nano* **2014**, *8*, 2686-2696.
- [100] S. Jaksch, A. Schulz, Z. Di, R. Luxenhofer, R. Jordan, C. M. Papadakis, *Macromol. Chem. Phys.* **2016**, *217*, 1448-1456.
- [101] J. Liu, Y. Xiao, C. Allen, *J. Pharm. Sci.* **2004**, *93*, 132-143.
- [102] A. O. Kasimova, G. M. Pavan, A. Danani, K. Mondon, A. Cristiani, L. Scapozza, R. Gurny, M. Möller, *J. Phys. Chem. B* **2012**, *116*, 4338-4345.
- [103] H. Gelderblom, J. Verweij, K. Nooter, A. Sparreboom, *Eur. J. Cancer* **2001**, *37*, 1590-1598.
- [104] O. Naksuriya, S. Okonogi, R. M. Schiffelers, W. E. Hennink, *Biomaterials* **2014**, *35*, 3365-3383.
- [105] C. Lawatscheck, M. Pickhardt, S. Wieczorek, A. Grafmüller, E. Mandelkow, H. G. Börner, *Angew. Chem. Int. Ed.* **2016**, *55*, 8752-8756.
- [106] S. Wieczorek, E. Krause, S. Hackbarth, B. Röder, A. K. H. Hirsch, H. G. Börner, *J. Am. Chem. Soc.* **2013**, *135*, 1711-1714.
- [107] S. Wieczorek, D. Remmler, T. Masini, Z. Kochovski, A. K. H. Hirsch, H. G. Börner, *Bioconjug. Chem.* **2017**, *28*, 760-767.
- [108] S. Lv, Y. Wu, K. Cai, H. He, Y. Li, M. Lan, X. Chen, J. Cheng, L. Yin, *J. Am. Chem. Soc.* **2018**, *140*, 1235-1238.
- [109] Y. Shi, M. J. van Steenberg, E. A. Teunissen, L. s. Novo, S. Gradmann, M. Baldus, C. F. van Nostrum, W. E. Hennink, *Biomacromolecules* **2013**, *14*, 1826-1837.
- [110] A. L. Z. Lee, S. Venkataraman, S. B. M. Sirat, S. Gao, J. L. Hedrick, Y. Y. Yang, *Biomaterials* **2012**, *33*, 1921-1928.
- [111] H. Cabral, K. Kataoka, *J. Control. Release* **2014**, *190*, 465-476.
- [112] Y. Shi, R. van der Meel, B. Theek, E. Oude Blenke, E. H. E. Pieters, M. H. A. M. Fens, J. Ehling, R. M. Schiffelers, G. Storm, C. F. van Nostrum, T. Lammers, W. E. Hennink, *ACS Nano* **2015**, *9*, 3740-3752.
- [113] C. J. Rijcken, C. J. Snel, R. M. Schiffelers, C. F. van Nostrum, W. E. Hennink, *Biomaterials* **2007**, *28*, 5581-5593.
- [114] B. T. Surikutchi, S. P. Patil, G. Shete, S. Patel, A. K. Bansal, *J. Excip. Food Chem.* **2013**, *4*, 70-94.
- [115] K. M. Boje, M. Sak, H.-L. Fung, *Pharm. Res.* **1988**, *5*, 655-659.
- [116] H. Konno, L. S. Taylor, *J. Pharm. Sci.* **2006**, *95*, 2692-2705.
- [117] C. Bhugra, M. J. Pikal, *J. Pharm. Sci.* **2008**, *97*, 1329-1349.
- [118] T. Matsumoto, G. Zografi, *Pharm. Res.* **1999**, *16*, 1722-1728.
- [119] U. S. Kestur, L. S. Taylor, *CrystEngComm* **2010**, *12*, 2390-2397.
- [120] J. Lee, E. C. Cho, K. Cho, *J. Control. Release* **2004**, *94*, 323-335.
- [121] S. Yalkowsky, R. Dannenfelser, *Aquasol Database of Aqueous Solubility, 5th edition* College of Pharmacy, University of Arizona-Tucson, AZ, USA, **1992**.
- [122] X. Yuan, T.-X. Xiang, B. D. Anderson, E. J. Munson, *Mol. Pharm.* **2015**, *12*, 4518-4528.
- [123] T. N. Pham, S. A. Watson, A. J. Edwards, M. Chavda, J. S. Clawson, M. Strohmeier, F. G. Vogt, *Mol. Pharm.* **2010**, *7*, 1667-1691.
- [124] X. Yuan, D. Sperger, E. J. Munson, *Mol. Pharm.* **2014**, *11*, 329-337.
- [125] A. S. Tatton, T. N. Pham, F. G. Vogt, D. Iuga, A. J. Edwards, S. P. Brown, *Mol. Pharm.* **2013**, *10*, 999-1007.
- [126] Y. Song, X. Yang, X. Chen, H. Nie, S. Byrn, J. W. Lubach, *Mol. Pharm.* **2015**, *12*, 857-866.
- [127] H. Nie, Y. Su, M. Zhang, Y. Song, A. Leone, L. S. Taylor, P. J. Marsac, T. Li, S. R. Byrn, *Mol. Pharm.* **2016**, *13*, 3964-3975.
- [128] M. Callari, P. L. De Souza, A. Rawal, M. H. Stenzel, *Angew. Chem. Int. Ed.* **2017**, *56*, 8441-8445.
- [129] Y. Shi, T. Lammers, G. Storm, W. E. Hennink, *Macromol. Biosci.* **2017**, *17*, 1600160.
- [130] J. Woodcock, J. P. Griffin, R. E. Behrman, *N. Engl. J. Med.* **2011**, *364*, 985-987.

-
- [131] N. Singh, P. J. Yeh, *J. Antibiot.* **2017**, *70*, 1033-1042.
- [132] N. Yin, W. Ma, J. Pei, Q. Ouyang, C. Tang, L. Lai, *PLOS ONE* **2014**, *9*, e93960.
- [133] L. Ma, M. Kohli, A. Smith, *ACS Nano* **2013**, *7*, 9518-9525.
- [134] P. Parhi, C. Mohanty, S. K. Sahoo, *Drug Discov. Today* **2012**, *17*, 1044-1052.
- [135] Y. Han, Z. He, A. Schulz, T. K. Bronich, R. Jordan, R. Luxenhofer, A. V. Kabanov, *Mol. Pharm.* **2012**, *9*, 2302-2313.
- [136] L. Zhang, H. Sun, Z. Chen, Z. Liu, N. Huang, F. Qian, *Mol. Pharm.* **2017**, *14*, 3568-3576.
- [137] L. Zhang, Z. Chen, K. Yang, C. Liu, J. Gao, F. Qian, *Mol. Pharm.* **2015**, *12*, 3999-4010.
- [138] P. Simamora, J. M. Alvarez, S. H. Yalkowsky, *Int. J. Pharm.* **2001**, *213*, 25-29.
- [139] H.-C. Shin, A. W. G. Alani, H. Cho, Y. Bae, J. M. Kolesar, G. S. Kwon, *Mol. Pharm.* **2011**, *8*, 1257-1265.
- [140] H.-C. Shin, A. W. G. Alani, D. A. Rao, N. C. Rockich, G. S. Kwon, *J. Control. Release* **2009**, *140*, 294-300.
- [141] J. H. Hildebrand, R. L. Scott, *The solubility of nonelectrolytes*, 3rd ed., New York, Reinhold Pub. Corp., **1950**.
- [142] C. M. Hansen, *THE THREE DIMENSIONAL SOLUBILITY PARAMETER AND SOLVENT DIFFUSION COEFFICIENT*, COPENHAGEN DANISH TECHNICAL PRESS, **1967**.
- [143] L. Huynh, J. Grant, J.-C. Leroux, P. Delmas, C. Allen, *Pharm. Res.* **2007**, *25*, 147-157.
- [144] W. M. Payne, D. Svechkarev, A. Kyrychenko, A. M. Mohs, *Carbohydr. Polym.* **2018**, *182*, 132-141.
- [145] D. Svechkarev, A. Kyrychenko, W. M. Payne, A. M. Mohs, *Soft Matter* **2018**, *14*, 4762-4771.
- [146] K. N. Houk, A. G. Leach, S. P. Kim, X. Zhang, *Angew. Chem. Int. Ed.* **2003**, *42*, 4872-4897.
- [147] J. Liang, C. Woodward, H. Edelsbrunner, *Protein Science* **1998**, *7*, 1884-1897.
- [148] V. M. Alves, D. Hwang, E. Muratov, M. Sokolsky-Papkov, E. Varlamova, N. Vinod, C. Lim, C. H. Andrade, A. Tropsha, A. Kabanov, *Sci. Adv.* **2019**, *5*, eaav9784.
- [149] L. Breiman, *Mach. Learn.* **2001**, *45*, 5-32.
- [150] Y. Seo, A. Schulz, Y. Han, Z. He, H. Bludau, X. Wan, J. Tong, T. K. Bronich, M. Sokolsky, R. Luxenhofer, R. Jordan, A. V. Kabanov, *Polym. Adv. Technol.* **2015**, *26*, 837-850.

4 Results

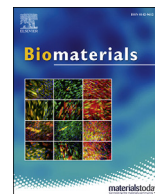
The research findings of this thesis will be divided into five chapters. The first chapter contains selected extracts of a review to introduce the polymer classes of POx and POzi from a pharmaceutical point of view. Following this, the formulation of non-water soluble drugs with POx and POzi based amphiphiles will be discussed with emphasize on polymer-drug compatibility. Among others, the latter will be mainly expressed by the loading capacity, *i.e.* the amount of drug solubilized per polymer, as well as long-term stability of the respective formulations. To get further insights into unexpected findings such as extraordinary high drug loadings as well as pronounced polymer-drug specificities, selected formulations will be investigated thoroughly using less conventional techniques such as fluorescence upconversion, small angle neutron scattering as well as solid-state NMR. To investigate the first ever reported POzi based drug formulations from a pharmaceutical point of view, the activity of POzi based curcumin and atorvastatin formulations against various kinds of cancer cell lines will be tested in conventional 2D cell culture as well as 3D tissue and spheroid models. Last, the desired application as intravenously administered drug-loaded micelles will be expanded to (sub)cutaneous drug depots by incorporating the micelles into cytocompatible hydrogels. This includes an introduction of the neat POx/POzi based hydrogels.

4.1 Poly(2-oxazoline) and Poly(2-oxazine) Based Biomaterials – an Overview

In the following, recent developments regarding the toxicity, immunogenicity, biodistribution as well as degradability of POx and POzi based biomaterials will be discussed. For further insights into POx and POzi based (i) hydrogels, (ii) conjugates, (iii) formulations, (iv) targeted and theranostic drug delivery systems as well as (v) protein and gene complexes, the reader is referred to the other parts of the review.

The following publication was reprinted in part with permission from *Biomaterials*, **2018**, *178*, 204-280.

<https://doi.org/10.1016/j.biomaterials.2018.05.022>; © 2018 Elsevier Ltd.



Poly(2-oxazoline)s based biomaterials: A comprehensive and critical update



Thomas Lorson ^{a,1}, Michael M. Lübtow ^{a,1}, Erik Wegener ^b, Malik S. Haider ^a, Solomiia Borova ^a, Daniel Nahm ^{a,c}, Rainer Jordan ^b, Marina Sokolski-Papkov ^d, Alexander V. Kabanov ^d, Robert Luxenhofer ^{a,*}

^a Functional Polymer Materials, Chair for Advanced Materials Synthesis, Department Chemistry and Pharmacy, Julius-Maximilians-University Würzburg, Röntgenring 11, 97070 Würzburg, Germany

^b Chair of Macromolecular Chemistry, Faculty of Chemistry and Food Chemistry, School of Science, Technische Universität Dresden, Mommsenstr. 4, 01069 Dresden, Germany

^c Department of Functional Materials in Medicine and Dentistry, University of Würzburg, Würzburg, 97070, Germany

^d Center for Nanotechnology in Drug Delivery, Division of Pharmacoengineering and Molecular Pharmaceutics, Eshelman School of Pharmacy, University of North Carolina at Chapel Hill, 125 Mason Farm Road, Chapel Hill, NC, 27599, United States

ARTICLE INFO

Article history:

Received 12 February 2018

Received in revised form

11 May 2018

Accepted 14 May 2018

Available online 2 June 2018

Keywords:

Drug delivery
Protein conjugate
Drug formulation
Non-fouling
Nanomedicine
Polyplex

ABSTRACT

Poly(2-oxazoline)s have been investigated for decades as biomaterials. Pioneering early work suggested that hydrophilic poly(2-oxazoline)s are comparable to poly(ethylene glycol) regarding their potential as biomaterials, but the ready commercial availability of the latter has led to its meteoric rise to become the gold standard of hydrophilic synthetic biomaterials. In contrast, poly(2-oxazoline)s almost fell into oblivion. However, in the last decade, this family of polymers has gained much more interest in general and as biomaterials in particular. The rich chemistry and comparably straightforward synthesis of poly(2-oxazoline)s gives many opportunities for tailoring the properties of the resulting biomaterials, allowing the chemist to explore new conjugation chemistry, and to fine-tune the molar mass, hydrophilic-lipophilic balance as well as architecture. Thus, the wide range of demands for various applications of biomaterials can be suitably addressed.

This review aims to give a comprehensive and critical update of the development of poly(2-oxazoline) based biomaterials, focusing on the last 5 years, which have seen an explosive increase of interest. We believe that the research regarding this diverse family of polymers will remain strong and will keep growing, in particular after the promising first-in-human studies of a poly(2-oxazoline) drug conjugate. This review aims at researchers and students new to this polymer family and seasoned poly(2-oxazoline) experts alike and attempts to showcase how the chemical diversity of poly(2-oxazoline)s allows a relatively facile and broad access to biomaterials of all kinds.

© 2018 Elsevier Ltd. All rights reserved.

1. Introduction

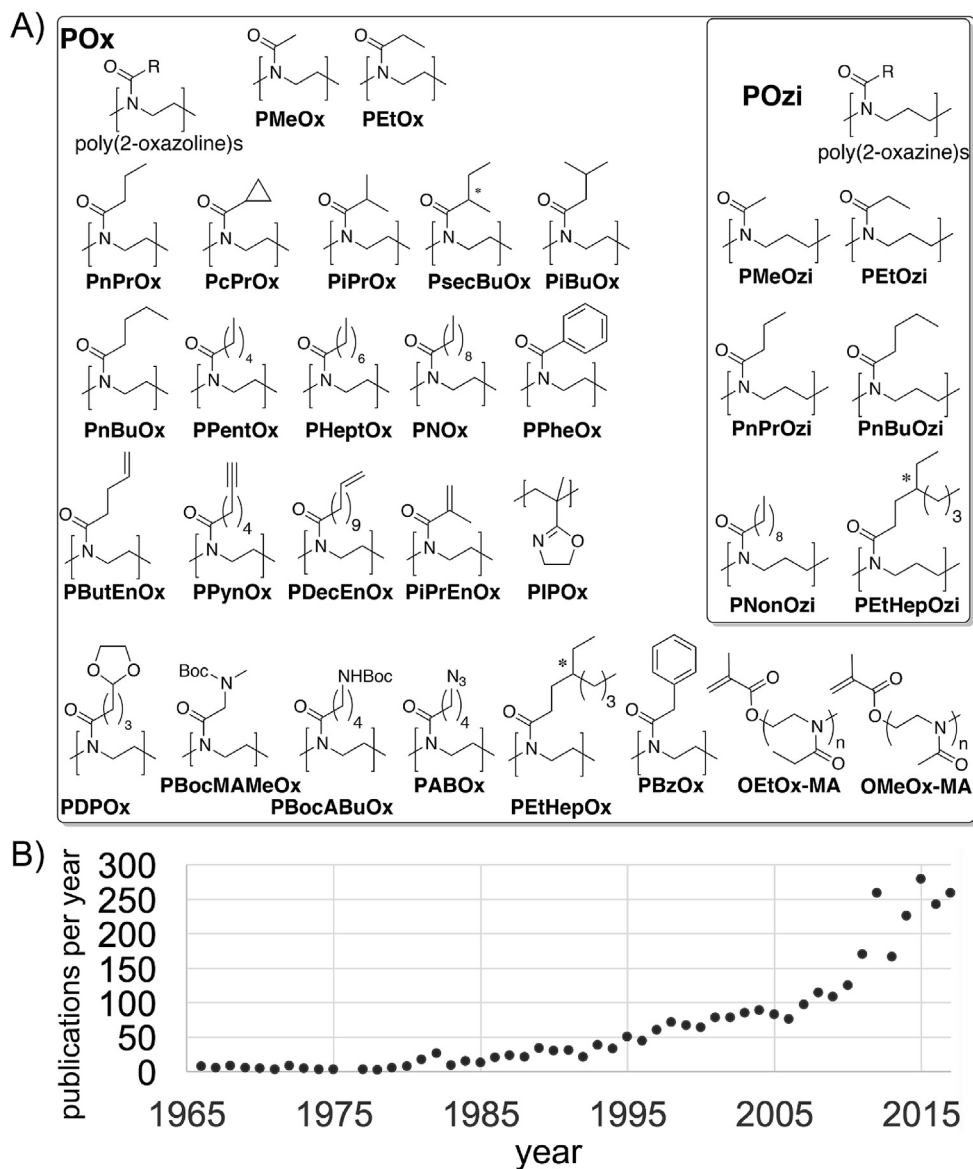
Poly(2-oxazoline)s (POx) have been known for a little over 50 years now [1] and this family of polymers has seen very variable interest by researchers and industry. For decades, only a few members of this diverse polymer family have been investigated in detail, first and foremost poly(2-ethyl-2-oxazoline) (PEtOx) even though the actual and potential chemical space is much larger (see

Scheme 1A for a selection of commonly used POx). PEtOx is an amphiphilic polymer that exhibits excellent water- and organo-solubility. The more hydrophilic poly(2-methyl-2-oxazoline) (PMeOx) has also been studied intensively, albeit less than PEtOx. Interestingly, PEtOx may also have interesting applications outside the field of biomaterials, for example in organic electronics, as demonstrated recently by Kim and co-workers [2]. POx with C3 side chains exhibit a lower critical solution temperature, an interesting thermoresponsive behavior, i.e. they are water soluble at cooler temperatures and become water insoluble at higher ones. The exact temperature of this transition can be controlled by composition [3,4], chain length and architecture [5,6], which has

* Corresponding author.

E-mail address: robert.luxenhofer@uni-wuerzburg.de (R. Luxenhofer).

¹ Authors contributed equally.



Scheme 1. A) Structures and abbreviations of commonly used poly(2-oxazoline)s (POx) and some poly(2-oxazine)s relevant for this review. B) Development of annual publications on poly(2-oxazoline)s (SciFinder® search term: poly AND oxazoline).

been employed by Jang and co-workers to realize a highly versatile and tunable multicolor emission material [7]. Hoogenboom and Schlaad recently excellently reviewed the state-of-the-art of thermoresponsive POx [8] which is why we will consider herein only select cases with a direct impact in the context of biomaterials. In addition, Dworak also reviewed thermoresponsive polymer-protein conjugates, which included also several examples of POx-protein conjugates [9]. POx with aliphatic side chains longer than C3 are typically non-water soluble and can be employed in amphiphilic systems, which will be reviewed in more detail herein.

In the last few years, several interesting reviews have been published, which give a comprehensive overview on the chemistry of POx and design strategies for functionalized POx [10–12] as well as their physico-chemical properties [13]. Hence, this wide field, which also has seen very interesting developments in recent years will not be covered in detail here. However, as new POx chemistry and novel functionalization strategies may also be directly connected to developments of POx as biomaterials, select examples

will also be addressed here. Apart from POx, there are other, closely related polymer families available for the design of biomaterials. For example, the higher homologues of POx, the poly(2-oxazine)s (POzi) have received very little attention so far [14]. Nevertheless, very recent work shows that they can also be used in drug delivery systems and to obtain stimulus-responsive hydrogels. Clearly, the potential of POzi is widely untapped. Also other POx derivatives, such as water-soluble 4-substituted POx [15] have not been investigated in any detail for their potential as biomaterials.

It should be noted that a variety of abbreviations for POx can be found in the literature (POZ, POXA, P(Ox) and others). For the sake of homogeneity, we will only use POx for poly(2-oxazoline)s and POzi for poly(2-oxazine)s even though the original literature might employ another. Similarly, we not always use the abbreviations for specific monomers from the primary literature as this would lead to an insufferable mess within this review.

Also, a few reviews have covered the topic of POx based hydrogels in recent years. Kelly and Wiesbrock reviewed the

various strategies to synthesize POx-based hydrogels and give selected examples for potential application [16]. Dargaville et al. reviewed briefly the up-and-coming field of 3D cell culture. The authors concentrated on POx based hydrogels for cell support and compared them to often used PEG based hydrogels [17]. Similarly, Hartlieb et al. reviewed covalently cross-linked POx hydrogels [18]. Although these excellent reviews give an overview until 2012 and 2014, respectively, we will comprehensively address this topic in the present contribution, especially covering work since 2015. Other reviews have covered the issue of POx at interfaces and on surfaces [19,20]. Nevertheless, we will also cover this topic in the present review, as a review on POx as biomaterials would be incomplete without this important aspect. In general, the research in POx has seen a very significant increase in recent years (Scheme 1B). Even though the simple search performed will certainly not portray the field accurately, the overall trend is likely to be reflective of the actual situation. While before 2010, the number of articles published in this field increased continuously but slowly, the number of articles are now increasing at a much higher rate.

A major breakthrough for the community was undoubtedly the first-in-human study of a POx-rotigotine conjugate initiated in 2015 [21]. Even though this study is ongoing and final results have not been published, it appears that preliminary results are promising [22].

This review will first look into recent development regarding the toxicity, degradability, immunogenicity, and biodistribution aspects of POx based biomaterials. Subsequently, the extensive work on POx hydrogels are reviewed. In addition, chapters on conjugates, formulations, and complexes are included. Finally, several chapters will summarize the recent research on POx at interfaces and surfaces as well as work on antimicrobial POx.

2. Toxicity, immunogenicity and biodistribution

It has been often written and considered established for some time that POx, in particular hydrophilic POx, are biocompatible. However, relatively little reliable data going beyond simple cytotoxicity has been available in the public domain and more caution should be exerted regarding the term biocompatible. The stealth effect of PEG and PMeOx has been probably one of the best established features [23], however new research by Szoka and Frechet questions important aspects of this issue (*vide infra*). Generally, POx have also been established to exhibit excellent cyto- and hemocompatibility and several reports have corroborated and extended our knowledge about this in the past 5 years (*vide infra*). However, it should never be assumed that this can be simply extended to POx with different composition, architectures or end-groups and must always be assessed on a case-by-case basis. Moreover, new studies have investigated the stability of POx with respect to hydrolysis, oxidative and environmental degradation, the latter of which has not been investigated before. For the interaction with biological systems, the solution properties of polymers in general are important. Very recently, Schubert, Nischang and co-workers [24] as well as Hoogenboom, Filippov and co-workers [25] investigated in great detail POx solution properties in aqueous solution (water and phosphate buffered saline (PBS), respectively) in two very interesting, detailed and valuable studies. In water, the hydrodynamic volumes of PMeOx and PEG are very similar at the same molar mass and systematically smaller than that of PEG [24]. Viscometric studies suggest that especially at lower molar masses, water is a better solvent for PEG than for PEG and, to a lesser extent, PMeOx. At higher molar masses (20 kg/mol and above), this difference becomes smaller or non-existent. Also, and very important to note, the authors caution that molar mass analysis of POx with molar masses of ≤ 10 kg/mol

using light scattering based detection should be viewed with some caution, as it may tend to overestimate the molar mass. This is not entirely surprising, as it is clear that sensitivity of light scattering becomes problematic with very small molar masses while the refractive index detectors are sensitive irrespective of the molar mass. While this study investigated PEG and PMeOx in water, Hoogenboom and Filippov studied PEG in PBS. This study concludes that the conformational rigidity of PEG is similar to that of PEG [25].

2.1. Cytocompatibility

Often cyto- and hemocompatibility of a certain polymer class is based on few experiments and generalized too readily, as both strongly depend on the utilized cell type, incubation time, polymer concentration, molar mass and of course, purity. PEG is currently the gold standard for hydrophilic polymers and can be seen as a benchmark for polymers that aim towards usage in medical application, drug delivery or biomaterials in general. Nevertheless, existing or perceived disadvantages or limitations of PEG such as undesired impurities, limited stability, high viscosity and accumulation in some organs have triggered search of new materials [26–29]. In the recent years, POx have been discussed as potential alternatives for PEG. Especially implications on the cell viability for various POx moved into focus. Fischer and co-workers investigated cyto- and hemocompatibility of PEG and PEG with different molar masses (0.4–200 kg/mol) at different incubation times (3, 12 and 24 h) [30]. It is important to note that some of the investigated PEG samples (5, 50 and 200 kg/mol) were ill-defined commercial polymers ($M_w = 2.4, 4.1$ and 4.7 , respectively). However, whether this dispersity would have any considerable impact in this simple assay is not clear. Even at very high polymer concentrations up to 80 g/L, no cytotoxicity was observed for short incubation times (3 h) in L929 mouse fibroblasts. After longer incubation (12 h), low molar mass PEG (0.4 and 2 kg/mol) as well as 20 kg/mol PEG decreased the cell viability below 70%. However, higher molar mass PEG (50 and 200 kg/mol) remained non-cytotoxic also after 24 h of incubation suggesting no influence of the broader molar mass distribution. Although no clear correlation between molar mass and cytotoxicity was found, medium molar masses appeared to exhibit somewhat higher cytotoxicity for unknown reason. A similar pattern was observed for PEG. Up to 40 g/L it was found to be non-toxic after 24 h incubation, the highest cytotoxicity was observed for 10 kg/mol PEG. None of the investigated polymers showed a pronounced influence on the aggregation behavior of erythrocytes or led to significant hemolysis. Specifically, PEG up to 40 kg/mol and 80 g/L did not cause erythrocyte aggregation and PEG with 200 kg/mol led to only minor erythrocyte aggregation at 40 g/L. Follow-up studies by the same group published in 2013 focused on PMeOx [31]. Similar to the study on PEG, *in vitro* cytotoxicity and hemocompatibility of PMeOx with a molecular weight from 2 to 20 kg/mol were assessed. None of the studied polymers caused release of hemoglobin, even at concentrations of 80 g/L. Cytotoxicity studies confirmed the generally high cytocompatibility of PMeOx. Only 2 kg/mol PMeOx (80 g/L) reduced the cell viability of L929 mouse fibroblasts to 60% and 44% after 3 and 12 h incubation, respectively. In general, a similar pattern as for PEG was observed [30].

Poly(2-*iso*-propenyl-2-oxazoline) is the product of the polymerization of 2-*iso*-propenyl-2-oxazoline (iPrEnOx), an interesting monomer that can alternatively be polymerized via radical, anionic polymerization or living cationic ring-opening polymerization (LCROP). For the sake of differentiation, we will call/abbreviate the product of the LCROP PiPrEnOx, while the product of radical or anionic polymerization, which leaves the 2-oxazoline ring intact,

PIPOx. Even though this review concentrates on POx obtained by LCROP, we would like to briefly mention a study investigating the cytocompatibility of PIPOx obtained via radical polymerization. Apart from PIPOx, Kronekova et al. studied the cytotoxicity of various 2-oxazoline monomers [32]. Specifically, MeOx, EtOx and iPrEnOx were tested using NIH 3T3 mouse fibroblasts (24 h incubation) and compared against acrylamide. Interestingly, iPrEnOx showed much more pronounced impact on the cell viability with an IC_{50} value of only approx. 0.7 mg/L (6 μ M). In contrast, the IC_{50} values of MeOx, EtOx and acrylamide were about 3–4 orders of magnitude higher. Therefore, iPrEnOx exhibits an extraordinarily high cytotoxicity and should be handled with considerable care. Moreover, it is advisable to make sure to remove even traces of this monomer when incorporated into biomaterials. In stark contrast to the monomer, PIPOx shows little if any effect on the cell viability (5 g/L, 24 h) in NIH 3T3 and P388.D1. Surprisingly, PIPOx seems to affect the cells even less than PEtOx tested in this study.

Very recently, Leiske et al. reported their approach to evaluate PMeOx, PEtOx, poly(vinyl alcohol) (PVA) and Pluronic® F127 as surfactants and cryoprotectant in the preparation of poly(lactic-co-glycolic acid) (PLGA) nanoparticle via nanoemulsion [33]. Cyto- and hemocompatibility is important in this context as it is almost impossible to completely remove the surfactants after nanoemulsion polymerization. For both POx investigated, no cytotoxic effect or hemolytic activity was found at 5 wt% concentration, corroborating earlier reports (Fig. 1 A). According to the authors, PVA and Pluronic® F127 could not be investigated at the highest concentration due to solubility issues. Regarding hemocompatibility, PVA and Pluronic® F127 did reveal increased hemolytic activity at 1 wt% whereas PMeOx and PEtOx remained inconspicuous (Fig. 1 B). The erythrocyte aggregation tests did not show significant differences between the tested polymers.

Also, the almost forgotten poly(2-oxazine)s (POzi) - the higher homologue of POx - regained interest as potential biomaterials [34–36]. An initial study conducted by Kroneková et al. regarding the cytotoxicity of different 2-oxazine monomers (2-methyl-2-oxazine (MeOzi), 2-ethyl-2-oxazine (EtOzi) and 2-*n*-propyl-2-oxazine (*n*PrOzi)) and homopolymers (PMeOzi (DP = 50), PEtOzi (DP = 50) and PEtOzi (DP = 150)) in 3T3 mouse fibroblasts was reported and is to the best of our knowledge the first on this topic

[37]. Cell viability after 24 h incubation decreased to or below IC_{50} at concentration exceeding 20 g/L for MeOzi, 10 g/L for EtOzi and 5 g/L for *n*PrOzi, compared to untreated control. Therefore, the cytotoxicity of 2-oxazines is about one order of magnitude lower compared to MeOx and EtOx [32]. POzi homopolymers were analyzed at concentrations ranging from 0.001 to 100 g/L. Those with a similar DP but different side chain (PMeOzi₅₀ vs. PEtOzi₅₀) showed similar cytotoxicity profiles (IC_{50} approx. 70 g/L). The comparison of PEtOzi₅₀ and PEtOzi₁₅₀ revealed a somewhat higher cytotoxicity (IC_{50} approx. 20 g/L) with increasing DP. *n*PrOzi could not be taken into account due to its lower critical solution temperature at around 12 °C [38] and the associated insolubility at physiological temperature. POx- or POzi-based biomaterials may comprise solely these two polymer families with different side chains, or be combined with other polymers like poly(ϵ -caprolactone) (PCL) [39,40] poly(sarcosine) (PSR) [41], poly(lactide) [42–44] or poly(ethylene imine) (PEI) [45–47]. Most typically, POx have been used as the hydrophilic constituent of amphiphilic block copolymers. Those that contain hydrophobic POx have been also investigated, but considerably less [48]. Recently, Lorson et al. found no dose dependent cytotoxicity up to 10 wt% in NIH 3T3 mouse fibroblast if incubated with PMeOx₅₀-*b*-*n*PrOzi₅₀ for 24 h [35]. Even at concentrations of 25 wt%, cells exhibited more than 80% metabolic activity, which is considered non-cytotoxic (Fig. 2 A). Please note that the aqueous solution of this polymer forms thermoresponsive hydrogels above a certain polymer concentration (which will be discussed in detail in the according chapter). Therefore, incubated cells do not sediment and remain 3-dimensionally distributed after incubation for 24 h (Fig. 2 B).

Very recently, Lübtow et al. reported the outstanding drug formulation capabilities of POx/POzi triblock copolymers (which will be discussed in detail in the according chapter) [36]. These polymers were also tested with respect to their cytotoxicity to different cell types (human dermal fibroblasts, Caco-2 and MD-MBA-231). Even at 100 g/L, no significant cytotoxicity was observed in Caco-2 and human dermal fibroblasts, while the cancer cell line MD-MBA-231 experienced a marked cytotoxicity with an IC_{50} of 10 g/L. This unexpected observation will require a more detailed investigation as it may have potential implications in cancer therapy, although the required polymer concentration is

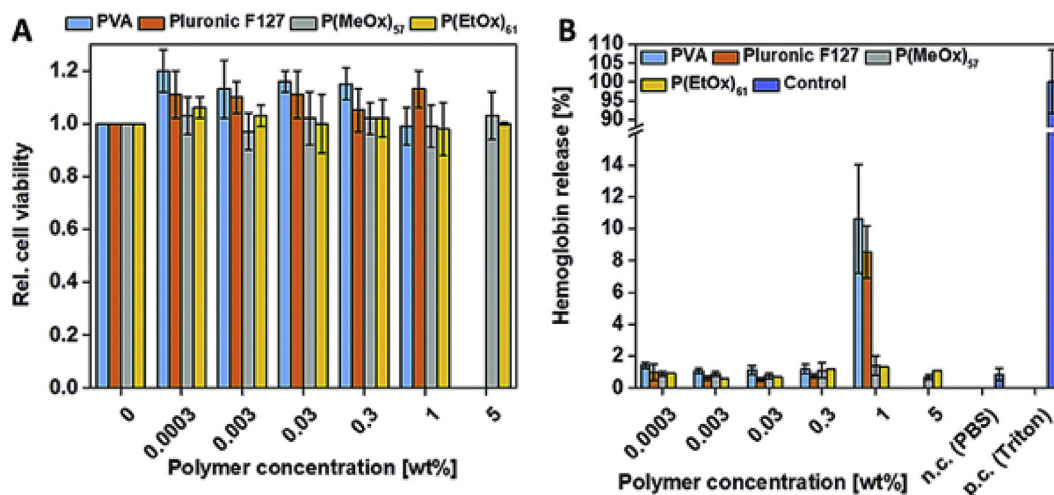


Fig. 1. Concentration dependent cytocompatibility of different non-ionic polymers suitable as surfactants in nanoemulsions. (A) Cell viability after incubation with poly(vinylalcohol) (PVA), Pluronic® F127 and two POx, PMeOx and PEtOx using AlamarBlue® assay, normalized to negative control. L929 cells were treated for 24 h with the indicated concentrations of the polymers. Values represent means \pm S.D. ($n = 3$). (B) Hemoglobin release of erythrocytes after incubation for 60 min at 37 °C with polymers at indicated concentrations. A value of less than 2% hemoglobin release is classified as non-hemolytic and >5% as hemolytic. Values represent means \pm S.D. ($n = 3$). Reprinted with permission from ref [33]. Copyright 2017 The Royal Society of Chemistry.

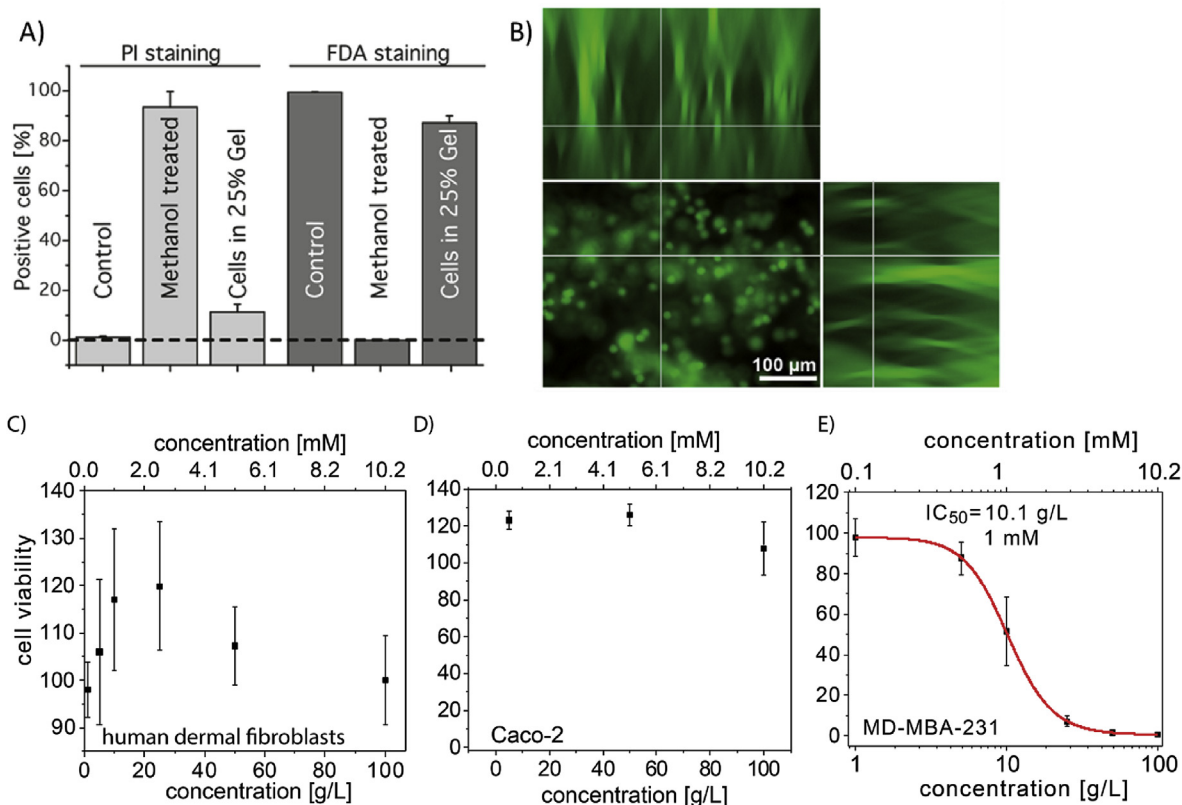


Fig. 2. A) Cell viability of NIH 3T3 fibroblasts and B) z-stack image of FDA stained cells, 24 h at 37 °C after incorporation into the aqueous solutions of PMeOx_{50} - b-PnPrOz_{150} (25 wt %), which forms a hydrogel at physiological temperature. The total volume in (B) comprises 559.54 μm (x) \times 419.25 μm (y) \times 355 μm (z) with 1 μm z-interval. Reprinted with permission from ref. [35]. Copyright 2017 American Chemical Society. C)–E) Cell viability for indicated cell lines upon incubation with the amphiphilic triblock copolymer $\text{PMeOx-b-PnPrOx-b-PMeOx}$ as determined by CellTiter-Glo[®] assay. Cells were incubated for 24 h (Caco-2) and 72 h (human dermal fibroblasts and MD-MBA-231), respectively. Reprinted, with modifications, from Ref. [36].

rather high.

Similar to POx, polypeptoids (POI) also belong to the group of pseudo-polypeptides and are being discussed as a promising alternative to PEG [49]. Guo and co-workers published a first report combining hydrophobic POx and a hydrophilic polypeptoid (POI) very recently [50]. Specifically, the authors reported the synthesis of amphiphilic POx-*b*-POI copolymers poly(2-but(3-enyl)-2-oxazoline)-*b*-polysarcosine (PButEnOx-*b*-PSR) by ring-opening polymerization via one-pot, three-step synthesis ($M_w = 4.7\text{--}10.8$ kg/mol; $\bar{D} = 1.15\text{--}1.21$) as potential biomaterials for drug delivery and gene therapy. Up to 10 g/L, the block copolymer PButOx₁₉-*b*-PSar₉₂ did not show pronounced cytotoxicity in L929 mouse fibroblasts after incubation for 24 h. This low cytotoxicity together with the small micellar size ($D_h \leq 100$ nm) of the spherical polymer particles in aqueous solution ($\rho(\text{polymer}) = 2$ g/L) makes this amphiphilic hybrid a potential candidate for further investigations in e.g. drug-delivery system.

Zwitterionic polymers are being discussed as promising non-fouling materials, drug delivery systems, implants and coating materials for medical devices. Tauhardt et al. investigated zwitterionic POx based on 1,3-propansultone (SB-POx) and β -propiolactone (CB-POx) modified PButEnOx as candidates for anticoagulants (Fig. 3) [51]. *In vitro* cytotoxicity tests of the homopolymer and copolymers show no cytotoxicity after incubation (24 h) at various concentrations (0.1–10 g/L) (Fig. 3).

Blood compatibility tests also showed no hemolytic effect as the hemoglobin release was below 2% (Fig. 4 A). Blood viscosity was not strongly affected by any of the investigated polymers up to concentrations of 5 g/L. Only a very small increase was noticed at the

highest concentration of 10 g/L (Fig. 4 B) There was no effect on the P-selectin (CD62p) membrane glycoprotein expression in CD42 (surface antigen) positive cells according to platelet activation test. Furthermore, no activation of the complement system was observed (C3a levels were observed) following the incubation with the zwitterionic polymers and the PETox control ($\rho(\text{polymer}) = 1, 5$, and 10 g/L) after incubation for 10, 30 and 60 min, most likely due to the pronounced hydrophilic character of the polymers. Prothrombin time was not affected in a clinically relevant manner (coagulation time >7 and <10 s). In contrast, the activated partial thromboplastin time was significantly affected, for CB-POx even at the lowest tested concentrations of 1 g/L, while PETox did not show any influence on the coagulation characteristics.

Yildirim et al. also synthesized amphiphilic, heterografted comb polymers based on oligomeric polylactide (PLA) and oligo-EtOx-methacrylate (OEtOx-MA) ($M_n = 21\text{--}41$ kg/mol; $\bar{D} = 1.17\text{--}1.37$) as potential drug carriers (Fig. 5 A) [52]. In this contribution, different hydrophilic (OEtOx)/hydrophobic (PLA) ratios were investigated, ranging from 70/30 (P1), 65/35 (P2), 80/20 (P3), 85/15 (P4), to 90/10 (P5). Neither polymer did show any cytotoxicity after 24 h, albeit only extremely low concentrations of up to 0.2 g/L were investigated (Fig. 5 B). One should be careful to consider the polymer as cytocompatible unless higher concentrations are tested.

Wang and co-workers synthesized PETox-*b*-poly(_{D,L}-lactide) (PETox-*b*-PDLLA) diblock copolymers that were also suggested for use as drug carrier for intravenous (i.v.) administration [53]. The hemolytic activity, platelet activation, blood coagulation and protein adsorption of PETox-*b*-PDLLA micelles was investigated and did not reveal problematic results. At all tested polymer

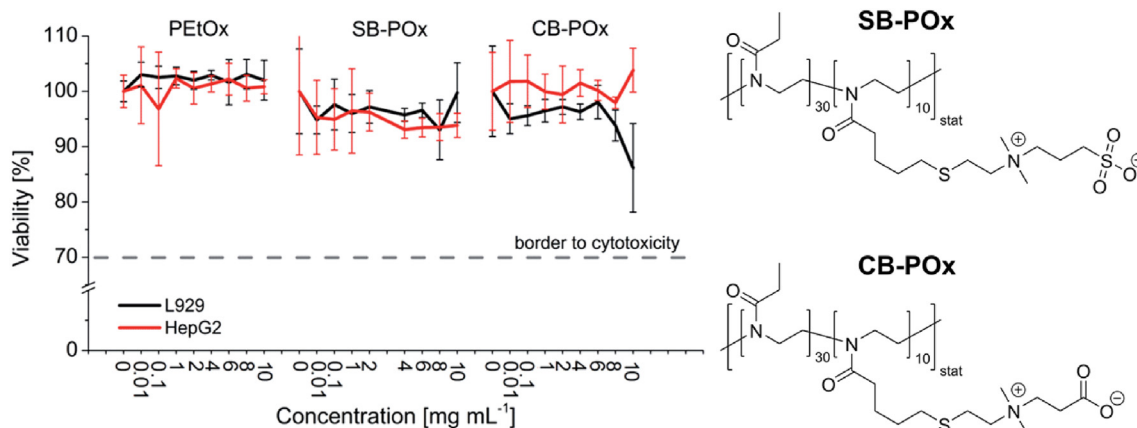


Fig. 3. Cell viability of L929 mouse fibroblasts and human hepatocytes HepG2 after incubation with zwitterionic polymers SB-POx and CB-POx (right side) up to 10 g/L after 24 h. Cells incubated with polymer free culture medium served as control. The cell viability was determined by XTT assay according to ISO 10993-5. Data are expressed as means \pm SD ($n = 6$). Reprinted with permission from ref. [51]. Copyright 2014 The Royal Society of Chemistry.

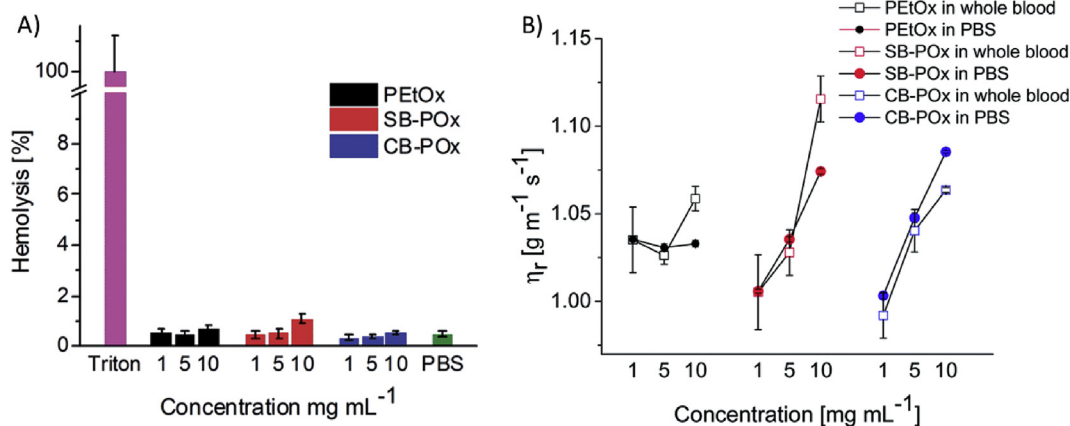


Fig. 4. (A) Photometric determination of hemolytic activity after incubation with different polymer concentrations for 1 h at 37 °C. Triton X-100 (1%) served as positive and PBS as negative control. Experiments were run in triplicate and were repeated once; data are presented as means \pm SD compared to the positive control set as 100%. (B) Blood compatibility of PETox and zwitterionic POx-based polymers concerning their influence on the whole blood viscosity: relative viscosity of the polymer solutions in PBS and in whole blood. Experiments were run in quadruplicate at three inclination angles, data are presented as the means \pm SD. Reprinted with permission from ref. [51]. Copyright 2014 The Royal Society of Chemistry.

concentration hemolysis percentage was below 0.3% and only $0.25 \pm 0.18\%$ hemolysis was detected at the highest (albeit still rather low) tested concentration of 0.82 g/L. *In vitro* blood coagulation study also did not reveal any significant effect of PETox-*b*-PDLLA on the blood/erythrocytes aggregation. Moreover, protein interaction, platelets activity and cytocompatibility did not show any significant effects at block copolymer concentration up to 12 g/L and 24 h incubation. Accordingly, this preliminary analysis suggests that PETox-*b*-PDLLA are potential candidates for further evaluation just as their well-established PEG analogs are.

The possibility to incorporate a positive charge into polymers opens up manifold opportunities in various biomedical applications such as drug delivery, gene engineering, tissue engineering, and cell encapsulations. PEI is one of the most intensively investigated polycations for biomedical applications. Due to its high condensation capability towards DNA, strong buffering capacity in a pH range of 5.1–7.4, and relatively high transfection efficiency, PEI is used for non-viral vectors design. However, the high charge density also contributes to its pronounced cytotoxicity. This problem has been addressed by partial hydrolysis of the POx, yielding P(Ox-co-EI). Early studies investigated P(Ox-co-EI) with at least 56 mol% EI [45,54]. Hoogenboom and co-workers studied

biocompatibility of partially hydrolyzed POx with a EI content ranging from 0.025 wt% (5 mol% EI) to 0.515 wt% (75 mol% EI) [55]. They used commercially available PETox with a molecular weight of 200 kDa, performed acidic hydrolysis and utilized human dermal fibroblast cells for toxicity test at concentrations up to 5 g/L. Compared to untreated PETox, up to 43 mol% EI, the cytotoxicity of P(EtOx-co-EI) was similar to PETox which did show some reduced cell viability compared to control, despite the relatively low concentrations. Increasing the degree of the hydrolysis up to 71% entails high cytotoxicity comparable to linear PEI. Important to note, the relatively high cytotoxicity of PETox reported in this study is in some contradiction to other reports, where comparable levels of cytotoxicity were typically found at higher concentrations of hydrophilic POx or PETox [30,48]. However, since the cell viability can be quite cell type specific, this nicely demonstrates that one has to be careful in generalizing “biocompatibility” of biomaterials from simply cytotoxicity tests with a few selected cell lines/types. Furthermore, the slug mucosal irritation test was applied to perform a simple but informative *in vivo* experiment. PETox and the P(EtOx-co-EI) with up to 25 mol% PEI show minimal mucus production that was on average lower compared with the negative control (PBS) indicating that they are non-irritating. Additionally,

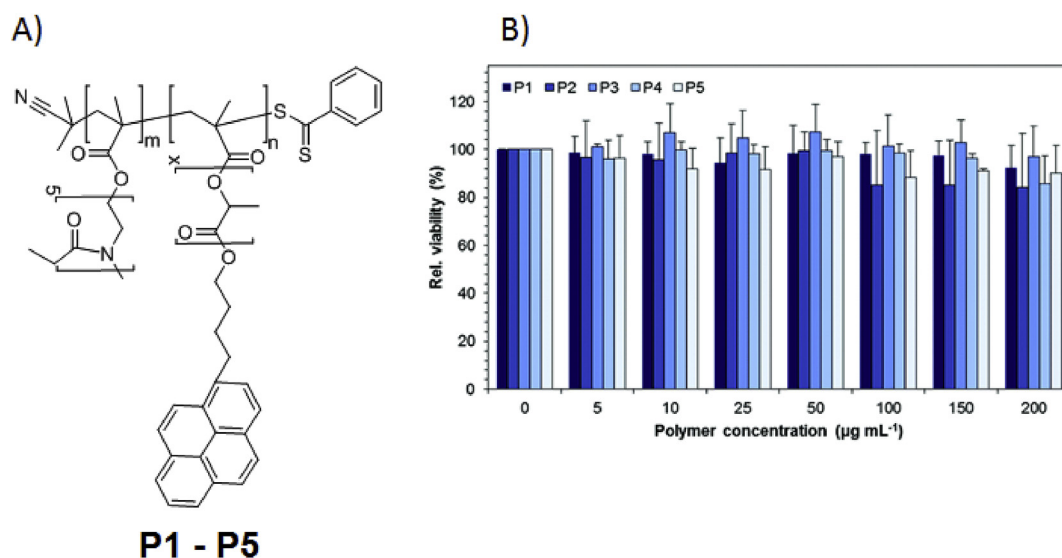


Fig. 5. (A) Schematic representation of the heterografted comb polymers obtained via RAFT polymerization. The molar ratios m/n defining the hydrophilic/hydrophobic balance were 70/30 (P1), 65/35 (P2), 80/20 (P3), 85/15 (P4), to 90/10 (P5). (B) Relative cell viability of L929 cells after 24 h of incubation with heterografted comb polymers (P1 to P5) at the indicated concentrations. Values represent the means \pm S.D. ($n = 3$). At these low concentrations, no cytotoxicity was found. Reprinted with permission from ref. [52]. Copyright 2016 The Royal Society of Chemistry.

no lactate dehydrogenase (LDH) release was induced implying that no tissue damage was caused. Polymers with a higher L-PEI content resulted in a mucus production that was statistically comparable with the negative controls and led to LDH release in one of five tested slugs. It is important to note that the described hydrolysis of POx only occurs at a reasonable rate under biologically irrelevant conditions (5.8 M HCl; $> 80^\circ\text{C}$). This is important to keep in mind regarding their use as biomaterials.

In 2015, Kronek et al. revisited this issue and reported *in vitro* studies of partially hydrolyzed PEtOx [56]. Cytotoxic studies were performed using copolymers with different molar mass (8–36 kg/mol), degree of hydrolysis (3–60 mol% PEI) using fibroblasts as the most common cells in connective tissue, βTC3 cells as secretory and regulatory cells and macrophages P388.D1 as the cells of immune system. Obtained results corroborated earlier work in that increasing degree of hydrolysis decreased the cell viability in all cases. The highest cytotoxic effect was seen for 19.6 kg/mol and a PEI content of 50 mol%. More detailed analysis of the dependence of the cytotoxicity on PEI content was done with PEtOx - 9.6 kg/mol (Fig. 6 A) and PEtOx - 19.6 kg/mol (Fig. 6 B) at concentrations of up to 20 g/L. After 48 h of incubation (0 mol% of EI), a partial decrease of cell viability was observed in the βTC3 and macrophages, while fibroblasts were unaffected. Not surprisingly, the cytotoxicity increased with increasing degree of hydrolysis, concentration and incubation time. Regarding partially hydrolyzed copolymers, it is evident that cytocompatibility is cell-type dependent with fibroblasts having the highest viability in this study and macrophages, as representatives of the immune system, being the most sensitive cells. PEtOx-19.6 kg/mol with a degree of hydrolysis of 59% (P388.D1; 48 h) showed a cytotoxicity comparable to PEI. The reason why the medium size copolymers exhibit the highest cytotoxicity remains unclear but again, corroborates findings by Bauer et al. [30,31].

Hsiue and co-workers also attempted to revisit block copolymers of PEtOx and a mixed P(EtOx-co-EI) block obtained by partial hydrolysis. Unfortunately, the presented synthetic route does not allow for any controlled synthesis and no adequate characterization of the resulting polymers is provided. Insufficient materials characterization notwithstanding, the commonly

observed trend that low hydrolysis degree results in relatively cytocompatible materials while high degree of hydrolysis leads to pronounced cytotoxicity is also found in this contribution [57].

England et al. investigated the cytocompatibility of poly(L-lysine) (PLL) dendrimers grafted with POx or PEG intended for use as drug carriers [58]. The molar mass of the studied polymer grafts was 2 kg/mol. Cytotoxicity studies confirmed that POx and PEG modified dendrimers were leading to less apoptosis than the unmodified dendrimer (2–3% compare to 36% for unmodified dendrimer) at a concentration of 0.5 g/L. Blood compatibility studies also showed that POx and PEG modified dendrimers did not result in hemolysis or red blood cell aggregation at 2 g/L.

Wang et al. recently reported a comparative study on the stealth properties of nano-graphene oxide grafted with PEG and PEtOx [59]. The protein corona cytotoxicity and haemolysis of the materials was investigated. While similar levels of complement proteins were found associated with the grafted nano-graphene oxide, some distinct differences in the protein corona were found.

2.2. POx for immunomodulation and immunocamouflage

Kronek and co-workers investigated possible immunomodulatory effects of POx prior to the period in focus of the present review [60,61]. These studies were later backed up by further work by the same group. Specifically, the activation of mouse lymphoid macrophages P388.D1 using PEtOx and a copolymer of EtOx and 2-(4-aminophenyl)-2-oxazoline (P(EtOx-co-AmPheOx)) [62]. The release of reactive oxygen species (ROS) and pro-inflammatory cytokines was investigated. Interestingly, PEtOx at 5 g/L was found to lead to a moderate increase in IL-1 α , IL-6 and TNF- α , as well as ROS levels compared to control. In contrast, P(EtOx-co-AmPheOx) only led to a minor increase in ROS. The authors try to put the results in context with the polarity of the two polymers. However, it should also be mentioned that the AmPheOx monomer leads to side reactions during polymerization, which is clearly apparent by the very large dispersity for this polymer. This can be easily understood as a free amine will lead to termination reactions and the resulting polymer will have invariably an unknown but likely very complex structure. Therefore, structure-

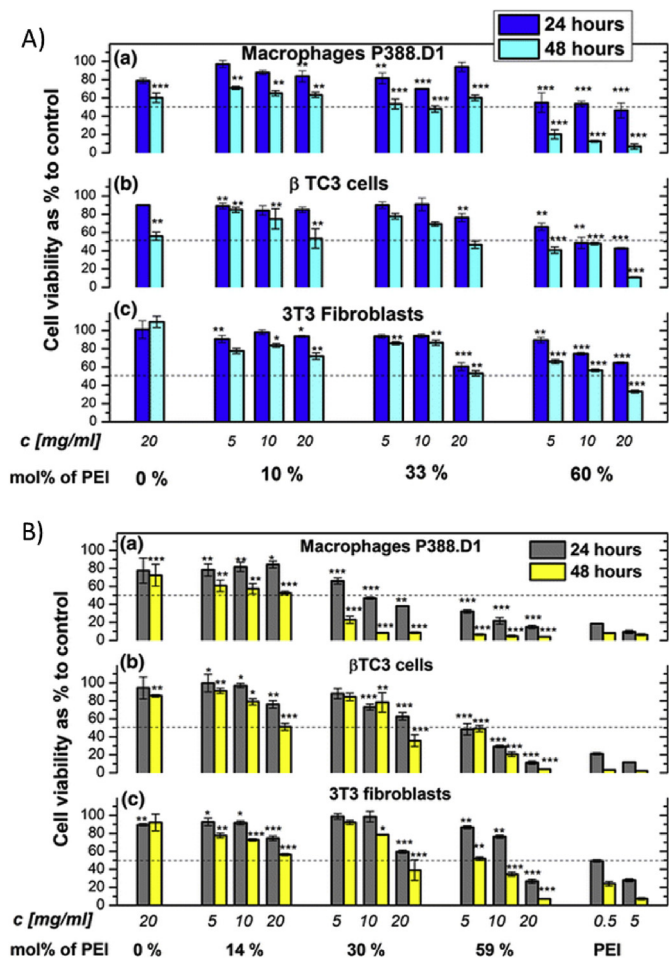


Fig. 6. (A) The cell viability of partially hydrolyzed PETox (9.6 kg/mol) with 10, 33 and 60 mol% degree of hydrolysis and (B) PETox (19.6 kg/mol) with 14, 30 and 59 mol% degree of hydrolysis after 24 and 48 h incubation in DMEM at 5, 10, and 20 g/L of copolymer. The MTT assays were performed using macrophages P388.D1 (a), pancreatic β TC3 cells (b), and 3T3 fibroblasts (c). The dashed line indicates the IC_{50} value. Mean viability and a standard deviation (SD) were computed for each group from triplicates ($n = 3$). Statistical significant difference in viability between the samples treated cells and untreated control is shown as * for ($P=0.05$), ** for ($P=0.01$), and *** for ($P=0.001$), using Dwass-Steel-Critchlow-Fligner post hoc test. Reprinted with permission from ref. [56]. Copyright 2015 Springer Science + Business Media.

property relationships should be viewed with great care. In our opinion, a careful study using a larger library of well defined POx with varying hydrophilic/lipophilic balance seems to be warranted to address this interesting and important point. As part of their research on PIPOx, Kronekova et al. observed a slight increase in apparent cell viability in P388 cells, which, according to the authors suggest the potential for immunomodulatory properties. This was backed up by a stimulatory effect of PIPOx on spleen cells [32].

Kyluik-Price and co-workers compared the ability of PETox and mPEG to protect blood cells from immune surveillance [63]. For this, both polymers were covalently grafted onto human red blood cells (RBC). The authors studied RBC morphology after grafting and report a slightly better result in the case of 30 kg/mol PETox compared to 30 kg/mol PEG. Apart from this, in the majority of experiments in this study, PETox and PEG were quite comparable. However, overall it was found that at similar surface grafting, mPEG exhibited superior immunocamouflage properties. This was demonstrated by antibody binding and phagocytosis of opsonized RBC. Testing the opsonization of PETox and PEG conjugated RBC,

the PEG modified RBC outperformed the PETox modified RBC. Regarding the comparison of PEG and POx of various molar masses, we would like to note an important difference between PEG and POx. Often the argument is made that POx have a lower viscosity than PEG at the same molar mass. This is of course true, and obviously attributable to the fact that the PEG chain length is much greater than the POx chain length at the same molar mass. Whereas one repeat unit for both polymers has similar dimensions regarding extended chain length, the molar mass of POx repeat unit is much higher than that of PEG. For example, the molar mass of PETox repeat unit is 99 g/mol, while in PEG, each repeat unit accounts only for 44 g/mol. In other words, at the same molar mass, the extended polymer chain of PEG is about 2.5 times longer than that of POx. Not surprisingly, this should lead to a higher viscosity of PEG at the same molar mass. Apart from this, it would be interesting to test PMeOx in such assay, as PMeOx is more hydrophilic and slightly more comparable to PEG with respect to the molar mass of the repeat unit.

2.3. Systemic compatibility or stealth properties

In this chapter, we review the knowledge on systemic compatibility and stealth properties of POx based polymers. The bio-distribution of hydrophilic PMeOx and PETox has been investigated before by Goddard et al. [64] as well as Jordan, Essler and co-workers [65]. Also, Woodle et al. reported very early on excellent bio-distribution of POxylated liposomes [23]. More recently, Hoo-genboom and co-workers revisited this issue. In one report, Wyffels et al. investigated the pharmacokinetic behavior of medium and high molar mass PETox and compared it to PEG [66]. The molar masses ranged from 5 kg/mol to 111 kg/mol for PETox and 20 kg/mol and 40 kg/mol for PEG. The polymers were labeled with ^{89}Zr and injected i.v. into mice. Not surprisingly and corroborating other studies, up to 20 kg/mol, the polymers were rapidly excreted via the kidneys. The overall bio-distribution found was similar to previous work by Goddard, including uptake in the skin, with the exception that Wyffels found significant uptake in the spleen for 70 and 111 kg/mol PETox. In a follow-up study, Glasner and co-workers investigated the effect of labels on the apparent bio-distribution [67]. Of course, the radiochemical purity and stability of the label is of great importance when assessing the bio-distribution of labeled compounds. This was corroborated in this contribution, comparing ^{18}F and ^{89}Zr labeled 5 kg/mol PETox. The ^{89}Zr was complexed using desferioxamine, while ^{18}F was covalently attached. It was shown, that the apparent kidney uptake was much higher for the ^{89}Zr labeled polymers, compared to the ^{18}F labeled polymer, with most of the radioactivity being retained in the renal cortex, most likely being attributable to retention in the proximal tubules. Also in this respect, results from an earlier study using ^{111}In labeled PETox (5 kg/mol) [65] were corroborated.

Apart from the bio-distribution of POx polymers themselves, polymer modified liposomes can be seen as a litmus-test for the respective polymer. As mentioned, Woodle reported long circulating liposomes employing POx lipopolymers early on [23]. Szoka, Frechet and co-workers revisited this issue and compared PEGylated and POxylated liposomes with liposomes bearing poly(-vinylpyrrolidone) (PVP), poly(hydroxypropylacrylate), poly(*N,N*-dimethyl acrylamide) (PDMA) and poly(*N*-acryloyl morpholine) (PACM) [68]. Important to note, the size of the liposomes was very similar, but the dispersity differed notably, from $PDI = 0.03\text{--}0.14$, which is quite a significant difference. Most importantly, the bio-distribution of liposomes was evaluated after single injection and after two consecutive injections spaced 6–8 days apart. After single injection, PMeOx (approx. 3 kg/mol as determined by mass spectrometry while the molar mass determined by GPC was much

higher) modified liposomes performed similar to PEGylated liposomes. Both outperformed all other liposomes in terms of circulation time ($t_{1/2} \approx 30$ h) and liver uptake (Fig. 7 A). An entirely different, essentially inverted picture presented when the labeled and polymer modified liposomes were injected a week after the first injection (Fig. 7 B). Here, both PEGylated and POxylated liposomes exhibited very short blood pool residence ($t_{1/2} < 2$ h), while the blood circulation of all other liposomes was essentially unaltered. Importantly, POxylated liposomes were unaffected by previous administration of PEGylated liposomes. The authors could connect the accelerated blood clearance with a pronounced increase in immunoglobulin M (IgM). Notably, these findings are somewhat contrasting data by Moreadith and co-workers, who could not elicit any antibody response for a copolymer of EtOx and 2-(pent-4-ynyl)-2-oxazoline (PynOx) [22]. Obviously, both materials were significantly different being a polymer modified liposome and a presumably unaggregated polymer chain, respectively. Moreover, in one case, essentially PMeOx was employed while a PEtOx copolymer was used in the other case. It should also be mentioned that some aspects of the polymer characterization are somewhat ambiguous. While the dispersities of the lipopolymers are quite low as determined by Maldi-ToF mass spectrometry, much higher values ($\bar{D} = 1.2$ and 1.5, as determined by GPC) are found in the supporting information.

Apart from liposomes, nanoparticles have been coated with hydrophilic polymers to provide stealth properties and to improve their blood circulation. Bludau and co-workers investigated the POxylation (i.e. the covalent modification of another entity such as proteins, drugs or particles with POx) of tobacco mosaic virus particles with PMeOx and its effect on the circulation of the particles *in vivo* [69]. It was reported that POxylation afforded a higher degree of polymer coating of the virus particles, compared to PEGylation. This was tentatively attributed to a different degree of hydration of the two polymers. In accordance with the higher coating density, the POxylated virus particles were better shielded from antibody recognition, as assessed by ELISA assay. Similarly, uptake by RAW 264.7 macrophages was reduced for the POxylated virus particles compared to PEGylated ones. Subsequently, the clearance of the polymer modified virus particles was investigated *in vivo*. The data suggest a somewhat slower initial clearing for the POxylated particles compared to the PEGylated ones. However, the difference was not pronounced and the initial clearing half-lives were very short in both cases. Moreover, considering a potential reduction of the immunogenicity of the virus particles by the polymer, a repeated injection experimental setup would have been

interesting.

Berke, Kampmann et al. reported on a novel strategy to radio-label nanoparticles to investigate their biodistribution [70]. An amphiphilic and telechelic block copolymer ($P[\text{MeOx}_{31}\text{-}b\text{-(2-heptyl-2-oxazoline}_4\text{-co-PynOx}_5)] = P[\text{MeOx}_{31}\text{-}b\text{-(HeptOx}_4\text{-co-PynOx}_5)]$ bearing a di-*tert*-butylfluorosilane moiety introduced via the initiator route was used as a reactive emulsifier. The micelles formed by the polymer were swollen with different amounts of 1,6-hexanediol dimethacrylate and subsequently crosslinked via free radical polymerization. The resulting nanoparticles ranged in size from 20 to 70 nm (hydrodynamic diameter) and were radiolabeled with simple isotope exchange using ^{19}F and investigated with respect to their biodistribution in tumor bearing (EMT6 shoulder grafts) mice using PET. Most of the injected nanoparticles ended up in the liver. While tumor-to-muscle ratio was reasonably high, the tumor-to-organ ratios in the organs of the mononuclear-phagocyte system were not quite promising. Tumor uptake was highest for 33 and 42 nm nanoparticles.

The biodistribution of an amphiphilic POx ABA triblock copolymer (10 kg/mol) with a modestly hydrophobic central B block (PMeOx-*b*-PBuOx-*b*-PMeOx) used as a drug carrier (*vide infra*) was investigated recently by He et al. [71]. The polymer was labeled using ^{64}Cu and biodistribution was evaluated by positron emission tomography (PET) and post-mortem necropsy. Interestingly, the biodistribution of the amphiphilic polymer mirrored that of a purely hydrophilic POx of the same molar mass. First-pass renal clearance with very little non-specific organ uptake was observed.

Kronek and co-workers also tested the toxicity of PEtOx and an amphiphilic copolymer P(EtOx-co-ButEnOx) to terrestrial plants, specifically seeds of *sinapis alba* [72]. No clear trends were found. In particular, at higher concentrations, no toxicity was found. At lower concentration, PEtOx with a DP of 100 exhibited some growth stimulation while P(EtOx-co-ButEnOx) (DP 100) exhibited growth inhibition, which were deemed significant. However, as PEtOx₂₀₀ exhibited growth inhibition in the same assay and any differences vanished at higher concentration, any deduction of actual structure-property relationships should be considered with utmost caution at this point.

2.4. Systemic toxicity

He et al. investigated the toxicity of PMeOx-*b*-PBuOx-*b*-PMeOx. In mice, the maximum tolerated dose was determined to be 500 mg/kg (i.v., q4dx4), corroborating the excellent biocompatibility profile of POx reported in other studies. For single

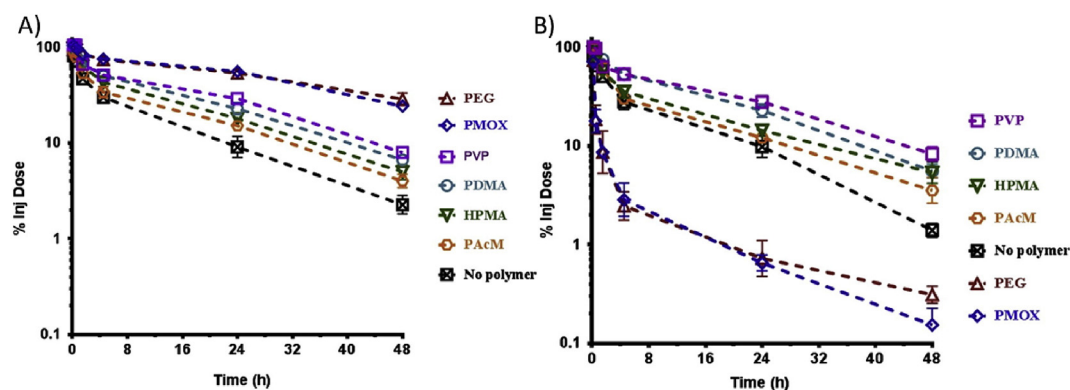


Fig. 7. Comparison of biodistribution (here: blood circulation) of polymer modified liposomes after a single injection (A) and a second injection one week after a first injection (B). Polymers investigated were poly(ethylene glycol) (PEG), PMeOx (here PMOX), poly(vinylpyrrolidone) (PVP), poly(hydroxypropyl acrylamide) (HPMA), poly(*N*-acryloyl morpholine) (PAcM) and poly(dimethyl acrylamide) (PDMA). As control, liposomes without lipopolymer modification were also studied. Reprinted with permission from ref. [68]. Copyright 2015 Elsevier.

administration, even higher doses were tolerated. Clinical chemistry and histology of major organs showed no major effects of the polymer after injection in Balb/c mice at MTD [71]. Also, neither platelet aggregation, hemolysis nor complement activation was observed at concentrations up to 1.52 g/L. On the one hand, this concentration is not particularly high, but since the polymer enables very high drug loading (*vide infra*) of approx. 50 wt%, this corresponds to a very high drug dose that can be safely administered. The blood coagulation parameters prothrombin time and thrombin time were not affected while the activated partial thromboplastin time was significantly prolonged. We would like to remind the reader, that Tauhardt et al. observed a similar effect for zwitterionic POx [51] but not for PEtOx (*vide supra*).

Akbulut and co-workers investigated the effects of PEtOx exposure on the development of ovarian follicle of zebrafish (*Danio rerio*) [73]. Unfortunately, the authors did not give any information regarding the used PEtOx, neither source, purity, molar mass nor dispersity are provided. Nevertheless, these studies appear to be the first studies of POx in zebrafish. Two concentrations of PEtOx in the aquaria were tested (10 mg/L and 50 mg/L) with exposure of 5 days. Such concentrations are well below the concentrations, for which any cytotoxicity would be expected in cell culture. The authors report that PEtOx induces apoptosis and inhibits oogenesis in female zebrafish. Even though the work by Akbulut lacks fundamental aspects of scientific work such as proper identification of materials studied, it would be interesting if these results could be reproduced using defined POx and different POx with variable molar mass.

One obvious application for hydrophilic polymers in a biomedical context are hydrogels. In turn, hydrogels are very interesting materials for an intraocular usage. For this purpose, it is necessary to investigate the respective long term *in vivo* biocompatibility. In 2013, Hwang et al. published a comparative study investigating the intraocular biocompatibility of PEtOx-*b*-poly(ϵ -caprolactone)-*b*-PEtOx (ECE), Matrigel® and Pluronic® F127 in albino rabbits [74]. After 2 weeks, Matrigel as well as Pluronic® F127 dispersed in the vitreous (Fig. 8 left side, Row B). In contrast, ECE hydrogel was still detectable. Furthermore, severe cataract with iris atrophic change was found in eyes containing Matrigel® or F127 two month after

injection. (Fig. 8 Insert, Row C). The authors attribute the ocular toxicity of Matrigel® to its biological origin (mouse-derived) while the cause of toxicity of F127 is unknown. Optical coherence tomography (OCT) revealed that the retina of the F127 and Matrigel® treated eyes were atrophic, whereas the retinal thickness of the ECE containing eye was still comparable to the control. Furthermore, electroretinography (ERG) was examined to evaluate the physiological retinal functions. Again significant decrease of the photoreceptor signals were observed for the Matrigel® and the Pluronic® treated eyes, while ECE injection revealed no significant changes compared to pre-injection. Furthermore, retinal histology demonstrated neither necrosis nor morphological changes in the ECE eyes. In contrast, the Matrigel® and the Pluronic® eyes showed signs of neuroretinal toxicity. The drastic loss of photoreceptors after injection of Matrigel® or Pluronic® was visualized via TEM micrographs (Fig. 8 right side) supporting the ERG results. The ECE eyes showed similar morphology as the control group. These results highlight the potential of POx-based hydrogels for biomedical applications while at the same time illustrates major issues for Pluronic® based gels or even Matrigel® which are both used widely in tissue engineering and biology *in vitro*.

2.5. Degradability

Every time exogenous materials are brought into the body, the question of their removal and degradability needs to be asked. As already mentioned above, POx are amendable to acidic and basic hydrolysis. However, at physiological conditions no significant hydrolysis was observed in simulated stomach and intestine fluid [55]. Of course, this is not the only possibility for the degradation of polymers. Another mechanism, relevant in a biological context is oxidative degradation by reactive oxygen species (ROS). Despite the fact that ROS are of major importance in physiological and pathological processes, generally little information can be found in the literature on the oxidative degradation of hydrophilic polymers/biomaterials in water. Although PEG and POx are in most cases regarded as non-biodegradable, PEG is long known to be sensitive to oxidative degradation [27,75]. Without giving any experimental data, Viegas et al. suggest that POx do not form

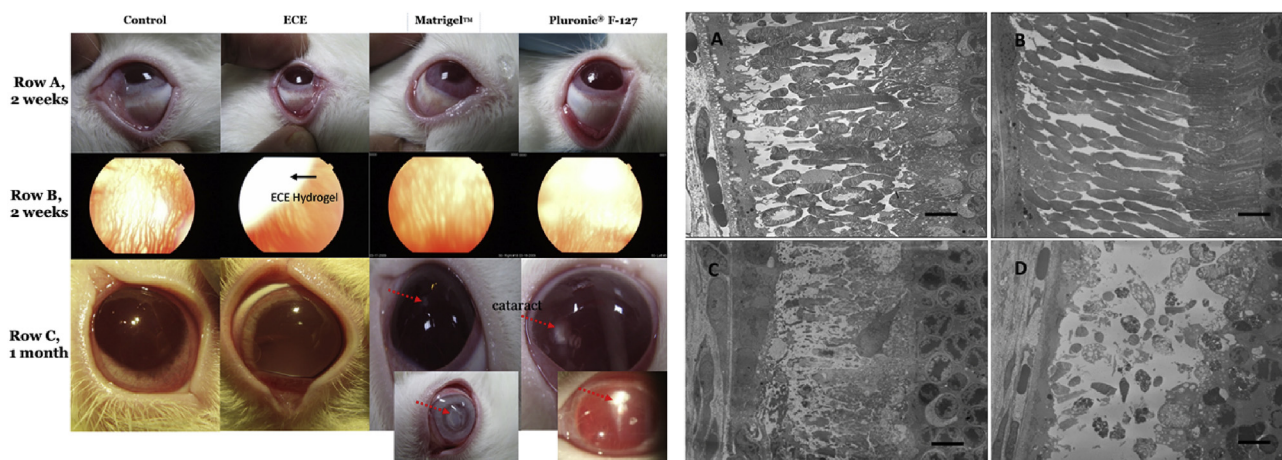


Fig. 8. Left Side: (**Row A**) External photos of control, 20 wt% PEtOx-*b*-poly(ϵ -caprolactone)-*b*-PEtOx (ECE) hydrogel, Matrigel®, and Pluronic F127® at two weeks after injection (from L to R). (**Row B**): The fundus oculi of control, 20 wt% ECE hydrogel, Matrigel, and Pluronic F127® at two weeks after injection (from L to R). (**Row C**) The external color photos of control, 20 wt% ECE hydrogel, Matrigel, and Pluronic F127 for ocular media at one month after injection (from L to R). The red arrows indicate the cataract formation. The black arrow indicates the ECE *in situ* hydrogel formation. The inset photo of Matrigel is at two months after injection, which had a denser cataract formation and perilimbal ciliary injection. The inset photo of Pluronic F127® is the high magnification of the cataract. Right Side: TEM micrographs of the outer retina, which demonstrates the morphology of outer nuclear layer (cell body of rod and cone cells). The control eyes (A), the 20 wt% ECE hydrogel (B), Matrigel® (C), Pluronic F127® (D) after two months of injection. (C) and (D) demonstrate more cell loss than ECE and control eyes. (scale bar is 6.1 μm). Reprinted with permission from ref. [74]. Copyright 2013 Public Library of Science (PLOS).

peroxides as PEG does [76]. In contrast, Luxenhofer and co-workers reported that PEG, POx and POI are degradable by oxidative degradation under conditions that have been claimed biologically relevant by others [77]. For their study, PEG, PEtOx and the watersoluble polypeptoid poly(*N*-ethylglycine)s with molar mass ranging from 2 to 11 kg/mol were used. The development of the apparent molar mass after incubation with different concentration of reactive oxygen species (ROS), generated from H₂O₂ and Cu(II) as catalyst, was determined as degradation. Surprisingly, the results show that PEG is the most stable of the three at peroxide concentrations below 50 mM, while there was no difference in the absence of catalyst. It was also found that the apparent degradation rate was dependent on the DP and molar mass, respectively. More recently, this study was expanded to higher molar masses and also to include poly(*N*-vinylpyrrolidone) (PVP) [78]. The trend that higher molar masses are degraded faster was corroborated, as was the result that PEG is more stable in this assay than PEtOx. These observations stand in contrast to the notion by Viegas and also to a report by Pidhatika et al., that showed that POx-modified surfaces retained their non-fouling character longer than PEG-modified ones when challenged with oxidative stress [79]. Taken together, these studies only begin to let us understand the stability of POx against oxidative degradation, and it is important to note that the actual concentration of ROS *in vivo* is difficult to assess and may be highly variable.

Recently, Luef et al. investigated the degradation of a poly(-EtOx₁₀₀-co-NonOx₅₀-co-ButEnOx₃₀) based hydrogel (UV-cross-linked with glycol dimercaptoacetate) at various pH values in the presence and in the absence of esterases [80]. Degradation was quantified through the release of encapsulated Eosin B (8 mg Eosin B per 2 g copolymer) by UV/Vis absorption. At the lowest investigated pH of 4, no degradation could be observed even after 2 weeks in the absence of enzymes. At pH 6 slight degradation started approx. after 8 days storage and after 14 days, 10% Eosin B were released. In general, the rate of dye release increased with increasing pH. However, still only modest release of 20% Eosin B occurred after 14 days at pH 10. Interestingly, degradation in the presence of rabbit liver esterase (RLE) at pH 8 was found to be very close to enzyme-free degradation at pH 10. The by far highest degradation was realized with porcine liver esterase (PLE) at pH 8 (Fig. 9). Unfortunately, the authors did not suggest any explanation,

as to why PLE is more effective than RLE.

Very recently, Kronek and co-workers also investigated the issue of degradability of POx using activated sludge (OECD guideline 209) [72]. Four different polymers were investigated, PEtOx and an amphiphilic copolymer P(EtOx-co-ButEnOx) with targeted DPs of 100 and 200 each. It should be noted that the synthesis of the higher degrees of polymerization apparently proved challenging, as the determined molar masses were much lower than expected, in case of PEtOx₂₀₀, the M_n (determined by GPC) was actually lower than that of PEtOx₁₀₀. The authors tested to oxygen consumption of activated sludge in the presence and absence of POx and found no difference, suggesting that these POx and perhaps POx in general cannot be degraded by activated sludge.

Summarizing the knowledge on safety of POx and interaction with biological systems, one can state that in general the picture has become much more detailed in the last few years. It has become evident beyond reasonable doubt that POx can be designed such that further development POx-based biomaterials into actual products seems feasible. However, some studies are raising important questions and indicate that, at least in certain circumstances, POx may not be able to overcome limitations seen also in other systems. Of course, any new material must always be thoroughly studied and scrupulously tested with respect to its safety. This process often starts with simple cytocompatibility studies. In this context, we'd like to posit a few comments and suggestions. First, it is always advisable to test new materials up to maximal concentrations possible in a given assay. In many reports, authors test their polymers only to a few hundred mg/L and deduce general biocompatibility from such miniscule concentrations. It is obvious that different cell lines may give a very different read-out, some may be robust, others may be more sensitive. Regarding endocytosis studies, also too often one finds very basic experimental protocols, where only one or a few concentrations and/or few time points are studied. A full concentration range is a prerequisite to properly assess concentration-dependent effects. The question of medium and long-time fate of POx in a biological and environmental context is insufficiently understood and should be studied with carefully designed experimental protocols. No doubt, the community will be following the further development of SER-214 very closely. To the best of our knowledge, at least four more companies (apart from Serina Therapeutics Inc.) have recently started evaluating commercial development of POx. In combination with the recently boosted academic interest, one can expect much more detailed information on the safety of POx in the near future.

3. POx-based hydrogels in biomaterials

In recent years, many excellent reviews have described the importance of hydrogels as soft biomaterials in tissue engineering, medicine as well as for the new and upcoming field of bio-fabrication [17,81–83]. In general, any watersoluble polymer can serve as a basis for hydrogels after cross-linking. Accordingly, POx-based hydrogels have been established for decades. Chujo and co-workers reported in a series of papers on POx based hydrogels [84–91]. In this series, thermo- and redox-responsive POx-based hydrogels were pioneered. Due to their good cytocompatibility, combined with tunable physicochemical properties, hydrophilic POx are ideally suitable as hydrogel based biomaterials. This was already summarized in a comprehensive review by Hartlieb et al. in 2015 [18] in which the authors focused on chemically cross-linked gels. These are polymeric networks based on covalently cross-linked macromolecules. According to the authors, POx-based hydrogels can be subdivided into three main classes: (1) polymeric networks that are formed *in situ* by the copolymerization of mono- and bis-functional monomers, (2) hydrogels prepared via

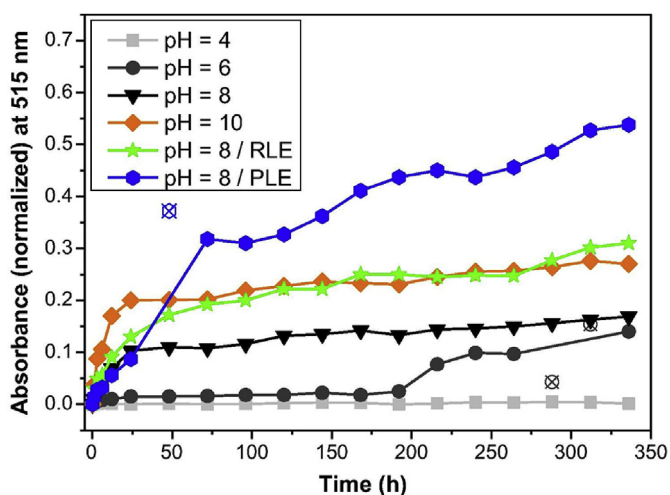


Fig. 9. (Normalized) Absorbance at 515 nm for the quantification of the released dye Eosin B during degradation studies of cross-linked poly(EtOx₁₀₀-co-NonOx₅₀-co-ButEnOx₃₀) at different conditions. Reprinted with permission from ref. [80]. Copyright 2017 Elsevier.

4.2 Polymer-Drug Compatibility

The impact of the smallest changes in the chemical structure of the polymeric drug carrier on the drug loading capacity became apparent when comparing POx and POzi based formulations of poorly water soluble PTX and CUR. By formally shifting a single methylene unit from the polymer sidechain (POx) to the polymer mainchain (POzi) of the core-forming monomer units caused distinct specificities for both hydrophobic compounds. Moreover, the co-formulation, *i.e.* simultaneous solubilization of both compounds with the same drug carrier, resulted in either synergistic or antagonistic solubilization patterns depending on the chemical structure of the polymer amphiphile. Solvatochromic Reichardt's dye showed a remodeling of the micellar microenvironment in the presence of PTX. Unexpectedly, highly hydrophobic PTX seemed to establish a more polar microenvironment which was attributed to the large number of polar moieties present in PTX. This gave first hints that the common perception of hydrophobic drugs being more or less unspecifically incorporated into the hydrophobic core should be regarded with great care. Apart from that, the extraordinary high LCs and small micellar sizes even at high drug loading suitable for IV administration showed the therapeutic potential of the first ever reported POzi based drug formulations. A more profound evaluation of the respective CUR formulations from a pharmaceutical point of view will be presented in chapter 4.4.

Drug Specificity, Synergy and Antagonism in Ultrahigh Capacity Poly(2-oxazoline)/Poly(2-oxazine) based Formulations

Michael M. Lübtow, Lukas Hahn, Malik Salman Haider, and Robert Luxenhofer*¹

Functional Polymer Materials, Chair for Chemical Technology of Material Synthesis and the Bavarian Polymer Institute, University of Würzburg, Röntgenring 11, 97070 Würzburg, Germany

S Supporting Information

ABSTRACT: Polymer micelles offer the possibility to create a nanoscopic environment that is distinct from the bulk phase. They find applications in catalysis, drug delivery, cleaning, etc. Often, one simply distinguishes between hydrophilic and hydrophobic, but fine-tuning of the microenvironment is possible by adjusting the structure of the polymer amphiphile. Here, we investigated a small library of structurally similar amphiphiles based on poly(2-oxazoline)s and poly(2-oxazine)s with respect to their solubilization capacity for two extremely water insoluble drugs, curcumin and paclitaxel. We found very significant and orthogonal specificities even if only one methylene group is exchanged between the polymer backbone and side chain. More strikingly, we observed profound synergistic and antagonistic solubilization patterns for the coformulation of the two drugs. Our findings shed new light on host–guest interaction in polymer micelles and such pronounced host–guest specificities in polymer micelles may not only be interesting in drug delivery but also for applications such as micellar catalysis.

Poor water solubility of the majority of drugs remains a tremendous challenge in pharmaceutical technology, despite decades of research and development. According to Ali and Kolter of BASF: “The continued trend of increased number of poorly soluble and permeable molecules is alarming and has brought the industry nearly to a standstill. The work continues to overcome these formulation challenges to find the appropriate solutions for these poorly soluble and permeable molecules.”¹ Polymer micelles have been discussed and evaluated as carriers for hydrophobic molecules for many years² but have limitations in the context of drug delivery. Despite tremendous efforts, few polymer micelles have been approved by regulatory agencies. One major limitation is that drug loading is low and rarely exceeds 20 wt %. A unusual exception are polymer micelles comprising a poly(2-oxazoline) (POx) based triblock copolymer, namely poly(2-methyl-2-oxazoline)-*block*-poly(2-butyl-2-oxazoline)-*block*-poly(2-methyl-2-oxazoline) (PMeOx-*b*-PBuOx-*b*-PMeOx \equiv A-pBuOx-A). Kabanov and co-workers have reported loading with almost 50 wt % of paclitaxel (PTX)^{3–5} into stable and injectable formulations, which exhibited a significantly increased therapeutic efficacy *in vivo*⁶ compared to clinically approved formulations. Interestingly, this combination of high loading and high stability was uniquely

found in block copolymers comprising poly(2-butyl-2-oxazoline) as hydrophobic core.⁷ PTX is one of the most commonly applied chemotherapeutic agents⁸ but is a high affinity substrate for P-glycoprotein (P-gp) leading to PTX resistance.⁹

Interestingly, similar high drug loading and stability of the formulation was achieved for a variety of structurally different taxanes,¹⁰ whereas etoposide and bortezomib, two important topoisomerase and proteasome inhibitors, respectively, did not give stable loading.^{3,4} Here, we also tested another extremely insoluble compound, curcumin (CUR),¹¹ which was solubilized well, but not excellently (maximum loading capacity: 24 wt %). Apparently, there is some sort of structural specificity for ultrahigh drug loaded micelles. CUR exhibits excellent safety,¹² but poor bioavailability and pharmacokinetic profile,^{13,14} is said to revert overexpression of P-gp¹⁵ and shows pharmacological synergy with PTX.¹⁶ However, because of its chemical instability in aqueous media, CUR is also very critically discussed as pan assay interference compound (PAIN) or invalid metabolic panacea (IMP).^{17,18} Nevertheless, its extremely low solubility, bioavailability and stability make it an excellent candidate to study the limitations and potential of polymer micelles for drug delivery.

To investigate the molecular basis of the drug specificity of A-pBuOx-A between PTX and CUR, we synthesized three other, structurally similar polymers, in which only the central hydrophobic block was changed minutely. Specifically, the three novel polymers were prepared (Figure 1). First, A-pPrOx-A, bearing a poly(2-*n*-propyl-2-oxazoline) core, which is a thermoresponsive polymer and lower homologue (polymer side chain) of pBuOx with a lower critical solution temperature (LCST) \approx 20 °C), second, A-pPrOzi-A, bearing poly(2-*n*-

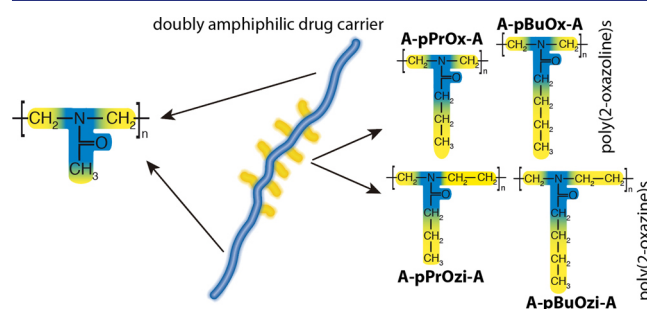


Figure 1. Schematic representation of polymers used in this study.

Received: May 25, 2017

Published: July 27, 2017

propyl-2-oxazine), a structural isomer of pBuOx with a LCST ≈ 10 °C, and third, **A-pBuOzi-A**, bearing poly(2-*n*-butyl-2-oxazine), a water-insoluble higher homologue (polymer backbone) of pBuOx.

Despite their structural similarity, poly(2-oxazine)s (POzi) have been much less investigated than POx.^{19–21} Both can be obtained via living cationic ring-opening polymerization (Figure S5) employing 2-substituted 2-oxazines (IUPAC: 2-*R*-5,6-dihydro-4*H*-1,3-oxazine) and 2-substituted 2-oxazolines, respectively (for monomer characterization, see Figures S1–S4).^{21,22} The polymers were characterized by ¹H NMR and GPC (Figures S5–S13). Comparison of structural isomers of POzi and POx revealed that POzi are more water-soluble, indicating that the side chain has a stronger impact on the polymer solubility than the polymer backbone.¹⁹ The four polymers were tested to formulate PTX and CUR using the thin film method (Figure S14), both drugs exhibiting a solubility of only around 1 mg/L.

Here, we investigate POzi as the central hydrophobic block in ABA triblock copolymers. Such polymers have not been reported and POzi have not been discussed as biomaterials before. As mentioned, **A-pBuOx-A** is an excellent solubilizer for paclitaxel, with a drug loading of almost 50 wt % ($m_{\text{Drug}}/(m_{\text{Drug}} + m_{\text{polymer}})$). We found that **A-pBuOzi-A** also gave excellent, if somewhat smaller loading of 40 wt % (Figure 2, Table S1,

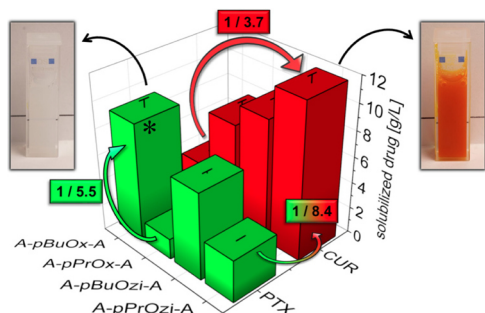


Figure 2. Maximum solubilized aqueous drug concentrations (PTX = green bars; CUR = red bars; $\rho(\text{polymer}) = 10$ g/L). Data is given as means \pm SD ($n = 3$). Selected ratios are given as [mol/mol]. * Data taken from ref 5.

Figures S15–S17). This may not be surprising, as a previous study showed that poly(2-*n*-pentyl-2-oxazoline), a structural isomer of **A-pBuOzi-A** was also an excellent taxane solubilizer.⁷ Interestingly, the structural isomer of **A-pBuOx-A**, **A-pPrOzi-A** was much less effective, solubilizing only 3.27 g/L (25 wt %).

Using the smaller main chain homologue, **A-pPrOx-A**, only 14 wt % (1.59 g/L) could be realized. Therefore, **A-pBuOx-A** solubilized 5.3 times more PTX than **A-pPrOx-A**. At first glance, this finding may seem unremarkable, considering that both PrOx and PrOzi bearing polymers are more hydrophilic than their 2-*n*-butyl counterparts. However, when we tested the formulation of CUR, a strikingly different pattern was observed. **A-pBuOx-A** failed to form ultrahigh loaded micelles, incorporating 25 wt % (3.2 g/L) CUR.

Even though this is exceeding any reported aqueous CUR concentration, including one very recent report based on POx diblock copolymers (12 wt %, 41 mg/L using 2-butenyl-2-oxazoline as hydrophobic core),²³ it is dwarfed by **A-pPrOx-A**, enabling solubilization of 7.8 g/L (44 wt %). The two 2-oxazine based block copolymers enabled even higher CUR concentrations. In particular, **A-pPrOzi-A** allowed stable nano-

formulations of CUR with a loading exceeding 50 wt % (≈ 12 g/L CUR@10 g/L polymer) and hydrodynamic diameters below 50 nm (Figure S18a). To put this into a stoichiometric perspective, per polymer molecule, about 27 drug molecules were incorporated, which is incidentally more than one CUR molecule per repeating unit of the pPrOzi block and 3.7 times more than **A-pBuOx-A** could solubilize. Comparing the amount of PTX and CUR solubilized in **A-pPrOzi-A**, the specificity for the latter was 8.4 (mol_{CUR}/mol_{PTX}). **A-pBuOx-A** showed a specificity factor of 5.3 over **A-pPrOx-A** for PTX solubilization, which in turn solubilized 11 times more CUR than PTX (mol/mol). Interestingly, **A-pBuOzi-A** did not exhibit any particular specificity and was an excellent solubilizer for both drugs, albeit less efficient than either best-in-class polymer. Apparently, the 2-oxazine backbone seems to be favorable for CUR while the 2-butyl side chains seem to be beneficial for PTX formulation.

Börner et al. have argued that the lack of specificity is a serious limitation of polymer micelles and have applied a high-throughput screening approach to identify drug specific drug carriers.^{24–28} The screening process revealed the importance of certain peptides within heptapeptide-PEG based drug carriers for drug binding. For example, the peptide sequence selected for Chlorin E6 (Ce6) formulation loaded 18 and 5 times more Ce6 than *meta*-tetra(hydroxyphenyl)chlorin (*m*-THPC) and Pheophorbide A (Pba), respectively. On the other hand, the peptide sequence selected for *m*-THPC was more compatible with Ce6 and Pba than with *m*-THPC. Moreover, the specificity of the polymers selected for Ce6, Pba and *m*-THPC with regard to Ce6 formulation was not pronounced (1/1.1/1.2). In comparison, the extraordinary drug loading and specificities of **A-pPrOx-A**, **A-pPrOzi-A**, **A-pBuOzi-A**, **A-pBuOx-A** for PTX of 1/2.1/4.2/5.5 are caused by the shift or addition of a single methylene group in the hydrophobic repeat units.

To explore the origin of this remarkable specificity, we employed Reichardt's dye, a hydrophobic and solvatochromic molecule, to probe the micellar microenvironment.²⁹ Though in the polymer films, the color appears identical in all samples (Figure 3a), the probe is clearly able to distinguish between the polymer side chains and the polymer backbone in the micellar form (Figure 3c).

Both polymers with propyl side chains result in a broad and comparably featureless UV/vis spectra whereas those of

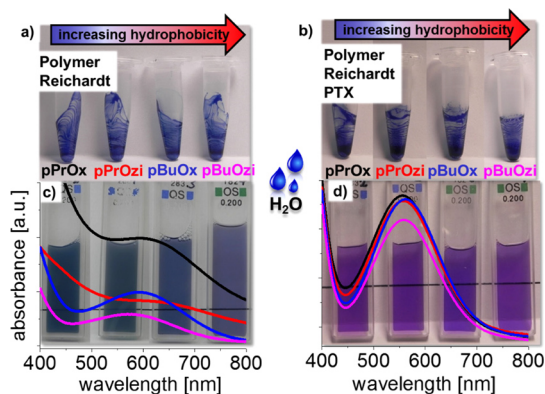


Figure 3. Polymer/Reichardt's dye films (10/0.5 w/w) in the absence (a) and in the presence of PTX (b; 10/0.5/1 w/w). Polymer micelles w/o (c; $\rho(\text{polymer/dye}) = 10/0.5$ [g/L]) and w/PTX (d; $\rho(\text{polymer/dye/PTX}) = 10/0.5/1$ [g/L]) with absorption spectra.

polymers bearing butyl side chains feature clearly distinguishable local maxima at around 580 nm (Figure 3c). Interestingly, as PTX was added, the spectra aligned (Figure 3d), indicating that the added drug remodels the micellar microenvironment. With increasing drug loading toward maximum drug loading, λ_{\max} gradually decreased to 550 nm, corresponding to an $E_T(30)$ value of 52 (Figures S19 and S21, Table S5). Although PTX is highly hydrophobic, its incorporation into polymer micelles seems to establish a more polar microenvironment for Reichardt's dye, which can be attributed to the large number of polar moieties present in PTX. Please note, the strong and broad absorbance of CUR does not allow a similar assessment of Reichardt's dye solvatochromicity in the presence of CUR.

Loading **A-pBuOx-A** micelles with PTX enabled coinorporation of drugs that alone did not give stable formulations.⁴ Similarly, when we combined PTX and CUR (1/1, w/w) in **A-pPrOzi-A** micelles, the polymer seemed to lose any specificity, as both drugs were incorporated neatly. Most interestingly, even higher overall drug loading was possible. In this 1/1 combination, 10 g/L polymer allowed solubilization of 7 g/L of each drug, totaling at a staggering 59 wt % drug loading (Figure 4a, Table S2) while the hydrodynamic diameters remain below 100 nm (Figure S18b).

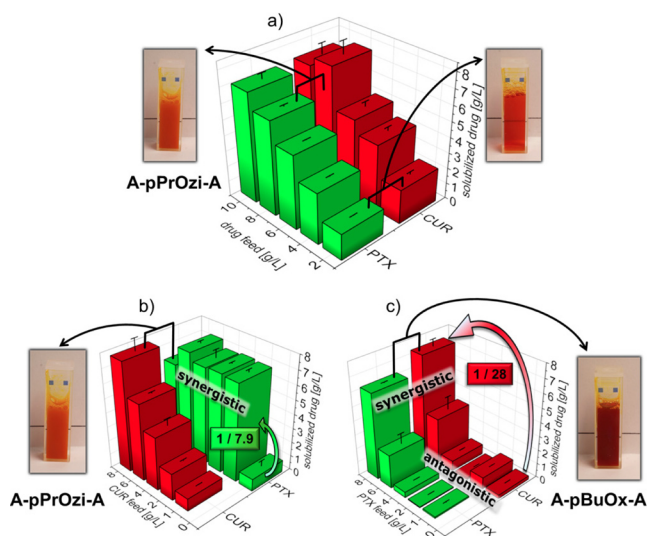


Figure 4. Coformulated aqueous drug concentrations in dependence of the drug feed concentration (PTX, green bars; CUR, red bars). At a certain drug feed concentration, both drugs were solubilized within a single formulation (\equiv coformulation). Data is given as means \pm SD ($n = 3$). (a) PTX and CUR were added at same feed concentrations and solubilized with **A-pPrOzi-A** ($\rho = 10$ g/L); (b) addition of increasing CUR feed concentrations ($\rho(\text{PTX}) = 8$ g/L; $\rho(\text{A-pPrOzi-A}) = 10$ g/L); (c) addition of increasing PTX feed concentrations ($\rho(\text{CUR}) = 8$ g/L; $\rho(\text{A-pBuOx-A}) = 10$ g/L).

To explore this loss in specificity, we investigated the loading of **A-pBuOx-A** with CUR and **A-pPrOzi-A** with PTX, i.e., the drugs the polymers are not specific for, with increasing amounts of the drugs the polymers are specific for. Please note, the polymer concentration was held constant at 10 g/L, the targeted concentration for the unfavorable drug at 8 g/L and the favorable drug was increased from 0 to 8 g/L. Also in this experiment, a remarkably different behavior of the two constitutional isomers was observed. In the case of **A-pPrOzi-A**, even the smallest addition of CUR (1 g/L) led to an immediate maximization and 8-fold increase of PTX loading

(Figure 4b, Table S3), which may be interpreted as a pronounced synergy between CUR and PTX loading in **A-pPrOzi-A**.

An entirely different situation presented itself for **A-pBuOx-A**. Not only did the addition of the preferred PTX do nothing to improve CUR loading, the presence of CUR even prevented efficient loading with PTX (Figure 4c, Table S4). This represents a clear antagonistic effect. Only when the PTX/CUR ratio approached unity, the loading efficiency of the otherwise "preferred" PTX exceeded 10%. At $\rho = 8/8$ g/L (PTX/CUR), loading efficiencies were excellent (80–90%) and overall loading exceeded 50 wt %. At this point, the loading with CUR is increased 28-fold compared with the absence of PTX, which is remarkable as this only happens when an amount of PTX is present, that is outstanding in its own right.

In short, when using **A-pBuOx-A**, the presence of the unfavorable CUR interferes with the loading of the favorable PTX (unless large relative amounts of PTX are added), the loading of PTX in **A-pPrOzi-A** is drastically enhanced by addition of minute amounts of CUR. This observation seems to be highly unusual. In fact, Kwon and co-workers clearly observed only simple additivity when combining PTX, 17-AAG and Rapamycin³⁰ or PTX, etoposide and docetaxel,³¹ respectively, in PEG-*b*-PLA micelles.

Previously, Hansen solubility parameters (HSPs) were used to predict incorporation of ellipticin in block copolymer micelles.³² Overall, a good correlation between drug formulation characteristics and calculated polymer–drug compatibility was obtained. However, the chemical structure of the polymers investigated differed significantly. More recently, Dargaville et al. used the HSP in the context of POx based diblock copolymer–CUR formulations.²³ Unfortunately, in our case, HSP calculated by group contribution methods are not able to explain the observed polymer–drug specificity.³³ Intrinsically, structural isomers such as **A-pBuOx-A** and **A-pPrOzi-A** cannot be distinguished, which requires a different approach to correlate experimental data with calculated HSP. This may help to improve the overall predictive power of HSP, which are currently not always suited for complex problems such as presented here.

In summary, we found that the smallest change in the polymer structure, a migration of a methylene group from the polymer side chain to the polymer main chain, led to a surprisingly specific drug loading of **A-pPrOzi-A** and **A-pBuOx-A** for CUR and PTX, respectively. In addition, very distinct drug loading profiles were observed for combinations of both drugs.

Ultrahigh loaded micelles carry the promise of improved therapeutic outcome.⁶ Combination drug therapy for cancer is a promising strategy to obtain maximum therapeutic response^{34,35} and ultrahigh coloaded micelles might combine both positive effects.

More generally, the observed host–guest specificity in combination with ultrahigh loading capacities may also offer new possibilities in substrate specific micellar catalysis^{36–39} and multiple step one-pot syntheses of water-soluble agents in aqueous media.³⁸

■ ASSOCIATED CONTENT

📄 Supporting Information

The Supporting Information is available free of charge on the ACS Publications website at DOI: 10.1021/jacs.7b05376.

Detailed experimental procedures, monomer and polymer characterization data, formulation data and dynamic light scattering data (PDF)

AUTHOR INFORMATION

Corresponding Author

*robert.luxenhofer@uni-wuerzburg.de

ORCID

Robert Luxenhofer: 0000-0001-5567-7404

Notes

The authors declare no competing financial interest.

ACKNOWLEDGMENTS

This work was supported by the Free State of Bavaria. Start-up funding for R.L. by the University Würzburg and SKZ Das Kunststoff-Zentrum is gratefully acknowledged. M.M.L. and M.S.H. thank the Evonik Foundation (M.M.L.) and the Higher Education Commission (HEC) of Pakistan and Deutscher Akademischer Austauschdienst (DAAD) Germany (M.S.H.), respectively, for providing doctoral fellowship. We also thank Christian May for technical support and Prof. J. Groll and PD Dr. J. Teßmar (University Clinic Würzburg) for instrument access and technical support.

REFERENCES

- (1) Ali, S.; Kolter, K. *Am. Pharm. Rev.* **2012**, *15*, 1.
- (2) Duncan, R.; Vicent, M. J. *Adv. Drug Delivery Rev.* **2013**, *65*, 60.
- (3) Luxenhofer, R.; Schulz, A.; Roques, C.; Li, S.; Bronich, T. K.; Batrakova, E. V.; Jordan, R.; Kabanov, A. V. *Biomaterials* **2010**, *31*, 4972.
- (4) Han, Y.; He, Z.; Schulz, A.; Bronich, T. K.; Jordan, R.; Luxenhofer, R.; Kabanov, A. V. *Mol. Pharmaceutics* **2012**, *9*, 2302.
- (5) Schulz, A.; Jaksch, S.; Schubel, R.; Wegener, E.; Di, Z.; Han, Y.; Meister, A.; Kressler, J.; Kabanov, A. V.; Luxenhofer, R.; Papadakis, C. M.; Jordan, R. *ACS Nano* **2014**, *8*, 2686.
- (6) He, Z.; Wan, X.; Schulz, A.; Bludau, H.; Dobrovolskaia, M. A.; Stern, S. T.; Montgomery, S. A.; Yuan, H.; Li, Z.; Alakhova, D.; Sokolsky, M.; Darr, D. B.; Perou, C. M.; Jordan, R.; Luxenhofer, R.; Kabanov, A. V. *Biomaterials* **2016**, *101*, 296.
- (7) Seo, Y.; Schulz, A.; Han, Y.; He, Z.; Bludau, H.; Wan, X.; Tong, J.; Bronich, T. K.; Sokolsky, M.; Luxenhofer, R.; Jordan, R.; Kabanov, A. V. *Polym. Adv. Technol.* **2015**, *26*, 837.
- (8) Zasadil, L. M.; Andersen, K. A.; Yeum, D.; Rocque, G. B.; Wilke, L. G.; Tevaarwerk, A. J.; Raines, R. T.; Burkard, M. E.; Weaver, B. A. *Sci. Transl. Med.* **2014**, *6*, 229ra43.
- (9) Pires, M. M.; Emmert, D.; Hrycyna, C. A.; Chmielewski, J. *Mol. Pharmacol.* **2009**, *75*, 92.
- (10) He, Z.; Schulz, A.; Wan, X.; Seitz, J.; Bludau, H.; Alakhova, D. Y.; Darr, D. B.; Perou, C. M.; Jordan, R.; Ojima, I.; Kabanov, A. V.; Luxenhofer, R. *J. Controlled Release* **2015**, *208*, 67.
- (11) Esatbeyoglu, T.; Huebbe, P.; Ernst, I.; Chin, D.; Wagner, A. E.; Rimbach, G. *Angew. Chem., Int. Ed.* **2012**, *51*, 5308.
- (12) Dhillon, N.; Aggarwal, B. B.; Newman, R. A.; Wolff, R. A.; Kunnumakkara, A. B.; Abbruzzese, J. L.; Ng, C. S.; Badmaev, V.; Kurzrock, R. *Clin. Cancer Res.* **2008**, *14*, 4491.
- (13) Aggarwal, B. B.; Sung, B. *Trends Pharmacol. Sci.* **2009**, *30*, 85.
- (14) Anand, P.; Kunnumakkara, A. B.; Newman, R. A.; Aggarwal, B. B. *Mol. Pharmaceutics* **2007**, *4*, 807.
- (15) Anuchapreeda, S.; Leechanachai, P.; Smith, M. M.; Ambudkar, S. V.; Limtrakul, P.-n. *Biochem. Pharmacol.* **2002**, *64*, 573.
- (16) Sreekanth, C.; Bava, S.; Sreekumar, E.; Anto, R. *Oncogene* **2011**, *30*, 3139.
- (17) Baell, J.; Walters, M. A. *Nature* **2014**, *513*, 481.
- (18) Baell, J. B. *J. Nat. Prod.* **2016**, *79*, 616.
- (19) Bloksma, M. M.; Paulus, R. M.; van Kuringen, H. P. C.; van der Woerd, F.; Lambermont-Thijs, H. M. L.; Schubert, U. S.; Hoogenboom, R. *Macromol. Rapid Commun.* **2012**, *33*, 92.
- (20) Bloksma, M. M.; Schubert, U. S.; Hoogenboom, R. *Macromol. Rapid Commun.* **2011**, *32*, 1419.
- (21) Lorson, T.; Jaksch, S.; Lübtow, M. M.; Jüngst, T.; Groll, J.; Lühmann, T.; Luxenhofer, R. *Biomacromolecules* **2017**, *18*, 2161.
- (22) Levy, A.; Litt, M. *J. Polym. Sci., Part B: Polym. Lett.* **1967**, *5*, 881.
- (23) Raveendran, R.; Mullen, K. M.; Wellard, R. M.; Sharma, C. P.; Hoogenboom, R.; Dargaville, T. R. *Eur. Polym. J.* **2017**, *93*, 682.
- (24) Wieczorek, S.; Dallmann, A.; Kochovski, Z.; Börner, H. G. *J. Am. Chem. Soc.* **2016**, *138*, 9349.
- (25) Wieczorek, S.; Remmler, D.; Masini, T.; Kochovski, Z.; Hirsch, A. K.; Börner, H. G. *Bioconjugate Chem.* **2017**, *28*, 760.
- (26) Lawatscheck, C.; Pickhardt, M.; Wieczorek, S.; Grafmüller, A.; Mandelkow, E.; Börner, H. G. *Angew. Chem., Int. Ed.* **2016**, *55*, 8752.
- (27) Wieczorek, S.; Krause, E.; Hackbarth, S.; Röder, B.; Hirsch, A. K. H.; Börner, H. G. *J. Am. Chem. Soc.* **2013**, *135*, 1711.
- (28) Wieczorek, S.; Schwaar, T.; Senge, M. O.; Börner, H. G. *Biomacromolecules* **2015**, *16*, 3308.
- (29) Reichardt, C. *Chem. Rev.* **1994**, *94*, 2319.
- (30) Shin, H.-C.; Alani, A. W. G.; Cho, H.; Bae, Y.; Kolesar, J. M.; Kwon, G. S. *Mol. Pharmaceutics* **2011**, *8*, 1257.
- (31) Shin, H.-C.; Alani, A. W. G.; Rao, D. A.; Rockich, N. C.; Kwon, G. S. *J. Controlled Release* **2009**, *140*, 294.
- (32) Liu, J.; Xiao, Y.; Allen, C. *J. Pharm. Sci.* **2004**, *93*, 132.
- (33) Van Krevelen, D. W.; Te Nijenhuis, K. *Properties of Polymers*; Elsevier: Amsterdam, 2009; Vol. 4.
- (34) Ma, L.; Kohli, M.; Smith, A. *ACS Nano* **2013**, *7*, 9518.
- (35) Mayer, L. D.; Janoff, A. S. *Mol. Interventions* **2007**, *7*, 216.
- (36) Rossbach, B. M.; Leopold, K.; Weberskirch, R. *Angew. Chem., Int. Ed.* **2006**, *45*, 1309.
- (37) Liu, Y.; Wang, Y.; Wang, Y.; Lu, J.; Pinon, V., 3rd; Weck, M. J. *Am. Chem. Soc.* **2011**, *133*, 14260.
- (38) Lempke, L.; Ernst, A.; Kahl, F.; Weberskirch, R.; Krause, N. *Adv. Synth. Catal.* **2016**, *358*, 1491.
- (39) Wang, F.; Wen, M.; Feng, K.; Liang, W. J.; Li, X. B.; Chen, B.; Tung, C. H.; Wu, L. *Z. Chem. Commun.* **2016**, *52*, 457.

The discussed POzi based drug carriers were designed having the observations of Luxenhofer *et al.* (Biomaterials **2010**, 31, 4972-4979) and Seo *et. al.* (Polym. Adv. Technol. **2015**, 26, 837-850) in mind, that only POx based micelles with a barely amphiphilic character enable extremely high drug loadings in selected cases. To see if this is also true for POzi based amphiphiles, strongly hydrophobic nonyl sidechains were introduced into the hydrophobic core, to achieve a more pronounced amphiphilic contrast. As sidechain crystallization has been suggested to be partly responsible for the lower LC of the nonyl sidechain comprising POx drug carriers compared to the butyl comprising ones, branching in the C₉ sidechain was introduced (3-ethylheptyl) to prevent crystallization. Interestingly, the POx with a nonyl sidechain was the only homopolymer exhibiting a pronounced crystallinity with a melting point around 90 °C. In contrast, the POzi counterpart with the same sidechain exhibited a much less distinct melting point (if any) at very low temperatures of -11 °C. However, these differences vanished in the corresponding triblock copolymers, all having glass transition temperatures T_g s between 54 and 60 °C without any sign of crystallinity. This is in violation of the Fox-equation, in which the T_g of block copolymers is derived from the T_g s of the respective homopolymers weighted with their respective mass fraction.

Although the POzi based amphiphiles enabled somehow higher CUR loadings than their POx counterparts, the solubilization patterns were less straightforward, with large deviations between the formulations prepared in triplicates especially at high drug-feed concentrations. Investigating the precipitate of the latter in more detail revealed that not only drug, but also polymer, most likely in the form of aggregated drug-loaded polymer micelles (= colloidal instabilities), precipitated. The latter hypothesis was supported by the observation that the precipitate partly re-dissolved over time which is only possible if CUR was still in solubilized state. Although we could not explain these observations on a molecular level at that point of time, the thorough analysis of the morphology of the CUR-loaded micelles shed new light on this phenomenon as will be discussed in more detail in chapter 4.3. Briefly, at higher drug loadings, more and more parts of the hydrophilic corona interact with encapsulated CUR to stabilize the latter. Conversely, an ever less pronounced hydrophilic corona struggles to facilitate water-solubility of the micelle finally causing agglomeration and therefore precipitation of the latter.

Despite their amphiphilic character, none of the triblock copolymers showed pronounced cell cytotoxicity (human dermal fibroblasts) as well as hemolytic activity which is in good agreement with the generally high cytocompatibility of various POx.

The following publication was reprinted with permission from *Macromol. Biosci.* **2018**, 18, 1800155

<https://doi.org/10.1002/mabi.201800155>; © 2018 WILEY-VCH Verlag GmbH & Co. KGaA



More Is Sometimes Less: Curcumin and Paclitaxel Formulations Using Poly(2-oxazoline) and Poly(2-oxazine)-Based Amphiphiles Bearing Linear and Branched C9 Side Chains

Michael M. Lübtow, Larissa Keßler, Antje Appelt-Menzel, Thomas Lorson, Niklas Gangloff, Marius Kirsch, Selma Dahms, and Robert Luxenhofer*

A known limitation of polymer micelles for the formulation of hydrophobic drugs is their low loading capacity (LC), which rarely exceeds 20 wt%. One general strategy to overcome this limitation is to increase the amphiphilic contrast, that is, to make the hydrophobic core of the micelles more hydrophobic. However, in the case of poly(2-oxazoline) (POx)-based amphiphilic triblock copolymers, a minimal amphiphilic contrast was reported to be beneficial. Here, this subject is revisited in more detail using long hydrophobic side chains that are either linear (nonyl) or branched (3-ethylheptyl). Two different backbones within the hydrophobic block are investigated, in particular POx and poly(2-oxazine) (POzi), for the solubilization and co-solubilization of the two highly water insoluble compounds, curcumin and paclitaxel. Even though high loading capacities can be achieved for curcumin using POzi-based triblock copolymers, the solubilization capacity of all investigated polymers with longer side chains is significantly lower compared to POx and poly(2-oxazine)s with shorter side chains. Although the even lower LC for paclitaxel can be somehow improved by co-formulating curcumin, this study corroborates that in the case of POx and POzi-based polymer micelles, an increased amphiphilic contrast leads to less drug solubilization.

logical activity of the drug candidate (dissolved in organic solvent) in conventional 2D cell cultures. As a result, a shift toward larger (high molecular weight) and more hydrophobic molecules with lower solubility is observed.^[2] The low water solubility of lead molecules poses substantial challenges for drug development. To overcome this challenge, drugs need to be formulated. Polymeric micelles exhibiting a core/shell structure offer the possibility to encapsulate drugs within their hydrophobic core.^[3–5] The hydrophilic shell not only modulates the water solubility, but is also thought to suppress interactions with blood components including the mononuclear phagocyte system. This increases strongly their half-life in vivo (so-called stealth effect).^[6–9] However, this is only relevant if the polymer micelle is stable in circulation. Despite a wide range of possible chemical compositions and favorable sizes in the nanometer-scale,^[10] the transfer of drug-loaded micelles into

1. Introduction

High-throughput combinatorial screenings to select “hit” molecules are the method of choice for modern drug discovery.^[1] However, the screening processes commonly evaluate the bio-

the clinics has been slow. Arguably, the translation is hampered by insufficient physical stability, thermodynamically driven disassembly, as well as reproducibility issues.^[11,12] In addition, low drug-loadings (commonly ≤ 20 wt%) and low overall drug concentrations remain issues. Following the concept “like dissolves like,” drug-loading is sometimes increased by covalent attachment of very hydrophobic moieties into the hydrophobic block. Typical examples include cholesterol (loading capacity, LC [Adriamycin] = 0.4 wt%;^[13] LC [quercetin] = 3.7 wt%;^[14] LC [docetaxel] = 4.7 wt%;^[15] or vitamin E [α -tocopherol]; LC [docetaxel] = 9.1 wt%).^[16] Overall however, this strategy only resulted in modest success. In recent years, an old but relatively little known polymer family of poly(2-oxazoline)s (POx) has gained some interest in the field of drug delivery.^[17–19] In 2010, Luxenhofer et al. reported a POx-based^[20,21] drug-carrier for the formulation of the hydrophobic chemotherapeutic paclitaxel (PTX).^[22,23] This enabled drug contents up to 50 wt% and a high overall aqueous solubility up to 40 g L⁻¹ PTX using only 50 g L⁻¹ polymer.^[24–26] Interestingly, this was achieved utilizing an ABA-triblock copolymer comprising only a modestly

M. M. Lübtow, L. Keßler, T. Lorson, N. Gangloff, M. Kirsch, S. Dahms, Prof. R. Luxenhofer
Polymer Functional Material, Chair for Advanced Materials Synthesis
Department of Chemistry and Pharmacy
Julius-Maximilians-University Würzburg
Röntgenring 11, 97070, Würzburg, Germany
E-mail: robert.luxenhofer@uni-wuerzburg.de

Dr. A. Appelt-Menzel
Lehrstuhl Tissue Engineering und Regenerative Medizin und Fraunhofer-
Institut für Silicatforschung ISC
University Hospital Würzburg
Röntgenring 11, 97070, Würzburg, Germany

The ORCID identification number(s) for the author(s) of this article can be found under <https://doi.org/10.1002/mabi.201800155>.

DOI: 10.1002/mabi.201800155

hydrophobic poly(2-*n*-butyl-2-oxazoline) (pBuOx ≡B) core. In contrast, a POx with a more hydrophobic poly(2-*n*-nonyl-2-oxazoline) (pNonOx ≡B) core enabled PTX contents of only 17–24 wt% and a much lower overall solubility ($\rho(\text{PTX}) = 2\text{--}3.2 \text{ g L}^{-1}$; $\rho(\text{polymer}) = 10 \text{ g L}^{-1}$).^[27] It was assumed that this decrease might be caused by crystallization of the long alkyl side-chains what might also be responsible for the lower drug-loading in the first place. To test this hypothesis, an ABA triblock copolymer containing poly(2-(3-ethylheptyl)-2-oxazoline) (pEtHepOx) is introduced as hydrophobic block B in which crystallization should be strongly hindered due to branching of the side-chain. To get better insights into the physicochemical properties of the hydrophobic core, the respective homopolymers were synthesized and characterized.

Very recently, Lübtow et al. compared the LC of A-pBuOx-A and its structural isomer comprising the same pMeOx shell and a barely hydrophobic poly(2-*n*-propyl-2-oxazine) (pPrOzi) core.^[28] The formal shift of a methylene group from the polymer side chain (A-pBuOx-A) to the polymer backbone (A-pPrOzi-A) caused distinct polymer/drug specificities with regard to the LC for PTX (LC [A-pBuOx-A] = 47.5 wt%; LC [A-pPrOzi-A] = 24.7 wt%) and curcumin^[29,30] (CUR; LC [A-pBuOx-A] = 24.4 wt%; LC [A-pPrOzi-A] = 54.3 wt%).^[31] It was wondered if such polymer/drug specificities would also occur in ABA triblock copolymers comprising C9-side-chains within their hydrophobic POx or POzi (POzi) core. Therefore, the ABA triblock copolymers bearing hydrophobic POzi blocks with 3-ethylheptyl and nonyl side chains were synthesized and evaluated with respect to the drug loading in comparison to their POx analogs.

2. Materials and Methods

2.1. Materials

All substances for the preparation of the polymers were purchased from Sigma-Aldrich (Steinheim, Germany) or Acros (Geel, Belgium) and were used as received unless otherwise stated. Curcumin powder from *Curcuma longa* (turmeric) was purchased from Sigma-Aldrich and analyzed in-house (curcumin = 79%; demethoxycurcumin = 17%; bisdemethoxycurcumin = 4%; determined by HPLC analysis). Paclitaxel was purchased from LC Laboratories (Woburn, MA). Deuterated solvents for NMR analysis were obtained from Deutero GmbH (Kastellaun, Germany). The substances used for polymerization, specifically methyl trifluoromethylsulfonate (MeOTf), MeOx, EtHepOx, EtHepOzi, NonOx, and NonOzi, were refluxed over CaH₂, distilled and stored under argon. Benzointrile (PhCN) was refluxed over phosphorus pentoxide, distilled and stored under argon.

2.2. Methods

2.2.1. Nuclear Magnetic Resonance Spectroscopy

NMR spectra were recorded on a Fourier 300 (300.12 MHz), Bruker Biospin (Rheinstetten, Germany) at 298 K. The spectra were calibrated to the signal of residual protonated solvent (CDCl₃ at 7.26 ppm; D₂O at 4.79 ppm).

2.2.2. Gel Permeation Chromatography

Gel permeation chromatography (GPC) was performed on an Agilent 1260 Infinity System, Polymer Standard Service (Mainz, Germany) with either HFIP containing 3 g L⁻¹ potassium trifluoroacetate; precolumn: 50 × 8 mm PSS PFG linear M; 2 columns: 300 × 8 mm PSS PFG linear M (particle size 7 μm; pore size 0.1–1,000 kDa) or DMF containing 1 g L⁻¹ LiBr; precolumn: 50 × 8 mm PSS GRAM; columns: 30 Å and 1,000 Å 300 × 8 mm PSS GRAM (particle size 10 μm; pore size 0.1–1,000 kDa) as eluent. The columns were kept at 40 °C and flow rates were 1.0 mL min⁻¹ (DMF) or 0.7 mL min⁻¹ (HFIP). Prior to each measurement, samples were filtered through 0.2 μm PTFE filters, Roth (Karlsruhe, Germany). Conventional calibration was performed with PEG standards (0.1–1,000 kg mol⁻¹) and data was processed with WinGPC software.

2.2.3. Matrix-Assisted Laser Desorption/Ionization–Time of Flight Mass Spectroscopy

MALDI-TOF was performed on a Daltonics autoflex II LRF, Bruker (Bremen, Germany). Sample preparation: 1:1 mixture of matrix solution (5 wt% DCTB (trans-2-[3-(4-tert-butylphenyl)-2-methyl-2-propenylidene]malononitrile) in CHCl₃) and sample solution (10 g L⁻¹ in methanol with 1 vol% TFA) spotted onto stainless steel target plate (0.7 μL, three times per spot). Measuring parameters: laser power: 30%; number of shots: ≥1000; ion source 1: 20.02 kV; ion source 2: 17.86 kV; lens: 8.91 kV; reflector: 20.02 kV; PIE: 500 ns; polarity: positive; matrix suppression mode: deflection; suppress up to: 1,000 Da; mass range: 1,000–6,000 Da; detector gain: 10.0x reflector; electronic gain: 100 mV; sample rate: 2.00 GS s⁻¹; realtime smooth: Off. calibration: CsI.

2.2.4. Infrared Spectroscopy

The IR-spectra of neat CUR, physically mixed powders of CUR and polymer, or formulated CUR were recorded on a FT-IR-4100, Jasco (Gross-Umstadt, Germany) from 500–4,000 cm⁻¹ at ambient temperature. Prior to the measurements, the aqueous CUR formulations were lyophilized to obtain the respective powders.

2.2.5. Fluorescence Spectroscopy–Critical Micelle Concentration

Pyrene features an emission spectrum with five distinct peaks between 360 and 400 nm.^[32] The ratio of I₁:I₃ can be utilized to determine changes in the polarity of the microenvironment surrounding pyrene which occur, for example, after encapsulation into polymeric micelles.^[33]

Pyrene solutions (24 μM, 5.0 mg L⁻¹ in acetone) were added to glass vials (do not use plastic vials!) and the solvent was removed by a gentle stream of argon. Subsequently, various amounts of polymer stock solutions were added and the solutions diluted with water (Millipore) to yield a final pyrene concentration of 5 × 10⁻⁷ M. The samples were stored overnight

at ambient temperature ($\approx 25\text{ }^\circ\text{C}$) under the exclusion of light. Pyrene fluorescence was recorded on a FP-8300, Jasco from 360 to 400 nm ($\lambda_{\text{ex}} = 333\text{ nm}$) at $25\text{ }^\circ\text{C}$. The critical micelle concentration (CMC) was determined as the concentration at which the fitted $I_1:I_3$ ratio decreased to 90% of its initial value.

2.2.6. Thermogravimetric Analysis

Thermogravimetric analysis of the polymers was performed on a TG 209 F1 IRIS, NETZSCH (Selb, Germany). The samples (5–10 mg) were added to aluminum oxide crucibles (NETZSCH) and heated under synthetic air from $30\text{ }^\circ\text{C}$ to $900\text{ }^\circ\text{C}$ with a heating rate of 10 K min^{-1} while detecting the mass loss.

2.2.7. Differential Scanning Calorimetry

DSC was performed on a DSC 204 F1 Phoenix, NETZSCH under N_2 -atmosphere (20.0 mL min^{-1}). The samples were placed in aluminum pans with crimped-on lids and heated from $25\text{ }^\circ\text{C}$ to $200\text{ }^\circ\text{C}$ (10 K min^{-1}) and subsequently cooled to $-50\text{ }^\circ\text{C}$ (10 K min^{-1}). The samples were heated/cooled two additional times from $-50\text{ }^\circ\text{C}$ to $200\text{ }^\circ\text{C}$ (10 K min^{-1}).

2.2.8. Drug-Loaded Polymer Micelles

Drug-loaded polymer micelles were prepared by thin film method.^[24] Ethanolic polymer (20 g L^{-1}), paclitaxel (20 g L^{-1}), and curcumin (5.0 g L^{-1}) stock solutions were mixed in the desired ratio. After complete removal of the solvent at $50\text{ }^\circ\text{C}$ under a mild stream of argon, the films were dried in vacuo ($\leq 0.2\text{ mbar}$) for at least 3 h. Subsequently, $300\text{ }\mu\text{L}$ preheated ($37\text{ }^\circ\text{C}$) H_2O were added. Complete solubilization was facilitated by shaking the solutions at $1,250\text{ rpm}$ at $55\text{ }^\circ\text{C}$ for 12 min with a Thermomixer comfort, Eppendorf AG (Hamburg, Germany). Non-solubilized drug (if any) was removed by centrifugation for 5 min at $10,000\text{ rpm}$ with a 3-Speed micro centrifuge, neoLab (Heidelberg, Germany). Solubilization experiments were performed with three individually prepared samples and results are presented as means \pm standard deviation (SD).

Curcumin quantification was performed by UV-Vis absorption on a BioTek Eon Microplate Spectrophotometer, Thermo Fisher Scientific (Waltham, MA) using a calibration curve obtained with known amounts of CUR, dissolved in EtOH. Samples were prepared in Rotilabo F-Type 96 well plates, Carl Roth GmbH & Co. KG (Karlsruhe, Germany) at a constant volume of $100\text{ }\mu\text{L}$. Spectra were recorded from 260 to 600 nm at $25\text{ }^\circ\text{C}$. Curcumin absorption was detected at 428 nm . Prior to UV-Vis absorption measurements, the aqueous formulations were appropriately diluted with ethanol to give a final absorbance between 0.3 and 2.5 (diluted at least $1/20\text{ v/v}$).

The following equations were used to calculate LC and loading efficiency (LE):

$$LE = \frac{m_{\text{drug}}}{m_{\text{drug, added}}} \quad (1)$$

$$LC = \frac{m_{\text{drug}}}{m_{\text{drug, added}} + m_{\text{polymer}}} \quad (2)$$

where m_{drug} and m_{polymer} are the weight amounts of the solubilized drug and polymer excipient in solution and $m_{\text{drug, added}}$ is the weight amount of the drug initially added to the dispersion. No loss of polymer during micelles preparation was assumed.

2.2.9. High-Performance Liquid Chromatography

HPLC analysis was carried out on a LC-20A Prominence HPLC, Shimadzu (Duisburg, Germany) equipped with a system controller CBM-20A, a solvent delivery unit LC-20 AT (double plunger), an on-line degassing unit DGU-20A, an auto-sampler SIL-20AC, a photo-diode array detector SPD-M20A, and a column oven CTO-20AC. As stationary phase, a ZORBAX Eclipse Plus, Agilent (Santa Clara, CA) C18 column ($4.6 \times 100\text{ mm}$; $3.5\text{ }\mu\text{m}$) was used. The mobile phase was a gradient of $\text{H}_2\text{O}/\text{ACN}$ (Figure S31, Supporting information) at $40\text{ }^\circ\text{C}$ and a flow rate of 1 mL min^{-1} . Quantification of Paclitaxel was performed at 227 nm .

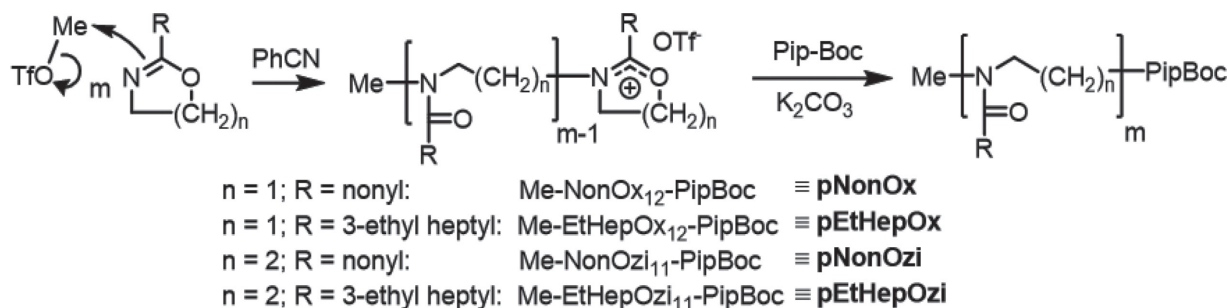
2.2.10. Dynamic Light Scattering

Dynamic light scattering (DLS) was measured at scattering angles from $22\text{ }^\circ\text{C}$ to $151\text{ }^\circ\text{C}$ at $25\text{ }^\circ\text{C}$ on a CGS-3 multi detection (eight simultaneous working APD Avalanche diodes and eight glass fiber detectors) goniometer system, ALV (Langen, Germany) equipped with a He-Ne-laser (22 mW , $\lambda = 632.8\text{ nm}$). Data was analyzed using HDRC-Software Version 6.3.1. developed by Schmidt and co-workers at Johannes Gutenberg University Mainz. Prior to each measurement, samples were filtered through $0.45\text{ }\mu\text{m}$ regenerated cellulose filters (Rotilabo) and polymer concentration was 10 or 1 g L^{-1} in H_2O . The decay of the electric field-time autocorrelation function was fitted by a triexponential function (equation (3)), as described in more detail by Rausch et al.^[34] with the amplitudes a_i and the decay times $\tau_i = \frac{1}{q^2 \cdot D_i}$, where D_i is Brownian diffusion coefficient of component i ; and q being the absolute value of the scattering vector.

$$g_1(t) = a_1 \cdot e^{\left(\frac{-t}{\tau_1}\right)} + a_2 \cdot e^{\left(\frac{-t}{\tau_2}\right)} + a_3 \cdot e^{\left(\frac{-t}{\tau_3}\right)} \quad (3)$$

2.2.11. Cell Viability Assay

Primary human dermal fibroblasts (HDF) were cultured in DMEM, GlutaMAX (Gibco, Darmstadt, Germany) medium supplemented with 10% fetal calf serum, and 1% sodium pyruvate. For cell cytotoxicity studies, cells were seeded in a white 96-well plate with a transparent bottom in triplicate per condition ($3 \times 10^5\text{ cells cm}^{-2}$) and cultured for 24 h at $37\text{ }^\circ\text{C}$ and 5% CO_2 . Subsequently, medium was removed and polymer stock solutions in cell-specific culture medium were added to the cells and applied for 24 h or 48 h. After the treatment, CellTiter-Glo Luminescent Cell Viability Assay (Promega, Mannheim,



Scheme 1. Synthesis of POx and POzi homopolymers by living cationic ring opening polymerization (LCROP).

Germany) was performed according to the manufacturer's instructions. Briefly, medium was removed and cells were washed 3x with PBS(+). Equal amounts of cell culture medium and CellTiter-Glo reagent were added to the wells. After shaking for 2 min and resting for 10 min to achieve cell lysis, luminescence was measured with an Infinite 200 (Tecan, Männedorf, Switzerland) at $\lambda_{em} = 590$ nm ($\lambda_{ex} = 560$ nm).

Cell viability was determined with equation (4):

$$\text{Cell viability} = \frac{F_{\text{treated}} - F_{\text{medium}}}{F_{\text{untreated}} - F_{\text{medium}}} \times 100\% \quad (4)$$

where F_{treated} and $F_{\text{untreated}}$ are the luminescence of treated and untreated cells, respectively, and F_{medium} is the luminescence of the culture medium. As negative control, cells were lysed with 10% SDS. Cell viability experiments were performed in three biological independent experiments and results are presented as means \pm SD. Cells were obtained by three individual isolations.

2.2.12. Hemolysis Assay

Blood from three healthy human donors, collected in heparinized tubes was centrifuged at $4,500 \times g$ for 5 min. Subsequently, the supernatant was removed and the pellet washed 3x times with cold PBS(-) (4 °C–10 °C). Centrifugation and washing step was repeated two additional times. After dilution with PBS(-) (pellet/PBS = 1:8 v/v), aliquots of erythrocyte suspension were mixed 1:1 v/v with polymer solution in PBS(-), mixed by gentle inverting and incubated at 37 °C for 60 min while slowly rotating the samples. After centrifugation at $2,400 \times g$ for 5 min, the supernatants were transferred into a transparent 96-well plate and the hemoglobin release was determined spectrophotometrically with an Infinite 200 (Tecan) at $\lambda_{abs} = 544$ nm. Complete hemolysis (100%) was achieved using 1% Triton X-100 serving as positive control. PBS(-) served as negative control (0%). A value less than 2% hemolysis was taken as non-hemolytic. Experiments were performed with three individual blood donors with four replicates each. The blood donors were 29 and 30 years of age including one female and two male donors. The hemolytic activity of the polymers was calculated using equation (5):

$$\% \text{ Hemolytic activity} = \frac{A_{\text{treated}} - A_{\text{negative control}}}{A_{\text{positive control}} - A_{\text{negative control}}} \times 100\% \quad (5)$$

3. Results and Discussion

3.1. Synthesis and Characterization of Homopolymers

To get better insights into the physicochemical properties of the hydrophobic core of the polymer amphiphiles, the respective homopolymers were synthesized and characterized first. To do so, the two 2-oxazine monomers (**NonOzi** and **EtHepOzi**) were prepared. Synthesis and characterization of both monomers is described in the Supporting Information (Figures S1–S4). To the best of our knowledge, neither has been described in literature. The literature known POx homopolymers (or rather short oligomers) poly(2-(3-ethylheptyl)-2-oxazoline) (**pEtHepOx**)^[35] and poly(2-*n*-nonyl-2-oxazoline) (**pNonOx**)^[36–39] as well as the newly introduced POzi homopolymers poly(2-(3-ethylheptyl)-2-oxazine) (**pEtHepOzi**) and poly(2-*n*-nonyl-2-oxazine) (**pNonOzi**) were prepared by living cationic ring-opening polymerization (LCROP, Scheme 1).

The homopolymers were characterized by ¹H-NMR, GPC, and MALDI-TOF as exemplified in the following for **pEtHepOzi**. For synthesis and characterization of the other homopolymers please refer to Supporting Information (Figures S5–S14, Tables S1–S4) and Table 1.

End-group analysis via ¹H-NMR gave a degree of polymerization (DP) of 9 (Figure 1a, $M_n = 2.1$ kg mol⁻¹; obtained as mean of all relevant signals), which is reasonably close to the targeted DP of 11 (from monomer to initiator ratio $[M]_0/[I]_0$). However, even at such low DP, slight differences in the integration limits of the initiator (signal 2) impacts the apparent DP. The signal of the tert-butyl group of PipBoc (Figure 1a, peak 7) showed a slightly larger integral than expected, which can be attributed to the insufficient base line separation of the adjacent polymer signals. This larger integral was not due to unreacted PipBoc, as the triplet at 2.83 ppm (in CDCl₃), characteristic for unreacted PipBoc, was absent. Also, all other signals could be unambiguously attributed to the target polymer using ¹³C-NMR, DEPT-135 and 2D-HSQC (Figure 1b–d). The GPC elugram of **pEtHepOzi** exhibited an essentially monomodal distribution with a dispersity of 1.05 (Figure 1g). The narrow molar mass distribution was further supported by mass spectrometry. The MALDI-TOF mass spectrum revealed a Poisson-like distribution with a dispersity of 1.07 (Figure 1e; calculated for the main distribution) and a maximum at a DP of 10 (based on the most intense peak at 2,236.2 m z⁻¹; $m/z_{\text{theor}} = 2,236.0$ [Na^+]), closer to the targeted DP of 11. In contrast, GPC slightly underestimated the molar mass ($M_n = 2.0$ kg mol⁻¹; DP = 8).

Table 1. Physicochemical characterization of the homopolymers including the yield, molecular weight M_n , dispersity D , glass transition temperature T_g , and melting point T_m .

Polymer	Yield [%]	$M_n^{a)}$	$M_n^{b)}$	$M_n^{c)}$	$M_n^{d)}$	$\bar{D}^{e)}$	$\bar{D}^{f)}$	$T_g^{f)}$	$T_m^{f)}$	$T_d^{g)}$
		[kg mol ⁻¹]						[°C]	[°C]	
pMeOx ₃₅	79	3.2	3.3	2.3	—	1.05	—	74	*	—
pEtHepOx	49	2.5	2.7	2.2	3.0	1.03	1.04	-26	*	369
pEtHepOzi	22	2.5	2.1	2.0	2.4	1.05	1.07	*	*	360
pNonOx	77	2.3	2.1	1.9	2.5	1.04	1.05	*	89	359
pNonOzi	31	2.5	2.7	2.1	2.3	1.08	1.11	(-35)	(-11)	361

^{a)}According to reactants weighed in; ^{b)}Obtained by ¹H-NMR (CDCl₃; 300 MHz) evaluated as mean of all relevant signals; ^{c)}Obtained by GPC (eluent: HFIP, calibrated with PEG standards); ^{d)}According to the most intense peak of MALDI-TOF spectrum; ^{e)}Obtained with a Poisson distribution from the MALDI-TOF spectrum; ^{f)}Mean T_g and T_m obtained from second and third heating curve (DSC); ^{g)}Onset temperature of major mass loss (TGA); *No value obtained; —not measured.

This can be attributed to the use of PEG-standards for calibration and their different solution behavior in the GPC eluent. The MALDI-TOF spectrum exhibited several distributions (one major and six sub-distributions), however the distance of 211.2 m z⁻¹ between the signals of every species fits very well to the molecular weight of **EtHepOzi** ($m/z_{\text{theor}} = 211.19$). Partial or complete removal of the terminal Boc probably occurred during ionization. Accordingly, the main distribution at 2,236.2 m z⁻¹ (signal set 2, Figure 1f) can be assigned to a deprotected **pEtHepOzi** with a Na⁺ counterion (for a more detailed information of the different MALDI-TOF species please refer to Table S2, Supporting Information).

It is well established that POx exhibit a good thermal stability (onset temperature of major mass loss $T_d > 300$ °C^[40,41]) comparable with other water soluble, organic polymers used for drug delivery ($T_d = 210$ °C [γ -polyglutamic acid];^[42] 330 °C [polyethylene glycol]^[43]). The T_d of the homopolymers comprising C9-side chains was above 350 °C (Figure S23a, Supporting Information, Table 1). However, a first mass loss step occurred already at approximately 250 °C (most pronounced for **pEtHepOzi** exhibiting a weight loss of 12% up to 300 °C), which may be attributed to either thermal, solvent-free degradation of the Boc-group (accounts for approximately 5 wt% of the polymer) or residual solvent/triflate present in the polymer, even though ¹H-NMR spectra did not show the presence of residual solvent.

To get further understandings of the thermal behavior of the homopolymers, DSC measurements were conducted (Figure S24a, Supporting Information). **pNonOx** was the only polymer exhibiting a melting transition ranging from 50 to 100 °C ($T_{m,\text{max}} = 89$ °C). Recrystallization occurred upon cooling between 50 and 10 °C. Not surprisingly, the absence of melting peaks in the case of **pEtHepOx** and **pEtHepOzi** confirmed the hindered alignment of the branched 3-ethyl heptyl side chains causing a decrease in packing density and efficiently preventing crystallization.^[44] The glass transition temperature (T_g) is commonly used to determine the chain segment mobility of a polymer. The higher the glass transition temperature, the lower the chain segment mobility.^[45] Neither **pNonOx** nor **pEtHepOzi** presented clear T_g values at the investigated temperature range from -50 to 200 °C. It should be noted that Rettler and co-workers also did not identify a T_g for **pNonOx** with higher DP of 60 or 100.^[46] For **pEtHepOx**, a T_g of -26 °C was observed.

The shape of the heating curves of **pNonOzi** was rather irregular and may suggest an overlap of a glass transition and a melting point. On the one hand, a gradual increase in the heat capacity c_p from -40 to -30 °C (corresponding to a glass transition), and on the other hand a more or less defined maximum in the heat flow at -11.2 °C (corresponding to an unusually low melting point) appeared. This overlap was corroborated using a lower heating rate (Figure S24b, Supporting Information).

Nevertheless, the less pronounced (if any) melting point suggests a higher chain mobility of POzi (**pNonOzi**) compared to POx (**pNonOx**) homopolymers.^[47] For **pEtHepOx** with a DP of 100, Kempe et al. reported a T_g of -5.6 °C,^[35] which is approximately 20 °C

higher than the T_g obtained presently. Furthermore, **pNonOx** with a DP of 50 exhibited a melting point of 150 °C^[44] (compared to 89 °C in this study). Both observations are in accordance with the common trend that the T_g as well as the melting point increases with increasing chain length for small chain lengths.

3.2. ABA Triblock Copolymers

Next, the ABA triblock copolymers comprising **pNonOx**, **pNonOzi**, **pEtHepOx**, and **pEtHepOzi** as hydrophobic block B as well as **pMeOx** as hydrophilic blocks A were prepared by consecutive LCROP. As all block copolymers comprise the same hydrophilic blocks A, they will be labeled according to their hydrophobic block **A-pNonOx-A**,^[25,27,48] **A-pNonOzi-A**, **A-pEtHepOx-A**, and **A-pEtHepOzi-A**.

All triblock copolymers were thoroughly characterized by ¹H-NMR and GPC, exemplified here using the novel **A-pEtHepOzi-A**. For further characterization of all other copolymers please refer to Supporting Information (Figures S15–S22) and Table 2. Analogue to the homopolymers, ¹H-NMR revealed a good synthetic control via $[M]_0/[I]_0$ (Figure 2a,b). Again, the signal of the tert-butyl group of PipBoc (signal 7) was overestimated, which could be explained by insufficient base line separation of the adjacent polymer signals as mentioned above. After full monomer consumption (verified by ¹H-NMR) and before subsequent monomer addition, small amounts of the reaction mixtures were sampled and analyzed by GPC (Figure 2c) without further purification (first and second block) and after dialysis (third block). A distinct shift to higher molar masses was clearly visible after consumption of each block. In particular, the eluogram of the final product appeared essentially monomodal with a reasonably low dispersity ($D < 1.2$).

Thermally, the ABA triblock copolymers were slightly more stable than the respective homopolymers exhibiting onsets of major mass loss >360 °C (Figure S23b, Supporting Information, Table 2). Again, a first minor mass loss step occurred already at approximately 250 °C. However, this first weight loss was less pronounced compared to the homopolymers, corroborating that this may be caused by degradation of the Boc-group

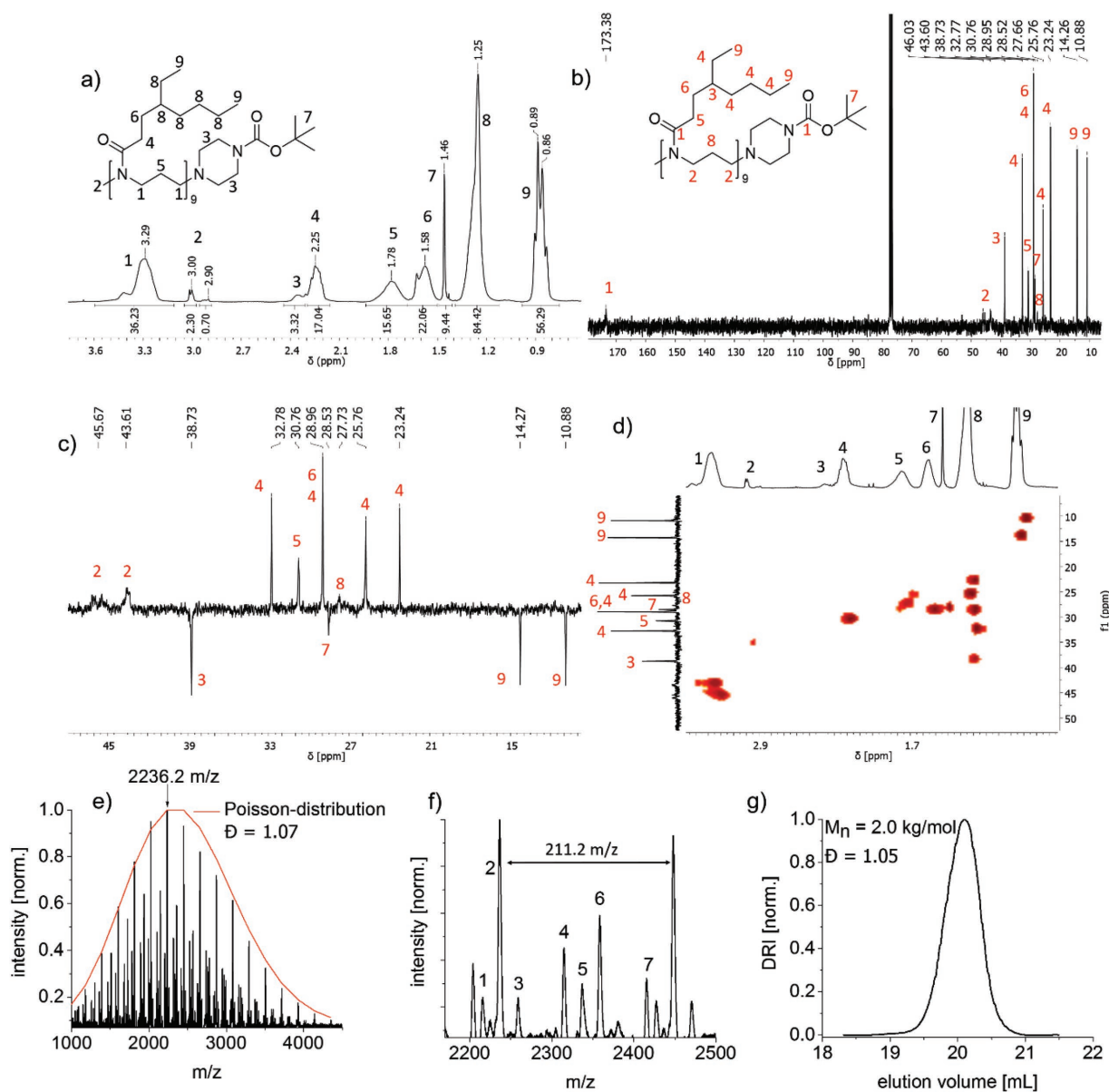


Figure 1. a) ¹H-NMR; b) ¹³C-NMR; c) DEPT-135 and d) HSQC (CDCl₃; 300 MHz; 298 K) of pEtHepOzi with signal assignment of all major signals; e) MALDI-TOF of pEtHepOzi with Poisson distribution of the main distribution (red curve, calculated); f) enlarged MALDI-TOF spectrum; g) GPC elugram (HFIP) of pEtHepOzi.

or residual triflate present in the polymer. A good thermal stability will be favorable for the formulation of different drugs by hot melt extrusion (vide infra), where the melting temperature of the drug often needs to be exceeded without compromising the polymer integrity.^[49] This issue needs to be evaluated further for the present polymers, investigating, for example, other polymer termini.

Unexpectedly, the ABA triblock copolymers exhibited similar T_g values in the narrow range of 54 °C to 61 °C (Figure S25, Supporting Information) with no melting transition. This is rather surprising, as the homopolymers corresponding to the hydrophobic blocks differed strongly in their thermal behavior (vide supra). Therefore, one might expect that according to the

Fox equation (Equation (6)), the T_g of the triblock copolymers should also differ significantly, as the hydrophilic blocks remain essentially the same in all cases.

$$\frac{1}{T_{g,mix}} = \frac{w_1}{T_{g,1}} + \frac{w_2}{T_{g,2}} \quad (6)$$

where $T_{g,mix}$ is T_g of the mixture; $T_{g,1}$ and $T_{g,2}$ are the T_g values of compound 1 and 2, respectively; and w_1 and w_2 are the weight fractions of compound 1 and 2, respectively.

The homopolymer pMeOx with a DP of 35 (pMeOx35) representing the hydrophilic A blocks of the ABA-triblock copolymers was synthesized (for synthesis and characterization please

Table 2. Physicochemical characterization of ABA-triblock copolymers including the yield, molecular weight M_n , dispersity D , glass transition temperature T_g , critical micelle concentration CMC, and mean hydrodynamic radius R_h .

Polymer	Yield [%]	$M_n^{a)}$	$M_n^{b)}$	$M_n^{c)}$	$D^{d)}$	$T_d^{d)}$ [°C]	$T_g^{e)}$ [°C]	CMC ^{f)} [mM·10 ⁻⁴]	CMC ^{f)} [mg L ⁻¹]	$R_h^{g)}$ [µm]
A-pEtHepOx-A	88	8.9	8.9	4.9	1.16	368	60	5.6	4.9	32
A-pEtHepOzi-A	90	8.7	9.5	4.4	1.15	375	54	4.8	4.1	11
A-pNonOx-A	83	8.5	6.5	5.0	1.17	379	60	6.2	5.3	60
A-pNonOzi-A	69	8.5	8.1	4.5	1.24	362	60	12.7	10.8	20

^{a)}According to reactants weighed in; ^{b)}Obtained by ¹H-NMR (CDCl₃; 300 MHz); ^{c)}Obtained by GPC (eluent: HFIP, calibrated with PEG standards); ^{d)}Onset temperature of major mass loss (TGA); ^{e)}Mean T_g obtained from second and third heating curve (DSC); ^{f)}Obtained by pyrene assay at 25 °C; ^{g)}Mean R_h obtained by DLS from the average diffusion coefficient at 25 °C.

refer to Table 1 and Figures S13–S14, Supporting Information) and characterized by DSC ($T_g = 74$ °C; Figure S24, Supporting Information). Thus, the T_g of all homopolymers would have to be about -13 °C (calculated using equation (6) with the measured T_g value of pMeOx35 and the respective values of the triblock copolymers), which clearly does not fit the experimental results. This could mean that in the solid state, the intra- and intermolecular interactions between the hydrophilic pMeOx chains, and the hydrophobic segments of the triblock copolymers are significant compared to the intra- and intermolecular interactions of the hydrophobic block itself, increasing the relative stiffness of the ABA-triblocks and therefore $T_{g,mix}$. This is in accordance with the observation that only a single $T_{g,mix}$ was observed, elucidating a homogeneous structure with no (micro) phase separation present.

The CMC in aqueous solution was determined by pyrene assay.^[33,50] The calculated CMCs of all ABA triblock copolymers were very similar, except for A-pNonOzi-A, exhibiting a somewhat higher CMC (Figure 3a; Table 2). However, the higher CMC is due to the somehow smaller $I_1:I_3$ ratio at $c(\text{A-pNonOzi-A}) = 10^{-7}$ M, causing a flattening of the baseline and therefore a delayed decay of the fitting curve. Apart from that, the $I_1:I_3$ ratio decreased for all polymers within the same concentration range, displaying limitations of the pyrene assay to determine CMCs. It should be noted that the aqueous stock solution of A-pNonOx-A had to be annealed at 80 °C for 12 h in order to avoid large non-equilibrium aggregates^[51] (for apparent CMC of non-annealed A-pNonOx-A, see Figure S27a, Supporting Information). It is interesting that the shape of $I_1:I_3$ ratio versus concentration plot is much steeper for the tempered A-pNonOx-A, compared to the other triblock copolymers and compared to the non-annealed polymer. Considering the thermal properties of the core-forming homopolymers, one may be tempted to attribute this to the solid nature of the hydrophobic core, but the thermal analysis of the triblock copolymers does not support this notion, as all four triblocks show almost identical thermograms (Figure S25, Supporting Information).

Furthermore, the size of the unloaded polymer micelles was analyzed by DLS (Figure 3b,c). Due to solubility issues, A-pNonOx-A had to be diluted to 1 g L⁻¹, whereas the other polymers were measured at 10 g L⁻¹. The micelles/aggregates formed by A-pEtHepOx-A, A-pEtHepOzi-A, and A-pNonOzi-A

exhibited apparent hydrodynamic radii (R_h) below 50 nm. The apparent R_h of A-pNonOx-A exhibits a pronounced angle dependence, which could be explained by a broad particle size distribution or non-spherical aggregates (or both). As it is previously confirmed that formation of worm-like micelles from A-pNonOx-A,^[52,53] it can be assumed that this will be the case here for this new batch. (Figure 3c; for DLS of non-annealed A-pNonOx-A, see Figure S27b,c, Supporting Information). Interestingly, both block copolymers with a POzi-based hydrophobic core exhibited a smaller R_h compared to the POx-based polymers (Table 2).

3.3. In Vitro Cell Cytotoxicity and Hemolysis

The low CMCs and small micellar sizes of the present ABA triblock copolymers make them potentially suitable for in vivo applications. For this, the cell compatibility as well as hemolytic activity of the respective copolymers is of interest. After 24 h treatment, none of the triblock copolymers decreased the cell viability of HDF compared to untreated control (Figure 4a). It should be noted, that the solution of A-pNonOx-A in cell culture medium was not completely clear at 10 g L⁻¹, exhibiting whitish streaks which could not be removed by centrifugation (A-pNonOx-A was completely soluble at concentrations ≤ 1 g L⁻¹). Nevertheless, the cytotoxicity of A-pNonOx-A was still evaluated at 10 g L⁻¹ for comparison reasons with no sign of reduction in viability. After 48 h treatment, only A-pNonOzi-A appears slightly cytotoxic with a corresponding reduction in cell viability to $70 \pm 4\%$ (Figure 4b). However, such relatively high concentrations for comparable long periods of time would not be expected in case of in vivo administration due to the significant dilution upon injection. Nevertheless, it should be noted that previously POx-based triblocks with a less pronounced amphiphilic contrast, such as A-pPrOzi-A, but also those with a very hydrophobic poly(2-benzyl-2-oxazoline) central block (A-pBzOx-A) did not show any sign of cytotoxicity up to even higher polymer concentrations of 100 g L⁻¹ against HDF.^[31,54]

We also investigated these new polymer amphiphiles with respect to their hemolytic potential. Non-ionic hydrophilic POx^[55,56] and POx amphiphiles with a weak hydrophilic/lipophilic contrast^[26] have been described to show very little hemolysis. However, the polymers described here exhibit a much stronger hydrophilic/lipophilic contrast, which may lead to more pronounced hemolysis. However, none of the POx-based triblock copolymers was hemolytic (Figure 4c; a hemoglobin release below 2% is considered to be non-hemolytic). To the best of our knowledge, the presently investigated POzi represent the first POzi to be investigated with respect to their hemolytic activity and also did not show any sign of hemolysis. As stated before, A-pNonOx-A was not fully soluble at polymer concentrations >1 g L⁻¹. Nevertheless, the hemolysis assay was also performed with the slightly turbid solution of 5 g L⁻¹ A-pNonOx-A. Due to the turbidity, no spectrophotometric quantification of the hemoglobin release could be performed.

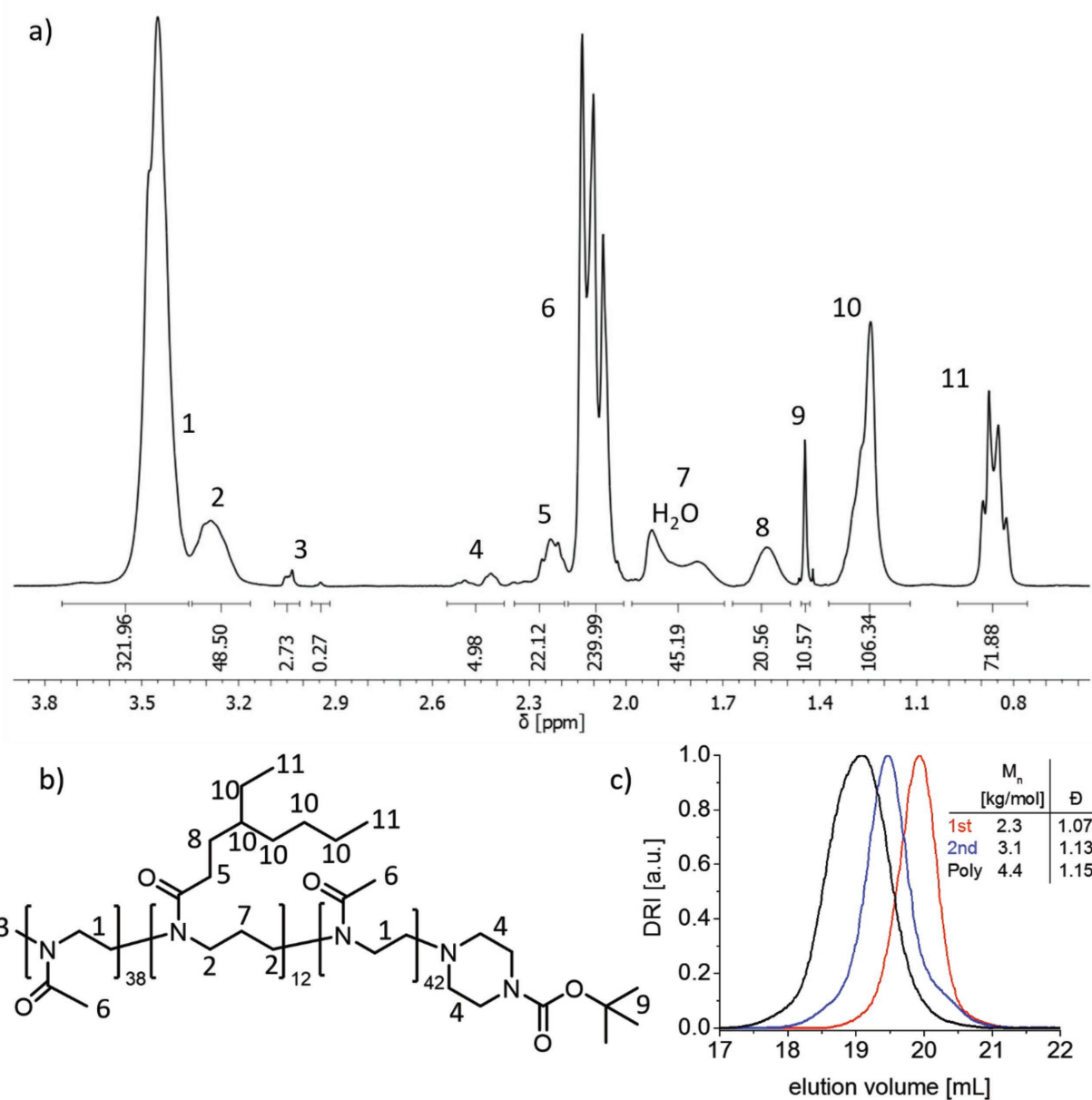


Figure 2. a) ¹H-NMR spectra (CDCl₃; 300 MHz; 298 K) of A-pEtHepOzi-A with signal assignment of all major signals; b) chemical structure of A-pEtHepOzi-A; c) GPC elugrams (HFIP) with corresponding data of A-pEtHepOzi-A after each block.

However, as judged by visual inspection, no hemoglobin was released (lack of red color).

3.4. Drug Formulation

The good cytocompatibility and absence of any hemolytic activity of the investigated ABA triblock copolymers corroborates the potential for in vivo applications. Thus, they were employed to formulate the highly water insoluble drugs curcumin (CUR; log *P* = 3.28,^[57] solubility [H₂O] = 0.01–0.6 mg L⁻¹^[58,59]) and paclitaxel (PTX; log *P* = 3.96^[60]; solubility [H₂O] =

0.4–4 mg L⁻¹^[61]) using the thin film method (Figure S28, Supporting Information).^[24]

During the preparation of the CUR-loaded micelles by thin film hydration, pronounced differences between the respective formulations were already apparent by visual inspection. Apart from the visual solvatochromicity, at the lowest CUR feed of 2 g L⁻¹ ($\rho(\text{polymer}) = 10 \text{ g L}^{-1}$ for all formulations), noticeable precipitation occurred in the case of the POx-based A-pEtHepOx-A (Figure 5a,d) and A-pNonOx-A (Figure 5c). The resulting supernatant appeared only slightly yellow, corroborating a very low CUR formulation (Figure 5a, left tube). In contrast, no precipitate was observed at the same CUR feeds

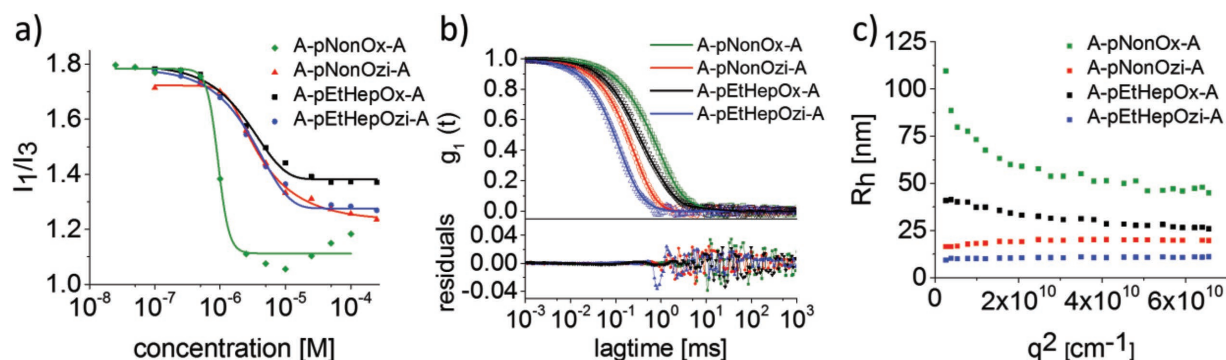


Figure 3. a) $I_1:I_3$ ratio (pyrene assay) in dependence of the ABA triblock copolymer concentration with corresponding fits. CMC was defined as a decrease of the $I_1:I_3$ ratio to 90% of its initial value; b) $g_1(t)$ (top graph, empty symbols) as well as corresponding fits (top graph, solid lines) with residuals (bottom graph) of the copolymers at a measurement angle of 90° . The polymer concentration was 10 g L^{-1} (**A-pNonOx-A**: 1 g L^{-1}); c) apparent hydrodynamic radii of aqueous ABA triblock copolymer solutions as a function of the scattering vector q^2 .

using the POzi with the same side chains, namely **A-pEtHepOzi-A** (Figure 5a,f) and **A-pNonOzi-A** (Figure 5b,e).

For PTX^[25] or CUR^[31] formulations with ABA triblock copolymer comprising a modestly hydrophobic **pBuOx** core, the *LE* decreased dramatically from 90% to essentially 0% after exceeding a certain drug-feed. In the case of **A-pEtHepOx-A** the situation appears to be vice versa, as doubling the CUR feed from 2 to 4 g L^{-1} enabled much better encapsulation ($LE = 0.2\%$ vs. 47.1% ; Figure 5a,d). A similar, however less pronounced increase in the *LE* could be obtained with the structural isomer **A-pNonOx-A** (Figure 5e). At higher CUR feed concentrations, higher standard deviations between the individually prepared formulations were observed (Figure 5c–f). This is in contrast to earlier reports using POx with short aliphatic side chains, where the standard deviations were typically very low ($\leq 8\%$) even at the highest drug loadings and also inter-lab reproducibility was excellent over many years. For example, in the case of **A-pNonOzi-A**, individual *LC* differed between $17.7 \text{ wt}\%$ ($\rho(\text{CUR}) = 2.2 \text{ g L}^{-1}$; $LE = 17.9\%$) and $51.1 \text{ wt}\%$ ($\rho(\text{CUR}) = 10.4 \text{ g L}^{-1}$; $LE = 87\%$) at CUR feeds of 12 g L^{-1} . Such poor reproducibility would not be favorable for further development. The reason for this poor reproducibility is unknown at this point, but it may hint toward a high dependency with respect

to formulation parameters such as temperature or air stream flow, even though these were kept constant to the best of our abilities. Apart from the high standard deviation, increasing the drug feed up to 8 g L^{-1} increased the mean *LC* for all triblock copolymers. However, at very high CUR-feeds (10 and 14 g L^{-1} , respectively) (Figure 5c,e,f), *LC* and *LE* decreased again. In the case of **A-pNonOzi-A**, this was particularly pronounced with a reduction of *LE* from $79.0 \pm 2.0\%$ (CUR feed = 10 g L^{-1}) to $12.0 \pm 2.0\%$ (CUR feed = 14 g L^{-1}).

Generally, the POzi-based ABA triblock copolymers exhibited significantly higher maximum CUR-loadings compared to the POx-based formulations ($\rho_{\text{max}}(\text{CUR}) = 3.21 \pm 2.46$ [**A-pNonOx-A**] vs. $7.90 \pm 0.24 \text{ g L}^{-1}$ [**A-pNonOzi-A**] and 2.79 ± 1.08 [**A-pEtHepOx-A**] vs. $5.74 \pm 0.44 \text{ g L}^{-1}$ [**A-EtHepOzi-A**]) resulting in polymer drug-specificities of $1/2.5$ for nonyl and $1/2.1$ for 3-ethylheptyl-based copolymers with respect to the *LC*. Such polymer-CUR specificities have already been observed previously for **A-pPrOx-A** and **A-pBuOx-A** versus **A-pPrOzi-A** and **A-pBuOzi-A**, respectively.^[28] Also in this case, the POzi-based triblock copolymers were superior to the POx-based ones with respect to the *LC* for curcumin. Also, CUR solvatochromicity was observed with formulations with POzi-based hydrophobic blocks appeared yellowish,

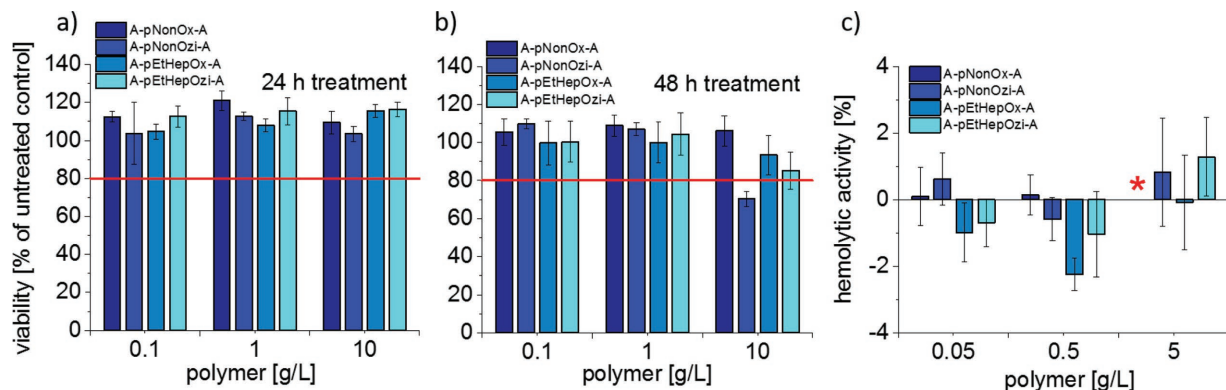


Figure 4. Cell viability of primary human dermal fibroblasts treated with increasing polymer concentrations (0.1 – 10 g L^{-1}) for a) 24 h and b) 48 h. Cell viability was assessed using CellTiter-Glo. Data are presented as means \pm SD ($n = 3$); c) hemolysis assay of erythrocytes after incubation with ABA-triblock copolymers at indicated concentrations. A value of less than 2% hemoglobin release is classified as non-hemolytic and more than 5% as hemolytic. The missing value for **A-pNonOx-A** at 5 g L^{-1} (red star) is due to solubility issues causing turbidity and therefore interfering with spectrophotometric quantification. Values are presented as means \pm SD ($n = 4$).

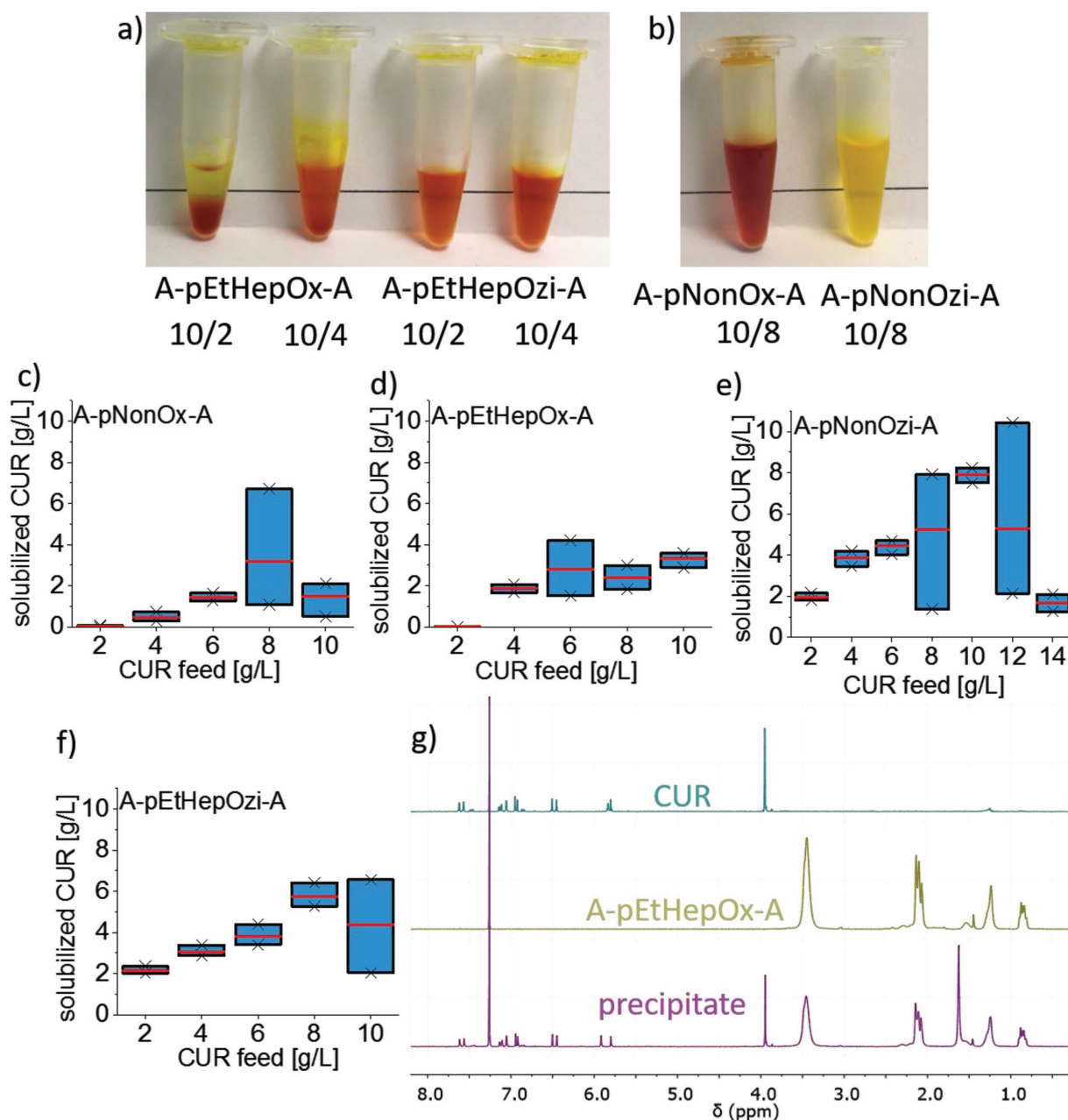


Figure 5. a) Optical appearance of CUR formulations of **A-pEtHepOx-A** and **A-pEtHepOzi-A** at polymer/drug-feed ratios of 10/2 & 10/4 [g L^{-1}]; b) appearance of CUR formulated with **A-pNonOx-A** and **A-pNonOzi-A** at a polymer/drug-feed ratio of 10/8 [g L^{-1}]; c) $^1\text{H-NMR}$ (CDCl_3 ; 300 MHz; 298 K) of the precipitate in the left tube shown in Figure 5a, neat **A-pEtHepOx-A** and neat CUR. Aqueous CUR-concentrations in dependence of the CUR-feed concentration at $\rho(\text{polymer}) = 10 \text{ g L}^{-1}$ of d) **A-pNonOzi-A**; e) **A-pNonOx-A**; f) **A-pEtHepOx-A**; and g) **A-pEtHepOzi-A**. The three individually prepared formulations at a certain CUR-feed concentration are shown as boxplot (red line = mean) with the highest and lowest solubilized CUR concentration being the upper and lower limit, respectively.

whereas POx-based copolymers exhibited a rather red color (Figure 5b).^[28,31]

A closer look at the precipitate of $\rho(\text{A-pEtHepOx-A/CUR}) = 10/2 \text{ g L}^{-1}$ (Figure 5a, left tube) revealed a rather voluminous, gel-like agglomerate or coacervate, instead of crystalline particles. To obtain a better perception of the composition of the precipitate, the clear and slightly yellow supernatant was removed, and the remaining solid/gel was carefully washed five times with water to remove any residual soluble formulation.

The remaining coacervate/gel was freeze-dried, dissolved in CDCl_3 , and characterized by $^1\text{H-NMR}$ spectroscopy (Figure 5g). Clearly, the precipitate did not only consist of precipitated curcumin, but also polymer. More strikingly, the ratio of polymer/CUR = 10:2.9 w/w correlated well to the initially added concentrations of **A-pEtHepOx-A/CUR** = 10/2 w/w. Important to note, in the absence of drug, **A-pEtHepOx-A** dissolved neatly. Therefore, the presence of CUR is necessary for coacervate formation.

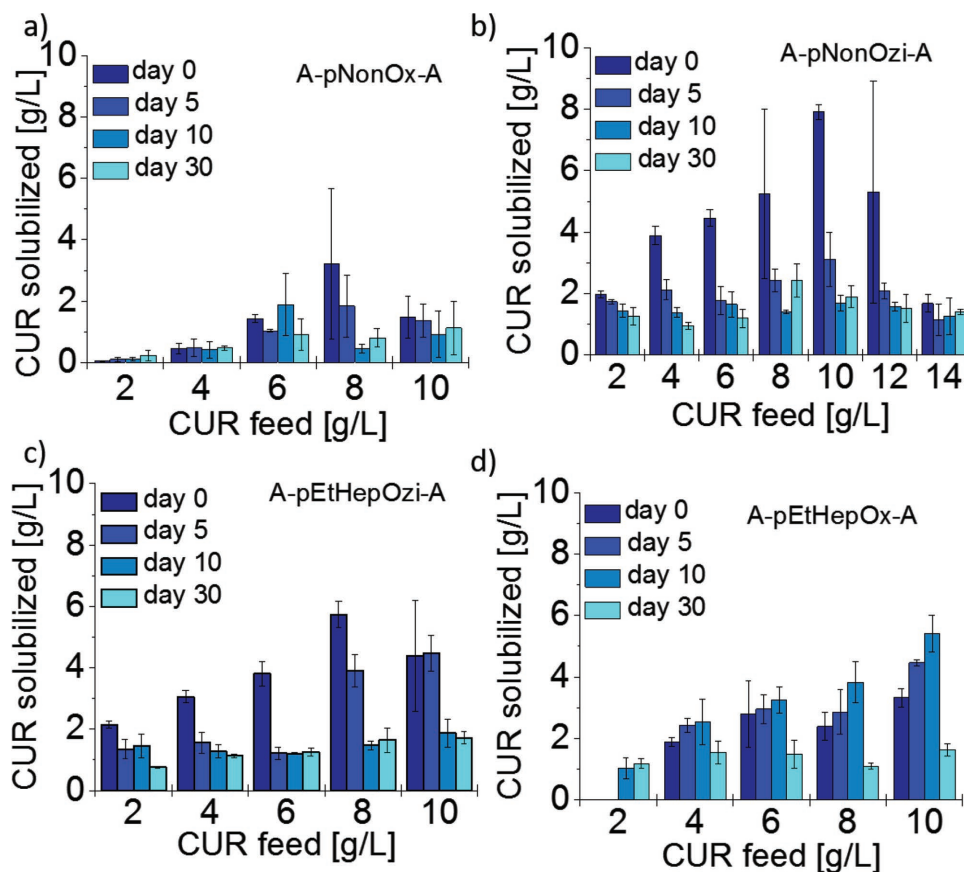


Figure 6. Long-term stability of CUR formulated with a) **A-pNonOx-A**, b) **A-pNonOzi-A**, c) **A-pEtHepOx-A**, and d) **A-pEtHepOzi-A** in dependence of the CUR-feed concentration ($\rho(\text{polymer}) = 10 \text{ g L}^{-1}$). Data is given as mean \pm SD ($n = 3$).

An unexpected difference between POx- and POzi-based CUR formulations was observable also with regard to the long-term stability of the respective formulations (Figure 6a–d). In the case of **A-pNonOzi-A** and **A-pEtHepOzi-A**, CUR-loading decreased over a 30-day period (Figure 6b,c). In the same period, the drug loading of **A-pNonOx-A** remained rather constant (Figure 6a). Unexpectedly, in the case of **A-EtHepOx-A**, the drug loading increased at all CUR-feed concentrations from day 0 to day 10 (Figure 6d). Even though in some cases the means are not significantly different due to the large standard deviations (e.g., drug feed 6 g L^{-1}), the overall trend appears reasonably clear. At 10 g L^{-1} CUR feed, a 1.6-fold increase in the drug loading from $3.3 \pm 0.3 \text{ g L}^{-1}$ (day 0) to $5.41 \pm 0.6 \text{ g L}^{-1}$ (day 10) was observed. At this point, it should be noted that all formulations were stored in Eppendorf tubes containing the initial gel/coacervate. Therefore, in the case of **A-pEtHepOx-A**, it seemed that either initially precipitated CUR was dissolved by neat polymer present in solution, or that the initial coacervate dissolved over the 10-day period.

The latter assumption is supported by the previously discussed observation, that the precipitate not only contained CUR, but also polymer (Figure 5g). As a control experiment, neat CUR was dispersed in water and **A-pEtHepOx-A** was added ($\rho(\text{A-pEtHepOx-A/CUR}) = 10/3 \text{ g L}^{-1}$). The dispersion was stored in the dark at ambient conditions ($T \approx 25 \text{ }^\circ\text{C}$) and samples were withdrawn after centrifugation after predefined

time intervals. No CUR was detectable in the supernatant by UV-VIS absorption (as well as visual inspection) within the first 24 h. Subsequently, the dispersion was shaken at $55 \text{ }^\circ\text{C}$ in the dark up to 15 days. Again, no CUR was detectable in the supernatant, clearly refuting the assumption that polymer in solution might be able to formulate initially precipitated CUR. Obviously, the polymer is unable to overcome the lattice energy of crystalline CUR. To further proof that drug/polymer coacervate re-dissolves in the case of **A-pEtHepOx-A**, the initial precipitate occurring during thin-film method (Figure 5a) was gently washed five times with water. Subsequently, a defined amount of water was added and the dispersion stored at ambient conditions in the dark. Whereas no CUR was detectable immediately after rehydration, the aqueous drug concentration continuously increased over a 23-day period (Figure S29, Table S19, Supporting Information). Therefore, it seemed that the POx/POzi-based amphiphiles not only slowed down the kinetics of CUR crystallization, but also drastically shift the thermodynamic equilibrium with regard to the CUR solubility, as at least 2.500 to 300.000-fold increase ($\rho(\text{CUR}) = 1.5\text{--}3 \text{ g L}^{-1}$) in CUR solubility (CUR solubility in $\text{H}_2\text{O} = 0.01\text{--}0.6 \text{ mg L}^{-1}$) occurred. This is quite remarkable, considering that few reported CUR formulations achieve such CUR solubilities at any given point. Also, it is important to note that the signs for chemical degradation were not observed, which is often reported for the relatively reactive/unstable CUR.^[62]

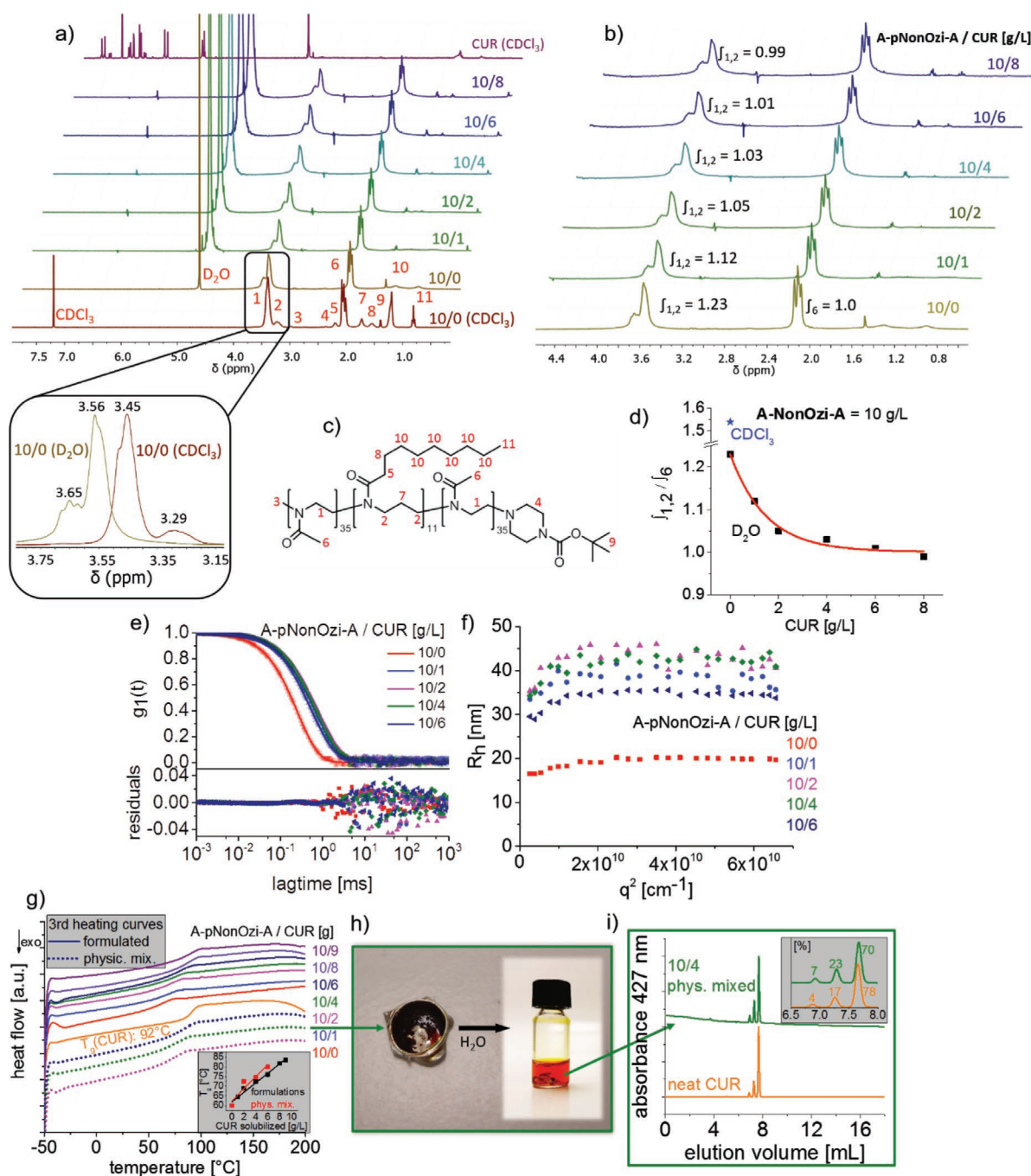


Figure 7. a) ¹H-NMR spectra (300 MHz, 298 K) of neat A-pNonOzi-A in CDCl₃ (bottom, red spectrum) and D₂O (golden spectrum), CUR-loaded A-pNonOzi-A micelles with increasing CUR content (CDCl₃; bottom to top) and neat CUR (CDCl₃; top, purple spectrum) with signal assignment of all major polymer signals. Polymer concentration was kept constant at ρ(A-pNonOzi-A) = 10 g L⁻¹. For better visibility, enlarged section of neat A-pNonOzi-A in D₂O and CDCl₃ is shown; b) enlarged spectra of CUR-loaded micelles with increasing drug content (bottom to top) in D₂O. Integral of methyl-side chain (signal 6) was set to 1 and corresponding integrals of POx/POzi backbone (signals 1 & 2) are shown; c) chemical structure and signal labeling of A-pNonOzi-A; d) ratio of the signal intensity of the POx/POzi backbone (signals 1 & 2) and the methyl side chain (signal 6) with increasing CUR content in D₂O (red curve = exponential decay fit). For comparison, ratio in CDCl₃ is shown (blue asterisk); e) Autocorrelation curves and fit residuals from dynamic light scattering of the various A-pNonOzi-A/CUR nanoformulations in DI water and f) apparent hydrodynamic radii of aqueous A-pNonOzi-A/CUR nanoformulations as a function of the scattering vector q². g) Heat flow (DSC) of the 3rd heating (10 °C min⁻¹) from -50 °C to 200 °C of CUR (orange), A-pNonOzi-A (red) or A-pNonOzi-A/CUR mixtures which were either formulated and subsequently lyophilized (solid lines) or physically mixed (dotted lines). Inset shows the T_g values in dependence of the amount of CUR solubilized (formulations) or added (physical mixtures); h) photograph of opened DSC crucible and of its content dissolved in DI water (A-pNonOzi-A/CUR mix 10/4 after three heating/cooling cycles) as well as the redispersed (H₂O) sample; i) HPLC elugram of the redispersed sample compared to neat CUR. Enlarged section shows all relevant signals as well as the relative amount [%] of BDMC, DMC, and CUR.

The study the interactions between CUR and **A-pNonOzi-A** (which is forming the nanoformulations with the highest CUR concentration), neat polymer and CUR-loaded nanoformulations were investigated by $^1\text{H-NMR}$ spectroscopy (Figure 7). Not surprising, already in the absence of CUR, major differences between the spectra of **A-pNonOzi-A** in CDCl_3 and D_2O are observed (Figure 7a, red and golden spectra). Whereas in CDCl_3 all $^1\text{H-NMR}$ signals of **A-pNonOzi-A** (Figure 7c) were clearly visible, the signals correlating to the hydrophobic **pNonOzi** block (signals 2, 5, 8, 10, 11) were significantly attenuated in D_2O . At the investigated concentration ($\rho = 10 \text{ g L}^{-1}$), **A-pNonOzi-A** is present almost exclusively (>99%) in form of micelles (CMC = 10.8 mg L^{-1} ; Figure 3a) in D_2O . Within the hydrophobic domain, the **pNonOzi** block is strongly hindered in its mobility causing a broadening and disappearance of the correlating $^1\text{H-NMR}$ signals by shortening its transverse relaxation time T_2 (spin–spin relaxation). In contrast and as expected, predominantly unimers were present in CDCl_3 . A closer look at the polymeric backbone (Figure 7a, enlarged section) revealed a downfield shift and a modified appearance of the $^1\text{H-NMR}$ signals of the polymeric backbone in D_2O compared to CDCl_3 . The downfield shift might be caused by hydrogen bonding, withdrawing electronic density from the tertiary amide of POx/POzi. The broad shape of the POx/POzi backbone is generally explained by cis/trans isomerism of the tertiary amide moiety. Therefore, the modified intensities might also be caused by a different ratio of cis/trans isomers, which can be expected changing the solvent. As the signal of the central methylene unit of the POzi-backbone (signal 7) completely disappeared in D_2O , it is unlikely that the signal at 3.65 ppm (Figure 7a, enlarged section) corresponds to the initial signal of the POzi backbone at 3.29 ppm.

None of the spectra of CUR-loaded micelles ($\rho(\text{CUR}) = 1\text{--}8 \text{ g L}^{-1}$) exhibited the signals characteristic for curcumin (Figure 7a, top spectrum). Furthermore, the signals of the NonOzi-side chain, which were still slightly detectable in the absence of CUR in D_2O (signals 8, 10, 11), completely disappeared in all formulations hinting a further reduction in chain mobility. In contrast, the methyl side chain of the hydrophilic pMeOx block (signal 6) was much less affected, indicating no major interaction with CUR. With increasing drug content, the ratio between the signals of the POx/POzi backbone (signals 1, 2) and the methyl side chain (signal 6) decreased essentially exponentially toward unity (Figure 7d). This indicates either interactions between the POx backbone and CUR, or that the signal of the POzi backbone (signal 2) underneath the signal of the POx backbone (signal 1) is more and more disappearing. However, in this case the ratio should decrease to a minimum 4:3, wherefore the obtained value of 1 hints toward a more complex situation which warrants further investigations.

Interactions between CUR and the ABA triblock copolymers were also apparent in the solid state (Figure S30, Supporting Information). Lyophilized drug-loaded polymer micelles exhibited a modified IR-spectra with a signal occurring at 1579 cm^{-1} , whereas simply physical mixed polymer/CUR with the same polymer and CUR contents did not show this absorption. As this absorption was close to the vibration band of the amide group of POx/POzi at $1,624 \text{ cm}^{-1}$, this signal could be related to the amide groups of the hydrophobic core interacting with

CUR. However, a more in-depth investigation is necessary to confirm this. Furthermore, the signal at $1,601 \text{ cm}^{-1}$ characteristic for CUR disappeared within the formulations, whereas mixed polymer/CUR clearly showed this signal. In addition, this signal became more dominant with increasing CUR content in the physical mixture.

The apparent hydrodynamic radii of the CUR-loaded polymer micelles of **A-pNonOzi-A** were slightly larger ($R_h \approx 40 \text{ nm}$) than of the neat polymer micelles ($R_h = 20 \text{ nm}$) (Figure 7e,f). The amount of CUR solubilized had a minor effect on R_h . None of the lyophilized CUR-loaded **A-pNonOzi-A** formulations showed a sign of CUR crystallinity in the first DSC-heating curve (after freeze drying, Figure S26a, Supporting Information). This is important, as the bioavailability of amorphous drugs is generally higher than that of crystalline ones, as the lattice energy does not need to be overcome. Furthermore, only a single T_g occurred in the third (and second) heating curves. This shows that the formulation forms a homogenous mixture without (micro)phase-separation (Figure 7g). In accordance with the Fox-equation (equation (6)), the T_g linearly increased with increasing drug content ($T_g(\text{CUR}) = 92 \text{ }^\circ\text{C}$ ($LC = 1 \text{ wt}\%$) to $84 \text{ }^\circ\text{C}$ ($LC = 47 \text{ wt}\%$; Figure 7g). In contrast to the formulations, an endothermic peak (more intense at higher CUR-content) occurred between $120 \text{ }^\circ\text{C}$ and approximately $180 \text{ }^\circ\text{C}$ (Figure S26b, Supporting Information) in the heat flows of the first heating cycle of physically mixed **A-pNonOzi-A/CUR** blends. However, the second and third heating curves also exhibited only a single T_g comparable to the ones of the formulations with no sign of CUR-crystallinity or microphase separation (Figure 7g). This indicates that CUR can be formulated solvent free within the polymer melt essentially representing the hot-melt extrusion process. To corroborate this, the aluminum pan was opened after the third heating curve and its contents were dispersed in water. A complete dissolution of the solid occurred without any residual solids (Figure 7h). HPLC analysis (Figure 7i, green curve) is in accordance with CUR ($R_t = 7.7 \text{ min}$), demethoxycurcumin (DMC, $R_t = 7.3 \text{ min}$), and bis-demethoxycurcumin (BDCM, $R_t = 6.9 \text{ min}$). The ratio of these curcuminoids slightly differed from that of neat CUR used in this study, derived from the rhizome of *C. longa*. Nevertheless, it is found that it is promising that the rather instable CUR is readily formulated in the melt without major degradation. This approach should be particularly suitable for more stable drugs. Altogether, CUR was clearly formulated in the solid state during the DSC measurements. The enthalpy of dissolution during the first heating cycle of any **A-pNonOzi-A/CUR** physical mixtures is obviously endothermic.

Compared to the formulations of CUR, the PTX formulations of **A-pEtHepOx-A**, **A-pEtHepOzi-A**, **A-pNonOx-A**, and **A-pNonOzi-A** exhibited an even more inordinate pattern with respect to the LC and long-term stability (Figure 8a–d). Visible precipitation occurred in all samples after rehydration of the dried films prepared by thin film method. At the day of preparation, maximum PTX concentrations of only $1.24 \pm 0.76 \text{ g L}^{-1}$ for **A-pNonOx-A** ($LC = 11.0 \pm 7.1 \text{ wt}\%$), $2.13 \pm 1.60 \text{ g L}^{-1}$ for **A-pNonOzi-A** ($LC = 21.0 \pm 16.7 \text{ wt}\%$), $0.74 \pm 0.07 \text{ g L}^{-1}$ for **A-pEtHepOx-A** ($LC = 6.9 \pm 0.7 \text{ wt}\%$), and $1.86 \pm 0.10 \text{ g L}^{-1}$ for **A-pEtHepOzi-A** ($LC = 15.7 \pm 1.0 \text{ wt}\%$) could be obtained. Previously, using another batch of **A-pNonOx-A**, slightly higher

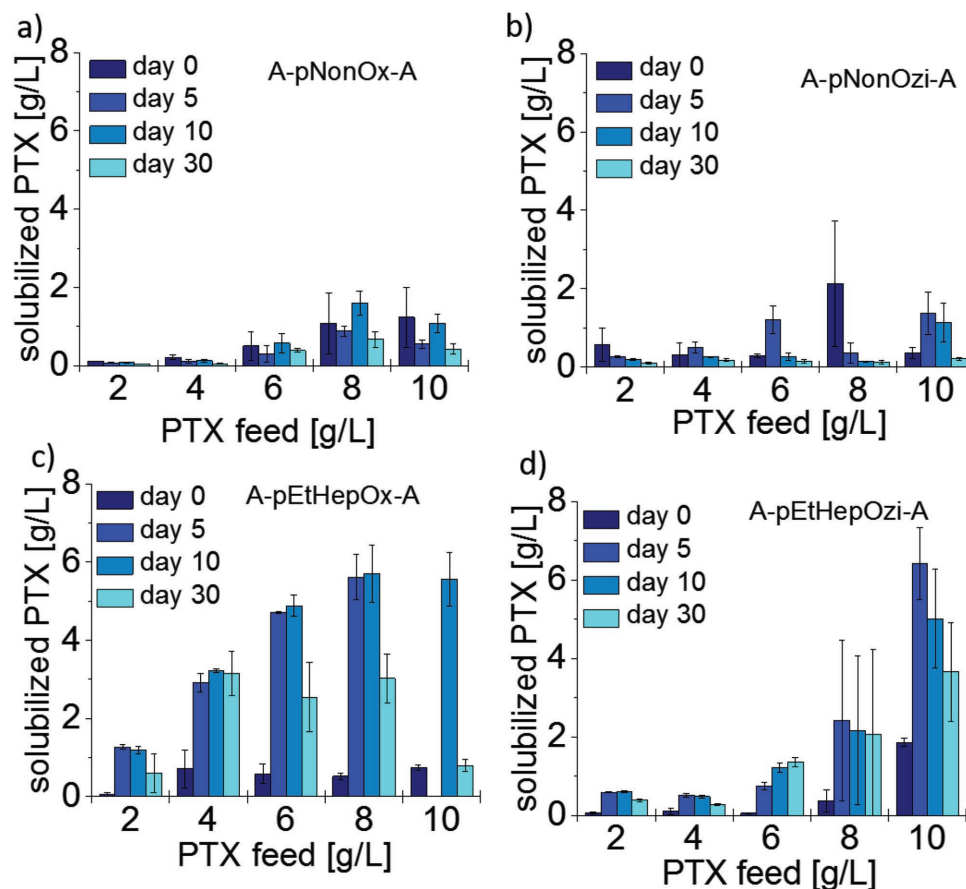


Figure 8. Long-term stability PTX formulated with a) A-pNonOx-A, b) A-pNonOzi-A, c) A-pEtHepOx-A, and d) A-pEtHepOzi-A in dependence of CUR-feed concentration ($\rho(\text{polymer}) = 10 \text{ g L}^{-1}$). Data is given as mean \pm SD ($n = 3$).

maximum aqueous PTX contents of $3.2 \pm 0.4 \text{ g L}^{-1}$ ($LC = 24 \text{ wt\%}$) with much lower standard deviations between the samples (prepared in triplicates) were reported.^[27] However, in this case, the volume of the aqueous formulations was 0.1 mL. Increasing the volume up to 1.5 mL at same polymer and drug concentrations lead to a significant decrease in the LC and maximum PTX contents less than 2 g L^{-1} . Unfortunately, only a single sample was investigated at a 1.5 mL scale, which is why no statement about the standard deviation can be made. In our case, all aqueous formulations exhibited a volume of 0.3 mL, which is somewhere between the two mentioned volumes of 0.1 and 1.5 mL and might explain the reduced LC compared to the formulation at 0.1 mL.

In the previous report, it was hypothesized that the decrease in the LC at larger scale was assumed to be caused by side-chain crystallization of the long, hydrophobic C9-side chains (as, e.g., greater thickness of the dried films and slower drying may facilitate crystallization), as triblock copolymers containing short C4-side chains (*sec*-butyl, *n*-butyl) did not display such a dependency of the encapsulation efficiency. This assumption was the initial driving force to compare the LC of nonyl-based copolymers with ABA triblock copolymers comprising hydrophobic pEtHepOx and pEtHepOzi blocks in which side chain crystallization is hindered due to branching. However, no such benefit with respect to the LC could be observed at

the day of preparation. Nevertheless, noticeable were the significantly smaller standard deviations of the pEtHepOx- and pEtHepOzi-based PTX formulations compared to the pNonOx- and pNonOzi-based PTX formulations especially at maximum drug content.

Taking into account the error bars, no significant differences in the PTX content of both nonyl-based formulations within 30 days of storage in the dark at ambient conditions was found (Figure 8a,b). In contrast, the PTX content of A-pEtHepOx-A-based formulations significantly increased at all PTX-feed concentrations after 5-day storage, that is, 21- and 11-fold increase at PTX feed = 2 and 8 g L^{-1} , respectively (Figure 8c). The increase in drug content of A-pEtHepOzi-A-based formulations was more pronounced at high PTX-feed concentrations of 8 and 10 g L^{-1} (Figure 8d). All PTX formulations were stored in Eppendorf tubes containing the initial coacervate. Therefore, analogue to the CUR formulations of A-pEtHepOx-A, initial A-pEtHepOx-A/PTX, and A-pEtHepOzi-A/PTX polymer/drug coacervates appear to dissolve over time, which points toward a kinetic rather than thermodynamic effect. Nevertheless, PTX contents of all formulations irrespective of the time of quantification were significantly lower than that of the extensively investigated PTX formulations of A-pBuOx-A exhibiting LC s of almost 50 wt% ($\rho(\text{PTX}) = 10 \text{ g L}^{-1}$ @ $\rho(\text{A-pBuOx-A}) = 10 \text{ g L}^{-1}$ ^[26]) and extraordinary long-term stabilities in PBS of at

least 7 months.^[25] Clearly, our hypothesis that side-chain crystallization may somehow interfere with drug loading does not stand.

As previously reported, in the case of **A-pPrOzi-A** and **A-pBuOx-A**, *LC* for the unfavorable drug (PTX for **A-pPrOzi-A**; CUR for **A-pBuOx-A**) could be significantly increased (eightfold for **A-pPrOzi-A**; 28-fold for **A-pBuOx-A**) by co-formulating the favorable drug in a 1:1 w/w ratio. Here, the *LC*s for PTX could also be strongly increased at all drug-feed concentrations irrespective of the utilized polymer by co-formulating CUR in a 1:1

w/w ratio (**Figure 9**, green bars). At low drug-feed concentrations of $\rho(\text{CUR \& PTX}) = 2 \text{ \& } 2 \text{ g L}^{-1}$, the *LC* for CUR (**Figure 9**, brown bars) could also be increased in the POx based triblocks. Interestingly, in all other cases, $\rho(\text{CUR})$ either remained the same as in the single formulation or slightly decreased. Generally, the triblock copolymers comprising a POzi-based hydrophobic core exhibited higher maximum drug loadings (*LC* [**A-pNonOzi-A**] = 38.8 wt%, $\rho(\text{CUR \& PTX}) = 3.5 \text{ \& } 5.1 \text{ g L}^{-1}$; *LC* [**A-pEtHepOzi-A**] = 37.4 wt%, $\rho(\text{CUR \& PTX}) = 4.2 \text{ \& } 5.8 \text{ g L}^{-1}$) compared to POx-based polymers (*LC* [**A-pNonOx-A**] = 26.1

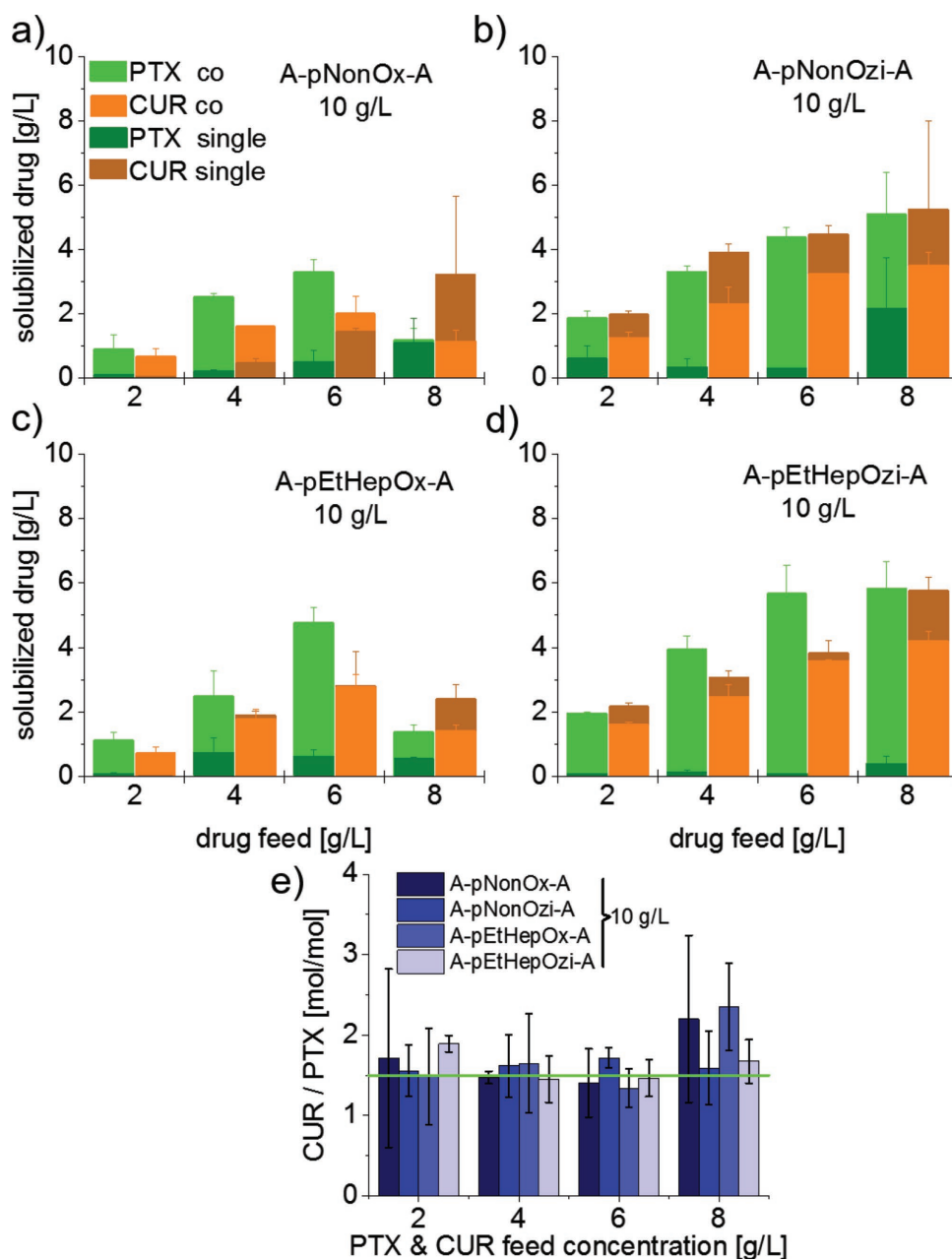


Figure 9. Aqueous CUR & PTX concentrations co-formulated with a) **A-pNonOx-A**, b) **A-pNonOzi-A**, c) **A-pEtHepOx-A**, and d) **A-pEtHepOzi-A** in dependence of drug-feed concentrations (PTX: bright green; CUR: bright orange; $\rho(\text{polymer}) = 10 \text{ g L}^{-1}$). For comparison, aqueous CUR (dark orange) and PTX (dark green) concentrations of the single drug formulations at same drug-feed ratios are shown. Data is given as mean \pm SD ($n = 3$); e) molar ratio of CUR & PTX co-encapsulated within the polymeric micelles \pm SD ($n = 3$, calculated with error propagation).

wt%, $\rho(\text{CUR} \& \text{PTX}) = 1.6 \& 2.5 \text{ g L}^{-1}$; $LC [\text{A-pEtHepOx-A}] = 32.9 \text{ wt\%}$, $\rho[\text{CUR} \& \text{PTX}] = 2.8 \& 4.8 \text{ g L}^{-1}$.

Surprisingly, a closer look at the molar ratios of the co-encapsulated drugs (Figure 9e) revealed a more or less constant CUR/PTX molar ratio of 1.5:1 (Table S18, Supporting Information). This might be a hint toward specific interactions between CUR and PTX as this considerably differed from the initial feed ratio of CUR/PTX = 2.3 [mol/mol]. Interestingly, PTX & CUR co-formulated with the shorter side chain homologue **A-pPrOzi-A** at the same drug-feed ratios resulted in solubilized CUR/PTX molar ratios of around 2.8:1 (being closer to the initial feed ratio of 2.3). Therefore, it appears that the nature of the hydrophobic block seems to somehow influence the co-loading ratio, the reason for this being unknown at the moment. It should be noted that the drug ratio chosen in this exploratory work has no particular biological rationale.

Intermolecular interactions between co-encapsulated drugs have already been observed for β -lapachone (LPC) and tanshinone IIA (THA) co-encapsulated with PTX.^[63,64] According to molecular dynamics simulation, PTX disrupted stacking interactions between the LPC molecules, strongly decreasing its crystallization propensity. A similar disruption might be present in the co-formulations of PTX and CUR, being responsible for the observed synergism with respect to the LC for PTX. However, this needs to be investigated further.

4. Conclusion

It has been reported previously, that despite its strongly hydrophilic/lipophilic contrast, **A-pNonOx-A** was much less suitable to formulate PTX than **A-pBuOx-A**, a polymer amphiphile with a poor hydrophilic/lipophilic contrast. It was assumed that this may have been due to side chain crystallization of the long alkyl chains, which has been described for the NonOx homopolymers.^[27] To study this, four ABA triblock copolymer amphiphiles with linear (nonyl) and branched (3-ethylheptyl) C9 side chains were synthesized, respectively. The backbone of the hydrophobic block was POx- and POzi-based, respectively. Apart from **A-pNonOx-A**, these polymers have not been described previously. It was not possible to identify any melting points for the polymers with the branched side chains while the ones with linear side chains are semicrystalline. However, in form of triblock copolymers with flanking MeOx blocks, none of the investigated polymers show signs of crystallization. Interestingly, the glass transition temperatures of the ABA triblock copolymers were almost identical, irrespective of the nature of the central hydrophobic blocks.

Interestingly, **A-pEtHepOx-A** bearing a branched side chain enabled much higher PTX concentrations in aqueous formulations compared to **A-pNonOx-A**, but still much lower than less hydrophobic **A-pBuOx-A**. However, this higher concentration could only be achieved after several days, hinting at a kinetic effect in the dissolution of the corresponding thin film. In the case of CUR as payload, previous reports suggested that hydrophobic poly(2-oxazine) moieties would be beneficial for CUR formulation. This was confirmed also for **A-pNonOzi-A** and **A-pEtHepOzi-A**, even though the drug loadings fell short compared to **A-pBuOzi-A** and **A-pPrOzi-A**.

While this contribution sheds more light on structure–formulation relationships, the molecular origin of the peculiar and highly unusual solubilization capacity of certain POx- and POzi-based polymer micelles remains to be elucidated.

Supporting Information

Supporting Information is available from the Wiley Online Library or from the author.

Acknowledgments

This work was supported by the Free State of Bavaria. Start-up funding for R.L. by the University Würzburg and SKZ Das Kunststoff-Zentrum is gratefully acknowledged. Moreover, financial support by the Deutsche Forschungsgemeinschaft is gratefully acknowledged (Project number 398461692, awarded to R.L.). M.M.L. would like to thank the Evonik Foundation for providing a doctoral fellowship. The authors would also like to thank Christian May and Alevtina Cubukova as well as colleagues at the Juliusspital Würzburg for technical support as well as the blood donors for their donation.

We are very grateful for the HDRC-Software Version 6.3.1., provided by O. Nirschl and K. Fischer, Physical Chemistry of Polymers at the Johannes Gutenberg University Mainz led by Prof. Sebastian Seiffert (formerly Prof. Manfred Schmidt). Light-scattering experiments were possible through support of the Deutsche Forschungsgemeinschaft (INST 93/774-1 FUGG).

Conflict of Interest

The authors declare no conflict of interest.

Keywords

curcumin, drug delivery, nanoformulations, paclitaxel, structure–property relationships

Received: April 27, 2018

Revised: July 31, 2018

Published online:

- [1] P. Szymański, M. Markowicz, E. Mikiciuk-Olasik, *Int. J. Mol. Sci.* **2012**, *13*, 427.
- [2] Z. Johannes, A. C. Matthew, *Curr. Top. Med. Chem.* **2012**, *12*, 1500.
- [3] Z. Ahmad, A. Shah, M. Siddiq, H.-B. Kraatz, *RSC Adv.* **2014**, *4*, 17028.
- [4] R. Cheng, F. Meng, C. Deng, H.-A. Klok, Z. Zhong, *Biomaterials* **2013**, *34*, 3647.
- [5] S. Mura, J. Nicolas, P. Couvreur, *Nat. Mater.* **2013**, *12*, 991.
- [6] U. Prabhakar, H. Maeda, R. K. Jain, E. M. Sevick-Muraca, W. Zamboni, O. C. Farokhzad, S. T. Barry, A. Gabizon, P. Grodzinski, D. C. Blakey, *Cancer Res.* **2013**, *73*, 2412.
- [7] S. Schöttler, K. Landfester, V. Mailänder, *Angew. Chem. Int. Ed.* **2016**, *55*, 8806.
- [8] G. Caracciolo, S. Palchetti, V. Colapicchioni, L. Digiacomio, D. Pozzi, A. L. Capriotti, G. La Barbera, A. Laganà, *Langmuir* **2015**, *31*, 10764.
- [9] N. J. Butcher, G. M. Mortimer, R. F. Minchin, *Nat. Nanotechnol.* **2016**, *11*, 310.

- [10] R. Toy, P. M. Peiris, K. B. Ghaghada, E. Karathanasis, *Nanomedicine* **2013**, *9*, 121.
- [11] A. Sosnik, M. Menaker Raskin, *Biotechnol. Adv.* **2015**, *33*, 1380.
- [12] R. Luxenhofer, *Nanomedicine* **2015**, *10*, 3109.
- [13] J.-P. Xu, J. Ji, W.-D. Chen, J.-C. Shen, *J. Control. Release* **2005**, *107*, 502.
- [14] J. Li, Z. He, S. Yu, S. Li, Q. Ma, Y. Yu, J. Zhang, R. Li, Y. Zheng, G. He, X. Song, *J. Biomed. Nanotechnol.* **2012**, *8*, 809.
- [15] Y. Yu, Y. He, B. Xu, Z. He, Y. Zhang, Y. Chen, Y. Yang, Y. Xie, Y. Zheng, G. He, J. He, X. Song, *J. Pharm. Sci.* **2013**, *102*, 1054.
- [16] Y. Mi, Y. Liu, S.-S. Feng, *Biomaterials* **2011**, *32*, 4058.
- [17] T. Lorson, M. M. Lübtow, E. Wegener, M. S. Haider, S. Borova, D. Nahm, R. Jordan, M. Sokolski-Papkov, A. V. Kabanov, R. Luxenhofer, *Biomaterials* **2018**, *178*, 204.
- [18] R. Luxenhofer, Y. Han, A. Schulz, J. Tong, Z. He, A. V. Kabanov, R. Jordan, *Macromol. Rapid Commun.* **2012**, *33*, 1613.
- [19] V. R. de la Rosa, *J. Mater. Sci. Mater. Med.* **2014**, *25*, 1211.
- [20] R. Luxenhofer, Y. Han, A. Schulz, J. Tong, Z. He, A. V. Kabanov, R. Jordan, *Macromol. Rapid Commun.* **2012**, *33*, 1613.
- [21] V. R. de la Rosa, *J. Mater. Sci. Mater. Med.* **2014**, *25*, 1211.
- [22] A. M. Sofias, M. Dunne, G. Storm, C. Allen, *Adv. Drug Deliv. Rev.* **2017**, *122*, 20.
- [23] L. M. Zasadil, K. A. Andersen, D. Yeum, G. B. Rocque, L. G. Wilke, A. J. Tevaerwerk, R. T. Raines, M. E. Burkard, B. A. Weaver, *Sci. Transl. Med.* **2014**, *6*, 229ra43.
- [24] R. Luxenhofer, A. Schulz, C. Roques, S. Li, T. K. Bronich, E. V. Batrakova, R. Jordan, A. V. Kabanov, *Biomaterials* **2010**, *31*, 4972.
- [25] A. Schulz, S. Jaksch, R. Schubel, E. Wegener, Z. Di, Y. Han, A. Meister, J. Kressler, A. V. Kabanov, R. Luxenhofer, C. M. Papadakis, R. Jordan, *ACS Nano* **2014**, *8*, 2686.
- [26] Z. He, X. Wan, A. Schulz, H. Bludau, M. A. Dobrovolskaia, S. T. Stern, S. A. Montgomery, H. Yuan, Z. Li, D. Alakhova, M. Sokolsky, D. B. Darr, C. M. Perou, R. Jordan, R. Luxenhofer, A. V. Kabanov, *Biomaterials* **2016**, *101*, 296.
- [27] Y. Seo, A. Schulz, Y. Han, Z. He, H. Bludau, X. Wan, J. Tong, T. K. Bronich, M. Sokolsky, R. Luxenhofer, R. Jordan, A. V. Kabanov, *Polym. Adv. Technol.* **2015**, *26*, 837.
- [28] M. M. Lübtow, L. Hahn, M. S. Haider, R. Luxenhofer, *J. Am. Chem. Soc.* **2017**, *139*, 10980.
- [29] O. Naksuriya, S. Okonogi, R. M. Schifflers, W. E. Hennink, *Biomaterials* **2014**, *35*, 3365.
- [30] S. C. Gupta, S. Patchva, B. B. Aggarwal, *AAPS J.* **2013**, *15*, 195.
- [31] M. M. Lübtow, L. C. Nelke, A. Brown, G. Sahay, G. Dandekar, R. Luxenhofer, *ChemRxiv* **2017**, <https://doi.org/10.26434/chemrxiv.5661736.v1>.
- [32] L. Piñeiro, M. Novo, W. Al-Soufi, *Adv. Colloid Interface Sci.* **2015**, *215*, 1.
- [33] K. Kalyanasundaram, J. K. Thomas, *J. Am. Chem. Soc.* **1977**, *99*, 2039.
- [34] K. Rausch, A. Reuter, K. Fischer, M. Schmidt, *Biomacromolecules* **2010**, *11*, 2836.
- [35] K. Kempe, S. Jacobs, H. M. L. Lambermont-Thijs, M. M. W. M. Fijten, R. Hoogenboom, U. S. Schubert, *Macromolecules* **2010**, *43*, 4098.
- [36] R. Hoogenboom, M. W. M. Fijten, H. M. L. Thijs, B. M. van Lankvelt, U. S. Schubert, *Des. Monomers Polym.* **2005**, *8*, 659.
- [37] R. Hoogenboom, F. Wiesbrock, M. A. M. Leenen, M. A. R. Meier, U. S. Schubert, *J. Comb. Chem.* **2005**, *7*, 10.
- [38] C. Diehl, I. Dambowsky, R. Hoogenboom, H. Schlaad, *Macromol. Rapid Commun.* **2011**, *32*, 1753.
- [39] A. M. Kelly, V. Kaltenhauser, I. Mühlbacher, K. Rametsteiner, H. Kren, C. Slugovc, F. Stelzer, F. Wiesbrock, *Macromol. Biosci.* **2013**, *13*, 116.
- [40] V. V. Jerca, K. Lava, B. Verbraeken, R. Hoogenboom, *Polym. Chem.* **2016**, *7*, 1309.
- [41] J. P. Bouten, K. Lava, C. J. van Hest, R. Hoogenboom, *Polymers* **2015**, *7*.
- [42] B. Manocha, A. Margaritis, *J. Nanomater.* **2010**, *2010*, 9.
- [43] C. Wang, L. Feng, H. Yang, G. Xin, W. Li, J. Zheng, W. Tian, X. Li, *Phys. Chem. Chem. Phys.* **2012**, *14*, 13233.
- [44] K. Kempe, E. F. J. Rettler, R. M. Paulus, A. Kuse, R. Hoogenboom, U. S. Schubert, *Polymer* **2013**, *54*, 2036.
- [45] H. Cheradame, J. F. L. Nest, in *Polymer Electrolyte Reviews* (Eds: J. R. MacCallum, C. A. Vincent), Springer, Amsterdam, the Netherlands **1987/1989**, p. 338.
- [46] E. F. J. Rettler, J. M. Kranenburg, H. M. L. Lambermont-Thijs, R. Hoogenboom, U. S. Schubert, *Macromol. Chem. Phys.* **2010**, *211*, 2443.
- [47] M. M. Bloksma, U. S. Schubert, R. Hoogenboom, *Macromol. Rapid Commun.* **2011**, *32*, 1419.
- [48] S. Jaksch, A. Schulz, Z. Di, R. Luxenhofer, R. Jordan, C. M. Papadakis, *Macromol. Chem. Phys.* **2016**, *217*, 1448.
- [49] H. Patil, R. V. Tiwari, M. A. Repka, *AAPS PharmSciTech* **2016**, *17*, 20.
- [50] A. V. Kabanov, I. R. Nazarova, I. V. Astafeva, E. V. Batrakova, V. Y. Alakhov, A. A. Yaroslavov, V. A. Kabanov, *Macromolecules* **1995**, *28*, 2303.
- [51] T. B. Bonné, K. Lüdtke, R. Jordan, P. Štěpánek, C. M. Papadakis, *Colloid. Polym. Sci.* **2004**, *282*, 833.
- [52] A. Schulz, S. Jaksch, R. Schubel, E. Wegener, Z. Di, Y. Han, A. Meister, J. Kressler, A. V. Kabanov, R. Luxenhofer, C. M. Papadakis, R. Jordan, *ACS Nano* **2014**, *8*, 2686.
- [53] S. Jaksch, A. Schulz, Z. Di, R. Luxenhofer, R. Jordan, C. M. Papadakis, *Macromol. Chem. Phys.* **2016**, *217*, 1448.
- [54] L. Hahn, M. M. Lübtow, T. Lorson, F. Schmitt, A. Appelt-Menzel, R. Schobert, R. Luxenhofer, *Biomacromolecules* **2018**, *19*, 3119.
- [55] M. Bauer, S. Schroeder, L. Tauhardt, K. Kempe, U. S. Schubert, D. Fischer, *J. Polym. Sci. A: Polym. Chem.* **2013**, *51*, 1816.
- [56] M. Bauer, C. Lautenschlaeger, K. Kempe, L. Tauhardt, U. S. Schubert, D. Fischer, *Macromol. Biosci.* **2012**, *12*, 986.
- [57] Y. B. Pawar, B. Munjal, S. Arora, M. Karwa, G. Kohli, J. K. Paliwal, A. K. Bansal, *Pharmaceutics* **2012**, *4*, 517.
- [58] B. T. Kurien, A. Singh, H. Matsumoto, R. H. Scofield, *Assay Drug Dev. Technol.* **2007**, *5*, 567.
- [59] H. H. Tønnesen, M. Måsson, T. Loftsson, *Int. J. Pharm.* **2002**, *244*, 127.
- [60] M. S. Surapaneni, S. K. Das, N. G. Das, *ISRN Pharmacol.* **2012**, *2012*, 623139.
- [61] P. Ma, R. J. Mumper, *J. Nanomed. Nanotechnol.* **2013**, *4*, 1000164.
- [62] C. Schneider, O. N. Gordon, R. L. Edwards, P. B. Luis, *J. Agric. Food Chem.* **2015**, *63*, 7606.
- [63] L. Zhang, H. Sun, Z. Chen, Z. Liu, N. Huang, F. Qian, *Mol. Pharm.* **2017**, *14*, 3568.
- [64] L. Zhang, Z. Chen, K. Yang, C. Liu, J. Gao, F. Qian, *Mol. Pharm.* **2015**, *12*, 3999.

As discussed in the state of knowledge, π - π stacking has been utilized to increase the LC of polymer micelles for hydrophobic drugs containing aromatic moieties. To investigate this systematically, four different triblock copolymers with increasing amount of aromatic moieties within their hydrophobic core have been synthesized to formulate three different hydrophobic drugs with varying aromatic content. Indeed, the LC of POx based amphiphiles with increasing amount of benzyl moieties in the sidechain (0 wt.%, 50 wt.%, 100 wt.%) increased linearly for CUR, having the highest amount of aromaticity. In contrast, the LC for PTX, having the lowest amount of aromatic moieties, decreased with increasing benzyl content. The first high capacity and stable formulations of the natural compound Schizandrin A (medium aromatic content) were barely affected by the polymer structure. Although these findings sound straightforward at first, the LC of a polymer comprising solely phenyl sidechains within the hydrophobic core was invariant of the drug structure. Therefore, a generalization of the impact of π - π stacking is not possible, although in selected cases LCs > 40 wt.% can be realized.

Investigating the Influence of Aromatic Moieties on the Formulation of Hydrophobic Natural Products and Drugs in Poly(2-oxazoline)-Based Amphiphiles

Lukas Hahn,[†] Michael M. Lübtow,[†] Thomas Lorson,[†] Frederik Schmitt,^{†,‡} Antje Appelt-Menzel,[‡] Rainer Schobert,[§] and Robert Luxenhofer^{*,†,§}

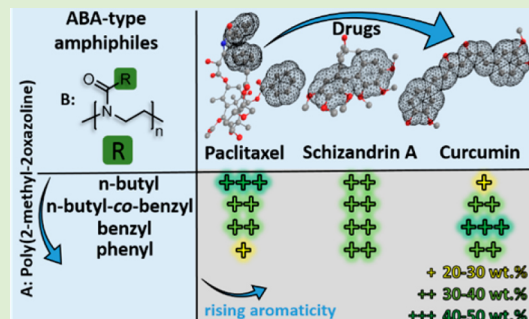
[†]Functional Polymer Materials, Chair for Advanced Materials Synthesis, Department of Chemistry and Pharmacy, Julius-Maximilians-Universität Würzburg, Röntgenring 11, 97070 Würzburg, Germany

[‡]Lehrstuhl Tissue Engineering und Regenerative Medizin and Fraunhofer-Institut für Silicatforschung ISC, Universitätsklinikum Würzburg, Röntgenring 11, 97070 Würzburg, Germany

[§]Organic Chemistry Laboratory, Universität Bayreuth, Universitätsstrasse 30, 95447 Bayreuth, Germany

Supporting Information

ABSTRACT: Many natural compounds with interesting biomedical properties share one physicochemical property, namely, low water solubility. Polymer micelles are, among others, a popular means to solubilize hydrophobic compounds. The specific molecular interactions between the polymers and the hydrophobic drugs are diverse, and recently it has been discussed that macromolecular engineering can be used to optimize drug-loaded micelles. Specifically, π - π stacking between small molecules and polymers has been discussed as an important interaction that can be employed to increase drug loading and formulation stability. Here, we test this hypothesis using four different polymer amphiphiles with varying aromatic content and various natural products that also contain different relative amounts of aromatic moieties. In the case of paclitaxel, having the lowest relative content of aromatic moieties, the drug loading decreases with increasing relative aromatic amount in the polymer, whereas the drug loading of curcumin, having a much higher relative aromatic content, is increased. Interestingly, the loading using schizandrin A, a dibenzo[*a,c*]cyclooctadiene lignan with intermediate relative aromatic content is not influenced significantly by the aromatic content of the polymers employed. The very high drug loading, long-term stability, ability to form stable highly loaded binary coformulations in different drug combinations, small-sized formulations, and amorphous structures in all cases corroborate earlier reports that poly(2-oxazoline)-based micelles exhibit an extraordinarily high drug loading and are promising candidates for further biomedical applications. The presented results underline that the interaction between the polymers and the incorporated small molecules may be more complex and are significantly influenced by both sides, the used carrier and drug, and must be investigated in each specific case.



INTRODUCTION

For many years, natural products have played an important part in drug discovery. In the late 20th century, a majority of drugs were either natural compounds or their derivatives.¹ At the end of their review concerning the importance of natural products for drug discovery, Newman et al. argued that well-defined drug delivery systems could overcome unfavorable physicochemical properties, like aqueous solubility, in the future.² Likewise, via high-throughput screening, new chemical entities or lead structures are being identified and evaluated every day,³ but only a minute fraction ever ripen into an approved drug. Obviously, a large proportion of drug candidates are poorly water-soluble,^{4,5} which calls for effective formulation strategies. Traditionally used surfactants like Cremophor EL and Tween 80 have drawbacks as they can elicit potentially life-threatening side effects and are limited with respect to their solubilizing ability.^{6,7} Polymeric micelles have been discussed and evaluated

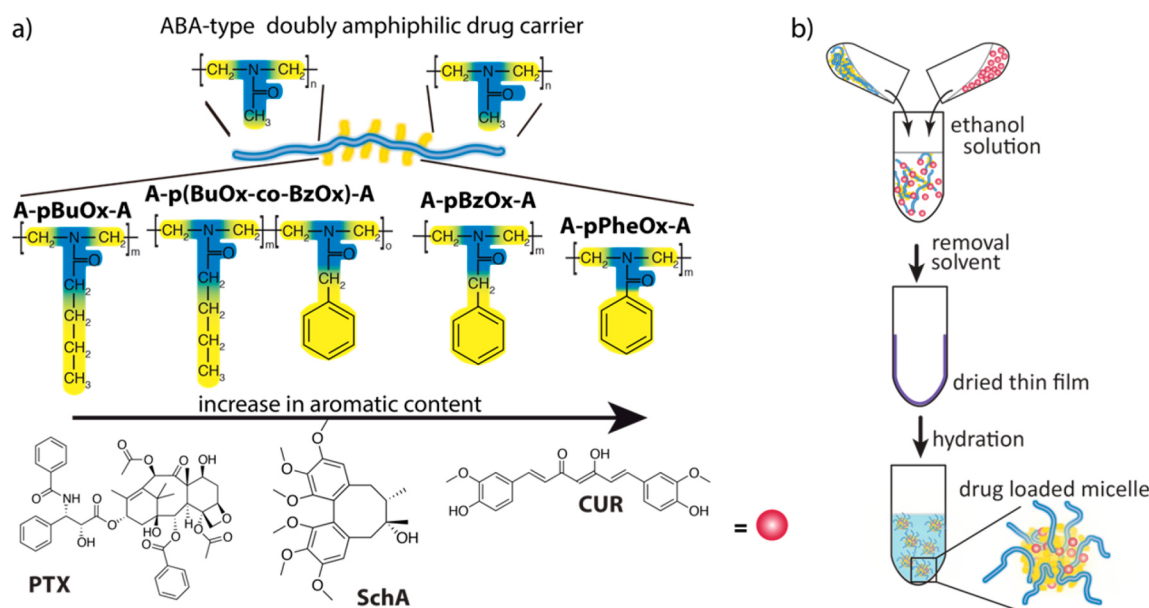
as carriers for hydrophobic molecules for many years, and thousands of papers praising the potential of polymer-based drug delivery systems are published every year.⁸ However, until now, only one micelle-based formulation (Genexol-PM, South Korea) has been used in the clinic with several others being under clinical development.⁹ Zhang et al. argued that the low drug loading capacity and poor in vivo stability typically displayed by polymeric micelles are responsible for this major discrepancy.¹⁰ These major problems concerning nanoformulations, drug delivery, and the advancement of polymeric micelles for clinical cancer therapy were also critically reviewed by other researchers.^{11–13}

Polymer micelles comprising a poly(2-oxazoline) (POx)-based amphiphilic triblock copolymer (poly(2-methyl-2-oxazo-

Received: May 2, 2018

Published: May 10, 2018

Scheme 1. Schematic Representation of (a) the Polymers and Insoluble Small Molecules Employed in the Present Study as Well as (b) the Formulation Procedure via the Thin Film Method



line)-*block*-poly(2-butyl-2-oxazoline)-*block*-poly(2-methyl-2-oxazoline) (PMeOx-*b*-PBuOx-*b*-PMeOx = A-pBuOx-A)) constitute an unusual exception. Loading capacities (LC) of almost 50 wt % for one of the most commonly used chemotherapeutic agents, paclitaxel (PTX),¹⁴ were reported by Kabanov, Jordan, Luxenhofer, and co-workers.^{15–19} The drug-loaded polymer micelles formed stable and injectable formulations and showed significantly increased therapeutic efficacy in vivo.^{20,21} The combination of high drug loading and stability was specific to block copolymers with poly(2-*n*-butyl-2-oxazoline) as hydrophobic core when a variety of formulations based on amphiphilic ABA POx with structurally different B blocks were investigated.¹⁹ Testing a variety of structurally different taxanes led to similar high drug loadings and stability of the formulations.²² Lübtow et al. investigated a small library of structurally similar ABA-triblock copolymers based on poly(2-oxazoline)s and poly(2-oxazine)s and explored their solubilization capacity for PTX and curcumin (CUR²³), another well-known natural compound featuring extremely low aqueous solubility, bioavailability, and stability.²⁴ The authors observed significant and orthogonal specificities dependent on the positioning of one methylene group in the more hydrophobic repeat unit. This outlines the complexity of drug/carrier interactions.²⁵ More recently, this CUR nanoformulation was characterized in more detail.²⁶

Schisandra chinensis is widely used in traditional Chinese and Japanese herbal medicines for a variety of pharmacological properties.^{27,28} Dibenzo[*a,c*]cyclooctadiene lignan metabolites are thought to be responsible for the majority of these effects.²⁸ Many such lignans have been extracted^{29,30} and chromatographically isolated.^{31–37} Schobert and co-workers established a simplified extraction method followed by one saponification step to obtain the pure dibenzo[*a,c*]cyclooctadiene lignan schisandrol A by column chromatography.³⁸ This was converted to a cinnamate and a titanocene derivative, which both showed promising P-gp inhibition and increased activity against cervix and breast cancer cells.^{38,39} The formation of nanoparticles and nanocrystals to formulate schisantherin A, a related dibenzo[*a,c*]cyclooctadiene lignan, was described by

Cheng et al. The drug/carrier aggregates could pass the hematoencephalic barrier and showed effects potentially useful for the treatment of Parkinson's disease.^{40,41} A recent review on the neuroprotective and cognitive enhancement properties of dibenzo[*a,c*]cyclooctadiene lignans from *Schisandra chinensis* concludes that, before such lignans can enter clinical settings to treat diseases, more studies are needed to improve their bioavailability.⁴²

Several strategies for the development of drug-specific drug delivery platforms have been followed recently. In particular, Luo, Nangia, and co-workers backed the synthetic work with extensive modeling and achieved very high drug loadings paired with excellent therapeutic efficacy.^{43–45} The driving forces considered relevant for drug incorporation are hydrophobic and electrostatic interactions, hydrogen bonding, π - π stacking, and van der Waals forces. The relevance of these interactions for drug formulations is widely discussed.⁴⁶ To stabilize polymeric micelles and thus increase their loading capacity for PTX (28 wt %) and docetaxel (34 wt %), Shi et al. synthesized amphiphilic block copolymers comprising the aromatic monomer *N*-2-benzoyloxypropyl methacrylamide (HPMAm-Bz) as a hydrophobic building block. The π - π interaction significantly increased the stability, loading capacity, and therapeutic index of drug-loaded polymeric micelles.^{47,48} Previously, amphiphilic diblock copolymers containing poly(2-phenyl-2-oxazolin) (PPheOx) and PMeOx were tested on their self-assembly in aqueous milieu, and the hydrophobic indomethacin could be successfully formulated, but potential effects of aromatic moieties on drug loading in POx based micelles have not been investigated in any considerable detail.⁴⁹

Here, we present a small library of POx-based amphiphiles in which the aromatic character was increased systematically and the solubilization capacity for drugs with different aromatic content was investigated (Scheme 1).

■ MATERIALS AND METHODS

All substances and reagents for the polymerizations were obtained from Sigma-Aldrich (Steinheim, Germany) or Acros (Geel, Belgium) and were used as received unless otherwise stated. Curcumin powder

from *Curcuma longa* (Turmeric) was obtained from Sigma-Aldrich (curcumin = 79%; demethoxycurcumin = 17%, bisdemethoxycurcumin = 4%; determined by HPLC analysis). Paclitaxel was purchased from LC Laboratories (Woburn, MA, USA). Deuterated solvents for NMR analysis were obtained from Deutero GmbH (Kastellaun, Germany). All substances used for polymerization, specifically methyl trifluoromethylsulfonate (MeOTf), MeOx, BuOx, PheOx, and BzOx, were refluxed over CaH₂ and distilled and stored under argon. Benzonitrile (PhCN) was dried over phosphorus pentoxide. The monomers 2-*n*-butyl-2-oxazoline (BuOx) and 2-benzyl-2-oxazoline (BzOx) were synthesized following the procedure by Seeliger et al.⁵⁰ The Pt-NHC-complex (Pt-NHC)⁵¹ and the fluorinated curcuminoid derivative (CUR-F₆)⁵² were synthesized according to the literature (Figure S7). Fruits of *Schisandra chinensis* were obtained from Naturwaren-Blum (Revensdorf, Germany) and were dried and powdered prior to the extraction procedure. Schizandrin (SchA) was obtained from powdered *Schisandra chinensis* using the simplified extraction procedure reported by Schobert et al.³⁸ Thin layer chromatography (TLC), NMR-, IR-, UV-vis spectroscopy and electrospray ionization mass spectrometry (ESI-MS) were used for analytical issues. TLC was performed on Sigma-Aldrich TLC Plates containing silica gel matrix (stationary phase) using *n*-hexane/ethylacetate (1:1) as mobile phase. For NMR measurements, a small fraction of the purified compound SchA was dissolved in deuterated dichloromethane and ¹H, ¹³C, correlation spectroscopy (COSY), heteronuclear single quantum coherence (HSQC), and heteronuclear multiple bond correlation (HMBC) experiments were performed. ATR-IR spectroscopic analysis was performed on an FT-IR spectrometer 4100 from 500 to 4000 cm⁻¹ from Jasco (Gross-Umstadt, Germany). For the UV-vis measurement, a 1 g/L ethanolic solution of SchA was filtered through 0.2 μm PTFE filters (Rotilabo, Karlsruhe) and recorded at 25 °C from 700 to 180 nm.

The purity of SchA was determined to be 97.9% by analytical high-pressure liquid chromatography (HPLC). The polymers A-pBuOx-A, A-p(BuOx-co-BzOx)-A, A-pBzOx-A and A-pPheOx-A were synthesized by living cationic ring opening polymerization (LCROP) as described previously.¹⁵ The reactions were controlled by ¹H NMR spectroscopy. The lyophilized polymers were characterized by ¹H NMR and gel permeation chromatography (GPC). The critical micellar concentrations (CMC) of the ABA-triblock copolymers were determined by pyrene fluorescence measurements.^{53,54} The I₁/I₃ ratio in dependence of varying polymer concentrations and the total redshift of I₁ in dependence of varying polymer concentrations were detected and used for the determination of the CMC values. Drug-loaded polymeric micelles were prepared by thin film method (Scheme 1). The loading capacities (LC) and efficiencies (LE) were determined by HPLC measurements according to eqs 1 and 2.

$$LC = \frac{m_{\text{drug}}}{m_{\text{drug}} + m_{\text{excipient}}} \times 100\% \quad (1)$$

$$LE = \frac{m_{\text{drug}}}{m_{\text{drug, added}}} \times 100\% \quad (2)$$

where m_{drug} and $m_{\text{excipient}}$ are the weight amounts of the solubilized drug and polymer excipient in solution and $m_{\text{drug, added}}$ is the weight amount of the drug initially added. It was assumed that no loss of polymer occurred during micelle preparation. The aggregation behavior of the polymers (10 g/L in PBS) and polymer/drug solutions (1:0.5 g/L in PBS) were investigated by dynamic light scattering (DLS) measurements at 27 different angles (temperature was fixed at 25 °C) as outlined in the supporting information in more detail. The glass transition temperatures (T_g) and melting points (mp) were determined by differential scanning calorimetry (DSC) measurements (see Supporting Information).

Primary human dermal fibroblasts (HDF) were cultured in DMEM, GlutaMAX (Gibco, Darmstadt, Germany) culture medium supplemented with 10% fetal calf serum (FCS), and 1% sodium pyruvate. For cell cytotoxicity studies, cells were seeded in a white 96-well plate with a transparent bottom in triplicate per condition (3×10^5 cells/

cm²) and cultured for 24 h at 37 °C and 5% CO₂. Subsequently, medium was removed, and polymer stock solutions in cell specific culture medium ($\rho = 100$ g/L) were diluted with cell-specific culture medium to desired concentrations and applied for 24 h. After the treatment, CellTiter-Glo Luminescent Cell Viability Assay (Promega, Mannheim, Germany) was performed according to the manufacturer's instructions. Briefly, medium was removed, and cells were washed 3× with PBS(+). Equal amounts of cell culture medium and CellTiter-Glo reagent were added to the wells. After shaking for 2 min and resting for 10 min to achieve cell lysis, luminescence was measured with an Infinite 200 (Tecan, Männedorf, Switzerland) at $\lambda_{\text{em}} = 590$ nm ($\lambda_{\text{ex}} = 560$ nm).

Cell viability was determined by eq 3

$$\text{cell viability} = \frac{F_{\text{treated}} - F_{\text{medium}}}{F_{\text{untreated}} - F_{\text{medium}}} \times 100\% \quad (3)$$

where F_{treated} and $F_{\text{untreated}}$ are the luminescence of treated and untreated cells, respectively, and F_{medium} is the luminescence of the culture medium. As negative control, cells were lysed with 10% sodium dodecyl sulfate (SDS). Cell viability experiments were performed with three individual 96-well plates containing each sample concentration in triplicate (considered as one experiment), and results are presented as means ± SD. Cells were obtained by three individual isolations. All methods are described in more detail in the Supporting Information.

RESULTS AND DISCUSSION

Inspired by reports on benefits for drug delivery via π - π stacking between drug carrier and loaded API,⁵⁵ we wanted to investigate this issue in poly(2-oxazoline)-based polymer amphiphiles to gain more insights into the structure-property relationship. In particular, the Hansen solubility parameters calculated by Dargaville and co-workers suggested a benefit regarding drug loading using polymer amphiphiles comprising a hydrophobic poly(2-phenyl-2-oxazoline) block.⁵⁶ In the case of paclitaxel and docetaxel, Hennink and co-workers reported that incorporation of aromatic side chains into thermosensitive block copolymers of modified hydroxypropyl methacrylamides improves drug loading.⁴⁷ However, it is important to note that, in this study, PTX precipitation rather than release was quantified.^{47,48} The authors argue that this was done as it is difficult to upload proper sink conditions for the extremely poorly soluble PTX. In contrast, in a preliminary study, we did not observe any benefit with respect to PTX formulation when we included aromatic moieties into the hydrophobic block.¹⁹ The inclusion of an aromatic moiety (A-p(BuOx-co-BzOx)-A; LC_{PTX}: 36 wt %) led to significant loss of loading capacity in comparison to A-pBuOx-A (LC_{PTX}: 49 wt %). Therefore, the present study investigates the influence of different proportions of aromatic moieties within poly(2-oxazoline)-based ABA triblock copolymers on the formulation of different hydrophobic drugs with varying aromatic content in more detail. To this end, we used a small library of four different polymers. As in previous work, the hydrophilic block A was poly(2-methyl-2-oxazoline) (pMeOx).²⁵ The hydrophobic blocks were in order of increasing aromatic content poly(2-butyl-2-oxazoline) (A-pBuOx-A), poly(2-butyl-2-oxazoline-co-2-benzyl-2-oxazoline) (A-p(BuOx-co-BzOx)-A), poly(2-benzyl-2-oxazoline) (A-pBzOx-A), and poly(2-phenyl-2-oxazoline) A-pPheOx-A, respectively. The polymers were prepared by living cationic ring opening polymerization (LCROP) and characterized by ¹H NMR and GPC (Table 1 and Supporting Information).

All polymers exhibited CMC values in the low μM range (determined by pyrene fluorescence, Figure S4) often deemed favorable for intravenous administration (Figure S4, Table S1). Interestingly, in the present library, it appears that the

Table 1. Number Average Molar Mass, Dispersity \mathcal{D} , and Yield of the Synthesized Triblock Copolymers

polymer	M_n^a [kg/mol]	M_n^b [kg/mol]	M_n^c [kg/mol]	\mathcal{D}^d	yield [%]
A-pBuOx-A	8.6	8.7	5.6	1.10	88
A-p(BuOx-co-BzOx)-A	9.0	7.8	5.9	1.12	91
A-pBzOx-A	8.7	10.3	5.2	1.25	77
A-pPheOx-A	8.5	8.5	5.3	1.10	92

^aTheoretical value obtained by $[M]_0/[I]_0$. ^bCalculated from ^1H NMR end-group and side chain analysis. ^cObtained from GPC ($T = 40^\circ\text{C}$, flow rate was set to 0.7 mL/min (HFIP) and calibrated using poly(ethylene glycol) standards). ^dObtained from GPC (M_w/M_n).

introduction of aromatic side chains has no marked influence on the CMC values. For polymeric micelles to be used as drug delivery vehicles, the synthesized carriers should exhibit no significant cytotoxicity against human cells. Luxenhofer et al. studied the cytotoxicity of different POx-based homo and block copolymers including A-pBuOx-A in different cell lines.⁵⁷ In this study, even at relatively high carrier concentrations (20 g/L), no significant cytotoxicity could be observed. However, to the best of our knowledge, amphiphilic POx-bearing aromatic moieties have not been investigated regarding their cytotoxicity. Therefore, we evaluated these polymers using primary human dermal fibroblasts (Figure 1).

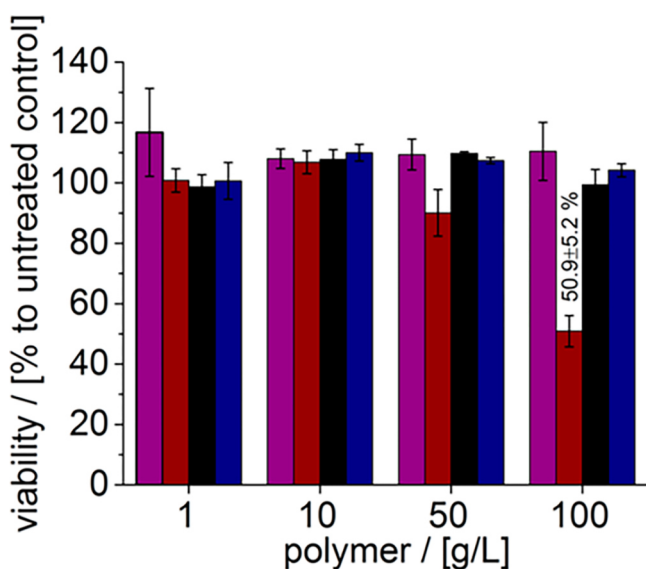


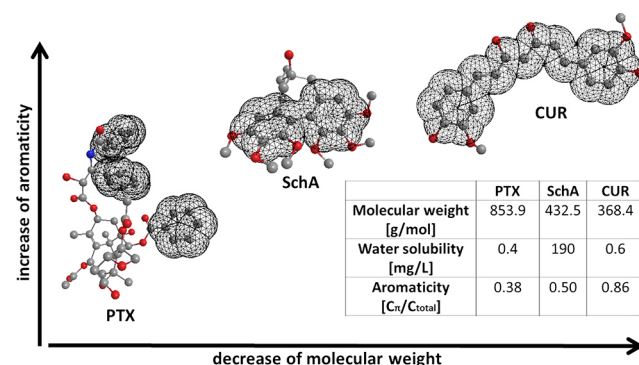
Figure 1. Cell viability of primary human dermal fibroblasts treated with increasing polymer concentrations (1–100 g/L). A-pBuOx-A (purple), A-p(BuOx-co-BzOx)-A (dark red), A-pBzOx-A (black), and A-pPheOx-A (dark blue). Cell viability was assessed using CellTiter-Glo after a 24 h incubation. Data are given as means \pm SD ($n = 3$).

The polymers A-pBzOx-A and A-pPheOx-A, which are comprised solely of aromatic moieties as the building blocks for the hydrophobic core, exhibited no cytotoxicity even at very high polymer concentration of 100 g/L. Interestingly, during the treatment of fibroblasts using the polymer A-p(BuOx-co-BzOx)-A, the viability decreased to $50.9 \pm 5.2\%$ at a polymer concentration of 100 g/L. Only a minor but noticeable reduction of the cell viability was observed at 50 g/L. This is interesting, as neither A-pBuOx-A nor A-pBzOx-A exhibit any cytotoxicity against human fibroblasts. The polymers used in

this study exhibit low dispersities and CMC values in μM range and show a favorable cytotoxicity profile; therefore, they are promising candidates for the solubilization of hydrophobic drugs.

For formulation, we focused on three natural compounds. On one hand, we employed the well-known and extremely water-insoluble compounds paclitaxel (PTX, 0.4 mg/L)⁵⁸ and turmeric curcumin (CUR, 0.6 mg/L).²⁴ On the other hand, we tested the poorly soluble dibenzo[*a,c*]cyclooctadiene lignan schizandrin (SchA, solubility: 0.19 g/L determined via HPLC). These three natural compounds differ in their relative aromatic contents. Whereas PTX contains three phenyl rings at a molar mass of 854 g/mol, SchA contains two rings at 432 g/mol, and CUR also contains two phenyl rings, however, connected with a bridging π -system at a molar mass of 368 g/mol. The ratio of C_{arom} , the carbon atoms, which are included in the conjugated/aromatic system, and C_{total} , the total number of carbon atoms in the hydrophobic compound, represents the aromaticity of the three different cargos (Scheme 2).

Scheme 2. Comparison of the Hydrophobic Drugs PTX, SchA, and CUR with Regard to Aromaticity, Solubility, and Molecular Weight



Additionally, the insoluble compounds Pt-NHC and CUR-F₆ (for structures, please see Figure S7) were investigated, the latter of which can be viewed as derivative of natural compound CUR.

All four polymers were tested for the solubilization of PTX, CUR, and SchA. As previously reported, A-pBuOx-A is an excellent solubilizer for PTX but much less so for CUR²⁵ (Figure 2). Interestingly, SchA, having an intermediate relative aromatic content, was solubilized very well but less than PTX. As previously reported¹⁹ and independently reproduced here using a newly synthesized polymer, the introduction of benzylic moieties (A-p(BuOx-co-BzOx)-A) does not help in the formulation of PTX but rather reduces the maximum drug loading. Interestingly, whereas in the case of SchA the maximum drug loading increased slightly, the LC_{CUR} that could be achieved increased significantly (Figure 2). In the case of A-pBzOx-A, the LC_{PTX} decreased further (35.6 ± 2.1 wt %), whereas LC_{SchA} (44.0 ± 0.3 wt %) and in particular LC_{CUR} (41.0 ± 2.1 wt %) increased further compared to A-pBuOx-A-based formulations. Interestingly, within this small library, A-pBzOx-A is the least selective of the tested polymers. Previously, comparable but somewhat higher loading capacities for PTX and CUR could be achieved (LC_{PTX} : 40.1 ± 1.5 wt %, LC_{CUR} : 48.5 ± 1.7 wt %) using A-p(2-*n*-butyl-2-oxazine)-A.²⁵ Thus, with increasing aromatic character of the polymeric solubilizer, more CUR ($LC_{\text{A-pBuOx-A}}$: 24.4 ± 1.1 wt %, 25

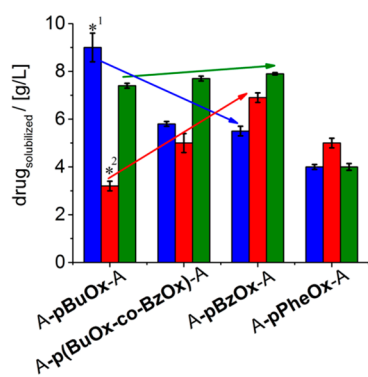


Figure 2. Maximum solubilized aqueous drug concentrations in formulation with the drug carriers (A-pBuOx-A, A-p(BuOx-co-BzOx)-A, A-pBzOx-A, A-pPheOx-A). Maximum solubilization (LE_{minimum} 79%) of the drugs PTX (blue), CUR (red), and SchA (green) using the four polymers. ^{*1} were taken from ref 18; ^{*2} were taken from ref 25. In all cases, the polymer concentration was fixed at 10 g/L. Data are given as means \pm SD ($n = 3$).

$LC_{A-p(\text{BuOx-co-BzOx})-A}$: 33.2 ± 3.7 wt %, $LC_{A-p\text{BzOx}-A}$: 41.0 ± 2.1 wt %) and less PTX ($LC_{A-p\text{BuOx}-A}$: 47.5 ± 0.1 wt %, ²⁵ $LC_{A-p(\text{BuOx-co-BzOx})-A}$: 36.8 ± 1.0 wt %, $LC_{A-p\text{BzOx}-A}$: 35.6 ± 2.1 wt %) could be solubilized, whereas little if any influence was found for SchA. Interestingly, A-pPheOx-A did show a markedly different performance as solubilizer. Although the LC_{PTX} did decrease further (28.6 ± 0.6 wt %), the solubilizations of CUR (LC_{CUR} : 33.4 ± 2.3 wt %) and SchA (LC_{SchA} : 28.6 ± 1.4 wt %) were also less efficient compared to A-pBzOx-A. We hypothesize that the reduced molecular flexibility of pPheOx and the close proximity of the phenyl ring to the polymer backbone may be one contributing factor (as shown, e.g., by a higher T_g , vide infra). It may be noted that this comparably low loading of PTX using A-pPheOx-A was still higher, albeit only slightly, than the highest PTX loading reported by Hennink et al.⁴⁷ In this report, the authors found an increased PTX loading with increasing content of aromatic comonomer, which was attributed to π - π stacking between polymer and drug molecules. Although apparently valid in some cases, it appears that this rationale is not generally helpful to increase drug loading in polymer micelles.

It should be noted that we also attempted formulation of CUR- F_6 , but no stable formulation could be obtained by film hydration method with either polymer. The NHC-Pt complex was solubilized with A-pPheOx-A by film hydration method using dichloromethane. However, it appears the complex does not exhibit sufficient stability as HPLC analysis revealed multiple signals after formulation, whereas the compound was pure initially. Therefore, quantification was not possible.

The drug content was quantified immediately after preparation. To gain a basic understanding of the stability of the drug formulations, we stored the formulation under ambient conditions containing the initial precipitate and took samples after 10 and 30 days. The formulations were centrifuged prior to each measurement. By using this method, it is possible that first precipitated drug could be dissolved over time.⁵⁹ For A-pBuOx-A, we have previously observed excellent stability of the PTX formulation without any precipitation after several months.^{15,17,18} In general, all presently tested formulations of PTX, CUR, and SchA showed very good stability over 30 days (Figure 3). No significant loss of SchA and very little variability of the drug concentration was

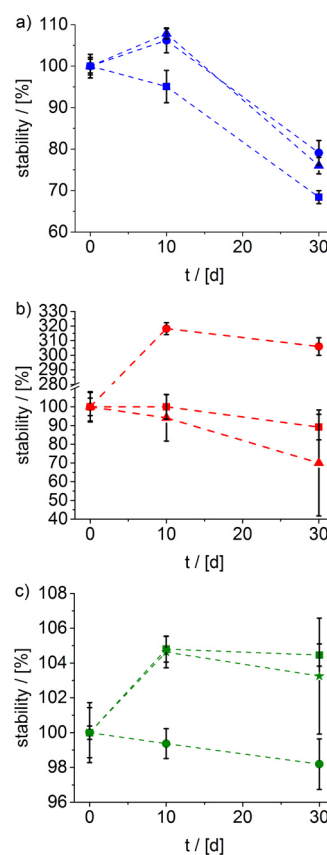


Figure 3. Long-term stability of drug/polymer formulations of PTX (a), CUR (b), and SchA (c). For this study, the maximum loaded formulations were used. The d0 values were set to 100%. In all cases, the polymer concentration was fixed at 10 g/L (squares: A-p(BuOx-co-BzOx)-A, circles: A-pBzOx-A, triangles: A-pPheOx-A, and stars: A-pBuOx-A). Data are given as means \pm SD ($n = 3$).

observed. In the case of PTX, the variability was somewhat higher; nevertheless, overall formulation stability was excellent. The stability compares favorably with π - π interaction stabilized PTX formulations reported by Hennink et al. In that report, 50–100% of the solubilized PTX precipitated within 10 days depending on the aromatic content of the micelles.⁴⁷ In the case of CUR, we made unexpected observations. First of all, the stability of CUR formulated in the POx-based micelles was remarkably high, especially considering the well-established low chemical stability of CUR in aqueous media.²⁴ In the case of A-p(BuOx-co-BzOx)-A and A-pPheOx-A, we did observe some loss of CUR concentration and increased variability after 30 days, but the average drug loading remained high. Notably, according to HPLC analysis, CUR did not show any signs of degradation even though it is often reported that CUR is not stable in an aqueous environment. Interestingly, in the case of A-pBzOx-A, the CUR concentration in solution (after centrifugation and filtration) was much higher on day 10 (LC_{CUR} : 45.6 ± 3.3 wt %) and day 30 (LC_{CUR} : 44.6 ± 4.6 wt %) than on day 0 (LC_{CUR} : 20.8 ± 2.1 wt %). It should be noted, for our stability studies, that the drug formulations were stored under ambient conditions over the pellet of unformulated drug (if any). Thus, it appears that CUR that initially precipitated/coacervated during thin film hydration became incorporated over time into the micelles. We observed a similar phenomenon with POx-based amphiphiles with long aliphatic side chains. Analysis of the precipitate/coacervate revealed that

both drug and polymer are present.⁵⁹ We cannot explain this observation at this point, but more detailed studies are certainly warranted.

In addition to the described single-drug formulations, we also investigated binary coformulations. Previously, several POx-based binary and ternary drug formulations with very high loading of ≥ 58 wt % were reported.^{17,25} Here, we investigated A-pBzOx-A for coformulation of PTX with SchA and CUR, respectively. Both combinations could show interesting pharmaceutical synergies.^{60,61} For these preliminary studies, we fixed the relative drug weight ratio at 1/1 for both combinations (10 g/L A-pBzOx-A and 6 g/L in the case of PTX/SchA and 8 g/L in the case of PTX/CUR). In both combinations, the loading efficiency was excellent, and total LC exceeded 50 wt %. The individual LC for PTX (40.8 wt %) and CUR (40.1 wt %) yielded an overall LC of 58.8 wt %, whereas with the combination of PTX (35.6 wt %) and SchA (36.9 wt %), an overall LC of 53.2 wt % was obtained (Figure 4).

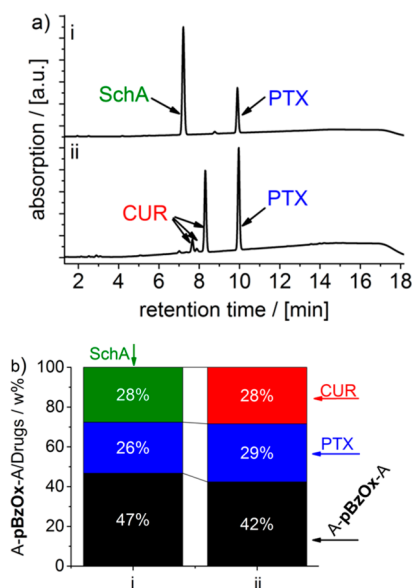


Figure 4. (a) HPLC elugrams ($\lambda = 220$ nm) of coformulations ((i) A-pBzOx-A/PTX/SchA = 10:6:6 w/w/w, (ii) A-pBzOx-A/PTX/CUR = 10:8:8 w/w/w). (b) Overall LCs of coformulations (i) and (ii).

Previously, we have investigated the PTX formulation with A-pBuOx-A in great detail using electron microscopy, dynamic light scattering (DLS), and small-angle neutron scattering.^{16,18} For preliminary elucidation of the aggregation behavior, we investigated aqueous polymer solutions and formulations by DLS (Figure 5). All polymers form aggregates in the size range expected for polymer micelles. The polymers containing aromatic moieties form very small and rather defined polymer micelles. At 10 g/L in PBS, hydrodynamic radii between 10 and 20 nm were found (Figure 5a, Figure S6c). In the case of A-pBuOx-A, we found a rather broad distribution centered around a hydrodynamic radius of $R_h = 25$ nm. Previously, using a different batch of the same polymer, we observed a bimodal size distribution originating from spherical and wormlike micelles.¹⁸ The broad distribution observed in the present case could likely be caused by an unresolved bimodal distribution.

Moreover, we investigated drug formulations of A-pBzOx-A by DLS at a polymer/drug-ratio of 10:5 in PBS. The

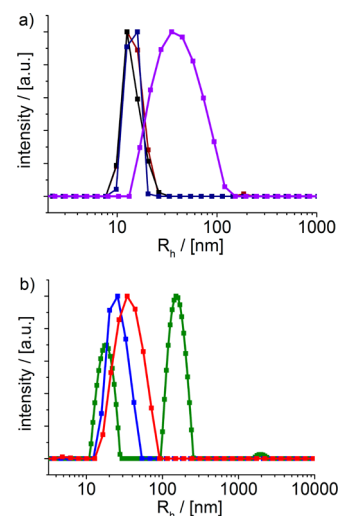


Figure 5. (a) Relative intensity dependent on the unweighted hydrodynamic radius R_h [nm] of the polymers (A-pPheOx-A = dark blue bars, A-p(BuOx-co-BzOx)-A = dark red bars, A-pBzOx-A = black bars, A-pBuOx-A = purple bars) of 10 g/L in PBS solution (scattering angle = 90° , $T = 25^\circ\text{C}$). (b) Relative intensity dependent on the unweighted hydrodynamic radius R_h [nm] of the formulation of the drugs PTX (blue), CUR (red), and SchA (green) with the drug carrier A-pBzOx-A with a polymer/drug-ratio of 10:5 (w/w) in 1 g/L of PBS solution (scattering angle = 90° , $T = 25^\circ\text{C}$).

formulation with SchA exhibited three species with weighted average mean of 23 nm (Figure 5b, Figure S6d). A large species at 2000 nm had a very low intensity and may be attributed to an artifact. In addition, two major distributions at approximately 20 and 150 nm were observed. In contrast, for PTX and CUR nanoformulations, only single and rather narrow distributions were observed with hydrodynamic radii of 21 nm (PTX) and 27 nm (CUR) (Figure 5b, Figure S6e). Obviously, such small sizes are typically considered favorable for parental administration, in particular for cancer chemotherapy.⁶²

The drug formulations studied here are not only potentially interesting as drug-loaded micelles but also in the form of solid dispersions. In this context, it is particularly interesting whether the drug is present in amorphous or crystalline form. Neither polymer exhibited a melting point, therefore being fully amorphous structures with glass transitions temperatures predictable by the Fox equation⁶³ using the T_g values of the homopolymers^{64–66} (Figure 6a, Table S9, eq 6, Table S10). SchA did not undergo thermal degradation at temperatures up to 200°C but exhibited a melting point of 129°C (Figure 6b), which corroborates values found in the literature.⁶⁷ Upon cooling, we did not observe recrystallization at the chosen experimental parameters, but a T_g value was detectable. The second heating cycle revealed a T_g of 30.7°C for SchA. For comparison, we also analyzed a simple physical mixture of SchA and A-pBzOx-A with the nanoformulation (both 1:2, w/w) obtained via thin film hydration and subsequent lyophilization. For the nanoformulation of A-pBzOx-A and SchA, no melting point could be detected in the first heating cycle (Figure 6c). Only a T_g of 67.5°C could be discerned, showing that the nanoformulation with an LC of $\sim 30\%$ was fully amorphous. The fact that only one T_g is observed demonstrates that no independent domains of amorphous drug and amorphous polymer are present but rather that the two entities are

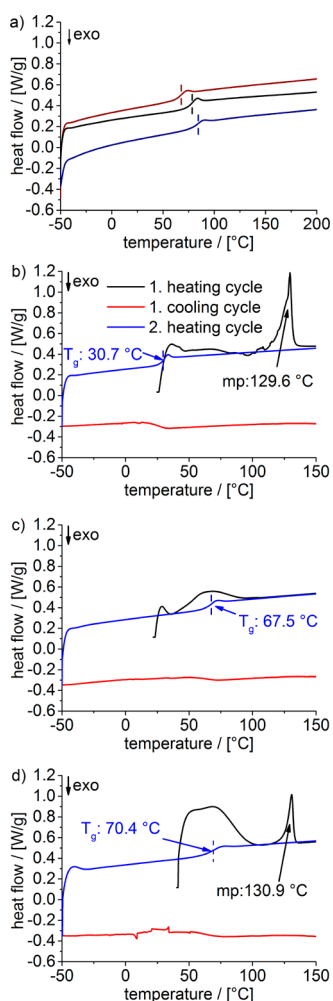


Figure 6. (a) DSC analysis of the triblock copolymers (A-pPheOx-A = dark blue line, $T_g = 81.3$ °C; A-p(BuOx-co-BzOx)-A = dark red line, $T_g = 67.5$ °C; A-pBzOx-A = black line, $T_g = 76.7$ °C). The heat flow [W/g] dependence on the temperature [°C] is shown with the particular glass transition T_g of each polymer marked with vertical lines. DSC analysis of SchA (b), nanoformulation with the polymer A-p(BuOx-co-BzOx)-A (c), and physical mixture of SchA/A-p(BuOx-co-BzOx)-A (d). The heat flow [W/g] dependence on the temperature [°C] is shown for the first heating cycle (black), first cooling cycle (red), and second heating cycle (blue). Melting points (endothermal maximum) were determined in the first heating cycle. The particular T_g values were determined in the second heating cycle. The scans were performed under a N_2 atmosphere using constant cooling and a heating rate of 10 K/min.

intimately and molecularly intertwined.⁶⁸ In the case of the physical mixture, we could clearly observe the melting point of SchA in the first heating cycle (Figure 6d). Also in this case, no recrystallization of SchA was observed upon cooling. The second heating cycle only revealed a T_g at 70.4 °C. Interestingly, the Fox equation predicts a much lower T_g for a mixture of 33 wt % SchA and 66 wt % A-pBzOx-A. Using the experimentally determined T_g values of both components, the Fox equation yields an expected T_g of only 52 °C. The origin of this discrepancy is unclear at this point.

CONCLUSIONS

We investigated the influence of incorporation of aromatic moieties into poly(2-oxazoline)-based ABA triblock copoly-

mers. In addition to the varying degree of aromaticity within the polymers, three cargo compounds with different relative aromatic contents were tested. In contrast to previous reports on a different polymeric system, incorporation of 2-benzyl-2-oxazoline or 2-phenyl-2-oxazoline did not increase drug loading or formulation stability in the case of paclitaxel. The first high capacity and stable formulations of the dibenzo[*a,c*]-cyclooctadiene lignan schizandrin A were realized. Interestingly, the formulation of the natural compound schizandrin A was barely affected by the different polymer structures, whereas the loading with curcumin benefitted significantly from incorporation of 2-benzyl-2-oxazoline but less so for 2-phenyl-2-oxazoline. Therefore, it appears that π - π interactions may be beneficial for drug loading and formulation stability in some cases, but it may not be considered a general phenomenon and must be assessed on a case-by-case basis. Not only are the nature of the drug and the amount of the aromatic moieties in the polymer important, but the nature of the aromatic moieties is also relevant as shown by the different behaviors of benzyl- and phenyl-containing triblock copolymers. Cell viability studies revealed that all studied polymers were highly cytocompatible with negligible effect on the cell viability at 50 g/L or less. Moreover, the first combination formulation could be realized, and the amorphous character of solid dispersions was confirmed by DSC.

ASSOCIATED CONTENT

Supporting Information

The Supporting Information is available free of charge on the ACS Publications website at DOI: 10.1021/acs.biomac.8b00708.

Detailed experimental procedures, monomer and polymer characterization data, extraction procedure, detailed methods description, results of the pyrene fluorescence assay (CMC values), formulation data, dynamic light scattering data, differential scanning calorimetry data, and chemical structures of Pt-NHC and CUR- F_6 (PDF)

AUTHOR INFORMATION

Corresponding Author

*E-mail: robert.luxenhofer@uni-wuerzburg.de.

ORCID

Rainer Schobert: 0000-0002-8413-4342

Robert Luxenhofer: 0000-0001-5567-7404

Notes

The authors declare the following competing financial interest(s): RL is listed as inventor on patents pertinent to the subject matter of the present contribution and co-founder of DelAqua Pharmaceuticals Inc. intent on commercial development of POx-based drug formulations.

ACKNOWLEDGMENTS

We thank Christian May for technical support. We are very grateful for the HDRC-Software version 6.3.1 provided by O. Nirschl and K. Fischer, Physical Chemistry of Polymers at the Johannes Gutenberg University Mainz led by Prof. Dr. Sebastian Seiffert (formerly Prof. Dr. Manfred Schmidt). This work was supported by the Free State of Bavaria and the Deutsche Forschungsgemeinschaft (project #398461692). Start-up funding for R.L. by the University Würzburg and SKZ Das Kunststoff-Zentrum is gratefully acknowledged.

M.M.L. thanks the Evonik Foundation for providing a doctoral fellowship. Light scattering experiments were possible through support of the Deutsche Forschungsgemeinschaft (INST 93/774-1 FUGG).

■ ABBREVIATIONS

API, active pharmaceutical ingredient; DMEM, Dulbecco's modified Eagle medium; Exo, exothermal; FT-IR, Fourier-transform infrared spectroscopy; HFIP, hexafluoroisopropanol; HPLC, high-pressure liquid chromatography; NMR, nuclear magnetic resonance; PBS, phosphate-buffered saline; P-gp, permeability glycoprotein; PTFE, polytetrafluoroethylene; SD, standard deviation; UV-vis, ultraviolet-visible

■ REFERENCES

- (1) Li, J. W.; Vederas, J. C. Drug discovery and natural products: end of an era or an endless frontier? *Science* **2009**, *325* (5937), 161–165.
- (2) Newman, D. J.; Cragg, G. M.; Snader, K. M. The influence of natural products upon drug discovery. *Nat. Prod. Rep.* **2000**, *17* (3), 215–234.
- (3) Lombardino, J. G.; Lowe, J. A. The role of the medicinal chemist in drug discovery—then and now. *Nat. Rev. Drug Discovery* **2004**, *3* (10), 853–862.
- (4) Yang, M.; Gong, W.; Wang, Y.; Shan, L.; Li, Y.; Gao, C. Bioavailability improvement strategies for poorly water-soluble drugs based on the supersaturation mechanism: an update. *J. Pharm. Pharm. Sci.* **2016**, *19* (2), 208–225.
- (5) Lipinski, C. A. Drug-like properties and the causes of poor solubility and poor permeability. *J. Pharmacol. Toxicol. Methods* **2000**, *44* (1), 235–249.
- (6) Gelderblom, H.; Verweij, J.; Nooter, K.; Sparreboom, A. Cremophor EL: the drawbacks and advantages of vehicle selection for drug formulation. *Eur. J. Cancer* **2001**, *37* (13), 1590–1598.
- (7) Bromberg, L. Polymeric micelles in oral chemotherapy. *J. Controlled Release* **2008**, *128* (2), 99–112.
- (8) Duncan, R.; Vicent, M. J. Polymer therapeutics—prospects for 21st century: the end of the beginning. *Adv. Drug Delivery Rev.* **2013**, *65* (1), 60–70.
- (9) Werner, M. E.; Cummings, N. D.; Sethi, M.; Wang, E. C.; Sukumar, R.; Moore, D. T.; Wang, A. Z. Preclinical evaluation of Genexol-PM, a nanoparticle formulation of paclitaxel, as a novel radiosensitizer for the treatment of non-small cell lung cancer. *Int. J. Radiat. Oncol., Biol., Phys.* **2013**, *86* (3), 463–468.
- (10) Zhang, Y.; Ren, T.; Gou, J.; Zhang, L.; Tao, X.; Tian, B.; Tian, P.; Yu, D.; Song, J.; Liu, X.; Chao, Y.; Xiao, W.; Tang, X. Strategies for improving the payload of small molecular drugs in polymeric micelles. *J. Controlled Release* **2017**, *261*, 352–366.
- (11) Houdaihed, L.; Evans, J. C.; Allen, C. Overcoming the road blocks: Advancement of block copolymer micelles for cancer therapy in the clinic. *Mol. Pharmaceutics* **2017**, *14* (8), 2503–2517.
- (12) Sofias, A. M.; Dunne, M.; Storm, G.; Allen, C. The battle of “nano” paclitaxel. *Adv. Drug Delivery Rev.* **2017**, *122*, 20–30.
- (13) Leroux, J. C. Drug delivery: Too much complexity, not enough reproducibility? *Angew. Chem., Int. Ed.* **2017**, *56* (48), 15170–15171.
- (14) Johnson, D. H.; Fehrenbacher, L.; Novotny, W. F.; Herbst, R. S.; Nemunaitis, J. J.; Jablons, D. M.; Langer, C. J.; DeVore, R. F., 3rd; Gaudreault, J.; Damico, L. A.; Holmgren, E.; Kabbinavar, F. Randomized phase II trial comparing bevacizumab plus carboplatin and paclitaxel with carboplatin and paclitaxel alone in previously untreated locally advanced or metastatic non-small-cell lung cancer. *J. Clin. Oncol.* **2004**, *22* (11), 2184–2191.
- (15) Luxenhofer, R.; Schulz, A.; Roques, C.; Li, S.; Bronich, T. K.; Batrakova, E. V.; Jordan, R.; Kabanov, A. V. Doubly amphiphilic poly(2-oxazoline)s as high-capacity delivery systems for hydrophobic drugs. *Biomaterials* **2010**, *31* (18), 4972–4979.
- (16) Luxenhofer, R.; Han, Y.; Schulz, A.; Tong, J.; He, Z.; Kabanov, A. V.; Jordan, R. Poly(2-oxazoline)s as polymer therapeutics. *Macromol. Rapid Commun.* **2012**, *33* (19), 1613–1631.
- (17) Han, Y.; He, Z.; Schulz, A.; Bronich, T. K.; Jordan, R.; Luxenhofer, R.; Kabanov, A. V. Synergistic combinations of multiple chemotherapeutic agents in high capacity poly(2-oxazoline) micelles. *Mol. Pharmaceutics* **2012**, *9* (8), 2302–2313.
- (18) Schulz, A.; Jaksch, S.; Schubel, R.; Wegener, E.; Di, Z.; Han, Y.; Meister, A.; Kressler, J.; Kabanov, A. V.; Luxenhofer, R.; Papadakis, C. M.; Jordan, R. Drug-induced morphology switch in drug delivery systems based on poly(2-oxazoline)s. *ACS Nano* **2014**, *8* (3), 2686–2696.
- (19) Seo, Y.; Schulz, A.; Han, Y.; He, Z.; Bludau, H.; Wan, X.; Tong, J.; Bronich, T. K.; Sokolsky, M.; Luxenhofer, R.; Jordan, R.; Kabanov, A. V. Poly(2-oxazoline) block copolymer based formulations of taxanes: effect of copolymer and drug structure, concentration, and environmental factors. *Polym. Adv. Technol.* **2015**, *26* (7), 837–850.
- (20) He, Z.; Wan, X.; Schulz, A.; Bludau, H.; Dobrovolskaia, M. A.; Stern, S. T.; Montgomery, S. A.; Yuan, H.; Li, Z.; Alakhova, D.; Sokolsky, M.; Darr, D. B.; Perou, C. M.; Jordan, R.; Luxenhofer, R.; Kabanov, A. V. A high capacity polymeric micelle of paclitaxel: Implication of high dose drug therapy to safety and in vivo anti-cancer activity. *Biomaterials* **2016**, *101*, 296–309.
- (21) Wan, X.; Min, Y.; Bludau, H.; Keith, A.; Sheiko, S. S.; Jordan, R.; Wang, A. Z.; Sokolsky-Papkov, M.; Kabanov, A. V. Drug combination synergy in worm-like polymeric micelles improves treatment outcome for small cell and non-small cell lung cancer. *ACS Nano* **2018**, *12* (3), 2426–2439.
- (22) He, Z.; Schulz, A.; Wan, X.; Seitz, J.; Bludau, H.; Alakhova, D. Y.; Darr, D. B.; Perou, C. M.; Jordan, R.; Ojima, I.; Kabanov, A. V.; Luxenhofer, R. Poly(2-oxazoline) based micelles with high capacity for 3rd generation taxoids: preparation, in vitro and in vivo evaluation. *J. Controlled Release* **2015**, *208*, 67–75.
- (23) Perrone, D.; Ardito, F.; Giannatempo, G.; Dioguardi, M.; Troiano, G.; Lo Russo, L.; De Lillo, A.; Laino, L.; Lo Muzio, L. Biological and therapeutic activities, and anticancer properties of curcumin. *Exp. Ther. Med.* **2015**, *10* (5), 1615–1623.
- (24) Anand, P.; Kunnumakkara, A. B.; Newman, R. A.; Aggarwal, B. B. Bioavailability of curcumin: problems and promises. *Mol. Pharmaceutics* **2007**, *4* (6), 807–818.
- (25) Lübtow, M. M.; Hahn, L.; Haider, M. S.; Luxenhofer, R. Drug specificity, synergy and antagonism in ultrahigh capacity poly(2-oxazoline)/poly(2-oxazine) based formulations. *J. Am. Chem. Soc.* **2017**, *139* (32), 10980–10983.
- (26) Lübtow, M. M.; Nelke, L. C.; Brown, A.; Sahay, G.; Dandekar, G.; Luxenhofer, R. Drug induced micellization into ultra-high capacity and stable curcumin nanoformulations. *Comparing in vitro 2D and 3D-tumor model of triple-negative breast cancer* **2017**, DOI: 10.26434/chemrxiv.5661736.v1.
- (27) Hancke, J. L.; Burgos, R. A.; Ahumada, F. Schisandra chinensis (Turcz.) Baill. *Fitoterapia* **1999**, *70* (5), 451–471.
- (28) Lu, Y.; Chen, D. F. Analysis of Schisandra chinensis and Schisandra sphenanthera. *J. Chromatogr. A* **2009**, *1216* (11), 1980–1990.
- (29) Ikeya, Y.; Taguchi, H.; Yosioka, I.; Kobayashi, H. The constituents of schizandra chinensis BAILL. I. isolation and structure determination of five new lignans, Gomisin A, B, C, F and G, and the absolute structure of Schizandrin. *Chem. Pharm. Bull.* **1979**, *27* (6), 1383–1394.
- (30) Dean, J. R.; Liu, B. Supercritical fluid extraction of chinese herbal medicines: investigation of extraction kinetics. *Phytochem. Anal.* **2000**, *11* (1), 1–6.
- (31) He, X. G.; Lian, L. Z.; Lin, L. Z. Analysis of lignan constituents from Schisandra chinensis by liquid chromatography-electrospray mass spectrometry. *J. Chromatogr. A* **1997**, *757* (1), 81–87.
- (32) Zhu, L.; Li, B.; Liu, X.; Huang, G.; Meng, X. Isolation and purification of schisandrol A from the stems of Schisandra chinensis and cytotoxicity against human hepatocarcinoma cell lines. *Pharmacogn. Mag.* **2015**, *11* (41), 131–135.

- (33) Štěrbová, H.; Sevcikova, P.; Kvasnickova, L.; Glatz, Z.; Slanina, J. Determination of lignans in *Schisandra chinensis* using micellar electrokinetic capillary chromatography. *Electrophoresis* **2002**, *23* (2), 253–258.
- (34) Wang, L.; Chen, Y.; Song, Y.; Chen, Y.; Liu, X. GC-MS of volatile components of *Schisandra chinensis* obtained by supercritical fluid and conventional extraction. *J. Sep. Sci.* **2008**, *31* (18), 3238–3245.
- (35) Li, X. Y.; Yang, M.; Huang, J. Y.; Yu, X. X.; Zhao, M. Q.; Liang, Z. K.; Xie, Z. S.; Xu, X. J. Preparative separation and purification of deoxyschizandrin from *Schisandrae Sphenantherae Fructus* by high-speed counter-current chromatography. *J. Pharm. Anal.* **2013**, *3* (6), 429–433.
- (36) Xia, Y. G.; Yang, B. Y.; Liang, J.; Wang, J. S.; Kuang, H. X. Simultaneous quantification of five dibenzocyclooctadiene lignans in *Schisandra chinensis* by HPLC separation and fluorescence detection. *Anal. Methods* **2014**, *6* (15), 5981–5985.
- (37) Hu, B.; Xin, G. Z.; So, P. K.; Yao, Z. P. Thin layer chromatography coupled with electrospray ionization mass spectrometry for direct analysis of raw samples. *J. Chromatogr. A* **2015**, *1415*, 155–160.
- (38) Schobert, R.; Kern, W.; Milius, W.; Ackermann, T.; Zoldakova, M. Synthesis of the first unnatural schisantherins and their effects in multidrug-resistant cancer cells. *Tetrahedron Lett.* **2008**, *49* (21), 3359–3362.
- (39) Gmeiner, A.; Effenberger-Neidnicht, K.; Zoldakova, M.; Schobert, R. A methyltitanocene complex of schisandrol A with high efficacy against multi-drug resistant cervix and breast carcinoma cells. *Appl. Organomet. Chem.* **2011**, *25* (2), 117–120.
- (40) Chen, T.; Li, C.; Li, Y.; Yi, X.; Lee, S. M. Y.; Zheng, Y. Oral delivery of a nanocrystal formulation of schisantherin A with improved bioavailability and brain delivery for the treatment of parkinson's disease. *Mol. Pharmaceutics* **2016**, *13* (11), 3864–3875.
- (41) Chen, T.; Li, C.; Li, Y.; Yi, X.; Wang, R.; Lee, S. M. Y.; Zheng, Y. Small-sized mPEG–PLGA nanoparticles of Schisantherin A with sustained release for enhanced brain uptake and anti-parkinsonian activity. *ACS Appl. Mater. Interfaces* **2017**, *9* (11), 9516–9527.
- (42) Sowndhararajan, K.; Deepa, P.; Kim, M.; Park, S. J.; Kim, S. An overview of neuroprotective and cognitive enhancement properties of lignans from *Schisandra chinensis*. *Biomed. Pharmacother.* **2018**, *97*, 958–968.
- (43) Shi, C.; Guo, D.; Xiao, K.; Wang, X.; Wang, L.; Luo, J. A drug-specific nanocarrier design for efficient anticancer therapy. *Nat. Commun.* **2015**, *6*, 7449.
- (44) Jiang, W.; Wang, X.; Guo, D.; Luo, J.; Nangia, S. Drug-specific design of telodendrimer architecture for effective doxorubicin encapsulation. *J. Phys. Chem. B* **2016**, *120* (36), 9766–9777.
- (45) Jiang, W.; Luo, J.; Nangia, S. Multiscale approach to investigate self-assembly of telodendrimer based nanocarriers for anticancer drug delivery. *Langmuir* **2015**, *31* (14), 4270–4280.
- (46) Li, Y.; Yang, L. Driving forces for drug loading in drug carriers. *J. Microencapsulation* **2015**, *32* (3), 255–272.
- (47) Shi, Y.; Van Steenberg, M. J.; Teunissen, E. A.; Novo, L.; Gradmann, S.; Baldus, M.; Van Nostrum, C. F.; Hennink, W. E. II–II stacking increases the stability and loading capacity of thermosensitive polymeric micelles for chemotherapeutic drugs. *Biomacromolecules* **2013**, *14* (6), 1826–1837.
- (48) Shi, Y.; Van der Meel, R.; Theek, B.; Blenke, E. O.; Pieters, E. H. E.; Fens, M. H. A. M.; Ehling, J.; Schiffelers, R. M.; Storm, G.; Van Nostrum, C. F.; Lammers, T.; Hennink, W. E. Complete regression of xenograft tumors upon targeted delivery of paclitaxel via II–II stacking stabilized polymeric micelles. *ACS Nano* **2015**, *9* (4), 3740–3752.
- (49) Milonaki, Y.; Kaditi, E.; Pispas, S.; Demetzos, C. Amphiphilic gradient copolymers of 2-methyl- and 2-phenyl-2-oxazoline: self-organization in aqueous media and drug encapsulation. *J. Polym. Sci., Part A: Polym. Chem.* **2012**, *50* (6), 1226–1237.
- (50) Feinauer, R.; Seeliger, W. Über die Anlagerung von Epoxiden an cyclische Iminoester. *Justus Liebigs Ann. Chem.* **1966**, *698* (1), 174–179.
- (51) Muenzner, J. K.; Rehm, T.; Biersack, B.; Casini, A.; De Graaf, I. A. M.; Worawutputtpong, P.; Noor, A.; Kempe, R.; Brabec, V.; Kasparkova, J.; Schobert, R. Adjusting the DNA interaction and anticancer activity of Pt(II) N-heterocyclic carbene complexes by steric shielding of the trans leaving Group. *J. Med. Chem.* **2015**, *58* (15), 6283–6292.
- (52) Schmitt, F.; Gold, M.; Begemann, G.; Andronache, I.; Biersack, B.; Schobert, R. Fluoro and pentafluorothio analogs of the antitumoral curcuminoid EF24 with superior antiangiogenic and vascular-disruptive effects. *Bioorg. Med. Chem.* **2017**, *25* (17), 4894–4903.
- (53) Nakajima, A. Solvent effect on the vibrational structures of the fluorescence and absorption spectra of pyrene. *Bull. Chem. Soc. Jpn.* **1971**, *44* (12), 3272–3277.
- (54) Kalyanasundaram, K.; Thomas, J. K. Environmental effects on vibronic band intensities in pyrene monomer fluorescence and their application in studies of micellar systems. *J. Am. Chem. Soc.* **1977**, *99* (7), 2039–2044.
- (55) Ding, J.; Chen, L.; Xiao, C.; Chen, L.; Zhuang, X.; Chen, X. Noncovalent interaction-assisted polymeric micelles for controlled drug delivery. *Chem. Commun.* **2014**, *50* (77), 11274–11290.
- (56) Raveendran, R.; Mullen, K. M.; Wellard, R. M.; Sharma, C. P.; Hoogenboom, R.; Dargaville, T. R. Poly(2-oxazoline) block copolymer nanoparticles for curcumin loading and delivery to cancer cells. *Eur. Polym. J.* **2017**, *93*, 682–694.
- (57) Luxenhofer, R.; Sahay, G.; Schulz, A.; Alakhova, D.; Bronich, T. K.; Jordan, R.; Kabanov, A. V. Structure-property relationship in cytotoxicity and cell uptake of poly(2-oxazoline) amphiphiles. *J. Controlled Release* **2011**, *153* (1), 73–82.
- (58) Hamada, H.; Ishihara, K.; Masuoka, N.; Mikuni, K.; Nakajima, N. Enhancement of water-solubility and bioactivity of paclitaxel using modified cyclodextrins. *J. Biosci. Bioeng.* **2006**, *102* (4), 369–371.
- (59) Lübtow, M. M.; Keßler, L.; Lorson, T.; Gangloff, N.; Kirsch, M.; Dahms, S.; Luxenhofer, R. More Is less: Curcumin and paclitaxel formulations using poly(2-oxazoline) and poly(2-oxazine) based amphiphiles bearing linear and branched C9 side chains. *ChemRxiv* **2018**, DOI: [10.26434/chemrxiv.5883109.v1](https://doi.org/10.26434/chemrxiv.5883109.v1).
- (60) Sreekanth, C. N.; Bava, S. V.; Sreekumar, E.; Anto, R. J. Molecular evidences for the chemosensitizing efficacy of liposomal curcumin in paclitaxel chemotherapy in mouse models of cervical cancer. *Oncogene* **2011**, *30* (28), 3139–3152.
- (61) Huang, M.; Jin, J.; Sun, H.; Liu, G. T. Reversal of P-glycoprotein-mediated multidrug resistance of cancer cells by five schizandrins isolated from the chinese herb fructus schizandrae. *Cancer Chemother. Pharmacol.* **2008**, *62* (6), 1015–1026.
- (62) Cabral, H.; Matsumoto, Y.; Mizuno, K.; Chen, Q.; Murakami, M.; Kimura, M.; Terada, Y.; Kano, M. R.; Miyazono, K.; Uesaka, M.; Nishiyama, N.; Kataoka, K. Accumulation of sub-100 nm polymeric micelles in poorly permeable tumours depends on size. *Nat. Nanotechnol.* **2011**, *6*, 815–823.
- (63) Fox, T. Static analysis of dilute materials to study surrounding temperature for the polymer. *Bull. Am. Phys. Soc.* **1956**, *1*, 23–135.
- (64) Rettler, E. F. J.; Kranenburg, J. M.; Lambermont-Thijs, H. M. L.; Hoogenboom, R.; Schubert, U. S. Thermal, mechanical, and surface properties of poly(2-N-alkyl-2-oxazoline)s. *Macromol. Chem. Phys.* **2010**, *211* (22), 2443–2448.
- (65) Culbertson, B. M.; Xue, Y. A novel simultaneous semi-interpenetrating polymer network of crosslinked poly(methyl methacrylate) and poly(2-benzyl-2-oxazoline). *J. Macromol. Sci., Part A: Pure Appl. Chem.* **1996**, *33* (11), 1601–1608.
- (66) Beck, M.; Birnbrich, P.; Eicken, U.; Fischer, H.; Fristad, W. E.; Hase, B.; Krause, H. J. Polyoxazoline auf fettchemischer Basis. *Angew. Makromol. Chem.* **1994**, *223* (1), 217–233.
- (67) Kochetkov, N. K.; Khorlin, A. Y.; Chizhov, O. S. Chemical study of *Schizandra chinensis*. I. Schizandrin and related compounds. *Zh. Obshch. Khim.* **1961**, *31*, 3454–3460.

(68) Rausch, K.; Reuter, A.; Fischer, K.; Schmidt, M. Evaluation of nanoparticle aggregation in human blood serum. *Biomacromolecules* **2010**, *11* (11), 2836–2839.

The chemical versatility of POx and POzi facilitates the design of polymeric drug carriers enabling extremely high drug loadings > 50 wt.% in selected cases. Nevertheless, the selection of suitable drug vehicles was mainly based on trial and error, in combination with some intuition and empirical knowledge. Flory-Huggins interaction and Hansen solubility parameters (HSPs) are widely used to predict polymer-drug compatibility. Although both group contribution methods are intrinsically unable to distinguish between structural isomers such as some of the discussed POx and POzi based amphiphiles, the prediction of general trends regarding drug loading might still be feasible. In order to obtain conclusive results, a sufficient large polymer and drug platform is necessary. Therefore, five different hydrophobic drugs were formulated with 18 different POx and POzi based amphiphiles, all comprising the same hydrophilic corona but slightly different hydrophobic cores. Surprisingly, HSPs were indeed able to correctly estimate some trends regarding good and poor solubilizers. However, this was only true for amphiphiles which strongly differed in their chemical structure such as barely hydrophobic C₃ or C₄ vs strongly hydrophobic C₉ sidechains. In contrast, the effect of e.g. branching or cyclization in the sidechain could not be predicted. This was also true when determining the solubility parameters of the various drugs and polymers empirically with their respective solubility profiles. The determination of the solubility of block copolymers has proven challenging, as solubility is a measure of the degree of molecular mixing between two substances at thermodynamic equilibrium. For micelles, efficient molecular mixing is not guaranteed anymore, as the hydrophobic (polar solvent) or hydrophilic (nonpolar solvent) part might be segregated from the solvent although macroscopically no precipitation/segregation occurs. Interestingly, drugs which were selectively soluble mainly in solvents comprising a high amount of hydrogen-bond acceptors also yielded the highest loading capacity et *vice versa*. This is in accordance with the chemical structure of the POx and POzi based amphiphiles, comprising a high density of tertiary amides (= hydrogen-bond acceptors).

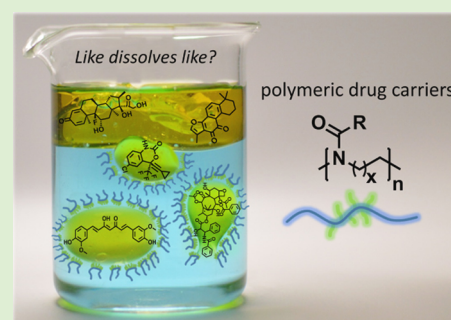
Like Dissolves Like? A Comprehensive Evaluation of Partial Solubility Parameters to Predict Polymer–Drug Compatibility in Ultrahigh Drug-Loaded Polymer Micelles

Michael M. Lübtow, Malik Salman Haider, Marius Kirsch, Stefanie Klisch, and Robert Luxenhofer*¹

Functional Polymer Materials, Chair for Advanced Materials Synthesis, Department of Chemistry and Pharmacy and Bavarian Polymer Institute, University of Würzburg, Röntgenring 11, 97070 Würzburg, Germany

S Supporting Information

ABSTRACT: Despite decades of research, our understanding of the molecular interactions between drugs and polymers in drug-loaded polymer micelles does not extend much beyond concepts such as “like-dissolves-like” or hydrophilic/hydrophobic. However, polymer–drug compatibility strongly affects formulation properties and therefore the translation of a formulation into the clinics. Specific interactions such as hydrogen-bonding, π – π stacking, or coordination interactions can be utilized to increase drug loading. This is commonly based on trial and error and eventually leads to an optimized drug carrier. Unfortunately, due to the unique characteristics of each drug, the deduction of advanced general concepts remains challenging. Furthermore, the introduction of complex moieties or specifically modified polymers hampers systematic investigations regarding polymer–drug compatibility as well as clinical translation. In this study, we reduced the complexity to isolate the crucial factors determining drug loading. Therefore, the compatibility of 18 different amphiphilic polymers for five different hydrophobic drugs was determined empirically. Subsequently, the obtained specificities were compared to theoretical compatibilities derived from either the Flory–Huggins interaction parameters or the Hansen solubility parameters. In general, the Flory–Huggins interaction parameters were less suited to correctly estimate the experimental drug solubilization compared to the Hansen solubility parameters. The latter were able to correctly predict some trend regarding good and poor solubilizers, yet the overall predictive strength of Hansen solubility parameters is clearly unsatisfactory.



INTRODUCTION

The limited water solubility of active pharmaceutical ingredients (APIs) is becoming ever more problematic, as drug discovery led to a shift toward larger, more hydrophobic compounds.¹ To address the problem of formulating such drugs with polymer excipients, a critical consideration of the term hydrophobic is warranted. At first glance, hydrophobicity seems to be straightforward; however, it is limited to water as a solvent and a crude, binary assessment.² Arguably, the best known parameter for drug hydrophobicity and drug formulation which builds on this simplification is the partition coefficient between octanol and water ($\log P$ value). Although being useful to give, e.g., a rough estimation about the permeability of a drug through cell membranes,^{3,4} it is not able to give conclusive insights into the properties of a drug. This becomes evident by comparing the two drugs pentobarbital and clobazam. Apart from the shared $\log P$ value of 2.1,⁵ they differ in many aspects: halogenated vs nonhalogenated, presence and number or absence of H-bond donors, and aromatic vs nonaromatic. Changing the point of view to a potential drug-delivery system, such structural differences are expected to influence the compatibility of drug carrier and encapsulated, non-water-soluble drug and therefore crucial characteristics such as drug loading,⁶ formulation stability,⁷ or

drug release.⁸ Due to the unique chemical and physical properties of each drug, no universal delivery vehicle is likely to be found. Luckily, polymer chemistry offers an essentially unlimited variety of potential polymeric drug carriers.^{9,10} To determine which kind of polymer is compatible with which drug commonly remains on trial and error and is associated with major efforts.^{11–17} The scope of such effort is beautifully displayed by the work of Börner and co-workers, using a combinatorial approach to identify suitable peptide sequences out of 7⁷ possible heptamers to efficiently formulate non-water-soluble anti-Alzheimer compounds.¹⁸ Also, a targeted tuning of the polymer–drug compatibility by specific coordination interactions was realized in selected cases.¹⁹ Allen and co-workers²⁰ considered the Hansen solubility parameters (HSPs) to predict the compatibility of different polymers with the API ellipticine. Overall, a good correlation between experimental formulation characteristics and calculated polymer–drug compatibilities was observed. Important to note, the investigated polymers differed strongly in their chemical structure. In contrast, distinct polymer–drug specificities in

Received: May 6, 2019

Revised: June 22, 2019

Published: June 24, 2019

chemically very similar poly(2-oxazoline) (POx) and poly(2-oxazine) (POzi)-based drug-delivery systems for the non-water-soluble drugs paclitaxel (PTX) and curcumin (CUR) have been reported recently.¹⁷ By shifting a single methylene group from the polymer side chain to the polymer main chain in the building blocks of the hydrophobic core caused pronounced specificities for CUR and PTX. As theoretical calculations of HSPs are an incremental or group contribution method (GCM), both polymers—being structural isomers—would yield the same HSPs thus being unable to predict the observed compatibilities. A shortcoming of the solubility parameters to predict polymer–drug compatibility of amorphous solid dispersions of 54 polymer–drug pairs was also reported by Turpin et al.²¹ It was suggested that the deviation between experimental results and predicted compatibility is among others due to the absence of an entropic term in all conventional GCMs. Important to note, the different homo- and copolymers employed in this study varied quite significantly in their chemical structure.

However, this failure of theoretically determined solubility parameters notwithstanding, it could be possible that an experimental determination rather than a theoretical derivation of the HSPs could give more in depth insights into the solubilization capacity of polymeric drug carriers. To obtain conclusive results, a sufficiently large polymer and drug platform is necessary. Therefore, we compared the solubilization properties of 18 different ABA triblock copolymers, all comprising the same hydrophilic poly(2-methyl-2-oxazoline) (PMeOx) shell A to focus on the impact of the hydrophobic core B. Previously, a small library of such ABA triblock copolymers with varying B blocks have been tested for taxane formulations. Others have studied pseudo-diblocks for solubilization of indomethacin with some success.²² However, as we already observed distinct polymer–drug specificities incorporating POx- and POzi-based hydrophobic cores B with barely hydrophobic C₃ and C₄ aliphatic side chains, we kept this pattern, included POzi, introduced branching and cyclization and tested compatibility with a range of structurally diverse drugs. Strongly hydrophobic C9 side chains were included to investigate the common, somewhat simplistic assumption of like dissolves like. Besides the chemotherapeutic PTX²³ and the biologically active CUR,²⁴ antiretroviral efavirenz (EFV),²⁵ the corticosteroid dexamethasone (DEX),²⁶ and antioxidative tanshinone IIA (T2A)²⁷ were included, all being highly water-insoluble. The pronounced specificities obtained in this study clearly show how a presumably simple system such as a drug-loaded polymer micelle can be highly susceptible to rather minute changes in the chemical composition of the drug carrier. This study systematically reduces the complexity of polymer–drug interactions to the extent that it becomes possible to isolate crucial factors such as necessity of hydrogen bonding between host and guest molecules, the influence of sterics, or the determination of polymer–drug compatibility on polymer backbone or polymer side-chain interactions.

MATERIALS AND METHODS

Reagents and Solvents. All substances for the preparation of the polymers were purchased from Sigma-Aldrich (Steinheim, Germany) or Acros (Geel, Belgium) and were used as received unless otherwise stated. Soluplus (poly(vinyl caprolactame)–poly(vinyl acetate)–poly(ethylene glycol) graft copolymer) and Resomer (poly(ethylene glycol)–poly(L-lactide); 35 wt % PEG) were a generous gift by BASF

SE (Ludwigshafen, Germany) and Evonik Industries AG (Essen, Germany), respectively. Curcumin powder from *Curcuma longa* (turmeric) was purchased from Sigma-Aldrich and analyzed in-house (curcumin = 79%, demethoxycurcumin = 17%, bisdemethoxycurcumin = 4%; determined by high-performance liquid chromatography (HPLC) analysis; Figure S22). Paclitaxel (>99%, HPLC) was purchased from LC Laboratories (Woburn, MA). Efavirenz (>98%, HPLC) and dexamethasone (>99%, HPLC) were purchased from TCI (Eschborn, Germany). Tanshinone IIA (>98%, HPLC) was purchased from Shanghai Yuanye Bio-Technology (Shanghai, China). Deuterated chloroform (CDCl₃) for NMR analysis was obtained from Deutero GmbH (Kastellaun, Germany).

The monomers 2-*iso*-propyl-2-oxazoline (iPrOx), 2-*iso*-propyl-2-oxazine (iPrOzi), 2-*n*-propyl-2-oxazoline (nPrOx), 2-*n*-propyl-2-oxazine (nPrOzi), 2-*cyclo*-2-propyl-2-oxazoline (cPrOx), 2-*cyclo*-2-propyl-2-oxazine (cPrOzi), 2-(*cyclo*-propyl-methylene)-2-oxazoline (cPrMeOx), 2-(*cyclo*-propyl-methylene)-2-oxazine (cPrMeOzi), 2-*n*-butyl-2-oxazoline (nBuOx), 2-*n*-butyl-2-oxazine (nBuOzi), 2-*iso*-butyl-2-oxazoline (iBuOx), 2-*iso*-butyl-2-oxazine (iBuOzi), 2-*sec*-butyl-2-oxazoline (sBuOx), and 2-*sec*-butyl-2-oxazine (sBuOzi) were synthesized according to Seeliger et al.²⁸ (Figures S1–S14). The synthesis of the monomers 2-(3-ethyl heptyl)-2-oxazoline (EtHepOx) and 2-(3-ethyl heptyl)-2-oxazine (EtHepOzi) was adapted from Kempe et al.,²⁹ which in turn was derived from the synthesis of Taubmann et al.³⁰ (Figures S15 and S16). The monomers 2-*n*-nonyl-2-oxazoline (nNonOx) and 2-*n*-nonyl-2-oxazine (nNonOzi) were synthesized according to Beck et al.³¹ (Figures S17 and S18).

The monomers cPrOzi, cPrMeOx, cPrMeOzi, iBuOzi, and sBuOzi were synthesized and characterized for the first time to the best of our knowledge. Experimental procedures as well as characterization can be found in the Supporting Information.

All substances used for polymerization, namely, methyl trifluoromethylsulfonate (MeOTf), propargyl p-toluenesulfonate, benzonitrile (PhCN), sulfolane, and all monomers were refluxed over CaH₂ (PhCN was refluxed over P₂O₅) and distilled under argon.

Polymer Synthesis. The polymerizations and workup procedures were carried out as described previously.¹⁷ For polymer synthesis and characterization, see Figures S19–S54. Briefly, the preparation of all ABA triblock copolymers was performed as follows: initiator was added to a dried and nitrogen-flushed flask and dissolved in the respective amount of solvent. The monomer 2-methyl-2-oxazoline (MeOx) was added and the reaction mixture was heated to 100 °C for approximately 4 h. The reaction progress was controlled using Fourier transform infrared and ¹H NMR spectroscopies. After complete consumption of MeOx, the mixture was cooled to room temperature and the monomer for the second block was added. The reaction mixture was heated to 100 °C (2-*R*-2-oxazoline) or 120 °C (2-*R*-2-oxazine) overnight. The procedure was repeated for the third block MeOx, and after monomer consumption was confirmed, termination was carried out by addition of 1-*tert*-butyl piperazine 1-carboxylate (PipBoc) or piperidine at 50 °C for 4 h. Subsequently, K₂CO₃ was added and the mixture was stirred at 50 °C for 4 h. Precipitates were removed by centrifugation, and the solvent was removed under reduced pressure. The supernatant was transferred into a dialysis bag (MWCO 1 kDa, cellulose acetate) and dialyzed against deionized water overnight. The solution was recovered from the bag and lyophilized.

EXPERIMENTAL SECTION

Nuclear Magnetic Resonance (NMR) Spectroscopy. NMR spectra were recorded on a Fourier 300 (¹H: 300 MHz), Bruker Biospin (Rheinstetten, Germany) at 298 K. The spectra were calibrated to the signal of residual protonated solvent signal (CDCl₃; 7.26 ppm). Multiplicities of signals are depicted as follows: s, singlet; d, doublet; t, triplet; q, quartet; quin, quintet; dt, doublet of triplets; m, multiplet; b, broad.

Dialysis. Dialysis was performed using Spectra/Por membranes with a molecular weight cutoff (MWCO) of 1 kDa (material: cellulose acetate) obtained from neoLab (Heidelberg, Germany). Deionized

water was renewed after 1 h, 4 h, and every 12 h subsequently, until end of dialysis.

Gel Permeation Chromatography. Gel permeation chromatography (GPC) was performed on an Agilent 1260 Infinity System, Polymer Standard Service (Mainz, Germany) with either HFIP containing 3 g/L potassium trifluoroacetate; precolumn: 50 × 8 mm² PSS PFG linear M; 2 columns: 300 × 8 mm² PSS PFG linear M (particle size 7 μm) or dimethylformamide (DMF) containing 1 g/L LiBr; precolumn: 50 × 8 mm² PSS GRAM; columns: 30 Å and 1000 Å 300 × 8 mm² PSS GRAM (particle size 10 μm) as eluent. The columns were kept at 40 °C, and flow rates were 1.0 mL/min (DMF) or 0.7 mL/min (HFIP). Prior to each measurement, samples were filtered through 0.2 μm poly(tetrafluoroethylene) filters, Roth (Karlsruhe, Germany). Conventional calibration was performed with PEG standards (0.1–1000 kg/mol), and data were processed with WinGPC software.

Differential Scanning Calorimetry (DSC). Differential scanning calorimetry (DSC) was performed on a DSC 204 F1 Phoenix, NETZSCH (Selb, Germany) under N₂ atmosphere (20.0 mL/min). The samples were placed in aluminum pans with crimped-on lids and heated from 25 to 200 °C (10 K/min) and subsequently cooled to −50 °C (10 K/min). The samples were heated/cooled two additional times from −50 to 200 °C (10 K/min).

Fluorescence Spectroscopy—Critical Micelle Concentration (CMC). Pyrene stock solution (24 μM, 5.0 mg/L in acetone) was added to glass vials (do not use plastic vials!), and the solvent was removed by a gentle stream of argon. Subsequently, various amounts of polymer stock solutions (H₂O) were added and the solutions diluted with deionized water to yield a final pyrene concentration of 5 × 10^{−7} M. The samples were stored overnight at ambient temperature (≈25 °C) under the exclusion of light. Pyrene fluorescence was recorded on an FP-8300, Jasco (Gross-Umstadt, Germany) from 360 to 400 nm (λ_{ex} = 333 nm) at 25 °C. The CMC was determined as the concentration at which the fitted I₁/I₃ ratio increased/decreased 10% of its initial value.

Drug-Loaded Polymer Micelles. Drug-loaded polymer micelles were prepared by thin-film method.³² Ethanolic polymer (20 g/L), PTX (20 g/L), CUR (5.0 g/L), EFV (20 g/L), dexamethasone (10 g/L), and tanshinone IIa (2 g/L) stock solutions were mixed in the desired ratio (polymer = 10 g/L, drug feed = 2, 4, 6, 8, 10, 12 g/L (2 and 4 g/L for T2A)). Due to its insolubility in ethanol, Resomer stock solutions were prepared in CHCl₃ (20 g/L). To avoid polymer precipitation during preparation of thin films, all drug stock solutions were also prepared in CHCl₃ in the case of Resomer. After complete removal of the solvent at 50 °C under a mild stream of argon, the films were dried in vacuo (≤0.2 mbar) for 20 min. Subsequently, 300 μL of preheated (37 °C) H₂O was added. Complete solubilization was facilitated by shaking the solutions at 1250 rpm and 55 °C for 12 min with a Thermomixer comfort, Eppendorf AG (Hamburg, Germany). Nonsolubilized drug (if any) was removed by centrifugation for 5 min at 9000 rpm with a MIKRO 185 (Hettich, Tuttlingen, Germany). Solubilization experiments were performed with 3 individually prepared samples, and the results are presented as means ± standard deviation (SD). Due to the large number of samples, a more sophisticated setup was used to prepare multiple thin films simultaneously (Figure S55).

CUR and T2A quantification was performed by UV–vis absorption on a BioTek Eon Microplate Spectrophotometer, Thermo Fisher Scientific (MA) using a calibration curve obtained with known amounts of CUR and T2A, respectively (Figure S56). Samples were prepared in Rotilabo F-Type 96 well plates, Carl Roth GmbH & Co. KG (Karlsruhe, Germany) at a constant volume of 100 μL. Spectra were recorded from 300 to 600 nm at 25 °C. CUR was quantified at 428 nm and T2A at 459 nm. Prior to UV–vis absorption measurements, the aqueous formulations were appropriately diluted with ethanol. The following equations were used to calculate loading capacity (LC) and loading efficiency (LE)

$$LE = \frac{m_{\text{drug}}}{m_{\text{drug,added}}} \quad (1)$$

$$LC = \frac{m_{\text{drug}}}{m_{\text{drug}} + m_{\text{polymer}}} \quad (2)$$

where m_{drug} and m_{polymer} are the mass of solubilized drug and polymer excipient in solution, respectively, and $m_{\text{drug,added}}$ is the amount of drug initially added to the dispersion. No loss of polymer during micelles preparation was assumed.

PTX, EFV, and DEX quantification was performed by HPLC analysis on an LC-20A Prominence HPLC, Shimadzu (Duisburg, Germany) equipped with a system controller CBM-20A, a solvent delivery unit LC-20 AT (double plunger), an on-line degassing unit DGU-20A, an autosampler SIL-20AC, and an SPD-20A UV–vis detector. As stationary phase, a ZORBAX Eclipse Plus, Agilent (Santa Clara, CA) C18 column (4.6 × 100 mm²; 3.5 μm) was used. The mobile phase was a gradient of H₂O/ACN at 40 °C and a flow rate of 1 mL/min. PTX was quantified at 227 nm, EFV at 248 nm, and DEX at 240 nm using a calibration curve obtained with known amounts of PTX, EFV,¹⁷ and DEX, respectively (Figure S57).

For long-term stability studies, the aqueous formulations were stored in Eppendorf tubes containing the precipitate (if any occurred) at ambient conditions (≈25 °C) under the exclusion of light. Prior to the drug quantification after d5, d10, and d30, all formulations were centrifuged again to remove any precipitate.

Solubility Parameters. The Hildebrand solubility parameter δ provides a numerical estimate of the degree of interaction between materials.³³ Materials with similar δ values are likely to be miscible. It is defined as the square root of a molecule's cohesive energy density (CED) and is commonly given in MPa^{1/2}. The CED of a liquid is the cohesive energy E_{coh} per molar volume V_m and corresponds to the energy needed to completely remove a unit volume of molecules from their neighbors to infinite.³⁴

$$\delta = \sqrt{\text{CED}} = \sqrt{\frac{E_{\text{coh}}}{V_m}} \quad (3)$$

As the cohesive energy E_{coh} needs to be exceeded while vaporizing, it can be derived from the heat of vaporization ΔH_{vap} at a given temperature. The Flory–Huggins interactions parameter χ can be used to estimate drug polymer compatibility

$$\chi_{\text{solvent-solute}} = (\delta_{T,\text{solvent}} - \delta_{T,\text{solute}})^2 \cdot \frac{V_{M,\text{solute}}}{RT} \quad (4)$$

where δ_T is the total solubility parameter of solvent and solute, V_m is the molar volume of solute, R is the Avogadro constant, and T is the temperature. The lower χ , the higher the solvent–solute compatibility (for complete miscibility, $\chi_{\text{solvent-solute}} \leq 0.5$ at the respective temperature³⁵).

In contrast to the one-dimensional Hildebrand solubility parameter, the Hansen solubility parameter (HSP) divides δ into three different kinds of interactions between solvent and solute³⁶

$$\delta_T = \sqrt{\delta_D^2 + \delta_p^2 + \delta_H^2} \quad (5)$$

where δ_D , δ_p , and δ_H comprise contributions from intermolecular van der Waals forces, dipole–dipole interactions, and hydrogen bonding, respectively.

HSPs can be calculated by group contribution method (GCM). Each functional or structural group exhibits a certain molar attractive force (F) and hydrogen-bond energy (E). The solubility parameter δ of a molecule is the sum of F and E with respect to its molar volume V_m

$$\delta = \frac{\sum F, E}{V_m} \quad (6)$$

According to the Hoftyzer–van Krevelen method (HVK),³⁴ the three partial solubility parameters can be calculated according to

$$\delta_D = \frac{\sum F_{di}}{V_m} \quad (7)$$

Table 1. Physicochemical Characterization of ABA Triblock Copolymers, Including the Molecular Weight, M_n , Dispersity, D , Glass-Transition Temperature, T_g , and Critical Micelle Concentration, CMC

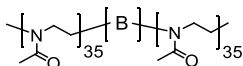
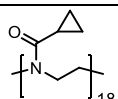
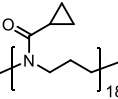
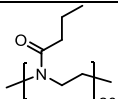
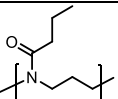
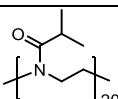
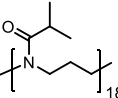
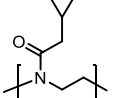
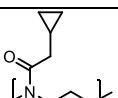
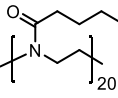
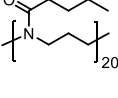
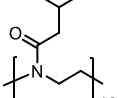
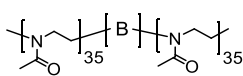
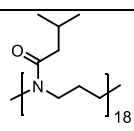
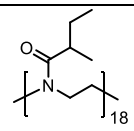
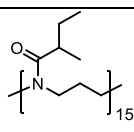
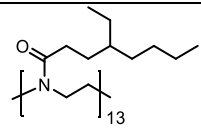
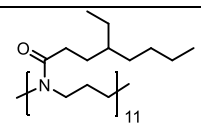
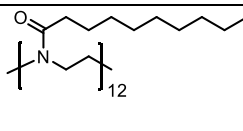
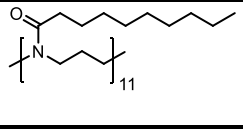
Polymer	Label	$M_n^{(a)}$ [kg/mol]	$M_n^{(b)}$ [kg/mol]	$M_n^{(c)}$ [kg/mol]	$D^{(c)}$	$T_g^{(d)}$ [°C]	CMC ^(e) [10 ⁻⁶ M] [mg/L]
	A-B-A						
	A-cPrOx-A	8.2	8.0	3.3	1.17	72	4 33
	A-cPrOzi-A	8.6	7.9	4.8	1.23	64	6 53
	A-nPrOx-A	8.6	8.3	4.6	1.17	61	---
	A-nPrOzi-A	8.7	8.2	5.6	1.16	52	---
	A-iPrOx-A	8.3	7.8	4.3	1.06	72	---
	A-iPrOzi-A	8.4	7.5	3.8	1.15	62	---
	A-cPrMeOx-A	8.5	8.5	4.2	1.12	67	---
	A-cPrMeOzi-A	8.0	8.9	3.8	1.20	52	5 42
	A-nBuOx-A	8.6	8.7	5.6	1.10	56	1 8
	A-nBuOzi-A	9.0	13.3	5.6	1.20	46	0.5 5
	A-iBuOx-A	8.5	9.1	5.0	1.11	65	1 12

Table 1. continued

Polymer	Label	$M_n^{a)}$ [kg/mol]	$M_n^{b)}$ [kg/mol]	$M_n^{c)}$ [kg/mol]	$\bar{D}^{d)}$	$T_g^{d)}$ [°C]	CMC ^{e)} [10 ⁻⁶ M] [mg/L]
	A-B-A						
	A-iBuOzi-A	8.5	8.6	3.9	1.17	51	4 35
	A-sBuOx-A	8.4	7.8	4.9	1.11	66	---
	A-sBuOzi-A	8.2	8.8	4.8	1.13	59	---
	A-EtHepOx-A	8.9	8.9	4.9	1.16	60	0.6 5
	A-EtHepOzi-A	8.7	9.5	4.4	1.15	54	0.5 4
	A-nNonOx-A	8.5	6.5	5.0	1.17	60	0.6 5
	A-nNonOzi-A	8.5	8.1	4.5	1.24	60	1 11

^aAccording to $[M]_0/[I]_0$. ^bObtained by ¹H NMR analysis (CDCl₃; 300 MHz) evaluated as mean of all relevant signals. ^cObtained by GPC analysis (eluent: HFIP, calibrated with PEG standards). ^dMean T_g obtained from second and third heating curves (DSC). ^eObtained by pyrene assay at 25 °C.

$$\delta_p = \frac{\sqrt{\sum F_{pi}^2}}{V_m} \quad (8)$$

$$\delta_H = \sqrt{\frac{\sum E_{hi}}{V_m}} \quad (9)$$

where F_{di} represents the van der Waals force, F_{pi} is the dipole–dipole interaction, and E_{hi} is the hydrogen bonding. Their values were taken from the literature.³⁴ Therefore, the CED is the sum of contributions from all functional and structural groups of a molecule. Important to note, δ_p and δ_H are affected by the symmetry of a certain molecule.

According to Fedor's method,³⁷ each functional or structural group of a molecule contributes to the molar volume V_m

$$V_m = \sum v_i \quad (10)$$

where v_i is the group-specific volume.

Another method to calculate HSPs is the Yamamoto Molecule Break (YMB) method, which is a subprogram of the commercially available software Hansen Solubility Parameters in Practice (HSPiP). The HSPs can be directly obtained from the chemical structure of a molecule, which can be inserted as SMILES code, which was obtained from ChemDraw Professional 15.1. YMB is a GCM as well; however, compared to HVK, it exhibits a larger data set of functional groups, such as the tertiary amide moiety, which is of particular interest for POx- and POzi-based drug-delivery vehicles. Unfortunately, no information about the algorithm behind the calculation can be found in the literature.

Instead of comparing δ_T , the three solubility parameters δ_D , δ_p , and δ_H are correlated with each other in the three-dimensional Hansen space to predict the compatibility between solvent and solute

$$R_a^2 = (4(\delta_{D1} - \delta_{D2})^2 + (\delta_{p1} - \delta_{p2})^2 + (\delta_{H1} - \delta_{H2})^2) \quad (11)$$

Important to note, the distance R_a of two substances in the Hansen space does not contain quantitative information about their miscibility

nor about the degree of intermolecular interactions. However, it can be used to qualitatively compare the solubility of a certain solute in various solvents.

Experimental Determination of HSP. The cohesive energy E_{coh} and therefore the solubility parameter of a certain molecule is directly linked to its heat of vaporization ΔH_{vap} at a given temperature. However, the determination of ΔH_{vap} is often unsuitable for drugs and excipients due to their thermal instabilities.³⁸ The software HSPiP provides a method to semiempirically obtain the partial solubility parameters of a certain compound by determining its solubility in a sufficiently large number of different solvents. Therefore, polymer or drug were dissolved at 20 g/L in the respective solvent and shaken at 160 rpm and 20 °C for 24 h. Samples exhibiting partial or complete precipitation were determined insoluble. If the formation of aggregates (micelles, etc.) was observed by visual inspection (in the case of triblock copolymers), the respective solutions were stored for additional 2 days. If no precipitation/sedimentation occurred, they were considered soluble.

RESULTS AND DISCUSSION

Polymer Synthesis and Characterization. All 18 ABA triblock copolymers used for drug formulation feature the same (within experimental reproducibility) hydrophilic PMeOx₃₅ shell A and a POx- or POzi-based hydrophobic core B comprising either barely hydrophobic C3 and C4 or strongly hydrophobic C9 aliphatic side chains (Table 1). Detailed description of monomer and polymer synthesis and characterization can be found in Figures S1–S18 and S19–S54, respectively. The polymers were designed to exhibit the same molecular weight to retain a somewhat comparable water solubility. Therefore, the degree of polymerization (DP) for hydrophobic blocks with C9 side chains is lower (DP = 11–13) than with C3/C4 side chains (DP = 15–20). The syntheses and characterization of A-*n*PrOx-A,¹⁷ A-*n*PrOzi-A,¹⁷ A-*n*BuOx-A,¹⁷ A-*n*BuOzi-A,¹⁷ A-EtHepOx-A,¹⁵ A-EtHepOzi-A,¹⁵ A-*n*NonOx-A,¹⁵ and A-*n*NonOzi-A¹⁵ used in this study have been already described in the literature. Polymers similar to A-*s*BuOx-A³⁹ and A-*i*BuOx-A³⁹ were previously described; however, the polymers of the present study were newly synthesized. All other ABA triblock copolymers were synthesized and characterized for the first time, to the best of our knowledge. Furthermore, the polymerization of *c*PrOzi, *c*PrMeOx, *c*PrMeOzi, *i*BuOzi, and *s*BuOzi has not been described previously. Except for A-*n*NonOzi-A ($\bar{D} = 1.24$), all polymers exhibited a narrow dispersity $\bar{D} \leq 1.2$ with an essential monomodal molar mass distribution (as judged by GPC, see Supporting Information (SI)). Furthermore, a distinct shift to higher molar masses after consumption of each block (determined by GPC) was observed, indicative of successful preparation of ABA triblock copolymers. The dispersity of the block copolymers comprising POzi hydrophobic cores was generally somewhat higher compared to their POx counterparts with the same side chain (except for *n*-propyl and EtHep). This may be attributed to the higher polymerization temperatures required for Ozi polymerization (POzi exhibits lower polymerization rate constants (k_p) than POx^{40,41}). Alternatively, slow initiation of Ozi polymerization by living PMeOx (1st block) or MeOx polymerization (3rd block) by living POzi chain ends may be responsible. However, no clear trend in the dispersity obtained after GPC measurements after each polymerized block was observed (for a comparison of elugrams obtained from samples directly drawn from the reaction mixture (1st and 2nd blocks) or after purification (3rd block), see SI).

Moreover, successful polymer synthesis was further corroborated by solid-state characterization of freeze-dried powders. All ABA triblock copolymers exhibited a single T_g between 46 °C (A-*n*BuOzi-A) and 72 °C (A-*c*PrOx-A and A-*i*PrOx-A) (Figure 1a). This is in accordance with previously

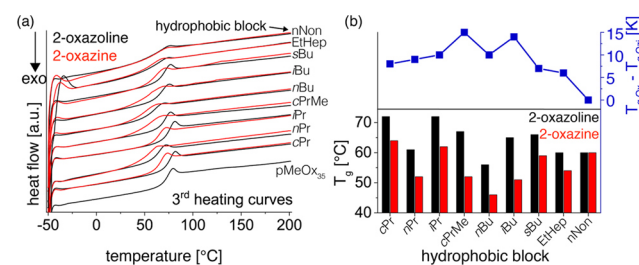


Figure 1. (a) Heat flow of the third heating cycle (10 °C/min) obtained by differential scanning calorimetry (DSC) measurements of ABA triblock copolymers (black: POx, red: POzi); (b) T_g (black bars: POx, red bars: POzi, left axis) and the corresponding difference in T_g of copolymers comprising the same side chain but different backbones (blue curve, right axis).

reported results from the triblock copolymers comprising C9 side chains, in which the thermal characteristics of the corresponding homopolymers (e.g., semicrystallinity of P*n*NonOx) is not observed in the triblocks, resulting in a single T_g .¹⁵ It should be noted that the single T_g is not in accordance with the Fox equation, according to which the T_g of block copolymers can be derived from the T_g 's of the corresponding homopolymers. However, the higher flexibility (i.e., lower T_g) of POzi-based homopolymers compared to POx-based ones with same side chains⁴² did result in lower T_g values of the corresponding triblock copolymers (Figure 1b) with the notable exception of *n*-nonyl side chain. Interestingly, the difference in T_g was less pronounced for polymers with long C9 side chains, and highest differences of T_g values between POx- and POzi-containing triblocks were observed for intermediate side-chain lengths, in particular cyclopropylmethyl and isobutyl side chains, which both feature branching units at the terminal positions of the side chains. Generally, the T_g of triblock copolymers comprising unbranched side chains (*n*-propyl) were lower than for corresponding polymers with branched ones (*i*-propyl and *c*-propyl). This is expected, as for the corresponding homopolymers, an increase in T_g from linear (n PrOx₁₀₀ = 40 °C) to cyclic (*c*PrOx₁₀₀ = 80 °C) was reported.⁴³

To get first insights into the amphiphilicity of the ABA triblock copolymers, the critical micelle concentration (CMC) was determined by pyrene assay. Pyrene is an extremely poorly water-soluble (water solubility: 0.7 μmol/L; 0.135 mg/L⁴⁴), aromatic compound that exhibits five distinct emission bands termed I_1 – I_5 between 370 and 400 nm.⁴⁵ Alterations in the ratio of I_1/I_3 can be used to determine changes in the polarity of the surrounding microenvironment. With the formation of micelles, pyrene partitions into the hydrophobic core usually causing a decrease in I_1/I_3 . Here, pronounced changes in I_1/I_3 only occurred for polymers comprising *n*-butyl or C9 side chains (Figure 2a and Table 1). With increasing polymer concentration, I_1/I_3 increased for *n*-butyl and decreased for C9 side chains. As discussed previously,³² the increase in I_1/I_3 after encapsulation is highly unusual, as pyrene is commonly considered a measure of polarity and exhibits values between 1.6 and 1.9 in aqueous solution. This indicates that the polarity

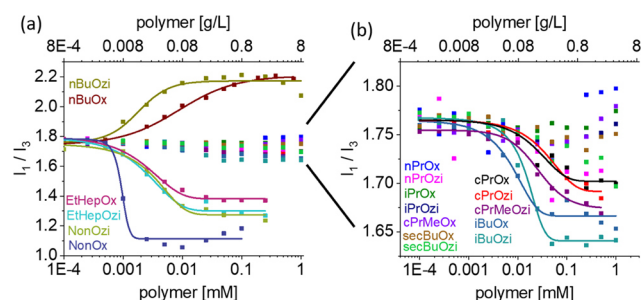


Figure 2. (a) Ratio of I_1/I_3 (pyrene assay) in dependence of the ABA triblock copolymer concentration with corresponding fits. Polymer concentration in mM (lower axis) corresponds to actual M_n of each triblock copolymer, whereas top axis (polymer [g/L]) is based on $M_n = 8.0$ kg/mol; (b) enlarged section shows the range $I_1/I_3 = 1.60$ – 1.80 .

inside the micellar core is greater than that of H_2O and even exceeds the one for dimethyl sulfoxide (DMSO) or ionic liquids. Taking a closer look at $I_1/I_3 = 1.6$ – 1.8 (Figure 2b) suggests minor but systematic changes that could be interpreted as CMCs for A-cPrMeOzi-A, A-iBuOx-A, A-iBuOzi-A, A-cPrOx-A, and A-cPrOzi-A. The apparent absence of micelle formation for most triblock copolymers comprising C3 side chains is in accordance with the general observation of increasing water solubility with decreasing side-chain length.³² Taking into account the cloud points (T_{cp}) of the corresponding homopolymers ($nPrOzi_{100} = 11$ °C;⁴⁰ $nPrOx_{100} = 25$ °C; $cPrOx_{100} = 30$ °C; and $iPrOx_{100} = 44$ °C, 5 mg/mL⁴³), a CMC for POx and POzi with *n*-propyl side chains may have been expected. However, the water solubility increases with decreasing chain length⁴⁶ ($nPrOx_{25} = 21$ °C; 20 mg/mL⁴⁷) and the flanking hydrophilic blocks can also influence the solubility of the central B block.⁴⁸ Apart from that, the differences in the I_1/I_3 ratios already illustrate how small changes in polymer structure such as branching in the side chain can have a large impact on the encapsulation properties (for pyrene) and on the polarity of the hydrophobic core.

Determination of Partial Solubility Parameters.

Solubility parameters δ and molar volume V_M of polymers and drugs were determined according to Hoftyzer–van Krevelen (HVK), Yamamoto Molecule Break (YMB), and Fedors' methods (eqs 6–10). As all drug carriers exhibit the same hydrophilic PMeOx shell A, only the hydrophobic block B of the ABA triblock copolymers was considered when predicting polymer–drug compatibility. This assumption seemed valid, as the hydrophobic drugs should be mainly associated with the hydrophobic block. In contrast to HVK, the degree of polymerization (DP) affects δ obtained by the YMB method. Important to note, with increasing DP, the solubility parameters of selected homopolymers became physically unreasonable, as, e.g., δ_H of PMeOx increased exponentially with increasing DP resulting in $\delta_H = 131.7$ MPa^{1/2} for PMeOx₁₈. Such a value is unreasonably high, especially when considering $\delta_H(H_2O) = 42.3$. Apart from a few outliers (e.g., δ_p for iPrOzi), the overall trend in δ_D , δ_p , and δ_H (YMB) for homopolymers with DP = 1 or DP > 5 was the same (Figure S58). Therefore, and for the sake of comparison with HVK, a single repeat unit (DP = 1) will be considered in the following for YMB.

HVK is a group contribution method, i.e., each group of a molecule contributes to the overall solubility parameters for the molecule. Therefore, HVK cannot differentiate between structural isomers such as cPrOzi and cPrMeOx (Figure 3 and Table S1). Apart from that, the following trends were observed:

- δ_D , δ_p , and δ_H decreased with increasing side-chain length, i.e., decreasing ratio of polar (tertiary amides) to nonpolar (aliphatics) moieties. The decrease was most pronounced in the case of δ_p for monomers containing highly hydrophobic C9 side chains. As a consequence, δ_T also decreased with increasing side-chain length. The trend becomes prominent by comparing δ of polymers with linear, branched, or cyclic side chains:
 - MeOx > nPrOx > nBuOx > nNonOx
 - iPrOx > iBuOx = sBuOx > EtHepOx
 - cPrOx > cPrMeOx

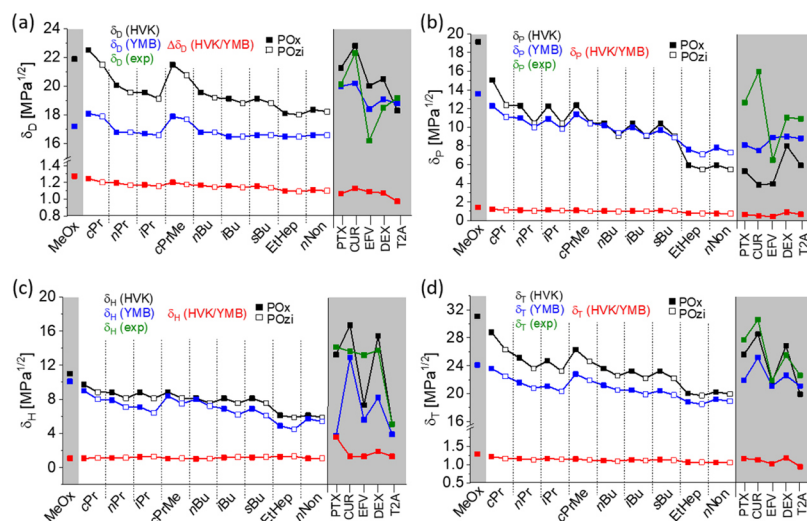


Figure 3. Partial (a–c) and total (d) solubility parameters δ_D , δ_p , δ_H , and δ_T of various repeat units (solid: POx, hollow: POzi) representing the hydrophilic shell (MeOx) or the hydrophobic core of ABA triblock copolymers as well as five different drugs. The solubility parameters were calculated by HVK (black), YMB (blue), or determined experimentally and obtained by HSPiP software (green). The difference in δ obtained by HVK or YMB is given as HVK/YMB (red).

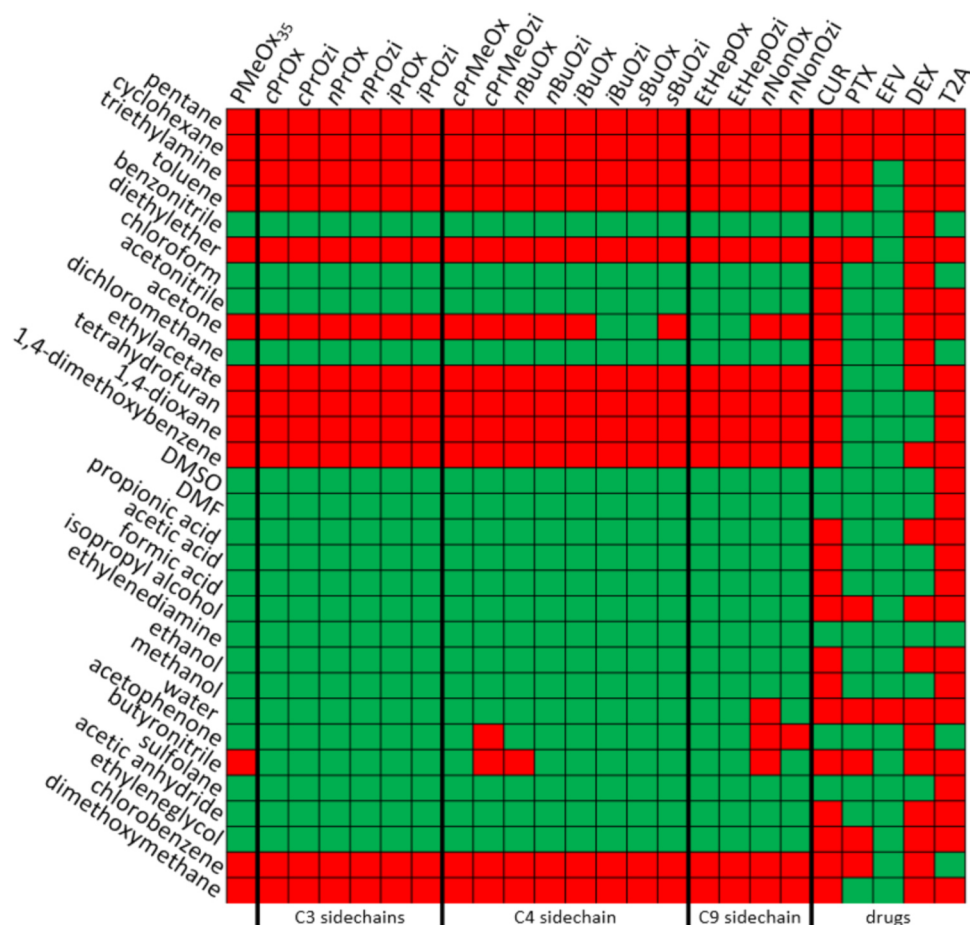


Figure 4. Solubility profiles of P(MeOx)₃₅, ABA triblock copolymers (labeled according to their hydrophobic core), as well as non-water-soluble drugs in 31 different solvents at 20 g/L and 20 °C (green: soluble; red: non-soluble).

- branching in the side chain decreased δ_D , δ_P , δ_H :
 - $n\text{BuOx} > i\text{BuOx} = s\text{BuOx}$
- cyclization in the side chain increased δ_D , δ_P , δ_H . The increase was most pronounced for δ_H :
 - $c\text{PrMeOx} > n\text{BuOx} > i\text{BuOx} = s\text{BuOx}$

As HVK is not able to differentiate between a methylene group in the side chain or the backbone, δ_D , δ_P , and δ_H of POx are generally greater than those of POzi with the same side chain.

Partial solubility parameters of a single repeat unit obtained by the YMB method resulted in the same trend of decreasing δ with increasing side-chain length. Furthermore, the extraordinarily high δ_D values for monomers with cyclic side chains were obtained for both methods. Interestingly, YMB was able to differentiate between structural isomers with $\Delta\delta_D$ (POx/POzi) < 1%, $\Delta\delta_P$ < 3%, and $\Delta\delta_H$ < 11% for POx- and POzi-based isomers such as $n\text{BuOx}$ and $n\text{PrOzi}$.

Comparing δ_D , δ_P , and δ_H of the five drugs gave similar trends irrespective of whether they were calculated using HVK or YMB (detailed description of how δ values were obtained can be found in Tables S2–S6). Only δ_H of PTX differed significantly with a value 4 times higher calculated by HVK. For a better understanding of the validity of the calculated solubility parameters, the solubility parameters of polymers and drugs were also determined experimentally.

Semiempirical determination of partial solubility parameters was performed by dissolving polymers or drugs at 20 g/L

(sparingly soluble according to the U.S. Pharmacopeia) in 31 solvents with varying polarities and functional groups at 20 °C (Figure 4 and see Table S7 for dielectric constants ϵ and $E_T(30)$ values of respective solvents). It is evident that the solubility of the ABA triblock copolymers (rows 2–19) is strongly affected by its hydrophilic P(MeOx)₃₅ shell (row 1). Homopolymers with C4 (or longer) side chains should not be soluble in water at the investigated concentration. With the notable exception of butyronitrile, all copolymers comprising C3 side chains exhibited the same solubility as P(MeOx)₃₅. The similar solubilities of all triblock copolymers display limitations of this approach, in particular regarding the crucial part, namely, the hydrophobic core of the drug carriers. In contrast to homopolymers, the solubility of block copolymers is highly complex due to their amphiphilic character and the associated aggregation behaviors.^{49,50} In this regard, even the term solubility needs to be discussed. According to the U.S. Pharmacopeia,⁵¹ soluble means that a substance yields a homogeneous mixture when mixed in the desired ratio with the designated solvent. The problem of this definition is illustrated in Figure S59. The two extremes completely soluble and non-soluble are easy to determine. Although no precipitation occurs, the in-between state caused by the formation of (nanosized) aggregates is hard to clearly assign to one of the two extremes. Generally, solubility is a measure of the degree of molecular mixing between two substances at thermodynamic equilibrium. In the case of micelles, efficient molecular mixing is not guaranteed anymore, as the hydro-

phobic (polar solvent) or hydrophilic (nonpolar solvent) part is segregated from the solvent. As we used a binary code (soluble, nonsoluble) to determine the solubility parameters, all solutions showing no precipitation after 2 day storage were regarded as soluble. Apart from that, the investigated polymer and drug concentration of 20 g/L was chosen at random. Important to note, different concentrations would result in altered solubility profiles further hampering the absolute determination of solubility parameters. At the chosen concentration, it is clear that the solubilities of all tested polymers only show minute differences. However, a minor difference for two polymers of particular interest, **A-pPrOzi-A** and **A-pBuOx-A**, which are constitutional isomers, was observed, as the former is soluble in butyronitrile, while the latter is not.

In contrast to the polymers, pronounced differences in the solubility behaviors of the drugs are obvious, which will be discussed in the context of drug formulations (Figures 6–10). The pronounced discrepancy in δ_D , δ_P , and δ_H between experimentally determined and calculated (HVK or YMB) values (Figure 3, green curve) averaged out, resulting in similar δ_T for all methods. This already gave a hint that the determination of polymer–drug compatibility by the Flory–Huggins interaction parameter χ (considering δ_T only; eq 4) might be inaccurate, as it is not able to distinguish between the different kinds of interactions.

To get a first understanding of the validity of the obtained solubility parameters, the water solubility of the repeat unit corresponding to the hydrophobic core or the hydrophilic shell was calculated and compared to their experimentally determined solubilities. Compatibility between solvent and solute can be qualified by the Flory–Huggins interactions parameter χ (eq 4) or the distance R_a between solvent and solute in three-dimensional Hansen space (eq 11). The experimentally determined trend of decreasing water solubility with increasing side-chain length could be reproduced by HVK (Figure 5, blue bars) or YMB (red bars) with both parameters, χ and R_a (Table S8). In all cases, MeOx exhibited the highest compatibility with water (i.e., lowest values of χ and R_a). In good agreement with experimental data, polymers comprising strongly hydrophobic C9 side chains were on the opposite side

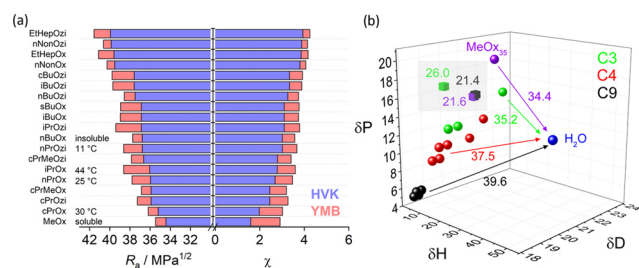


Figure 5. (a) Predicted water miscibility of different poly(2-oxazolin) and poly(2-oxazine) repeat units (Ox/Ozi) estimated by HVK (blue) or YMB (red) with either R_a (left bars) or χ (right bars). Polymers are sorted according to decreasing water solubility (bottom to top) obtained by HVK. Water solubility of selected homopolymers according to their T_{cp} is given. (b) Visualization of R_a between homopolymers (HVK method; DP = 1) with varying side-chain length and H₂O in three-dimensional Hansen space. R_a (H₂O) of MeOx₃₅ (purple) or selected triblock copolymers (green: **A-nPrOzi-A**; black: **A-nNonOx-A**) derived from their experimental solubility profile (Figure 4) are given in the gray inset.

with regard to water miscibility. As already suggested by their high δ_H values, polymers comprising cyclic side chains (*c*-propyl or *c*-propylmethylene; Figure 3) were predicted to have a higher water solubility than linear or branched ones (compatibility with H₂O is strongly influenced by δ_H due to its high value of 42.3). However, this does not correctly reflect the experimental solubility, as the cloud point (T_{cp}) of *i*PrOx₁₀₀ is approximately 14 °C higher than that of *c*PrOx₁₀₀.⁴³ Furthermore, the same χ and R_a values of *n*PrOzi and *n*BuOx (HVK) or even higher values of *n*PrOzi (YMB) do not correlate well with their actual water solubilities. Such small differences between experimental and calculated miscibilities may seem negligible. However, as we will see later, those small changes in the chemical structure can have tremendous impact on polymer–drug compatibility. In conclusion, it is possible to correctly classify the solubility of polymers with strongly varying solubility behaviors (C1 vs C3 vs C4 vs C9 side chains); however, the impact of small structural changes including shifts of single methylene groups seems to be unpredictable using Hansen solubility parameters. Important to note, water solubility of the polymers predicted with solubility parameters derived from their experimental solubility profile (Figure 4) correlated much worse, as **A-nNonOx-A** comprising a strongly hydrophobic core was predicted to have a higher water compatibility than MeOx₃₅ (Figure 5b, gray inset).

Drug Formulations. The drug formulations included in this study were prepared under identical conditions (as far as possible; for detailed description, the reader is referred to the Materials and Methods section). An overview of the maximum achieved drug concentrations of all formulations is given in Figure S60, whereas complete formulation data can be found in Figures S61–S83. The initial thought of comparing POx- and POzi-based drug formulations with the ones prepared with commercially available polymers was revoked due to the inability of Resomer and Soluplus to efficiently solubilize any of the investigated drugs (Figures S64, S68, S72, S76, S82). However, this is most likely due to inappropriate formulation conditions (thin-film method), as Soluplus is designed for hot melt extrusion and Resomer for nanoprecipitation. In fact, curcumin solubilities up to 0.47 g/L were reported with solid dispersions of Soluplus⁵² while using the thin-film method only less than 0.1 g/L was achieved (Figure S68).

The PTX and CUR formulations of **A-EtHepOx-A**, **A-EtHepOzi-A**, **A-nNonOx-A**, and **A-nNonOzi-A** were already reported.¹⁵ CUR and PTX formulations of **A-nPrOx-A**, **A-nPrOzi-A**, **A-nBuOx-A**, and **A-nBuOzi-A** were already described,¹⁷ but prepared for the present study under slightly different conditions; however, the drug loadings were highly reproducible.⁵³

Paclitaxel Formulations. The solubility enhancement of PTX using POx triblock copolymers exhibiting a similar structure to some of the ones investigated in this study (**A-nBuOx-A**, **A-iBuOx-A**, **A-sBuOx-A**) was already assessed at slightly different conditions.³⁹ Except for **A-sBuOx-A**, the here obtained maximum PTX loadings (Figure 6a) correlated well to the ones reported previously. The difference for **A-sBuOx-A**/PTX (3.6³⁹ vs 5.6 g/L) might be due to poor formulations stability (Figure 10). Measuring the drug content not immediately after preparation (as performed here) might already have caused PTX precipitation. The drug feed concentrations of 2, 4, 6, 8, 10, and 12 g/L (polymer = 10 g/L) were chosen to obtain reliable maximum drug loadings.

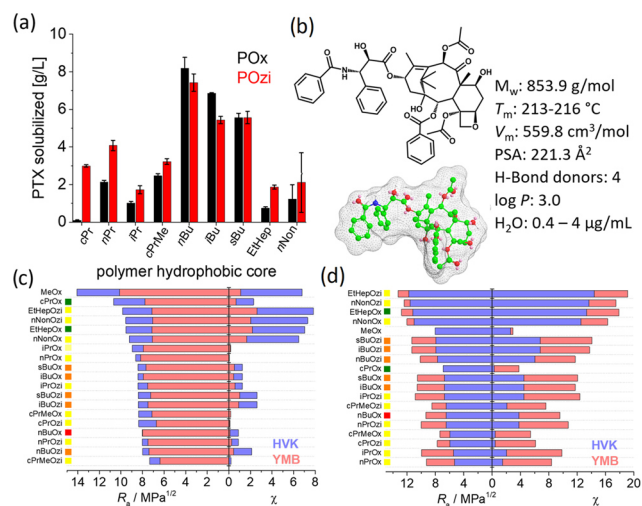


Figure 6. (a) Maximum achieved PTX concentrations directly after preparation in dependence of the polymer structure (polymer = 10 g/L; ABA triblock copolymers labeled according to their hydrophobic core). All samples were prepared in triplicate, and the results are presented as mean \pm SD. (b) Chemical and spatial (MM2 force-field minimum energy; Chem3D 15.1) structure of PTX. (c, d) Predicted compatibility between PTX and hydrophobic repeat units estimated by HVK (blue) or YMB (red) with either R_a (left bars) or χ (right bars). Polymers are sorted according to decreasing polymer–PTX compatibility (bottom to top) obtained by HVK. Solubility parameters of PTX were either calculated (c) or derived from its experimental solubility profile (d). Color code next to polymer labels: 8–10 g/L PTX (red); 5–8 g/L PTX (orange); 1–5 g/L PTX (yellow); and <1 g/L PTX (green).

This becomes clear by taking a closer look at the PTX formulations of A-*n*BuOzi-A (Figure 11). Up to PTX feed concentrations of 8 g/L, PTX was encapsulated quantitatively with loading efficiencies (LE) around 100%. Increasing PTX feed to 10 g/L already caused little precipitation with LE = 56%. At 12 g/L however, only 0.65 g/L PTX could be encapsulated (LE = 5.4 wt %). Therefore, investigating high drug feed concentrations >10 g/L only would have resulted in false maximum PTX loadings, i.e., wrong polymer–drug compatibilities.

As determined in a previous study,¹⁷ hydrophobic cores exhibiting a butyl side chain—irrespective if linear or branched—were found preferable in terms of maximum PTX loadings (Figure 6a). Furthermore, no pronounced difference between POx and POzi hydrophobic cores was observed. Interestingly, HVK correctly classified the worst-performing polymers comprising C9 side chains or A-*c*PrOx-A and A-*i*PrOx-A with R_a (Figure 6c and Tables S4, S9). This was not true for YMB, which, e.g., predicted (R_a) a higher compatibility for A-*i*PrOx-A than for the best-performing polymer A-*n*BuOx-A. Interestingly, the two best-performing polymers A-*n*BuOx-A and A-*n*BuOzi-A were included within the four best polymers according to HVK and R_a . As χ does not differentiate between the different contributions to the solubility parameters, the compatibility of the *c*PrOx core with PTX was overestimated due to their similar δ_T values. Generally, R_a was in better agreement with the experimental drug loadings than χ . Interesting to note, R_a and χ obtained from the experimentally determined solubility parameters of PTX (Figure 6d) performed worse than calculated compatibilities. This might be due to the large solubility range of PTX in the

31 chosen solvents at 20 g/L. Being soluble in many solvents makes it hard to determine crucial parameters resulting in nonexpressive, averaged values of δ_D , δ_P , and δ_H .

In summary, (1) R_a (being more discriminating) predicted polymer–PTX compatibility better than χ , (2) HVK was more precise than YMB, (3) HVK was able to classify the worst-performing polymers with R_a , (4) R_a and χ obtained with experimentally determined δ of PTX predicted worse than purely calculated ones, and finally, (5) none of the methods was able to correctly predict polymer–PTX compatibility of structurally similar polymers (e.g., *i*BuOx and *i*PrOzi).

Curcumin Formulations. In contrast to the situation with PTX, the polymer backbone seems to be a crucial parameter in the case of CUR. POzi-based CUR formulations were in all cases superior to their POx counterparts with the same side chains (Figure 7a), again in good agreement with previous

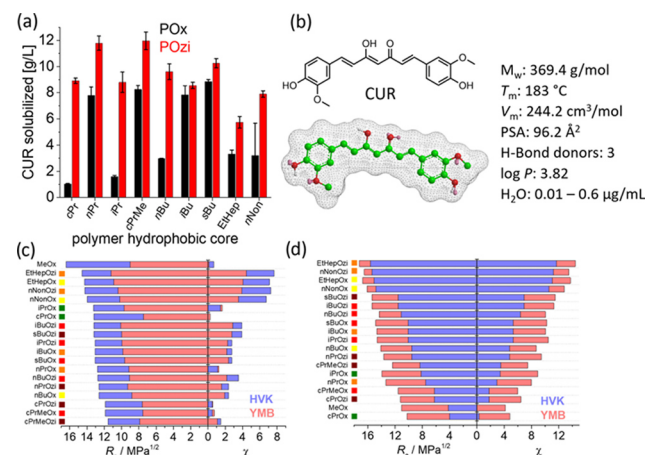


Figure 7. (a) Maximum achieved CUR concentrations directly after preparation in dependence of the polymer structure (polymer = 10 g/L; ABA triblock copolymers labeled according to their hydrophobic core). All samples were prepared in triplicate, and the results are presented as mean \pm SD. (b) Chemical and spatial (MM2 force-field minimum energy; Chem3D 15.1) structure of CUR. (c, d) Predicted compatibility between CUR and homopolymers (DP = 1) corresponding to the hydrophobic core estimated by HVK (blue) or YMB (red) with either R_a (left bars) or χ (right bars). Polymers are sorted according to decreasing polymer–CUR compatibility (bottom to top) obtained by HVK. Solubility parameters of CUR were either calculated (c) or derived from its experimental solubility profile (d). Color code next to polymer labels: 10–12 g/L CUR (dark red); 8–10 g/L CUR (red); 5–8 g/L CUR (orange); 1–5 g/L CUR (yellow); and <1 g/L CUR (green).

hypothesis of strong influence of polymer backbone on polymer–CUR compatibility based on a much smaller polymer library.¹⁷ Very recently, we have observed that a more dynamic structure inside the hydrophobic core of CUR-loaded A-PrOzi-A is conducive to achieve extremely high CUR loadings >50 wt %.⁵⁴ In contrast, CUR experiences a more rigid environment within A-*n*BuOx-A, which seems to prohibit such high CUR loadings. It should be noted that LC = 23 wt % (ρ (CUR) = 3.0 g/L) of A-*n*BuOx-A is still rather high as nanoformulations commonly not exceed CUR loadings of 20 wt %.⁵⁵

Interestingly, the difference in loading between POx and POzi was least pronounced for polymers comprising branched C4 side chains (*i*-butyl and *s*-butyl). Presumably, the branched side chains shield the amide moiety more efficiently, interfering

with rigid structure formation as in the case of **A-*n*BuOx-A**/CUR. However, this is mere speculation at this point and remains to be elucidated. Interesting to note, the differences in T_g , indicative of main-chain flexibility, was very pronounced for the *iso*-butyl side chains but rather small for *sec*-butyl. The polymers comprising *n*-propyl or *iso*-propyl side chains did not exhibit a clear CMC by pyrene assay (Figure 2). Nevertheless, they enabled CUR concentrations up to 11.6 g/L (54 wt %) in the case of **A-*c*PrOzi-A**. Such a CUR-induced micellization was already previously reported for **A-*n*PrOzi-A**.⁵⁶

Interestingly, the extremely high CUR loadings >50 wt % were somehow expressed in the solubility profile of CUR (Figure 4). At the investigated conditions, CUR was a very selective compound, being soluble in only 6 out of 31 solvents. Most interestingly, three out of these six solvents are strong hydrogen-bond donors comprising either a sulfoxide (DMSO, sulfolane) or a tertiary amide (DMF) moiety. Considering that both POx and POzi exhibit a high density on tertiary amides as well, this somehow rationalizes their unrivaled high CUR loadings in selected cases. However, the pronounced preference for POzi over POx is not explained by this.

It is well known^{53,57} that CUR is generally incorporated into the hydrophobic core of polymeric micelles as keto–enol tautomer. In the literature, the keto–keto tautomer of CUR has been used to predict polymer–CUR compatibility with solubility parameters,⁵⁸ while presently, the planar keto–enol CUR was chosen for the calculations (Table S2). However, discrepancy with the solubility parameters calculated here and values from the literature⁵⁹ occurred. Unfortunately, publications involving HSPs typically only show the final parameters without giving sufficient information on how they were obtained.

Similar as noted for PTX, HVK was able to classify the worst-performing polymers (except **A-*n*BuOx-A**) with R_a (Figure 7c and Table S10). YMB gave similar results but overestimated the CUR compatibility of **A-*i*PrOx-A** and **A-*c*PrOx-A**. Distinction between good (8–10 g/L CUR) and highly compatible (10–12 g/L CUR) polymers was not possible either way. Again, the Flory–Huggins interaction parameter χ yielded worse predictions than R_a , as, e.g., the poorly performing polymers **A-*n*BuOx-A**, **A-*i*PrOx-A**, and **A-*c*PrOx-A** were estimated more compatible than many of the best performers. As for PTX, compatibility predicted with experimental δ of CUR (Figure 7d) was worse than purely calculated one.

Efavirenz Formulations. To the best of our knowledge, no POx- or POzi-based EFV formulations have been reported in the literature. In contrast to PTX and CUR, no clear and consistent trend of the maximum achieved EFV concentration on the polymer side chain was observed (Figure 8a). With the exception of the *s*-butyl side chain, POzi were superior to POx throughout, but the difference was less pronounced than for CUR. For EFV, no marked difference between polymers comprising barely hydrophobic C₃ and C₄ or strongly hydrophobic C₉ side chains occurred. This seems to be correlated with the solubility profile of EFV (Figure 4) as it is soluble in a wide range of solvents (28 out of 31 solvents with various polarities and functional groups). The presently achieved EFV loadings of up to LC = 39 wt % (EFV = 6.4 g/L at 10 g/L **A-*n*BuOx-A**) surpass the LC of various EFV nanoformulations found in the literature exhibiting maximum LCs < 20 wt % (EFV = 20⁶⁰–23⁶¹ g/L at 100 g/L Pluronic) or < 25 wt % (EFV \approx 33⁶⁰ g/L at 100 g/L Tetronic). **A-*c*PrOx-A**

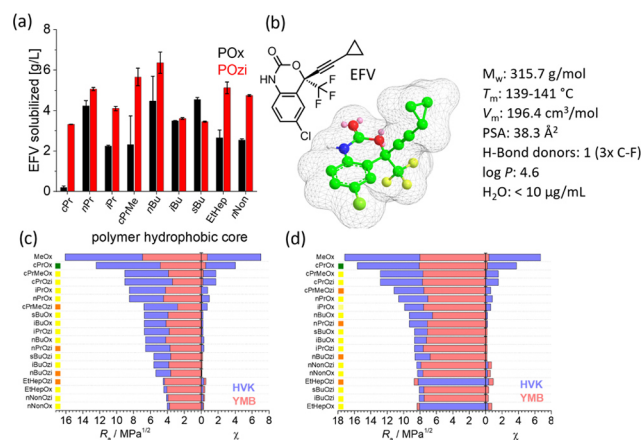


Figure 8. (a) Maximum achieved EFV concentrations directly after preparation in dependence of the polymer structure (polymer = 10 g/L; **ABA** triblock copolymers labeled according to their hydrophobic core). All samples were prepared in triplicate and results are presented as mean \pm SD. (b) Chemical and spatial (MM2 force-field minimum energy; Chem3D 15.1) structure of EFV. (c, d) Predicted compatibility between EFV and homopolymers (DP = 1) corresponding to the hydrophobic core estimated by HVK (blue) or YMB (red) with either R_a (left bars) or χ (right bars). Polymers are sorted according to decreasing polymer–EFV compatibility (bottom to top) obtained by HVK. Solubility parameters of EFV were either calculated (c) or derived from its solubility profile (d). Color code next to polymer labels: 10–12 g/L EFV (dark red); 8–10 g/L EFV (red); 5–8 g/L EFV (orange); 1–5 g/L EFV (yellow); and < 1 g/L EFV (green).

was the only polymer being unable to obtain moderate to high drug loadings. However, **A-*c*PrOx-A** could not incorporate any of the drugs investigated in this contribution efficiently. This could be due to steric effects, such as a shielding of the amide moiety by the *cyclo*-propyl residue, rather than insufficient hydrophobicity, as **cPrOx₁₀₀** has a lower water solubility than **iPrOx₁₀₀**.⁴³ In this case, the worst solubilizer **A-*c*PrOx-A** was corroborated by the HVK and YMB methods with R_a (Figure 8c and Table S11) and the YMB method was superior to categorize the polymers, as the three best solubilizers **A-*c*PrMeOzi-A**, **A-*n*BuOzi-A**, and **A-*n*PrOzi-A** were among the five best polymers predicted with R_a . Again, χ was much less accurate in predicting polymer–drug compatibility. Furthermore, due to the small molar volume V_m of EFV, most values of χ approach zero, which corroborates the good solubility in many solvents and polymers. Out of the five investigated drugs, EFV is the only one which can be efficiently solubilized with polymers comprising strongly hydrophobic C₉ side chains. Most interestingly and in contrast to CUR and PTX, HVK indeed predicted (R_a) a high compatibility of the polymers comprising C₉ side chains and EFV. Unlike previously, R_a and χ obtained with the experimentally determined solubility parameters of EFV correlated well with the purely calculated ones (Figure 8d).

Dexamethasone Formulations. So far, HVK and, to a lesser extent, YMB were able to classify the solubilization ability of the copolymers in a certain range with R_a . Especially, the worst-performing polymers could be identified reasonably well. However, POx- and POzi-based DEX formulations display strong limitations of the group contribution methods. Neither HVK nor YMB contain information on the rigidity of a molecule. Although DEX has a lower molecular weight (M_w = 392.5 g/mol) and calculated molar volume V_m (268.8 cm³/

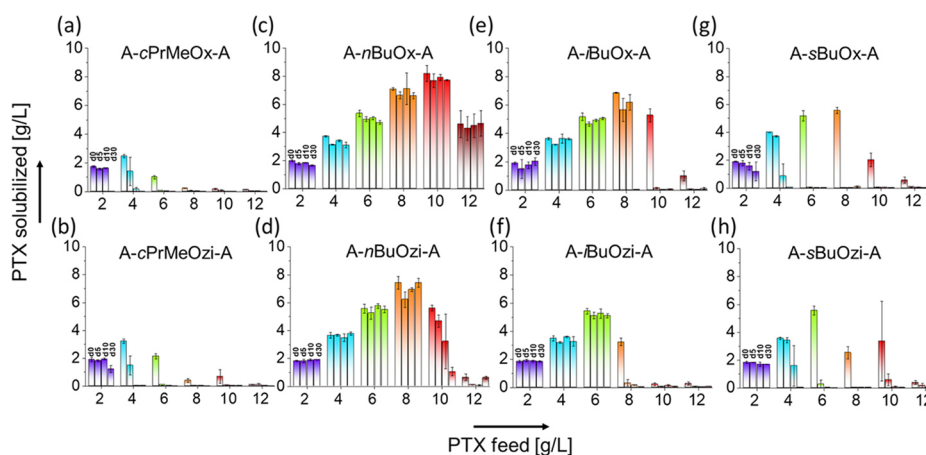


Figure 11. Aqueous PTX concentrations in dependence of the drug feed concentration (2–12 g/L) and polymer structure (polymer = 10 g/L). The samples were quantified directly after preparation (d0) or after storage at ambient conditions ($T \approx 25^\circ\text{C}$) under the exclusion of light for 5, 10, and 30 days. Prior to each quantification, the samples were centrifuged to remove any precipitate in the supernatant. For long-term stability studies, the formulations were stored in Eppendorf tubes containing the initial precipitate (if any occurred). Each formulation was prepared in triplicate, and the results are presented as mean \pm SD.

susceptibility of the drug loading on the polymer structure was shown. Due to the unique structure of each drug, no systematic trend in the influence of small structural changes in the polymer structure such as side-chain branching on the polymer–drug compatibility was observed. However, due to their versatility in terms of chemical structures, POx and POzi are a promising drug-delivery platform to handle such specificities enabling drug loadings close to or in excess of 50 wt % in selected cases. We are confident that the formulation of challenging molecules such as T2A could be facilitated by the introduction of, e.g., hydrogen-bond donors into the hydrophobic core of the investigated polymers. However, such strong structural changes were excluded on purpose for the present work, to challenge the idea of using partial solubility parameters to assess polymer–drug compatibilities. Polymers with strongly differing structures such as C3 vs C9 side chains could be successfully classified with experimental data employing polymers with strongly differing structures.²⁰ However, the impact of small structural changes in the polymer side or main chain remains unpredictable at this point. For the present work, HSPs were chosen due to their simplicity. They do not contain much information about complex interactions, and their easy calculation/determination makes them attractive to predict polymer–drug compatibility. Sophisticated calculations may give more insights into actual polymer–drug interactions on an atomic scale, but such approach is much more demanding.^{68,69} Although applicable for, e.g., the binding of substrates into well-defined pockets of enzymes⁷⁰ or cyclodextrins,⁷¹ this is more challenging for polymer micelles due to their dynamic structure.

Long-Term Stability of Drug Formulations. The different long-term stabilities of the presently investigated formulations will be exemplified by the PTX formulations of polymers comprising C4 side chains. For all other formulations, the reader is referred to Figures S61–S71. Generally, the drug loading increased with increasing drug feed up to the maximum obtainable PTX concentration (Figure 10). Further addition of PTX decreased the drug loading. This decrease was dependent on the polymer structure, as PTX loading of A-*n*BuOx-A decreased by 46% from 8.2 g/L (45 wt %; 10 g/L feed) to 4.6 g/L (32 wt %; 12 g/L feed), but by 64%

in the case of A-*s*BuOx-A (8 vs 10 g/L PTX feed). Not surprisingly, the long-term stability was generally higher when the initial drug feed was lower, as shown in the highest stability of the formulations at 2 g/L PTX feed for all polymers (purple bars). Formulations prepared at drug feeds surpassing the maximum obtainable drug concentrations exhibited the poorest long-term stabilities, as, e.g., PTX loading decreased from 5.6 g/L (36 wt %) to 0.04 g/L (0.4 wt %) after 5 day storage in the case of A-*s*BuOx-A (PTX feed: 8 g/L). Therefore, the drug loading of the initially highly loaded formulations fell short of the ones prepared at lower PTX feeds such as 2 g/L. If this is due to the presence of PTX precipitated after preparation (samples were stored upon the precipitate) acting as crystallization nucleus or to colloidal instabilities needs further investigation. It is quite remarkable how smallest changes in the polymer structure not only affect maximum obtainable drug loadings but also the long-term stabilities. A-*n*BuOx-A not only exhibited the highest PTX loading in the first place but also the best long-term stability without any sign of drug loss during the 30 day storage, corroborating earlier reported absence of aggregation of A-*n*BuOx-A/PTX formulations during 4 month storage as investigated by dynamic light scattering.³⁹ In contrast, drug content of initially highly loaded formulations of polymers comprising branched side chains collapsed the latest after 30 day storage for *iso*-butyl (Figure 11e,f) or already after 5 day storage in the case of *sec*-butyl side chains (Figure 11g,h).

In the case of CUR, all triblock copolymers comprising C₄ side chains exhibited an excellent long-term stability with no major loss in CUR content during 30 day storage (Figure S66). In contrast, polymers comprising C₃ side chains showed a decrease in CUR loading in all cases in which CUR already precipitated on the day of preparation (Figure S65). Therefore, it seems that precipitated CUR nanoformulations further affects the stability of the remaining nanoformulations. However, important to note, the precipitate does presumably not comprise crystalline but amorphous CUR, as was reported previously for A-EtHepOx-A.¹⁴ Only A-cPrOzi-A, exhibiting an excellent CUR loading >50 wt % in the first place, showed no loss of CUR within the 30 day storage (Figure S65b). Except for A-*i*PrOx-A (Figure S69e), EFV formulated with

triblock copolymers exhibiting C_3 (Figure S69) or C_4 (Figure S70) side chains generally exhibited excellent long-term stability with no major loss of drug content within 30 day storage. In contrast to CUR, initially precipitated EFV did not seem to affect long-term stability of the respective formulations.

CONCLUSIONS

A considerable library of structurally diverse triblock copolymers was tested for solubilization of five different, extremely water-insoluble drugs. In all cases in which an efficient encapsulation of the drug into polymer micelles was possible (PTX, CUR, EFV), almost all polymers could incorporate at least 20 wt % of drug, which seems to be a common limiting value for many drug formulations based on different polymer micelles. In these cases, HVK and, to a lesser extent, YMB were able to classify the polymer–drug compatibility in a certain range with R_a . Especially the least suitable polymers correlated reasonably well with a large R_a value. However, only relying on the absolute values of R_a is misleading, as also nonsolubilizable drugs (DEX and T2A) were predicted to have a high compatibility. Considering the broad parameter space in terms of investigated polymer structures, crucial parameters of the drugs hampering drug encapsulation are likely to be connected with rigidity or absence of hydrogen-bond-donating moieties. In all cases, the simple comparison of δ_T of polymer and drug as in the case of the Flory–Huggins interaction parameter χ leads to false predicted compatibilities and display a rationale to use the more detailed partial solubility parameters. Here, we investigated 1710 different formulations and 4626 individual samples, which highlights why it can be very challenging to develop polymer-based drug-delivery systems for water-insoluble drugs, as smallest changes in the chemical structures of the polymer carriers determine if a formulation is successful or not.

ASSOCIATED CONTENT

Supporting Information

The Supporting Information is available free of charge on the ACS Publications website at DOI: 10.1021/acs.biomac.9b00618.

Monomer synthesis and characterization (Schemes S1–S5 and Figures S1–S18); polymer synthesis and characterization (Scheme S6 and Figures S19–S54); partial and total solubility parameters (Tables S1–S6 and S8–S13); and formulation data (Figures S60–S83) (PDF)

AUTHOR INFORMATION

Corresponding Author

*E-mail: robert.luxenhofer@uni-wuerzburg.de.

ORCID

Robert Luxenhofer: 0000-0001-5567-7404

Notes

The authors declare the following competing financial interest(s): M.M.L. and R.L. are listed as inventors on a patent application pertinent to materials discussed in this contribution.

ACKNOWLEDGMENTS

This work was supported by the Free State of Bavaria and the Deutsche Forschungsgemeinschaft (Project number 398461692, awarded to R.L.). Moreover, M.M.L. acknowledges the Evonik Foundation for providing a doctoral fellowship. M.S.H. acknowledges the Higher Education Commission (HEC) of Pakistan and Deutscher Akademischer Austauschdienst (DAAD), Germany. The authors thank Christian May, Daniela Lautz, Thomas Bretschneider, and Maximilian Rist for technical support. They also thank Lukas Hahn for providing triblock copolymers comprising aromatic side chains and Florian Wagner for designing and fabricating the device for preparing multiple formulations simultaneously.

REFERENCES

- (1) Zuegg, J.; Matthew, A. C. Drug-Likeness and Increased Hydrophobicity of Commercially Available Compound Libraries for Drug Screening. *Curr. Top. Med. Chem.* **2012**, *12*, 1500–1513.
- (2) Abbot, S. *Solubility Science: Principles in Practice*; TCNF Ltd., 2017.
- (3) Levin, V. A. Relationship of octanol/water partition coefficient and molecular weight to rat brain capillary permeability. *J. Med. Chem.* **1980**, *23*, 682–684.
- (4) Wohnsland, F.; Faller, B. High-Throughput Permeability pH Profile and High-Throughput Alkane/Water log P with Artificial Membranes. *J. Med. Chem.* **2001**, *44*, 923–930.
- (5) Banerjee, R.; Chattopadhyay, S.; Basu, G. Conformational preferences of a short Aib/Ala-based water-soluble peptide as a function of temperature. *Proteins* **2009**, *76*, 184–200.
- (6) Lin, L. Y.; Lee, N. S.; Zhu, J.; Nyström, A. M.; Pochan, D. J.; Dorshow, R. B.; Wooley, K. L. Tuning core vs. shell dimensions to adjust the performance of nanoscopic containers for the loading and release of doxorubicin. *J. Controlled Release* **2011**, *152*, 37–48.
- (7) Ebrahim Attia, A. B.; Ong, Z. Y.; Hedrick, J. L.; Lee, P. P.; Ee, P. L. R.; Hammond, P. T.; Yang, Y.-Y. Mixed micelles self-assembled from block copolymers for drug delivery. *Curr. Opin. Colloid Interface Sci.* **2011**, *16*, 182–194.
- (8) Bariana, M.; Aw, M. S.; Kurkuri, M.; Losic, D. Tuning drug loading and release properties of diatom silica microparticles by surface modifications. *Int. J. Pharm.* **2013**, *443*, 230–241.
- (9) Liechty, W. B.; Kryscio, D. R.; Slaughter, B. V.; Peppas, N. A. Polymers for Drug Delivery Systems. *Annu. Rev. Chem. Biomol. Eng.* **2010**, *1*, 149–173.
- (10) Vlassi, E.; Papagiannopoulos, A.; Pispas, S. Amphiphilic poly(2-oxazoline) copolymers as self-assembled carriers for drug delivery applications. *Eur. Polym. J.* **2017**, *88*, 516–523.
- (11) Kothari, K.; Ragoonanan, V.; Suryanarayanan, R. The Role of Drug–Polymer Hydrogen Bonding Interactions on the Molecular Mobility and Physical Stability of Nifedipine Solid Dispersions. *Mol. Pharm.* **2015**, *12*, 162–170.
- (12) Wiczorek, S.; Schwaar, T.; Senge, M. O.; Börner, H. G. Specific Drug Formulation Additives: Revealing the Impact of Architecture and Block Length Ratio. *Biomacromolecules* **2015**, *16*, 3308–3312.
- (13) Johnson, L. M.; Li, Z.; LaBelle, A. J.; Bates, F. S.; Lodge, T. P.; Hillmyer, M. A. Impact of Polymer Excipient Molar Mass and End Groups on Hydrophobic Drug Solubility Enhancement. *Macromolecules* **2017**, *50*, 1102–1112.
- (14) Wiczorek, S.; Dallmann, A.; Kochovski, Z.; Börner, H. G. Advancing Drug Formulation Additives toward Precision Additives with Release Mediating Peptide Interlayer. *J. Am. Chem. Soc.* **2016**, *138*, 9349–9352.
- (15) Lübtow, M. M.; Keßler, L.; Appelt-Menzel, A.; Lorson, T.; Gangloff, N.; Kirsch, M.; Dahms, S.; Luxenhofer, R. More Is Sometimes Less: Curcumin and Paclitaxel Formulations Using Poly(2-oxazoline) and Poly(2-oxazine)-Based Amphiphiles Bearing

Linear and Branched C9 Side Chains. *Macromol. Biosci.* **2018**, No. 1800155.

(16) Hahn, L.; Lübtow, M. M.; Lorson, T.; Schmitt, F.; Appelt-Menzel, A.; Schobert, R.; Luxenhofer, R. Investigating the Influence of Aromatic Moieties on the Formulation of Hydrophobic Natural Products and Drugs in Poly(2-oxazoline)-Based Amphiphiles. *Biomacromolecules* **2018**, *19*, 3119–3128.

(17) Lübtow, M. M.; Hahn, L.; Haider, M. S.; Luxenhofer, R. Drug Specificity, Synergy and Antagonism in Ultrahigh Capacity Poly(2-oxazoline)/Poly(2-oxazine) based Formulations. *J. Am. Chem. Soc.* **2017**, *139*, 10980–10983.

(18) Lawatscheck, C.; Pickhardt, M.; Wiczorek, S.; Grafmüller, A.; Mandelkow, E.; Börner, H. G. Generalizing the Concept of Specific Compound Formulation Additives towards Non-Fluorescent Drugs: A Solubilization Study on Potential Anti-Alzheimer-Active Small-Molecule Compounds. *Angew. Chem., Int. Ed.* **2016**, *55*, 8752–8756.

(19) Lv, S.; Wu, Y.; Cai, K.; He, H.; Li, Y.; Lan, M.; Chen, X.; Cheng, J.; Yin, L. High Drug Loading and Sub-Quantitative Loading Efficiency of Polymeric Micelles Driven by Donor–Receptor Coordination Interactions. *J. Am. Chem. Soc.* **2018**, *140*, 1235–1238.

(20) Liu, J.; Xiao, Y.; Allen, C. Polymer–drug compatibility: A guide to the development of delivery systems for the anticancer agent, ellipticine. *J. Pharm. Sci.* **2004**, *93*, 132–143.

(21) Turpin, E. R.; Taresco, V.; Al-Hachami, W. A.; Booth, J.; Treacher, K.; Tomasi, S.; Alexander, C.; Burley, J.; Laughton, C. A.; Garnett, M. C. In Silico Screening for Solid Dispersions: The Trouble with Solubility Parameters and χ FH. *Mol. Pharmaceutics* **2018**, *15*, 4654–4667.

(22) Milonaki, Y.; Kaditi, E.; Pispas, S.; Demetzos, C. Amphiphilic gradient copolymers of 2-methyl- and 2-phenyl-2-oxazoline: self-organization in aqueous media and drug encapsulation. *J. Polym. Sci. A: Polym. Chem.* **2012**, *50*, 1226–1237.

(23) Sofias, A. M.; Dunne, M.; Storm, G.; Allen, C. The battle of “nano” paclitaxel. *Adv. Drug Delivery Rev.* **2017**, *122*, 20–30.

(24) Kunnumakkara, A. B.; Bordoloi, D.; Padmavathi, G.; Monisha, J.; Roy, N. K.; Prasad, S.; Aggarwal, B. B. Curcumin, the golden nutraceutical: multitargeting for multiple chronic diseases. *Br. J. Pharmacol.* **2017**, *174*, 1325–1348.

(25) Wit, F. W. N. M.; Tongeren, J.; Lange, J. M. A. Efavirenz: a review. *Expert Opin. Pharmacother.* **2007**, *8*, 851–871.

(26) de Gans, J.; van de Beek, D. Dexamethasone in Adults with Bacterial Meningitis. *N. Engl. J. Med.* **2002**, *347*, 1549–1556.

(27) Fu, J.; Huang, H.; Liu, J.; Pi, R.; Chen, J.; Liu, P. Tanshinone IIA protects cardiac myocytes against oxidative stress-triggered damage and apoptosis. *Eur. J. Pharmacol.* **2007**, *568*, 213–221.

(28) Witte, H.; Seeliger, W. Cyclische Imidsäureester aus Nitrilen und Aminoalkoholen. *Justus Liebigs Ann. Chem.* **1974**, *1974*, 996–1009.

(29) Kempe, K.; Jacobs, S.; Lambermont-Thijs, H. M. L.; Fijten, M. M. W. M.; Hoogenboom, R.; Schubert, U. S. Rational Design of an Amorphous Poly(2-oxazoline) with a Low Glass-Transition Temperature: Monomer Synthesis, Copolymerization, and Properties. *Macromolecules* **2010**, *43*, 4098–4104.

(30) Taubmann, C.; Luxenhofer, R.; Cesana, S.; Jordan, R. First Aldehyde-Functionalized Poly(2-oxazoline)s for Chemoselective Ligation. *Macromol. Biosci.* **2005**, *5*, 603–612.

(31) Beck, M.; Birnbrich, P.; Eicken, U.; Fischer, H.; Fristad, W. E.; Hase, B.; Krause, H. J. Polyoxazoline auf fettchemischer Basis. *Angew. Makromol. Chem.* **1994**, *223*, 217–233.

(32) Luxenhofer, R.; Schulz, A.; Roques, C.; Li, S.; Bronich, T. K.; Batrakova, E. V.; Jordan, R.; Kabanov, A. V. Doubly amphiphilic poly(2-oxazoline)s as high-capacity delivery systems for hydrophobic drugs. *Biomaterials* **2010**, *31*, 4972–4979.

(33) Hildebrand, J. H.; Scott, R. L. *The Solubility of Nonelectrolytes*, 3rd ed.; Reinhold Pub. Corp.: New York, 1950.

(34) Van Krevelen, D. W.; Te Nijenhuis, K. Cohesive Properties and Solubility. In *Properties of Polymers*, 4th ed.; Elsevier: Amsterdam, 2009; pp 189–227.

(35) Wypych, G. *Handbook of Solvents*; ChemTec Publishing: ChemTec Publishing, 2014; Vol. 1.

(36) Hansen, C. M. *Hansen Solubility Parameters*, 2nd ed.; CRC Press, 2007.

(37) Fedors, R. F. A method for estimating both the solubility parameters and molar volumes of liquids. *Polym. Eng. Sci.* **1974**, *14*, 147–154.

(38) Hancock, B. C.; York, P.; Rowe, R. C. The use of solubility parameters in pharmaceutical dosage form design. *Int. J. Pharm.* **1997**, *148*, 1–21.

(39) Seo, Y.; Schulz, A.; Han, Y.; He, Z.; Bludau, H.; Wan, X.; Tong, J.; Bronich, T. K.; Sokolsky, M.; Luxenhofer, R.; Jordan, R.; Kabanov, A. V. Poly(2-oxazoline) block copolymer based formulations of taxanes: effect of copolymer and drug structure, concentration, and environmental factors. *Polym. Adv. Technol.* **2015**, *26*, 837–850.

(40) Bloksma, M. M.; Paulus, R. M.; van Kuringen, H. P. C.; van der Woerd, F.; Lambermont-Thijs, H. M. L.; Schubert, U. S.; Hoogenboom, R. Thermoresponsive Poly(2-oxazine)s. *Macromol. Rapid Commun.* **2012**, *33*, 92–96.

(41) Saegusa, T.; Kobayashi, S.; Nagura, Y. Isomerization Polymerization of 1,3-Oxazine. II. Kinetic Studies of the Ring-Opening Isomerization Polymerization of Unsubstituted 5,6-Dihydro-4H-1,3-oxazine. *Macromolecules* **1974**, *7*, 265–272.

(42) Bloksma, M. M.; Schubert, U. S.; Hoogenboom, R. Poly(cyclic imino ether)s Beyond 2-Substituted-2-oxazolines. *Macromol. Rapid Commun.* **2011**, *32*, 1419–1441.

(43) Bloksma, M. M.; Weber, C.; Perevyazko, I. Y.; Kuse, A.; Baumgärtel, A.; Vollrath, A.; Hoogenboom, R.; Schubert, U. S. Poly(2-cyclopropyl-2-oxazoline): From Rate Acceleration by Cyclopropyl to Thermoresponsive Properties. *Macromolecules* **2011**, *44*, 4057–4064.

(44) Miller, M. M.; Wasik, S. P.; Huang, G. L.; Shiu, W. Y.; Mackay, D. Relationships between octanol-water partition coefficient and aqueous solubility. *Environ. Sci. Technol.* **1985**, *19*, 522–529.

(45) Piñeiro, L.; Novo, M.; Al-Soufi, W. Fluorescence emission of pyrene in surfactant solutions. *Adv. Colloid Interface Sci.* **2015**, *215*, 1–12.

(46) Christova, D.; Velichkova, R.; Loos, W.; Goethals, E. J.; Prez, F. D. New thermo-responsive polymer materials based on poly(2-ethyl-2-oxazoline) segments. *Polymer* **2003**, *44*, 2255–2261.

(47) Huber, S.; Jordan, R. Modulation of the lower critical solution temperature of 2-alkyl-2-oxazoline copolymers. *Colloid Polym. Sci.* **2008**, *286*, 395.

(48) Huber, S.; Hutter, N.; Jordan, R. Effect of end group polarity upon the lower critical solution temperature of poly(2-isopropyl-2-oxazoline). *Colloid Polym. Sci.* **2008**, *286*, 1653–1661.

(49) Nakashima, K.; Bahadur, P. Aggregation of water-soluble block copolymers in aqueous solutions: Recent trends. *Adv. Colloid Interface Sci.* **2006**, *123–126*, 75–96.

(50) Lambermont-Thijs, H. M. L.; Hoogenboom, R.; Fustin, C.-A.; Bomal-D’Haese, C.; Gohy, J.-F.; Schubert, U. S. Solubility behavior of amphiphilic block and random copolymers based on 2-ethyl-2-oxazoline and 2-nonyl-2-oxazoline in binary water–ethanol mixtures. *J. Polym. Sci., Part A: Polym. Chem.* **2009**, *47*, 515–522.

(51) *Pharmacopoeia of the United States of America and the National Formulary*, 27th ed.; USP31; 2009.

(52) Rani, S.; Mishra, S.; Sharma, M.; Nandy, A.; Mozumdar, S. Solubility and stability enhancement of curcumin in Soluplus polymeric micelles: a spectroscopic study. *J. Dispersion Sci. Technol.* **2019**, 1–14.

(53) Lübtow, M. M.; Nelke, L. C.; Seifert, J.; Kühnemundt, J.; Sahay, G.; Dandekar, G.; Nietzer, S.; Luxenhofer, R. Drug induced micellization into ultra-high capacity and stable curcumin nanoformulations: Physico-chemical characterization and in vitro evaluation in 2D/3D in vitro models. *J. Controlled Release* **2019**, *303*, 162–180.

(54) Lübtow, M. M.; Marciniak, H.; Schmiedel, A.; Roos, M.; Lambert, C.; Luxenhofer, R. Ultra-High to Ultra-Low Drug Loaded Micelles: Probing Host-Guest Interactions by Fluorescence Spectros-

copy. *Chem. Eur. J.* **2019**, No. in print, in print. DOI: 10.1002/chem.201902619.

(55) Naksuriya, O.; Okonogi, S.; Schiffelers, R. M.; Hennink, W. E. Curcumin nanoformulations: A review of pharmaceutical properties and preclinical studies and clinical data related to cancer treatment. *Biomaterials* **2014**, *35*, 3365–3383.

(56) Lorson, T.; Jaksch, S.; Lübtow, M. M.; Jüngst, T.; Groll, J.; Lüthmann, T.; Luxenhofer, R. A Thermogelling Supramolecular Hydrogel with Sponge-Like Morphology as a Cytocompatible Bioink. *Biomacromolecules* **2017**, *18*, 2161–2171.

(57) Moussa, Z.; Chebl, M.; Patra, D. Fluorescence of tautomeric forms of curcumin in different pH and biosurfactant rhamnolipids systems: Application towards on-off ratiometric fluorescence temperature sensing. *J. Photochem. Photobiol., B* **2017**, *173*, 307–317.

(58) Raveendran, R.; Mullen, K. M.; Wellard, R. M.; Sharma, C. P.; Hoogenboom, R.; Dargaville, T. R. Poly(2-oxazoline) block copolymer nanoparticles for curcumin loading and delivery to cancer cells. *Eur. Polym. J.* **2017**, *93*, 682–694.

(59) Doktorovova, S.; Souto, E. B.; Silva, A. M. Hansen solubility parameters (HSP) for prescreening formulation of solid lipid nanoparticles (SLN): in vitro testing of curcumin-loaded SLN in MCF-7 and BT-474 cell lines. *Pharm. Dev. Technol.* **2018**, *23*, 96–105.

(60) Chiappetta, D. A.; Hocht, C.; Sosnik, A. A Highly Concentrated and Taste-Improved Aqueous Formulation of Efavirenz for a More Appropriate Pediatric Management of the Anti-HIV Therapy. *Curr. HIV Res.* **2010**, *8*, 223–231.

(61) Chiappetta, D. A.; Hocht, C.; Taira, C.; Sosnik, A. Efavirenz-loaded polymeric micelles for pediatric anti-HIV pharmacotherapy with significantly higher oral bioavailability. *Nanomedicine* **2009**, *5*, 11–23.

(62) Pepić, I.; Hafner, A.; Lovrić, J.; Pirkić, B.; Filipović-Grcčić, J. A Nonionic Surfactant/Chitosan Micelle System in an Innovative Eye Drop Formulation. *J. Pharm. Sci.* **2010**, *99*, 4317–4325.

(63) Wang, Q.; Jiang, J.; Chen, W.; Jiang, H.; Zhang, Z.; Sun, X. Targeted delivery of low-dose dexamethasone using PCL–PEG micelles for effective treatment of rheumatoid arthritis. *J. Controlled Release* **2016**, *230*, 64–72.

(64) Chopra, P.; Hao, J.; Li, S. K. Sustained release micellar carrier systems for iontophoretic transport of dexamethasone across human sclera. *J. Controlled Release* **2012**, *160*, 96–104.

(65) Salgarella, A. R.; Zahoranová, A.; Šrámková, P.; Majerčíková, M.; Pavlova, E.; Luxenhofer, R.; Kronek, J.; Lacík, I.; Ricotti, L. Investigation of drug release modulation from poly(2-oxazoline) micelles through ultrasound. *Sci. Rep.* **2018**, *8*, No. 9893.

(66) Zhang, L.; Sun, H.; Chen, Z.; Liu, Z.; Huang, N.; Qian, F. Intermolecular Interactions between Coencapsulated Drugs Inhibit Drug Crystallization and Enhance Colloidal Stability of Polymeric Micelles. *Mol. Pharm.* **2017**, *14*, 3568–3576.

(67) Zhang, J.; Li, Y.; Fang, X.; Zhou, D.; Wang, Y.; Chen, M. TPGS-g-PLGA/Pluronic F68 mixed micelles for tanshinone IIA delivery in cancer therapy. *Int. J. Pharm.* **2014**, *476*, 185–198.

(68) Guo, X. D.; Tan, J. P. K.; Kim, S. H.; Zhang, L. J.; Zhang, Y.; Hedrick, J. L.; Yang, Y. Y.; Qian, Y. Computational studies on self-assembled paclitaxel structures: Templates for hierarchical block copolymer assemblies and sustained drug release. *Biomaterials* **2009**, *30*, 6556–6563.

(69) Ahmad, S.; Johnston, B. F.; Mackay, S. P.; Schatzlein, A. G.; Gellert, P.; Sengupta, D.; Uchehgbu, I. F. In silico modelling of drug–polymer interactions for pharmaceutical formulations. *J. R. Soc., Interface* **2010**, *7*, S423–S433.

(70) Tinberg, C. E.; Khare, S. D.; Dou, J.; Doyle, L.; Nelson, J. W.; Schena, A.; Jankowski, W.; Kalodimos, C. G.; Johnsson, K.; Stoddard, B. L.; Baker, D. Computational design of ligand-binding proteins with high affinity and selectivity. *Nature* **2013**, *501*, 212.

(71) Moghaddam, S.; Inoue, Y.; Gilson, M. K. Host–Guest Complexes with Protein–Ligand-like Affinities: Computational Analysis and Design. *J. Am. Chem. Soc.* **2009**, *131*, 4012–4021.

In all studies discussed so far, emphasize was put on the impact of the micellar hydrophobic core on polymer-drug compatibility. This approach seems valid, as hydrophobic drugs should be mainly associated with the hydrophobic block. However, as already briefly mentioned, especially at high drug loading, parts of the hydrophilic shell are likely to participate in the stabilization of the hydrophobic drug. To systematically investigate the influence of the hydrophilic shell on drug loading, the so far consistently kept hydrophilic poly(2-methyl-2-oxazoline) (PMeOx) shell of the ABA triblock copolymers (A = hydrophilic block; B = hydrophobic block) was either partly (A-B-A*) or completely (A*-B-A*) replaced with similarly water-soluble poly(2-ethyl-2-oxazoline) (PEtOx). A significant drop in the *LC* of all amphiphiles comprising PEtOx occurred. Interestingly, the interaction between the PEtOx shell and the incorporated hydrophobic small molecules was more pronounced than for its PMeOx counterparts, reducing colloidal stability of the respective drug-loaded micelles at much lower drug loading. Apart from the reduced overall drug loading, the specificity pattern with respect to the hydrophobic core was largely preserved irrespective of the corona, once more corroborating the relevance of the core identity. These findings demonstrate that a simple core-shell architecture, in which the core incorporates the hydrophobic drug and the corona facilitates micellar water solubility, is an oversimplification. The actual morphology of the drug-loaded micelles will be discussed in more detail in the following chapter.

Think beyond the core: The impact of the hydrophilic corona on the drug solubilization using polymer micelles

Malik Salman Haider[‡], Michael M. Lübtow[‡], Sebastian Endres[†], Vladimir Aseyev[‡], Ann-Christin Pöplert[†], Robert Luxenhofer^{‡,*}

[‡]Functional Polymer Materials, Chair for Chemical Technology of Material Synthesis and Bavarian Polymer Institute, Faculty of Chemistry and Pharmacy, University of Würzburg, Röntgenring 11, 97070 Würzburg, Germany

[‡]Department of Chemistry, University of Helsinki, PB 55, Helsinki FIN-00014, Finland

[†]Institute of Organic Chemistry, Faculty of Chemistry and Pharmacy, University of Würzburg, Am Hubland, 97074 Würzburg, Germany

Supporting Information Placeholder

ABSTRACT: Polymeric micelles are typically characterized as core-shell structures. The hydrophobic inner core is considered as depot for hydrophobic molecules such as drugs or catalysts and the corona forming block acts as protective, stabilizing and solubilizing interface between the hydrophobic core and the external aqueous milieu. Tremendous efforts have been made to tune the hydrophobic block to increase the drug loading and stability of the micelles, while the role of hydrophilic blocks regarding drug loading and stability of micelles is rarely studied in detail. To do so, we investigated a small library of structurally similar A-B-A type amphiphiles based on poly(2-oxazoline)s and poly(2-oxazine)s by varying the hydrophilic block A utilizing poly(2-methyl-2-oxazoline) (A) or poly(2-ethyl-2-oxazoline) (A*), both excellently water-soluble polymers that are able to provide beneficial stealth properties. Surprisingly, major differences in loading capacities from A-B-A > A*-B-A > A*-B-A* highlight the impact of the hydrophilic corona of the polymer micelles on drug loading and stability. ¹H-NMR spectroscopy revealed that the hydrophilic pEtOx exhibits a stronger interaction with the cargo compared with its more hydrophilic counterpart pMeOx, reducing colloidal stability of the drug loaded micelles at lower drug loading. To gain more insights, formulations were also characterized by diffusion ordered and nuclear Overhauser effect NMR spectroscopy, dynamic light scattering and (micro) differential scanning calorimetry. Our findings suggest that the interaction between the hydrophilic block and the guest molecule should be considered an important but previously largely ignored factor for the rational design of polymeric micelles.

1. INTRODUCTION

Amphiphilic block copolymers self-assemble into polymeric micelles (PM) in selective solvents above their critical micelle concentration (cmc)¹. These nanostructures can be employed for a variety of applications such as drug delivery², viscosity modifications³, catalysis and toughening of plastics⁴. The size, morphology, stability and surface chemistry of PM can be easily adjusted by fine tuning the hydrophilic/hydrophobic ratios and block lengths⁵⁻⁶. PMs are capable to encapsulate hydrophobic molecules, increasing their solubility and stability, thus often resulting in improved

drug bioavailability and/or delivery. It is frequently postulated and sometimes confirmed that micelles have core-shell structures, where the core hosts hydrophobic guest molecules, while the shell provides the solubility and colloidal stability in aqueous milieu⁷⁻⁸. Along these lines, Guo and Lu *et al.* demonstrated that increasing the chain length of the hydrophobic block has a positive impact on drug loading⁹⁻¹⁰ while Wang and coworkers reported that increasing the hydrophilic block length in case of diblock copolymers can increase the thickness of the corona and slow the exchange kinetics¹. With respect to the morphology of PMs, Schulz *et al.* and later Cao *et al.* reported that increasing the drug feed can induce a morphology transition from worm or rod like structures to small spherical micelles or vesicles^{5, 11}, while Lübtow *et al.* reported micelle formation of A-B-A triblock copolymers triggered only by the presence of a hydrophobic guest molecule¹². More recently, Wiest *et al.* showed that increasing the imatinib concentration in taurocholate/lecithin micelles above 250 μ M, not only caused morphology transition from vesicles (>110 nm) to micelles (<40 nm) but also lead to colloidal collapse because of the migration of drug from the core to the shell of the micelles¹³. PMs have been studied intensively for decades with respect to their physicochemical properties and general behavior in biological systems¹⁴⁻¹⁵. However, despite thousands of research papers on the use of polymer micelles for drug delivery, little information can be found on the impact of the hydrophilic block on the drug loading of PMs, the localization of the drug within the micelles⁵ or the colloidal stability¹⁶ of the drug delivery system. Recently, utilizing methylacrylate based block copolymers and curcumin (CUR), Cao and co-workers⁵ reported that at higher drug loading, CUR started to reside in the shell forming block leading to a reduction in water content in the shell from 73% (no drug) to 64% (high drug). In further contributions, Stenzel demonstrated that not only the different drug loadings¹⁷ but also the aspect ratio of non-spherical nanocarriers also impacts the endocytosis¹⁸. Recently, Li and coworkers have shown that a slightly hydrophobic micelle corona can efficiently sequester the hydrophobic drugs to preserve supersaturation, leading to better dissolution profile for oral drug delivery applications¹⁶.

Generally speaking, the hydrophilic corona in the vast majority of described systems for drug delivery is comprised of poly(ethylene

glycol) (PEG)¹⁹⁻²¹. However, for several years, alternatives for PEG as the gold standard of a non-fouling, stealth, non-toxic and non-immunogenic synthetic biomaterial have been heavily investigated²². One particularly debated issue is the potential immunogenicity of PEG²³. This discussion notwithstanding, alternative polymers used for the hydrophilic corona of PMs may be useful to tailor the properties of the corona. One such alternative are hydrophilic poly(2-oxazoline)s (POx), in particular poly(2-methyl-2-oxazoline) (pMeOx) and poly(2-ethyl-2-oxazoline) (pEtOx). More recently, poly(2-oxazine)s, their higher main-chain homologues have also raised some interest²⁴⁻²⁷.

In fact, POx based amphiphiles have high potential for drug formulation development, demonstrated in various tumor models²⁸⁻³³. Luxenhofer and coworkers reported an ultra-high paclitaxel (PTX) loaded POx based micellar formulation (loading capacity (LC) \approx 50 wt.% ($m_{Drug}/(m_{Drug}+m_{Polymer})$)³⁴ with excellent *in vivo* anti-tumor efficacy²⁹⁻³⁰. The lead amphiphile was an A-B-A type triblock copolymer, poly(2-methyl-2-oxazoline)-*b*-(poly(2-*n*-butyl-2-oxazoline)-*b*-poly(2-methyl-2-oxazoline) (A-pBuOx-A). For variation of the more hydrophobic central B block, a library of structurally related amphiphiles was studied with a variety of extremely water-insoluble molecules. Besides PTX, the solubilizing capacity was also tested for other highly hydrophobic natural products like curcumin³⁵⁻³⁷(CUR), tanshinone IIa and various hydrophobic drugs like efavirenz, dexamethasone and mitotane^{35, 38}. Notably, the small structural difference between A-pBuOx-A and A-pPrOzi-A (poly(2-methyl-2-oxazoline)-*b*-(poly(2-*n*-propyl-2-oxazine)-*b*-poly(2-methyl-2-oxazoline)) resulted in profound specificities in drug loading³⁹ (Figure 1b, Table S2), with pBuOx providing a more rigid environment for CUR which coincides with a lower maximum drug solubilization⁴⁰. To accelerate the development of effective drug delivery systems, Alves and coworkers built models predicting LC and loading efficiency (LE) of POx based polymer platform for hydrophobic drugs⁴¹. A computer aided strategy was conceived utilizing various descriptors of drug polymer complexes implying 75% prediction accuracy, but only one polymer composition, A-pBuOx-A was employed here.

After previously gaining first insights into the structure-property relationships with respect to the hydrophobic block for this family of polymers³⁹, we now turned our attention to the effect of the hydrophilic block/corona, which remains much in the dark. Considering these ultra-high drug loading capacities (Figure 1b, Table S2) we wondered, whether these ultra-high drug loadings can be explained by interactions with the hydrophobic blocks^{39, 42} alone or whether the hydrophilic block must be involved. From a stoichiometric perspective, the involvement of the hydrophilic corona may even seem inevitable. At maximum drug loading of A-pPrOzi-A (LC \approx 54 wt.%; 12 g/L CUR in 10 g/L polymer) 27 CUR molecules per polymer chain, or 1.34 CUR molecules ($C_{21}H_{20}O_6$, $M = 368$ g/mol) per repeat unit of pPrOzi ($C_7H_{13}NO$, $M = 127$ g/mol) are accommodated. Important to note, even at such large excess of CUR (or PTX with A-BuOx-A) with its high propensity for crystallization, the drugs remained fully amorphous¹². Considering this, it appears likely that the hydrophilic block should play a role in the drug solubilization besides creating a simple hydrophilic corona that stabilizes the micelles. Indeed, we recently investigated these drug loaded micelles in more detail using solid-state NMR⁴³ spectroscopy and found a very profound contribution of the hydrophilic corona (pMeOx). Accordingly, this work investigates the impact of chemically distinct hydrophilic blocks (pMeOx and pEtOx) on drug loading, solubilization and colloidal stability of POx based drug loaded micelles.

2. RESULTS AND DISCUSSIONS

2.1 SYNTHESIS AND FORMULATION STUDIES

We synthesized four structurally similar A-B-A triblock copolymers (Fig 1a) replacing pMeOx (A) with another highly hydrophilic POx, i.e. pEtOx (A*) resulting in A*-pPrOx-A*, A*-pPrOzi-A*, A*-pBuOx-A* and A*-pBuOzi-A* triblock copolymer amphiphiles. For a full characterization (¹H-NMR, GPC, TGA, DSC and cmc), the reader is referred to the supporting information (Figures S1-S9, S23, S25 and Table S1). The four polymers were tested for their solubilizing capacity for PTX and CUR by using the thin film method (Figures S26-S30). Compared to the polymers bearing pMeOx hydrophilic blocks (Figure 1b)³⁹, we found a significant drop in the LC for all newly synthesized amphiphiles with pEtOx as hydrophilic block. In no case, LCs values exceeding 30 wt.% could be obtained (Figure 1c, Table S3). Interestingly, 20-30 wt.% is typically the upper limit for micellar LC found in literature⁴⁴⁻⁴⁶. It should be noted though, that the LC with A*-B-A* based amphiphiles is much higher than many reported CUR formulations in the literature⁴⁷. Interestingly, the specificity pattern with respect to the hydrophobic core and drug is largely preserved irrespective of the corona, corroborating the relevance of the core identity. For pBuOx as hydrophobic block, being the best solubilizer for PTX²⁹, the LC dropped from 50 wt.% (A as corona) to 30 wt.% (A* as corona). Similarly, for pPrOzi as hydrophobic block, being the best solubilizer for CUR³⁹, a drop from 54 wt.% (A as corona) to 28 wt.% (A* as corona) was observed. However, both remained the best solubilizers for PTX and CUR, respectively, in the A*-B-A* series. Irrespective of the corona forming block, the barely hydrophobic block pPrOx results in poor solubilization for PTX while CUR is solubilized rather well with pMeOx corona but not pEtOx.

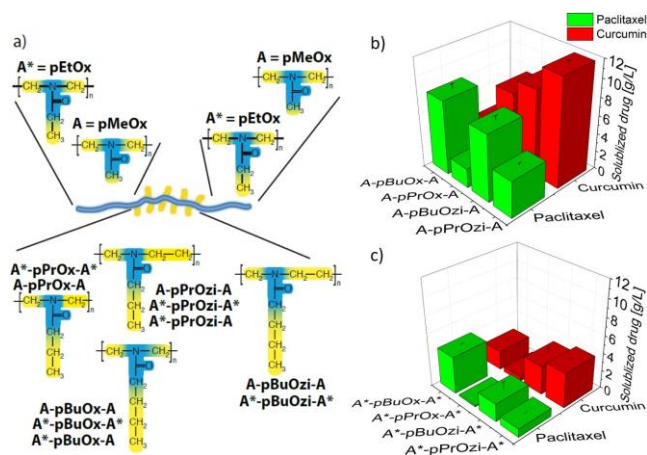


Figure 1 | a) Schematic representation of the polymers used in this study. Maximum solubilized aqueous paclitaxel (green) and curcumin (red) concentrations using four different A-B-A triblock copolymers (four different hydrophobic blocks) with b) pMeOx (represented as A) and c) pEtOx (represented as A*) as hydrophilic blocks. The polymer feed was kept constant at 10 g/L with an increasing drug feed from 0 to 10 g/L in each case. Data is given as means \pm SD (n=3). The data shown in b) was taken from ref. [39]. See Table S2-S3 for tabulated values.

In case of pBuOzi and A* as shell, again a dramatic decrease in LC was observed (48 to 24 wt.% for CUR and 40 to 16 wt.% for PTX) (see Table S2-S3 for tabulated values). Important to note, the restricted solubilization capacity cannot be attributed to poor solubility of the newly synthesized A*-B-A* triblock copolymers themselves, as the aqueous solubility of the neat polymers well exceeded 100 g/L. In all the cases with A*-B-A* copolymers, the thin-

film method resulted in an undissolved gel-like agglomerate after film-hydration once a critical LC is reached. $^1\text{H-NMR}$ revealed that the agglomerate dissolved in non-selective CDCl_3 clearly contains both, the polymer and the drug itself⁴⁸ (Figure S32-33). Differential scanning calorimetry (DSC) analysis of pristine CUR, PTX and freeze-dried agglomerate for both PTX and CUR formulations with $\text{A}^*\text{-pBuOx-A}^*$ and $\text{A}^*\text{-pPrOzi-A}^*$ amphiphiles, respectively, confirmed their amorphous character. Clearly, the sharp endothermic peak appearing as the melting point of pristine CUR (175°C) and solid-solid transition of PTX (170°C)⁴⁹, were absent in the DSC thermograms of both agglomerates confirming their amorphous character (Figure S34-35). Similarly, Wiest et al. found completely amorphous drug in their taurocholate micelle agglomerates¹³. To further probe this interesting effect of the hydrophilic corona, we synthesized two new $\text{A}^*\text{-B-A}$ triblock terpolymers with mixed hydrophilic blocks (for characterization, see Figure S10-S13, S18-S19, S23, S25 and Table S1), selecting the two best performing hydrophobic blocks, pBuOx and pPrOzi (for PTX and CUR, respectively). The resulting triblock terpolymers are denoted as $\text{A}^*\text{-pBuOx-A}^*$ and $\text{A}^*\text{-pPrOzi-A}^*$ and their solubilizing capacity for CUR and PTX was also compared to a physical mixture of $\text{A}^*\text{-B-A}^*$ and A-B-A polymers (5/5 g/L each $\approx 10\text{g/L}$).

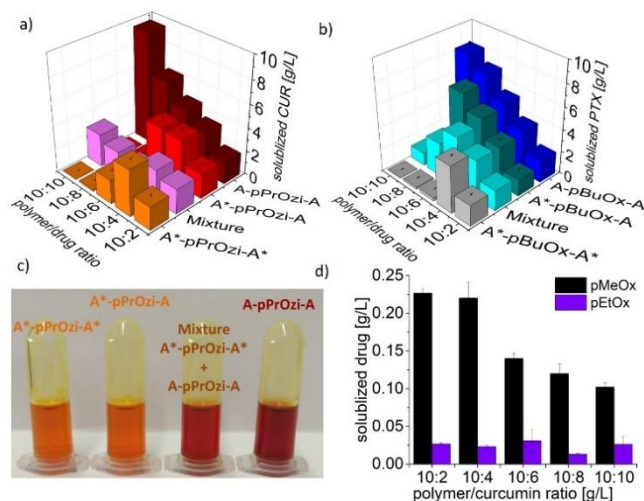


Figure 2 | a) Solubilized curcumin (CUR) using triblock co- and terpolymers with pPrOzi as hydrophobic and varying hydrophilic blocks i.e. A-pPrOzi-A ($\text{A}=\text{pMeOx}$) (wine), A-pPrOzi-A ($\text{A}^*=\text{pEtOx}$) (red), $\text{A}^*\text{-pPrOzi-A}^*$ (orange) and mixture (1:1 ratio w/w) of A-pPrOzi-A and $\text{A}^*\text{-pPrOzi-A}^*$ (magenta). b) Solubilized paclitaxel (PTX) using triblock co- and terpolymers with pBuOx as hydrophobic and varying hydrophilic blocks i.e. A-pBuOx-A (blue), $\text{A}^*\text{-pBuOx-A}$ (dark cyan), $\text{A}^*\text{-pBuOx-A}^*$ (grey) and the mixture (cyan). c) Visual appearance of CUR aqueous formulation prepared with four different setups of hydrophilic blocks at polymer/CUR feed ratio of 10/2 g/L. d) The CUR solubilizing capacity of corona forming blocks as homopolymers pMeOx (black) and pEtOx (violet). The polymer feed is 10 g/L with the increasing drug feed from 0 to 10 g/L in each case. Data is given as means \pm SD ($n=3$). See Tables S6-S8 for tabulated values.

Solubilization experiments revealed that the LC of $\text{A}^*\text{-pBuOx-A}$ and $\text{A}^*\text{-pPrOzi-A}$ for CUR (Figure 2a) and PTX (Figure 2b) aligned between A-B-A and $\text{A}^*\text{-B-A}^*$, respectively. Solubilizing CUR, immediate differences could be noted by virtue of the solvatochromicity of CUR⁵⁰. The formulations with $\text{A}^*\text{-pPrOzi-A}^*$ and $\text{A}^*\text{-pPrOzi-A}$ appeared orange while A-pPrOzi-A based formulations appeared dark red (Figure 2c) indicating the different microenvironment for the guest molecule. It is clear that CUR solvatochromicity is not only determined by the hydrophobic blocks^{12, 48}, but also affected by the hydrophilic blocks in these particular micellar formulations,

evidencing the involvement of the hydrophilic blocks. The LC of $\text{A}^*\text{-pBuOx-A}$ (39 wt.%) for PTX is comparable with A-pBuOx-A (41 wt.%) up to a polymer/PTX feed of 10/8 g/L. Upon further increase in drug feed the LC significantly dropped to 3 wt.%, while A-pBuOx-A kept solubilizing increasing amounts of PTX (45 wt.%) (Figure 2b, Table S7). Similarly, for $\text{A}^*\text{-pPrOzi-A}$ and CUR, a dramatic decrease in LC was observed at a polymer/CUR feed of 10/6 (Figure 2a, Table S6). The formulation completely agglomerated upon further increase in drug feed. Therefore, the LC for both drugs follows the order of $\text{A-B-A} > \text{A}^*\text{-B-A} > \text{A}^*\text{-B-A}^*$. Considering the macromolecular structure of the $\text{A}^*\text{-B-A}$ triblock terpolymers, the resulting micelles must inevitably feature a mixed pMeOx/pEtOx corona. In contrast, if the corresponding, individual A-B-A and $\text{A}^*\text{-B-A}^*$ triblock copolymers were combined, the system could either form mixed micelles or phase separate into two distinct sets of micelles. We mixed both triblock copolymers (5 g/L each to obtain 10 g/L in total) and prepared nanoformulations of CUR and PTX, respectively. Interestingly, at first glance, the solubilization results do not clearly support either the picture of mixed micelles or two separate types of micelles. (Figure 2a, b). The formulation experiments were also performed for the drugs and the hydrophobic blocks, which are not preferred i.e. CUR with pBuOx and PTX with pPrOzi based amphiphiles, respectively (Figure S31, Tables S4-S5) and a similar picture was obtained.

It is well established that both, pMeOx and pEtOx are highly water soluble, but while pMeOx does not show a lower critical solution temperature (LCST) in water⁵¹, pEtOx can exhibit an LCST depending on the molar mass and polymer architecture with a cloud point temperature (T_{cp}) as low as 61°C to 69°C⁵². However, Schubert et al. reported that at least 100 repeat units are required for linear pEtOx to observe the T_{cp} below 100°C⁵³. To rule out that the poor solubilization in the case of the $\text{A}^*\text{-B-A}^*$ triblock copolymer can be attributed to a LCST type behavior, formulation experiments were also performed at room temperature but no significant differences were observed (Table S6). To aid with the solubilization of water-insoluble active pharmaceutical ingredients (APIs), also water soluble homopolymers are regularly employed⁵⁴⁻⁵⁵. Indeed, pEtOx has been employed in this context with some success⁵⁶. Here, pMeOx and pEtOx homopolymers (each with 35 repeat units) were synthesized (Figures S14-S17, S22, S24 and Table S1) and compared for CUR solubilization (Figure 2d, Table S8). We found that pMeOx is capable to solubilize eight times more CUR (0.23 g/L) than pEtOx (0.03 g/L), suggesting that pMeOx is a profoundly more expicent than pEtOx and a better alternative to polyvinylpyrrolidone (0.18 g/L at pH 5.2)^{55, 57} or hydroxypropyl methylcellulose, if necessary. These findings further corroborate the formulation results obtained by CUR formulations experiments (Figure 1b, c and Figure 2a, b) with triblock co- and terpolymers based on pMeOx (9.52 g/L) and pEtOx (3.96 g/L). Interestingly, CUR solvatochromicity was also observed when using the homopolymers pEtOx (orange) and pMeOx (dark red) for formulation (Figure 3a). A recent and excellent study by Nischang and co-workers suggested that both pEtOx and pMeOx are good alternatives to PEG from the perspective of hydrodynamic invariants⁵⁸. However, our results highlight important differences between pMeOx and pEtOx for pharmaceutical applications. Similarly, Morgese et al. have recently compared polymer brushes of PEG, pEtOx, pMeOx as well as mixtures thereof. Among the tested samples, pEtOx based polymer brushes have shown the least hydration and highest amount of physisorbed proteins when compared to pMeOx presumably via hydrophobic interactions between pEtOx and surface interacting protein by van der Waals forces⁵⁹. We can assume, that the profound differences observed in the LC with different hydrophilic

blocks are also connected to a difference in hydration between pMeOx and pEtOx.

2.2 FORMULATIONS WITH REICHARDT'S DYE

To further probe the micellar microenvironment, we employed the hydrophobic and solvatochromic Reichardt's dye (RD) to obtain the solvent polarity parameter $E_T(30)^{60}$, which has been widely used to measure the polarity of different systems⁶¹ (Figures S36-S37). RD clearly allowed to distinguish between the polymer sidechain and to a lesser extent polymer backbone in all the investigated triblock co- and terpolymers (polymer/RD 10/0.5 g/L) (Figure 3b). Albeit somewhat less obvious, the different hydrophilic blocks can also be distinguished. A-pPrOx-A and A-pPrOzi-A showed broad and comparably featureless UV/Vis spectra³⁹ while A*-pPrOzi-A* and A*-pPrOzi-A featured better resolved local maxima. The latter may be attributed to a more defined molecular environment. A more pronounced difference was observed for polymers featuring a butyl side chain, irrespective of the hydrophilic block. Very clearly distinguishable local maxima between 585 to 595 nm were observed. Upon incorporation of PTX along with RD (polymer/RD/PTX 10/0.5/1 g/L), all spectra narrowed and aligned with local maxima around 560 nm, indicating the remodeling of the micellar microenvironment by the addition of PTX (Figure 4c). With an increase in PTX feed (from 0 to 6 g/L), λ_{max} gradually decreased to 557, 554 and 552 nm for A*-pBuOx-A*, A*-pBuOx-A and A-pBuOx-A (Figure 4d, Table S10), respectively, with the corresponding $E_T(30)$ values of 51.3, 51.6 and 51.8. High $E_T(30)$ values corresponds to high solvent polarity and *vice versa* (Table S9). Interesting to note, at low PTX loading, the UV-vis spectrum of A-B-A is clearly separated from A*-B-A and A*-B-A*, which are essentially identical up to 9 wt.% (10/1 g/L). In contrast, at 23 wt.% (10/3 g/L), the spectra of all three formulations superimpose. At first sight, this seems to contradict the influence of the polymer corona. However, we need to keep in mind that we probe the microenvironment with RD while increasing PTX load. The present data can be interpreted that at low loading, the RD molecules can interact with both, the hydrophilic corona and the hydrophobic core. Above a critical loading (9 wt.% < LC < 23 wt.%) the RD only interacts with the core, presumably because PTX starts to interact more with the corona. This observation coincides with the formation of the raspberry-like morphology observed at similar LC values for A-pBuOx-A/PTX formulations, which can be explained in the light of the present work with the start of the interaction of the PTX with the micellar corona¹¹. Unfortunately, a similar analysis using RD is not possible for the CUR formulations, as CUR itself is highly colored and dominates the UV-Vis spectrum over RD.

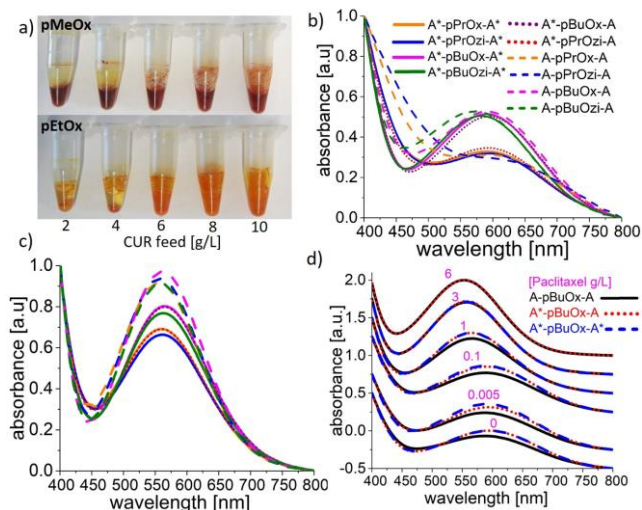


Figure 3 | a) Visual appearance of CUR formulations prepared with pMeOx (upper row) and pEtOx (lower row) homopolymer in dependence of CUR feed (0 to 10 g/L), with polymer feed of 10 g/L in each case. b) Normalized UV-vis absorption spectra of Reichardt's dye in the absence (polymer/dye 10/0.5 g/L) and presence c) of paclitaxel (PTX) (polymer/dye/PTX 10/0.5/1 g/L). d) Normalized absorption spectra of Reichardt's dye co-formulated with PTX into polymeric micelles of either A-pBuOx-A (black), A*-pBuOx-A (red) or A*-pBuOx-A* with the increasing PTX feed (0 to 6 g/L) (purple numbers above graph), with the constant polymer/dye feed of 10/0.5 g/L. For better visibility, the absorption spectra were shifted along y-axis.

2.3 CHARACTERIZATION OF FORMULATIONS

2.3.1 ¹H-NMR SPECTROSCOPY

To gain more insights into the structure of CUR loaded PMs, pure polymers and lyophilized formulations prepared with A-pPrOzi-A, A*-pPrOzi-A, A*-pPrOzi-A* triblocks and mixture of A-pPrOzi-A/A*-pPrOzi-A* (1/1, w/w) were dispersed in D₂O and subsequently analyzed by ¹H-NMR spectroscopy (Figure 4a, b, 5a, b and Figures S38-S49). Please note, any precipitate that occurred in the formulation will therefore be removed and not contribute to the NMR analysis. Nevertheless, we discuss all data with respect to the CUR feed, not the actual concentration, which can be found in the supporting information. In the absence of CUR, the ¹H-NMR spectra of A*-pPrOzi-A* and A*-pPrOzi-A in D₂O clearly present all signals from the polymers with the expected intensities (Figure S38-S39) showing that the polymers exist as unimers. The pyrene assay also confirmed the absence of micelles in the case of pPrOzi based amphiphiles (Figure S25, Table S1). These observations corroborate recent results which showed that A-pPrOzi-A self-assembles only in the presence of hydrophobic molecules¹². In the formulations, the characteristic signals for CUR were not observed^{12, 48}.

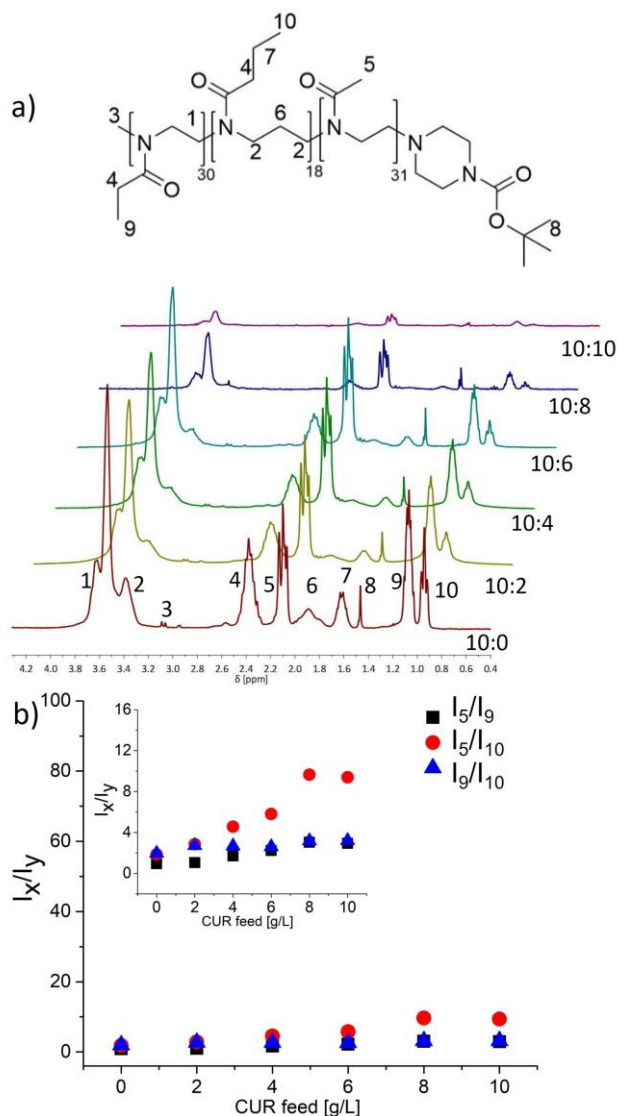


Figure 4 a) $^1\text{H-NMR}$ spectra (300 MHz, 298 K) and b) NMR integral ratios (I_x/I_y) of terpolymer (A*-pPrOzi-A)/CUR formulations in dependence of CUR feed (0 to 10 g/L). For better visibility, enlarged sections are added as insets.

This can be attributed to a hindered mobility resulting in short T_2 relaxation times. In contrast, the polymer signals were clearly distinguishable for all samples, but individual signal intensities strongly varied with CUR loading⁶². For A-pPrOzi-A/CUR formulation, comparison of signals attributed to the hydrophilic block vs. the hydrophobic block provide clear evidence for reduced mobility in the latter (Figure S44). However, after a strong initial increase of the integral ratio between I_1/I_8 ($\text{CH}_2^{\text{MeOx}}/\text{CH}_3^{\text{PrOzi}}$) and I_5/I_8 ($\text{CH}_3^{\text{MeOx}}/\text{CH}_3^{\text{PrOzi}}$), the ratio decreases again at CUR feed ≥ 6 g/L, suggesting also a lowered mobility of the hydrophilic block (Figure S45, blue and magenta triangles). Obviously, the hydrophilic block becomes involved in the coordination of CUR above a critical CUR concentration. This observation corroborates a recent, more extensive solid state NMR analysis of A-pPrOzi-A/CUR formulations⁴³. In contrast, for A*-pPrOzi-A*/CUR formulations, the integral ratio I_1/I_9 (pEtOx backbone/ $\text{CH}_3^{\text{PrOzi}}$) and I_8/I_9 ($\text{CH}_3^{\text{EtOx}}/\text{CH}_3^{\text{PrOzi}}$) kept on increasing with the increasing CUR feed (Figure S46-S47, blue triangle and green diamond) even while overall drug solubilization deteriorated. Comparing the spectra of the terpolymer A*-pPrOzi-A formulations (Figure 4) and those employing the mixture

A*-pPrOzi-A*/A-pPrOzi-A (Figure 5) inform us in more detail on the involvement of different moieties of the hydrophilic coronas and their interactions with CUR.

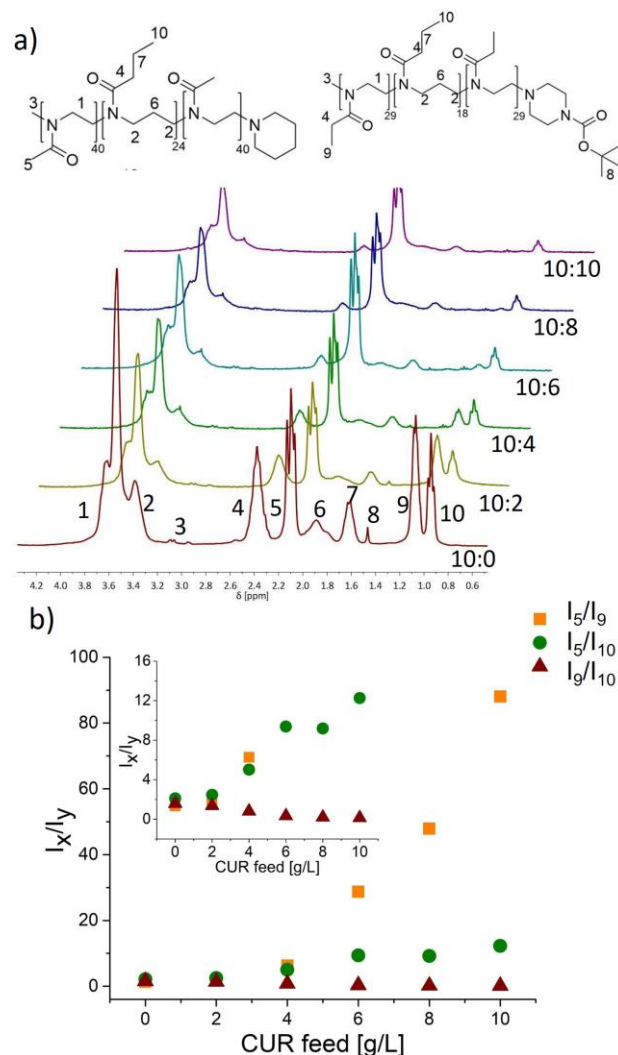


Figure 5 a) $^1\text{H-NMR}$ spectra (300 MHz, 298 K) and b) NMR integrals (I_x/I_y) of mixture (A*-pPrOzi-A*/A-pPrOzi-A)/CUR formulation in dependence of CUR feed (0 to 10 g/L). For better visibility, enlarged sections are added as insets.

In case of A*-pPrOzi-A, (Figure 4a, b and Figure S48), the increase in the integral ratio I_5/I_{10} ($\text{CH}_3^{\text{MeOx}}/\text{CH}_3^{\text{PrOzi}}$, red circle) again indicates the higher mobility of pMeOx compared to pPrOzi with the increasing CUR feed, while the integral ratio I_9/I_{10} ($\text{CH}_3^{\text{EtOx}}/\text{CH}_3^{\text{PrOzi}}$, blue triangle) did not change significantly (Figure 4b). More interestingly, in case of the A*-pPrOzi-A*/A-pPrOzi-A mixture, the integral ratio I_5/I_{10} ($\text{CH}_3^{\text{EtOx}}/\text{CH}_3^{\text{PrOzi}}$, green circle) (Figure 5a, b and Figure S49) increased much more with increasing drug content. This shows a stronger reduction of the mobility of pEtOx in the mixture compared to terpolymer. The signal of the Boc-protected piperazine terminating reagent (signal 8) attached either at the pMeOx (A*-pPrOzi-A) or pEtOx (A*-pPrOzi-A*) block further corroborate this picture. While the signal remains clearly visible when attached to pMeOx (Figure 4a), it essentially vanishes even at low drug loading when attached to pEtOx (Figure 5a).

It appears that a slightly lower hydration of the pEtOx shell is exacerbated with increasing drug loading. The mobility of the hydrophilic pEtOx blocks suffer much more compared to pMeOx for

both mixed corona systems. Quantitatively, however, the increase in the ratio pMeOx side chain/pEtOx side chain with increasing drug feed was much lower in the case of the triblock terpolymer (black square, Figure 4) vs. the triblock copolymer mixture (orange square, Figure 5), especially as the polymer/drug ratio exceeded 10/4 and was 30 times higher at a 10/10 ratio (Figure 5b, orange square). This profound loss in pEtOx signal intensity can have two reasons. First, the pEtOx moieties become more solid-like because they interact more strongly with CUR and lose their mobility, probably also segregate more towards the interior of the micelles. Second, the polymers in the mixture could undergo phase separation and micelles that contain more pEtOx, agglomerate/precipitate preferentially, which also let them appear more solid-like but also removes them from the analysis of the supernatant. Therefore, we next analysed the precipitate of the formulations after freeze-drying, in a non-selective solvent. Strikingly, the $^1\text{H-NMR}$ analysis in CDCl_3 of freeze-dried agglomerate/precipitate of $\text{A}^*\text{-pPrOzi-A}^*/\text{A-pPrOzi-A}$ /CUR formulation revealed exclusively $\text{A}^*\text{-pPrOzi-A}^*$ and CUR (Figure S50). This means that the mixture phase separates and $\text{A}^*\text{-pPrOzi-A}^*/\text{CUR}$ precipitates, while micelles enriched in A-pPrOzi-A remain in solution. In contrast, pMeOx and pEtOx are covalently linked in the case of $\text{A}^*\text{-pPrOzi-A}$ terpolymer and cannot separate. The characteristic signal of the methyl group of pMeOx in case of $\text{A}^*\text{-pPrOzi-A}/\text{CUR}$ formulation is clearly distinguishable in the $^1\text{H-NMR}$ spectra (in CDCl_3 at 2 ppm) of the lyophilized agglomerate (Figure S51). In contrast, the $^1\text{H-NMR}$ analysis of lyophilized supernatant in CDCl_3 revealed the presence of both component of the mixture in the expected ratio up to polymer/CUR feed of 10/4 g/L (Figure S52). Upon further increase the signal for the EtOx side chain (signal 9) starts to decrease but does not completely vanish even at maximum CUR feed (10 g/L). It is obvious that the increasing CUR feed leads to higher interaction with $\text{A}^*\text{-pPrOzi-A}^*$ resulting in agglomeration of pure $\text{A}^*\text{-pPrOzi-A}^*/\text{CUR}$, while the A-pPrOzi-A remains in solution and available to solubilize some CUR along with a few $\text{A}^*\text{-pPrOzi-A}^*$ chains. However, it appears that CUR has a much higher affinity for pEtOx as most of the added CUR is agglomerated with $\text{A}^*\text{-pPrOzi-A}^*$, therefore CUR solubilized by A-pPrOzi-A did not increase with higher feeding ratio (Table S6). In the light of this, we also prepared a formulation with an excessive CUR feed (polymer/CUR = 10/16 g/L) (Table S6) expected to saturate $\text{A}^*\text{-pPrOzi-A}^*$. However, no significant increase in solubilized CUR was observed. Again, the agglomerate formed was analyzed by $^1\text{H-NMR}$ in CDCl_3 , indicating the massive amount of CUR (polymer/CUR \approx 5/12 w/w) (Figure S53) further indicating concentration dependent higher interaction of pEtOx with CUR than pMeOx.

Based on these results, we can build a tentative model of the micelle architecture with different hydrophilic coronas and drug loading (Figure 6). At no or very low drug loading, no major difference is observable in any case but with increasing drug loading pEtOx interacts stronger with the hydrophobic guest molecules, loses its hydration and mobility. Upon further increase of drug loading the $\text{A}^*\text{-B-A}^*$ micelles agglomerate and precipitate while $\text{A}^*\text{-B-A}$ micelles still have hydrated pMeOx chains, stabilizing and solubilizing them. However, eventually also its capacity is reached and the $\text{A}^*\text{-B-A}$ micelles precipitate earlier than the A-B-A micelles containing only pMeOx.

2.3.2 DIFFUSION AND NOE DATA

To support the findings based on comparison of $^1\text{H-NMR}$ and integrations as well as to gain more insights into the assembly of the micelles, in particular with respect to the mixture of polymers, ^1H diffusion (DOSY) NMR experiments were performed for a set of

four polymer/CUR (10/2 g/L) formulations. Please note, at this CUR feed, solubilization in all formulation was quantitative. From agreement of the diffusion coefficients for water (residual HDO signal) and comparison between a stimulated BPP-LED and a double stimulated echo pulse sequence for all four samples, differences in viscosity or convection effects could be excluded. The diffusion coefficients were determined by fitting the experimental diffusion data with a log normal function⁶³ and the values are in comparable range for all four samples indicating similar hydrodynamic radii (Table S11). From comparison of the averaged diffusion coefficients over the functional groups for each sample, the smallest value (and thus largest particles size) was observed for $\text{A}^*\text{-pPrOzi-A}^*$ and increases in the order $\text{A}^*\text{-pPrOzi-A} \approx$ polymer mixture $>$ A-pPrOzi-A , which thus shows the smallest hydrodynamic volume.

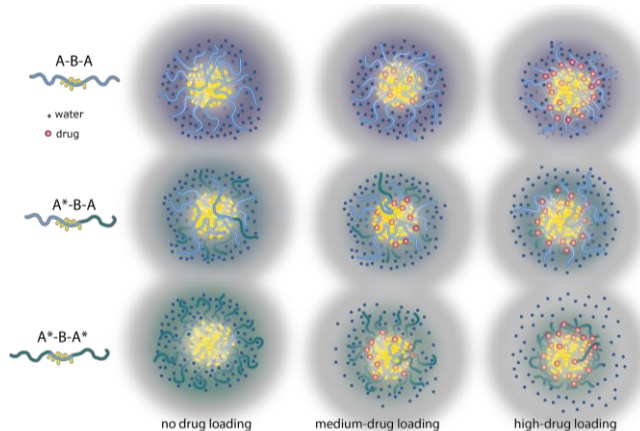


Figure 6 | Schematic illustration of the effect of drug loading on the corona of drug loaded micelles in dependence of the corona composition.

The individual diffusion coefficients for the moieties in the terpolymer and the polymer mixture do not differ in a significant or systematic way. This hints at the presence of mixed micelles for the polymer mixture. This was further supported by the direct comparison of the respective ^1H (Figure S54) and $^1\text{H-}^1\text{H}$ NOESY NMR spectra (Figure 7a). $^1\text{H-}^1\text{H}$ NOESY spectra were recorded with different mixing times $d_8 = 50$ (Figure S55), 100, 200 and 400 ms (Figure 7b and c). Each spectrum was carefully phase and baseline corrected before the rows containing the $\text{CH}_3(\text{PrOzi})$ and $\text{CH}_3(\text{EtOx})$ groups were extracted to investigate the proximities of these fragments. For the overlay of these 1D extracted slices, the spectra were scaled to equal height of the diagonal peak to compare the relative intensity of the cross-peak. The similarity of the two NOESY spectra (Figure 7a) confirms that, for low CUR loading, the mixture ($\text{A}^*\text{-pPrOzi-A}^*/\text{A-pPrOzi-A}$) forms mixed micelles. The cross peaks observed in the spectra are largely identical. At strongly increased intensity, cross-peaks between the CH_3 groups of EtOx and the PrOzi fragments start to appear. As this cross-peak is very close to the intense diagonal signal, a series of NOESY spectra with the increasing mixing time (100, 200 and 400 ms) were recorded. For each of these spectra, the rows 1728 and 1684, corresponding to CH_3 groups of PrOzi and EtOx, respectively, were extracted (Figure 7b and c). The CH_3 group of PrOzi shows indeed a cross-peak with the EtOx signal at 1.02 ppm, which increases with increasing mixing time. In fact, this cross-peak is observed for both the terpolymer ($\text{A}^*\text{-pPrOzi-A}$) and the mixture. The CH_3 group of EtOx also exhibits clearly visible cross-peaks to the adjacent CH_2 group and to the POx backbone, but also a low intensity signal to the CH_2 group of the PrOzi side chain at 1.57 ppm (Figure 7c). Interestingly, for both CH_3 groups, no contact to MeOx at 2.05 ppm

can be observed at 100 ms mixing time and only a low intensity signal barely above the noise is detected for the two longer mixing times (200 and 400 ms). Presumably this weak, residual contact results from the direct connection of the polymer blocks. All NOESY data strongly suggest that while EtOx units are in close proximity of PrOzi units, the MeOx units remain more separated.

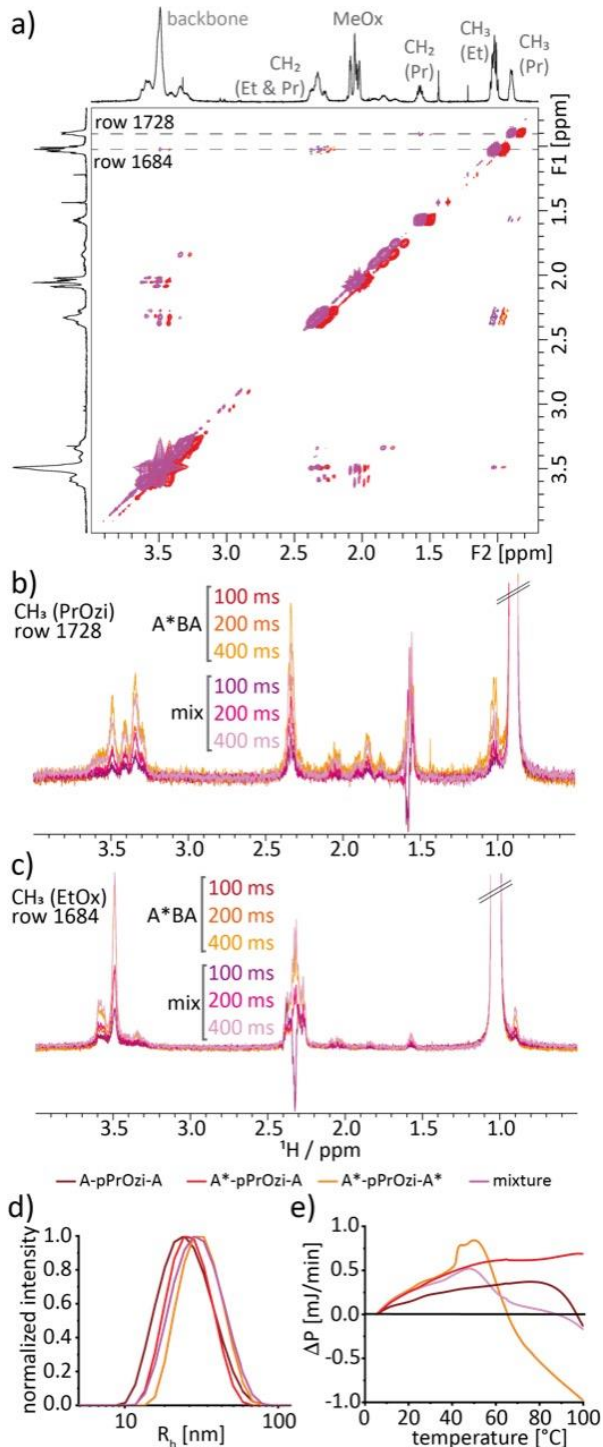


Figure 7 a) Overlay of the ^1H - ^1H NOESY spectra of terpolymer, A*-pPrOzi-A (red) and the mixture of A-pPrOzi-A/A*-pPrOzi-A* (magenta) (1:1 ratio w/w) with low CUR feed (2 g/L) recorded with a mixing time of 100 ms. For easier comparison, the red spectrum is slightly shifted to the right. b, c) Overlay of the slices from ^1H - ^1H NOESY experiments at different mixing times extracted for the two spectral rows as indicated by the grey dashed

lines in a). d) The size distribution of CUR nanoformulations (10/2 g/L) by dynamic light scattering (90°) with different setups of hydrophilic blocks (A=pMeOx and A*=pEtOx) $n=1$. e) Raw microcalorimetry heating curves obtained for CUR nanoformulations (10/2 g/L) with different hydrophilic blocks (60 °C/h). ΔP represents the measured power, the difference between the sample solution and the solvent reference (DI water) $n=1$.

2.3.3 DYNAMIC LIGHT SCATTERING (DLS)

To support the results from DOSY NMR spectroscopy, we analyzed the polymer/CUR (10/2 g/L) formulations with four different setups of hydrophilic coronas by nanosizer (at 90°). All the tested aqueous formulations self-assemble to form micelles with the hydrodynamic radii (R_h) ranging between 12 to 15 nm (Figure 7d). Previously, we had observed A-pBuOx-A/PTX and A-pPrOzi-A/CUR based formulation (with polymer/drug feed of 10/2 and 10/3 g/L) appeared with the R_h of 8 and 11 nm, respectively¹¹⁻¹². In short, at CUR feed of 2 g/L, where all the employed CUR nanoformulations were completely soluble, no significant differences in size of the micelles were observed for different hydrophilic coronas.

2.3.4 MICRO CALORIMETRY STUDIES (micro DSC)

Differences in hydration of the hydrophilic corona may exacerbate with increasing temperature. Therefore, we also conducted microcalorimetric studies on nanoformulations with a polymer/CUR feed of 10/2 g/L. Samples were heated from 5 to 100 °C with a heating rate of 60 °C/h and the power difference (ΔP) between reference (DI water) and sample was recorded (Figure 7e). Clearly, the four different formulations yielded four distinct thermograms. The CUR nanoformulations of A-pPrOzi-A and A*-pPrOzi-A did not provide evidence of any obvious thermal transition. In contrast, the CUR nanoformulations of A*-pPrOzi-A* as well as A-pPrOzi-A/A*-pPrOzi-A* mixture gave clear evidence of a thermal transition as peaks in the thermograms. Interestingly, A-pPrOzi-A nanoformulations showed a decrease in ΔP above 80 °C, which is absent for the A*-pPrOzi-A formulation. This may be attributed to the interaction of CUR with the pMeOx hydrophilic block in A-pPrOzi-A, which decreases pMeOx strength in the interaction with water, leading to a loss of hydration with increasing temperature. In contrast, for the A*-pPrOzi-A formulation, besides pMeOx, pEtOx is also present as a hydrophilic block. Due to the higher affinity of pEtOx to CUR compared to pMeOx, pMeOx hydration is not affected at this loading, corroborating the results from NMR experiments showing the preferential condensation and dehydration of the pEtOx over pMeOx blocks upon CUR addition. Most interestingly, the mixture of A-pPrOzi-A/A*-pPrOzi-A* showed an entirely different picture from the terpolymer A*-pPrOzi-A formulation, although they comprise the same building blocks. Initially, the obtained curves are similar, but in the temperature range of 36 – 60 °C a small but distinct peak is observed in case of the mixture of A-pPrOzi-A/A*-pPrOzi-A* based formulation. We attribute this thermal transition to the dehydration of predominantly pEtOx chains interacting with CUR and concomitant reorganization of the hydrophilic corona. In contrast to the situation with the terpolymer A*-pPrOzi-A formulation, the mixture can undergo phase separation, which is in fact observed at higher drug loading as previously discussed. At this lower loading, the phase separation is induced by the increase in temperature. In addition, at very high temperature, the microcalorimetric trace of the mixture resembles the trace for the A-pPrOzi-A, suggesting also in the mixture, CUR remains to some extent in the corona of A-pPrOzi-A micelles and decrease pMeOx hydration. Again, this corroborates the data obtained by ^1H -NMR for higher loading. Finally, A*-pPrOzi-A* formulations show the most pronounced thermal transition and profound negative ΔP values above 60 °C. Notably, A*-pPrOzi-A*/CUR

was the only formulation in this series that showed macroscopic agglomeration and precipitation at this loading with increased temperature, which is in line with the strong negative values of ΔP . Notably, the observed bimodal peak supports the idea that the pEtOx corona dehydrates. Such bimodality maybe attributed to dynamics/kinetics of the transition of the chains in the micellar corona. Such behavior has been reported for core-shell particles and more pronounced for thermoresponsive polymers of higher molar mass in the corona⁶⁴. It may also be related to release of curcumin and reorganization of the polymer in corona. It should also be noted that the cooling curves of A-pPrOzi-A/A*-pPrOzi-A* formulations also showed this bimodality (Figure S56).

3. SUMMARY

In summary, we show conclusively using a range of complementary analytical tools that the hydrophilic corona of polymer micelles may not only be involved in the solubilization of hydrophobic cargo, but also that a minor change in the hydrophilic block of a polymer amphiphile (pMeOx vs. pEtOx vs. pMeOx/pEtOx) can have a significant impact on drug loading and/or colloidal stability of the micelles. Our results show that a simple core-shell architecture, where the core incorporated the drug and the corona solubilized the micelle can be an oversimplification. Clearly, the nature of the hydrophobic block and the guest molecule are not the only determinants and more scrutiny must be applied to the interactions between cargo and hydrophilic corona. It also interacts with the system in various ways which can ultimately affect the physicochemical properties of nanocarriers. In fact, the highly unusual ultra-high drug loading now well-established for POx based micelles are apparently in part possible due to the choice of the hydrophilic pMeOx. Our results shed new light and give clearer instructions on how to design and optimize drug delivery systems and polymeric excipients. Considering that the vast majority of drug delivery systems contain poly(ethylene glycol) as a hydrophilic polymer, which is very similar to pEtOx in its amphiphilicity, we can raise the question whether the limited drug loading of polymeric micelles found in the literature, may be strongly correlated to the choice of the hydrophilic polymer. In addition, our finding may also suggest that major differences of the interaction between different hydrophilic polymers and drugs in polymer-drug conjugates or even polymer-protein conjugates can be expected.

ASSOCIATED CONTENT

Supporting Information

The Supporting Information is available free of charge on the ACS Publications website. Detailed experimental procedures, polymer characterization, formulation data, additional ¹NMR analysis, DSC, DOSY and NOESY experiments.

AUTHOR INFORMATION

Corresponding Author

robert.luxenhofer@uni-wuerzburg.de

Notes

M.M.L. and R.L. are listed as inventors on a patent application pertinent to some of the materials discussed in this contribution. R.L. is co-founder and has a financial interest in DeLaqua Pharmaceuticals Inc. which is intent on commercializing poly(2-oxazoline) based excipients.

ACKNOWLEDGMENT

This work was supported by Deutsche Forschungsgemeinschaft (DFG, Project no. 398461692 awarded to R.L.). Moreover, M.S.H. and M.M.L. are grateful to the Higher education commission of Pakistan and German academic exchange services (HEC-DAAD Pakistan) (M.S. Haider) and Evonik foundation (M.M. Lübtow), respectively for the award of PhD scholarships. Financial support from the Fonds der Chemischen Industrie (FCI) in form of a material cost allowance is acknowledged (A.-C. P.). We thank Lukas Hahn and Dr. Matthias Grüne for valuable discussion.

REFERENCES

1. Wang, E.; Lu, J.; Bates, F. S.; Lodge, T. P., Effect of Corona Block Length on the Structure and Chain Exchange Kinetics of Block Copolymer Micelles. *Macromolecules* **2018**, *51* (10), 3563-3571.
2. Garcia Daza, F. A.; Colville, A. J.; Mackie, A. D., Chain architecture and micellization: A mean-field coarse-grained model for poly (ethylene oxide) alkyl ether surfactants. *J. Chem. Phys.* **2015**, *142* (11), 114902.
3. Declet-Perez, C.; Francis, L. F.; Bates, F. S., Deformation processes in block copolymer toughened epoxies. *Macromolecules* **2015**, *48* (11), 3672-3684.
4. Li, T.; Zhang, J.; Schneiderman, D. K.; Francis, L. F.; Bates, F. S., Toughening glassy poly (lactide) with block copolymer micelles. *ACS Macro Lett.* **2016**, *5* (3), 359-364.
5. Cao, C.; Zhao, J.; Chen, F.; Lu, M.; Khine, Y. Y.; Macmillan, A.; Garvey, C. J.; Stenzel, M. H., Drug-Induced Morphology Transition of Self-Assembled Glycopolymers: Insight into the Drug-Polymer Interaction. *Chem. Mater.* **2018**, *30* (15), 5227-5236.
6. Antonietti, M.; Förster, S., Vesicles and liposomes: a self-assembly principle beyond lipids. *Adv. Mater.* **2003**, *15* (16), 1323-1333.
7. Smart, T.; Lomas, H.; Massignani, M.; Flores-Merino, M. V.; Perez, L. R.; Battaglia, G., Block copolymer nanostructures. *Nano Today* **2008**, *3* (3-4), 38-46.
8. Adair, J. H.; Parette, M. P.; Altinoglu, E. I.; Kester, M., Nanoparticulate alternatives for drug delivery. *ACS nano* **2010**, *4* (9), 4967-4970.
9. Lu, W.; Li, F.; Mahato, R. I., Poly (ethylene glycol)-block-poly (2-methyl-2-benzoxycarbonyl-propylene carbonate) micelles for rapamycin delivery: in vitro characterization and biodistribution. *J. Pharm. Sci.* **2011**, *100* (6), 2418-2429.
10. Guo, X. D.; Qian, Y.; Zhang, C. Y.; Nie, S. Y.; Zhang, L. J., Can drug molecules diffuse into the core of micelles? *Soft Matter* **2012**, *8* (39), 9989-9995.
11. Schulz, A.; Jaksch, S.; Schubel, R.; Wegener, E.; Di, Z.; Han, Y.; Meister, A.; Kressler, J. r.; Kabanov, A. V.; Luxenhofer, R., Drug-induced morphology switch in drug delivery systems based on poly (2-oxazoline) s. *ACS nano* **2014**, *8* (3), 2686-2696.
12. Lübtow, M. M.; Nelke, L. C.; Seifert, J.; Kühnemundt, J.; Sahay, G.; Dandekar, G.; Nietzer, S. L.; Luxenhofer, R., Drug induced micellization into ultra-high capacity and stable curcumin nanoformulations: Physico-chemical characterization and evaluation in 2D and 3D in vitro models. *J. Control. Release* **2019**, *303*, 162-180.
13. Wiest, J.; Saedtler, M.; Böttcher, B.; Grüne, M.; Reggane, M.; Galli, B.; Holzgrabe, U.; Meinel, L., Geometrical and structural

- dynamics of Imatinib within biorelevant colloids. *Mol. Pharm.* **2018**, *15* (10), 4470-4480.
14. Cabral, H.; Matsumoto, Y.; Mizuno, K.; Chen, Q.; Murakami, M.; Kimura, M.; Terada, Y.; Kano, M.; Miyazono, K.; Uesaka, M., Accumulation of sub-100 nm polymeric micelles in poorly permeable tumours depends on size. *Nat. Nanotechnol.* **2011**, *6* (12), 815.
15. Win, K. Y.; Feng, S.-S., Effects of particle size and surface coating on cellular uptake of polymeric nanoparticles for oral delivery of anticancer drugs. *Biomaterials* **2005**, *26* (15), 2713-2722.
16. Li, Z.; Lenk, T. I.; Yao, L. J.; Bates, F. S.; Lodge, T. P., Maintaining hydrophobic drug supersaturation in a micelle corona reservoir. *Macromolecules* **2018**, *51* (2), 540-551.
17. Noy, J.-M.; Cao, C.; Stenzel, M., Length of the Stabilizing Zwitterionic Poly (2-methacryloyloxyethyl phosphorycholine) Block Influences the Activity of the Conjugated Arsenic Drug in Drug-Directed Polymerization-Induced Self-Assembly Particles. *ACS Macro Lett.* **2018**, *8* (1), 57-63.
18. Zhao, J.; Lu, H.; Xiao, P.; Stenzel, M. H., Cellular uptake and movement in 2D and 3D multicellular breast cancer models of fructose-based cylindrical micelles that is dependent on the rod length. *ACS Appl. Mater. Interfaces* **2016**, *8* (26), 16622-16630.
19. Gref, R.; Domb, A.; Quellec, P.; Blunk, T.; Müller, R.; Verbavatz, J.-M.; Langer, R., The controlled intravenous delivery of drugs using PEG-coated sterically stabilized nanospheres. *Adv. Drug Deliv. Rev.* **1995**, *16* (2-3), 215-233.
20. Turecek, P. L.; Bossard, M. J.; Schoetens, F.; Ivens, I. A., PEGylation of biopharmaceuticals: a review of chemistry and nonclinical safety information of approved drugs. *J. Pharm. Sci.* **2016**, *105* (2), 460-475.
21. Ivens, I. A.; Achanzar, W.; Baumann, A.; Brändli-Baiocco, A.; Cavagnaro, J.; Dempster, M.; Depelchin, B. O.; Irizarry Rovira, A. R.; Dill-Morton, L.; Lane, J. H., PEGylated biopharmaceuticals: current experience and considerations for nonclinical development. *Toxicol. Pathol.* **2015**, *43* (7), 959-983.
22. Barz, M.; Luxenhofer, R.; Zentel, R.; Vicent, M. J., Overcoming the PEG-addiction: well-defined alternatives to PEG, from structure–property relationships to better defined therapeutics. *Polym. Chem.* **2011**, *2* (9), 1900.
23. Schellekens, H.; Hennink, W. E.; Brinks, V., The immunogenicity of polyethylene glycol: facts and fiction. *Pharm. Res.* **2013**, *30* (7), 1729-1734.
24. Bloksma, M. M.; Paulus, R. M.; van Kuringen, H. P.; van der Woerd, F.; Lambermont-Thijs, H. M.; Schubert, U. S.; Hoogenboom, R., Thermoresponsive Poly (2-oxazine) s. *Macromol. Rapid Commun.* **2012**, *33* (1), 92-96.
25. Klein, T.; Parkin, J.; de Jongh, P. A.; Esser, L.; Sephezadeh, T.; Zheng, G.; De Veer, M.; Alt, K.; Hagemeyer, C. E.; Haddleton, D. M., Functional Brush Poly (2-ethyl-2-oxazine) s: Synthesis by CROP and RAFT, Thermoresponsiveness and Grafting onto Iron Oxide Nanoparticles. *Macromol. Rapid Commun.* **2019**, (40), 1800911.
26. Morgese, G.; Verbraeken, B.; Ramakrishna, S. N.; Gombert, Y.; Cavalli, E.; Rosenboom, J. G.; Zenobi-Wong, M.; Spencer, N. D.; Hoogenboom, R.; Benetti, E. M., Chemical Design of Non-Ionic Polymer Brushes as Biointerfaces: Poly (2-oxazine) s Outperform Both Poly (2-oxazoline) s and PEG. *Angew. Chem.* **2018**, *57* (36), 11667-11672.
27. Lorson, T.; Jaksch, S.; Lübtow, M. M.; Jüngst, T.; Groll, J. r.; Lühmann, T.; Luxenhofer, R., A thermogelling supramolecular hydrogel with sponge-like morphology as a cytocompatible bioink. *Biomacromolecules* **2017**, *18* (7), 2161-2171.
28. Han, Y.; He, Z.; Schulz, A.; Bronich, T. K.; Jordan, R.; Luxenhofer, R.; Kabanov, A. V., Synergistic combinations of multiple chemotherapeutic agents in high capacity poly (2-oxazoline) micelles. *Mol. Pharm.* **2012**, *9* (8), 2302-2313.
29. Luxenhofer, R.; Schulz, A.; Roques, C.; Li, S.; Bronich, T. K.; Batrakova, E. V.; Jordan, R.; Kabanov, A. V., Doubly amphiphilic poly (2-oxazoline) s as high-capacity delivery systems for hydrophobic drugs. *Biomaterials* **2010**, *31* (18), 4972-4979.
30. He, Z.; Schulz, A.; Wan, X.; Seitz, J.; Bludau, H.; Alakhova, D. Y.; Darr, D. B.; Perou, C. M.; Jordan, R.; Ojima, I., Poly (2-oxazoline) based micelles with high capacity for 3rd generation taxoids: Preparation, in vitro and in vivo evaluation. *J. Control. Release* **2015**, *208*, 67-75.
31. He, Z.; Wan, X.; Schulz, A.; Bludau, H.; Dobrovolskaia, M. A.; Stern, S. T.; Montgomery, S. A.; Yuan, H.; Li, Z.; Alakhova, D., A high capacity polymeric micelle of paclitaxel: Implication of high dose drug therapy to safety and in vivo anti-cancer activity. *Biomaterials* **2016**, *101*, 296-309.
32. Paál, K.; Müller, J.; Hegedüs, L., High affinity binding of paclitaxel to human serum albumin. *Eur. J. Biochem.* **2001**, *268* (7), 2187-2191.
33. Wan, X.; Min, Y.; Bludau, H.; Keith, A.; Sheiko, S. S.; Jordan, R.; Wang, A. Z.; Sokolsky Papkov, M.; Kabanov, A. V., Drug Combination Synergy in worm-like Polymeric Micelles Improves Treatment Outcome for Small Cell and Non-Small Cell Lung Cancer. *ACS nano* **2018**, *12* (3), 2426-2439.
34. Ma, P.; Mumper, R. J., Paclitaxel nano-delivery systems: a comprehensive review. *J. Nanomed. Nanotechnol.* **2013**, *4* (2), 1000164.
35. Esatbeyoglu, T.; Huebbe, P.; Ernst, I. M.; Chin, D.; Wagner, A. E.; Rimbach, G., Curcumin—from molecule to biological function. *Angew. Chem.* **2012**, *51* (22), 5308-5332.
36. Naksuriya, O.; Okonogi, S.; Schiffelers, R. M.; Hennink, W. E., Curcumin nanoformulations: a review of pharmaceutical properties and preclinical studies and clinical data related to cancer treatment. *Biomaterials* **2014**, *35* (10), 3365-3383.
37. Baell, J. B., Feeling nature's PAINS: natural products, natural product drugs, and pan assay interference compounds (PAINS). *J. Nat. Prod.* **2016**, *79* (3), 616-628.
38. Lübtow, M. M.; Haider, M. S.; Kirsch, M.; Klisch, S.; Luxenhofer, R., Like Dissolves Like? A Comprehensive Evaluation of Partial Solubility Parameters to Predict Polymer-Drug Compatibility in Ultra-High Drug Loaded Polymer Micelles. *Biomacromolecules* **2019**, (20), 3041-3056.
39. Lübtow, M. M.; Hahn, L.; Haider, M. S.; Luxenhofer, R., Drug specificity, synergy and antagonism in ultrahigh capacity poly (2-oxazoline)/poly (2-oxazine) based formulations. *J. Am. Chem. Soc.* **2017**, *139* (32), 10980-10983.
40. Lübtow, M. M.; Marciniak, H.; Schmiedel, A.; Roos, M.; Lambert, C.; Luxenhofer, R., Ultra-high to ultra-low drug loaded micelles: Probing host-guest interactions by fluorescence spectroscopy. *Chem. Eur. J.* **2019**, in print, DOI: 10.1002/chem.201902619.
41. Alves, V. M.; Hwang, D.; Muratov, E.; Sokolsky-Papkov, M.; Varlamova, E.; Vinod, N.; Lim, C.; Andrade, C. H.; Tropsha, A.; Kabanov, A., Cheminformatics-driven discovery of polymeric micelle formulations for poorly soluble drugs. *Sci. Adv.* **2019**, *5* (6), 9784.
42. Hahn, L.; Lübtow, M. M.; Lorson, T.; Schmitt, F.; Appelt-Menzel, A.; Schobert, R.; Luxenhofer, R., Investigating the Influence of Aromatic Moieties on the Formulation of Hydrophobic Natural Products and Drugs in Poly (2-oxazoline)-Based Amphiphiles. *Biomacromolecules* **2018**, *19* (7), 3119-3128.

43. Pöppler, A.-C.; Lübtow, M. M.; Schlauersbach, J.; Wiest, J.; Meinel, L.; Luxenhofer, R., Loading dependent Structural Model of Polymeric Micelles by Solid-State NMR. *ChemRxiv* **2019**, DOI: 10.26434/chemrxiv.8943251.v1.
44. Yu, Y.; Chen, C.-K.; Law, W.-C.; Weinheimer, E.; Sengupta, S.; Prasad, P. N.; Cheng, C., Polylactide-graft-doxorubicin nanoparticles with precisely controlled drug loading for pH-triggered drug delivery. *Biomacromolecules* **2014**, *15* (2), 524-532.
45. Cheetham, A. G.; Zhang, P.; Lin, Y.-a.; Lock, L. L.; Cui, H., Supramolecular nanostructures formed by anticancer drug assembly. *J. Am. Chem. Soc.* **2013**, *135* (8), 2907-2910.
46. Maksimenko, A.; Dosio, F.; Mougín, J.; Ferrero, A.; Wack, S.; Reddy, L. H.; Weyn, A.-A.; Lepeltier, E.; Bourgaux, C.; Stella, B., A unique squalenoylated and nonpegylated doxorubicin nanomedicine with systemic long-circulating properties and anticancer activity. *Proc. Natl. Acad. Sci. U.S.A* **2014**, *111* (2), E217-E226.
47. Raveendran, R.; Mullen, K. M.; Wellard, R. M.; Sharma, C. P.; Hoogenboom, R.; Dargaville, T. R., Poly (2-oxazoline) block copolymer nanoparticles for curcumin loading and delivery to cancer cells. *Eur. Polym. J.* **2017**, *93*, 682-694.
48. Lübtow, M. M.; Keßler, L.; Appelt Menzel, A.; Lorson, T.; Gangloff, N.; Kirsch, M.; Dahms, S.; Luxenhofer, R., More Is Sometimes Less: Curcumin and Paclitaxel Formulations Using Poly (2-oxazoline) and Poly (2-oxazine)-Based Amphiphiles Bearing Linear and Branched C9 Side Chains. *Macromol. Biosci* **2018**, *18* (11), 1800155.
49. Liggins, R. T.; Hunter, W.; Burt, H. M., Solid-state characterization of paclitaxel. *J. Pharm. Sci.* **1997**, *86* (12), 1458-1463.
50. Patra, D.; Barakat, C., Synchronous fluorescence spectroscopic study of solvatochromic curcumin dye. *Spectrochim. Acta A* **2011**, *79* (5), 1034-1041.
51. Hoogenboom, R.; Schlaad, H., Thermoresponsive poly (2-oxazoline)s, polypeptoids, and polypeptides. *Polym. Chem.* **2017**, *8* (1), 24-40.
52. Lin, P.; Clash, C.; Pearce, E. M.; Kwei, T.; Aponte, M., Solubility and miscibility of poly (ethyl oxazoline). *J. Polym. Sci. B* **1988**, *26* (3), 603-619.
53. Hoogenboom, R.; Thijs, H. M.; Jochems, M. J.; van Lankvelt, B. M.; Fijten, M. W.; Schubert, U. S., Tuning the LCST of poly (2-oxazoline)s by varying composition and molecular weight: alternatives to poly (N-isopropylacrylamide)? *ChemComm* **2008**, (44), 5758-5760.
54. Li, B.; Konecke, S.; Wegiel, L. A.; Taylor, L. S.; Edgar, K. J., Both solubility and chemical stability of curcumin are enhanced by solid dispersion in cellulose derivative matrices. *Carbohydrate polymers* **2013**, *98* (1), 1108-1116.
55. Paradkar, A.; Ambike, A. A.; Jadhav, B. K.; Mahadik, K., Characterization of curcumin-PVP solid dispersion obtained by spray drying. *Int. J. Pharm.* **2004**, *271* (1-2), 281-286.
56. Bender, J. C. M. E.; Hoogenboom, R.; Van Vliet, P. A. A., Drug delivery system comprising polyoxazoline and a bioactive agent. WO/2011/002285: **2014**.
57. Hernandez-Patlan, D.; Solis-Cruz, B.; Pontin, K. P.; Latorre, J. D.; Baxter, M. F.; Hernandez-Velasco, X.; Merino-Guzman, R.; Méndez-Albores, A.; Hargis, B. M.; Lopez-Arellano, R., Evaluation of a solid dispersion of curcumin with polyvinylpyrrolidone and boric acid against Salmonella Enteritidis infection and intestinal permeability in broiler chickens: A pilot study. *Front. Microbiol.* **2018**, *9*.
58. Grube, M.; Leiske, M. N.; Schubert, U. S.; Nischang, I., POx as an alternative to PEG? A hydrodynamic and light scattering study. *Macromolecules* **2018**, *51* (5), 1905-1916.
59. Morgese, G.; Gombert, Y.; Ramakrishna, S. N.; Benetti, E. M., Mixing Poly (ethylene glycol) and Poly (2-alkyl-2-oxazoline)s Enhances Hydration and Viscoelasticity of Polymer Brushes and Determines Their Nanotribological and Antifouling Properties. *ACS Appl. Mater. Interfaces* **2018**, *10* (48), 41839-41848.
60. Reichardt, C., Solvatochromic dyes as solvent polarity indicators. *Chem. Rev.* **1994**, *94* (8), 2319-2358.
61. Cerón-Carrasco, J. P.; Jacquemin, D.; Laurence, C.; Planchat, A.; Reichardt, C.; Sraïdi, K., Solvent polarity scales: determination of new ET (30) values for 84 organic solvents. *J. Phys. Org. Chem.* **2014**, *27* (6), 512-518.
62. de Graaf, A. J.; Boere, K. W.; Kemmink, J.; Fokkink, R. G.; van Nostrum, C. F.; Rijkers, D. T.; van der Gucht, J.; Wienk, H.; Baldus, M.; Mastrobattista, E., Looped structure of flowerlike micelles revealed by ¹H NMR relaxometry and light scattering. *Langmuir* **2011**, *27* (16), 9843-9848.
63. Guo, X.; Laryea, E.; Wilhelm, M.; Luy, B.; Nirschl, H.; Guthausen, G., Diffusion in Polymer Solutions: Molecular Weight Distribution by PFG-NMR and Relation to SEC. *Macromol. Chem. Phys.* **2017**, *218* (1), 1600440.
64. Shan, J.; Chen, J.; Nuopponen, M.; Tenhu, H., Two phase transitions of poly (N-isopropylacrylamide) brushes bound to gold nanoparticles. *Langmuir* **2004**, *20* (11), 4671-4676.

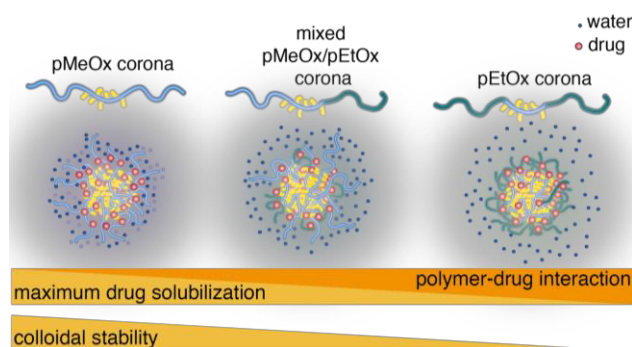


Table of contents artwork

4.3 Structure of Drug-Loaded Micelles

Before revealing the morphology of selected micelles in dependence of the drug loading, the state of the solubilized drug was investigated by fluorescence spectroscopy. Therefore, two isomeric polymer micelles were compared, one which enables ultra-high CUR loadings exceeding 50 wt.% (POzi core with propyl sidechain), while the other only allows a drug loading of 25 wt.% (POx core with butyl sidechain). Taking a closer look at the steady state fluorescence spectra revealed a new, high energy emission band at low CUR loading only for the low capacity, POx based micelles. Whereas the normal CUR emission showed a time-dependent drift in the wavelength of maximum fluorescence ($\lambda_{em,max}$; investigated by fluorescence upconversion), $\lambda_{em,max}$ of the new emission band was more or less unaffected. Therefore, the high-energy emission was attributed to CUR molecules closely embedded in the polymer matrix of the micellar core. As the lifetime of the high energy emission was much lower in the high capacity, POzi based micelle (preventing its detection in steady state), the molecular mobility of CUR seemed to be much more restricted in the low capacity, POx micelle. This is in accordance with the higher overall fluorescence intensity in POx/CUR compared to POzi/CUR, as an increase in fluorescence quantum yield of fluorophores is connected with a decrease of the rate of (non-emitting) internal conversion of excited states. This decrease in the rate of internal conversions can be linked to an increase in the viscosity of the immediate environment, *i.e.* the molecular mobility of the fluorophore. Stronger POx-CUR interactions were also apparent by more strongly suppressed conformational changes of CUR during temperature dependent absorption measurements. Therefore, contradicting suggestions found in the literature, stronger polymer-drug interactions do not always correlate with higher overall drug loading.

Drug Delivery

Ultra-High to Ultra-Low Drug-Loaded Micelles: Probing Host–Guest Interactions by Fluorescence Spectroscopy

Michael M. Lübtow,^[a] Henning Marciniak,^[b] Alexander Schmiedel,^[b] Markus Roos,^[b] Christoph Lambert,^[b] and Robert Luxenhofer^{*,[a]}

Abstract: Polymer micelles are an attractive means to solubilize water insoluble compounds such as drugs. Drug loading, formulations stability and control over drug release are crucial factors for drug-loaded polymer micelles. The interactions between the polymeric host and the guest molecules are considered critical to control these factors but typically barely understood. Here, we compare two isomeric polymer micelles, one of which enables ultra-high curcumin loading exceeding 50 wt.%, while the other allows a drug loading of

only 25 wt.%. In the low capacity micelles, steady-state fluorescence revealed a very unusual feature of curcumin fluorescence, a high energy emission at 510 nm. Time-resolved fluorescence upconversion showed that the fluorescence life time of the corresponding species is too short in the high-capacity micelles, preventing an observable emission in steady-state. Therefore, contrary to common perception, stronger interactions between host and guest can be detrimental to the drug loading in polymer micelles.

Introduction

Curcumin (CUR) is a yellow, natural phenolic compound, which can be isolated from the rhizome of *curcuma longa* (turmeric).^[1] Besides its use as a popular spice and food supplement in major parts of the world, it regained significant scientific attention due to its various biological effects reported in recent years.^[2] These include antioxidant,^[3] cardioprotective,^[4] neuroprotective,^[5] antidiabetic,^[6] anti-inflammatory^[7] and even anti-tumor^[8] activities, which are presumably elicited by modulating various signaling molecules including interleukin-1,^[9] NF- κ B^[10] and many more.^[11] This versatility is most likely due to the chemical reactivity of CUR (making it a non-discriminating pharmaceutically active component), as well as its instability,^[12] as its degradation products display biological properties as well.^[13] However, in combination with its intense color, CUR is also considered a so-called pan-assay interference compound (PAIN) or invalid metabolic panacea (IMP), making it appear to

be active even if it is not.^[14] Apart from this ongoing debate,^[15] the instability and extremely low water solubility ($\log P = 3.28$,^[16] solubility (H₂O) = 0.6 mg L⁻¹^[17]) result in a formidable challenge to formulate and safely deliver CUR,^[18] making it arguably an ideal model to test and challenge drug delivery systems. In recent decades, nanoformulations—that is, drug-loaded particles or micelles in the nanosize range—have been investigated as promising drug delivery vehicles for numerous drugs, including CUR.^[19] Although being able to increase CUR water solubility, most of such nano-systems suffer rather low overall drug-loadings below 20 wt.%.^[20] and overall CUR solubility typically remains low. In the last few years, considerable efforts have been made to understand and utilize specific host–guest interactions such as donor–acceptor interactions,^[21] H-bonding,^[22] complexation^[23] and π – π interactions^[24] to improve drug loading and formulations stability. A simple poly(2-oxazoline) (POx)^[25] based micellar drug delivery system was previously reported featuring unexpected high drug loadings up to almost 50 wt.% paclitaxel (PTX) in combination with very high aqueous concentrations of > 40 g L⁻¹.^[26] Using this ABA-triblock copolymer with two hydrophilic poly(2-methyl-2-oxazoline) (pMeOx) blocks **A** and a modest hydrophobic poly(2-*n*-butyl-2-oxazoline) (pBuOx) block **B** = **A-pBuOx-A** for the encapsulation of CUR, drug loadings up to 25 wt.% could be achieved.^[27] However, a structural isomer of **A-pBuOx-A** with the same hydrophilic pMeOx shell, but a barely hydrophobic poly(2-*n*-propyl-2-oxazine) (pPrOzi) core = **A-pPrOzi-A** enabled extremely high drug loadings up to 54 wt.% with a corresponding CUR solubility of 55 g L⁻¹ (approximately 10⁵ fold increase in water solubility) while PTX loading was mediocre.^[28] Therefore, a simple formal shift of a methylene group from the polymer side chain (BuOx) to the polymer main chain (PrOzi) significantly affected drug compatibilities. Despite detailed mi-

[a] M. M. Lübtow, Prof. Dr. R. Luxenhofer
Functional Polymer Materials, Chair for Advanced Materials Synthesis
Department of Chemistry and Pharmacy and Bavarian Polymer Institute
University of Würzburg, Röntgenring 11, 97070 Würzburg (Germany)
E-mail: robert.luxenhofer@uni-wuerzburg.de

[b] Dr. H. Marciniak, A. Schmiedel, M. Roos, Prof. Dr. C. Lambert
Institute of Organic Chemistry and Center for Nanosystems Chemistry
University of Würzburg, Am Hubland, 97070 Würzburg (Germany)

Supporting information and the ORCID identification number(s) for the author(s) of this article can be found under:
<https://doi.org/10.1002/chem.201902619>.

© 2019 The Authors. Published by Wiley-VCH Verlag GmbH & Co. KGaA.
This is an open access article under the terms of Creative Commons Attribution NonCommercial-NoDerivs License, which permits use and distribution in any medium, provided the original work is properly cited, the use is non-commercial and no modifications or adaptations are made.

cellular analysis using for example, small angle neutron scattering,^[29] we were unable to describe the polymer–drug interactions that explain the ultra-high drug loading and the unexpected specificities on a molecular basis.^[28,30] Therefore, we wondered if we could get a better understanding of the **A-pBuOx-A/CUR** and **A-pPrOzi-A/CUR** formulations by taking a closer look at the very inside of those drug-loaded micelles, namely the drug itself. CUR is highly solvatochromic, that is, its absorption and emission properties strongly depend on its microenvironment^[31] causing Stokes shifts between 2000 and 6000 cm⁻¹ in organic media (Figure 1).^[32] While in aprotic solvents, CUR lacks any specific interactions, hydrogen-bonding is present in protic solvents.^[33] Furthermore, the bis- α,β -unsatu-

ties to enable efficacious therapy. Insights into the interactions between polymer and drug gained from this study may help to improve our understanding of drug delivery systems and eventually improve their design. The relevance of such improved understanding will not be limited to the case of CUR. After all, the molecular interactions, that is, H-bonding, dipole-dipole and Van der Waals interactions will be relevant for most drug delivery systems where the drug is solubilized by physical interactions. However, even if drugs are covalently bound to carrier molecules, these non-covalent interactions must be expected to influence the stability and morphology of drug delivery systems.

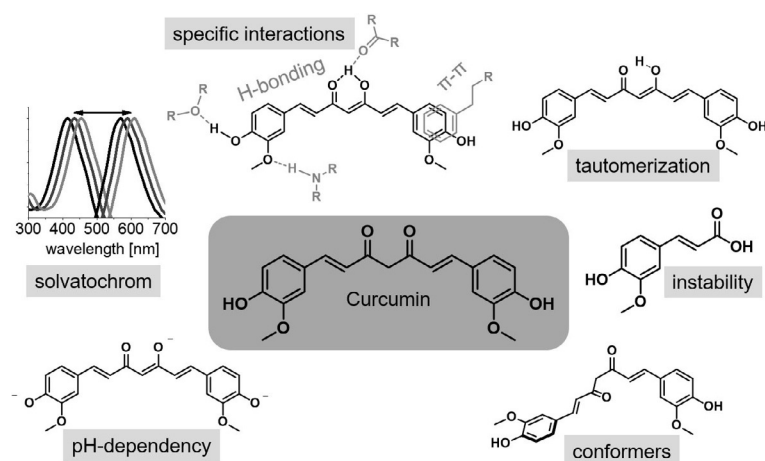


Figure 1. Scheme of the various influences that affect the optical properties of CUR including chemical stability,^[12a,b,13a] solvatochromicity,^[31a,b,33] tautomerization,^[34a,b,35,37,38,42,43] pH,^[18,44] conformers,^[32,34,45] as well as specific interactions.^[33,46,47]

rated β -diketone exhibits keto-enol tautomerism with three main tautomers, each of them with various isomers.^[34] Stabilization of a certain tautomer can be facilitated by addition of surfactants, as shown by the stabilization of the keto-enol tautomer in the presence of anionic^[35] or zwitterionic^[36] surfactants, as well as non-ionic micelles^[37] or nanodiscs.^[38] The effects of the microenvironment on CUR fluorescence in polymer micelles were previously investigated. The stronger the interference of the surrounding surfactant with non-radiative relaxation processes, the longer relaxation times were observed hinting towards stronger intermolecular interactions.^[39] Such dependency of the photorelaxation on the surrounding media is generally well established and has been first described by Schmidt in 1896. With increasing viscosity, internal conversion processes are suppressed. Therefore, fluorescence quantum yields strongly increase.^[40]

Having these observations in mind, we wondered if the photophysical properties of CUR could help us to understand the different compatibilities and loading capacities of **A-pBuOx-A** and **A-pPrOzi-A**. As in modern drug-discovery programs a shift towards ever more hydrophobic compounds with poor water solubility is observed,^[41] a good compatibility between carrier and drug is necessary to achieve sufficiently high drug solubili-

Experimental Section

Reagents

The polymers **A-pBuOx-A** (Me-MeOx₃₅-BuOx₂₀-MeOx₃₅-Pip) and **A-pPrOzi-A** (Me-MeOx₃₅-PrOzi₂₀-MeOx₃₅-PipBoc) were synthesized and described previously.^[27] Curcumin powder from *Curcuma longa* (turmeric) was purchased from *Sigma-Aldrich* and analyzed in-house (curcumin = 79%; demethoxycurcumin = 17%, bisdemethoxycurcumin = 4%; determined by HPLC analysis; no difference in fluorescence upconversion experiments between this curcuminoid mixture and pure CUR (>98%) were observed by Petrich and co-workers^[48]).

Curcumin encapsulation

Curcumin-loaded polymer micelles were prepared by the thin film method.^[26a] Ethanolic polymer (20 g L⁻¹) and curcumin (5.0 g L⁻¹) stock solutions were mixed in desired ratio. After complete removal of the solvent at 55 °C under a mild stream of argon, the films were dried in vacuo (≤ 0.2 mbar) for at least 20 min. Subsequently, preheated (37 °C) H₂O (Millipore) was added to obtain final polymer and curcumin concentrations as mentioned in the main text. To ensure complete solubilization, the solutions were shaken at 55 °C for 15 min at 1250 rpm with a Thermomixer comfort (*Eppendorf AG*, Hamburg, Germany). Non-solubilized curcumin (if any) was removed by centrifugation for 5 min at 9000 rpm with a MIKRO 185 (*Hettich*, Tuttlingen, Germany). Curcumin quantification was performed by UV/Vis absorption of diluted samples in ethanol using a BioTek Eon Microplate Spectrophotometer (*Thermo Fisher Scientific*, MA, USA) using a calibration curve obtained with known amounts of CUR.^[27]

Absorption

Absorption spectra at room temperature were recorded from 200–800 nm with a Cary 50 UV/Vis Spectrophotometer (*Agilent*, Waldbronn, Germany). Neat CUR was dispersed in H₂O (1 mg L⁻¹; 2.7 μ m; undissolved particles were removed by centrifugation) and measured in quartz cuvettes ($d = 10$ mm, QS, *Hellma*, Müllheim, Germany). CUR encapsulated into polymer micelles was measured undiluted (polymer = 10 g L⁻¹, CUR = 0.05–12 g L⁻¹) in quartz cuvettes ($d = 0.01$ mm).

All temperature-dependent measurements were performed in quartz cuvettes ($d = 10$ mm) with a Cary 5000 UV/Vis-NIR (*Agilent*) equipped with a Cary Dual Cell Peltier Accessory (*Agilent*) from 235 nm to 800 nm (bandwidth = 2 nm) at 600 nm min⁻¹. Neat CUR

dissolved in H₂O ($\approx 1 \text{ mg L}^{-1}$) was heated from 15 °C to 80 °C (steps of 5 °C) and cooled from 80 °C to 15 °C (steps of 10 °C). Stock solutions of polymer-formulated CUR ([CUR]=0.1–12 g L⁻¹) were diluted to [CUR] $\approx 0.01 \text{ g L}^{-1}$ (27 μM) and heated from 20 °C to 60 °C (steps of 5 °C) and cooled from 60 °C to 20 °C (steps of 10 °C). At each temperature, the samples were allowed to equilibrate for 10 min.

Steady-state fluorescence

Steady-state emission ($\lambda_{\text{ex}}=420 \text{ nm}$; $\lambda_{\text{em}}=430 \text{ nm}$ –700 nm) and excitation ($\lambda_{\text{em}}=540 \text{ nm}$; $\lambda_{\text{ex}}=300 \text{ nm}$ –530 nm) spectra were recorded in quartz cuvettes ($d=10 \text{ mm}$) with a Spectrofluorometer FP8300 (JASCO, Pfungstadt, Germany) equipped with a F250 recirculating chiller (Julabo, Seelbach, Germany) at a response of 0.1 sec and a scan speed of 1000 nm min⁻¹ (Xe lamp, ex and em bandwidth: 2.5 nm) at 25 °C. Spectra are presented as the average of 3 accumulated measurements of the same sample. Stock solutions of polymer-formulated CUR ([CUR]=0.05–12 g L⁻¹, [polymer]=10 g L⁻¹) were diluted prior to the measurements to [CUR]=0.05 g L⁻¹ (136 μM). For **A-pPrOzi-A/CUR**, detector sensitivity was set to “high”. Due to the stronger fluorescence, detector sensitivity was set to “medium” in the case of **A-pBuOx-A/CUR**. A comparison of the CUR fluorescence at identical instrument settings is given in the supporting information (Figure S5). Fluorescence spectra were smoothed using OriginPro 2015G.

For temperature dependent measurements, neat CUR dissolved in H₂O ($\approx 1 \text{ mg L}^{-1}$) was heated from 15 °C to 80 °C (steps of 5 °C) and re-cooled from 80 °C to 15 °C (steps of 10 °C). Stock solutions of polymer-formulated CUR ([CUR]=0.1–12 g L⁻¹) were diluted to [CUR] $\approx 0.01 \text{ g L}^{-1}$ (27 μM) and heated from 20 °C to 60 °C (steps of 5 °C) and re-cooled from 60 °C to 20 °C (steps of 10 °C). At each temperature, the samples were allowed to equilibrate for 10 min.

Fluorescence upconversion studies

We used a commercial broadband fluorescence upconversion setup (FLUPS)^[49] from LIOPTEC which can simultaneously measure 395–850 nm fluorescence, with an intrinsic resolution of 0.9 nm (303–516 nm upconverted, intrinsic resolution 0.42 nm). The fluorescence is focused onto a BBO crystal (BBO type II with a thickness of 100 μm , theta=40° and phi=0°) where it temporally and spatially overlaps with a gate pulse. The pump pulse, which was used to excite the sample, was guided over a delay stage to provide the temporal shift between gate pulse and fluorescence signal. Except of two lenses all optics were reflective to prevent pulse broadening.

The laser source was a chirped pulse amplification system “Solstice” from Newport-Spectra-Physics. This system provided a fundamental wavelength of 800 nm with 100 fs pulse length and ca. 3.5 mJ pulse energy at a repetition rate of 1 kHz. To operate the FLUPS we split off about 0.75 mJ.

To produce the gate pulse, we used a two-stage optical parametric amplifier (OPA) which was set to $\approx 1300 \text{ nm}$. The pump energy for the OPA was around 0.25 mJ and the output energy was around 0.06 mJ. Afterwards the gate pulse was guided onto the crystal through a compressor comprising only three instead of the usual four prisms. In order to shorten the instrument response function (ca. 150 fs) the 4th prism was removed to retain the tilt of the wavefront and to match it with the wavefront from the fluorescence. The position where the 4th prism is in a typical 4 prism compressor was projected by a lens onto the BBO crystal.

The 400 nm pump pulse was created by frequency doubling of the 800 nm fundamental and guided over a delay line with a maximum delay of 1.5 ns and an intrinsic resolution of 0.5 fs to the sample (1 mm optical path length quartz cuvette).

The upconverted signal is guided over curved mirrors into a fiber coupled polychromator. To detect the signal a CCD-camera with full vertical binning and 2 pix horizontal binning was used (Andor iDus DV420A-BU, backside illuminated, 1024×255 Pixel, 26 μm ×26 μm).

The recorded fluorescence spectra were corrected for group velocity dispersion and photometric accuracy using a set of reference dyes with known spectral distribution.

Anisotropy studies

Polarized steady-state emission spectra ($\lambda_{\text{ex}}=420 \text{ nm}$; $\lambda_{\text{em}}=450 \text{ nm}$ –800 nm) were recorded in quartz cuvettes ($d=10 \text{ mm}$) with a fluorescence lifetime spectrometer FLS980 (Edinburgh Instruments, Livingston, United Kingdom, software F980 version 1.2.2) equipped with a 450 W Xenon lamp, a PMT detector (R928P) and Glan-Thompson polarizers for excitation and emission at 25 °C. Measurements were performed as sequences with parallel and perpendicular orientation of the polarizers. Aqueous solutions were purged with argon for 10 min before the measurement.

Addition of polymer to drug formulations

Dynamics of CUR-loaded polymers were investigated by preparing aqueous stock solutions of **A-pBuOx-A/CUR**=10/4 g L⁻¹ and **A-pPrOzi-A/CUR**=10/12 g L⁻¹. Subsequently, stock solutions were diluted 1/40 (v/v) with H₂O and dry powder of the respective polymer was added to obtain the desired polymer/CUR ratios as mentioned in main text. For fluorescence measurements, all samples with added polymer were diluted to [CUR]=0.03 g L⁻¹.

DLS measurements

DLS measurements were performed on a Zetasizer Nano ZSP (Malvern Panalytical GmbH, Kassel, Germany) with a 633 nm HeNe-laser at 173°. Autocorrelations for each sample were obtained 3 times for 40 seconds and results are presented as mean. Prior to the measurements, all samples (polymer=10 g L⁻¹) were diluted 1/10 (v/v) with H₂O to polymer=1 g L⁻¹ and filtered with 0.45 μm PVDF syringe filters (Carl Roth GmbH + Co. KG, Karlsruhe, Germany). Selected samples were measured unfiltered to exclude any influence of the filtering on particle sizes < 1000 nm. Samples were measured in quartz cuvettes ($d=10 \text{ mm}$, QS, Hellma).

For temperature-dependent DLS measurements, the same regimen as for the photophysical studies was used. Briefly, the samples were heated from 20 °C to 60 °C (steps of 5 °C) and cooled from 60 °C to 20 °C (steps of 10 °C). At each temperature, the samples were allowed to equilibrate for 10 min.

Results and Discussion

When dissolved in H₂O, CUR exhibits two major absorption bands at $\lambda > 300 \text{ nm}$ (Figure S1a in the Supporting Information), attributed to a π - π^* transition of the single feruloyl ($\lambda_{\text{abs}}=345 \text{ nm}$) and a π - π^* transition of the two conjugated feruloyl chromophores ($\lambda_{\text{abs}}=420 \text{ nm}$), as reported in literature.^[36,50] With increasing temperature, the diketo-form is favored^[43] and the band at $\lambda_{\text{abs}}=345 \text{ nm}$ becomes more promi-

ment (Figure S1a). This was found to be partially reversible upon cooling. When excited at $\lambda_{ex}=420$ nm, CUR exhibited a broad fluorescence emission with $\lambda_{em,max}=540$ nm (Figure S1b; corresponding excitation spectra at $\lambda_{em}=540$ nm are shown in Figure S1c). With increasing temperature, the fluorescence intensity decreased and $\lambda_{em,max}$ shifted slightly from 556 nm (20 °C) to 551 nm (80 °C) representing minor changes in the microenvironment of CUR.^[33] Similar to the absorbance, the fluorescence returned to approximately 80% of its initial intensity upon cooling. A 20% degradation of CUR heated to 80 °C is surprisingly low (heating/cooling cycle took approximately 4 h), as much more pronounced degradation even at room temperature is reported in the literature.^[51]

When encapsulated in POx- and POzi-based micelles, major changes in the absorption properties of CUR were observed. It should be noted, that CUR in the POx/POzi micelles was found invariably amorphous, irrespective of the drug loading or the polymer employed.^[28,30a] Irrespective whether CUR was solubilized by POx based **A-pBuOx-A** or the POzi based **A-pPrOzi-A**, the absorption at $\lambda_{abs}=345$ nm completely disappeared (Figure 2a,d) which may be attributed to hydrogen bonding between the keto-enol group of CUR (H-bond donor) and the carbonyl groups of the polymer (H-bond acceptor).^[36] The absorbance linearly increased with increasing CUR content until maximum drug-loading was achieved (12 gL⁻¹ for **A-pPrOzi-A**; 4 gL⁻¹ for **A-pBuOx-A**). The corresponding molar extinction coefficient ϵ of 8.5×10^4 dm³ mol⁻¹ cm⁻¹ ($\epsilon_{MeOH}=6.8 \times 10^4$; $\epsilon_{EtOH}=5.5 \times 10^4$)^[52] demonstrated the strong absorption of CUR

in these aqueous formulations. A pronounced hypsochromic shift of $\lambda_{abs,max}$ from 432 nm ([CUR]=0.05 gL⁻¹) to 414 nm ([CUR]=12 gL⁻¹) was observed in the case of **A-pPrOzi-A** (Figure 2b), which is commonly attributed to a less polar microenvironment of CUR.^[38,43] We posit that particularly at low loading, the micellar core might still contain a certain amount of water, which becomes expelled as more CUR is incorporated. In accordance with this assumption, the size of **A-pPrOzi-A**/CUR micelles which only form in the presence of CUR initially decreased with increasing CUR content ([CUR] \leq 6 gL⁻¹), before they increased in size (Figure 2c), as reported previously.^[28] A similar initial shrinkage was observed for **A-pBuOx-A** loaded with paclitaxel (PTX).^[26b,29] While $\lambda_{abs,max}$ at a certain CUR concentration was the same for both polymers (Figure 2b,e), the size of the CUR-loaded micelles differed significantly. At 0.5 gL⁻¹, only a single species with a hydrodynamic diameter (D_h) of 14 nm was present in the case of **A-pBuOx-A** (Figure 2f, Figure S3). However, with increasing CUR content, a second, much larger population occurred which became dominant at higher CUR-loadings. Hydrodynamic diameters between 550 nm ([CUR]=1 gL⁻¹) and 120 nm ([CUR]=4 gL⁻¹) suggested the presence of larger aggregates such as worm-like micelles or polymersomes and/or indicates colloidal instabilities which cause the **A-pBuOx-A**/CUR formulations to collapse at [CUR] > 4 gL⁻¹.^[27–28] However, we would like to stress that these values should be considered with considerable care, as they were obtained using a rather simplistic equipment (Zeta-sizer Nano ZSP) observing only a single scattering angle. Also,

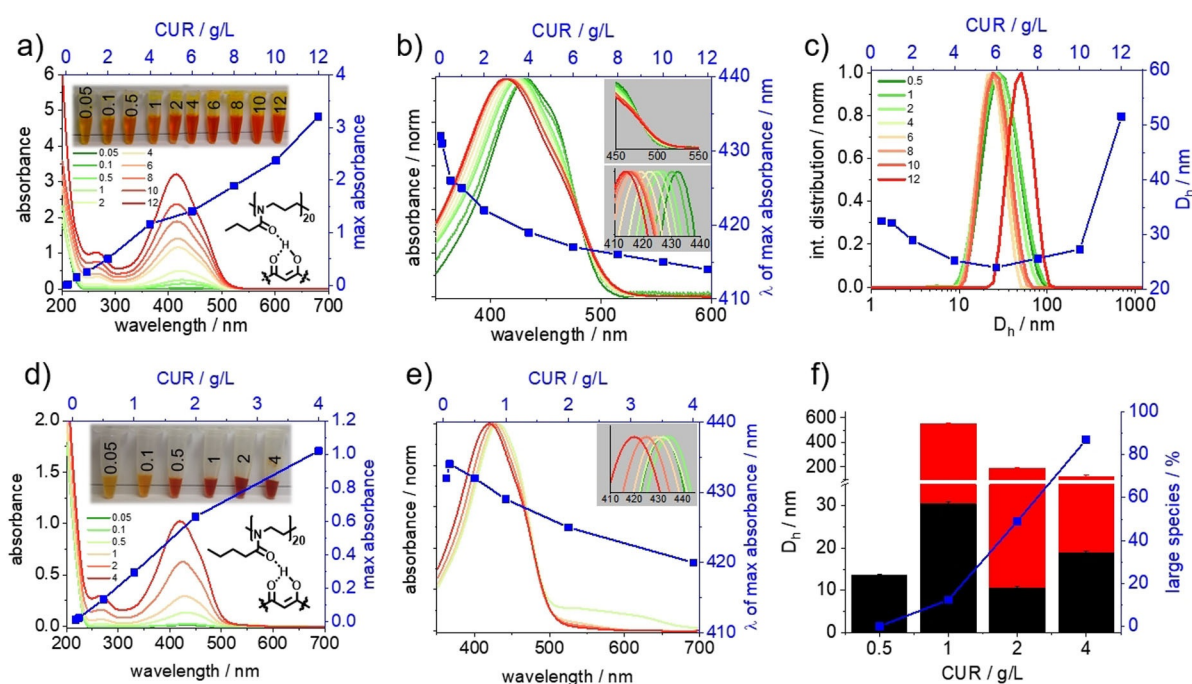


Figure 2. Absorption spectra and DLS measurements of **A-pPrOzi-A**/CUR (a,b,c) and **A-pBuOx-A**/CUR (d,e,f) formulations at a constant polymer concentration of 10 gL⁻¹ and various CUR concentrations (legend in figures). Absorption spectra of **A-pPrOzi-A**/CUR (a) and **A-pBuOx-A** (d) with corresponding maximum absorbances (blue curve; top, right axis). Normalized absorption spectra of **A-pPrOzi-A**/CUR (b) and **A-pBuOx-A**/CUR (e) with corresponding λ_{max} (blue curve; top, right axis). All absorption measurements were conducted undiluted in quartz cuvettes with $d=10$ μ m. c) Size distribution (intensity) of **A-pPrOzi-A**/CUR formulations with corresponding D_h (blue curve; top, right axis). f) D_h of **A-pBuOx-A**/CUR formulations (black bars: smaller species; red bars: larger species; left axis) and corresponding percentage of the larger species (blue curve; right axis). Prior to the DLS measurements, the aqueous samples were diluted 1/10 (v/v) with H₂O to yield a polymer concentration of 1 gL⁻¹.

we should stress that the differences between the sizes and morphologies at higher drug loading are interesting, but most likely only to be attributed to differences in colloidal stabilities of the drug-loaded micelles. This phenomenon is currently under more detailed investigation but bears only little relevance to the subject matter of the current contribution, where we concentrate on the interactions of the micellar core and the incorporated molecules.

Fluorescence measurements were conducted after dilution to $[CUR] = 0.05 \text{ g L}^{-1}$ (0.14 mM) and varying corresponding polymer concentrations. For the sake of comparison with previous spectra, the samples are labeled according to the polymer/CUR (w/w; P/C) ratio, but the reader should bear in mind that the actual CUR concentration was the same in all samples. When excited at $\lambda_{\text{ex}} = 420 \text{ nm}$, the fluorescence intensity decreased with increasing CUR loading, irrespective of the polymer (Figure 3a,c), which is attributed to self-quenching. At $P/C = 10/0.1$, only approx. 0.2 CUR molecules per macromolecule (or approx. 20 hydrophobic repeat units) comprise the micelles. At $P/C = 10/4$, already approx. nine CUR molecules per polymer chain are present, meaning per CUR molecule only two relatively small hydrophobic repeat units with their respective amides are available. Following this, at $P/C = 10/12$, a staggering 27 CUR molecules per polymer chains are incorporated. At this point, the number of CUR molecules outnumbers hydrophobic repeat units in the polymers.

The wavelength of maximum emission ($\lambda_{\text{em,max}}$) increased with increasing CUR content by approximately 15 nm, irrespec-

tive of the polymer (Figure 3b,d). This led to an increased Stokes shift from 5200 cm^{-1} ($P/C = 10/0.05$) to 6600 cm^{-1} ($P/C = 10/12$) in the case of **A-pPrOzi-A** (Figure S4a) and from 5000 cm^{-1} ($P/C = 10/0.05$) to 6000 cm^{-1} ($P/C = 10/4$) in the case of **A-pBuOx-A** (Figure S4b). In aprotic as well as protic solvents, the Stokes shift of CUR generally increases with increasing solvent polarity.^[33,53] In accordance with the Lippert–Mataga equation, this was correlated to solvent polarity. In our case, especially at high CUR loadings, CUR itself would dominate the surrounding media, that is, most CUR molecules are surrounded by other CUR molecules with some polymer chains in between preventing crystallization. Steady-state fluorescence anisotropy studies showed a significant difference between the two micelle types. With increasing CUR content, CUR anisotropy r_0 decreased in both polymeric systems. However, while for **A-pPrOzi-A/CUR** r_0 decreased gradually, **A-pBuOx-A/CUR** exhibited a steep decay from $[CUR] = 0.05 \text{ g L}^{-1}$ to 1 g L^{-1} (Figure S6). This steep decrease in anisotropy coincided well with the occurrence of the second, much larger aggregates observed by DLS (Figure 2f). Such decrease in anisotropy is often attributed to an increased molecular flexibility of the fluorophore. However, in the present system, it seems more reasonable to assume energy transfer between different CUR molecules within the micelles, which is well known to depolarize fluorescence.

A closer look at the shape of the emission spectra revealed two types of emissions for **A-pBuOx-A/CUR** (Figure 3d). Besides the emission at $\lambda_{\text{em}} \approx 550 \text{ nm}$, a second, higher energy

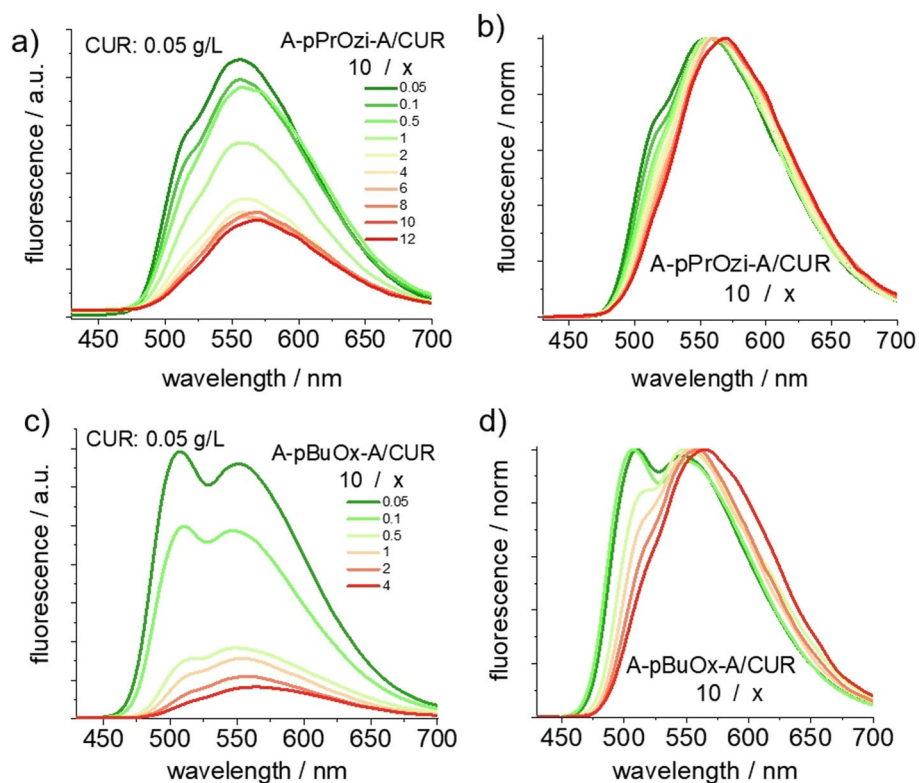


Figure 3. Fluorescence spectra of **A-pPrOzi-A/CUR** (a) and **A-pBuOx-A/CUR** (c) at $c(\text{CUR}) = 0.05 \text{ g L}^{-1}$ and different polymer/CUR ratios, measured in quartz cuvettes with $d = 10 \text{ mm}$. Normalized emission spectra of **A-pPrOzi-A/CUR** (b) and **A-pBuOx-A/CUR** (d).

emission at $\lambda_{em} \approx 510$ nm is visible. This emission became dominant at very low drug loadings ($P/C \geq 10/0.1$). In contrast, for **A-pPrOzi-A**, only a small shoulder appeared in this region (Figure 3b). The keto-enol form of CUR undergoes a fast intramolecular proton transfer in the excited state (ESIPT).^[45] One may be tempted to argue that one of the emissions at $\lambda_{em} \approx 550$ nm and 510 nm derives from the emission of the proton-transferred isomer, and the other one from the non-transferred geometry.^[54] However, in that case energetically different S_1 and S_0 states of the different isomers are a prerequisite. Although otherwise stated in literature,^[55] this is not the case for CUR due to its highly symmetric structure. Banerjee et al.^[56] also observed two emission bands ($\lambda_{em} = 461$ nm and 485 nm) for CUR encapsulated in the polar core of reverse micelles dissolved in *n*-heptane. With increasing amount of polar solvents incorporated into the micellar core, the high-energy emission vanished. This was attributed to the transition of CUR from the bulk *n*-heptane phase ($\lambda_{em} = 461$ nm) to the micellar core ($\lambda_{em} = 485$ nm). However, in the present case, the concentration of CUR in the bulk phase water is negligible (water solubility of [CUR] < 1 mg L⁻¹[17]). As we kept the absolute concentration of CUR the same in all samples ([CUR] = 50 mg L⁻¹), the polymer concentration was the only significant variable. As the high-energy emission at $\lambda_{em} \approx 510$ nm occurred only at high P/C ratios it seems reasonable that this emission band is due to specific polymer-CUR interactions with a corresponding stabilized S_1 -state. At P/C = 10/0.05, approximately 9 polymer chains or 170 repeat units of the hydrophobic core are present per CUR molecule. At such high P/C ratios, the interactions between CUR and the excess polymer should dominate and one can expect that individual CUR molecules only interact with the polymer repeat units, presumably via H-bonding. In contrast, at P/C = 10/4, only 2 repeat units of the hydrophobic block are available per CUR molecule and interactions between individual CUR molecules appear to dominate the spectroscopic behavior. Most interestingly, **A-pPrOzi-A**, enabling much higher CUR-loadings than **A-pBuOx-A**, did only exhibit a small shoulder at the high-energy emission (Figure 3b). In addition, the measured fluorescence intensity of **A-pBuOx-A/CUR** was much higher compared to the fluorescence intensity measured in the **A-pPrOzi-A/CUR** system at P/C > 10/2 (Figure S5).

Considering that the absorbance at identical CUR content is the same, the higher fluorescence intensity must be correlated with a higher fluorescence quantum yield. Such increase in fluorescence quantum yield of fluorophores is connected with a decrease of the rate of (non-emitting) internal conversion of excited states.^[40b] This decrease in the rate of internal conversions may be attributed to an increase in the viscosity of the immediate environment, that is, the molecular mobility of the fluorophore.^[40a] In the present case, this may be interpreted as measure of the interaction between the fluorophore and the host polymer in combination with the flexibility of the polymer chain surrounding the fluorophore. The inherent flexibility of **pPrOzi** is higher compared to that of **pBuOx** due to the additional methylene group in the polymer backbone.^[57] In the case of reverse micelles, the fluorescence intensity of CUR was increased by modulation of the non-radiative rates associated

with excited-state intermolecular hydrogen bonding between CUR and polar solvents incorporated into the micellar core.^[56] Similarly, solvents that interact with the enol (acting as H-donor) or with the ketone (acting as H-acceptor) of CUR can interfere with internal conversion relaxation, for example, prolonging the fluorescence lifetime.^[56] To investigate this in more detail, fluorescence upconversion experiments were performed at low drug loading (10/0.5 and 10/0.05), as under these conditions considerable differences in the steady-state spectra were observed.

Here, we excited the samples at 400 nm and detected the time resolved emission spectra by focusing the fluorescence onto a BBO nonlinear optical crystal and by upconverting the fluorescence with a time delayed gate pulse at 1320 nm. The resulting time resolved spectra were corrected for chirp and photometric intensity (Figure 4). For the analysis, we integrated spectral ranges at 488–526 nm and at 540–588 nm which correspond to the two fluorescence peaks observed in the steady state spectra (Figure 3). However, because the steady state fluorescence intensity is the integral of the intensity vs. time and depends on both, the fluorescence lifetime of the respective state as well as the transition probability between the excited and the ground-state, the time resolved spectra look different from the steady state spectra. Thus, for the analysis, the decay in the selected spectral regions was fitted by multiple exponential functions also considering the instrument response function (for fitting parameters, please see Table S1). Comparing the high (540–588 nm) and low (488–526 nm) wavelength emission ranges immediately reveals that all samples decay significantly faster at shorter wavelengths (see Figure 4a vs. b and the amplitude average lifetimes^[59] which are proportional to the steady state emission intensity in the last column of Table S1). In the time-resolved fluorescence spectra the different decay rates of different wavelength regions appears as a more or less continuous shift of the emission maximum, particularly at higher P/C ratios (10/0.5) (Figure 4d,f). However, a closer look at the spectra at lower P/C ratios (10/0.05) shows that the peak maximum of the low wavelength region is in fact almost constant and it is the ratio of the two decay regions which produced this apparent shift. At both emission ranges, **A-pBuOx-A** based formulations exhibited longer fluorescence lifetimes than the corresponding **A-pPrOzi-A** based CUR formulations (Figure 4a,b and Table S1). The difference between the two polymers was more pronounced at low CUR loadings. For both polymers, the higher loaded micelles exhibit shorter lifetimes. Both observations are in accordance with the higher fluorescence intensities of the polymer/CUR formulations at low CUR loadings in steady state emission measurements (Figure 3a,c). The life time measurements also clearly show that the difference in steady state fluorescence between **A-pPrOzi-A** and **A-pBuOx-A** cannot be attributed to different species of the fluorophores, but only to different fluorescence lifetimes of the same species. The influence of the polymer/CUR ratio on fluorescence quantum yields was not further investigated, but the correlation of fluorescence quantum yields and local viscosities are well established.^[40a,c] The high-energy emission can therefore be attribut-

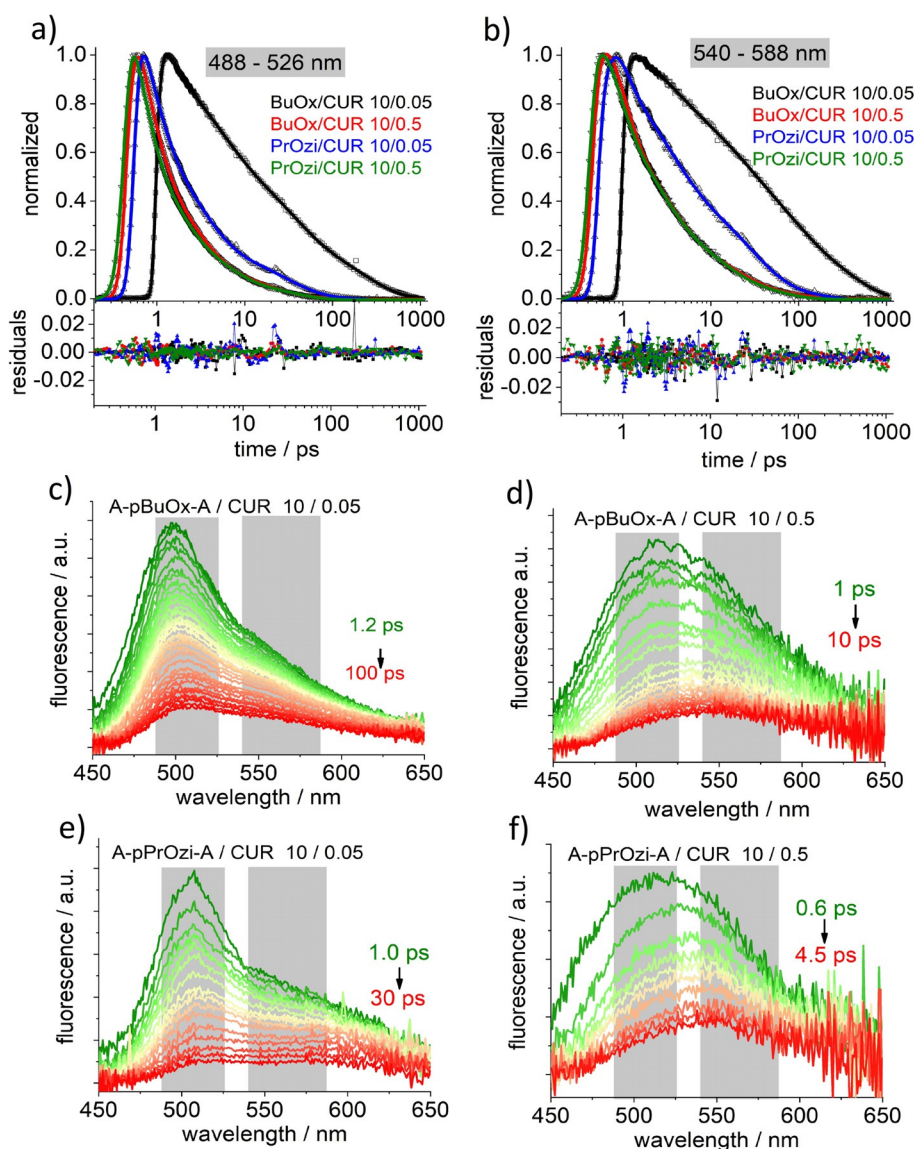


Figure 4. Fluorescence upconversion decays of **A-pBuOx-A/CUR** = 10/0.05 (black) & 10/0.5 (red) and **A-pPrOzi-A/CUR** = 10/0.05 (blue) and 10/0.5 (green) at a) 488–526 nm and b) 540–588 nm. Decays were fitted with a multi-exponential function exhibiting 5 independent lifetimes. Time resolved emission spectra at different delay times of **A-pBuOx-A/CUR** = 10/0.05 (c) and 10/0.5 (d) and **A-pPrOzi-A/CUR** = 10/0.05 (e) and 10/0.5 (f). Before the measurements, all samples were diluted with H₂O to a constant CUR concentration of 0.05 g L⁻¹ and measured in quartz cuvettes (*d* = 10 mm).

ed to CUR molecules closely embedded in the polymer matrix of the micellar core.

To get a better understanding about the dynamics of the micellar CUR formulations, dry powder of **A-pPrOzi-A** or **A-pBuOx-A** was added to aqueous formulations of **A-pPrOzi-A/CUR** = 10/12 and **A-pBuOx-A/CUR** = 10/4, respectively. Therefore, the CUR concentration in all samples was kept essentially constant, whereas the P/C ratio increased with increasing amount of polymer added. Both, $\lambda_{\text{abs,max}}$ (Figure S7 a,d) as well as $\lambda_{\text{em,max}}$ (Figure S7 b,e) were only dependent on the P/C ratio, irrespective if obtained by addition of polymer or by direct formulation. This illustrates the highly dynamic structure of the CUR-loaded micelles (Stokes shifts are shown in Figure S8). Most interestingly, the high-energy emission at $\lambda_{\text{em}} = 510$ nm also occurred when additional **A-pBuOx-A** was added to the

A-pBuOx/CUR = 10/4 g L⁻¹ formulation (Figure S7 e). This was accompanied with a strong increase in fluorescence intensity at high P/C ratios as observed for the formulated samples (Figure 3c). The increase in emission at high **A-pBuOx-A/CUR** ratios was also clearly visible after exciting the samples with a conventional UV/Vis lamp at $\lambda_{\text{ex}} = 365$ nm (Figure S7 c,f). That the photophysical properties were determined predominantly by the P/C ratio was corroborated by comparing formulated samples at different polymer and CUR concentrations, but constant P/C ratio (Figure S9). One may argue that such fast exchange dynamics may be detrimental for the envisioned application. That may be the case, in particular if drug targeting is envisioned. However, even though drug targeting using nanoparticles (not antibodies) is a concept that has been heavily investigated for decades, it produced little if any products that

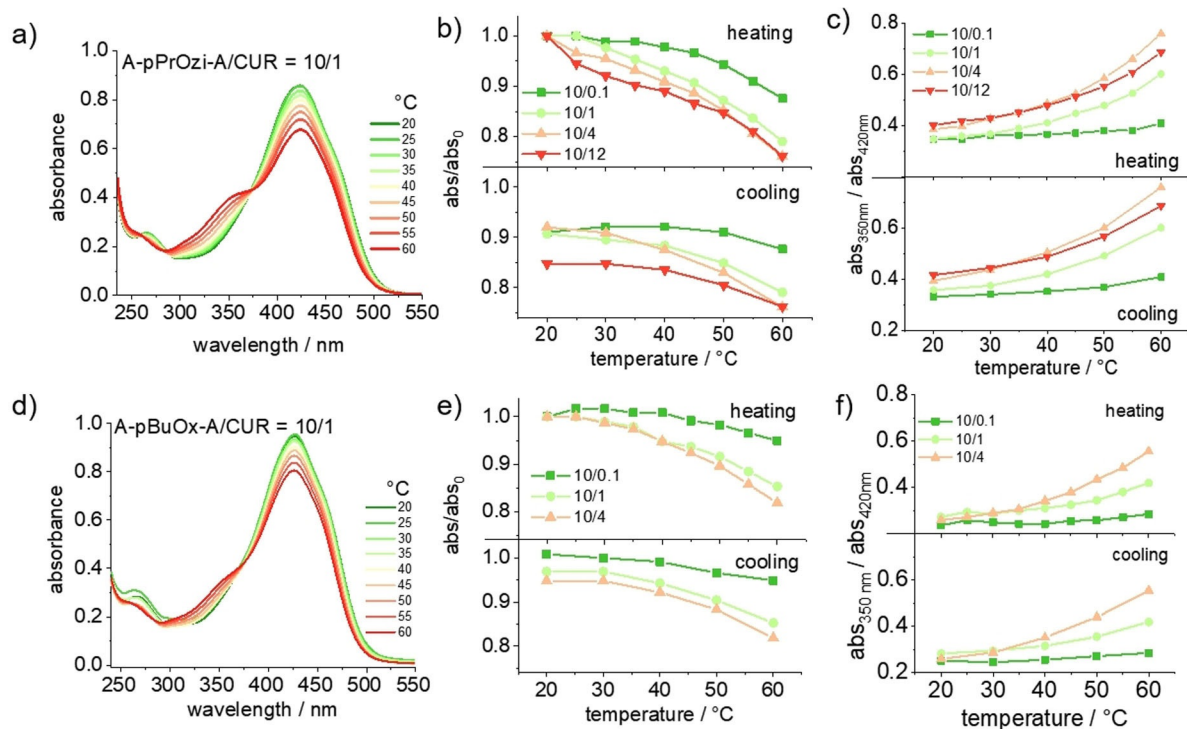


Figure 5. Temperature dependent, normalized absorption spectra of a) **A-pPrOzi-A/CUR** = 10/1 and b) **A-pBuOx-A/CUR** = 10/1 g L^{-1} heated from 20 °C to 60 °C. Ratio of the maximum absorbance at a respective temperature and the initial absorbance at 20 °C (abs/abs_0) during heating (red curve; top, right axis) and cooling (blue curve; top, right axis). Ratios of (b,e) abs/abs_0 and (c,f) $\text{abs}_{350\text{nm}}/\text{abs}_{420\text{nm}}$ for (b,c) **A-pPrOzi-A/CUR** = 10/0.1; 10/1; 10/4; 10/12 g L^{-1} and (e,f) **A-pBuOx-A/CUR** = 10/0.1; 10/1; 10/4 g L^{-1} while heating (top curves) and cooling (bottom curves). Prior to the measurements, all samples were diluted with H_2O to a similar CUR concentration of $\approx 0.01 \text{ g L}^{-1}$ and measured in quartz cuvettes with $d = 10 \text{ mm}$.

benefit patients, while drug solubilization/formulation is a trusted method that has proven its value time and again, including employing the **A-pBuOx-A** platform discussed here.^[60]

Temperature-dependent measurements give additional insights into the stability of the two formulations (Figure 5; for absorbance spectra at different P/C ratios, the reader is referred to Figure S10 for **A-pPrOzi-A/CUR** and Figure S11 for **A-pBuOx-A/CUR**). With increasing temperature, the absorbance at $\lambda_{\text{abs}} \approx 420 \text{ nm}$ decreased and a new absorption at $\lambda_{\text{abs}} = 355 \text{ nm}$ occurred, resembling the absorption band of the diketo tautomer of CUR, accompanied by an isosbestic point at $\lambda_{\text{abs}} \approx 370 \text{ nm}$ (Figure 5a,d). The new band became more prominent at elevated temperatures for all samples (Figure 5c,f). The tautomerization led to a distinct change in color (Figure S12) and is more prominent at higher P/C ratio (Figure 5c,f). This further corroborates the hypothesis that the intermolecular hydrogen bonds between polymer and CUR weaken with increasing CUR content, due to fewer polymer amide groups available per CUR molecule as well as an increasingly disordered and dynamic situation in the micelles. Moreover, the keto-enol/diketo ratio at a certain CUR concentration and temperature was higher for **A-pBuOx-A** than for **A-pPrOzi-A** based formulations, also corroborating stronger **A-pBuOx-A/CUR** interactions. Furthermore, in the case of **A-pBuOx-A**, the shift in the tautomeric ratio was completely reversible upon cooling, indicating a higher thermal stability of the **A-pBuOx-A/CUR** micelles (Figure 5c,f). Most interestingly,

for P/C = 10/0.1, only a small shoulder occurred at $\lambda_{\text{abs}} \approx 355 \text{ nm}$, irrespective of the polymer structure. Although not detectable in steady state, this fits well to the results obtained from the fluorescence up-conversion studies, in which both polymers exhibited a high-energy emission indicative for strong polymer-CUR interactions only at low CUR content.

Interesting to note, the steady-state fluorescence intensity of **A-pPrOzi-A/CUR** (Figure S13a,b) as well as **A-pBuOx-A/CUR** (Figure S14a,b) increased with increasing temperature at low loading (P/C = 10/0.1). The increase was more pronounced for **A-pBuOx-A/CUR** (Figure S14). Such increase is unexpected, as the fluorescence quantum yields (and fluorescence intensities) are expected to decrease with increasing temperature (i.e. decreasing viscosity), as internal conversion rates increase with temperature.^[40c] We hypothesize that at such low CUR loadings, water molecules present at low temperature are excluded from the micellar core with increasing temperature, which increases the local viscosity (i.e. decreases mobility) despite the increased temperature. This is supported by the more pronounced increase of the high-energy emission at $\lambda_{\text{em}} = 510$ in the case of **A-pBuOx-A** which is attributed to CUR molecules closely embedded in the polymer matrix of the micellar core. Interestingly at lower P/C ratios, the fluorescence increased only in the case of **A-pBuOx-A**, whereas with **A-pPrOzi-A** a decrease in fluorescence intensity occurred. Again, this highlights the highly unusual character of the **A-pBuOx-A/CUR** nanoformulations. The hypothesis of water exclusion at low P/C ratios

in the case of **A-pBuOx-A** is further corroborated by the temperature-dependence with respect to the respective micellar morphology. While **A-pPrOzi-A** based CUR-formulations were more or less unaffected by the heating/cooling cycle (Figure S15 a; S16), **A-pBuOx-A/CUR** exhibited a much stronger, temperature-dependent behavior (Figure S15 b,c and S17).

Conclusions

Curcumin (CUR) is one of the most intensively studied bioactive natural compounds even though its viability as an active pharmaceutical ingredient is heavily debated.^[14–15] Key limiting factors to study and use CUR are its low solubility and stability. We studied micellar CUR nanoformulations of the two amphiphiles **A-pPrOzi-A** and **A-pBuOx-A**, which are constitutional isomers but exhibit very different CUR loading. While **A-pPrOzi-A** gives access to CUR formulations with drug loadings exceeding 50 wt.%, **A-pBuOx-A** micelles cannot be loaded beyond 25 wt.%. Since CUR is solvatochromic, we probed the interactions between CUR and the polymers using spectroscopic methods. With increasing drug loading, the absorbance of CUR showed a profound hypsochromic shift and steady-state fluorescence intensity decreased. At low drug loading, a pronounced emission was observed at 510 nm in **A-pBuOx-A** formulations, which was essentially absent in the case of **A-pPrOzi-A/CUR**. To the best of our knowledge, **A-pBuOx-A** is the first non-ionic, polymeric system revealing two steady-state emission bands for encapsulated CUR. Fluorescence up-conversion experiments revealed that the species responsible for the emission at 510 nm is in fact present in both micelles, but decays much faster in the case of **A-pPrOzi-A**. This makes the emission virtually non-observable in steady-state spectroscopy. We attribute this observation to a more restricted molecular mobility of CUR within the hydrophobic core of **A-pBuOx-A** at very low drug loading. In contrast, CUR embedded in **A-pPrOzi-A** micelles retains more flexibility, probably in part due to the higher polymer flexibility. The stronger interactions between CUR and **A-pBuOx-A** were corroborated by temperature dependent measurements. We find it particularly intriguing that the polymer with the weaker interaction allows much higher drug loading.

Despite the very high loading, the drug loaded micelles exchanged rapidly with free polymer or empty micelles in solution, as was evidenced by the reversal of the hypsochromic shifts in the absorption as well as the appearance of the emission at 510 nm in the case of **A-pBuOx-A**.

Even though employing only the model compound CUR in the present contribution, it is clear that similar mechanisms for drug loading and molecular interaction are relevant for many other drug molecules and probably other polymer platforms. Indeed, we have observed similar specificities with respect to drug loading and polymer/drug structure with several other drugs, including different taxanes,^[61] antiretroviral efavirenz,^[62] and mitotane,^[63] used in treatment for adrenocortical carcinoma. Our results clearly show that the concept of a hydrophobic polymer that solubilizes a hydrophobic cargo is much too simplistic and a much more detailed look into the interactions be-

tween polymer micelle and cargo is necessary. In fact, we provide conclusive evidence that stronger interaction between drug and polymer must not correlate with higher drug loading or the stability of nanoformulations and corroborate that smallest structural changes can significantly affect the interactions between drug and polymer, which must be considered in developing advanced drug nanoformulations.

Acknowledgements

This work was supported by the Deutsche Forschungsgemeinschaft (Project number 398461692, awarded to R.L.). Moreover, M.M.L. would like to thank the Evonik Foundation for providing a doctoral fellowship. We would also like to thank Christian May for technical support. C.L. is grateful to the Bavarian Ministry of Education, Culture, Research, and the Fine Arts for support within the SolTech consortium. Moreover, we thank Prof. Ann-Christin Pöppler for valuable discussions.

Conflict of interest

M.M.L. and R.L. are listed as inventors on a patent application pertinent to materials discussed in this contribution.

Keywords: curcumin · drug delivery · fluorescence · poly(2-oxazine) · poly(2-oxazoline) · polymer–drug interaction · upconversion

- [1] a) T. Kita, S. Imai, H. Sawada, H. Kumagai, H. Seto, *Biosci. Biotechnol. Biochem.* **2008**, *72*, 1789–1798; b) T. Esatbeyoglu, P. Huebbe, I. M. A. Ernst, D. Chin, A. E. Wagner, G. Rimbach, *Angew. Chem. Int. Ed.* **2012**, *51*, 5308–5332; *Angew. Chem.* **2012**, *124*, 5402–5427.
- [2] S. C. Gupta, S. Patchva, W. Koh, B. B. Aggarwal, *Clin. Exp. Pharmacol. Physiol.* **2012**, *39*, 283–299.
- [3] T. Ak, İ. Gülçin, *Chem.-Biol. Interact.* **2008**, *174*, 27–37.
- [4] S. Miriyala, M. Panchatcharam, P. Rengarajulu, in *The Molecular Targets and Therapeutic Uses of Curcumin in Health and Disease*, Springer, **2007**, pp. 359–377.
- [5] G. M. Cole, B. Teter, S. A. Frautschy, *Adv. Exp. Med. Biol.* **2007**, *595*, 197–212.
- [6] D.-w. Zhang, M. Fu, S.-H. Gao, J.-L. Liu, *Evid.-Based Complementary Altern. Med.* **2013**, 636053.
- [7] J. S. Jurenka, *Altern. Med. Rev.* **2009**, *14*, 141–153.
- [8] X. Yang, Z. Li, N. Wang, L. Li, L. Song, T. He, L. Sun, Z. Wang, Q. Wu, N. Luo, C. Yi, C. Gong, *Sci. Rep.* **2015**, *5*, 10322.
- [9] N. Jurrmann, R. Brigelius-Flohé, G.-F. Böhl, *J. Nutr.* **2005**, *135*, 1859–1864.
- [10] J. U. Marquardt, L. Gomez-Quiroz, L. O. Arreguin Camacho, F. Pinna, Y.-H. Lee, M. Kitade, M. P. Domínguez, D. Castven, K. Breuhahn, E. A. Conner, P. R. Galle, J. B. Andersen, V. M. Factor, S. S. Thorgeirsson, *J. Hepatol.* **2015**, *63*, 661–669.
- [11] a) A. Goel, C. R. Boland, D. P. Chauhan, *Cancer Lett.* **2001**, *172*, 111–118; b) A. L. Clutterbuck, D. Allaway, P. Harris, A. Mobasheri, *F1000Research* **2013**, *2*, 147.
- [12] a) C. Schneider, O. N. Gordon, R. L. Edwards, P. B. Luis, *J. Agric. Food Chem.* **2015**, *63*, 7606–7614; b) O. N. Gordon, P. B. Luis, H. O. Sintim, C. Schneider, *J. Biol. Chem.* **2015**, *290*, 4817–4828.
- [13] a) L. Shen, H.-F. Ji, *Trends Mol. Med.* **2012**, *18*, 138–144; b) K. Lirdprapa-mongkol, H. Sakurai, S. Suzuki, K. Koizumi, O. Prangsaengtong, A. Viriyaroy, S. Ruchirawat, J. Svasti, I. Saiki, *In Vivo* **2010**, *24*, 501–506.
- [14] M. A. W. Jonathan Baell, *Nature* **2014**, *513*, 481–483.
- [15] M. Heger, *Nature* **2017**, *543*, 40–40.

- [16] Y. B. Pawar, B. Munjal, S. Arora, M. Karwa, G. Kohli, J. K. Paliwal, A. K. Bansal, *Pharmaceutics* **2012**, *4*, 517–530.
- [17] B. T. Kurien, A. Singh, H. Matsumoto, R. H. Scofield, *Assay Drug Dev. Technol.* **2007**, *5*, 567–576.
- [18] P. Anand, A. B. Kunnumakkara, R. A. Newman, B. B. Aggarwal, *Mol. Pharm.* **2007**, *4*, 807–818.
- [19] J. Jeevanandam, Y. S. Chan, M. K. Danquah, *Biochimie* **2016**, *128*–129, 99–112.
- [20] a) O. Naksuriya, S. Okonogi, R. M. Schiffelers, W. E. Hennink, *Biomaterials* **2014**, *35*, 3365–3383; b) W.-H. Lee, C.-Y. Loo, P. M. Young, D. Traini, R. S. Mason, R. Rohanizadeh, *Expert Opin. Drug Delivery* **2014**, *11*, 1183–1201; c) S. Datta, A. Jutková, P. Šrámková, L. Lenkavská, V. Huntošová, D. Chorvát, P. Miškovský, D. Jancura, J. Kronek, *Biomacromolecules* **2018**, *19*, 2459–2471.
- [21] S. Lv, Y. Wu, K. Cai, H. He, Y. Li, M. Lan, X. Chen, J. Cheng, L. Yin, *J. Am. Chem. Soc.* **2018**, *140*, 1235–1238.
- [22] S. Wiczorek, A. Dallmann, Z. Kochovski, H. G. Börner, *J. Am. Chem. Soc.* **2016**, *138*, 9349–9352.
- [23] a) Y. Li, Q. Zou, C. Yuan, S. Li, R. Xing, X. Yan, *Angew. Chem. Int. Ed.* **2018**, *57*, 17084–17088; *Angew. Chem.* **2018**, *130*, 17330–17334; b) K. Mitra, S. Gautam, P. Kondaiah, A. R. Chakravarty, *Angew. Chem. Int. Ed.* **2015**, *54*, 13989–13993; *Angew. Chem.* **2015**, *127*, 14195–14199.
- [24] Y. Shi, M. J. van Steenberg, E. A. Teunissen, L. S. Novo, S. Gradmann, M. Baldus, C. F. van Nostrum, W. E. Hennink, *Biomacromolecules* **2013**, *14*, 1826–1837.
- [25] T. Lorson, M. M. Lübtow, E. Wegener, M. S. Haider, S. Borova, D. Nahm, R. Jordan, M. Sokolski-Papkov, A. V. Kabanov, R. Luxenhofer, *Biomaterials* **2018**, *178*, 204–280.
- [26] a) R. Luxenhofer, A. Schulz, C. Roques, S. Li, T. K. Bronich, E. V. Batrakova, R. Jordan, A. V. Kabanov, *Biomaterials* **2010**, *31*, 4972–4979; b) A. Schulz, S. Jaksch, R. Schubel, E. Wegener, Z. Di, Y. Han, A. Meister, J. Kressler, A. V. Kabanov, R. Luxenhofer, C. M. Papadakis, R. Jordan, *ACS Nano* **2014**, *8*, 2686–2696; c) Z. He, X. Wan, A. Schulz, H. Bludau, M. A. Dobrovolskaia, S. T. Stern, S. A. Montgomery, H. Yuan, Z. Li, D. Alakhova, M. Sokolsky, D. B. Darr, C. M. Perou, R. Jordan, R. Luxenhofer, A. V. Kabanov, *Biomaterials* **2016**, *101*, 296–309.
- [27] M. M. Lübtow, L. Hahn, M. S. Haider, R. Luxenhofer, *J. Am. Chem. Soc.* **2017**, *139*, 10980–10983.
- [28] M. M. Lübtow, L. C. Nelke, J. Seifert, J. Kühnemundt, G. Sahay, G. Dandekar, S. Nietzer, R. Luxenhofer, *J. Controlled Release* **2019**, *303*, 162–180.
- [29] S. Jaksch, A. Schulz, Z. Di, R. Luxenhofer, R. Jordan, C. M. Papadakis, *Macromol. Chem. Phys.* **2016**, *217*, 1448–1456.
- [30] a) M. M. Lübtow, L. Keßler, A. Appelt-Menzel, T. Lorson, N. Gangloff, M. Kirsch, S. Dahms, R. Luxenhofer, *Macromol. Biosci.* **2018**, *18*, 1800155; b) L. Hahn, M. M. Lübtow, T. Lorson, F. Schmitt, A. Appelt-Menzel, R. Schobert, R. Luxenhofer, *Biomacromolecules* **2018**, *19*, 3119–3128.
- [31] a) C. Párkányi, M. R. Stem-Beren, O. R. Martínez, J.-J. Aaron, M. Bulaceanu-MacNair, A. F. Arrieta, *Spectrochim. Acta Part A* **2004**, *60*, 1805–1810; b) S. N. Margar, N. Sekar, *Mol. Phys.* **2016**, *114*, 1867–1879.
- [32] K. I. Priyadarsini, *J. Photochem. Photobiol. C* **2009**, *10*, 81–95.
- [33] D. Patra, C. Barakat, *Spectrochim. Acta Part A* **2011**, *79*, 1034–1041.
- [34] a) T. M. Kolev, E. A. Velcheva, B. A. Stamboliyska, M. Spittler, *Int. J. Quantum Chem.* **2005**, *102*, 1069–1079; b) E. Benassi, F. Spagnolo, *Theor. Chem. Acc.* **2009**, *124*, 235–250.
- [35] A. Dutta, B. Boruah, A. K. Manna, B. Gohain, P. M. Saikia, R. K. Dutta, *Spectrochim. Acta Part A* **2013**, *104*, 150–157.
- [36] C. Banerjee, S. Ghosh, S. Mandal, J. Kuchlyan, N. Kundu, N. Sarkar, *J. Phys. Chem. B* **2014**, *118*, 3669–3681.
- [37] S. Ghosh, J. Kuchlyan, D. Banik, N. Kundu, A. Roy, C. Banerjee, N. Sarkar, *J. Phys. Chem. B* **2014**, *118*, 11437–11448.
- [38] M. Ghosh, A. T. K. Singh, W. Xu, T. Sulchek, L. I. Gordon, R. O. Ryan, *Nanomedicine* **2011**, *7*, 162–167.
- [39] a) R. Adhikary, P. J. Carlson, T. W. Kee, J. W. Petrich, *J. Phys. Chem. B* **2010**, *114*, 2997–3004; b) C. Banerjee, S. Maiti, M. Mustafi, J. Kuchlyan, D. Banik, N. Kundu, D. Dhara, N. Sarkar, *Langmuir* **2014**, *30*, 10834–10844.
- [40] a) G. Oster, Y. Nishijima, *J. Am. Chem. Soc.* **1956**, *78*, 1581–1584; b) S. Sharafy, K. A. Muszkat, *J. Am. Chem. Soc.* **1971**, *93*, 4119–4125; c) T. Förster, G. Hoffman, *Z. Phys. Chem.* **1971**, *75*, 63–76; d) G. C. Schmidt, *Annalen der Physik* **1896**, *294*, 103–130; e) G. C. Schmidt, *Annalen der Physik* **1921**, *370*, 247–256; f) J. Stark, F. Lipp, *Z. Phys. Chem.* **1914**, *86U*, 36–50.
- [41] J. Zuegg, M. A. Cooper, *Curr. Top. Med. Chem.* **2012**, *12*, 1500–1513.
- [42] Y. Manolova, V. Deneva, L. Antonov, E. Drakalska, D. Momekova, N. Lambov, *Spectrochim. Acta Part A* **2014**, *132*, 815–820.
- [43] Z. Moussa, M. Chebl, D. Patra, *J. Photochem. Photobiol. B* **2017**, *173*, 307–317.
- [44] M. Bernabé-Pineda, M. T. Ramírez-Silva, M. Romero-Romo, E. González-Vergara, A. Rojas-Hernández, *Spectrochim. Acta Part A* **2004**, *60*, 1091–1097.
- [45] R. Ghosh, J. A. Mondal, D. K. Palit, *J. Phys. Chem. B* **2010**, *114*, 12129–12143.
- [46] K. Muthoosamy, I. B. Abubakar, R. G. Bai, H.-S. Loh, S. Manickam, *Sci. Rep.* **2016**, *6*, 32808.
- [47] I. O. Omotuyi, M. O. Abiodun, K. Komolafe, O. C. Ejelonu, O. Olusanya, *J. Mol. Model.* **2015**, *21*, 109.
- [48] R. Adhikary, P. Mukherjee, T. W. Kee, J. W. Petrich, *J. Phys. Chem. B* **2009**, *113*, 5255–5261.
- [49] M. Gerecke, G. Bierhance, M. Gutmann, N. P. Ernsting, A. Rosspointner, *Rev. Sci. Instrum.* **2016**, *87*, 053115.
- [50] D. Ke, X. Wang, Q. Yang, Y. Niu, S. Chai, Z. Chen, X. An, W. Shen, *Langmuir* **2011**, *27*, 14112–14117.
- [51] Y. J. Wang, M. H. Pan, A. L. Cheng, L. I. Lin, Y. S. Ho, C. Y. Hsieh, J. K. Lin, *J. Pharm. Biomed. Anal.* **1997**, *15*, 1867–1876.
- [52] R. Waranyoupalin, S. Wongnawa, M. Wongnawa, C. Pakawatchai, P. Panichayupakaranant, P. Sherdshoopongse, *Cent. Eur. J. Chem.* **2009**, *7*, 388–394.
- [53] S. M. Khopde, K. Indira Priyadarsini, D. K. Palit, T. Mukherjee, *Photochem. Photobiol.* **2007**, *72*, 625–631.
- [54] a) J. Zhao, S. Ji, Y. Chen, H. Guo, P. Yang, *Phys. Chem. Chem. Phys.* **2012**, *14*, 8803–8817; b) A. S. Klymchenko, A. P. Demchenko, *New J. Chem.* **2004**, *28*, 687–692.
- [55] M. Mouslmani, D. Patra, *RSC Adv.* **2014**, *4*, 8317.
- [56] C. Banerjee, C. Ghatak, S. Mandal, S. Ghosh, J. Kuchlyan, N. Sarkar, *J. Phys. Chem. B* **2013**, *117*, 6906–6916.
- [57] G. Morgese, B. Verbraeken, S. N. Ramakrishna, Y. Gombert, E. Cavalli, J.-G. Rosenboom, M. Zenobi-Wong, N. D. Spencer, R. Hoogenboom, E. M. Benetti, *Angew. Chem. Int. Ed.* **2018**, *57*, 11667–11672; *Angew. Chem.* **2018**, *130*, 11841–11846.
- [58] a) L. Nardo, D. Paderno, A. Andreoni, M. Másson, T. Haukvik, H. H. Tønnesen, *Spectroscopy* **2008**, *22*, 187–198; b) S. M. Khopde, K. Indira Priyadarsini, D. K. Palit, T. Mukherjee, *Photochem. Photobiol.* **2000**, *72*, 625–631.
- [59] A. Sillen, Y. Engelborghs, *Photochem. Photobiol.* **1998**, *67*, 475–486.
- [60] a) Z. He, A. Schulz, X. Wan, J. Seitz, H. Bludau, D. Y. Alakhova, D. B. Darr, C. M. Perou, R. Jordan, I. Ojima, A. V. Kabanov, R. Luxenhofer, *J. Controlled Release* **2015**, *208*, 67–75; b) X. Wan, Y. Min, H. Bludau, A. Keith, S. S. Sheiko, R. Jordan, A. Z. Wang, M. Sokolsky-Papkov, A. V. Kabanov, *ACS Nano* **2018**, *12*, 2426–2439; c) X. Wan, J. J. Beaudoin, N. Vinod, Y. Min, N. Makita, H. Bludau, R. Jordan, A. Wang, M. Sokolsky, A. V. Kabanov, *Biomaterials* **2019**, *192*, 1–14.
- [61] Y. Seo, A. Schulz, Y. Han, Z. He, H. Bludau, X. Wan, J. Tong, T. K. Bronich, M. Sokolsky, R. Luxenhofer, R. Jordan, A. V. Kabanov, *Polym. Adv. Technol.* **2015**, *26*, 837–850.
- [62] M. M. Lübtow, M. S. Haider, M. Kirsch, S. Klisch, R. Luxenhofer, *Biomacromolecules* **2019**, *20*, 3041–3056.
- [63] M. S. Haider, J. Schreiner, S. Kendl, M. Kroiß, R. Luxenhofer, *ChemRxiv* **2019**, <https://doi.org/10.26434/chemrxiv.8055773.v1>.

Manuscript received: June 7, 2019

Accepted manuscript online: July 10, 2019

Version of record online: September 2, 2019

Up to now, the state of the solubilized drug provided information about the microenvironment within the micelles in dependence of the drug loading as well as chemical structure of the polymeric drug carrier. However, knowledge about the interactions between polymer and drug on a molecular level is still missing. Therefore, a loading dependent structural model based on the chemical shifts and respective line widths within solid state NMR spectra of freeze-dried CUR formulations was developed. As already suggested by powder x-ray diffraction, none of the formulations showed signs of CUR crystallinity in the NMR spectra irrespective of the drug loading ($LC = 17, 38$ and 52 wt.%). However, increasing CUR loading led to an increasing resemblance with the NMR spectrum of non-formulated, quench-cooled amorphous CUR corresponding to a more diverse molecular environment for CUR. This correlates to the results obtained by fluorescence spectroscopy, suggesting a less ordered microenvironment with increasing CUR loading. On an atomic level, pronounced alterations in the aromatic OCH_3 and OH signals of CUR in dependence of the CUR loading were assigned to be strongly involved in polymer-CUR interactions. Interestingly, CUR enol moiety seemed to be mostly involved in intramolecular interactions. As expected, polymer carbonyl moieties acting as hydrogen bond acceptor sites were highly sensitive to the presence of CUR. Most interestingly, with increasing loading, the occurrence of additional carbonyl signals indicated that not only the amide groups of the hydrophobic core, but also of the hydrophilic shell interacted with CUR. Therefore, as the interactions sites within the core become saturated with increasing CUR loading, an increasing amount of the repeating units of the hydrophilic block stabilize the solubilized cargo. Conversely, the hydrophilic corona gets more and more physically crosslinked, finally causing colloidal instabilities and precipitation. This is in line with the above-mentioned precipitation not only of CUR, but of polymer/CUR in the case of the polymers comprising nonyl sidechains at high CUR loading. Important to note, physical crosslinking of the hydrophilic shell was also expressed in decreasing dissolution rates of the freeze-dried CUR-loaded micelles with increasing CUR loading.

Loading-Dependent Structural Model of Polymeric Micelles Encapsulating Curcumin by Solid-State NMR Spectroscopy**

Ann-Christin Pöppler,* Michael M. Lübtow, Jonas Schlauersbach, Johannes Wiest, Lorenz Meinel, and Robert Luxenhofer

Abstract: Detailed insight into the internal structure of drug-loaded polymeric micelles is scarce, but important for developing optimized delivery systems. We observed that an increase in the curcumin loading of triblock copolymers based on poly(2-oxazolines) and poly(2-oxazines) results in poorer dissolution properties. Using solid-state NMR spectroscopy and complementary tools we propose a loading-dependent structural model on the molecular level that provides an explanation for these pronounced differences. Changes in the chemical shifts and cross-peaks in 2D NMR experiments give evidence for the involvement of the hydrophobic polymer block in the curcumin coordination at low loadings, while at higher loadings an increase in the interaction with the hydrophilic polymer blocks is observed. The involvement of the hydrophilic compartment may be critical for ultrahigh-loaded polymer micelles and can help to rationalize specific polymer modifications to improve the performance of similar drug delivery systems.

Only when molecular level understanding of polymer–drug formulations is available is it possible to make targeted changes to the components with the aim to optimize physico-chemical properties. Ideally, drug delivery platforms should carry large amounts of cargo, while simultaneously maintaining suitable stability and efficient release. In practice, drug formulations such as solid dispersions and soluble drug

delivery systems (DDS) comprising polymeric micelles have attracted a lot of attention^[1] and several have made their way onto the market in the form of drug delivery platforms, health care products, and biomaterials.^[2] However, the large body of published reports on DDS is not mirrored by therapeutic advances and benefit to the patient.^[3] Complexity and reproducibility are important points to be considered for applications of polymers in nanomedicine.^[4] A molecular level understanding of these combined “macromolecule/small molecule” materials that would help to systematically address these points is difficult to obtain due to their complex nature and lack of long-range order. Therefore, the prevailing picture across the literature for self-assembled polymeric micelles encapsulating drug molecules is that of a well-defined core–shell particle, where the hydrophobic core contains the drug molecules and the hydrophilic shell of the particle has a protection and solubilisation function.^[5] This image is dominated by the view from the outside. In this context, the work of Callari et al. was inspirational, because they were amongst the first to analyse how the structure of a polymer micelle might be affected by the presence of drug molecules.^[6] Their study shows that a higher loading reduces the cellular uptake and cytotoxicity in vitro; this is attributed to an increased packing density of the particle. In this case, a glycopolymer with discrete anchoring points for the Pt drug was used. However, the majority of DDS rely on physical encapsulation featuring less well-defined interactions. For such physically loaded micelles, this effect—a decrease in dissolution with increasing drug loading—is also well known.^[7] Here, we utilize solid-state NMR spectroscopy in combination with complementary tools to generate detailed insight into ultrahigh-drug-loaded polymeric micelles on the molecular level to understand the interplay between drug loading and the bulk properties, for example, dissolution behaviour, of such formulations. We envisage this structure–property relationship to serve as the basis for defined and systematic modifications aimed at extracting the best from both worlds—high loading and high release.

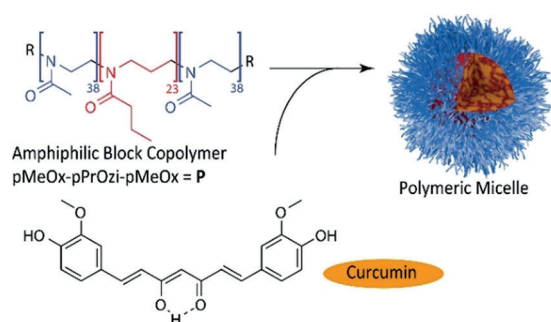
To build a bridge from experimental observations to a structural model, we used the amphiphilic triblock copolymer poly(2-methyl-2-oxazoline)-*block*-poly(2-*n*-propyl-2-oxazine)-*block*-poly(2-methyl-2-oxazoline) (pMeOx-*b*-pPrOzi-*b*-pMeOx = A-pPrOzi-A = P) (Scheme 1). Due to the weak hydrophobic character of pPrOzi, the polymer chains self-assemble in aqueous solution only in the presence of hydrophobic guest molecules.^[8] These assemblies could be identified as spherical and worm-like micellar structures in SANS and cryo-TEM experiments.^[8,9] The natural product curcumin (CUR) is encapsulated as a model compound due to

[*] Jun.-Prof. A.-C. Pöppler
Institute of Organic Chemistry
University of Würzburg
Am Hubland, 97074 Würzburg (Germany)
E-mail: ann-christin.poeppler@uni-wuerzburg.de
M. M. Lübtow, Prof. R. Luxenhofer
Lehrstuhl für Chemische Technologie der Materialsynthese
University of Würzburg
Röntgenring 11, 97070 Würzburg (Germany)
J. Schlauersbach, Dr. J. Wiest, Prof. L. Meinel
Institute for Pharmacy and Food Chemistry
University of Würzburg
Am Hubland, 97074 Würzburg (Germany)

[**] A previous version of this manuscript has been deposited on a preprint server (<http://doi.org/10.26434/chemrxiv.8943251.v1>).

Supporting information and the ORCID identification number(s) for the author(s) of this article can be found under:
<https://doi.org/10.1002/anie.201908914>.

© 2019 The Authors. Published by Wiley-VCH Verlag GmbH & Co. KGaA. This is an open access article under the terms of the Creative Commons Attribution Non-Commercial NoDerivs License, which permits use and distribution in any medium, provided the original work is properly cited, the use is non-commercial, and no modifications or adaptations are made.



Scheme 1. Structural formula of the components used in this study: The amphiphilic block copolymer P encapsulates curcumin by self-assembly into polymeric micelles (schematic drawing on the right).

its very low aqueous solubility, straightforward spectroscopic detection at very low concentrations, and the absence of signal overlap with the polymer in the NMR spectra. CUR with 77% purity was used as received. Additionally, A-pPrOzi-A (**P**) can incorporate large quantities of curcumin (> 50 wt. %) enabling the preparation of formulations with different, well-defined loadings.^[10] A set of three different formulations, CUR-2-P, CUR-6-P, and CUR-11-P, was prepared.^[10,11] This corresponds to 2, 6, and 11 gL⁻¹ CUR per 10 gL⁻¹ of the polymer, respectively, before freeze-drying (Chapter S1 of the Supporting Information). At the highest loading, the number of curcumin molecules per polymer chain exceeds the number of repeating units of the inner, more hydrophobic polymer block.

In standard dissolution tests using pressed tablet discs, no detectable dissolution was observed for crystalline curcumin within two hours, while amorphous CUR exhibited a low but noticeable dissolution (Table 1 and Figure S2). Formulating CUR with A-pPrOzi-A improved the dissolution rate up to 6000-fold (CUR-2-P) with the dissolution behaviour strongly depending on the drug loading (Table 1 and Figure S3). For all formulations, required tablet discs were prepared from freeze-dried samples.

CUR-2-P with the lowest CUR loading began to dissolve immediately after the start of the experiment with a dissolution rate of 6.2 μmol min⁻¹ cm⁻², which was the highest among the tested samples. When the CUR loading is increased (CUR-6-P), the dissolution rate drops by a factor of two and a lag period of 24 min is observed. This change is even more pronounced at the highest CUR loading (CUR-11-P) with the dissolution rate decreasing by a factor of 100. Although this dissolution rate is still 20 times faster than that

Table 1: Experimentally determined dissolution rates with lag times as well as results from hydrophobicity testing.

Sample	Lag time [min]	Dissolution rate [μmol min ⁻¹ cm ⁻²] ^[a]	Water uptake (wt. %) at 80% RH ^[b]
CUR-2-P	0	6.2 ± 0.5	30
CUR-6-P	24	2.6 ± 0.8	16
CUR-11-P	N/A	0.025 ± 0.008	15
amorphous CUR	N/A	0.001 ± 0.0004	–

[a] Mean ± SD (n = 3). [b] n = 1.

of amorphous CUR, it shows that the highest loading of a compound may not always be the most desirable formulation for (oral) administration. A two-sided t-test confirmed that the observed differences between CUR-2-P and CUR-6-P as well as between CUR-11-P and amorphous CUR are statistically significant ($p \leq 0.05$). To explain the differences in the dissolution behaviour, crystallisation could be excluded based on a longer PXRD measurement of the swollen tablet which gave no indication of crystallisation (Figure S16). The high stirring speed (4800 rpm) used here also suffices to exclude a resident water layer as a diffusion barrier. However, the formation of a highly viscous gel layer is conceivable. The dissolution studies were supplemented by water uptake experiments at 80% relative humidity. After 24 h, the formulations with lowest loading showed a 30% weight gain, while weight gains of 16% and 15% were observed for CUR-6-P and CUR-11-P, respectively, illustrating the increasing hydrophobicity of the latter.

To derive a structural model that can explain these experimentally observed bulk properties, the freeze-dried formulations were characterized by powder X-ray diffraction (Figure S13). For neat CUR, a distinct pattern of clear diffraction peaks was observed in agreement with the most stable, monoclinic crystal form (CSD ref. code: BINMEQ05^[12]). In contrast, all formulations lacked long-range order; they were X-ray amorphous. However, trends observed for the broad halo indicate changes in local order. NMR spectroscopy is particularly sensitive to the local environment of NMR-active nuclei and can thus be a powerful probe of such local or short-range-order phenomena. Therefore, the samples were dissolved in the non-selective solvent CDCl₃ (no micelles, individual components) or selective D₂O (CUR loaded micelles) and subsequently analysed by NMR spectroscopy in solution (Figures S4–S6). While CDCl₃ readily dissolves both CUR and the polymer, the CUR signals could barely be observed in D₂O. Only the polymer resonances were clearly distinguishable, suggesting that CUR in the micellar core behaves more solid-like, which agrees with recent fluorescence spectroscopic analysis at very low loadings.^[13] This hampers the detailed analysis and shows that NMR analysis in solution is not a suitable tool to study proximities and intermolecular interactions in these polymeric micelles. Diffusion (DOSY) NMR measurements of the three formulations in solution yielded diffusion coefficients and thus approximate radii, which agree with previously determined values from dynamic light scattering (both in Table S3).^[10] This shows that information on the size and exterior of these micelles is readily available, while information on the molecular arrangement of and within the micellar core is more difficult to obtain.

Therefore, we turned our attention to solid-state NMR spectroscopy, which has been shown to be a very powerful analytical technique in the pharmaceutical context for studying amorphous dosage forms in general^[14] and which is particularly sensitive to intermolecular interactions and subtle changes in the local arrangement. For example, Procházková et al. recently used solid-state NMR spectroscopy complemented by calculations and PXRD for a detailed investigation of polymorphic transformations in glycopoly-

meric vesicles.^[15] Freeze-dried formulations were subjected to ^1H and ^{13}C CP/MAS NMR experiments at 24 kHz MAS and 14.1 T. To ensure sample stability upon MAS, the ^1H NMR spectrum was observed at different times and PXRD was measured after completion of the NMR experiments (Figure S14b). For a first proof-of-principle, the NMR spectroscopic data from the three formulations were compared to spectra for the individual components (as-received CUR and pure polymer), a 1:1 physical mixture, and quench-cooled amorphous curcumin (Figure 1, scaled according to the individual number of scans). The ^{13}C CP/MAS NMR spectra

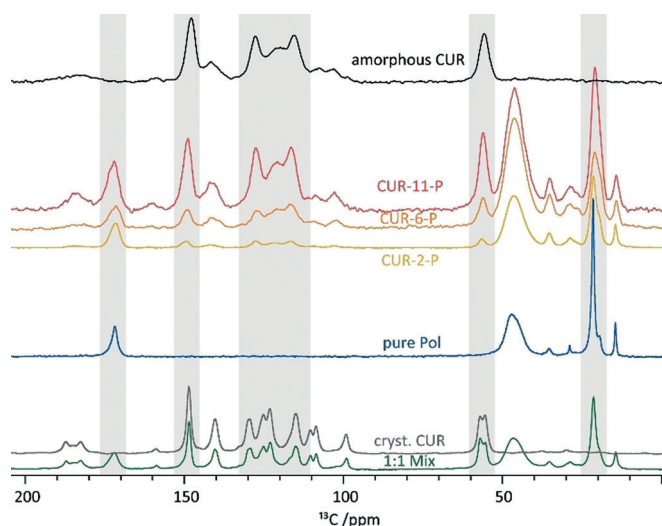


Figure 1. ^{13}C CP/MAS NMR spectra of amorphous CUR (black), the three formulations (yellow, orange, red with increasing CUR concentration), pure polymer (blue), as-received CUR (grey), and a 1:1 mixture of the two components (green). All spectra were recorded at 14.1 T and 24 kHz and scaled according to the number of scans of the individual datasets.

of as-received CUR and the polymer used for sample preparation are shown in grey and blue. The resonances were assigned based on NMR spectra in solution and previously published assignments based on solid-state NMR and calculations.^[16] The spectrum of the 1:1 physical mixture (green) is the simple sum of the spectra of the individual components. In contrast, the spectra of the three formulations (yellow, orange, red) clearly differ from the other spectra in peak number, position, width, and relative intensities. Increasing curcumin loading results in a corresponding increase in the relative CUR signal intensities and increasing similarity to the spectrum of quench-cooled amorphous CUR. Together, this shows that solid-state NMR spectroscopy provides a solid basis for the systematic analysis of these polymer–drug self-assemblies, allowing us a detailed look at distinct, loading-dependent changes. In the following, several regions in the spectra (Figure 1, grey highlights) will be discussed in more detail to point out specific aspects of the formulations (Figure 2 and Figure 4). For this discussion, the scaling of the spectra was adjusted for each signal area to show signals with practically equal heights. This facilitates the identification of changes in chemical shifts and the respective

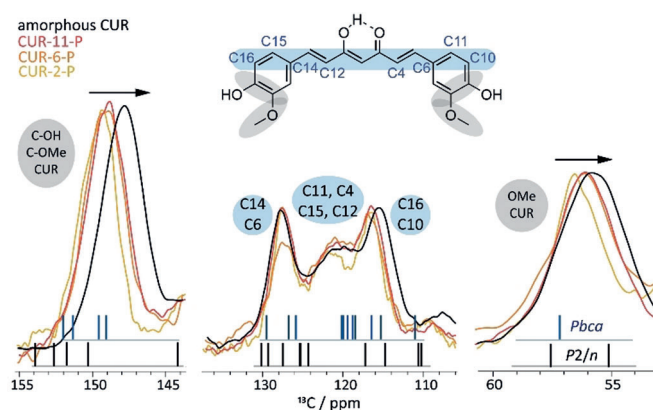


Figure 2. Enlarged sections from the overlay of the ^{13}C CP/MAS NMR spectra of CUR-2-P (yellow), CUR-6-P (orange), and CUR-11-P (red) compared to the spectrum of amorphous CUR (black) from Figure 1. Here, the signal intensities were scaled to approximately equal height for each individual signal area to facilitate direct comparison. Calculated chemical shifts are represented by vertical lines.

line widths. For an overview of all extracted spectral parameters, the reader is referred to the Supporting Information (Table S4). As a general trend, the signals in the formulations attributed to the polymer are all broader than those observed for the pure compound (no micelles present), while those resulting from CUR are narrower than the signals of fully amorphous CUR. This corroborates the concept of an X-ray amorphous material with different degrees of short-range order.

Firstly, the signals corresponding to the quaternary C–OH/C–OMe carbon atoms at ≈ 150 ppm as well as the signals of the CH_3 groups of curcumin (≈ 56 ppm) are compared as they appear to be affected most by increased loading (Figure 2, grey ellipsoids). These are the polar groups that are expected to be involved in intermolecular hydrogen bonding, while the enol moiety is mostly involved in intramolecular interactions. This was also underlined by a comparison of theoretical chemical shifts in a complete crystal and for an isolated molecule (Figures S19 and S20). Upon going from low (CUR-2-P) to high loading (CUR-11-P), the corresponding ^{13}C chemical shifts decrease, approaching that of amorphous CUR and the line widths increase. Hence, with higher loadings, the curcumin molecules experience a less uniform molecular environment. Interestingly, the changes in absolute values are greater between CUR-2-P and CUR-6-P than between the two higher loadings (6 vs. 11). Secondly, the signals of CUR between 110 and 130 ppm give additional insights. These signals belong to the backbone of the CUR molecule (highlighted in light blue). Curcumin in its most stable crystalline form (monoclinic space group $P2_1/n$) does not show any ^{13}C signals around 120 ppm as indicated by the calculated chemical shifts (Figure 2, black lines). In contrast, analogous calculations for the two other known polymorphs, in which CUR shows a significantly smaller torsion angle (16.1° vs. 46.0°), predict ^{13}C resonances in this region of the spectrum (blue lines). Therefore, we can deduce that CUR inside the micelles adopts a range of conformations with little molecular twist.

For further evidence of the involvement of the hydroxy group of CUR in hydrogen bonding with the amide functionality of the polymer, ^1H NMR spectra at fast MAS were recorded for CUR-11-P, CUR-6-P, as-received CUR, and a 1:1 mixture (Figure 3). For the formulations, a broad

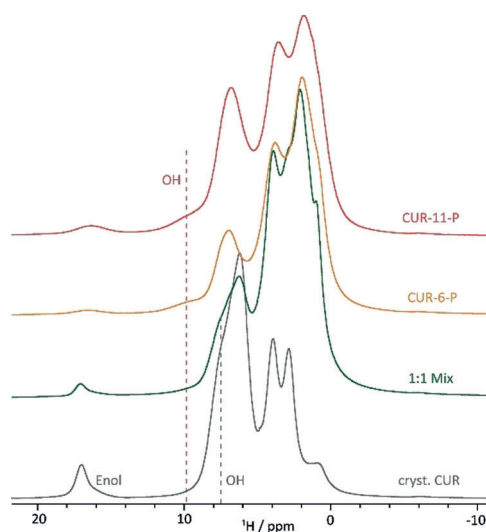


Figure 3. Overlay of the ^1H solid-state NMR spectra of CUR-11-P, CUR-6-P, a physical 1:1 mixture, and as-received CUR recorded at 14.1 T and 65 kHz MAS. The enol and the hydroxy moieties of the curcumin are indicated for the respective samples.

resonance at 9–10 ppm indicated by the red dotted line can be observed, which increases from CUR-6-P to CUR-11-P and is not present for the as-received CUR sample or the physical mixture. Resonances at such high ppm values are indicative of hydrogen-bonding interactions and the signal can be assigned to the OH group. For CUR and the physical mixture, the OH group resonates at a lower value of 7.5 ppm. We attribute this difference to the stronger hydrogen bonds formed between the hydroxyl moieties and the carbonyl of the amide group compared those to the methoxy group of the curcumin molecule, in agreement with GIPAW (CASTEP) calculations on a set of model structures containing similar $\text{OH}\cdots\text{O}=\text{CN}$ interactions (Chapter S8). Here, a shift of about 5–6 ppm to higher ppm values was predicted for resonances involved in such hydrogen-bonding arrangements, which is 1–2 ppm higher than predicted for CUR in form 1 (Chapter S7).

Focussing on the polymer, the resonance of the amidic $\text{C}=\text{O}$ group (≈ 172 ppm), which can serve as a hydrogen-bond-acceptor site, should be sensitive to the presence of CUR. For the neat polymer, only one resonance is observed in the 1D ^{13}C CP/MAS NMR spectrum, such that pMeOx and pPrOzi cannot be distinguished. However, in the ^1H - ^{13}C HETCOR spectrum with longer contact times (1.5 ms) three distinct resonances at 172.8, 171.7, and 171.0 ppm are observed, which can be assigned to the pPrOzi carbonyl moiety and the *cis/trans* isomers of pMeOx by comparison with ^{13}C NMR data in solution (Figure 4a). The existence of *cis/trans* isomers is well known for tertiary amides such as poly(2-oxazoline)s.^[17] For the pure polymer, the presence of the isomers is also observed in the solid state, which needs to be taken into account for the

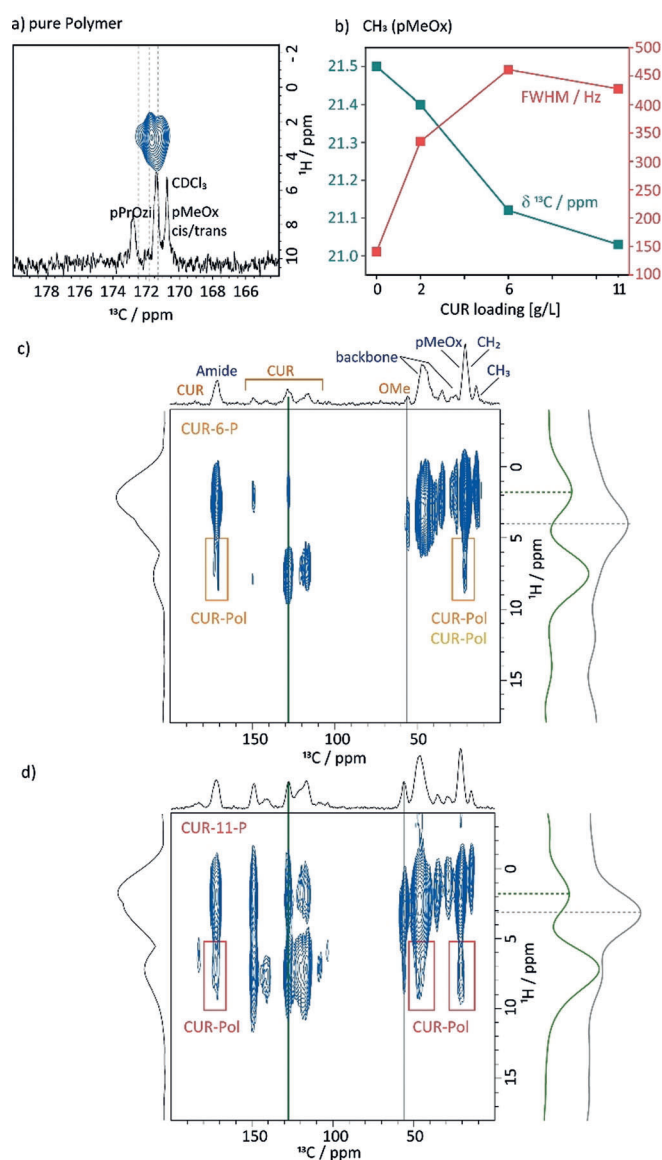


Figure 4. a) Amide region of the ^1H - ^{13}C FSLG HETCOR spectrum of the pure polymer recorded with a contact time of 1.5 ms alongside the ^{13}C NMR spectrum in CDCl_3 (full 2D spectrum in the Supporting Information). b) Comparison of the chemical shift (green) and line width (red) of the CH_3 group of the hydrophilic polymer block pMeOx for the pure polymer and the three formulations. c) and d) ^1H - ^{13}C FSLG HETCOR spectra of CUR-6-P and CUR-11-P recorded at 14.1 T and 20 kHz MAS with a contact time of 5 ms alongside the vertical slices extracted as highlighted by the coloured bars. Coloured boxes indicate cross-peaks originating from CUR–Pol intermolecular contacts. The 2D dataset of CUR-2-P can be found in the Supporting Information.

construction of a more detailed structural model. Upon CUR loading, the lines broaden and overlapping resonances can be observed. This is due to the distribution of environments and the presence of uncoordinated as well as coordinated amide moieties. To investigate the role of the different polymer blocks and their involvement in the CUR coordination more closely, changes in the chemical shift and line widths for the CH_3 group of the pMeOx polymer blocks are analysed (Figure 4b). The line width increases significantly on going

from the unassembled polymer to self-assembled CUR-2-P and further to the CUR-6-P and CUR-11-P formulations, which lie in the same range. The chemical shift shows only a minor change on going from the pure polymer to the formulation with low loading (0.1 ppm) as expected from the simplified image that CUR is located in the micellar core in the proximity of the more hydrophobic PrOzi residues. With increasing CUR loading, however, a more pronounced change in chemical shift is observed. This indicates that at higher loadings, the hydrophilic polymer blocks become involved in the coordination of CUR. In agreement with this picture, the chemical shift as well as the line width of the propyl-CH₃ signal do not differ between the CUR-6- and CUR-11-P formulations, for which we hypothesize that the interactions with the hydrophobic micellar core are largely saturated (Figure S9). To confirm this hypothesis, ¹H-¹³C 2D HETCOR spectra with a long contact time of 5 ms were recorded to probe intermolecular interactions between CUR and the polymer. The corresponding 2D spectra of CUR-6-P and CUR-11-P are shown in Figure 4c and 4d, respectively. As the polymer does not contain any aromatic moieties, cross-peaks at the ¹³C chemical shift of the polymer observed in this spectral area must originate from CUR–Pol contacts. Such contacts are highlighted by boxes in the colour code introduced in Figure 1. The 2D HETCOR spectrum of CUR-2-P can be found in the Supporting Information (Figure S11b). For the formulation with lowest loading, mostly intramolecular cross-peaks are observed apart from one weak cross-peak with the CH₂ unit of the propyl chain at 20.5 ppm. However, the overall intensity is low so that further contacts cannot be fully excluded. For medium loading, additional contacts between CUR and pMeOx are observed, proving the involvement of the pMeOx polymer block. Interestingly, two contacts of different intensity are observed to the carbonyl group. This could be due to *cis/trans* isomerism or different degrees of interaction with pMeOx and pPrOzi segments; this requires further investigation. Finally, many cross-peaks can be observed between CUR and the polymer for CUR-11-P. Contacts to all carbonyl environments and the polymer backbone are observed to the already described interactions for the formulations with lower CUR loading. Cross-peaks

located at ¹³C CUR resonances with protons at low chemical shifts could also indicate intermolecular CUR–Pol contacts; however, the interpretation is more complex as the methoxy group of CUR is also observed around 3.5 ppm. Horizontal slices indicate that the peak centre for the cross-peak at 128 ppm (green) is at lower ppm values than the OMe resonance (grey), but CUR–CUR contacts or intramolecular spin-diffusion cannot be fully excluded as a source of this cross-peak. A HETCOR spectrum with an additional spin-diffusion block of 50 ms according to Duan et al.^[18] showed spin diffusion between the different components (Figure S12a). This is an indication that no phase separation into domains takes place even at high CUR loadings, which is supported by the observation of only one glass transition for these formulations in a previous study.^[8] As a negative control, a HETCOR experiment for a 1:1 physical mixture did not yield cross-peaks between CUR and the polymer (Figure S12b).

Based on these observations, we can now assemble the puzzle pieces from the various experiments to obtain an overall loading-dependent, molecular level structural model (Figure 5): The unimers self-assemble into micelles only in the presence of curcumin. For the formulation with the lowest concentration of CUR (CUR-2-P), the poorly water-soluble CUR molecules with only a small molecular twist are mainly located in the micellar core with a distribution of rather defined environments due to hydrogen bonding between the phenolic OH moieties and the amide moiety of the hydrophobic block (depicted in red, Figure 5). As these preferred interaction sites become saturated at increasing CUR loading (CUR-6-P), the local order of CUR molecules is reduced. Furthermore, CUR molecules are now envisaged to be located at the hydrophilic–hydrophobic interface (in agreement with the raspberry model fitted for SANS data of a comparable system^[9]) and therefore interact increasingly with the repeating units of the hydrophilic block as evidenced by distinct changes in chemical shifts and corresponding cross-peaks in the 2D HETCOR spectra. These amide functionalities of the hydrophilic blocks (Figure 5, in blue) otherwise hydrate and stabilize the micelle. Consequently, in the hydration/dissolution process, CUR molecules now block

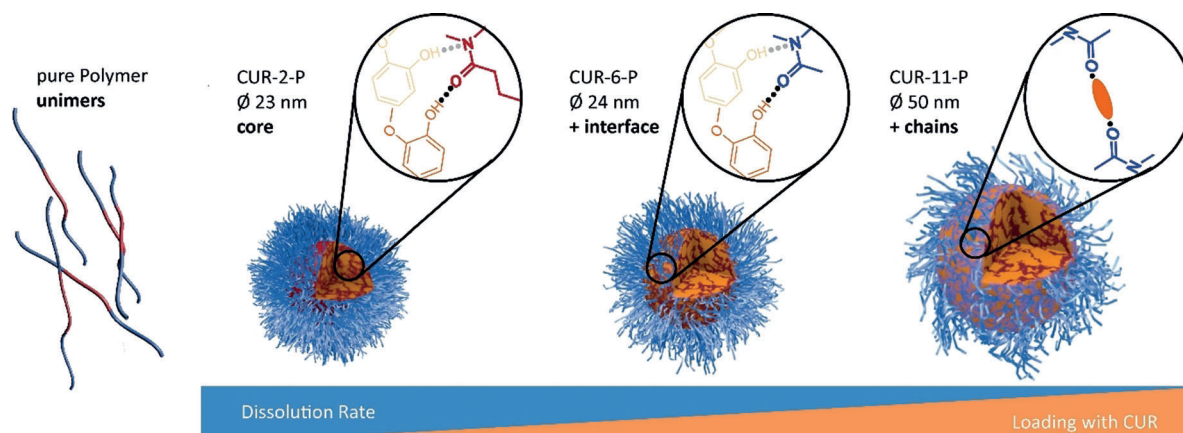


Figure 5. Schematic model of the structural changes of the polymeric micelles upon loading with curcumin based on the solid-state NMR data and complementary insights. For each loading stage, the additionally occurring interaction site is depicted.

the hydrogen bond acceptor sites within the shell of the micelle. This correlates with the observed retardation of the dissolution for CUR-6- and CUR-11-P. Finally, at the highest loading, not only the core is essentially filled with CUR molecules (smallest degree of short-range order in the NMR spectra), also the hydrophilic amide units become saturated, essentially physically crosslinking the hydrophilic corona, significantly affecting hydration. This is in accordance with the strongly decreased dissolution rate as observed for CUR-11-P1 and an increased radius of the particle, because of the shell being more rigid for these ultrahigh loadings. This overall picture would suggest an increased hydrophobicity of the micelles at higher loadings in agreement with the results in Table 1 and with a different study on glycopolymers using SAXS and SANS.^[19]

In general, structural information and understanding on the molecular level is difficult to obtain for drug-loaded polymeric micelles. In this work, we could show that solid-state NMR spectroscopy is a versatile toolbox, which can—complemented by other approaches—facilitate the detailed analysis of polymeric micelles, thus improving our structural understanding. NMR spectroscopic data probed changes in the interaction profile with increasing loading. At higher loadings, the hydrophilic polymer blocks were found to participate in the coordination of CUR, which is presumably of critical importance to obtain the unusually high drug loadings of approximately 50 wt. % observed with this platform. This can now serve as a starting point for the rational modification of polymers to maintain ultrahigh loadings, while not having to compromise the release behaviour. Experimental studies will now need to verify if and how optimized nanoparticles for drug delivery can be obtained through this approach. Additionally, the NMR experiments used here can be expanded including further proton-detected experiments at fast MAS. This would allow the drawing of an even more accurate picture for this and other drug–polymer arrangements. A systematic investigation by varying both polymer and guest molecules potentially also employing isotopic labelling schemes is necessary to, for example, explain the extremely different loading efficiencies observed for structurally similar polymers.^[10,20] Investigation of the samples during storage at a defined relative humidity might give insights into the dissolution mechanism. Moreover, exploration of the complementary insights from pair-distribution functions based on PXRD or probing the internal micellar structure by SANS should also be very valuable to learn more about these interesting systems.

Acknowledgements

We thank Prof. Roland Mitric for access to his workgroup cluster for the GIPAW (CASTEP) calculations and in particular to Matthias Wohlgemuth for helping us with the setup of the program package. We thank Dr. Matthias Grüne for helpful and stimulating discussions. We further thank Dominik Heuler for his support with the PXRD measurements and Malik Salman Haider for sharing his experience with respect to quench-cooling of curcumin. Tessa Lühmann

is acknowledged for proof reading and Thomas Lorson for help with the DLS data. Special thanks goes to the Pöppler group for their support with proof reading, discussion, and enthusiasm. Financial support from the Verband der Chemischen Industrie (VCI) in the form of a material cost allowance is acknowledged (A.-C.P.). M.M.L. thanks the Evonik Foundation for providing a doctoral fellowship. We would like to thank all reviewers for their effort and helpful comments to improve the initial version of this manuscript. Experimental and calculated data for this study is available through the repository Zenodo.

Conflict of interest

M.M.L. and R.L. are listed as inventors on a patent application pertinent to some of the materials discussed in this contribution. R.L. is co-founder and has a financial interest in DelAqua Pharmaceuticals Inc. which is intent on commercializing poly(2-oxazoline)-based excipients.

Keywords: dissolution rates · micelles · polymers · short-range order · solid-state NMR spectroscopy

- [1] a) R. Duncan, *Nat. Rev. Drug Discovery* **2003**, *2*, 347–360; b) Y. Huang, W.-G. Dai, *Acta Pharm. Sin. B* **2014**, *4*, 18–25; c) G. S. Kwon, K. Kataoka, *Adv. Drug Delivery Rev.* **2012**, *64*, 237–245; d) H. Cabral, K. Kataoka, *J. Controlled Release* **2014**, *190*, 465–476.
- [2] a) V. Wagner, A. Dullaart, A.-K. Bock, A. Zweck, *Nat. Biotechnol.* **2006**, *24*, 1211–1217; b) N. Kamaly, Z. Xiao, P. M. Valencia, A. F. Radovic-Moreno, O. C. Farokhzad, *Chem. Soc. Rev.* **2012**, *41*, 2971–3010.
- [3] J.-C. Leroux, *Angew. Chem. Int. Ed.* **2017**, *56*, 15170–15171; *Angew. Chem.* **2017**, *129*, 15368–15369.
- [4] R. Luxenhofer, *Nanomedicine* **2015**, *10*, 3109–3119.
- [5] a) H. Chen, S. Kim, L. Li, S. Wang, K. Park, J.-X. Cheng, *Proc. Natl. Acad. Sci. USA* **2008**, *105*, 6596–6601; b) H. Cho, T. C. Lai, K. Tomoda, G. S. Kwon, *AAPS PharmSciTech* **2015**, *16*, 10–20; c) Y. T. Tam, J. Gao, G. S. Kwon, *J. Am. Chem. Soc.* **2016**, *138*, 8674–8677; d) H. Cabral, K. Miyata, K. Osada, K. Kataoka, *Chem. Rev.* **2018**, *118*, 6844–6892.
- [6] M. Callari, P. L. De Souza, A. Rawal, M. H. Stenzel, *Angew. Chem. Int. Ed.* **2017**, *56*, 8441–8445; *Angew. Chem.* **2017**, *129*, 8561–8565.
- [7] a) R. Gref, Y. Minamitake, M. T. Peracchia, V. Trubetskoy, V. Torchilin, R. Langer, *Science* **1994**, *263*, 1600; b) M. Polakovič, T. Görner, R. Gref, E. Dellacherie, *J. Controlled Release* **1999**, *60*, 169–177.
- [8] M. M. Lübtow, L. C. Nelke, J. Seifert, J. Kühnemundt, G. Sahay, G. Dandekar, S. L. Nietzer, R. Luxenhofer, *J. Controlled Release* **2019**, *303*, 162–180.
- [9] A. Schulz, S. Jaksch, R. Schubel, E. Wegener, Z. Di, Y. Han, A. Meister, J. Kressler, A. V. Kabanov, R. Luxenhofer, C. M. Papadakis, R. Jordan, *ACS Nano* **2014**, *8*, 2686–2696.
- [10] M. M. Lübtow, L. Hahn, M. S. Haider, R. Luxenhofer, *J. Am. Chem. Soc.* **2017**, *139*, 10980–10983.
- [11] R. Luxenhofer, A. Schulz, C. Roques, S. Li, T. K. Bronich, E. V. Batrakova, R. Jordan, A. V. Kabanov, *Biomaterials* **2010**, *31*, 4972–4979.

- [12] P. Sanphui, N. R. Goud, U. B. R. Khandavilli, S. Bhanoth, A. Nangia, *Chem. Commun.* **2011**, 47, 5013–5015.
- [13] M. M. Lübtow, H. Marciniak, A. Schmiedel, M. Roos, C. Lambert, R. Luxenhofer, *Chem. Eur. J.* **2019**, 25, 12601–12610.
- [14] a) R. Lefort, A. De Gussemme, J. F. Willart, F. Danède, M. Descamps, *Int. J. Pharm.* **2004**, 280, 209–219; b) T. N. Pham, S. A. Watson, A. J. Edwards, M. Chavda, J. S. Clawson, M. Strohmeier, F. G. Vogt, *Mol. Pharm.* **2010**, 7, 1667–1691; c) J. Brus, M. Urbanova, I. Sedenkova, H. Brusova, *Int. J. Pharm.* **2011**, 409, 62–74.
- [15] E. Procházková, C. Cao, A. Rawal, M. Dračínský, S. Bhattacharyya, I. Císařová, J. M. Hook, M. H. Stenzel, *ACS Appl. Mater. Interfaces* **2019**, 11, 28278–28288.
- [16] a) X. Kong, A. Brinkmann, V. Terskikh, R. E. Wasylshen, G. M. Bernard, Z. Duan, Q. Wu, G. Wu, *J. Phys. Chem. B* **2016**, 120, 11692–11704; b) M. A. Matlinska, R. E. Wasylshen, G. M. Bernard, V. V. Terskikh, A. Brinkmann, V. K. Michaelis, *Cryst. Growth Des.* **2018**, 18, 5556–5563.
- [17] a) M. Sisido, Y. Imanishi, T. Higashimura, *Biopolymers* **1972**, 11, 399–408; b) Q. Sui, D. Borchardt, D. L. Rabenstein, *J. Am. Chem. Soc.* **2007**, 129, 12042–12048; c) B. C. Gorske, J. R. Stringer, B. L. Bastian, S. A. Fowler, H. E. Blackwell, *J. Am. Chem. Soc.* **2009**, 131, 16555–16567.
- [18] P. Duan, J. C. Moreton, S. R. Tavares, R. Semino, G. Maurin, S. M. Cohen, K. Schmidt-Rohr, *J. Am. Chem. Soc.* **2019**, 141, 7589–7595.
- [19] C. Cao, J. Zhao, F. Chen, M. Lu, Y. Y. Khine, A. Macmillan, C. J. Garvey, M. H. Stenzel, *Chem. Mater.* **2018**, 30, 5227–5236.
- [20] M. M. Lübtow, L. Keßler, A. Appelt-Menzel, T. Lorson, N. Gangloff, M. Kirsch, S. Dahms, R. Luxenhofer, *Macromol. Biosci.* **2018**, 18, 1800155.

Manuscript received: July 17, 2019

Revised manuscript received: September 4, 2019

Accepted manuscript online: September 17, 2019

Version of record online: ■■■■■, ■■■■■

Although the structure of the micelles including the micellar microenvironment, CUR amorphicity as well as polymer-CUR interactions on a molecular scale was resolved, one last important information, the actual morphology of the drug-loaded micelles is still missing. Although dynamic light scattering suggested small sizes and most likely spherical aggregates for POzi/CUR, an in depth-investigation of the morphology was not possible with previous used techniques. Small angle neutron scattering (SANS) as one of various scattering techniques offers the required scattering contrast to investigate morphological transitions or the actual composition within different aggregate layers. To obtain structure-property relationships, the morphology of three different polymer amphiphiles with different maximum LC s for CUR was evaluated. Two of the investigated polymers formed micelles by themselves, whereas the amphiphilic contrast of the third one was not pronounced enough, being present in aqueous solution mainly as single polymer chains (unimers). Important to note, the former two polymers formed rather spherical aggregates with no core-shell differentiation than actual micelles. However, after solubilization of small amounts of CUR (polymer/CUR = 10/1 g/L), distinct core-shell spherical micelles appeared (also in the case of the polymer not forming micelles by itself). Further increasing the CUR loading (polymer/CUR \geq 10/3 g/L) caused the formation of a second shell, *i.e.* spherical micelles with a core-shell-shell structure. This second, inner shell is in good agreement with the participation of the hydrophilic polymer block in the stabilization of solubilized CUR at higher CUR loadings, investigated by solid state NMR. Considering the scattering length densities (SLD), increasing CUR loading caused a dehydration of the initially hydrated core, as well as inner shell due to increasing amounts of CUR in the respective layers. Especially the SLD of the core approaches the one of neat CUR, suggesting a dense accumulation of CUR within the core. The increasing SLD of the outer shell approaching the SLD of heavy water can be assigned to ever more parts of the hydrophilic block being part of the inner shell, in order to stabilize the increasing amounts of CUR. This causes a dehydration of the micelle as a whole, finally causing agglomeration and precipitation. This is in accordance with cryo-TEM images, showing a potential bridging and connection of single micelles at polymer/CUR = 10/12 g/L, as will be discussed in the following publication.

Probing the complex loading dependent structural changes in ultra-high drug loaded polymer micelles by small-angle neutron scattering

Benedikt Sochor^{1,+}, Özgür Dündükcü^{1,+}, Michael M. Lübtow², Bernhard Schummer³, Sebastian Jaksch⁴, Robert Luxenhofer^{2,5*}

¹Chair of X-Ray Microscopy, Department of Physics and Astronomy, University Würzburg, Campus Hubland Nord, Josef-Martin-Weg 63, 97074 Würzburg, Germany

²Functional Polymer Materials, Chair for Advanced Materials Synthesis, Department of Chemistry and Pharmacy and Bavarian Polymer Institute, University of Würzburg, Röntgenring 11, 97070 Würzburg, Germany

³Fraunhofer Institute for Integrated Circuits, X-Ray Development Center EZRT, Flugplatzstraße 75, 90768 Fürth, Germany

⁴Forschungszentrum Jülich GmbH, Jülich Center for Neutron Science (JCNS) at Heinz Maier-Leibnitz Zentrum, Lichtenberstraße 1, 85747 Garching, Germany

⁵Soft Matter Chemistry, Department of Chemistry, Helsinki University, 00014 Helsinki, Finland

⁺ authors contributed equally

*correspondence to: robert.luxenhofer@uni-wuerzburg.de

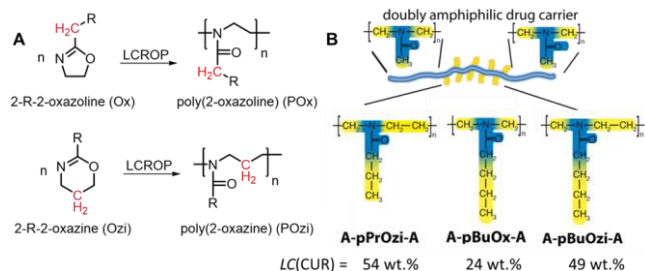
Keywords: nanomedicine, nanoformulations, drug solubilization, drug-polymer interaction, drug-corona interactions

ABSTRACT: Drug loaded polymer micelles or nanoparticles are being continuously explored in the fields of drug delivery and nanomedicine. Commonly, a simple core-shell structure is assumed, in which the core incorporates the drug and the corona provides steric shielding, colloidal stability, and prevents protein adsorption. Recently, the interactions of the dissolved drug with the micellar corona have received increasing attention. Here, using small-angle neutron scattering, we provide an in-depth study of the differences in polymer micelle morphology of a small selection of structurally closely related polymer micelles at different loadings with the model compound curcumin. This work supports a previous study using solid state nuclear magnetic resonance spectroscopy and we confirm that the drug resides predominantly in the core of the micelle at low drug loading. As the drug loading increases, neutron scattering data suggests that an inner shell is formed, which we interpret as the corona also starting to incorporate the drug, whereas the outer shell mainly contains water and the polymer. The presented data clearly shows that a better understanding of the inner morphology and the impact of the hydrophilic block can be important parameters for improved drug loading in polymer micelles as well as provide insights into structure-property relationships.

1. INTRODUCTION

Promising new active pharmaceutical ingredients (API) are discovered in pharmaceutical industry and academia on a daily basis, but one major challenge remains the formulation of the API. According to estimates, 40%¹ - 60%² of all new drugs are practically insoluble in water. Therefore, a plethora of methods is used to increase

their solubility.³ Polymer micelles are nanoscopic structures formed by amphiphilic (block) copolymers.⁴ In a simplified picture, hydrophobic APIs are dissolved in the hydrophobic core, whereas the hydrophilic shell acts as a protective layer to prevent premature disintegration or unwanted protein interactions and to ensure a sufficient water solubility. However, the actual situation may be more complex as recently shown for a variety of drug loaded micelles, as the nature of the hydrophobic block can significantly affect the drug loading.^{5,6} A particularly strong effect was reported for the different solubilization behaviors of structurally very similar poly(2-oxazoline) (POx) and poly(2-oxazine) (POzi) based drug delivery vehicles (Scheme 1).



Scheme 1: A) Schematic synthesis of the structural isomers poly(2-oxazoline)s (POx) and poly(2-oxazine)s (POzi) by living cationic ring opening polymerization (LCROP) of 2-substituted 2-oxazolines and 2-substituted 2-oxazines; B) Schematic representation of the amphiphilic triblock copolymers all bearing two hydrophilic poly(2-methyl-2-oxazoline) blocks (blue) and different hydrophobic cores (yellow) as well as their maximum loading capacity (LC) for curcumin (CUR).

Small structural changes in the polymer sidechain and polymer backbone of the hydrophobic core caused pronounced differences

in the solubilization capacity for different hydrophobic compounds such as curcumin (CUR)⁷⁻⁹ and paclitaxel (PTX).¹⁰⁻¹³ The investigated formulations are of particular interest as extremely high CUR-loading > 50 wt.% were observed, which is highly unusual for drug-loaded micelles, since they generally suffer, with notable exceptions^{14, 15}, from rather low drug-loadings < 20 wt.%.¹⁶⁻¹⁸ Repeatedly, a stronger hydrophobic contrast resulted in lower drug loadings in this family of amphiphilic block copolymers, clearly stressing the point that the simplistic picture of a hydrophobic core, which dissolves hydrophobic drugs⁶, may often be inadequate.^{12, 19-21} Since the drug loading (in wt.% vs. polymer) and final drug solubilization (in g/L) are critical parameters dictating, to a certain extent, the clinical potential of a formulation, a closer look at the interactions between polymeric drug carriers and solubilized drug has recently received attention.²¹⁻²³ This includes a critical evaluation of the traditional core-shell concept as evident by the drug-induced morphology switch of POx based micelles from worm-like, to spherical and raspberry-like structures with increasing PTX-loading (0 – 50 wt.%)^{24, 25}. In contrast, the formation of a worm-like morphology was observed at high-loading (50 wt.%) of the same drug-carrier loaded with etoposide and a platinum (Pt)-based prodrug.²⁶ It was recently confirmed by Callari *et al.* using solid state nuclear magnetic resonance (NMR) and endocytosis studies²², that the different morphologies can have direct impact on biological properties.²⁷ Micelles at low-loading of a Pt-based drug had a rather loose structure, whereas the high-loaded micelles were much more condensed with aggregated Pt-species surrounded by a densely packed hydrophilic corona. The cellular uptake of these micelles, bearing fructose moieties in the hydrophilic corona, depended on fructose-specific cellular uptake transporters. Accordingly, endocytosis was significantly higher at lower loading due to the less-restricted interaction of the flexible polymer chains. In contrast, the apparently too densely packed fructose moieties at higher loading reduced the cellular uptake. Using solid-state NMR, it was recently reported that the hydrophilic corona is also significantly involved in the drug/polymer interactions in POx/POzi micelles, in particular at higher drug loadings, which impeded dissolution of the lyophilized polymer micelle powders, which can be understood as a unusual solid amorphous dispersions.²⁸ Moreover, using fluorescence spectroscopy and lifetime measurements, significant differences for the molecular environment of the incorporated drug were found at very low drug loading where no involvement of the hydrophilic corona is expected.¹³ Inspired by this, we set out to determine if the involvement of the hydrophilic corona in this formulation and distinct polymer-drug specificities observed for POx and POzi based CUR formulations¹⁰ also result in different micellar morphologies or sizes. The analytical techniques utilized so far were not able to address these questions.

To gain extensive insights into the micellar structure, small-angle neutron scattering (SANS) curves of CUR solubilized with three different POx and POzi based amphiphiles (Scheme 1) were obtained at various polymer/CUR ratios. Following this, not only morphological transitions from a distinct core-shell to a core-shell-shell model with increasing CUR-loading could be observed, but also the content of polymer, water or CUR in the different layers could be estimated.

2. MATERIALS AND METHODS

Reagents

Curcumin powder from *Curcuma longa* (turmeric) was purchased from *Sigma-Aldrich* and analyzed in-house (curcumin = 79%; demethoxycurcumin = 17%, bisdemethoxycurcumin = 4%; determined by HPLC analysis). The ABA triblock copolymers, all comprising the same hydrophilic poly(2-methyl-2-oxazoline) (pMeOx) corona A and structurally similar hydrophobic cores based on either poly(2-*n*-2-propyl-oxazine) (pPrOzi; Me-MeOx₃₅-PrOzi₂₀-MeOx₃₅-1-Boc-piperazine = A-pPrOzi-A), poly(2-*n*-2-butyl-oxazoline) (pBuOx; Me-MeOx₃₅-BuOx₂₀-MeOx₃₅-piperidine = A-pBuOx-A) or poly(2-*n*-2-butyl-oxazine) (pBuOzi; Me-MeOx₃₅-BuOzi₂₀-MeOx₃₅-1-Boc-piperazine = A-pBuOzi-A), were synthesized and described previously.²⁹

Preparation of CUR-loaded micelles

CUR loaded polymer micelles were prepared by thin film method as described elsewhere.²⁹ Briefly, ethanolic polymer (20 g/L) and curcumin (5.0 g/L) stock solutions were mixed in the desired ratio. After complete removal of the solvent at 55 °C under a mild stream of argon, the films were dried *in vacuo* (≤ 0.2 mbar) for at least 20 min. Subsequently, preheated (37 °C), ultrapure H₂O was added to obtain the final polymer and CUR concentrations as mentioned in the main text. To ensure complete solubilization, the solutions were shaken at 55 °C for 15 min at 1250 rpm with a Thermomixer comfort (*Eppendorf AG*, Hamburg, Germany). Non-solubilized curcumin, if any, was removed by centrifugation for 5 min at 9.000 rpm with a MIKRO 185 (*Hettich*, Tuttlingen, Germany). CUR quantification was performed by UV-Vis absorption of samples diluted in ethanol using a BioTek Eon Microplate Spectrophotometer (*Thermo Fisher Scientific*, MA, USA) and a calibration curve obtained with known amounts of CUR.¹⁰ For SANS measurements, the freshly prepared aqueous formulations were freeze-dried and redissolved in deuterated water (D₂O) right before measurements. Note that the densimetric measurements were performed in H₂O.

Densimetry

The densimetric measurements were performed using a DMA 4100 M density meter (*Anton Paar*, Graz, Austria). The samples were diluted/dissolved using ultrapure water (H₂O) and the density of each sample was measured from 5 °C to 55 °C. For the estimation of the scattering length densities (SLD) in solution and to calculate the volume fraction, densities obtained at 25°C were used.

Small-angle-neutron-scattering (SANS)

The SANS experiments were performed on the KWS-1 beamline³⁰ at Heinz Maier-Leibnitz Zentrum (Garching, Germany). The samples were measured in standard Hellma quartz cuvettes with a path-length of 1 mm and kept at 25 °C throughout the experiment. For the measurements, a neutron wavelength of 7 Å was used. To cover the desired Q-range, the samples were measured at three sample to detector distances of 19.6 m, 7.6 m and 1.6 m for 1200 s, 600 s and 300 s respectively. Calibration to absolute intensities was done using poly(methyl methacrylate) (PMMA) as a secondary standard. For data correction, merging and reduction (azimuthal averaging) the toolkit QtiKWS by JCNS was used. The shape model (core-shell-shell sphere) is commonly used and readily available in most software. The model-dependent data analysis was carried out using the macro IRENA for IgorPro.³¹

3. RESULTS AND DISCUSSION

Densimetry

To estimate the volume fractions and neutron scattering length densities (SLD) of polymer-CUR formulations at 25°C (at which SANS experiments were conducted), the densities of the formulations were determined at this temperature. For the complete temperature dependent density data, the reader is referred to supporting information (Figure S1-S6). As expected, the solution density increased with increasing drug concentration (at constant polymer concentration, Table 1).

To derive the density of the polymer-CUR formulations, ρ_{sample} , the amount of water in solution was subtracted:

$$\rho_{sample} = \frac{\rho_{solution}\rho_{water}c_{sample}}{\rho_{water}-\rho_{solution}(1-c_{sample})} \quad (1)$$

with the measured solution density $\rho_{solution}$, the water density ρ_{water} and the total sample mass concentration $c_{sample} = \frac{m_{sample}}{m_{sample}+m_{water}}$, in weight percent. The values for the water density were obtained from calculations at ambient pressure (1013 hPa).³²

Table 1: Densimetric data of the nanoformulations at different drug loading at 25°C.

polymer/CUR		$\rho_{solution}$ [g/ml] ^{a)}	ρ_{sample} [g/ml] ^{b)}	$\phi^c)$
A-pPrOzi-A				
[g/l]	mmol/mmol			
10/0	n.a.	0.9976	1.0282	0.0091
10/1	1.1/2.7	0.9981	1.0724	0.0096
10/3	1.1/8.1	0.9988	1.1246	0.0109
10/5	1.1/13.6	0.9993	1.1533	0.0122
10/10	1.1/27.1	1.0010	1.2145	0.0154
A-pBuOzi-A				
10/0	n.a.	0.9979	1.0611	0.0094
10/1	1.1/2.7	0.9982	1.0973	0.0095
10/3	1.1/8.1	0.9988	1.1295	0.0108
10/5	1.1/13.6	0.9992	1.1446	0.0123
10/10	1.1/27.1	1.0003	1.1711	0.0160
A-pBuOx-A				
10/0	n.a.	0.9977	1.0389	0.0090
10/1	1.2/2.7	0.9985	1.1211	0.0092
10/3	1.2/8.1	0.9989	1.1530	0.0098
10/5	1.2/13.6	0.9992	1.1708	0.0104

a) measured solution density (system error: 0.0002 g/ml),

b) water subtracted polymer/CUR formulation density (calculated with eq. 1, propagated error: 0.0003)

c) volume fraction (propagated error: 0.0005).

As the polymer and CUR concentrations were ≤ 1 wt.%, it was assumed that the excess volume (polymer & CUR) during mixing of the samples is negligible. The obtained densities of the polymer/CUR formulations were used to calculate the respective volume fractions, ϕ . Here the polymer and CUR concentration can be transformed from weight to volume percent using:

$$\phi \text{ (vol. \%)} = \frac{\rho_{solution}}{\rho_{sample}} c_{sample} \quad (2)$$

The obtained values were used as a fixed fit parameter during the modeling of the SANS data. Using the densities of the pure polymer solutions without any CUR (10-0 samples), the corresponding neutron scattering length densities (SLD_n) of the polymers can be calculated by:

$$SLD_n = \rho \cdot (\sum_j n_j b_j) / (\sum_j n_j m_j) \quad (3)$$

where ρ is the macroscopic density, b_j the element- and isotope-specific neutron scattering length, m_j the element specific molecular weight and n_j the stoichiometric composition of the compound. For the estimation of the CUR-SLD the density was taken from literature³³ (Table 2).

Table 2: Neutron scattering length densities (SLD) of the polymers, CUR and heavy water (D₂O). The values were calculated from the macroscopic densities using equation (3) or, in case of D₂O, taken from literature³⁴.

Sample	ρ_{sample} [g/ml]	SLD_n [10^{-6} \AA^{-2}]
A-pPrOzi-A	1.0282	0.9721
A-pBuOzi-A	1.0611	0.9246
A-pBuOx-A	1.0389	0.9416
CUR	1.30±0.05	1.790
D ₂ O	---	6.3351

Small-angle neutron scattering

The experimentally determined scattering intensities

$$I(Q) = \sum_i F(Q) \cdot \Delta(Q) \cdot S(Q) \quad (4)$$

can be modeled using different form factors, $F(Q)$, size distribution functions, $\Delta(Q)$ and structure factors, $S(Q)$. In all scattering related theories and experiments, the main variable is always the scattering vector $Q = \frac{4\pi}{\lambda} \sin(\theta)$, which depends on the used wavelength, λ , and the angle, θ , under which the scattered neutrons are collected. The measured SANS data can be used to study the structural properties of the nanoformulations under investigation (Scheme 1).

The scattering curve of pure A-pPrOzi-A in D₂O without any added CUR (A-pPrOzi-A/CUR=10/0, Figure 1, A) shows a flat curve which can be described by the Debye function, indicating a Gaussian chain-like behavior, supporting earlier results, which suggested that this polymer does not form micelles by itself under ambient condition at this concentration (10 g/L).²⁹ Upon CUR addition, polymer micelles form, as shown by the change in the plateau intensities at low Q -values, and the overall appearances of the scattering curves, indicative of discrete and compact objects. The increasing plateau intensity can be caused by larger particles or a higher scattering contrast. A recent report by Lübtow *et al.*²³ showed that

the hydrodynamic radii of A-pPrOzi-A-CUR aggregates initially decrease slightly at low CUR content (10/0.9: hydrodynamic diameter (D_h) = 26 nm; 10-4.8: D_h = 20 nm) and only start to increase at $\rho(\text{CUR}) > 5$ g/L (10/11.9: D_h = 46 nm) as determined by dynamic light scattering (DLS). Since DLS measures the hydrodynamic radius, which involves a water corona around the particle, and SANS probes the radius of gyration without this corona, differences are expected. The increasing scattering intensities probably indicate a higher scattering contrast due to the higher CUR amounts, which is solubilized in the polymer micelles. At 50 wt.% drug loading, i.e. same concentrations of polymer and drug, the scattering intensity increases by nearly an order of magnitude compared to the polymer alone (Figure 1, A and B). The already mentioned DLS results as well as cryo-TEM images²⁹ have also shown the presence of larger and worm-like particles. These larger structures were also observable by SANS, as the increasing scattering intensities at the lowest measured Q -values indicate (Figure 1, D). To investigate these particles in more detail, power-law or model-based fitting techniques could be used. However, for accurate results, either their shape and size or the exact ratio between micelles and larger particles must be known. In the present study, we concentrate on the morphological study of the spherical micelles and hence only the corresponding Q -range for single micelles (0.007 - 0.3 \AA^{-1}) was considered for further data analysis.

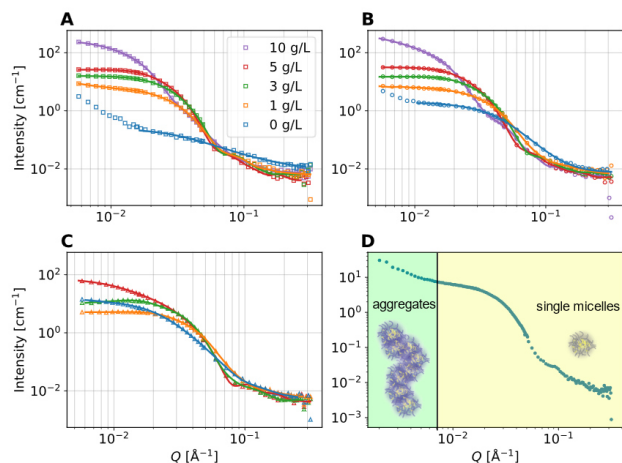


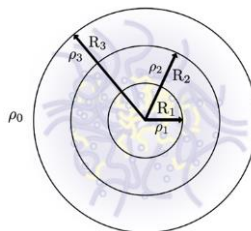
Figure 1: Measured SANS data for A) A-pPrOzi-A, B) A-pBuOzi-A and C) A-pBuOx-A and their CUR nanoformulations. The concentration of the polymer was kept constant at 10 g/L, while the CUR concentration was varied from 0 to 10 g/L. In the case of A-pBuOx-A, CUR concentrations above 3 g/L already caused precipitation. Only one third of the data points is shown to increase visibility. The solid lines are fits to the data obtained by the core-shell-shell model (all fit parameters can be found in the supporting information); D) to show the presence of larger aggregates, the whole data range extended to very small Q -values is shown for A-pPrOzi-A at $c(\text{CUR}) = 1$ g/L (bottom right). The data analysis however, was done on the cropped Q -range shown in the other graphs neglecting those aggregates.

Choice of fitting model

For the analysis of the SANS data, three different spherical form factor models were considered: A simple sphere, a core-shell sphere and a core-shell-shell sphere. Each model is available in the Irena modelling suite and was used to fit the data. The resulting χ^2 -values of the best obtained fits were used as an indicator for the most suitable model for data evaluation. A full example and explanation of one sample data set and the fitting results can be found in the supporting information (Figure S7, S8). Based on these results, the core-shell-shell form factor model³¹

$$F(Q) = \frac{3V_1}{QR_1}(\rho_1 - \rho_2)J_1(QR_1) + \frac{3V_2}{QR_2}(\rho_2 - \rho_3)J_1(QR_2) + \frac{3V_3}{QR_3}(\rho_3 - \rho_0)J_1(QR_3) \quad (5)$$

was chosen and used to fit all data for comparability. Here V_1 to V_3 are the volumes of each compartment (core, first (inner) or second (outer) shell), R_1 to R_3 their respective radii, ρ_1 to ρ_3 the SLD of each compartment, ρ_0 the SLD of the solvent and J_1 is the Bessel function of the first kind. A schematic overview of this model is given in Scheme 2.



Scheme 2: A graphic representation of the employed core-shell-shell sphere model with its parameters as are defined in Eq. 5.

However, we must note that for several samples the core or one of the shells practically vanish, reducing the model effectively to a simple core-shell model. This may also be attributed to the co-existence of different morphologies, which cryo-TEM images of A-pPrOzi-A formulations suggest and which makes accurate fitting extremely challenging²⁹.

In addition to the form factor, a structure factor for samples with CUR concentrations above 1 g/L was used for describing the intermicelle interactions. In the present analysis, the hard sphere structure factor³⁵⁻³⁷ was used. This factor assumes a spherically shaped interaction potential between the particles. Hence, the sphere's diameter, D , and volume fraction of the spheres, ϕ , are not parameters of the micelles, but of the modeled spheres around them, which represent their interaction potential. For the highest CUR concentration (10 g/L), a sticky hard sphere structure factor³⁵ was used, because sticky micelles and inter-micellar contacts were observed for A-pPrOzi-A/CUR = 10/10 g/L by cryo-TEM²⁹.

Fit Results

The possible parameter set of the chosen model is rather large including eight (without structure factor) or more fit variables. For reasons of clarity, only the micellar structure defining parameters (size parameters and SLDs) will be shown (Figure 2 and 3). Moreover, to constrain the fitting procedure, it was attempted to match the overall particle size with the results from DLS and cryo-TEM. The full list of model parameters for each sample can be found in the supporting information. As mentioned, A-pBuOzi-A and A-pBuOx-A form micelles without the need of added CUR with critical micelle concentration (cmc) values of 5 mg/L (0.5 μM) and 8 mg/L (1 μM), respectively. Only A-pPrOzi-A needs CUR to form micelles, i.e. shows CUR-induced micellization.²⁹ Hence, there are no values for the core and shell sizes as well as their respective SLDs for pure A-pPrOzi-A in heavy water without any CUR. Obviously, the micellar sizes and structures develop differently in dependence of the CUR-content for all three polymers (Figure 2, 3). Therefore, the different formulations will be evaluated separately in the following. Important to note, the formulation of A-pBuOx-A at polymer/CUR = 10/5 is already above the maximum drug loading, and precipitation occurs. This resulted in very unstable fits in our current work. Therefore, we will not discuss the data analysis of this formulation at this loading any further.

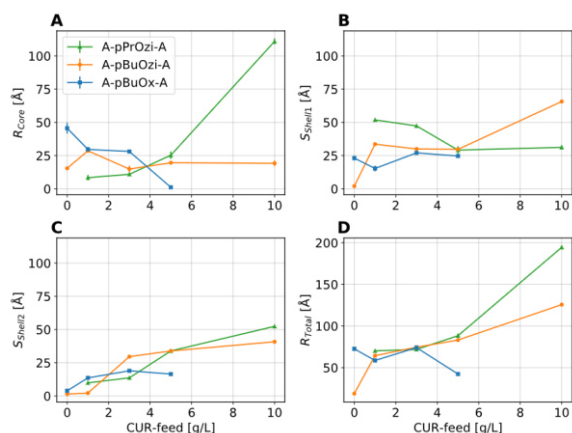


Figure 2: Graphic representation of the micellar size parameters: A) core radius, B) shell 1 thickness, C) shell 2 thickness and D) total micelle radius. Please note, when size parameters of a particular compartment approach zero, one can consider the resulting morphology again as core-shell instead of core-shell-shell.

A-pBuOzi-A

The core radius of pure A-pBuOzi-A micelles in water is approximately 18 Å (Figure 2, A). Since both shell thicknesses are negligibly small, the observed A-pBuOzi-A aggregates can be described as simple, surprisingly small spheres. Adding CUR (10/1) causes an increase of the micellar core to roughly 30 Å and the development of a first shell with nearly the same size (≈ 35 Å) (Figure 2, B). Increasing the CUR-content (10/3) further, the core of the A-BuOzi-A/CUR-micelles appears to shrink to its initial value and remains almost constant at around 18-20 Å upon further increase of CUR. The first (inner) shell remains at the same size as well for intermediate CUR loadings, but a second, outer shell becomes noticeable

for a CUR-concentration of 3 g/L, which has nearly the same size as the first shell (Figure 2, C). This shell also increases slightly in size with increasing CUR feed.

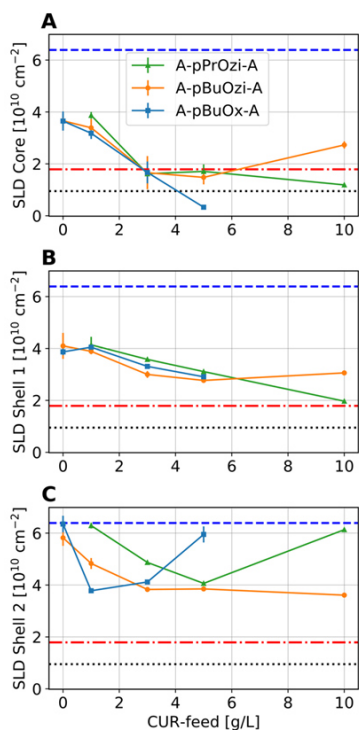


Figure 3: Graphic representation of the fitted SLDs of A) the micelles core, B) its first shell and C) second shell. Additionally, the SLDs of heavy water (blue dashed line), CUR (red dash-and-dot line) and the polymers (black dotted line) are marked.

At maximum loading (10/10), another notable change of the A-pBuOzi-A micelles is observed with the thickness of shell 1 doubling in size to approximately 60 Å. In general, we found that the data analysis at CUR concentrations of 10 g/L with only one fitting

model was very challenging. Our fit describes the vast majority of the particles in solution. Additional particles at lower concentrations can only be described with better *a priori* knowledge about their size and shape.

Apart from the size, further insights into the actual composition of the different micellar layers can be obtained from the fitted SLDs (Figure 3). Pure A-pBuOzi-A (CUR = 0 g/L) forms spherical aggregates with no core-shell differentiation. The fitted SLD is approx. $3.6 \times 10^{-6} \text{ \AA}^{-2}$ and therefore almost perfectly in between the SLDs of A-pBuOzi-A and D₂O (Table 2), suggesting that the ratio of A-pBuOzi-A/D₂O is roughly 1/1. In other words, these micelles do not exhibit a core-shell structure but are rather homogenous in composition, which we tentatively attribute to excellent hydration of the hydrophobic repeat units by virtue of the polar and flexible poly(2-oxazine) backbone. By adding CUR (CUR = 1 g/L), SLD_{core} decreases slightly (Figure 3, A), which could be an indication of the dehydration of the core in favor of CUR inclusion. The SLD of the first shell is slightly above the initial value of the spherical aggregates (roughly $4 \times 10^{-6} \text{ \AA}^{-2}$) (Figure 3, B), which hints towards a A-pBuOzi-A/D₂O mixture with a slightly higher D₂O-fraction. The second, very small, shell contains almost only D₂O as judged by the SLD (Figure 3, C). Being very small and essentially D₂O, this second shell is negligible. With increasing CUR concentration, the SLDs of the core and both shells decrease indicating further dehydration. After reaching a CUR concentration of 3 g/L, the SLDs of the system remain almost constant. This indicates a possibly stable composition in every part of the micelle. According to the SLDs, it appears as though CUR is mostly present in the core. At the highest possible CUR concentration of 10 g/L, the morphological situation is somewhat similar to the situation without CUR, as the composition of all components appears to be quite similar, according to the SLDs (Figure 3). Accordingly, we cannot consider the micelles anymore as core-shell-shell structure but rather a large homogeneous sphere. A similar distribution of CUR into the outer, hydrophilic shell of glycopolymers was previously observed by Stenzel and coworkers using SANS.²³ Increasing amount of CUR dehydrated the nanoparticle shell, which coincided well with a lower cellular uptake of the respective nanoparticles.

A-pBuOx-A

In contrast to A-pBuOzi-A, neat A-pBuOx-A micelles have a core-shell structure and are significantly larger than the A-pBuOzi-A assemblies at the same concentration with a total radius of approximately 75-80 Å (Figure 2, D). However, the SLDs of the core and this shell are also very similar (Figure 3, A and B). Again, the size of the second shell is negligible, resulting in an overall core-shell structure (Figure 2, C). This seems inconsistent as BuOzi should be more hydrophobic than BuOx, and thus, a stronger core-shell contrast would be expected. However, preliminary comparison of ¹H-NMR spectra in CDCl₃ and D₂O indeed suggest a highly hydrated and thus mobile BuOzi core, but this will have to be studied separately in more detail.

In contrast to the other two polymers, A-pBuOx-A micelles seem to shrink in size in the presence of CUR. At a CUR concentration of 1 g/L, the overall size of the micelles reduces to approximately 60 Å, even though a second shell becomes apparent (Figure 2, C and D). This can be explained by splitting of the initial shell into shell 1 and shell 2. Therefore, the thickness of the first shell is reduced by half and also the core size is reduced (Figure 2, A and B). Such a compaction of the aggregate structure could be a hint towards

strong polymer-CUR interactions. Interestingly, stronger drug-polymer interactions were recently suggested in the system A-pBuOx-A/CUR compared to A-pPrOzi-A/CUR by fluorescence up-conversion studies.¹³ Although A-pPrOzi-A enables extremely high CUR-loadings up to 54 wt.%, in contrast to 24 wt.% of A-pBuOx-A¹⁰, at low loading, the molecular mobility of CUR within A-pBuOx-A was lower than in A-pPrOzi-A. This was interpreted with stronger, more defined A-pBuOx-A/CUR interactions, whereas CUR seemed to be more loosely incorporated into A-pPrOzi-A.

With increasing CUR loading (10/3), the core size of A-pBuOx-A remains nearly constant while the first and second shell thickness slightly increases for the nanoformulations. This is in contrast to the other to polymer, where core slightly increases at this point. The total micelle radius approaches again 80 Å (Figure 2, D). Above this concentration, CUR starts to precipitate, which results in the failure of the fitting model, since more than one particle population is present in solution. Considering the SLD values, the core and first shell are heavily and almost equally well hydrated in the absence of CUR (Figure 3, A and B). The second shell of negligible size consists only of D₂O (Figure 3, C). At low loading (10/1), fitting revealed that the first and second shell exhibit same SLD-values and therefore should have a similar composition. Therefore, a simple core-shell morphology can be assumed. This is an indication of a dehydration of the core and the second shell. The lower core SLD can be explained by the presence of CUR, while the SLD reduction of the second shell could result from a higher polymer content. This is in good agreement with the overall smaller micellar size, and significantly reduced core size (Figure 2, A and D). Further increasing the CUR concentration to 3 g/L, the core SLD reduces to a point, where it can be assumed that the core is almost entirely consisting of CUR and A-pBuOx-A with little to no D₂O left (Figure 3, A). The SLD of the first shell reduces as well, while the SLD of the second shell increases (Figure 3, B and C). This could again indicate an incorporation of CUR in the first shell and increasing D₂O fraction in the outer shell.

A-pPrOzi-A

At a CUR concentration of 1 g/L, A-pPrOzi-A exhibits a pronounced core-shell-shell structure with a relatively small core and outer shell, but very big first shell (Figure 2). The total micelle radius is roughly 70-80 Å (Figure 2, D), which is in reasonably good agreement with data from DLS.²⁹ With increasing CUR concentrations, both the core and outer shell grow, while the inner shell shrinks. Reaching a CUR concentration of 10 g/L, the core dimension increases very profoundly, which is in line with data from DLS²⁹.

The SLDs of all A-pPrOzi-A-micelle parts decrease with increasing CUR concentration (Figure 3). Starting from a highly hydrated core and first shell, it is quickly evident that the largest amount of CUR is stabilized in the core of the micelles, since the SLDs of the core decrease much steeper and the SLD stabilizes in between the SLDs of pure CUR and A-pPrOzi-A (Figure 3, A). The involvement of the first shell in the solubilization of CUR is clearly evidenced by its SLD, which is smaller than the one of the second shell (Figure 3, B and C). The SLD of the large core corroborates a mixture of CUR and polymer. The relatively thin first shell remains hydrated as evident by a larger SLD value. The second shell vanishes again at this point as the SLD is essentially that of pure D₂O.

CUR spatial distribution at different loadings

Using the fitted sizes of each micelle section (Figure 2) and their respective SLDs (Figure 3), it is possible to estimate the amount of CUR, which is present in the respective component, *i.e.* the micellar core and shell. In this regard, the method established by Stenzel *et al.*^{22, 23} was used and modified. Since each micelle component can comprise polymer, CUR and D₂O, the fitted SLD can be written as

$$SLD_{Fit} = \phi_{polymer} \cdot SLD_{polymer} + \phi_{CUR} \cdot SLD_{CUR} + \phi_{D_2O} \cdot SLD_{D_2O}$$

with the volume fraction in each micelle component ϕ and the calculated SLDs of polymer, CUR and D₂O (Table 2). Additionally, the two boundary conditions

$$\phi_{polymer} + \phi_{CUR} + \phi_{D_2O} = 1,$$

$$\phi_{CUR}^{Core} + \phi_{CUR}^{shell1} + \phi_{CUR}^{shell2} = LC$$

can be used, where the loading capacity $LC = \frac{V_{CUR}}{V_{polymer} + V_{CUR}}$ constrains the total amount of CUR in the micelle. The extremely high values for LC were determined experimentally and are already reported by Lübtow *et al.*¹⁰ The following assumptions were made for the calculation of ϕ_{CUR} : Firstly, the second shell never incorporates any CUR, which may however not be entirely correct. Secondly, the D₂O amount in the core is negligible for all CUR concentrations. The last assumption guarantees a solvable equation system. If the CUR amount in the core is not sufficient for obtaining the measured loading capacity, the CUR amount in the first shell will be increased accordingly. The resulting CUR volume fractions ϕ_{CUR} of the core and the first shell show a clear trend for all three polymers (Figure 4).

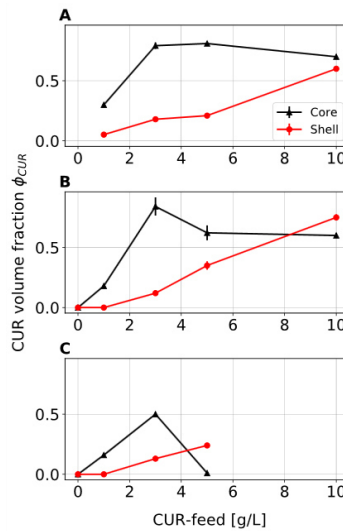


Figure 4: Calculated CUR volume fractions using the fitted SLDs of the core and first shell (Figure 3) for A) A-pPrOzi-A, B) A-pBuOzi-A and C) A-pBuOx-A. The total volume fraction was constrained by the sum of both ϕ_{CUR} of the core and first shell being identical to the reported loading capacities²⁹. Here, the volume of each micelle section (core and shell 1) was calculated using the structural parameters shown in Figure 3.

Additionally, the results are summarized and sketched in Figure 5. While the core mainly receives CUR at low [CUR]=1-3 g/L, the first shell must include small amounts of CUR here as well to obtain the measured LC. With increasing CUR feed, both core and shell 1 incorporate more CUR. ϕ_{CUR} in the shell reaches estimated values of up to 20-30% for all three polymers (3 and 5 g/L). Only at high polymer concentrations, the values for ϕ_{CUR} become less reasonable and trustworthy, since the nanoformulations either aggregated and precipitated (A-pBuOx-A) or the particle shape becomes more heterogenic due to the presence of larger agglomerates or

worm-like structures (A-pPrOzi-A and A-pBuOzi-A). Nevertheless, the analysis of SANS data unambiguously shows that the micellar shell is involved in incorporating large amounts of CUR and plays an essential role in the stabilization process. This corroborates recent finding, where solid-state NMR spectroscopy also revealed interaction of CUR with the amide moieties in the hydrophilic corona of A-pPrOzi-A which lead to a decrease in dissolution rates at higher loadings.²⁸ In addition, when the hydrophilic blocks were exchanged to the slightly less hydrophilic poly(2-ethyl-2-oxazoline), solubilization capacity of the corresponding ABA triblock copolymers for CUR and paclitaxel drastically decreased.³⁸ Similarly, stabilization of CUR and paclitaxel using a methacrylate based system featuring fructose containing corona forming blocks has also been previously reported.^{22, 23}

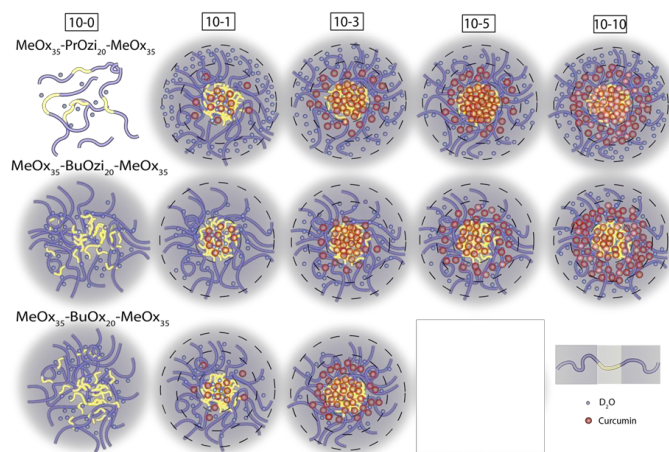


Figure 5: Schematic illustration of the different micellar morphologies at various CUR contents shown in Figure 5. The sizes of the micelle compartments are not to scale to facilitate comparability. To visualize the amount of CUR in each micellar section, the number of red dots roughly represents the respective CUR concentration.

4. CONCLUSION

Poly(2-oxazoline)/poly(2-oxazine) based micelles have been shown to be highly unusual as they enable extraordinary high drug loading of more than 50 wt.% in select cases. Increasing experimental evidence suggests that this high drug loading is intimately linked with interactions of the drug with the hydrophilic corona. Here, we investigated the influence of the loading of three different but structurally similar ABA triblock copolymers with the model compound curcumin on the morphology of the resulting micelles. While without CUR no pronounced core shell character was found, addition of small amounts of CUR enhanced the contrast between core and corona. In all cases, CUR concentrated in the core at low drug loadings. With increasing CUR concentrations, the picture becomes more complicated and the scattering data could not be reasonably fitted using the previously employed core-shell model. Our data suggests a core-shell-shell morphology, with parts of the hydrophilic corona filling up with CUR and effectively forming a second, inner shell, while the other shell remains hydrated and colloidally stabilizes the micelles. With more CUR added, this situation eventually becomes unstable, finally causing precipitation. This happens already at about 25 wt.% drug loading for the A-pBuOx-A micelles, while those with poly(2-oxazine) based B block allow overall drug loading of 50 wt.%. The insufficient difference in scattering length density between the hydrophilic and hydrophobic block of the studied block copolymers

made hampered a more detailed analysis of the presently investigated systems. However, to overcome this limitation will require block copolymer, in which the different blocks are deuterium labeled.

Acknowledgments

Financial support by the Deutsche Forschungsgemeinschaft is gratefully acknowledged (Project number 398461692, awarded to R.L.). The authors thank JCNS for allocating beamtime (proposal #12083) and providing excellent equipment and support, before, during and after the beam-time. Also, we appreciate valuable feedback by Ann-Christin Pöppler. M.M.L. would like to thank the Evonik Foundation for providing a doctoral fellowship.

References

- (1) Merisko-Liversidge, E. M.; Liversidge, G. G. Drug Nanoparticles: Formulating Poorly Water-Soluble Compounds. *Toxicol. Pathol.* **2008**, *36*, 43-48.
- (2) Giliyar, C.; Fikstad, D.; Tyavanagimatt, S. Challenges and opportunities in oral delivery of poorly water-soluble drugs. *Drug Deliv. Technol* **2006**, *6*, 57-63.
- (3) Williams, H. D.; Trevaskis, N. L.; Charman, S. A.; Shanker, R. M.; Charman, W. N.; Pouton, C. W.; Porter, C. J. H. Strategies to Address Low Drug Solubility in Discovery and Development. *Pharmacol. Rev.* **2013**, *65*, 315.
- (4) Cabral, H.; Miyata, K.; Osada, K.; Kataoka, K. Block Copolymer Micelles in Nanomedicine Applications. *Chem. Rev.* **2018**, *118*, 6844-6892.
- (5) Liu, J.; Xiao, Y.; Allen, C. Polymer-drug compatibility: A guide to the development of delivery systems for the anticancer agent, ellipticine. *J. Pharm. Sci.* **2004**, *93*, 132-143.
- (6) Kasimova, A. O.; Pavan, G. M.; Danani, A.; Mondon, K.; Cristiani, A.; Scapozza, L.; Gurny, R.; Möller, M. Validation of a Novel Molecular Dynamics Simulation Approach for Lipophilic Drug Incorporation into Polymer Micelles. *J. Phys. Chem. B* **2012**, *116*, 4338-4345.
- (7) Jonathan Baell, M. A. W. Chemical con artists foil drug discovery. *Nature* **2014**, *513*, 481-483.
- (8) Heger, M. Drug screening: Don't discount all curcumin trial data. *Nature* **2017**, *543*, 40-40.
- (9) Gupta, S. C.; Patchva, S.; Aggarwal, B. B. Therapeutic Roles of Curcumin: Lessons Learned from Clinical Trials. *AAPS J.* **2013**, *15*, 195-218.
- (10) Lübtow, M. M.; Hahn, L.; Haider, M. S.; Luxenhofer, R. Drug Specificity, Synergy and Antagonism in Ultrahigh Capacity Poly(2-oxazoline)/Poly(2-oxazine) based Formulations. *J. Am. Chem. Soc.* **2017**, *139*, 10980-10983.
- (11) Seo, Y.; Schulz, A.; Han, Y.; He, Z.; Bludau, H.; Wan, X.; Tong, J.; Bronich, T. K.; Sokolsky, M.; Luxenhofer, R.; Jordan, R.; Kabanov, A. V. Poly(2-oxazoline) block copolymer based formulations of taxanes: effect of copolymer and drug structure, concentration, and environmental factors. *Polym. Adv. Technol.* **2015**, *26*, 837-850.
- (12) Lübtow, M. M.; Haider, M. S.; Kirsch, M.; Klisch, S.; Luxenhofer, R. Like Dissolves Like? A Comprehensive Evaluation of Partial Solubility Parameters to Predict Polymer-Drug Compatibility in Ultrahigh Drug-Loaded Polymer Micelles. *Biomacromolecules* **2019**, *20*, 3041-3056.
- (13) Lübtow, M. M.; Marciniak, H.; Schmiedel, A.; Roos, M.; Lambert, C.; Luxenhofer, R. Ultra-high to ultra-low drug loaded micelles: Probing host-guest interactions by fluorescence spectroscopy. *Chem.: Eur. J.* **2019**, *25*, 12601-12610.

- (14) Milonaki, Y.; Kaditi, E.; Pispas, S.; Demetzos, C. Amphiphilic gradient copolymers of 2-methyl- and 2-phenyl-2-oxazoline: self-organization in aqueous media and drug encapsulation. *J. Polym. Sci. Pol. Chem.* **2012**, *50*, 1226-1237.
- (15) Zhang, Y.; Ren, T.; Gou, J.; Zhang, L.; Tao, X.; Tian, B.; Tian, P.; Yu, D.; Song, J.; Liu, X.; Chao, Y.; Xiao, W.; Tang, X. Strategies for improving the payload of small molecular drugs in polymeric micelles. *J. Control. Release* **2017**, *261*, 352-366.
- (16) Naksuriya, O.; Okonogi, S.; Schiffelers, R. M.; Hennink, W. E. Curcumin nanoformulations: A review of pharmaceutical properties and preclinical studies and clinical data related to cancer treatment. *Biomaterials* **2014**, *35*, 3365-3383.
- (17) Raveendran, R.; Mullen, K. M.; Wellard, R. M.; Sharma, C. P.; Hoogenboom, R.; Dargaville, T. R. Poly(2-oxazoline) block copolymer nanoparticles for curcumin loading and delivery to cancer cells. *Eur. Polym. J.* **2017**, *93*, 682-694.
- (18) Datta, S.; Jutková, A.; Šrámková, P.; Lenkavská, L.; Huntošová, V.; Chorvát, D.; Miškovský, P.; Jancura, D.; Kronek, J. Unravelling the Excellent Chemical Stability and Bioavailability of Solvent Responsive Curcumin-Loaded 2-Ethyl-2-oxazoline-grad-2-(4-dodecyloxyphenyl)-2-oxazoline Copolymer Nanoparticles for Drug Delivery. *Biomacromolecules* **2018**, *19*, 2459-2471.
- (19) Lübtow, M. M.; Keßler, L.; Appelt-Menzel, A.; Lorson, T.; Gangloff, N.; Kirsch, M.; Dahms, S.; Luxenhofer, R. More Is Sometimes Less: Curcumin and Paclitaxel Formulations Using Poly(2-oxazoline) and Poly(2-oxazine)-Based Amphiphiles Bearing Linear and Branched C9 Side Chains. *Macromol. Biosci.* **2018**, *18*, 1800155.
- (20) Johnson, L. M.; Li, Z.; LaBelle, A. J.; Bates, F. S.; Lodge, T. P.; Hillmyer, M. A. Impact of Polymer Excipient Molar Mass and End Groups on Hydrophobic Drug Solubility Enhancement. *Macromolecules* **2017**, *50*, 1102-1112.
- (21) Li, Z.; Lenk, T. I.; Yao, L. J.; Bates, F. S.; Lodge, T. P. Maintaining Hydrophobic Drug Supersaturation in a Micelle Corona Reservoir. *Macromolecules* **2018**, *51*, 540-551.
- (22) Cao, C.; Zhao, J.; Lu, M.; Garvey, C. J.; Stenzel, M. H. Correlation between Drug Loading Content and Biological Activity: The Complexity Demonstrated in Paclitaxel-Loaded Glycopolymer Micelle System. *Biomacromolecules* **2019**, *20*, 1545-1554.
- (23) Cao, C.; Zhao, J.; Chen, F.; Lu, M.; Khine, Y. Y.; Macmillan, A.; Garvey, C. J.; Stenzel, M. H. Drug-Induced Morphology Transition of Self-Assembled Glycopolymers: Insight into the Drug-Polymer Interaction. *Chem. Mater.* **2018**, *30*, 5227-5236.
- (24) Schulz, A.; Jaksch, S.; Schubel, R.; Wegener, E.; Di, Z.; Han, Y.; Meister, A.; Kressler, J.; Kabanov, A. V.; Luxenhofer, R.; Papadakis, C. M.; Jordan, R. Drug-Induced Morphology Switch in Drug Delivery Systems Based on Poly(2-oxazoline)s. *ACS Nano* **2014**, *8*, 2686-2696.
- (25) Jaksch, S.; Schulz, A.; Di, Z.; Luxenhofer, R.; Jordan, R.; Papadakis, C. M. Amphiphilic Triblock Copolymers from Poly(2-oxazoline) with Different Hydrophobic Blocks: Changes of the Micellar Structures upon Addition of a Strongly Hydrophobic Cancer Drug. *Macromol. Chem. Phys.* **2016**, *217*, 1448-1456.
- (26) Wan, X.; Min, Y.; Bludau, H.; Keith, A.; Sheiko, S. S.; Jordan, R.; Wang, A. Z.; Sokolsky-Papkov, M.; Kabanov, A. V. Drug Combination Synergy in Worm-like Polymeric Micelles Improves Treatment Outcome for Small Cell and Non-Small Cell Lung Cancer. *ACS Nano* **2018**, *12*, 2426-2439.
- (27) Callari, M.; De Souza, P. L.; Rawal, A.; Stenzel, M. H. The Effect of Drug Loading on Micelle Properties: Solid-State NMR as a Tool to Gain Structural Insight. *Angew. Chem. Int. Ed.* **2017**, *56*, 8441-8445.
- (28) Pöppler, A.-C.; Lübtow, M. M.; Schlauersbach, J.; Wiest, J.; Meinel, L.; Luxenhofer, R. Loading dependent Structural Model of Polymeric Micelles Encapsulating Curcumin by Solid-State NMR Spectroscopy. *Angew. Chem. Int. Ed.* **2019**, doi:10.1002/anie.201908914.
- (29) Lübtow, M. M.; Nelke, L. C.; Seifert, J.; Kühnemundt, J.; Sahay, G.; Dandekar, G.; Nietzer, S. L.; Luxenhofer, R. Drug induced micellization into ultra-high capacity and stable curcumin nanoformulations: Physico-chemical characterization and evaluation in 2D and 3D in vitro models. *J. Control. Release* **2019**, *303*, 162-180.
- (30) Feoktystov, A. V.; Frielinghaus, H.; Di, Z.; Jaksch, S.; Pipich, V.; Appavou, M.-S.; Babcock, E.; Hanslik, R.; Engels, R.; Kemmerling, G.; Kleines, H.; Ioffe, A.; Richter, D.; Bruckel, T. KWS-1 high-resolution small-angle neutron scattering instrument at JCNS: current state. *J. Appl. Cryst.* **2015**, *48*, 61-70.
- (31) Ilavsky, J.; Jemian, P. R. Irena: tool suite for modeling and analysis of small-angle scattering. *J. Appl. Cryst.* **2009**, *42*, 347-353.
- (32) National Institute of Standards and Technology (NIST) Chemistry WebBook (SRD 69), Thermophysical Properties of Fluid Systems, <https://webbook.nist.gov/chemistry/fluid/> (accessed June 2019).
- (33) Balasubramanian, S.; Mohite, A. M.; Singh, K. K.; Zachariah, T. J.; Anand, T. Physical properties of turmeric (*Curcuma longa* L.). *JOSAC* **2012**, *21*, 178-181.
- (34) Sears, V. F. Neutron scattering lengths and cross sections. *Neutron News* **1992**, *3*, 26-37.
- (35) Kline, S. Reduction and analysis of SANS and USANS data using IGOR Pro. *J. Appl. Cryst.* **2006**, *39*, 895-900.
- (36) Hammouda, B. *Probing Nanoscale Structures – The SANS Toolbox*. National Institute of Standards and Technology (NIST), Center for Neutron Research, Gaithersburg: 2016; Vol. chapter 32 - Structure factors for particulate systems.
- (37) Percus, J. K.; Yevick, G. J. Analysis of Classical Statistical Mechanics by Means of Collective Coordinates. *Phys. Rev.* **1958**, *110*, 1-13.
- (38) Haider, M. S.; Lübtow, M. M.; Endres, S.; Aseyev, V.; Pöppler, A.-C.; Luxenhofer, R. Think Beyond the Core: The Impact of the Hydrophilic Corona on the Drug Solubilization Using Polymer Micelles. *ChemRxiv* **2019**, <https://doi.org/10.26434/chemrxiv.9710579.v1>.
-

4.4 Pharmaceutical Properties of Drug-Loaded Micelles

So far, critical formulation parameters as well as the structure of drug-loaded POx and POzi based micelles were investigated systematically. CUR was chosen as model compound due to its extremely low water solubility as well as chemical instability. Although a plethora of papers claim health benefits by CUR, a growing number of reports highlight that many experimental results may be artefacts or outright deny any suitability of CUR as drug due to its problematic physicochemical properties. Nevertheless, the small micellar sizes, extremely high loadings as well as sufficient long-term stabilities of some of the here presented CUR formulations are promising for IV administration. Therefore, the anti-tumoral activity of the latter was critically evaluated in conventional 2D cell culture as well as more sophisticated 3D tumor test systems. Although nanoformulated CUR prevented the adherence of malignant SW480 cells to a collagen scaffold in a flow bioreactor, suggesting anti-metastatic potential of CUR, the stability of the CUR-loaded micelles as well as their efficient transport to the site of action *in vivo* remains highly challenging and needs to be evaluated.



Drug induced micellization into ultra-high capacity and stable curcumin nanoformulations: Physico-chemical characterization and evaluation in 2D and 3D *in vitro* models



Michael M. Lübtow^a, Lena C. Nelke^b, Julia Seifert^b, Johanna Kühnemundt^b, Gaurav Sahay^{d,e}, Gudrun Dandekar^{b,c}, Sarah L. Nietzer^{b,**}, Robert Luxenhofer^{a,*}

^a Functional Polymer Materials, Department of Chemistry and Pharmacy and Bavarian Polymer Institute, Würzburg University, Röntgenring 11, 97070 Würzburg, Germany

^b University Hospital Würzburg, Röntgenring 11, 97070 Würzburg, Germany

^c Translational Center 'Regenerative Therapies' (TLC-RT), Fraunhofer Institute for Silicate Research (ISC), Neunerplatz 2, 97082 Würzburg, Germany

^d Department of Pharmaceutical Sciences, College of Pharmacy, Oregon State University, Collaborative Life Science Building, 2730 SW Moody Avenue, Portland, OR 97201, United States

^e Department of Biomedical Engineering, Oregon Health and Science University, Collaborative Life Science Building, 2730 SW Moody Avenue, Portland, OR 97201, United States

ARTICLE INFO

Keywords:

Nanomedicine
Drug delivery
Poly(2-oxazoline)
Poly(2-oxazine)
3D tumor model
Solid amorphous dispersion

ABSTRACT

Curcumin (CUR) is a natural extract from the plant *Curcuma longa* and part of turmeric, a spice and herbal remedy in traditional medicine. Thousands of papers claim a plethora of health benefits by CUR, but a growing number of reports and contributions caution that many experimental data may be artifacts or outright deny any suitability of CUR due to its problematic physicochemical properties. Two major issues often encountered with CUR are its extraordinarily low solubility in water and its limited chemical stability. Here, we report on a novel nanoformulation of CUR that enables CUR concentrations in water of at least 50 g/L with relative drug loadings of > 50 wt% and high dose efficacy testing in 3D tumor models. Despite this high loading and concentration, the CUR nanoformulation comprises polymer-drug aggregates with a size < 50 nm. Most interestingly, this is achieved using an amphiphilic block copolymer, that by itself does not form micelles due to its limited hydrophilic/lipophilic contrast. The ultra-high loaded nanoformulations exhibit a very good stability, reproducibility and redispersibility. In order to test effects of CUR in conditions closer to an *in vivo* situation, we utilized a 3D tumor test system based on a biological decellularized tissue matrix that better correlates to clinical results concerning drug testing. We found that in comparison to 2D culture, the invasively growing breast cancer cell line MDA-MB-231 requires high concentrations of CUR for tumor cell eradication in 3D. In addition, we supplemented a 3D colorectal cancer model of the malignant cell line SW480 with fibroblasts and observed also in this invasive tumor model with stroma components a decreased tumor cell growth after CUR application accompanied by a loss of cell-cell contacts within tumor cell clusters. In a flow bioreactor simulating cancer cell dissemination, nanoformulated CUR prevented SW480 cells from adhering to a collagen scaffold, suggesting an anti-metastatic potential of CUR. This offers a rationale that the presented ultra-high CUR-loaded nanoformulation may be considered a tool to harness the full therapeutic potential of CUR.

1. Introduction

For many years, high-throughput screenings [1] have been seen as a game changer for the discovery of lead molecules for active pharmaceutical ingredients (API). However, when it comes to the development of a dosage form, one major challenge, the appropriate formulation of the API, remains. An estimated 40% [2] – 60% [3] of all NCEs (new

chemical entities) developed in medicinal chemistry and pharmaceutical industry are practically insoluble in water. In addition, 90% of all APIs in today's drug delivery pipelines are reported to be poorly water-soluble [4], which poses a major challenge for the pharmaceutical industry [4,5]. Obviously, the demand for excipients that increase the water solubility and thus, the bioavailability of hydrophobic compounds is enormous.

* Corresponding author at: University of Würzburg, Röntgenring 11, 97070 Würzburg, Germany.

** Corresponding author.

E-mail addresses: sarah.nietzer@uni-wuerzburg.de (S.L. Nietzer), robert.luxenhofer@uni-wuerzburg.de (R. Luxenhofer).

Naturally, amphiphilic compounds are of paramount interest in this context. First thoughts of using polymeric micelles for medicinal applications were already reviewed in the early 1980s by Ringsdorf and coworkers [6]. Polymeric micelles are nanoscopic, typically core/shell structures formed by amphiphilic block copolymers. Both, the inherent and modifiable properties of polymeric micelles make them particularly well suited for formulation purposes [7]. Several polymeric micellar formulations are currently undergoing preclinical [8], phase I [9], phase II [10,11], and phase III [12] clinical trials, which have shown improved antitumor efficacy and reduced systemic toxicity [13].

Poly(2-oxazoline)s (POx) are currently intensively discussed as a promising and highly versatile class of biomaterials [14–16]. Hydrophilic and amphiphilic POx have been reported to exhibit a high cytocompatibility [17–20], easy modulation of solubility and size [21], architecture [22–24] as well as chemical functionality [25]. Although their synthesis was already reported in the mid-1960s [26–28], it took almost 30 years until first attempts towards POx-based systems for non-fouling surfaces [29] and drug delivery systems [30] were explored. Block copolymers of poly(2-oxazoline)s (POx) are accessible via living cationic ring-opening polymerization (LCROP) of 5 membered cyclic imino ethers (2-oxazolines) (Fig. 1a) [28]. The combination of LCROP of 2-oxazolines with other types of polymerization can further increase the structural variety of the polymer amphiphiles. In 2015, Zhao et al. utilized pH-responsive polymeric micelles based on poly(2-ethyl-2-oxazoline)-poly(*D,L*-lactide) (pEtOx-PLA) prepared by combining LCROP with anionic ring-opening polymerization of *D,L*-lactide for co-delivery of the chemotherapeutic doxorubicin and a P-glycoprotein inhibitor in a targeted and controlled manner [31]. In addition, attaching poly-ethylenimine (PEI) onto pEtOx-PLA micelles enabled the co-delivery of minicircle DNA vectors and doxorubicin achieving cell internalization resulting in effective gene expression and anti-tumoral activity [32]. However, also pure POx based micelles have shown excellent formulation abilities. Luxenhofer et al. [33] utilized polymeric micelles based on amphiphilic ABA triblock-copolymers to solubilize paclitaxel (PTX), which is characterized by an extremely low aqueous solubility ($\log P = 3.70$ [34] – 3.96 [35]; solubility (H_2O) = 0.4 mg/L [36]). The investigated amphiphile comprised of two hydrophilic poly(2-methyl-2-oxazoline) (pMeOx) blocks A and a modestly hydrophobic poly(2-butyl-2-oxazoline) (pBuOx) block B (Fig. 1b) exhibited high loading capacities of almost 50 wt% PTX as well as a high water solubility of the resulting formulation, corresponding to an increase of solubility of PTX over five orders of magnitude to 50 g/L. [37,38] *In vivo* studies revealed superior antitumor efficacy of the obtained POx/PTX nanoformulations compared to commercially available formulations Taxol® or Abraxane® with maximum tolerated doses (MTD) of 150 mg/kg (c.f. 20 mg/kg for Taxol® and 90 mg/kg for Abraxane®, respectively) [39]. Schulz et al. [38], Seo et al. [37] and Jaksch et al. [40] explored some facets of the

interplay of POx and drug structure on the solubilization behavior and micellar morphology and found marked polymer/drug specificities. In these reports, the POx side chain was varied. However, changes in the polymer main chain may also be used to tailor polymer-drug compatibility, which makes this system even more versatile and interesting.

Poly(2-oxazine)s (POzi) can be formally derived from poly(2-oxazoline)s (POx) by shifting a methylene group from the polymer side chain to the polymer main chain (Fig. 1a). Although similar in chemical structure and discovered along with POx some decades ago [41], POzi have been much less investigated than POx with only a handful of papers published [42–47]. Similar to POx, POzi can be obtained via living cationic ring-opening polymerization (LCROP) employing 6-membered 2-substituted 2-oxazine (IUPAC: 2-*R*-5,6-dihydro-4*H*-1,3-oxazine) monomers instead of 2-substituted 2-oxazolines (IUPAC: 2-*R*-4,5-dihydrooxazole) (Fig. 1a) [44,48]. Thus, POzi and POx offer an interesting macromolecular design space via side chain and main chain variation, which cannot be realized in the same way by acrylate or vinyl based polymers.

Very recently, Lübtow et al. reported that the structural variation between POx and POzi can have a major effect with respect to drug formulation. Pronounced drug/polymer specificities with regard to the solubilization capacity for PTX and curcumin (CUR), were observed [49]. While being the most effective solubilizer for paclitaxel, the triblock-copolymer bearing a moderately hydrophobic poly(2-butyl-2-oxazoline) (A-pBuOx-A) core was least effective in solubilizing CUR. In contrast, its structural isomer bearing a poly(2-propyl-2-oxazine) core (A-pPrOzi-A, Fig. 1b) exhibited excellent solubilization for CUR even though this polymer is even less hydrophobic.

CUR ($\log P = 3.28$ [50], solubility (H_2O) = 0.6 $\mu\text{g}/\text{mL}$ [51]) is a natural yellow phenolic compound which is present in many kind of herbs, particularly in *Curcuma longa* (turmeric). It is a bis- α,β -unsaturated β -diketone which exhibits keto-enol tautomerism (Fig. 2).

Although a vast number of preclinical and clinical studies [52] pointed out the antioxidant [53], cardioprotective [54], neuroprotective [55,56], antidiabetic [57], anti-inflammatory [58,59] and anti-tumor [60] activities of CUR (and its related curcuminoids as well as its natural analogues [61]), the “generally regarded as safe” compound has not been approved as a drug for human use. As Baell and Walters [62] pointed out, “some of the compounds that should ring the most warning bells are toxoflavin and polyhydroxylated natural phytochemicals such as CUR [...]”. So-called pan-assay interference compounds (PAINS) can interfere with assays, making them appear to be active even if they are not. It is argued that eventually these compounds are condemned to fail, sometimes only in late stage clinical trials. However, this critical viewpoint is not unchallenged [63]. A reason for the many activities of CUR is that it may function as a reactive chemical rather than a specific binder for, e.g. a certain protein [64]. On the one hand, CUR is claimed

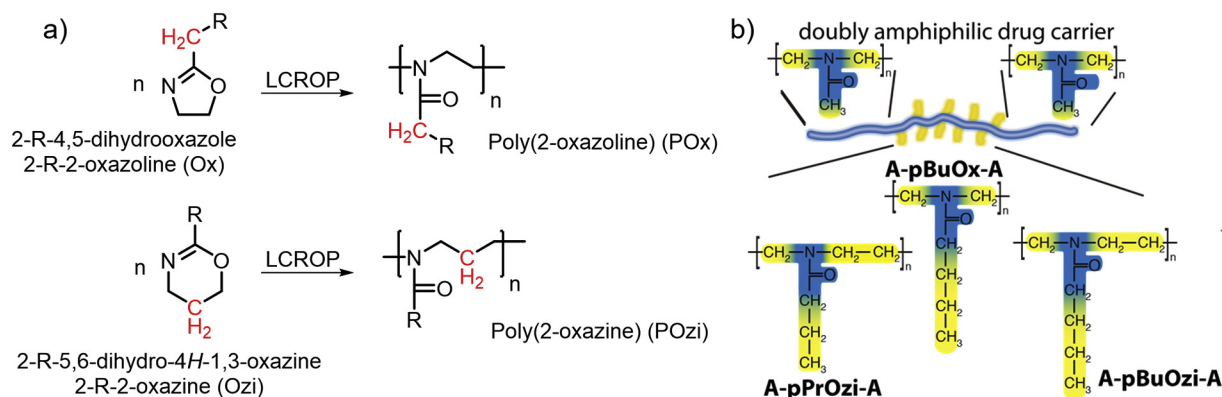


Fig. 1. a) Schematic synthesis of the structural isomers poly(2-oxazoline)s (POx) and poly(2-oxazine)s (POzi) by living cationic ring opening polymerization (LCROP) of 2-substituted 2-oxazolines (IUPAC: 2-*R*-4,5-dihydrooxazole) and 2-substituted 2-oxazines (IUPAC: 2-*R*-5,6-dihydro-4*H*-1,3-oxazines); b) Schematic representation of the amphiphilic triblock copolymers investigated in the present study.

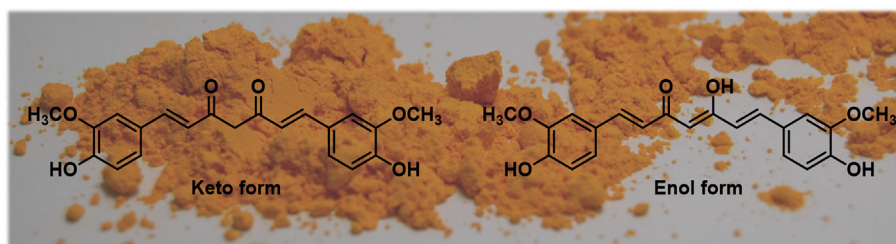


Fig. 2. Physical appearance and chemical structure of CUR showing the keto-enol tautomers of diferuloylmethane.

to modulate various signaling molecules (interleukin-1 β [65]; cyclooxygenase-2 [66], prostaglandin E₂ [67], NF- κ B [68]; etc.) making it a non-discriminating substance rather than a monotargeted therapeutic (taking into account that CUR degradation products might also display biological properties [69,70]). On the other hand, the chemical reactivity causes rapid metabolism *in vivo* which, in combination with its extremely low water solubility drastically reduces its bioavailability [71].

A plethora of studies to increase the bioavailability of CUR can be found in the literature, starting with the addition of simple adjuvants like piperine [72], however, only with modest success. More sophisticated approaches include the use of nanotechnology, but most CUR nanoformulations suffer from mediocre drug loading (approx. 10–20 wt %) [73,74] and low overall solubility (0.3 g/L (loading capacity (LC) = 13 wt%) [75]; 0.4 g/L (LC = 17 wt%) [76]; 41 mg/L (LC = 12%) [77]; 0.22 g/L (LC = 5.2%) [78], 1.1 g/L (LC = 22 wt%) [79]). Nevertheless, nanoformulated CUR [80] showed therapeutic efficacy in numerous *in vitro* [81,82] and *in vivo* [83] studies. Relying on these promising results, formulated CUR has actually reached the market as food supplement to increase the bioavailability of orally administered CUR in various forms: THERACURMIN® (colloidal nanoparticles comprising gum-ghatti and glycerin; LC = 10 wt%; 27 fold-increase [84,85]; Meriva® (curcumin-phospholipid [86,87]; LC = 20 wt% [88]; 29-fold increase [89]); BCM-95®CG (Biocurcumin™; micronized CUR mixed with turmeric essential oils; 6.9-fold-increase [90]). However, plasma concentrations were still significantly lower than those required for the inhibition of most anti-inflammatory targets of CUR (Meriva®: $c_{\max} = 206.9 \pm 54.9$ ng/mL [89]; THERACURMIN®: $c_{\max} = 29.5 \pm 12.9$ ng/mL; BCM-95®CG: $c_{\max} = 456.88$ ng/mL). This might be due to the still insufficient water solubility of the respective CUR-formulations. In contrast, using **A-pPrOzi-A**, CUR nanoformulations with an extremely high solubilization exhibiting 11.9 g/L (32.3 mM) CUR at 10 g/L polymer in aqueous media (LC = 54 wt%) was reported. This exceptional high solubility in combination with the observation, that the bioavailability of micellar curcuminoids (formulated with Tween-80; LC = 7 wt%) [91] was not only significantly higher than of native curcuminoids [92], but also 11-fold higher [92] than for curcuminoids simply mixed with solubilizing phytochemicals (LC = 33 wt%) and 20 fold higher than micronized CUR [93] makes it a promising candidate for CUR-based treatments. However, a good water solubility of the drug is only one aspect when it comes to administration. Others which have to be considered are the physical state of the drug (crystalline or amorphous), serum stability, size of the nanoparticles as well as shelf life and batch-to-batch reproducibility of the formulation.

It is well-known that two-dimensional (2D) cell culture has limitations regarding assessment of the therapeutic efficacy *in vivo*. Growing evidence suggests that three-dimensional (3D) tumor models may be able to reflect the complex situation *in vivo* more accurately. For this reason, we evaluated and compared our ultra-high loaded CUR nanoformulations in 2D and 3D cell culture using the triple negative breast cancer cell line MDA-MB-231 as well as the colorectal cancer cell line SW480 in mono- and co-culture with primary fibroblasts. The utilized 3D tumor models are based on a decellularized porcine intestinal matrix

(SISmuc, Small Intestinal Submucosa with preserved mucosa) that allows 3D tumor cell growth within the former crypt structures and the invasion into deeper parts of the tissue matrix across the basement membrane [94–98].

2. Materials and methods

2.1. Reagents and solvents

All substances for the preparation of the polymers were purchased from *Sigma-Aldrich* (Steinheim, Germany) or *Acros* (Geel, Belgium) and were used as received unless otherwise stated. CUR powder from *Curcuma longa* (turmeric) was purchased from *Sigma-Aldrich* and analyzed in-house (curcumin = 79%; demethoxycurcumin = 17%, bisdemethoxycurcumin = 4%; determined by HPLC analysis; Fig. S22). Deuterated solvents for NMR analysis were obtained from *Deutero GmbH* (Kastellaun, Germany).

Phosphate-buffered saline (PBS) was prepared by dissolving 8.0 g (137 mmol) NaCl, 0.2 g (2.7 mmol) KCl, 1.42 g (10 mmol) Na₂HPO₄ and 0.27 g (1.98 mmol) KH₂PO₄ in 1.0 L of deionized water (pH 7.4 at 25 °C). If necessary, pH was adjusted to pH 7.4 with aqueous HCl or NaOH solution.

The monomers 2-*n*-propyl-2-oxazine (PrOzi), 2-*n*-butyl-2-oxazoline (BuOx) and 2-*n*-butyl-2-oxazine (BuOzi) were prepared following the procedure by Seeliger et al. (Figs. S1–S4) [99]. All substances used for polymerization, methyl trifluoromethylsulfonate (MeOTf), propargyl p-toluenesulfonate, MeOx, BuOx, PrOzi, BuOzi, benzonitrile (PhCN), sulfolane, acetonitrile, and other solvents for polymer preparation were refluxed over CaH₂ (benzonitrile (PhCN) was refluxed over P₂O₅) and distilled under argon.

2.2. Polymer synthesis

The polymerizations and work-up procedures were carried out as described previously [100]. For polymer synthesis and characterization see Figs. S5–S19). Exemplary, the preparation of **A-pPrOzi-A** was performed as follows:

Under dry and inert conditions, 0.37 g (1.76 mmol, 1 eq) propargyl p-toluenesulfonate and 5.19 g (61.0 mmol, 35 eq) 2-methyl-2-oxazoline (MeOx) were dissolved in 35 mL dry sulfolane [101] (preheated to 37 °C) at room temperature. The mixture was stirred for 16 h at 90 °C. After cooling to RT, the monomer for the second block, 2-*n*-propyl-2-oxazine (4.41 g, 34.7 mmol, 20 eq) was added and the mixture was stirred for 20 h at 100 °C. The procedure was repeated for the third block with 5.19 g (61.0 mmol, 35 eq) MeOx. Termination was carried out with 0.97 g of 1-Boc-piperazine (5.23 mmol, 3 eq) at 50 °C overnight. K₂CO₃ (0.24 g, 1.74 mmol, 1 eq) was added and the mixture was stirred at 50 °C overnight. Precipitates were removed by centrifugation. The supernatant was transferred into a dialysis bag (MWCO 1 kDa) and dialyzed against deionized water (1 L) overnight. The solution was recovered from the bag and lyophilized.

3. Methods

3.1. Nuclear magnetic resonance spectroscopy (NMR)

NMR spectra were recorded on a Fourier 300 (^1H ; 300 MHz), Bruker Biospin (Rheinstetten, Germany) at 298 K. The spectra were calibrated to the signals of residual protonated solvent signals (CDCl_3 : 7.26 ppm; D_2O 4.79 ppm). Multiplicities of signals are depicted as follows: s, singlet; d, doublet; t, triplet; q, quartet; quin, quintet; dt; doublet of triplets; m, multiplet; b, broad.

3.2. Dialysis

Dialysis was performed using Spectra/Por membranes with a molecular weight cutoff (MWCO) of 1 kDa (material: cellulose acetate) obtained from neoLab (Heidelberg, Germany). Deionized water was renewed after 1 h, 4 h and every 12 h subsequently, until end of dialysis.

3.3. Gel permeation chromatography

Gel permeation chromatography (GPC) was performed on an Agilent 1260 Infinity System, Polymer Standard Service (Mainz, Germany) with either HFIP containing 3 g/L potassium trifluoroacetate; precolumn: 50×8 mm PSS PFG linear M; 2 columns: 300×8 mm PSS PFG linear M (particle size $7 \mu\text{m}$; pore size 0.1–1000 kDa) or DMF containing 1 g/L LiBr; precolumn: 50×8 mm PSS GRAM; columns: 30 \AA and 1000 \AA 300×8 mm PSS GRAM (particle size $10 \mu\text{m}$) as eluent. The columns were kept at 40°C and flow rates were 1.0 mL/min (DMF) or 0.7 mL/min (HFIP). Prior to each measurement, samples were filtered through $0.2 \mu\text{m}$ PTFE filters, Roth (Karlsruhe, Germany). Conventional calibration was performed with PEG standards (0.1–1000 kg/mol) and data was processed with WinGPC software.

3.4. DSC

For DSC studies, samples were placed into flat-bottom aluminum pans with crimped-on lids and heated/cooled on a calibrated DSC 204 F1 Phoenix equipped with a CC200 F1 Controller, (NETZSCH, Selb, Germany). The dynamic scans were recorded in nitrogen atmosphere with a heating rate of $5^\circ\text{C}/\text{min}$ (0°C – 180°C).

3.5. XRD

X-ray diffraction (XRD) was performed on a D Advance X-ray diffractometer (Bruker Axs Inc. Germany) using $\text{Cu-K}\alpha$ radiation ($\lambda = 1.54184 \text{ \AA}$) at 40 kV voltage, 40 mA current, a scanning rate of $5^\circ/\text{min}$ and a 2θ angle ranging from 5° to 60° .

3.6. Drug formulation

Drug-loaded polymer micelles were prepared using the thin film method [33]. Ethanolic polymer (20 g/L–50 g/L) and CUR (5.0 g/L) stock solutions were mixed in desired ratio. After complete removal of the solvent at 55°C under a mild stream of argon, the films were dried *in vacuo* (≤ 0.2 mbar) for at least 3 h (final polymer concentration: 10 g/L) or overnight (final polymer concentration: 50 g/L). Subsequently, preheated (37°C) deionized H_2O , PBS or aqueous serum albumin solution (10 g/L) was added to obtain desired polymer and CUR concentrations as mentioned in the main text. To ensure complete solubilization, the solutions were shaken at 55°C for 10 min at 1250 rpm (10 g/L polymer concentration) or at least 25 min (50 g/L polymer concentration) with a Thermomixer comfort (Eppendorf AG, Hamburg, Germany). Non-solubilized drug (if any) was removed by centrifugation for 5 min at 10,000 rpm (5,000 g) with a 3-Speed micro centrifuge, (neoLab, Heidelberg, Germany). Solubilization experiments were performed with 3 individually prepared samples and results are presented

as means \pm standard deviation (SD).

CUR quantification was performed by UV–Vis absorption on a BioTek Eon Microplate Spectrophotometer, Thermo Fisher Scientific (MA, USA) using a calibration curve obtained with known amounts of CUR in EtOH (Fig. S23). Samples were prepared in Rotilabo F-Type 96 well plates (Carl Roth GmbH & Co. KG, Karlsruhe, Germany) with a constant volume of 100 μL . Spectra were recorded from 260 to 600 nm at a constant reading speed of 1 nm at 298 K. Curcumin absorption was detected at 428 nm. Prior to UV–Vis absorption measurements, the aqueous formulations were appropriately diluted using ethanol to give a final absorbance between 0.3 and 2.5 (diluted at least 1/20 (v/v)). The following equations were used to calculate loading capacity (LC) (Eq. (1)) and loading efficiency (LE) (Eq. (2)):

$$LC = \frac{m_{\text{drug}}}{m_{\text{drug}} + m_{\text{excipient}}} \cdot 100\% \quad (1)$$

$$LE = \frac{m_{\text{drug}}}{m_{\text{drug,added}}} \cdot 100\% \quad (2)$$

where m_{drug} and $m_{\text{excipient}}$ are the weight amounts of the solubilized drug and polymer excipient in solution and $m_{\text{drug,added}}$ is the weight amount of the drug initially added to the dispersion. No loss of polymer during micelles preparation was assumed.

3.7. Longterm stability studies

For longterm stability studies, formulated CUR was stored at ambient conditions ($\approx 25^\circ\text{C}$) under the exclusion of light. Before the determination of the drug loading by UV/Vis absorption, all samples were centrifuged for 5 min at 10,000 rpm (5000g) with a 3-Speed micro centrifuge (neoLab, Heidelberg, Germany). Solubilization experiments were performed with 3 individually prepared samples and results are presented as means \pm SD, quantification was carried out as described above.

3.8. HPLC

HPLC analysis was carried out on a LC-20A Prominence HPLC (Shimadzu, Duisburg, Germany) equipped with a system controller CBM-20A, a solvent delivery unit LC-20 AT (double plunger), an on-line degassing unit DGU-20A, an auto-sampler SIL-20 AC, a photo-diode array detector SPD-M20A, a column oven CTO-20 AC, and a refractive index detector RID-20A. As stationary phase, a ZORBAX Eclipse Plus (Agilent, Santa Clara, CA, USA) C18 column (4.6×100 mm; $3.5 \mu\text{m}$) was used.

Quantification of CUR, demethoxycurcumin (DMC) and bisdemethoxycurcumin (BDMC) was performed with a stepwise gradient (Fig. S22a, blue curve). Within the first 10 min, the ratio of $\text{H}_2\text{O}/\text{ACN}$ was decreased from 60/40 (v/v) to 40/60 (v/v). Solvent ratio was kept constant for 5 min, prior to increasing it to the initial ratio of 60/40 (v/v) within 0.5 min. This ratio was kept for 5 min. Flow rate was 1 mL/min at 40°C . Detection was performed at 425 nm. Retention times R_t were 8.1 min (CUR), 7.3 min (DMC) and 6.5 min (BDMC) (Fig. S22b). Prior to each measurement, samples were centrifuged (10,000 rpm; 5000g) with a 3-speed-micro centrifuge (neoLab, Heidelberg, Germany) and filtered through $0.4 \mu\text{m}$ PTFE filter (Rotilabo, Karlsruhe, Germany).

3.9. Pyrene assay – critical micelle concentration (cmc) and critical micelle temperature (CMT)

Pyrene solutions (10 μL , 25 μM in acetone) were added to glass vials (polypropylene based containers should be avoided!) and the solvent was removed. Subsequently, various amounts of polymer stock solutions in H_2O were added and the solutions diluted with deionized water to yield a final pyrene concentration of 5×10^{-7} M. The samples were gently shaken overnight at ambient temperature ($\approx 25^\circ\text{C}$) under the

exclusion of light. Pyrene fluorescence was recorded on a FP-8300 (Jasco, Gross-Umstadt, Germany) from 360 to 400 nm ($\lambda_{\text{ex}} = 333$ nm) at 25 °C. The critical micelle concentration (CMC) was determined as the concentration, at which the I_1/I_3 ratio increased by 10% of its initial value. CMT was measured at two different polymer concentrations ($\rho(\text{A-pPrOzi-A}) = 1$ g/L & 10 g/L) from 25 to 70 °C with steps of 5 °C (samples were equilibrated for 20 min at each temperature). CMT was determined as the temperature, at which the I_1/I_3 ration decreased by 10% of its initial value.

3.10. Dynamic light scattering/zeta-potential

Dynamic light scattering (DLS) and zeta-potential were measured on a NICOMP 380 ZLS Zeta Potential/Particle Sizer, (PSS, Santa Barbara, California, USA) in quartz cuvettes (10 mm path length (Hellma GmbH & Co. KG, Müllheim, Germany)) at ambient temperatures (≈ 25 °C). Stock solutions ($\rho(\text{polymer}) = 10$ g/L) were diluted right before measurement (dilution 1/10). Selected samples were measured at multiple dilutions (1/5; 1/10; 1/13; 1/20) to exclude variation due to dilution effects. All samples were filtered through 0.45 μm regenerative cellulose filters (Rotilabo, Karlsruhe) prior to measurement. Selected samples were measured also unfiltered to exclude the loss of bigger particles by filtration. DLS experiments were performed in triplicate using three individually prepared samples and results are presented as means \pm standard deviation (SD). For determination of the zeta-potential, a sample containing deionized H_2O only was measured as reference. Zeta potential was measured once.

DLS measurements of samples stored for 3 years at ambient conditions under the exclusion of light were performed on a Zetasizer Nano ZSP (Malvern Panalytical GmbH, Kassel, Germany) with a 633 nm HeNe-laser at 173°. Autocorrelations for each sample were obtained 3 times for 60 s and results are presented as mean. Prior to the measurements, all samples (polymer = 10 g/L) were diluted 1/10 (v/v) with H_2O and were measured unfiltered. DLS experiments were performed in triplicate (except for CUR = 2.7 g/L; $n = 1$) using three individually prepared samples and results are presented as means \pm standard deviation (SD).

3.11. Cryo-TEM

Lyophilized (freeze-dried) polymer loaded with CUR were reconstituted in water supported by immersion in a bath sonicator. Liquid samples were vitrified in liquid ethane onto a 658–300-CU TEM grid (Ted Pella, Redding, CA, USA) using a Vitrobot Mark IV (FEI Company, Hillsboro, OR), and maintained in liquid nitrogen for the duration of the sample analysis. The conditions utilized for the cryopreservation were 100% humidity, blot force 1 and blotting time 3 s. Low-dose conditions were used to acquire images on a Krios-Titan equipped at 300 KV with a Falcon II direct electron detector (FEI, Hillsboro, OR, USA). Cryo-TEM images were collected with a defocus range of 2–4 μm .

3.12. Cell viability assay

Human dermal fibroblasts, Caco-2 and MDA-MB-231 cells (Deutsche Sammlung von Mikroorganismen und Zellkulturen GmbH, Braunschweig, Germany) were cultured in RPMI 1640 GlutaMax™ (Gibco, Darmstadt, Germany) supplemented with 10% fetal calf serum (FCS). SW480 cells (American Type Culture Collection) and human dermal fibroblasts were cultured in medium that was comprised equally of the SW480-specific 1640 RPMI medium containing GlutaMAX (L-alanyl-L-glutamine) as well as the fibroblast-specific DMEM containing GlutaMAX and HEPES and supplemented with 10% FCS. For Caco-2 cells and human dermal fibroblasts, 1% non-essential amino acids and 1% sodium-pyruvate were added. For the determination of IC_{50} , cells were seeded in white 96 well plates with transparent bottom in triplicates per condition (human dermal fibroblasts and MDA-MB-231:

6×10^3 cells/well, Caco-2: 5×10^3 cells/well and cultured for 1 d at 37 °C and 5% CO_2 , SW480 and fibroblasts in monoculture: 2×10^4 , coculture: 1×10^4 of each cell type and culture for 3 d at 37 °C and 5% CO_2). Subsequently, medium was removed and stock solutions of A-pPrOzi-A ($\rho = 100$ g/L in cell specific culture medium), nanoformulated CUR ($\rho(\text{A-pPrOzi-A/CUR}) = 10/11$ [g/L] in H_2O) or DMSO-formulated CUR (11 g/L) were diluted with cell specific culture medium to desired concentrations and applied for 24 h to Caco-2 as well as SW480, or 72 h to human dermal fibroblasts and MDA-MB-231, including a medium change (containing identical sample concentration) after 48 h. After the treatment, CellTiter-Glo® Luminescent Cell Viability Assay (Promega, Mannheim, Germany) was performed according to manufacturer's instructions. Briefly, medium was removed and cells were washed with PBS (+) until supernatant was clear. Equal amounts of cell culture medium and CellTiter-Glo® reagent were added to the wells. After shaking for 2 min and resting for 10 min to achieve cell lysis, luminescence was measured with an Infinite 200 (Tecan, Männedorf, Switzerland) at $\lambda_{\text{em}} = 590$ nm ($\lambda_{\text{ex}} = 560$ nm).

Cell viability was determined by Eq. (3):

$$\text{cell viability} = \frac{F_{\text{treated}} - F_{\text{medium}}}{F_{\text{untreated}} - F_{\text{medium}}} \cdot 100\% \quad (3)$$

where F_{treated} and $F_{\text{untreated}}$ are the luminescence of treated and untreated cells and F_{medium} is the luminescence of the culture medium.

As a reference, untreated MDA-MB-231 cells were incubated with sodium dodecyl sulfate (SDS) to cause cell death. Cell viability experiments were performed with 3 individual 96 well-plates containing each sample concentration in triplicates and results are presented as means \pm SD. IC_{50} was determined using OriginPro 2015G software using a logistic (CUR-nanoformulation), Boltzmann (DMSO/CUR) or logistic 5 fit (A-pPrOzi-A).

3.12.1. Efficacy screening of DMSO- and A-pPrOzi-A-formulated CUR in conventional 2D culture and 3D breast cancer tissue models

The efficacy of CUR formulated with DMSO or A-pPrOzi-A was comparatively assessed in conventional 2D cultures as well as 3D tumor tissue models of the breast cancer cell line MDA-MB-231. For 2D testing, MDA-MB-231 cells were cultured in 12 well plate format for 4 d. 3D breast cancer models were prepared on SISmuc scaffolds as described previously [98] and cultured for 14 d. CUR treatment (DMSO- or A-pPrOzi-A-formulated) was applied for the last three days of culture period in indicated concentrations with a medium change (containing initial sample concentration) after 48 h of treatment. Subsequently, one part of tissue models was fixed in 4% formaldehyde and paraffin-embedded for histological staining. The other part of the tumor tissue models as well as the 2D cultures were used to determine cell viability by MTT test. Briefly, 1 g/L MTT (Serva, Heidelberg, Germany) in cell culture medium was applied to the cells both in 2D and 3D for 3 h at 37 °C and 5% CO_2 . Subsequently, water-insoluble formazan formed by metabolically active cells was repeatedly extracted with isopropanol/0.04 N HCl and absorption of extracts was measured using a microplate (Infinite 200, Tecan, Männedorf, Switzerland) at $\lambda_{\text{abs}} = 570$ nm and a reference wavelength of $\lambda = 630$ nm. Background correction of MTT-values was performed for treatment with 500 μM CUR, as assay interference was observed for this concentration (Fig. S28, Table S4). Statistical analysis was performed with the open-source software R (Cran. The Comprehensive R Archive Network; available from: <https://cran.r-project.org/>). Statistical significance was calculated by Student's *t*-test (with Bonferroni correction) after test for normal distribution (Shapiro-Wilk test). Differences with a value of $p < 0.05$ were considered statistically significant. All experiments were performed four times.

3.13. Anti-metastatic effects of CUR in a dynamic metastasis model for colorectal cancer in a flow bioreactor and anti-tumor effects in a static 3D co-culture model using cell crowns

For the static 3D co-culture model, SW480 cells and dermal fibroblasts were cultured in co- or mono-culture on the scaffold SISmuc for 14 days under static cell culture conditions in cell crowns and medium was changed every 2–3 d [102]. On day 11 to 14, **A-pPrOzi-A**-formulated CUR (50 μ M) was applied. Tissue was then fixed in 4% formaldehyde, paraffin-embedded and H&E stainings as well as immunohistochemical stainings were performed.

For the dynamic metastasis model, the unseeded scaffold SISmuc was inserted in a flow bioreactor [102] and 6×10^6 SW480 cells were applied to the medium flask from day 3 to 6 of culture using a magnetic stirrer for preventing cell adhesion within the medium reservoir. On day 7 medium was changed and fresh medium supplemented with 50 μ M CUR was applied. On day 14, the tissue was removed from the bioreactor and fixed in 4% formaldehyde prior to paraffin-embedding. Immunohistological stainings were then performed after heat-induced epitope demasking with the following antibodies: Pan-Cytokeratin Mouse (Sigma-Aldrich, Munich, Germany), Vimentin Rabbit (Abcam, Cambridge, Great Britain), E-Cadherin Mouse (BD Biosciences, Heidelberg, Germany), β -catenin Rabbit (Abcam, Cambridge, GRB), Donkey Alexa Fluor 488 Anti-Mouse, Donkey Alexa Fluor 555 Anti-Rabbit (Invitrogen by Thermo Fisher Scientific, Dreieich, Germany). Images were taken with a digital microscope (BZ-9000, Keyence, Neu-Isenburg, Germany).

4. Results and discussion

4.1. Polymer synthesis and characterization

The synthesized amphiphilic ABA-triblock copolymers comprising moderately hydrophobic 2-oxazine repeating units were designed to feature the same hydrophilic PMeOx corona as the comprehensively studied **A-pBuOx-A** and will be labeled according to their hydrophobic block **A-pPrOzi-A** and **A-pBuOzi-A** (Fig. 3). The polymers were synthesized by LCROP using methyl trifluoromethylsulfonate (MeOTf) or propargyl p-toluenesulfonate (PropOTs) as initiator. The **A-pBuOx-A** were terminated with piperidine, piperazine (Pip) or N-Boc-piperazine (BocPip), whereas **A-pPrOzi-A** and **A-pBuOzi-A** were terminated

exclusively using BocPip to facilitate end-group analysis by ^1H NMR. Previous work on **A-pBuOx-A** featuring different end-groups has not revealed any considerable effect thereof on the formulation. Similarly, we did not expect considerable effects of the end-groups on the solubilization of CUR. Also, we synthesized additional polymer batches to be able to assess the batch-to-batch reproducibility of the formulation [103,104]. The polymers were synthesized and thoroughly characterized as is reported and discussed in supporting information (Fig. S5–S19). Briefly, the formation of triblock copolymers was verified using gel permeation chromatography (Fig. S20a) and ^1H NMR corroborated that polymer composition was as targeted (Fig. S20b).

The critical micelle concentration (CMC) and critical micelle temperature (CMT) can be used as indicators for the thermodynamic stability of micelles. The lower the CMC and CMT, the more stable the micelles [105]. Both can be determined, among other means, by changes in the emission spectra of the hydrophobic, aromatic compound pyrene which typically associates with polymeric micelles once they form. Pyrene features an emission spectrum with five distinct peaks between 360 and 400 nm [106]. For **A-pPrOzi-A**, the I_1/I_3 ratio did not considerably change, suggesting no micellization at the investigated concentration range of up to 10 g/L polymer (Fig. 4a). This corroborates the reported increased water solubility of POzi compared to their POx based structural isomers [42]. However, at first glance the absence of aggregation may surprise, as pPrOzi homopolymer with a chain length of 100 was reported to exhibit a cloud point of 11 $^\circ\text{C}$ at 5 g/L polymer [42]. On the other hand, Jordan et al. have reported a significant increase in the water solubility of a thermoresponsive block by adding even very short pMeOx blocks [107]. As a result, **A-pPrOzi-A** can be considered a triple hydrophilic block copolymer similar to pMeOx-b-pPrOx-b-pMeOx, which also shows thermoresponsive aggregation behavior in water [108]. In contrast, and as expected, **A-pBuOzi-A** exhibited a similar, if somewhat lower CMC (0.5 μM ; 5 mg/L) compared to its POx counterpart with the same side chain **A-pBuOx-A** (1 μM ; 9 mg/L). With the formation of micelles, pyrene partitions into the hydrophobic core usually resulting in a decrease in I_1/I_3 . As discussed previously [33], the observed increase in I_1/I_3 after encapsulation is highly unusual, as pyrene is commonly considered a measure of polarity and exhibits values between 1.6 and 1.9 in aqueous solution. The data indicate, that the polarity inside the micellar core is greater than H_2O and even exceeds the one for DMSO or ionic liquids. Both polymers exhibit a high density of highly polar tertiary amide moieties

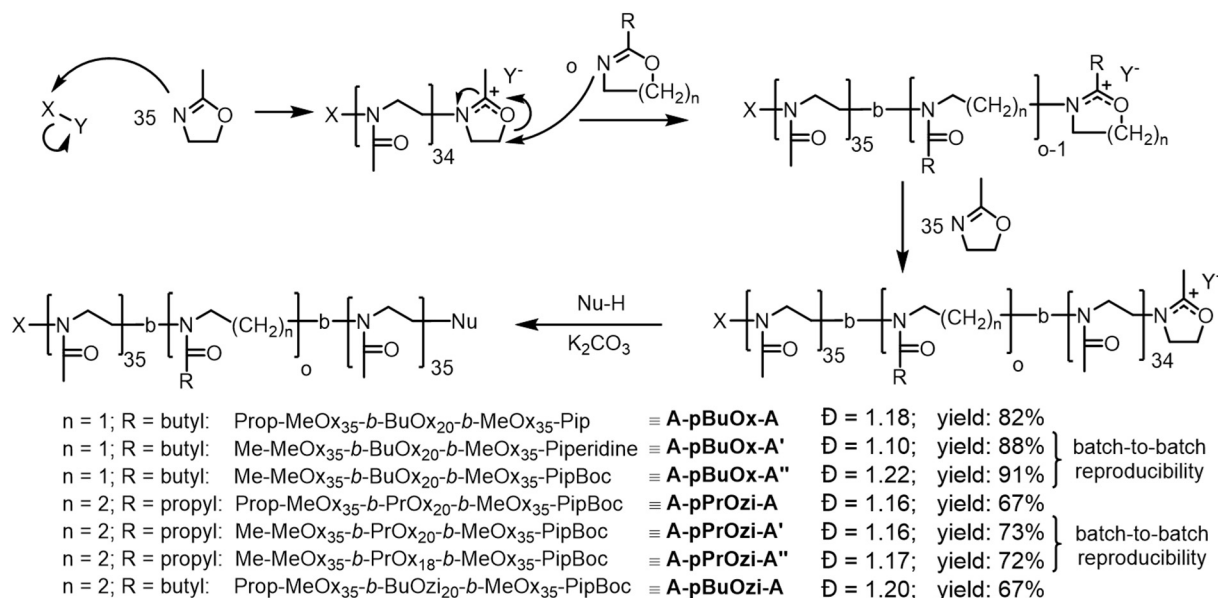


Fig. 3. Reaction scheme of the one-pot four-step synthesis of the ABA-triblock copolymers **A-pBuOx-A**, **A-pPrOzi-A** and **A-pBuOzi-A** in multiple batches for batch-to-batch reproducibility studies.

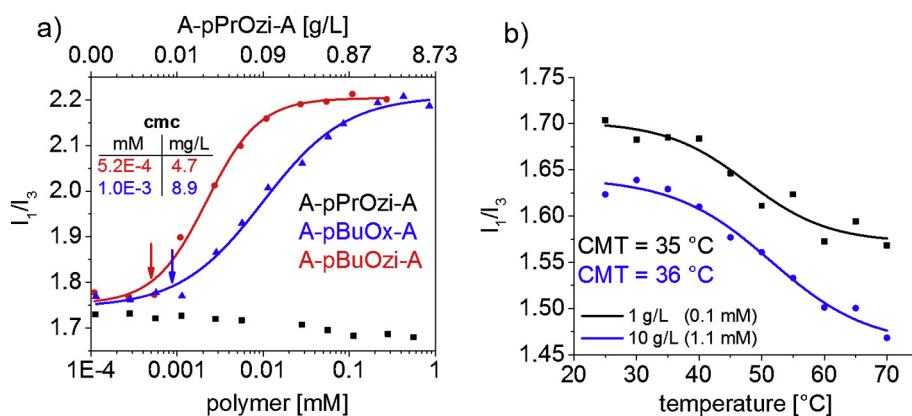


Fig. 4. a) Ratio of the I_1/I_3 emission of pyrene (0.5 μM in H_2O) in dependence of the polymer concentration after excitation at $\lambda_{\text{ex}} = 333 \text{ nm}$. Critical micelle concentration (CMC) was determined as the concentration at which the I_1/I_3 ratio increased by 10% from its initial value; b) ratio of the I_1/I_3 emission of pyrene (0.5 μM) in dependence of the temperature at two different A-pPrOzi-A concentrations (1 g/L and 10 g/L) after excitation at $\lambda_{\text{ex}} = 333 \text{ nm}$. Critical micelle temperature (CMT) was determined as the temperature at which the I_1/I_3 ratio decreased to 90% of its initial value.

within the barely hydrophobic central block. Therefore, the increase in I_1/I_3 with increasing polymer concentration might be due either to close interaction of pyrene with the amide groups or to the presence of residual water molecules in the micellar core undergoing H-bonding with the tertiary amides. In contrast, A-pPrOzi-A comprising a thermoresponsive pPrOzi core, changes in the I_1/I_3 ratio were observed with increasing temperature, which is attributed to a critical micellization temperature (CMT). We found very similar CMT values (35 $^{\circ}\text{C}$ and 36 $^{\circ}\text{C}$ at 1 g/L (0.1 mM) and 10 g/L (1.1 mM), respectively) (Fig. 4b). The absence of micelle formation at room temperature in the case of A-pPrOzi-A is particularly interesting considering the incorporation of CUR reported in a previous communication [49].

4.2. Preparation and characterization of CUR formulations

CUR was formulated using the aforementioned block copolymers A-pPrOzi-A, A-pBuOx-A and A-pBuOzi-A via the thin-film method [33] (Fig. S21).

The polymer A-pBuOx-A exhibited medium to high loading capacities LCs up to $24.4 \pm 1.1 \text{ wt}\%$ ($\rho(\text{A-pBuOx-A}) = 10 \text{ g/L}$; $\rho(\text{CUR}) = 3.2 \pm 0.2 \text{ g/L}$) and $21.6 \pm 0.7 \text{ wt}\%$ ($\rho(\text{A-pBuOx-A}) = 50 \text{ g/L}$; $\rho(\text{CUR}) = 13.7 \pm 0.5 \text{ g/L}$) (Fig. 5a, b). Therefore, A-pBuOx-A enables LCs similar to current CUR nanoformulations (LCs of 10–20 wt%) [73,79] but much higher overall CUR concentrations due to the

excellent water solubility of the drug-loaded micelles. Interestingly, A-pBuOzi-A and A-pPrOzi-A, exhibited much higher drug solubility with ($\text{CUR} = 37.4 \pm 0.5 \text{ g/L}$ ($\rho(\text{A-pBuOzi-A}) = 50 \text{ g/L}$) and $54.5 \pm 0.2 \text{ g/L}$ ($\rho(\text{A-pPrOzi-A}) = 50 \text{ g/L}$), respectively). Together with the previously communicated maximum CUR loadings of $11.9 \pm 0.6 \text{ g/L}$ at $\rho(\text{A-pPrOzi-A}) = 10 \text{ g/L}$ [49], this underscores the exceptional high solubility of this formulation.

With increasing CUR content, the appearance of the A-pPrOzi-A based formulations changed continuously from slightly yellow to dark red (Fig. 5c). Despite the high drug loading and concentration, no sign of precipitation or aggregation was observed in the A-pPrOzi-A/CUR = 50/55 [g/L] formulation. Upon dilution, the typical CUR colour (also known as Natural Yellow 3) became apparent again. This apparent solvatochromicity [109,110] within the novel nanoformulations are currently investigated in more detail and will be reported shortly.

Apart from the significant difference in maximum LC for CUR between the POx based A-pBuOx-A and the POzi based A-pPrOzi-A and A-pBuOzi-A, we observed a different behavior as the maximum LC was approached. In the case of A-pBuOx-A, LC initially increased with increasing CUR feed to $LC = 20\text{--}25 \text{ wt}\%$, but upon further increase in CUR feed, the LC dropped to essentially zero (Fig. 5a, b). The same effect has been observed with paclitaxel, however, only at $LC > 50 \text{ wt}\%$ [38]. Interestingly, A-pPrOzi-A and A-pBuOzi-A did not display this effect at the investigated parameters. As A-pBuOzi-A reached its

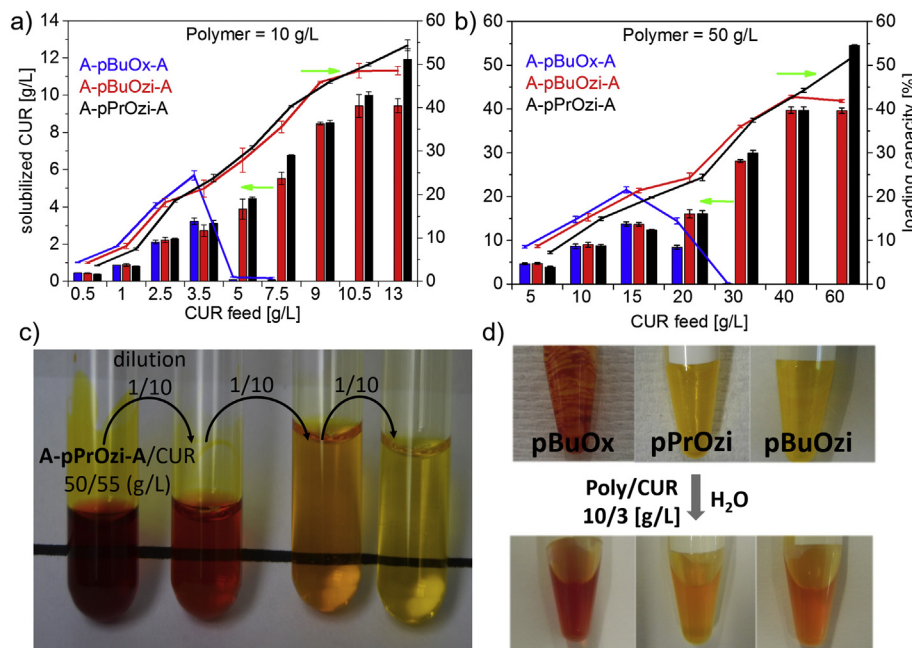


Fig. 5. a, b) Formulated aqueous CUR concentrations (bars, left axis) and corresponding loading capacities (lines, right axis) in dependence of the CUR feed by A-pBuOx-A (blue), A-pBuOzi-A (red) and A-pPrOzi-A (black). Polymer concentrations were a) 10 g/L or b) 50 g/L. Data is given as means \pm SD ($n = 3$). c) Images of serial dilution of an aqueous A-pPrOzi-A/CUR 50/55 [g/L] formulation to a final dilution of 1/1000 (v/v). d) Dried CUR/polymer films (polymer from left to right = A-pBuOx-A; A-pBuOzi-A; A-pPrOzi-A) and corresponding aqueous formulations ($\rho(\text{polymer}/\text{CUR}) = 10/3 \text{ [g/L]}$) depicting the solvatochromicity of CUR depending on the micellar core. (For interpretation of the references to color in this figure legend, the reader is referred to the web version of this article.)

maximum LC of about 40 wt%, additional CUR feed did not seem to affect the drug loading, while simply more CUR remained undissolved as a precipitate.

In addition, we observed CUR solvatochromicity in dried films and in solution, depending on the polymer used (Fig. 5d), indicating different microenvironment for the compound. At $\rho(\text{CUR}) = 3 \text{ g/L}$ ($\rho(\text{polymer}) = 10 \text{ g/L}$), both POzi based dried films exhibited a similar yellow colour, whereas the POx based formulations appeared reddish. In contrast, in the case of the solvatochromic Reichhardt's dye [49] and pyrene (Fig. 4a), the polymers with butyl side chains appeared more similar. Judging from the similar appearance of the POzi based CUR solid dispersions and aqueous formulations, it appears that the backbone has a stronger impact on the microenvironment for CUR while the side chains seem more important in the case of Reichhardt's dye and pyrene. Besides a low aqueous solubility, another important limitation of CUR is its limited stability as it suffers from rapid degradation in solution under ambient conditions. As the stability and photochemistry of CUR, including reaction with oxygen, depend on its microenvironment [111,112] this observation might also affect the stability of CUR in the different formulations presented here.

Interestingly, irrespective of the LC, the UV-Vis absorption spectra of CUR (recorded after dilution in ethanol) solubilized with A-pPrOzi-A did not show any signs of degradation after 3 days in water (Fig. S24). The spectral characteristics and λ_{max} were found in accordance with the literature [113]. The same was found for A-pBuOx-A and A-BuOzi-A, showing that no degradation of the nanoformulated CUR occurred in aqueous solution over a course of three days. In contrast, the UV-Vis spectra of formulated CUR ($\rho(\text{A-pPrOzi-A/CUR}) = 10/3 \text{ [g/L]}$) changed immediately under harsh basic conditions ($\text{CUR}/(10\% \text{ KOH in } \text{H}_2\text{O}) = 1/1 \text{ (v/v)}$), which is in line with the expedited degradation at high pH values reported in the literature (Fig. S24, dotted black line). For more details, please refer to the supporting information (Fig. S24, S25).

Moreover, to investigate the potential shelf-life of the formulations, the aqueous solutions were stored at ambient conditions ($\approx 25^\circ\text{C}$) in the dark for up to 3 years. Although A-pBuOx-A had the lowest loading capacity LC of the three polymers, it exhibited excellent 1 year stability (Fig. 6a) at LCs up to 25 wt%. This observation is reminiscent of the situation previously observed for POx/paclitaxel formulations, when a more hydrophobic 2-nonyl-2-oxazoline was used as the central block of triblock copolymers. Also in this case, the drug loading was mediocre (approx. 20 wt%) but the long-term stability was excellent [38]. Small variations (within the standard deviation) of the drug loadings may be attributed to a loss of solvent, variations during the UV/Vis measurements and/or minimal degradation/precipitation of CUR. Important to note, the spectral characteristics indicated no detectable degradation of CUR even after 3 years in solution which is particularly remarkable for CUR. At drug feeds above the maximum loading ($\geq 5 \text{ g/L}$), we made an unexpected observation (Fig. 6a). The amount of CUR solubilized increased within 1 year storage from $0.10 \pm 0.0 \text{ g/L}$ (day 1) to $3.03 \pm 0.02 \text{ g/L}$ (1 year) (3000% increase @ 5 g/L CUR feed) and from 0.42 ± 0.10 to 3.33 ± 0.10 (700% increase @ 7.5 g/L CUR feed). It should be noted that for the long-term stability studies, the formulations were stored in Eppendorf tubes containing the precipitates after centrifugation. Therefore, initially precipitated CUR/polymer aggregates must have re-dissolved after some time or initially unformulated CUR was incorporated into A-pBuOx-A micelles present in solution. Please note, the formulations at 5 and 7.5 g/L CUR feed have not been analyzed by UV/Vis after 30-day storage, however, per visual inspection, the supernatant was almost colorless, reminiscent of the situation after 1 day storage. A similar phenomenon was observed for POx/POzi micelles with more hydrophobic cores [114].

Formulations of A-pBuOzi-A and A-pPrOzi-A showed excellent 30 day stabilities up to very high LC of 47 wt%. Only when exceeding 50 wt%, some loss in CUR concentration was observed (Fig. 6b, c). This loss seemed to be more pronounced for A-pBuOzi-A as compared to A-

pPrOzi-A. For the latter polymer, extraordinary high drug loadings of $8.3 \pm 2.2 \text{ g/L}$ CUR (with 10 g/L A-pPrOzi-A) and corresponding loading capacities of 45 wt% were found even after 30 days. However, the LC of all nanoformulations seem to converge at $\approx 3 \text{ g/L}$ ($LC = 23 \text{ wt\%}$) after 1-year storage (Fig. 6d, top panel) or $\approx 2 \text{ g/L}$ after 3-year storage (Fig. 6d, bottom panel). According to the “spring and parachute” concept [115], amphiphiles can increase drug solubility by incorporating them into their hydrophobic core (spring), and act as an “parachute” to keep the drug in solution and maintain drug supersaturation. Conceptionally, the “parachute” only slows down the kinetics of the crystallization of the drug. However, after a certain period of time, the drug concentration will reach its thermodynamic equilibrium, which normally correlates to the water solubility of the drug itself. As all our formulations level-off at $\approx 2\text{--}3 \text{ g/L}$ ($\approx 5000\text{-fold}$ increase in CUR solubility), it seems that the POx/POzi-based amphiphiles not only slow down the kinetics of CUR crystallization but also drastically shift the thermodynamic equilibrium with regard to CUR solubility. Important to note, the size of selected CUR-loaded A-pPrOzi-A micelles after 3-year storage was essentially monomodal (Fig. 6f) with a narrow size distribution (Fig. 6e) as will be discussed in more detail below.

An often employed way to increase the shelf life of formulated drugs is to lyophilize the aqueous formulation after solubilization and redisperse them right before usage. POx based formulations of PTX already displayed excellent redispersibility without the need of cryoprotectants [33]. Here, lyophilized POx and POzi based CUR formulations displayed a similar ability for redispersion (Fig. 7a). Redispersion with PBS containing 10 g/L bovine serum albumin (BSA) was performed as a preliminary study for upcoming *in vitro* tests, as initially stable formulations can precipitate in the presence of albumin.

All formulations discussed so far have been prepared in triplicates by the thin film method exhibiting low standard deviations. However, deviations caused by batch to batch variation with regard to the polymer amphiphiles were not considered so far. Reproducibility and batch-to-batch variation is discussed as a significant problem in different fields, including nanomedicine [103,116]. Therefore, different batches ($n = 3$) of A-pPrOzi-A and A-pBuOx-A exhibiting the highest and lowest LC for CUR, respectively, were evaluated. Even though minor differences between that batches are observed, quantitatively the reproducibility is excellent, highlighting the platforms potential for further translation (Fig. 7b, c).

On a molecular level, the high loading in combination with excellent stability of the A-pPrOzi-A seems particularly surprising as the polymer itself does not form micelles on its own. To investigate this system further, ^1H NMR was employed. The spectra of neat CUR and lyophilized CUR nanoformulation dissolved in CDCl_3 confirmed loading and CUR stability (Fig. S26). When the lyophilized powders were dissolved in D_2O we made an unexpected observation (Fig. 8). In the absence of CUR, all polymer signals were clearly observed with expected intensities. This corroborates the results from the pyrene assay showing no formation of micelles at 10 g/L (Fig. 4). In contrast, even at the lowest drug content ($\rho(\text{A-pPrOzi-A/CUR}) = 10/1 \text{ [g/L]}$) the signals of the propyl side chains and the POzi backbone are significantly attenuated, but no ^1H NMR signal that can be attributed to CUR could be detected, presumably due to its low mobility in the core (Fig. 8a, b). The attenuation became more pronounced with increasing CUR feed concentration, whereas the hydrophilic corona remained largely unaffected. Correlating the integrals of the propyl side chain and methyl side chains to the integral of the POx backbone, it becomes clear that the micellar core increasingly eludes NMR analysis with increasing CUR loading (Fig. 8d).

The resolution of protons in ^1H NMR-spectra depends, among other things, on the relaxation time T_2 (transverse relaxation; spin-spin relaxation). Short T_2 causes a broadening of NMR-peaks and may lead to a complete disappearance of certain signals. Thus, systems, which are hindered in their mobility are destined for short T_2 . The disappearance

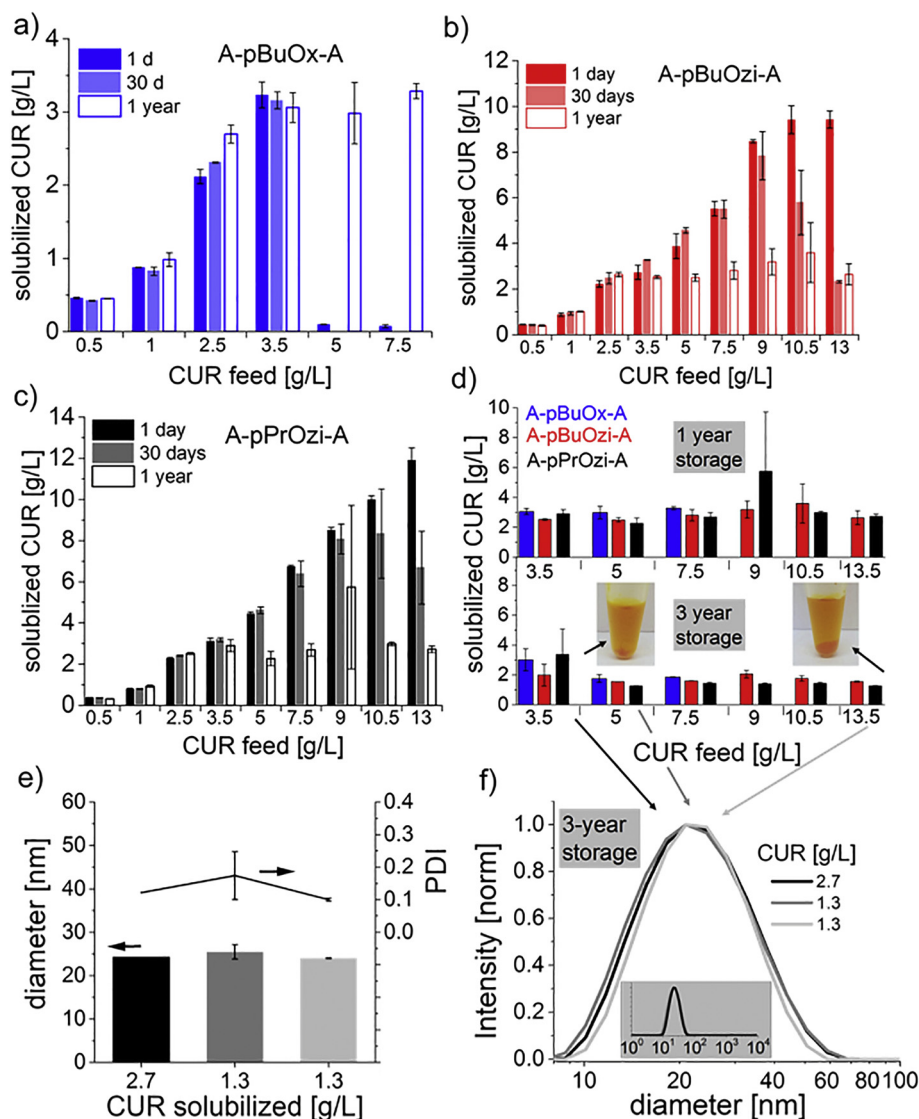


Fig. 6. Solubilized [CUR] in dependence of the CUR feed at $\rho(\text{polymer}) = 10$ [g/L] after 1d, 30 d and 1 year storage at ambient conditions under exclusion of light by a) **A-pBuOx-A** (blue); b) **A-pBuOzi-A** (red) and c) **A-pPrOzi-A** (black). Data is given as means \pm SD ($n = 3$). d) Solubilized [CUR] after 1-year (top) and 3-year (bottom) storage in dependence of the CUR feed. e) Mean diameter (intensity weighted) and PDI as well as f) particle size distribution determined by dynamic light scattering of selected CUR-loaded **A-pPrOzi-A** micelles after 3-year storage. The samples ($\rho(\text{A-pPrOzi-A}) = 10$ g/L) were centrifuged and subsequently diluted with H_2O 1/10 v/v prior to measurement and measured unfiltered. Each formulation (except CUR = 2.7 g/L; CUR feed: 3.5 g/L) was prepared three times and data is given as means \pm SD ($n = 3$). (For interpretation of the references to colour in this figure legend, the reader is referred to the web version of this article.)

of the ^1H NMR signals of formulated CUR clearly indicates a strong decrease in molecular mobility of CUR incorporated into the hydrophobic core of the polymer even at low loading, while the **pPrOzi** block only gradually disappears with increasing loading. Important to note, the ^1H NMR integrals of unloaded **A-pPrOzi-A** were identical in CDCl_3 and D_2O (Fig. 8d, green circled box) showing that neither solvents are selective for either block. No ^1H NMR signals that can be attributed to CUR could be observed in D_2O solution, neither at high nor at low drug-loading. In contrast, solid-state NMR of freeze-dried polymer/CUR formulations could give further insights into polymer/CUR interactions within the micelles. In fact, we observed distinct changes in CUR signals depending on the drug-loading in preliminary solid-state NMR experiments. However, as this is an extensive study by itself, it is outside the scope of the present contribution and will be published separately.

As suggested by ^1H NMR and pyrene assay, **A-pPrOzi-A** does not form micelles in the absence of CUR. This absence of micelles was also corroborated by dynamic light scattering (DLS) at room temperature ($\approx 25^\circ\text{C}$). In contrast, at $\rho(\text{CUR}) = 0.9$ g/L, small particles ($R_h = 13.1 \pm 1.4$ nm) were barely detectable, indicating that only few micelles were present in solution (Fig. 9a, b). With increasing CUR content, light scattering intensity increased markedly, even though micellar size decreased. Clearly, CUR not only triggered micellization but also compaction of **A-pPrOzi-A** micelles. The decrease in size corroborates the strong interactions between CUR and the hydrophobic

core of **A-pPrOzi-A** leading to loss of NMR intensity with increasing drug loading. A similar compaction of initially loose aggregates to compact micelles was already observed by the addition of ionic surfactants such as SDS to POx based block copolymers or with increasing temperature [117] as well as in paclitaxel/**A-pBuOx-A** formulations [38].

At CUR concentrations ≥ 6.8 g/L micellar size started to increase. However, even at extraordinary high CUR loadings of $\rho(\text{A-pPrOzi-A}/\text{CUR}) = 10/11.9$ [g/L] ($LC = 54.3$ wt%), the drug-loaded micelles exhibited relatively small hydrodynamic diameter of 48 nm. Cryogenic transmission electron microscopy (cryo-TEM) can be used to visualize such small entities. We investigated aqueous solutions of CUR nanoformulations at different loading. Unfortunately, we could not obtain a clear and unambiguous picture of the self-assemblies as sample preparation seems to affect the obtained morphologies to some extent. It appears that both at higher ($\geq 10/8$) and lower drug loading (10/3) spherical and worm-like structures co-exist (Fig. 9c and f-h). In contrast, at intermediate drug loading (10/4), only very small, spherical assemblies were found. This observation actually seems to corroborate the data obtained by light scattering, which also gave smallest sizes for intermediate loading (Fig. 9a). Similar worm-like micelles have been described for **A-pBuOx-A** before [38]. However, in this case, worm-like micelles were observed only in the absence of drug or low drug loading with paclitaxel. In contrast, when co-loaded with a combination of a

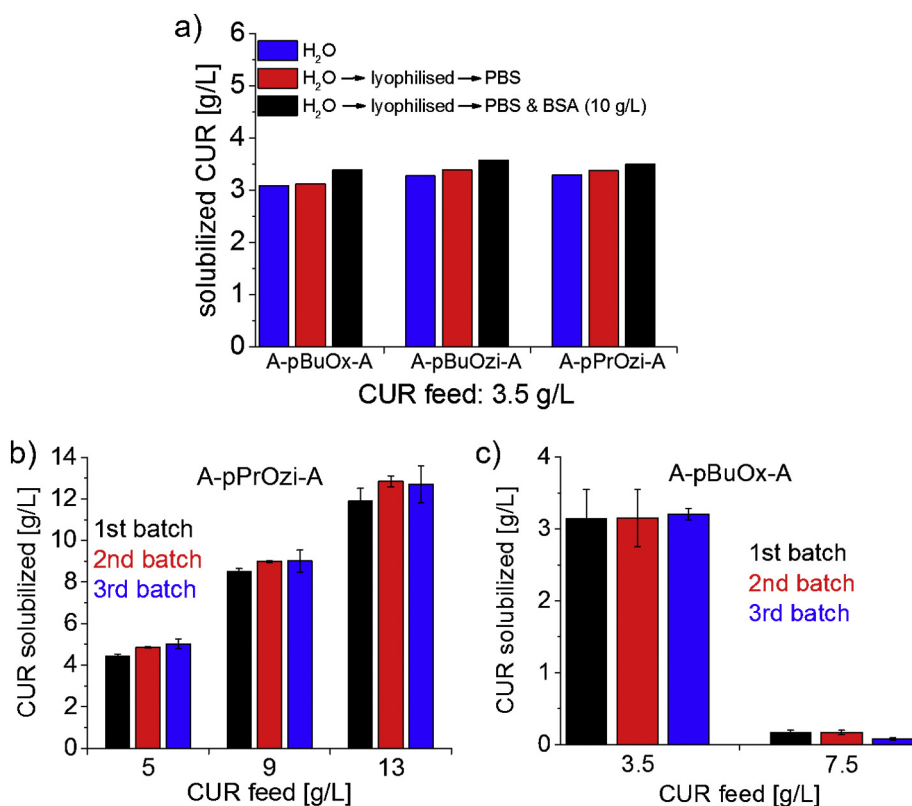


Fig. 7. a) Aqueous CUR concentrations (CUR feed: 3.5 g/L) formulated with **A-pBuOx-A**, **A-pBuOzi-A** or **A-pPrOzi-A** after redispersion of dried films in water (blue bars), lyophilisation of the aqueous formulations and redispersion in PBS (red bars) or redispersion in PBS containing 10 g/L bovine serum albumin (BSA, black bars). b, c) Aqueous CUR concentrations in dependence of the CUR feed formulated with 3 different polymer batches ($\rho(\text{polymer}) = 10 \text{ g/L}$) of b) **A-pPrOzi-A** and c) **A-pBuOx-A**. Data is given as means \pm SD ($n = 3$); (For interpretation of the references to colour in this figure legend, the reader is referred to the web version of this article.)

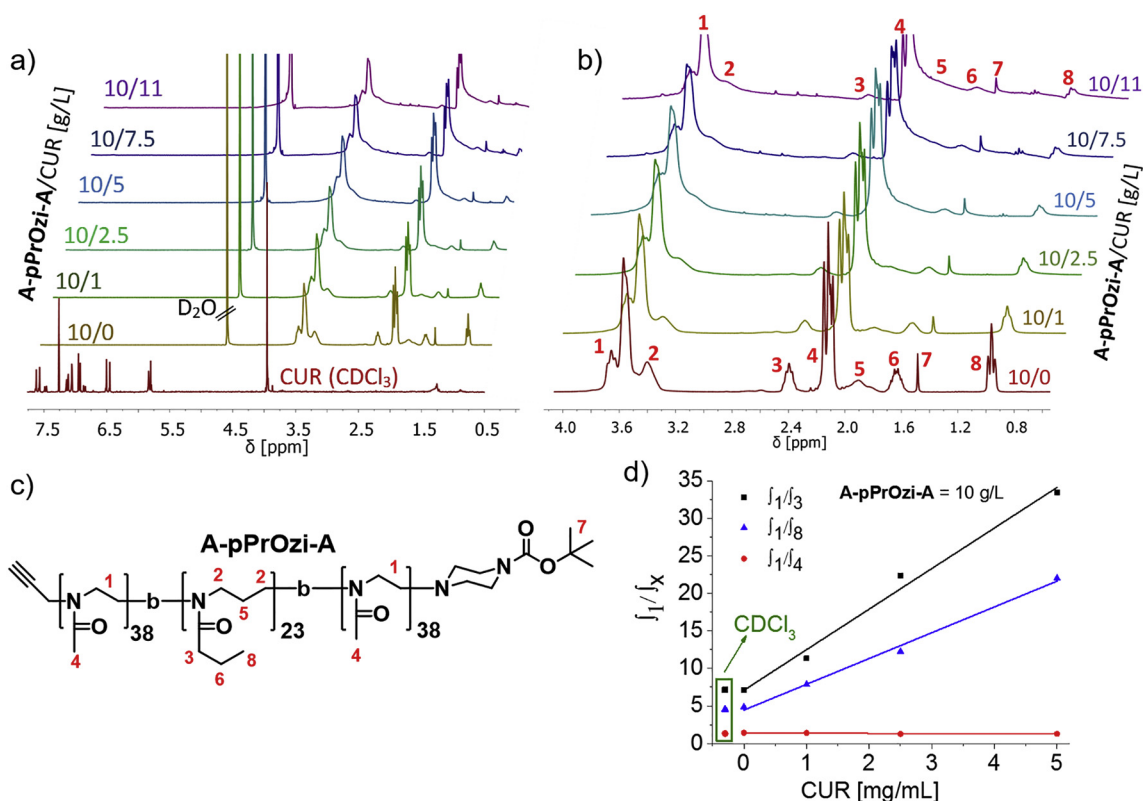


Fig. 8. a) ^1H NMR spectra (300 MHz, 298 K) of CUR (bottom red spectrum; CDCl_3) and **A-pPrOzi-A**/CUR formulations (D_2O). Concentration of **A-pPrOzi-A** was kept at 10 g/L, whereas CUR feed concentration was increased from 0 to 11 g/L (2nd bottom to top spectrum). b) Enlarged section of the **A-pPrOzi-A**/CUR formulations with increasing CUR content (bottom to top). c) Chemical structure and ^1H NMR signal assignment of **A-pPrOzi-A**. d) Ratio of ^1H NMR integrals (D_2O ; 300 MHz; 298 K) of different **A-pPrOzi-A**/CUR formulations in dependence of the CUR feed ($\rho(\text{A-pPrOzi-A}) = 10 \text{ g/L}$). Integrals were labeled according to Fig. 8c). The green encircled box shows the ratio of the ^1H NMR signals of **A-pPrOzi-A** (10 g/L; without CUR) in CDCl_3 instead in D_2O . (For interpretation of the references to colour in this figure legend, the reader is referred to the web version of this article.)

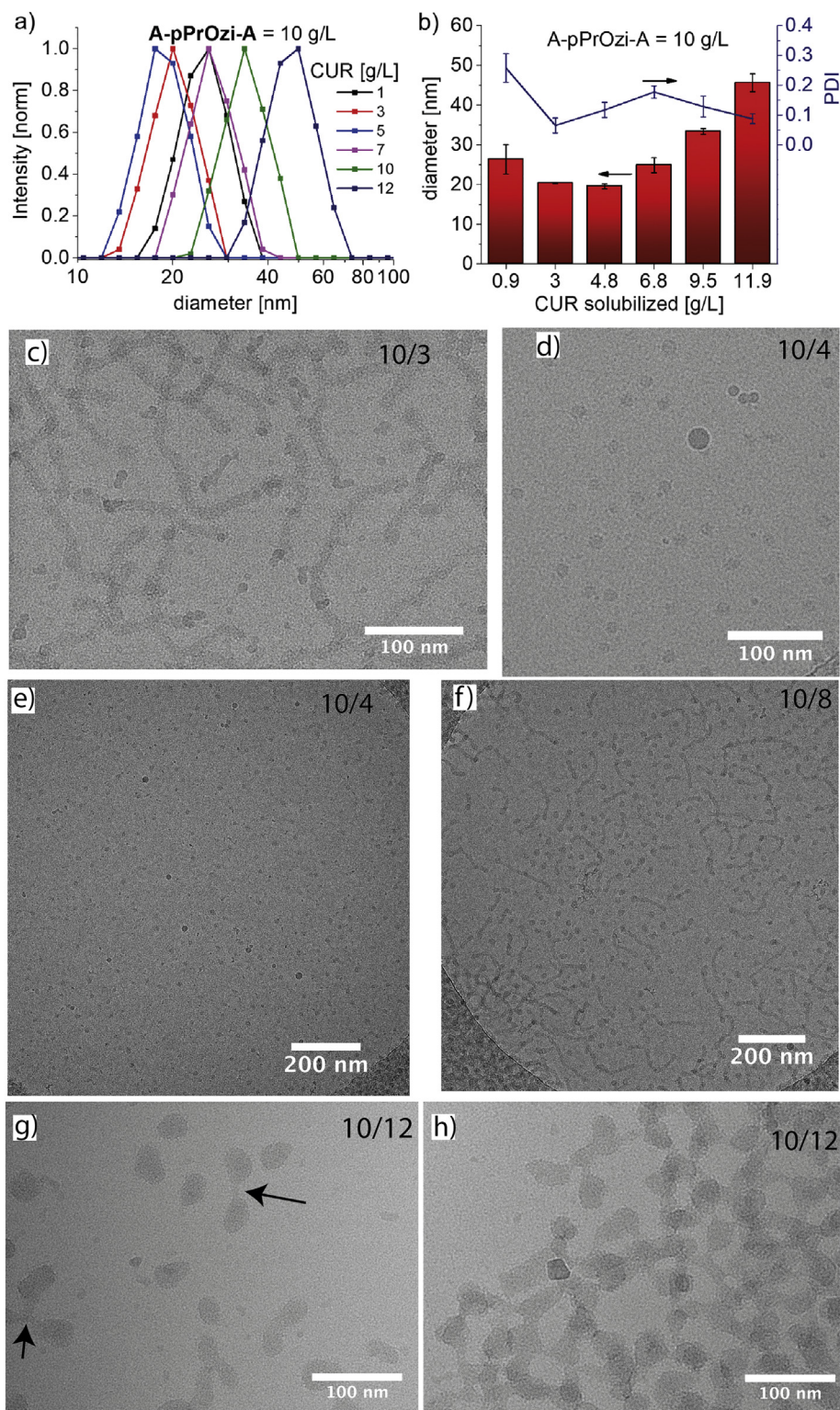


Fig. 9. a) Particle size distribution as determined by dynamic light scattering of CUR-loaded A-pPrOzi-A micelles in dependence of the solubilized CUR concentration at room temperature ($\approx 25^\circ\text{C}$). The samples ($\rho(\text{A-pPrOzi-A}) = 10 \text{ g/L}$) were diluted with H_2O 1/10 (v/v) prior to measurement; b) mean diameter (intensity weighted) of the CUR-loaded A-pPrOzi-A micelles. Each sample was prepared three times and data is given as means \pm SD ($n = 3$). c-h) cryo-TEM images of aqueous nanoformulations with drug loading ranging from c) $\rho(\text{A-pPrOzi-A}/\text{CUR}) = 10/3$ over d,e) 10/4 and f) 10/8 to g,h) 10/12 [g/L].

hydrophobic cis-platin prodrug and etoposide, the worm-like micelles were also observed at higher drug loading [118]. In the present case, the worm-like micelles are clearly observed to co-exist with spherical structures also at $LC < 40 \text{ wt}\%$. At the investigated concentration, it seems that the self-assemblies dynamically merge into larger structures

such as networks of worms. This is surprising, considering that even at much higher concentrations of 50/55 [g/L] macroscopically the solutions exhibit low viscosity and high colloidal stability, which would not be expected from a cross-linked network of polymer worms. Interestingly, in several images at very high drug loading (10/12) it seems that

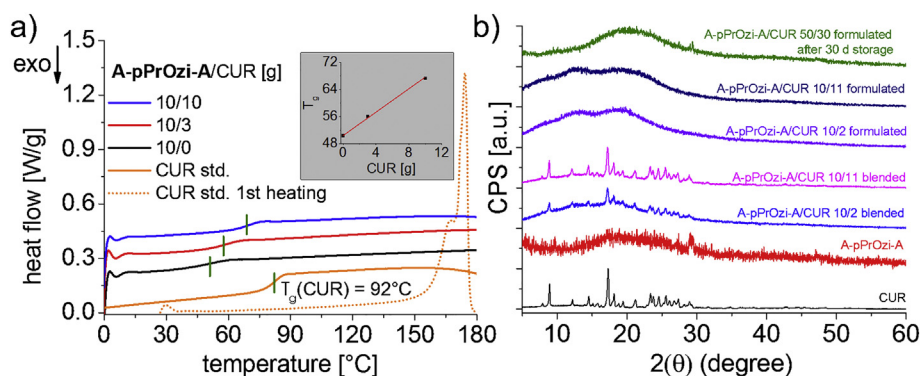


Fig. 10. a) DSC heat flow of the first (CUR standard; dotted line) and second heating cycle (solid lines) of **A-pPrOzi-A** and lyophilized **A-pPrOzi-A/CUR** formulations. The curves were shifted along the y-axis for better visibility (CUR: -0.1 ; $10/3$: $+0.1$; $10/10$; $+0.3$). Samples were heated to $180\text{ }^{\circ}\text{C}$ at $5\text{ }^{\circ}\text{C}/\text{min}$. Inset shows T_g in dependence of formulated CUR concentration (linear fit). b) XRD analysis of neat CUR, **A-pPrOzi-A** copolymer, blended **A-pPrOzi-A + CUR**, lyophilized **CUR/A-pPrOzi-A** nanoformulation ($\rho(\text{A-pPrOzi-A/CUR}) = 10/2$ & $10/11$ [w/w]) and lyophilized CUR-loaded **A-pPrOzi-A** micelles ($\rho(\text{A-pPrOzi-A/CUR}) = 50/30$ [w/w]) after 30 d storage at ambient conditions ($T \approx 25\text{ }^{\circ}\text{C}$) under the exclusion of light.

spherical micelles are just to merge or separate (arrows, Fig. 9g).

Apart from the size, also the zeta-potential of the CUR nanoformulations was investigated. The micellar solution of $\rho(\text{A-pPrOzi-A/CUR}) = 10/3$ [g/L] exhibited a neutral zeta-potential (0.07 mV), suitable for *in vitro* and *in vivo* applications (Fig. S27) [119]. The pronounced decrease in molecular mobility (as evidenced by $^1\text{H NMR}$) and micellar compaction (as evidenced by DLS) may point towards crystallization of CUR within the micellar core. We therefore investigated the lyophilized nanoformulations using differential scanning calorimetry (Fig. 10a) and x-ray powder diffraction (Fig. 10b).

For comparison, crystallinity of neat CUR (T_m at $167.8\text{ }^{\circ}\text{C}$ and $174.2\text{ }^{\circ}\text{C}$ [120]) was evaluated at the first heating cycle due to the absence of recrystallization during cooling under the experimental parameters (Fig. 10a). However, we did observe a T_g of CUR at $86\text{ }^{\circ}\text{C}$ during the second heating cycle. In contrast to neat CUR, its nanoformulations did not show any sign of melting peak in the first heating cycle, suggesting fully amorphous CUR, irrespective of LC . Glass transition temperatures (T_g s) of the polymer and nanoformulations were determined using the second heating cycle (Table S2). **A-pPrOzi-A** exhibited a lower T_g ($50.3\text{ }^{\circ}\text{C}$) than its structural isomer **A-pBuOx-A** ($62.4\text{ }^{\circ}\text{C}$ [121]), which can be attributed to the improved flexibility of the POzi backbone [43,47]. Interestingly, the T_g of the nanoformulations increased linearly with increasing CUR content (inset Fig. 10a). A similar phenomenon has been observed for **A-pBuOx-A/PTX** formulation [121]. It is more common to find a decrease in T_g with incorporation of APIs in solid dispersions [122,123]. However, the observed increase in T_g can be very well explained by the Fox-equation.

$$\frac{1}{T_{g,mix}} = \frac{w_1}{T_{g,1}} + \frac{w_2}{T_{g,2}} \quad (4)$$

where $T_{g,mix} = T_g$ of the mixture; $T_{g,1}$ and $T_{g,2}$ are the T_g s of compound 1 and 2, respectively; and w_1 and w_2 are the weight fractions of compound 1 and 2, respectively.

Using the T_g of **A-pPrOzi-A** and CUR, the Fox-equation yields a T_g of $56\text{ }^{\circ}\text{C}$ ($56\text{ }^{\circ}\text{C}$ observed experimentally) for the $10/3$ ($w_{CUR} = 0.23$) solid dispersion and $63\text{ }^{\circ}\text{C}$ ($67\text{ }^{\circ}\text{C}$ observed experimentally) for the $10/10$ ($w_{CUR} = 0.5$) solid dispersion. The fact that we observe only one T_g and that it can be described using the Fox-equation corroborates the notion that two compounds are molecularly mixed without formation of nanoscopic domains sufficient in size what would lead to two distinct T_g values.

Moreover, we analyzed CUR, **A-pPrOzi-A** copolymer, physical blend of CUR + **A-pPrOzi-A**, and the CUR nanoformulation by XRD (Fig. 10b) [60]. The XRD spectra of free CUR and CUR + **A-pPrOzi-A** blend showed various peaks (in the 2θ range of $10\text{--}30^{\circ}$) corresponding to crystalline CUR [124]. In contrast, **A-pPrOzi-A** only shows a broad, amorphous halo ranging from $2\theta = 10\text{--}30^{\circ}$. The sharp signals in the physical mixture of **A-pPrOzi-A + CUR** correlated with the CUR content, implying that the physical blending had no noticeable effect on the crystallinity of CUR. Strikingly, no evidence of crystalline peaks could be observed for the nanoformulation, even at extremely high drug

loadings ($LC = 52.4\text{ wt}\%$). It appears that **A-pPrOzi-A** micelles completely inhibited crystallization of incorporated CUR even in drug-dominant formulations. For long-term stability studies, **A-pPrOzi-A/CUR** = $50/30\text{ g/L}$ ($LC = 37.5\text{ wt}\%$) was lyophilized and stored at ambient conditions ($T \approx 25\text{ }^{\circ}\text{C}$) under the exclusion of light. Even after 30 days storage, the powder did not show any evidence for CUR crystallization (Fig. 10b, top green graph).

Whether an API is present in amorphous or crystalline state is of great importance for its bioavailability. Generally speaking, amorphous drugs have a better bioavailability since the crystalline state exhibits stronger interactions between the single drug molecules and requires more energy to break [125]. Therefore, the ability of **A-pPrOzi-A** to efficiently suppress CUR crystallization maybe highly relevant for future *in vivo* studies.

4.3. *In vitro* testing of **A-pPrOzi-A/CUR** in comparison to DMSO-formulated CUR

The **A-pPrOzi-A/CUR** nanoformulations showed very favorable characteristics as it may be able to overcome the limitations that have hindered CUR from reaching its therapeutic potential *in vivo*, but it may also lead to undesired toxicity. To compare the effects of **A-pPrOzi-A/CUR** and standard DMSO formulated CUR incubation, cell viability tests using different cell types were performed. Both **A-pPrOzi-A** and DMSO-formulated CUR clearly induced a dose-dependent cytotoxicity in all cases (Fig. 11). IC_{50} values were comparable for both formulations, but differed between the various cell types. In our experiments, Caco-2 cells showed lowest sensitivity with an $IC_{50, 24h}$ of 63 and $60\text{ }\mu\text{M}$ CUR in DMSO- or **A-pPrOzi-A**-formulation (Sakuma et al.: $IC_{50, 24h} \approx 40\text{ }\mu\text{M}$ (DMSO/CUR)) [126], respectively. Medium sensitivity with an $IC_{50, 72h}$ of 35 and $45\text{ }\mu\text{M}$ was determined for primary human dermal fibroblasts (Scharstuhl et al.: $IC_{50, 48h} \approx 20\text{ }\mu\text{M}$ (DMSO/CUR)) [127]. MDA-MB-231 were most sensitive with an $IC_{50, 72h}$ of 17 and $19\text{ }\mu\text{M}$ (Khosropanah et al.: $IC_{50, 72h} \approx 84\text{ }\mu\text{M}$ (DMSO/CUR) and $35\text{ }\mu\text{M}$ (myristic acid-chitosan/CUR)) [128].

Interestingly, in the case of MDA-MB-231 **A-pPrOzi-A** alone showed a dose-dependent cytotoxicity ($IC_{50, 72h} = 1\text{ mM}/10\text{ g/L}$), suggesting a cytotoxic effect of the polymer on the aggressive triple-negative breast cancer (TNBC) cell line, albeit at rather high doses. In contrast, even at very high concentrations of 100 g/L (10 mM), no cytotoxicity was observed for human dermal fibroblasts and Caco-2 cells, respectively. Interestingly though, a mild increase in apparent cell viability was observed in the case of fibroblasts at concentrations between 10 and 50 g/L **A-pPrOzi-A**. However, experimental variability was unusually high in this case and we are not sure whether this effect might not be an artifact.

It is well known that cancer cells grown in a 3D environment behave very differently from those cultured on 2D plastic dishes. Often, 3D cultured cells are more resistant to therapeutic compounds compared to the same cell lines grown in a conventional 2D format [97]. Particularly in the case of CUR, this aspect is important to reflect the situation in

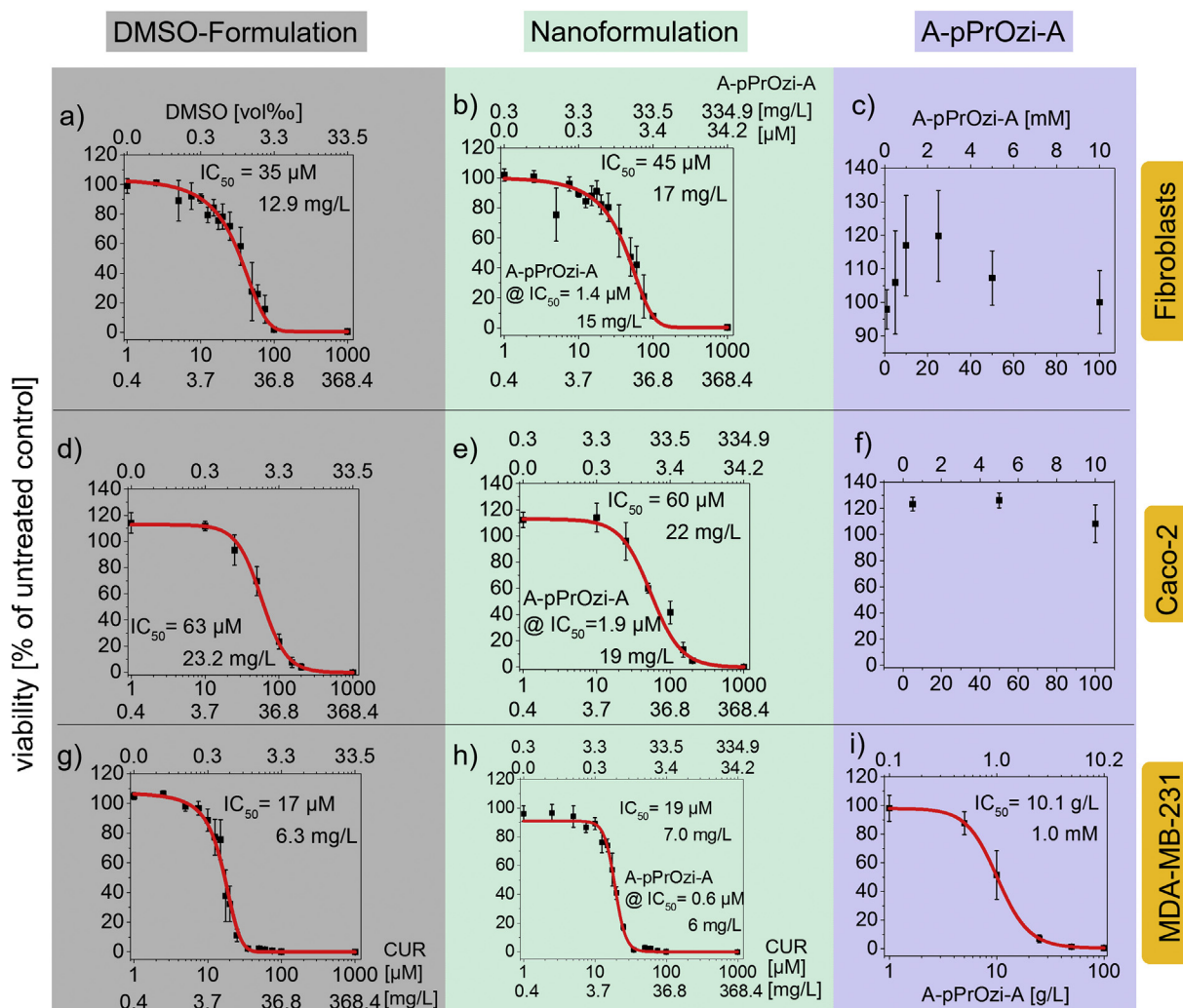


Fig. 11. Dose-dependent cytotoxicity of DMSO-formulated CUR, CUR-loaded **A-pPrOzi-A** micelles and **A-pPrOzi-A** block copolymer in (a–c) human dermal fibroblasts (72 h incubation); (d–f) Caco-2 (24 h incubation) and (g–i) MDA-MB-231 breast cancer cells (72 h incubation). DMSO-formulated CUR was prepared by dissolving 11 g/L CUR in DMSO with further dilution with cell specific medium to desired CUR concentration (a; g). CUR-loaded **A-pPrOzi-A** micelles ($\rho(\text{A-pPrOzi-A/CUR}) = 10/11$ [g/L]) were prepared by “thin film method” with further dilution in cell specific medium to obtain desired CUR concentrations (b; e; h). **A-pPrOzi-A** stock solution was prepared in cell specific medium (200 g/L) and further diluted to desired **A-pPrOzi-A** concentration (c; f; i). Data are presented as mean \pm SD ($n = 3 \times 3$) for every drug and polymer concentration. Cell Viability was determined by CellTiter-Glo® assay.

patients, as rather high doses are required. In 2000, a phase I clinical trial demonstrated that the average peak serum concentration after oral administration of 8 g/day CUR was as low as $1.77 \pm 1.87 \mu\text{M}$ [129]. Notably, no treatment-related toxicity was detectable even at these very high orally administered doses. Parenteral administration potentially increases drug concentrations in serum, however the development of a suitable CUR formulation has proven challenging. With low drug loading, excipients themselves may become toxic [130].

To evaluate the antitumor efficacy of our novel CUR-nanoformulations in a situation that potentially more closely resembles the situation *in vivo*, we directly compared cytotoxicity in 3D tissue models (Fig. 12b) with conventional 2D cell cultures (Fig. 12a) using MDA-MB-231. The tissue model is composed of human cancer cell lines seeded on a scaffold derived from a decellularized porcine jejunum. This matrix, termed SIS muc (Small Intestinal Submucosa with preserved mucosa), exhibits several characteristics that resembles actual tissue such as a maintained architecture including the basement membrane and extracellular matrix components. Extensions of this model allow vascularization with human endothelial cells [131]. Such 3D cancer models for drug testing have been established for colorectal cancer [132] and lung cancer [94,98]. Notably, it was shown that lung cancer cells grown on this

matrix predict the outcome of targeted therapies more accurately than the same cells in 2D culture [98,133]. Here, we investigate for the first time drug evaluation in a 3D breast cancer model based on SIS muc matrix. Importantly, we observed an increased resistance of the cancer cells to pharmacotherapy in this 3D tissue model compared to 2D cell culture. In 2D, reduction of viability was pronounced at CUR concentrations of $15 \mu\text{M}$ (Fig. 12a) according to MTT assay, corroborating previous CellTiter Glo results (Fig. 11g,h). In contrast, CUR concentrations of up to $25 \mu\text{M}$ did not appreciably reduce viability and cell numbers in the 3D tumor model (Fig. 12b, c). A reduction of tumor cell viability in 3D was only observed at 100 and $500 \mu\text{M}$ CUR. At these concentrations cell numbers were drastically reduced not only on top of the scaffold, but also in the deeper layers of the tissue as indicated in the H&E staining of the tumor models (Fig. 12c). This goes in line with the observations that clinical trials using CUR have regularly failed presumably due to poor bioavailability, and higher concentrations of CUR are not possible without a suitable drug carrier [134]. It is important to note, that DMSO-formulated CUR precipitated in cell culture medium at concentrations $\geq 500 \mu\text{M}$, whereas **A-pPrOzi-A** formulated CUR remained clear and seemingly unchanged (Fig. 11d, e). It should be noted that we observed a minor interference of CUR with the MTT-

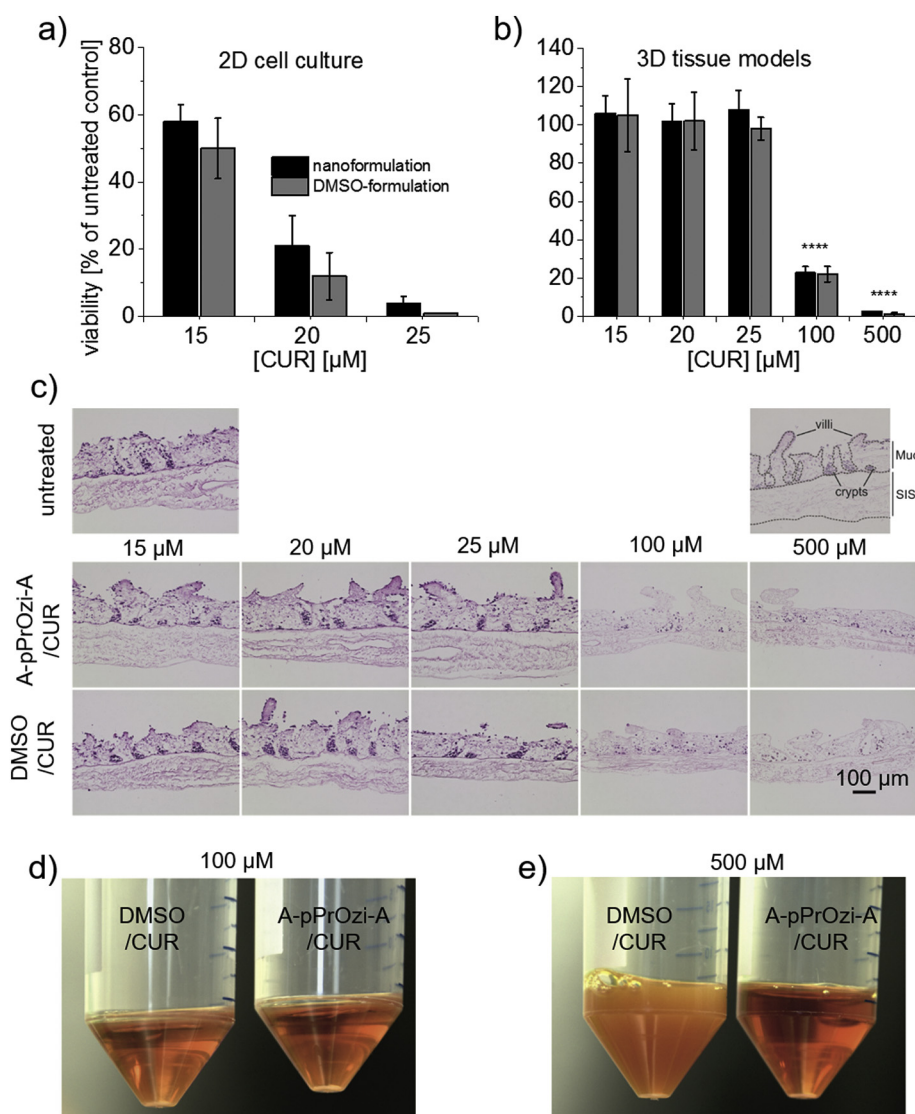


Fig. 12. a) Dose-dependent reduction of cell viability upon treatment with DMSO-formulated CUR and CUR-loaded **A-pPrOzi-A** micelles in MDA-MB-231 cancer cells grown in conventional 2D cell culture. b) Decrease in cell viability upon treatment with CUR in both formulations was achieved only for higher CUR concentrations in a tissue-like 3D culture of MDA-MB-231 cell line based on scaffold SISmuc according to MTT test. Data are presented as mean \pm SD ($n = 4$) for every drug and polymer concentration. Cell Viability was determined by MTT assay. c) H&E staining of the tissue models. The scaffold SISmuc is composed of the small intestinal submucosa (SIS) and the mucosa (Muc). Villi and crypt structures of the mucosal part are preserved and tumor cells (purple spots) grow on the mucosal surface and migrate into the former crypts as well as into the mucosal layer of the scaffold. Scale bar represents 100 μ m. d,e) Precipitation of CUR occurred from DMSO/CUR at a concentration of 500 μ M in cell specific medium while CUR nanoformulations remained clear. (For interpretation of the references to colour in this figure legend, the reader is referred to the web version of this article.)

assay in the case of the cell-free control and at the highest concentration of 500 μ M CUR (Table S4). This effect was more pronounced in the case of the DMSO-formulation and may have been caused by the precipitation and more pronounced adsorption of DMSO-formulated CUR to the scaffold (Fig. S28) leading back to its classification as a pan-assay interference substance. It is apparent that while the 3D tumor model leads to an increased resistance to pharmacotherapy with CUR, there is no difference between the nanoformulation and the DMSO control. This shows that the nanoformulated CUR is fully bioactive. This is not surprising as it has been observed repeatedly before in similar POx-based ultra-high loaded PTX formulations [39]. However, it should also be noted that the DMSO formulation would not be suitable for *in vivo* evaluation, considering the observed precipitation.

In order to further approximate the 3D model to *in vivo* conditions, we applied **A-pPrOzi-A**-formulated CUR to a 3D colorectal cancer model based on the same SISmuc matrix consisting of malignant SW480 tumor cells co-cultured with fibroblasts as a tumor stroma component. Here, fibroblasts induce invasive tumor cell growth leading to partly destroyed and overgrown crypt structures of the matrix. Moreover, we investigated effects of **A-pPrOzi-A** formulated CUR on tumor cell adhesion to our SISmuc scaffold as part of the metastatic cascade [135] by adding SW480 to the medium flow in a dynamic bioreactor setting.

Again, no cytotoxicity of the polymer **A-pPrOzi-A** alone was observed in 2D cell culture at 10 g/L, which is in fact a factor of 10^2 higher

than the highest polymer concentration used for CUR loaded nanoformulations at 500 μ M. Up to 100 μ M CUR, no cytotoxicity of **A-pPrOzi-A**-formulated CUR on SW480 cells was observed while human dermal fibroblasts in mono-culture and the co-culture showed minor growth inhibition by CUR in 2D, however, variability was rather high (Fig. 13a). It has been shown before in conventional 2D culture, that SW480 cells are not highly sensitive to CUR [136]. In contrast, in the more complex 3D model of co-cultured fibroblasts under static culture conditions, we observed markedly decreased tumor cell numbers and altered morphology not only in mono- but also in co-cultures of SW480 cells and fibroblasts after CUR treatment (50 μ M, Fig. 13b, for treatment protocol, please see supporting info Table S5). Apparently, the 3D culture, with and without the stromal component increased the chemosensitivity of SW480 cells to CUR (Fig. 13b I to VI). Just as in 2D, mono-cultured fibroblasts were affected by CUR in 3D, resulting in morphological changes (Fig. 13b III and IV). Notably, in our co-culture approach on the SISmuc, fibroblasts were less affected by CUR and did not change notably their morphology in contrast to the fibroblasts in monoculture (Fig. 13b VII and VIII).

This supports the generation of a malignant tumor stroma in our model which is difficult to target and stresses the urgent need to develop strategies to counteract the whole tumor tissue within appropriate models. In simple 2D co-cultures cues from the ECM and tissue architecture are neglected. Also in mouse models it is difficult to

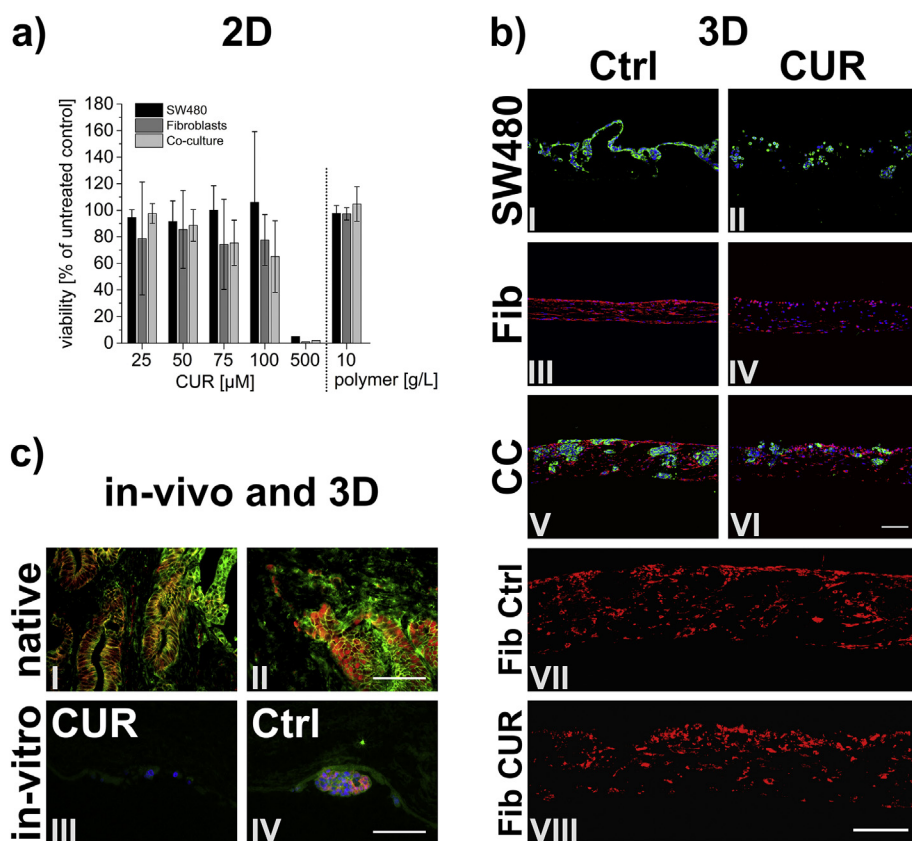


Fig. 13. A-pPrOzi-A-formulated CUR (50 μM) leads to reduced SW480 cell numbers under 3D but not 2D conditions and has anti-metastatic abilities in a metastasis model of colorectal cancer. a) In 2D, CUR has no significant effects on the viability of cells in mono-culture of SW480 cells up to 100 μM , while the viability of mono-cultured fibroblasts as well as the co-cultured fibroblasts with SW480 was somewhat diminished. b) Pan-Cytokeratin (green) / Vimentin (red) stainings of static 3D models. CUR diminishes tumor cell numbers in mono- and co-cultures as shown in I and II as well as V and VI. Fibroblasts in mono-culture are affected by CUR and changed their morphology as shown in III and IV. In contrast, co-cultured fibroblasts did not change their morphology after treatment as shown in VII (untreated control) and VIII (treatment with CUR). Fib = fibroblasts, CC = Co-culture, Ctrl = untreated control, CUR = A-pPrOzi-A-formulated CUR. Scale bar in VI = 100 μm for I to VI, Scale bar in VIII = 100 μm for VII and VIII. c) I: In a native non-invasive tumor, E-Cadherin (green) and β -Catenin (red) are co-localized at the cell boundaries. II: In an invasive carcinoma, β -Catenin translocates to the cytoplasm and into the nucleus. III: SW480 cells in the flowing medium of a flow bioreactor are hampered to adhere after CUR treatment and express neither β -Catenin nor E-Cadherin. IV: Untreated SW480 cells adhere to the matrix SIS muc in a flow bioreactor displaying β -Catenin in the cytoplasm and the nucleus as well as E-Cadherin at the cell boundaries of the tightly packed cells. Scale bar in II = 100 μm for I and II. Scale bar in IV = 100 μm for III and IV. (For interpretation of the references to colour in this figure legend, the reader is referred to the web version of this article.)

represent tumor-stroma interactions, as the human stroma is often lost after implantation of xenografts [137]. Moreover, mouse stroma is quite different from human stroma, as exemplified by the misfit of the murine growth factor HGF from stroma to the HGF receptor on human tumor cells [138,139].

The cell line SW480 is known to express β -catenin partly in the cytoplasm as well as in the nucleus, which is an important characteristic of invasive carcinoma (Fig. 13c I and II). Furthermore, SW480 show the adherens junction protein E-cadherin at cell boundaries when they grow in dense clusters (Fig. 13c IV) [140]. Metastatic cells are known to acquire mesenchymal properties by an epithelial-to-mesenchymal transition (EMT) to start migration from the primary tumor site. After reaching other tissues, tumor cells regain epithelial properties by the reverse process: the mesenchymal-to-epithelial transition (MET [135]) as seen in our model. With CUR treatment in this dynamic metastasis model only a few SW480 adhere to the matrix, and those that do have lost β -catenin as well as E-cadherin expression (Fig. 13c III, for treatment protocol, see Table S6). This points to anti-metastatic properties of CUR which can be detected in our 3D model of metastasizing colorectal cancer. The effect of CUR on β -Catenin expression in SW480 cells has been noted before [136].

It will be important to critically assess chemically unstable compounds such as CUR for biomedical application (e.g. as PAIN [62,64]), instead of relying on supposedly pleiotropic effects of natural compounds. It is quite remarkable that > 100 clinical studies were conducted even though the oral administration of unformulated CUR against various diseases including cancer are not very likely to result in more than “promising results”, as even extraordinary high doses of orally administered CUR (8 g/day) resulted in extremely low serum concentrations ($1.77 \pm 1.87 \mu\text{M}$) [129]. However, instead of refuting any biomedical potential of this small molecule outright, we may have to rethink the approach. Many water-insoluble drugs including one of

today's most prominent chemotherapeutics paclitaxel require appropriate formulation and must be administered parenterally to fully unfold their therapeutic potential. The reported ultra-high drug-loaded polymer micelles may be viewed as a promising candidate for CUR-based treatments. Needless to say, tolerability and safety need to be critically re-evaluated, as such nanoformulated CUR might have a significantly altered safety profile compared to its native form.

5. Conclusion

This work investigated poly(2-oxazoline) (POx) and poly(2-oxazine) (POzi) based amphiphiles for the formulation of the non-water soluble compound CUR. Interestingly, the triple-hydrophilic A-pPrOzi-A (Me-pMeOx₃₅-pPrOzi₂₀-pMeOx₃₅-PipBoc) enabled unrivalled high aqueous drug solubilities of 54.5 g/L at 50 g/L polymer representing a drug-dominant formulation with a loading capacity (LC) of 52 wt%. Moreover, only the addition of the hydrophobic drug promoted micellization as corroborated by ¹H NMR spectroscopy and DLS. The close interactions between polymer and CUR were also noticed in solid dispersion, as the T_g of A-pPrOzi-A/CUR formulations increased linearly with increasing CUR content and crystallization of CUR was prevented even at extraordinary 52 wt% CUR.

The IC₅₀ values of CUR formulated with DMSO or A-pPrOzi-A in conventional 2D models using three different cell lines were similar, showing that CUR was fully bioactive when incorporated into the polymer micelles. Interestingly, A-pPrOzi-A showed a dose-dependent cytotoxicity for MDA-MB-231, suggesting a cytotoxic effect of the polymer in high doses on this very aggressive triple-negative breast cancer cell line. This effect could not be observed for human dermal fibroblasts and Caco-2 cells and needs further investigation. At this point, we cannot rule out that A-pPrOzi-A may exhibit effects similar to the well-studied pluronics [141], with the difference that pluronics are

generally not capable to yield ultra-high drug-loaded micelles.

Compared to conventional 2D cell cultures, we observed an increase in resistance of the cancer cells in 3D tissue models. As stability in complex biological media was higher for **A-pPrOzi-A** formulated CUR compared to DMSO/CUR at 500 μM , we can assume that the presented nanoformulation might allow, for the first time, high-dose *in vivo* therapy using parenteral CUR administration necessary for effective therapeutic high-dose intervention. This might result in significant benefits for the pharmacotherapy using CUR *in vivo* as we could previously show in the case of high-dose therapy using POx/paclitaxel nanoformulations [39]. Moreover, in our metastasis model using a flow bioreactor we found fewer adhering cells expressing hardly any E-Cadherin or β -Catenin after CUR application. This points to a possible anti-metastatic effect of CUR.

The presented, highly unusual CUR nanoformulations warrants further investigation. Safety studies should first elucidate possible toxic effects of high doses of CUR administered parenterally, which has not been possible before. Thereafter, efficacy studies for the plethora of therapeutic interventions associated with CUR could be evaluated without the problem of CUR's poor bioavailability.

Author contributions

M. M. Lübtow synthesized and characterized polymers other than **A-pBuOx-A** and **A-pBuOzi-A**, performed all formulation experiments and conducted all CMC-, CMT-, NMR-, DLS-, DSC-, XRD- and zeta-potential measurements. 2D cell culture studies were conducted by M. M. Lübtow, J. Seifert and L. Nelke. L. Nelke, J. Kühnemund and J. Seifert conducted all 3D cell culture studies.

G. Sahay supervised cryo-TEM measurements. R. Luxenhofer designed and supervised the entire study. The manuscript was written by M. M. Lübtow, R. Luxenhofer, L. Nelke, S. L. Nietzer and G. Dandekar, all authors agreed to the final version of the manuscript.

Conflict of interest

R.L. and M.M.L. are listed on a patent application submitted by the Julius-Maximilians University of Würzburg which is pertinent to content of the report.

Acknowledgement

Financial support by the Deutsche Forschungsgemeinschaft is gratefully acknowledged (Project number 398461692, awarded to R.L.). This work was also supported by the Free State of Bavaria. Start-up funding for R.L. by the University Würzburg and SKZ Das Kunststoff-Zentrum is gratefully acknowledged. Furthermore, the work with 3D-tissue models was supported by the Bayern-Fit Program. M.M.L. would like to thank the Evonik Foundation (M.M.L.) for providing a doctoral fellowship.

We would also like to thank Christian May, Lisa Holz and Maria Krebs for technical support in monomer and polymer synthesis, respectively. We thank Ilona Zilkowsky, M. Sc. (University of Würzburg, Department for Functional Materials in Medicine and Dentistry) for support during DLS- and Zeta potential- measurements. We thank Isabell Biermann (University of Würzburg, Department for Functional Materials in Medicine and Dentistry) for support during XRD- measurements. Furthermore, we thank Maximilian Rist for the support regarding characterization of 3-year samples. Electron microscopy was performed at the Multiscale Microscopy Core (MMC) with technical support Anna Brown, Clemens Schulte and Siddharth Patel and from the Oregon Health & Science University (OHSU)-FEI Living Lab and the OHSU Center for Spatial Systems Biomedicine (OCSBS).

Appendix A. Supplementary data

Supplementary data to this article can be found online at <https://doi.org/10.1016/j.jconrel.2019.04.014>.

References

- [1] A. Persidis, High-throughput screening, *Nat. Biotechnol.* 16 (1998) 488–489.
- [2] E.M. Merisko-Liversidge, G.G. Liversidge, Drug nanoparticles: formulating poorly water-soluble compounds, *Toxicol. Pathol.* 36 (2008) 43–48.
- [3] C. Giliyar, D. Fikstad, S. Tyavanagimatt, Challenges and opportunities in oral delivery of poorly water-soluble drugs, *Drug Deliv. Technol.* 6 (2006) 57–63.
- [4] V. Bharti, V. Attal, A. Munde, A. Birajdar, S. Bais, Strategies to enhance solubility and dissolution of a poorly water soluble drug, *J. Innov. Pharm. Biol. Sci.* 2 (2015) 482–494.
- [5] S. Ali, K. Kolter, Challenges and opportunities in oral formulation development, *Am. Pharm. Rev.* 15 (2012) 1–8 dec.
- [6] L. Gros, H. Ringsdorf, H. Schupp, Polymeric antitumor agents on a molecular and on a cellular level? *Angew. Chem. Int. Ed.* 20 (1981) 305–325.
- [7] S.R. Croy, G.S. Kwon, Polymeric micelles for drug delivery, *Curr. Pharm. Des.* 12 (2006) 4669–4684.
- [8] J. Logie, A.N. Ganesh, A.M. Aman, R.S. Al-awar, M.S. Shoichet, Preclinical evaluation of taxane-binding peptide-modified polymeric micelles loaded with docetaxel in an orthotopic breast cancer mouse model, *Biomaterials* 123 (2017) 39–47.
- [9] Study of NC-6004 in Combination with 5-FU and Cetuximab in Patients with Head and Neck Cancer, <https://www.clinicaltrials.gov/ct2/show/NCT02817113>, (2016).
- [10] Study to Evaluate the Efficacy and Safety of Docetaxel Polymeric Micelle (PM) in Recurrent or Metastatic HNSCC, <https://www.clinicaltrials.gov/ct2/show/NCT02639858>, (2017).
- [11] A Phase II Study of Weekly Genexol-PM in Patients with Hepatocellular Carcinoma after Failure of Sorafenib, <https://www.clinicaltrials.gov/ct2/show/NCT03008512>, (2016).
- [12] Clinical Trial on the Efficacy and Safety of Sirolimus-Eluting Stent (MiStent® System) (DESSOLVE-C), <https://www.clinicaltrials.gov/ct2/show/NCT02448524>, (2016).
- [13] H. Cabral, K. Kataoka, Progress of drug-loaded polymeric micelles into clinical studies, *J. Control. Release* 190 (2014) 465–476.
- [14] R. Luxenhofer, Y. Han, A. Schulz, J. Tong, Z. He, A.V. Kabanov, R. Jordan, Poly(2-oxazoline)s as polymer therapeutics, *Macromol. Rapid Commun.* 33 (2012) 1613–1631.
- [15] V.R. de la Rosa, Poly(2-oxazoline)s as materials for biomedical applications, *J. Mater. Sci. Mater. Med.* 25 (2014) 1211–1225.
- [16] T. Lorson, M.M. Lübtow, E. Wegener, M.S. Haider, S. Borova, D. Nahm, R. Jordan, M. Sokolski-Papkov, A.V. Kabanov, R. Luxenhofer, Poly(2-oxazoline)s based biomaterials: a comprehensive and critical update, *Biomaterials* 178 (2018) 204–280.
- [17] J. Kronek, Z. Kroneková, J. Lustoň, E. Paulovičová, L. Paulovičová, B. Mendrek, In vitro bio-immunological and cytotoxicity studies of poly(2-oxazolines), *J. Mater. Sci. Mater. Med.* 22 (2011) 1725–1734.
- [18] M. Bauer, S. Schroeder, L. Tauhardt, K. Kempe, U.S. Schubert, D. Fischer, In vitro hemocompatibility and cytotoxicity study of poly(2-methyl-2-oxazoline) for biomedical applications, *J. Polym. Sci. A* 51 (2013) 1816–1821.
- [19] M. Bauer, C. Lautenschlaeger, K. Kempe, L. Tauhardt, U.S. Schubert, D. Fischer, Poly(2-ethyl-2-oxazoline) as alternative for the stealth polymer poly(ethylene glycol): comparison of in vitro cytotoxicity and Hemocompatibility, *Macromol. Biosci.* 12 (2012) 986–998.
- [20] R. Luxenhofer, G. Sahay, A. Schulz, D. Alakhova, T.K. Bronich, R. Jordan, A.V. Kabanov, Structure-property relationship in cytotoxicity and cell uptake of poly(2-oxazoline) amphiphiles, *J. Control. Release* 153 (2011) 73–82.
- [21] B. Verbraeken, B.D. Monnery, K. Lava, R. Hoogenboom, The chemistry of poly(2-oxazolines), *Eur. Polym. J.* 88 (2017) 451–469.
- [22] R. Luxenhofer, M. Bezen, R. Jordan, Kinetic investigations on the polymerization of 2-Oxazolines using Pluritriflate Initiators, *Macromol. Rapid Commun.* 29 (2008) 1509–1513.
- [23] N. Zhang, S. Huber, A. Schulz, R. Luxenhofer, R. Jordan, Cylindrical molecular brushes of poly(2-oxazoline)s from 2-Isopropenyl-2-oxazoline, *Macromolecules* 42 (2009) 2215–2221.
- [24] N. Zhang, R. Luxenhofer, R. Jordan, Thermoresponsive poly(2-Oxazoline) molecular brushes by living ionic polymerization: modulation of the cloud point by random and block copolymer pendant chains, *Macromol. Chem. Phys.* 213 (2012) 1963–1969.
- [25] B. Guillerme, S. Monge, V. Lapinte, J.-J. Robin, How to modulate the chemical structure of Polyoxazolines by appropriate functionalization, *Macromol. Rapid Commun.* 33 (2012) 1600–1612.
- [26] D.A. Tomalia, D.P. Sheetz, Homopolymerization of 2-alkyl- and 2-aryl-2-oxazolines, *J. Polym. Sci. A* 4 (1966) 2253–2265.
- [27] T. Kagiya, S. Narisawa, T. Maeda, K. Fukui, Preparation of a crystalline poly(esteramide) by the polyaddition reaction of bisoxazoline and a dicarboxylic acid, *J. Polym. Sci. B Polym. Phys.* 4 (1966) 257–260.
- [28] W. Seeliger, E. Aufderhaar, W. Diepers, R. Feinauer, R. Nehring, W. Thier, H. Hellmann, Neuere Synthesen und Reaktionen cyclischer Imidsäureester, *Angew. Chem.* 78 (1966) 913–927.
- [29] C. Maechling-Strasser, P. Déjardin, J.C. Galin, A. Schmitt, V. Housse-Ferrari,

- B. Sébille, J.N. Mulvihill, J.P. Cazenave, Synthesis and adsorption of a poly(*n*-acetylthyleneimine)-polyethyleneoxide-poly (*n*-acetylthyleneimine) triblock-copolymer at a silica/solution interface. Influence of its preadsorption on platelet adhesion and fibrinogen adsorption, *J. Biomed. Mater. Res. A* 23 (1989) 1395–1410.
- [30] P. Goddard, L.E. Hutchinson, J. Brown, L.J. Brookman, Soluble polymeric carriers for drug delivery. Part 2. Preparation and in vivo behaviour of *N*-acetylthyleneimine copolymers, *J. Control. Release* 10 (1989) 5–16.
- [31] Y. Zhao, Y. Zhou, D. Wang, Y. Gao, J. Li, S. Ma, L. Zhao, C. Zhang, Y. Liu, X. Li, pH-responsive polymeric micelles based on poly(2-ethyl-2-oxazoline)-poly(D,L-lactide) for tumor-targeting and controlled delivery of doxorubicin and P-glycoprotein inhibitor, *Acta Biomater.* 17 (2015) 182–192.
- [32] V.M. Gaspar, C. Gonçalves, D. de Melo-Diogo, E.C. Costa, J.A. Queiroz, C. Pichon, F. Sousa, I.J. Correia, Poly(2-ethyl-2-oxazoline)-PLA-g-PEI amphiphilic triblock micelles for co-delivery of minicircle DNA and chemotherapeutics, *J. Control. Release* 189 (2014) 90–104.
- [33] R. Luxenhofer, A. Schulz, C. Roques, S. Li, T.K. Bronich, E.V. Batrakova, R. Jordan, A.V. Kabanov, Doubly amphiphilic poly(2-oxazoline)s as high-capacity delivery systems for hydrophobic drugs, *Biomaterials* 31 (2010) 4972–4979.
- [34] K. Miyamoto, T. Shimada, K. Sawamoto, Y. Sai, Y. Yonemura, Disposition kinetics of Taxanes in peritoneal dissemination, *Gastroenterol. Res. Pract.* 2012 (2012) 963403.
- [35] M.S. Surapaneni, S.K. Das, N.G. Das, Designing paclitaxel drug delivery systems aimed at improved patient outcomes: current status and challenges, *ISRN Pharmacol.* 2012 (2012) 623139.
- [36] P. Ma, R.J. Mumper, Paclitaxel Nano-delivery systems: a comprehensive review, *J. Nanomed. Nanotechnol.* 4 (2013) 1000164.
- [37] Y. Seo, A. Schulz, Y. Han, Z. He, H. Bludau, X. Wan, J. Tong, T.K. Bronich, M. Sokolsky, R. Luxenhofer, R. Jordan, A.V. Kabanov, Poly(2-oxazoline) block copolymer based formulations of taxanes: effect of copolymer and drug structure, concentration, and environmental factors, *Polym. Adv. Technol.* 26 (2015) 837–850.
- [38] A. Schulz, S. Jaksch, R. Schubel, E. Wegener, Z. Di, Y. Han, A. Meister, J. Kressler, A.V. Kabanov, R. Luxenhofer, C.M. Papadakis, R. Jordan, Drug-induced morphology switch in drug delivery systems based on poly(2-oxazoline)s, *ACS Nano* 8 (2014) 2686–2696.
- [39] Z. He, X. Wan, A. Schulz, H. Bludau, M.A. Dobrovolskaia, S.T. Stern, S.A. Montgomery, H. Yuan, Z. Li, D. Alakhova, M. Sokolsky, D.B. Darr, C.M. Perou, R. Jordan, R. Luxenhofer, A.V. Kabanov, A high capacity polymeric micelle of paclitaxel: implication of high dose drug therapy to safety and in vivo anti-cancer activity, *Biomaterials* 101 (2016) 296–309.
- [40] S. Jaksch, A. Schulz, Z. Di, R. Luxenhofer, R. Jordan, C.M. Papadakis, Amphiphilic Triblock copolymers from poly(2-oxazoline) with different hydrophobic blocks: changes of the Micellar structures upon addition of a strongly hydrophobic Cancer drug, *Macromol. Chem. Phys.* 217 (2016) 1448–1456.
- [41] A. Levy, M. Litt, Polymerization of cyclic imino ethers. II. Oxazines, *Polym. Lett.* 5 (1967) 881–886.
- [42] M.M. Bloksma, R.M. Paulus, H.P.C. van Kuringen, F. van der Woerd, H.M.L. Lambermont-Thijs, U.S. Schubert, R. Hoogenboom, Thermoresponsive poly(2-oxazine)s, *Macromol. Rapid Commun.* 33 (2012) 92–96.
- [43] M.M. Bloksma, U.S. Schubert, R. Hoogenboom, Poly(cyclic imino ether)s beyond 2-Substituted-2-oxazolines, *Macromol. Rapid Commun.* 32 (2011) 1419–1441.
- [44] S. Sinnwell, H. Ritter, Microwave accelerated polymerization of 2-Phenyl-5,6-dihydro-4H-1,3-oxazine: kinetics and influence of end-groups on glass transition temperature, *Macromol. Rapid Commun.* 27 (2006) 1335–1340.
- [45] T. Lorson, S. Jaksch, M.M. Lübtow, T. Jüngst, J. Groll, T. Lühmann, R. Luxenhofer, A Thermogelling Supramolecular hydrogel with sponge-like morphology as a Cytocompatible bioink, *Biomacromolecules* 18 (2017) 2161–2171.
- [46] S. Kobayashi, T. Igarashi, Y. Moriuchi, T. Saegusa, Block copolymers from cyclic imino ethers: a new class of nonionic polymer surfactant, *Macromolecules* 19 (1986) 535–541.
- [47] G. Morgese, B. Verbraeken, S.N. Ramakrishna, Y. Gombert, E. Cavalli, J.G. Rosenboom, M. Zenobi-Wong, N.D. Spencer, R. Hoogenboom, E.M. Benetti, Chemical Design of non-Ionic Polymer Brushes as biointerfaces: poly(2-oxazine)s outperform both poly(2-oxazoline)s and PEG, *Angew. Chem. Int. Ed. Eng.* 57 (2018) 11667–11672.
- [48] A. Levy, M. Litt, Polymerization of cyclic imino ethers. II. Oxazines, *J. Polym. Sci. B Polym. Phys.* 5 (1967) 881–886.
- [49] M.M. Lübtow, L. Hahn, M.S. Haider, R. Luxenhofer, Drug specificity, synergy and antagonism in ultrahigh capacity poly(2-oxazoline)/poly(2-oxazine) based formulations, *J. Am. Chem. Soc.* 139 (2017) 10980–10983.
- [50] Y.B. Pawar, B. Munjal, S. Arora, M. Karwa, G. Kohli, J.K. Paliwal, A.K. Bansal, Bioavailability of a Lipidic formulation of Curcumin in healthy human volunteers, *Pharmaceutics* 5 (2012) 517–530.
- [51] B.T.S.A.M. Kurien, R.H. Scofield, Improving the solubility and pharmacological efficacy of curcumin by heat treatment, *Assay Drug Dev. Technol.* 5 (2007) 567–576.
- [52] S.C. Gupta, S. Patchva, B.B. Aggarwal, Therapeutic roles of curcumin: lessons learned from clinical trials, *AAPS J.* 15 (2013) 195–218.
- [53] T. Ak, İ. Gülçin, Antioxidant and radical scavenging properties of curcumin, *Chem. Biol. Interact.* 174 (2008) 27–37.
- [54] S. Miriyala, M. Panchatcharam, P. Rengarajulu, Cardioprotective effects of curcumin, *The Molecular Targets and Therapeutic Uses of Curcumin in Health and Disease*, Springer, 2007, pp. 359–377.
- [55] G.M. Cole, B. Teter, S.A. Fruitsch, Neuroprotective effects of Curcumin, *Adv. Exp. Med. Biol.* 595 (2007) 197–212.
- [56] Y. Li, J. Li, S. Li, Y. Li, X. Wang, B. Liu, Q. Fu, S. Ma, Curcumin attenuates glutamate neurotoxicity in the hippocampus by suppression of ER stress-associated TXNIP/NLRP3 inflammasome activation in a manner dependent on AMPK, *Toxicol. Appl. Pharmacol.* 286 (2015) 53–63.
- [57] D.W. Zhang, M. Fu, S.H. Gao, J.L. Liu, Curcumin and diabetes: a systematic review, *Evid. Based Complement. Alternat. Med.* 2013 (2013) 16.
- [58] J.S. Jurenka, Anti-inflammatory properties of Curcumin, a major constituent of Curcuma longa: a review of preclinical and clinical research, *Altern. Med. Rev.* 14 (2009) 141–153.
- [59] N. Chainani-Wu, Safety and anti-inflammatory activity of Curcumin: a component of Tumeric (*Curcuma longa*), *J. Altern. Complement. Med.* 9 (2003) 161–168.
- [60] X. Yang, Z. Li, N. Wang, L. Li, L. Song, T. He, L. Sun, Z. Wang, Q. Wu, N. Luo, C. Yi, C. Gong, Curcumin-encapsulated polymeric micelles suppress the development of Colon Cancer in vitro and in vivo, *Sci. Rep.* 5 (2015) 10322.
- [61] P. Anand, S.G. Thomas, A.B. Kunnumakkara, C. Sundaram, K.B. Harikumar, B. Sung, S.T. Tharakan, K. Misra, I.K. Priyadarisni, K.N. Rajasekharan, B.B. Aggarwal, Biological activities of curcumin and its analogues (congeners) made by man and mother nature, *Biochem. Pharmacol.* 76 (2008) 1590–1611.
- [62] J. Baell, M.A. Walters, Chemistry: chemical con artists foil drug discovery, *Nature* 513 (2014) 481–483.
- [63] M. Heger, Drug screening: Don't discount all curcumin trial data, *Nature* 543 (2017) 40.
- [64] K.M. Nelson, J.L. Dahlin, J. Bisson, J. Graham, G.F. Pauli, M.A. Walters, The essential medicinal chemistry of Curcumin, *J. Med. Chem.* 60 (2017) 1620–1637.
- [65] N. Jurrmann, R. Brigelius-Flohé, G.-F. Böl, Curcumin blocks Interleukin-1 (IL-1) Signaling by inhibiting the recruitment of the IL-1 receptor-associated kinase IRAK in murine Thymoma EL-4 cells, *J. Nutr.* 135 (2005) 1859–1864.
- [66] A. Goel, C.R. Boland, D.P. Chauhan, Specific inhibition of cyclooxygenase-2 (COX-2) expression by dietary curcumin in HT-29 human colon cancer cells, *Cancer Lett.* 172 (2001) 111–118.
- [67] A.L. Clutterbuck, D. Allaway, P. Harris, A. Mobasher, Curcumin reduces prostaglandin E2, matrix metalloproteinase-3 and proteoglycan release in the secretome of interleukin 1 β -treated articular cartilage, *F1000Res.* 2 (2013) 147.
- [68] J.U. Marquardt, L. Gomez-Quiroz, L.O. Arreguin Camacho, F. Pinna, Y.-H. Lee, M. Kitade, M.P. Domínguez, D. Castven, K. Breuhahn, E.A. Conner, P.R. Galle, J.B. Andersen, V.M. Factor, S.S. Thorgeirsson, Curcumin effectively inhibits oncogenic NF- κ B signaling and restrains stemness features in liver cancer, *J. Hepatol.* 63 (2015) 661–669.
- [69] L. Shen, H.-F. Ji, The pharmacology of curcumin: is it the degradation products? *Trends Mol. Med.* 18 (2012) 138–144.
- [70] K. Lirdprapamongkol, H. Sakurai, S. Suzuki, K. Koizumi, O. Prangsaengtong, A. Viriyaraj, S. Ruchirawat, J. Svasti, I. Saiki, Vanillin enhances TRAIL-induced apoptosis in Cancer cells through inhibition of NF- κ B activation, *In Vivo* 24 (2010) 501–506.
- [71] P. Anand, A.B. Kunnumakkara, R.A. Newman, B.B. Aggarwal, Bioavailability of Curcumin: problems and promises, *Mol. Pharm.* 4 (2007) 807–818.
- [72] G. Shoba, D. Joy, T. Joseph, M. Majeed, R. Rajendran, P.S.S.R. Srinivas, Influence of Piperine on the pharmacokinetics of Curcumin in animals and human volunteers, *Planta Med.* 64 (1998) 353–356.
- [73] O. Naksuriya, S. Okonogi, R.M. Schiffelers, W.E. Hennink, Curcumin nanoformulations: a review of pharmaceutical properties and preclinical studies and clinical data related to cancer treatment, *Biomaterials* 35 (2014) 3365–3383.
- [74] W. Liu, Y. Zhai, H. Heng, F.Y. Che, W. Chen, D. Sun, G. Zhai, Oral bioavailability of curcumin: problems and advancements, *J. Drug Target.* 24 (2016) 694–702.
- [75] L. Song, Y. Shen, J. Hou, L. Lei, S. Guo, C. Qian, Polymeric micelles for parenteral delivery of curcumin: preparation, characterization and in vitro evaluation, *Colloids Surf. A Physicochem. Eng. Asp.* 390 (2011) 25–32.
- [76] C. Gonçalves, J.-P. Gomez, W. Mème, B. Rasolonjatovo, D. Gosset, S. Nedellec, P. Hulin, C. Huin, T. Le Gall, T. Montier, P. Lehn, C. Pichon, P. Guégan, H. Cheradame, P. Midoux, Curcumin/poly(2-methyl-2-oxazoline-b-tetrahydrofuran-b-2-methyl-2-oxazoline) formulation: an improved penetration and biological effect of curcumin in F508del-CFTR cell lines, *Eur. J. Pharm. Biopharm.* 117 (2017) 168–181.
- [77] R. Raveendran, K.M. Mullen, R.M. Wellard, C.P. Sharma, R. Hoogenboom, T.R. Dargaville, Poly(2-oxazoline) block copolymer nanoparticles for curcumin loading and delivery to cancer cells, *Eur. Polym. J.* 93 (2017) 682–694.
- [78] F. Novelli, S. De Santis, M. Diociaiuti, C. Giordano, S. Morosetti, P. Punzi, F. Sciubba, V. Viali, G. Masci, A. Scipioni, Curcumin loaded nanocarriers obtained by self-assembly of a linear d,l-octapeptide-poly(ethylene glycol) conjugate, *Eur. Polym. J.* 98 (2018) 28–38.
- [79] S. Datta, A. Jutková, P. Šrámková, L. Lenkavská, V. Huntošová, D. Chorvát, P. Miškovský, D. Jancura, J. Kronek, Unravelling the excellent chemical stability and bioavailability of solvent responsive Curcumin-loaded 2-Ethyl-2-oxazoline-grad-2-(4-dodecyloxyphenyl)-2-oxazoline copolymer nanoparticles for drug delivery, *Biomacromolecules* 19 (2018) 2459–2471.
- [80] S. Bisht, A. Maitra, Systemic delivery of curcumin: 21st century solutions for an ancient conundrum, *Curr. Drug Discov. Technol.* 6 (2009).
- [81] S. Bisht, G. Feldmann, S. Soni, R. Ravi, C. Karikar, A. Maitra, A. Maitra, Polymeric nanoparticle-encapsulated curcumin (“nanocurcumin”): a novel strategy for human cancer therapy, *J. Nanobiotechnology* 5 (2007) 3.
- [82] K.J. Lim, S. Bisht, E.E. Bar, A. Maitra, C.G. Eberhart, A polymeric nanoparticle formulation of curcumin inhibits growth, clonogenicity and stem-like fraction in malignant brain tumors, *Cancer Biol. Ther.* 11 (2011) 464–473.
- [83] S. Bisht, M. Mizuma, G. Feldmann, N.A. Ottenhof, S.-M. Hong, D. Pramanik, V. Chenna, C. Karikari, R. Sharma, M.G. Goggins, M.A. Rudek, R. Ravi, A. Maitra, A. Maitra, Systemic Administration of Polymeric Nanoparticle-Encapsulated

- Curcumin (NanoCurc) blocks tumor growth and metastases in preclinical models of pancreatic Cancer, *Mol. Cancer Ther.* 9 (2010) 2255.
- [84] H. Sasaki, Y. Sunagawa, K. Takahashi, A. Imaizumi, H. Fukuda, T. Hashimoto, H. Wada, Y. Katanasaka, H. Kakeya, M. Fujita, K. Hasegawa, T. Morimoto, Innovative preparation of Curcumin for improved Oral bioavailability, *Biol. Pharm. Bull.* 34 (2011) 660–665.
- [85] Y. Sunagawa, S. Hirano, Y. Katanasaka, Y. Miyazaki, M. Funamoto, N. Okamura, Y. Hojo, H. Suzuki, O. Doi, T. Yokoji, E. Morimoto, T. Takahashi, H. Ozawa, A. Imaizumi, M. Ueno, H. Kakeya, A. Shimatsu, H. Wada, K. Hasegawa, T. Morimoto, Colloidal submicron-particle Curcumin exhibits high absorption efficiency - a double-blind, 3-way crossover study, *J. Nutr. Sci. Vitaminol.* 61 (2015) 37–44.
- [86] G. Belcaro, M.R. Cesarone, M. Dugall, L. Pellegrini, A. Ledda, M.G. Grossi, S. Togni, G. Appendino, Efficacy and safety of Meriva®, a Curcumin-phosphatidylcholine complex, during extended Administration in Osteoarthritis Patients, *Altern. Med. Rev.* 15 (2010) 337–344.
- [87] G. Belcaro, M.R. Cesarone, M. Dugall, L. Pellegrini, A. Ledda, M.G. Grossi, S. Togni, G. Appendino, Product-evaluation registry of Meriva®, a curcumin-phosphatidylcholine complex, for the complementary management of osteoarthritis, *Painmanerva Med.* 52 (2010) 55–62.
- [88] B. Yoo, K. Kirshenbaum, Peptoid architectures: elaboration, actuation, and application, *Curr. Opin. Chem. Biol.* 12 (2008) 714–721.
- [89] J. Cuomo, G. Appendino, A.S. Dern, E. Schneider, T.P. McKinnon, M.J. Brown, S. Togni, B.M. Dixon, Comparative absorption of a standardized Curcuminoid mixture and its lecithin formulation, *J. Nat. Prod.* 74 (2011) 664–669.
- [90] B. Antony, B. Merina, V.S. Iyer, N. Judy, K. Lennertz, S. Joyal, A pilot cross-over study to evaluate human Oral bioavailability of BCM-95(®)CG (Biocurcmax™), a novel bioenhanced preparation of Curcumin, *Indian J. Pharm. Sci.* 70 (2008) 445–449.
- [91] A. Kocher, L. Bohnert, C. Schiborr, J. Frank, Highly bioavailable micellar curcuminoids accumulate in blood, are safe and do not reduce blood lipids and inflammation markers in moderately hyperlipidemic individuals, *Mol. Nutr. Food Res.* 60 (2016) 1555–1563.
- [92] A. Kocher, C. Schiborr, D. Behnam, J. Frank, The oral bioavailability of curcuminoids in healthy humans is markedly enhanced by micellar solubilisation but not further improved by simultaneous ingestion of sesamin, ferulic acid, naringenin and xanthohumol, *J. Funct. Foods* 14 (2015) 183–191.
- [93] C. Schiborr, A. Kocher, D. Behnam, J. Jandasek, S. Toelstede, J. Frank, The oral bioavailability of curcumin from micronized powder and liquid micelles is significantly increased in healthy humans and differs between sexes, *Mol. Nutr. Food Res.* 58 (2014) 516–527.
- [94] C. Göttlich, L.C. Müller, M. Kunz, F. Schmitt, H. Walles, T. Walles, T. Dandekar, G. Dandekar, S.L. Nietzer, A combined 3D tissue engineered *in vitro/in Silico* lung tumor model for predicting drug effectiveness in specific mutational backgrounds, *J. Vis. Exp.* 110 (2016) e53885.
- [95] P. Benien, A. Swami, 3D tumor models: history, advances and future perspectives, *Future Oncol.* 10 (2014) 1311–1327.
- [96] A. Villasante, G. Vunjak-Novakovic, Tissue-engineered models of human tumors for cancer research, *Expert Opin. Drug Discov.* 10 (2015) 257–268.
- [97] X. Xu, M.C. Farach-Carson, X. Jia, Three-dimensional *in vitro* tumor models for Cancer research and drug evaluation, *Biotechnol. Adv.* 32 (2014) 1256–1268.
- [98] A.T. Stratmann, D. Fecher, G. Wangorsch, C. Göttlich, T. Walles, H. Walles, T. Dandekar, G. Dandekar, S.L. Nietzer, Establishment of a human 3D lung cancer model based on a biological tissue matrix combined with a Boolean *in silico* model, *Mol. Oncol.* 8 (2014) 351–365.
- [99] H. Witte, W. Seeliger, Cyclische Imidäureester aus Nitrilen und Aminoalkoholen, *Liebigs Ann. Chem.* 1974 (1974) 996–1009.
- [100] R. Luxenhofer, R. Jordan, Click chemistry with poly(2-oxazoline)s, *Macromolecules* 39 (2006) 3509–3516.
- [101] M. Vergaelen, B. Verbraeken, B.D. Monnery, R. Hoogenboom, Sulfolane as common rate accelerating solvent for the cationic ring-opening polymerization of 2-Oxazolines, *ACS Macro Lett.* 4 (2015) 825–828.
- [102] S. Nietzer, F. Baur, S. Sieber, J. Hansmann, T. Schwarz, C. Stoffer, H. Häfner, M. Gasser, A.M. Waaga-Gasser, H. Walles, G. Dandekar, Mimicking metastases including tumor Stroma: a new technique to generate a three-dimensional colorectal Cancer model based on a biological Decellularized intestinal scaffold, *Tissue Eng. Part C* 22 (2016) 621–635.
- [103] R. Luxenhofer, Polymers and nanomedicine: considerations on variability and reproducibility when combining complex systems, *Nanomedicine* 10 (2015) 3109–3119.
- [104] J.C. Leroux, Drug delivery: too much complexity, not enough reproducibility? *Angew. Chem. Int. Ed. Eng.* 56 (2017) 15170–15171.
- [105] V.P. Torchilin, Targeted polymeric micelles for delivery of poorly soluble drugs, *Cell. Mol. Life Sci.* 61 (2004) 2549–2559.
- [106] L. Piñeiro, M. Novo, W. Al-Soufi, Fluorescence emission of pyrene in surfactant solutions, *Adv. Colloid Interf. Sci.* 215 (2015) 1–12.
- [107] S. Huber, N. Hutter, R. Jordan, Effect of end group polarity upon the lower critical solution temperature of poly(2-isopropyl-2-oxazoline), *Colloid Polym. Sci.* 286 (2008) 1653–1661.
- [108] A. Zahoranová, M. Mrlík, K. Tomanová, J. Kronek, R. Luxenhofer, ABA and BAB Triblock copolymers based on 2-Methyl-2-oxazoline and 2-n-Propyl-2-oxazoline: synthesis and Thermoresponsive behavior in water, *Macromol. Chem. Phys.* (2017) 1700031 (n/a).
- [109] D. Patra, C. Barakat, Synchronous fluorescence spectroscopic study of solvatochromic curcumin dye, *Spectrochim. Acta A* 79 (2011) 1034–1041.
- [110] S.N. Margar, N. Sekar, Nonlinear optical properties of curcumin: solvatochromism-based approach and computational study, *Mol. Phys.* 114 (2016) 1867–1879.
- [111] J.L.S. Gonçalves, S.R. Valandro, A.L. Poli, C.C. Schmitt, Influence of clay minerals on curcumin properties: stability and singlet oxygen generation, *J. Mol. Struct.* 1143 (2017) 1–7.
- [112] O. Naksuriya, M.J. van Steenberg, J.S. Torano, S. Okonogi, W.E. Hennink, A kinetic degradation study of Curcumin in its free form and loaded in polymeric micelles, *AAPS J.* 18 (2016) 777–787.
- [113] K. Priyadarsini, The chemistry of Curcumin: from extraction to therapeutic agent, *Molecules* 19 (2014) 20091.
- [114] M.M. Lübtow, L. Keßler, A. Appelt-Menzel, T. Lorson, N. Gangloff, M. Kirsch, S. Dahms, R. Luxenhofer, More is sometimes less: Curcumin and paclitaxel formulations using poly(2-oxazoline) and poly(2-oxazine)-based Amphiphiles bearing linear and branched C9 side chains, *Macromol. Biosci.* 18 (2018) 1800155.
- [115] C. Liu, Z. Chen, Y. Chen, J. Lu, Y. Li, S. Wang, G. Wu, F. Qian, Improving Oral bioavailability of Sorafenib by optimizing the “spring” and “parachute” based on molecular interaction mechanisms, *Mol. Pharm.* 13 (2016) 599–608.
- [116] J.-C. Leroux, Drug delivery: too much complexity, not enough reproducibility? *Angew. Chem. Int. Ed.* 56 (2017) 15170–15171.
- [117] A. Bogomolova, S.K. Filippov, L. Starovoytova, B. Angelov, P. Konarev, O. Sedlacek, M. Hruby, P. Stepanek, Study of complex Thermosensitive Amphiphilic Polyoxazolines and their interaction with ionic surfactants. Are hydrophobic, Thermosensitive, and hydrophilic moieties equally important? *J. Phys. Chem. B* 118 (2014) 4940–4950.
- [118] X. Wan, Y. Min, H. Bludau, A. Keith, S.S. Sheiko, R. Jordan, A.Z. Wang, M. Sokolsky-Papkov, A.V. Kabanov, Drug combination synergy in worm-like polymeric micelles improves treatment outcome for small cell and non-small cell lung cancer, *ACS Nano* 12 (2018) 2426–2439.
- [119] S.E. McNeil, Nanoparticle therapeutics: a personal perspective, *Wiley Interdiscip. Rev. Nanomed. Nanobiotechnol.* 1 (2009) 264–271.
- [120] P. Sanphui, N.R. Goud, U.B.R. Khandavilli, S. Bhanoth, A. Nangia, New polymorphs of curcumin, *Chem. Commun.* 47 (2011) 5013–5015.
- [121] A. Schulz, Investigation of Structure-Property Relationships of Poly(2-Oxazoline) Based Drug Delivery Systems, In, Investigation of Structure-Property Relationships of Poly(2-Oxazoline) Based Drug Delivery Systems, thesis Technische Universität Dresden, 2014.
- [122] C. de Brabander, G. van den Mooter, C. Vervaeke, J.P. Remon, Characterization of ibuprofen as a nontraditional plasticizer of ethyl cellulose, *J. Pharm. Sci.* 91 (2002) 1678–1685.
- [123] C. Wu, J.W. McGinity, Non-traditional plasticization of polymeric films, *Int. J. Pharm.* 177 (1999) 15–27.
- [124] W. Wang, R. Zhu, Q. Xie, A. Li, Y. Xiao, K. Li, H. Liu, D. Cui, Y. Chen, S. Wang, Enhanced bioavailability and efficiency of curcumin for the treatment of asthma by its formulation in solid lipid nanoparticles, *Int. J. Nanomedicine* 7 (2012) 3667–3677.
- [125] P. Khadka, J. Ro, H. Kim, I. Kim, J.T. Kim, H. Kim, J.M. Cho, G. Yun, J. Lee, Pharmaceutical particle technologies: an approach to improve drug solubility, dissolution and bioavailability, *Asian J. Pharm.* 9 (2014) 304–316.
- [126] Y. Fujimoto, S. Sakuma, C. Maruyama, T. Kohda, Curcumin inhibits the proliferation of a human colorectal cancer cell line Caco-2 partially by both apoptosis and G2/M cell cycle arrest, *Int. J. Clin. Pharmacol. Res.* 4 (2014) 84–90.
- [127] A. Scharstuhl, H.A.M. Mutsaers, S.W.C. Pennings, W.A. Szarek, F.G.M. Russel, F.A.D.T.G. Wagener, Curcumin-induced fibroblast apoptosis and *in vitro* wound contraction are regulated by antioxidants and heme oxygenase: implications for scar formation, *J. Cell. Mol. Med.* 13 (2009) 712–725.
- [128] M.H. Khosropanah, A. Dinavand, A. Nezhadhosseini, A. Haghighi, S. Hashemi, F. Nirouzas, S. Khatamsaz, M. Entezari, M. Hashemi, H. Dehghani, Analysis of the antiproliferative effects of curcumin and nanocurcumin in MDA-MB231 as a breast cancer cell line, *Iran. J. Pharm. Res.* 15 (2016) 231–239.
- [129] A.-L. Cheng, C.-H. Hsu, J.-K. Lin, M.-M. Hsu, Y.-F. Ho, T.-S. Shen, J.-Y. Ko, J.-T. Lin, B.-R. Lin, W. Ming-Shiang, Phase I clinical trial of curcumin, a chemopreventive agent, in patients with high-risk or pre-malignant lesions, *Anticancer Res.* 21 (2001) 2895–2900.
- [130] H. Gelderblom, J. Verweij, K. Nooter, A. Sparreboom, Cremophor EL: the drawbacks and advantages of vehicle selection for drug formulation, *Eur. J. Cancer* 37 (2001) 1590–1598.
- [131] J. Schanz, J. Pusch, J. Hansmann, H. Walles, Vascularised human tissue models: a new approach for the refinement of biomedical research, *J. Biotechnol.* 148 (2010) 56–63.
- [132] S. Nietzer, F. Baur, S. Sieber, J. Hansmann, T. Schwarz, C. Stoffer, H. Häfner, M. Gasser, A.M. Waaga-Gasser, H. Walles, G. Dandekar, Mimicking metastases including tumor Stroma: a new technique to generate a three-dimensional colorectal Cancer model based on a biological Decellularized intestinal scaffold, *Tissue Eng. Part C Methods* 22 (2016) 621–635.
- [133] C. Göttlich, M. Kunz, C. Zapp, S.L. Nietzer, H. Walles, T. Dandekar, G. Dandekar, A combined tissue-engineered/*in silico* signature tool patient stratification in lung cancer, *Mol. Oncol.* 12 (2018) 1264–1285.
- [134] C.-H. Hsu, A.-L. Cheng, Clinical studies with curcumin in, in: B.B. Aggarwal, Y.-J. Surh, S. Shishodia (Eds.), *The Molecular Targets and Therapeutic Uses of Curcumin in Health and Disease*, Springer US, Boston, MA, 2007, pp. 471–480.
- [135] A.W. Lambert, D.R. Pattabiraman, R.A. Weinberg, Emerging biological principles of metastasis, *Cell* 168 (2017) 670–691.
- [136] H. Dou, R. Shen, J. Tao, L. Huang, H. Shi, H. Chen, Y. Wang, T. Wang, Curcumin suppresses the Colon Cancer proliferation by inhibiting Wnt/ β -catenin pathways via miR-130a, *Front. Pharmacol.* 8 (2017).
- [137] E. Yada, S. Wada, S. Yoshida, T. Sasada, Use of patient-derived xenograft mouse

- models in cancer research and treatment, *Future Sci. OA* 4 (2017) FSO271.
- [138] T.D. Francone, R.G. Landmann, C.-T. Chen, M.Y. Sun, E.J. Kuntz, Z. Zeng, R.P. Dematteo, P.B. Paty, M.R. Weiser, Novel xenograft model expressing human hepatocyte growth factor shows ligand-dependent growth of c-met-expressing tumors, *Mol. Cancer Ther.* 6 (2007) 1460.
- [139] M. Jeffers, S. Rong, G.F. Vande Woude, Hepatocyte growth factor/scatter factor—met signaling in tumorigenicity and invasion/metastasis, *J. Mol. Med.* 74 (1996) 505–513.
- [140] T. Brabletz, A. Jung, S. Reu, M. Porzner, F. Hlubek, L.A. Kunz-Schughart, R. Knuechel, T. Kirchner, Variable β -catenin expression in colorectal cancers indicates tumor progression driven by the tumor environment, *PNAS* 98 (2001) 10356–10361.
- [141] A.V. Kabanov, E.V. Batrakova, D.W. Miller, Pluronic block copolymers as modulators of drug efflux transporter activity in the blood-brain barrier, *Adv. Drug Deliv. Rev.* 55 (2003) 151–164.

The pharmaceutical potential of drug-loaded POzi based micelles was further evaluated in the treatment of very aggressive and up to date incurable glioblastoma. Although statins are widely used for the treatment of hypercholesterolemia, recent research effort gives increasing evidence on anti-tumoral properties including activity against glioblastoma. Interestingly, especially hydrophobic statins such as atorvastatin (ATV), showed permeability through the blood-brain-barrier *in vitro* and *in vivo*. Although this sounds promising at first, the very low aqueous solubility of ATV prevents IV administration necessary to reach sufficiently high blood concentrations. ATV water solubility could be strongly increased by solubilization with polymer amphiphiles. As observed for CUR, an amphiphile with a POzi core enabled the highest drug loading. However, at ATV concentrations ≥ 3 g/L (polymer = 10 g/L), large aggregates with hydrodynamic diameters > 600 nm were formed. Nevertheless, the nanosized ATV-loaded micelles (polymer/ATV = 10/1 g/L; $D_h = 26$ nm) exhibited pronounced cytotoxicity against various mouse and human glioblastoma cells in 2D cell culture. This was also true for 3D spheroid models of highly aggressive and rapidly proliferating mouse brain tumor initiating bRITS-G2 cells. Permeability of the POzi formulated ATV through an artificial blood-brain-barrier (BBB) derived from human induced pluripotent stem cells was not enhanced compared to DMSO/ATV. However, co-administration of agents temporarily permeabilizing the BBB could assist to increase ATV transport across the BBB.

***In vitro* blood-brain-barrier permeability and cytotoxicity of atorvastatin-loaded nanoformulation against glioblastoma in 2D and 3D models**

Michael M. Lübtow¹, Sabrina Oerter², Sabina Quader³, Elisabeth Jeanclos^{4,5}, Alevtina Cubukova⁶, Marion Krafft², Clemens Schulte¹, Laura Meier, Maximilian Rist¹, Oltea Sampetean⁷, Hiroaki Kinoh³, Antje Gohla⁴, Kazunori Kataoka^{3,8}, Antje Appelt-Menzel^{2,6}, Robert Luxenhofer^{1,9*}

¹ *Functional Polymer Materials, Chair for Advanced Materials Synthesis, Department of Chemistry and Pharmacy and Bavarian Polymer Institute, University of Würzburg, Röntgenring 11, 97070 Würzburg, Germany*

² *University Hospital Würzburg, Chair Tissue Engineering and Regenerative Medicine (TERM), Röntgenring 11, 97070 Würzburg, Germany*

³ *Innovation Center of Nanomedicine (iCONM), Kawasaki Institute of Industrial Promotion, 3-25-14 Tonomachi, Kawasaki-Ku, Kawasaki-Shi 210-0821, Japan*

⁴ *Institut of Pharmacology and Toxicology, University of Würzburg, Versbacher Straße 9, 97078 Würzburg, Germany*

⁵ *Rudolf Virchow Center for Experimental Biomedicine, University of Würzburg, Josef-Schneider-Straße 2, 97080 Würzburg, Germany*

⁶ *Fraunhofer Institute for Silicate Research ISC, Translational Center Regenerative Therapies TLC-RT, Röntgenring 11, 97070 Würzburg, Germany*

⁷ *Institute for Advanced Medical Research (IAMR), Division of Gene Regulation, Keio University School of Medicine, 35 Shinanomachi, Shinjuku-ku, Tokyo, 160-8582, Japan*

⁸ *Policy Alternatives Research Institute, The University of Tokyo, 7-3-1 Hongo, Bunkyo-ku, Tokyo, 113-0033 Japan*

⁹ *Soft Matter Chemistry, Department of Chemistry, Helsinki University, 00014 Helsinki, Finland*

correspondence to: robert.luxenhofer@uni-wuerzburg.de

Keywords

drug-loaded micelles, poly(2-oxazoline), poly(2-oxazine), nanomedicine, human induced-pluripotent stem cells, cancer stem cells

ABSTRACT: Inhibitors of 3-hydroxy-3-methylglutaryl-coenzyme A (HMG-CoA) reductase of the family of statins have been suggested as therapeutic options in various tumors. Atorvastatin is a statin with potential to cross the blood-brain-barrier, however, the concentrations necessary for a cytotoxic effect against cancer cells exceeds the concentration achievable via oral administration, which made the development of a novel atorvastatin formulation necessary. We characterized the drug loading and basic physicochemical characteristics of micellar atorvastatin formulations and tested their cytotoxicity against a panel of different glioblastoma cell lines. In addition, activity against tumor spheroids formed from mouse glioma and mouse cancer stem cells, respectively, was evaluated. Our results show good activity of atorvastatin against all tested cell lines. Interestingly, in the 3D models, growth inhibition was more pronounced for the micellar formulation compared to free atorvastatin. Finally, atorvastatin penetration across a blood-brain-barrier model obtained from human induced-pluripotent stem cells was evaluated. Our results suggest that the presented micelles may enable much higher serum concentrations than possible by oral administration, however, if transport across the blood-brain-barrier is sufficient to reach therapeutic atorvastatin concentration for the treatment of glioblastoma via intravenous administration remains unclear.

1. INTRODUCTION

Glioblastoma (GBM) is the most common and most aggressive cancer of the central nervous system exhibiting dismal 5-year survival rates of 5%.^[1, 2] Currently, surgical resection (limited due to diffuse and infiltrative nature of GBM) and concomitant chemoradiotherapy offer highest median survival rates of 14 months.^[3] Chemotherapy of GBM is especially challenging due to the rapid proliferative rate of GBM cells^[4], the appearance of treatment resistant cell clones shortly after initial treatment^[5, 6] as well as the limited access of systemically administered agents to the brain parenchyma due to the blood-brain-barrier (BBB)^[7, 8]. Despite these drawbacks, chemoradiotherapy greatly improves mean 3-year survival rates from 1.9 to 16% compared to radiotherapy alone in the case of the most widely used chemotherapeutic agent for GBM treatment, temozolomide (TMZ).^[3] However, rapid development of TMZ resistance underline the urgent clinical need for better treatment options, potentially by using alternative active pharmaceutical ingredients (APIs) for GBM chemotherapy.^[9]

Statins are a family of widely used drugs for the treatment of hypercholesterolemia.^[10] They act as inhibitors of 3-hydroxy-3-methylglutaryl-coenzyme A (HMG-CoA) reductase thus being potent inhibitors of cholesterol biosynthesis.^[11] However, beyond their effects on serum cholesterol levels, recent research effort gives increasing evidence on cancer prevention and/or treatment properties of statins through interactions with essential cellular functions such as cell proliferation and differentiation.^[12] Several

in vitro and *in vivo* studies have demonstrated tumor growth inhibition as well as induction of apoptosis in various melanoma^[13], glioma^[14], neuroblastoma^[15], leukemia^[16] as well as glioblastoma cell lines^[17]. The underlying modes of action of statins causing (i) inhibition of tumor cell growth, (ii) repression of tumor metastases, (iii) inhibition of angiogenesis and (iv) induction of apoptosis were comprehensively reviewed by Hindler *et al.*^[12], Pisanti *et al.*^[18] and Gizzo *et al.*^[19]

As cell replication of GBM is highly dependent on the mevalonate (MVA) pathway for the synthesis of lipid moieties, their growth is naturally highly vulnerable to statins acting as competitive inhibitors of the enzyme regulating MVA synthesis – HMG-CoA reductase.^[20, 21] Furthermore, lovastatin increases the expression of the peroxisome proliferator-activated receptor, a transcription factor implicated in the control of lipid metabolism, cell growth and differentiation thus strongly reducing glioma proliferation.^[20] Real-time PCR analysis of U87 glioma spheroids revealed that atorvastatin (ATV) induced cell apoptosis by down-regulating the expression of anti-apoptotic Bcl-2 and up-regulating apoptotic caspase-3 and caspase-8 factors.^[22] Increase in caspase-3 activity in glioblastoma was also confirmed for other statins.^[17] Investigating the Ras downstream cascade, it was found that the increase was due to a reduced phosphorylation of extracellular signal-regulated kinase 1/2 (ERK1/2) and Akt. As the activation levels of these signal transduction molecules were restored in the presence of geranylgeranyl-pyrophosphate (GGPP), the inhibition of ERK1/2 and Akt activation in C6 glioma cells was correlated to the inhibition of GGPP biosynthesis.^[17] ATV also reduced the pro-tumorigenic effects of microglia on glioma migration and invasion by reducing the microglial expression of membrane type 1 metalloproteinase (MT1-MMP).^[23] It was suggested that the down-regulation of MT1-MMP was controlled by a p38 MAPK pathway in microglia. Furthermore, ATV was suggested to decrease the expression of pro-inflammatory proteins and interleukins (IL).^[24] This is important, as inflammatory microenvironment generally promotes malignant progression^[25] which is especially true for GBM^[26]. Although not discussed in direct correlation with GBM but worth mentioning, statins have been reported to sensitize cells to ferroptosis and induce ferroptosis in selected cell lines (however, further studies are necessary to confirm this).^[27] Furthermore, combination therapy of temozolomide and ATV in combination with radiotherapy in newly diagnosed GBM patients was promising (progression free survival (PFS) rate at 6 months: 67 % and median PFS of 9.1 months), meeting criteria for continued accrual in a phase II clinical study (NCT02029573).^[28] In addition, considerable evidence suggests that statins also exhibit immunomodulatory properties,^[18] as e.g. the number and suppressive function of regulatory T cells was decreased by ATV in patients with rheumatoid arthritis.^[29]

Although both, hydrophilic and lipophilic statins demonstrated antitumor effects, hydrophobic APIs generally exhibit a higher permeability through the BBB by e.g. passive diffusion.^[30] However, lipophilic substances also tend to be substrates for P-glycoprotein, potentially reversing this effect^[31, 32]. That this general trend is also true for statins was confirmed by Tsuji *et al.*^[33], observing permeation of lipophilic lovastatin and simvastatin but not of hydrophilic pravastatin through an artificial BBB *in vitro*, later this was also confirmed *in vivo*^[34]. Important to note, among various statins, ATV is the most frequently reported one for causing adverse neurocognitive effects compared to less lipophilic statins which was associated with its increased permeability through the BBB.^[35, 36]

Therefore, we chose lipophilic ATV as potential cytotoxic API against various glioblastoma cell lines.

However, besides the issue of passing the BBB, transportation of APIs to the BBB at sufficient high drug concentration is crucial. This can be especially challenging for hydrophobic APIs such as ATV which cannot simply be administered e.g. intravenously and oral bioavailability may not be sufficient to achieve concentrations necessary to reliably exhibit anti-tumor activity. Nanomedicine offers great potential regarding intravenous administration of water-insoluble drugs.^[37, 38] A few ATV-loaded polymer micelles based on amphiphilic polylactic acid-*b*-PEG-*b*-polylactic acid (PLA-PEG-PLA) triblock copolymers^[39], PEG-poly(ϵ -caprolactone) (PEG-PCL) diblock copolymers^[40], PEG-*b*-vitamin E succinate (PEG-VES)^[41], stearyl grafted chitosan (SC)^[42] or ATV-loaded bovine serum albumin (BSA) nanoparticles^[43] can be found in the literature. However, to the best of our knowledge, none of these systems was investigated with respect to GBM treatment. Interestingly though, polysorbate 80 coated, ATV-loaded poly(lactic-*co*-glycolic acid)-*b*-PEG (PLGA-PEG) nanoparticles have been designed to investigate the influence of the coating on the transport of ATV to the brain.^[44] Important to note, both – coated and uncoated nanoparticles – were able to penetrate the BBB *in vivo* reaching maximum brain-concentration 1 h post-intravenous injection. Pioneering work by Kabanov and co-workers revealed that several amphiphilic polymers can facilitate transport of small molecules and proteins across the BBB.^[45-48]

2. MATERIALS AND METHODS

Reagents and Solvents

The monomers 2-*n*-propyl-2-oxazoline (PrOx), 2-*n*-propyl-2-oxazine (PrOzi), 2-*n*-butyl-2-oxazoline (BuOx) and 2-*n*-butyl-2-oxazine (BuOzi) were synthesized according to Seeliger *et al.*^[49] as reported recently^[50]. The polymers **A-pPrOx-A** (Me-MeOx₃₆-PrOx₂₀-MeOx₃₆-1-Boc-piperazine (PipBoc)), **A-pBuOx-A** (Me-MeOx₃₅-BuOx₂₀-MeOx₃₅-piperidine), **A-pPrOzi-A** (Me-MeOx₃₅-PrOzi₂₀-MeOx₃₅-PipBoc) and **A-pBuOzi-A** (Prop-MeOx₃₅-BuOzi₂₀-MeOx₃₅-PipBoc) were synthesized recently.^[50] Pluronic® was a mixture of Pluronic® F127 and L61 at 8/1 (w/w) corresponding to the ratio reported for SP1049C®. Atorvastatin (calcium salt trihydrate) was purchased from *Sigma-Aldrich* (HPLC \geq 98 %). Deuterated chloroform (CDCl₃), dimethyl sulfoxide (DMSO-*d*₆) or water (D₂O) for ¹H-NMR analysis were obtained from *Deutero GmbH* (Kastellaun, Germany).

Experiments

Nuclear Magnetic Resonance Spectroscopy (NMR)

NMR spectra were recorded on a Fourier 300 (300 MHz), *Bruker Biospin* (Rheinstetten, Germany) at 298 K. The spectra were calibrated to the signal of residual protonated solvent signal (CDCl₃: 7.26 ppm; DMSO-*d*₆: 2.50 ppm, D₂O: 4.79 ppm).

ATV-loaded Polymer Micelles

ATV-loaded polymer micelles were prepared by thin film method.^[51] Methanolic polymer (20 g/L) and ATV (20 g/L) stock solutions were mixed in desired ratio. After complete removal of the solvent at 40 °C under a mild stream of argon, the films were dried *in vacuo* (\leq 0.2 mbar) for 20 min. Subsequently, H₂O was added. Complete solubilization was facilitated by shaking the solutions at 1250 rpm at 35 °C for 12 min with a Thermomixer comfort, *Eppendorf AG* (Hamburg, Germany). Non-solubilized drug (if any) was removed by centrifugation for 5 min at 9.000 rpm with a

MIKRO 185 (Hettich, Tuttlingen, Germany). Solubilization experiments were performed with 3 individually prepared samples and results are presented as mean \pm standard deviation (SD).

ATV Quantification by HPLC

ATV quantification was performed by HPLC on a LC-20A Prominence HPLC, Shimadzu (Duisburg, Germany) equipped with a system controller CBM-20A, a solvent delivery unit LC-20 AT (double plunger), an on-line degassing unit DGU-20A, an auto-sampler SIL-20AC, and a SPD-20A UV-Vis detector. As stationary phase, a ZORBAX Eclipse Plus, Agilent (Santa Clara, CA, USA) C18 column (4.6 x 100 mm; 3.5 μ m) was used. The mobile phase was a gradient of H₂O/ACN (60 % - 40 % H₂O; Figure S1a) at 40 °C and a flow rate of 1 mL/min. Prior to ATV quantification, all formulations were centrifuged to remove any precipitate, diluted with ACN/H₂O = 60/40 (v/v) and quantified at 245 nm (Figure S1b). The following equations were used to calculate loading capacity (LC) and loading efficiency (LE):

$$LC = \frac{m_{drug}}{m_{drug} + m_{polymer}} \quad (1)$$

$$LE = \frac{m_{drug}}{m_{drug,added}} \quad (2)$$

where m_{drug} and $m_{polymer}$ are the weight amounts of solubilized drug and polymer excipient in solution and $m_{drug,added}$ is the weight amount of drug initially added to the dispersion. No loss of polymer during micelle preparation was assumed.

Long-term Stability Studies

For long-term stability studies, ATV-loaded polymer micelles were stored in Eppendorf tubes containing the precipitate (if any occurred) at ambient conditions (\approx 25 °C) under the exclusion of light. Prior to ATV quantification, all formulations were centrifuged to remove any precipitate, diluted with ACN/H₂O = 60/40 (v/v) and quantified by HPLC analysis at 245 nm.

Dynamic Light Scattering (DLS)

DLS measurements were performed on a Zetasizer Nano ZS (Malvern Panalytical GmbH, Kassel, Germany) with a 633 nm HeNe-laser at 173°. Autocorrelations for each sample were obtained 3 times for 40 seconds and results are presented as mean. Prior to the measurements, all samples (polymer = 10 g/L) were diluted 1/5 (v/v) with ultrapure H₂O to polymer = 2 g/L. The samples were measured unfiltered in quartz cuvettes (d = 10 mm, QS, Hellma) at 25 °C.

2D Cell Viability and Migration Studies

Mouse glioma cells (CT-2A and GL261) as well as human glioblastoma cells U373, U251 and U87 were cultured in Dulbecco's Modified Eagle's medium (DMEM; Sigma-Aldrich, St. Louis, USA) (high glucose) supplemented with 10 % fetal bovine serum (FBS). In the case of CT-2A, U373 and GL261, 1 % penicillin/streptomycin (P/S) was added. For U373, Gibco® MEM non-essential amino acids were added as well. For the determination of IC₅₀, cells were seeded at 3×10^3 cells/well in transparent flat-bottom 96 well-plates and cultured for 1 d in humidified atmosphere of 5 % CO₂ at 37 °C. DMSO/ATV was prepared by dissolving 10 g/L ATV in DMSO and diluted with D-PBS(-) (PBS = phosphate buffered saline, FUJIFILM Wako Pure Chemicals Corporation (Osaka, Japan) to 1 g/L ATV before further dilution with cell specific medium to desired ATV concentrations. ATV-loaded A-pBuOzi-A micelles were prepared by thin-film method ($\rho(\text{A-pBuOzi-A/ATV}) = 10/1$ [g/L])

and diluted with cell-specific medium to desired ATV concentrations. The respective solutions were applied for 24 h, 48 h and 72 h. After treatment, Cell Counting Kit-8 (CCK8) cell proliferation/cytotoxicity assay was performed according to manufacturer's instructions. Briefly, 10 μ L of CCK-8 solution were added per well and the samples incubated for 2 h at 37 °C and 5 % CO₂. Absorption was measured at $\lambda_{abs} = 450$ nm with an Infinite 200 (Tecan, Männedorf, Switzerland).

Cell viability was determined by equation 3:

$$cell\ viability = \frac{F_{treated} - F_{medium}}{F_{untreated} - F_{medium}} \times 100\% \quad (4)$$

where $F_{treated}$ and $F_{untreated}$ correspond to the absorption of treated and untreated cells, respectively, and F_{medium} is the absorption of the culture medium.

Cell viability experiments were performed with three individual 96 well-plates containing each sample concentration in quadruplicate and results are presented as means \pm SD. IC₅₀ was determined with OriginPro 2019 software using a Boltzmann or biphasic dose-response fit.

Human pediatric cerebellar glioblastoma multiforme GBM6840 cells were cultured in DMEM (high glucose) supplemented with 10 % FBS. Cell viability studies and IC₅₀ determinations were conducted by live/dead cell staining and flow cytometric analysis. Briefly, cells were seeded in 96 well-plates (10⁴ cells/well). The next day, ATV (solubilized in DMSO or formulated with A-pBuOzi-A) was added to the medium at a final concentration of 0 to 80 μ M. The corresponding concentrations of DMSO and A-pBuOzi-A alone served as controls. After 48 h incubation, cells were rinsed with PBS, trypsinized, and resuspended in 250 μ L PBS containing 0.5 g/L soybean trypsin inhibitor (Invitrogen, Carlsbad, USA). Cell culture medium, wash solution and trypsinized cells were collected and incubated for 15 min at 22 °C with the live cell indicator calcein-AM (Invitrogen, Carlsbad, USA) at a final concentration of 10 nM. Immediately before flow cytometry, cell suspensions were incubated with the dead cell indicator propidium iodide (1 mg/L, Invitrogen) for 1 min. Cells were analyzed on a FACS Calibur flow cytometer (Beckton Dickinson, Heidelberg, Germany); at least 5,000 cells were analyzed per condition. Data are presented as means \pm SEM of $n=3$ independent experiments. Cell viability was expressed as the percentage of calcein-positive cells. IC₅₀ values were determined by non-linear regression (log(inhibitor) vs. response – variable slope (four parameters)) using Prism v7.04 (GraphPad, San Diego, U.S.A.).

For cell migration studies, 2×10^5 GBM6840 cells were seeded in 3 cm dishes and treated with 0, 2.5 or 5 μ M ATV formulated with A-pBuOzi-A for 65 h. GBM6840 cells were trypsinized, resuspended in 1 mL DMEM containing 0.5 mg/mL soybean trypsin inhibitor, and washed once by centrifugation (300 \times g, 5 min at RT). The cell suspension (2.5×10^4 cells/0.5 mL DMEM) was added to the upper compartment of a transwell (Falcon cell culture inserts for 24 well-plates, 8 μ m pore size; ThermoFisher Scientific). The bottom side of the membrane was pre-coated with fibronectin (10 mg/mL; Sigma-Aldrich) to assure attachment of the transmigrated cells; epidermal growth factor (100 ng/mL; Sigma-Aldrich) was used as a chemoattractant in the lower transwell compartment. Cells were allowed to migrate for 8 h in a humidified tissue culture incubator (37 °C, 5 % CO₂) in the presence of 0, 2.5 or 5 μ M ATV. Remaining cells on the upper side of the transwell membranes were removed with cotton swabs, and cells on the lower side of

the membranes were fixed with 4 % (w/v) para-formaldehyde for 20 min. Nuclei were stained with 4',6-diamidino-2'-phenylindole (DAPI, 1 µg/mL) in PBS, and transwells were mounted on coverslips using Immunomount (*ThermoFisher Scientific*). Cell nuclei were visualized on a Leica SP5 confocal microscope (*Leica Microsystems*) equipped with a 10× objective, and four images covering ≈ 75 % of the total transwell membrane surface area were taken for each transwell. Cell numbers were quantified semi-automatically using ImagePro-Plus software, version 7.0 (*Media Cybernetics*, Rockville, U.S.A.).

3D Spheroid studies

CT-2A cells were cultured in DMEM supplemented with 10 % FBS and 1 % P/S. Mouse brain tumor initiating bRiTS-G2 cells were cultured in DMEM/F12 (*Wako*, Osaka, Japan) supplemented with 20 ng/mL epidermal growth factor, 20 ng/mL basic fibroblast growth factor (both *PeprTech*, Rocky Hill, NJ), B27 supplement without vitamin A (*Invitrogen*, Carlsbad, USA) and 200 ng/mL heparan sulfate (*Sigma-Aldrich*, St. Louis, USA). For spheroid studies, cells were seeded at 5×10^3 cells/well in all white U-bottom 96 well-plates (*PrimeSurface96U*, *Sumitomo Bakelite Co.* Tokyo, Japan) and incubated for 1 d in humidified atmosphere of 5 % CO₂ at 37 °C. Within this time, 3D cell aggregates of around 400 µm diameter were spontaneously formed (Figure S2). Subsequently, stock solutions of **A-pBuOzi-A/ATV** ($\rho(\text{A-pBuOzi-A/ATV}) = 10/1$ [g/L] in ultrapure H₂O) or DMSO/ATV (ATV = 10 g/L) were diluted with cell specific culture medium to desired concentrations and applied for 48 h and 72 h. After treatment, CellTiter-Glo® 3D Luminescent Cell Viability Assay (*Promega*, Madison, USA) was performed according to manufacturer's instructions. Briefly, 100 µL of CellTiterGlo® 3D solution were added per well (100 µL) and stored for 30 min at ambient conditions (≈ 25 °C) under the exclusion of light. Luminescence was measured with a GloMax®-Multi+ Detection System (*Promega*, Madison, USA). Spheroid studies were performed with three individual 96 well-plates containing each sample concentration in quadruplicate and results are presented as means ± SD.

2D human iPSC-BBB Studies

Human induced-pluripotent stem cells (hiPSC; IMR90-4, *WiCell Research Institute*, USA) were cultured in mTeSR™1 medium (*Stem-Cell Technologies*, Canada). The iPSC-derived BBB model was built as previously described.^[52] Cytotoxicity of **A-pBuOzi-A/ATV** or DMSO/ATV against hiPSC-derived endothelial cells (hiPS-ECs) was evaluated for three concentrations (45 µM, 90 µM and 150 µM) after 4 h and 24 h incubation. After treatment, CellTiter-Glo® 3D Luminescent Cell Viability Assay (*Promega*, Mannheim, Germany) was performed according to manufacturer's instructions. Luminescence was measured with an Infinite M200 fluorescence reader (*Tecan Group*, Switzerland). Cytotoxicity studies were performed in triplicates and three independent biological replicates and results are presented as means ± SEM.

To evaluate human BBB-like characteristic, transendothelial electrical resistances (TEER) were determined with a Millicell ERS-2 voltohmmeter (*Millipore*, USA) equipped with a STX3 electrode (*World Precision Instruments*, Germany) prior transport assay. TEER measurements were performed 40 min after medium change. Each model was measured three times, monitoring and excluding a possible data drift due to temperature fluctuations and duplicates were used for each experiment in three independent biological replicates. To yield the TEER values [$\Omega \cdot \text{cm}^2$] resulted

from BBB hiPS-ECs, average TEER of empty inserts coated with collagen IV/fibronectin were subtracted and values were multiplied by insert surface. Results are presented as means ± SEM.

Permeation through BBB endothelium

Transport assays were performed in transwells (24-well format) on an orbital shaker (*Edmund Bühler GmbH*, Germany) at 100 rpm, 37 °C, 95 % humidity, and 5 % CO₂. Stock solutions of **A-pBuOzi-A/ATV** or DMSO/ATV were diluted with human endothelial-SFM (*Thermo Fisher Scientific*, USA) containing 1 % platelet poor-plasma derived serum (PPDS; *Alfa Aesar*, USA) to the desired concentrations ([ATV] = 90 µM and 150 µM). Test concentrations of **A-pBuOzi-A/ATV** or DMSO/ATV (200 µL) were applied to the apical side of the BBB model. The basolateral side was supplied with 800 µL of human endothelial-SFM containing 1 % PPDS and the respective concentration of sterile water (**A-pBuOzi-A**) or DMSO. The permeation was evaluated after incubation times of 4 h and 24 h. Apical and basolateral media were analyzed by HPLC to quantify the transport of **A-pBuOzi-A/ATV** or DMSO/ATV. As control, the substances were incubated on empty collagen IV-/fibronectin-coated inserts to exclude major ATV adsorption on the membrane. All permeability studies were performed in duplicates and three independent biological replicates, results are presented as means ± SD. The level of statistical significance was set at $p < 0.05$, indicated with asterisk (*). Grading in significance is indicated as follows: * $p < 0.05$, ** $p < 0.01$, *** $p < 0.001$.

3. RESULTS AND DISCUSSION

ATV solubilization

As reported recently, poly(2-oxazoline) (POx) and poly(2-oxazine) (POzi) based ABA triblock copolymers, all comprising the same hydrophilic poly(2-methyl-2-oxazoline) (PMeOx) shell **A** and structurally very similar, hydrophobic cores **B** exhibit different loading capacities for various hydrophobic drugs^[50, 53-57] as well as varying drug/polymer interactions in dependence of the drug-loading^[58, 59]. Whereas the triblock copolymer with a barely hydrophobic poly(2-*n*-butyl-2-oxazoline) (pBuOx, = **A-pBuOx-A**) core enabled moderately high loadings of 24 wt.% of the hydrophobic compound curcumin (CUR), its structural isomer with a poly(2-*n*-propyl-2-oxazine) (pPrOzi; = **A-pPrOzi-A**) core was able to yield exceptionally high loadings up to 54 wt.%.^[53] Interestingly, in the case of hydrophobic paclitaxel (PTX), the situation was *vice versa*, **A-pBuOx-A** being the best performer with PTX loadings up to 48 wt.% compared to 25 wt.% in the case of **A-pPrOzi-A**. As the drug loading is a crucial parameter concerning the translation of drug-loaded polymer micelles into the clinics, we investigated both polymers with regard to their solubilization capacity for the non-water soluble drug atorvastatin (ATV; water solubility of ATV calcium salt trihydrate by thin film-method = 60 mg/L (0.1 mM); analyzed in house). Additionally, two polymers comprising either a poly(2-*n*-propyl-2-oxazoline) (pPrOx; = **A-pPrOx-A**) or poly(2-*n*-butyl-2-oxazine) (pBuOzi; = **A-pBuOzi-A**) core were investigated for solubilization. The mixture of two Pluronic® SP1049C, which was developed by Kabanov for the interference with P-glycoprotein (P-gp) and therefore, improved delivery of hydrophobic molecules across biological barriers such as the BBB overexpressing P-gp^[60-62] was included for comparison (Figure 1a). As expected, distinct polymer-ATV solubilization specificities were observed for the formulations prepared by thin film method (Figure 1b). Whereas **A-pPrOx-A** enabled ATV concentrations of only 0.7 g/L ($LC = 6.4$

wt.%; ATV-feed = 10 g/L), its POzi counterpart with the same propyl-side chain **A-pPrOzi-A** solubilized up to 4.2 g/L ATV ($LC = 29$ wt.%; ATV feed = 10 g/L), being outperformed only by **A-pBuOzi-A** with up to 6.9 g/L ATV ($LC = 41$ wt.%; ATV feed = 10 g/L) (Figure 1c). Again, the POx with the same side chain **A-pBuOx-A** exhibited lower LC s of up to 25 wt.% (3.3 g/L; ATV feed = 10 g/L). The LC of Pluronic® was 6 times lower with ATV = 0.7 g/L ($LC = 6.4$ wt.% ATV-feed = 10 g/L), showing the same LC as **A-pPrOx-A**. As **A-pBuOzi-A** also exhibited the best long-term stability showing only minor loss in ATV-content up to ATV feed concentrations of 5 g/L within 30 d storage (Figure 1d; for 30 d long-term stability of all other formulations, please see Figure S3) this carrier was deemed most promising for further studies. Therefore, the physicochemical properties of **A-pBuOzi-A/ATV** formulations were investigated in more detail.

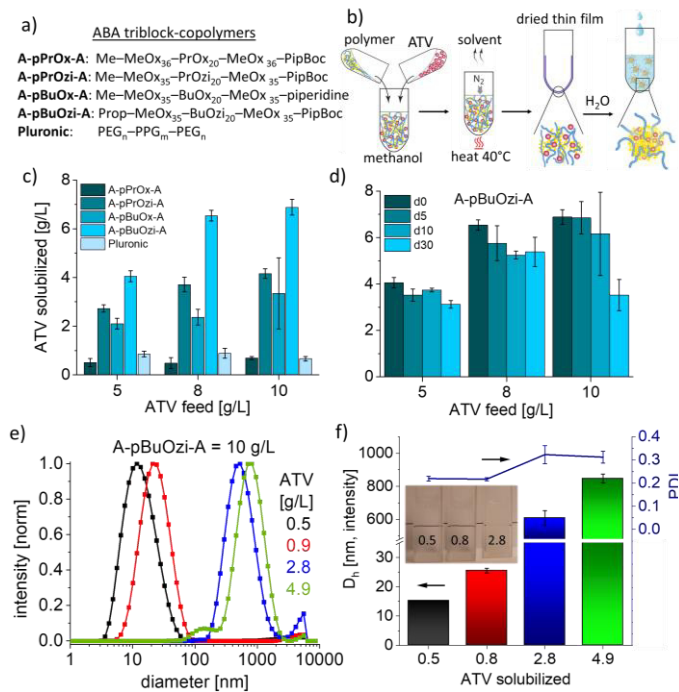


Figure 1: a) ABA triblock-copolymers used for ATV solubilization by b) thin-film method; c) solubilized aqueous ATV concentrations in dependence of the ATV feed by **A-pPrOx-A**, **A-pPrOzi-A**, **A-pBuOx-A**, **A-pBuOzi-A** or Pluronic® F127/L61 8/1 (w/w) at polymer = 10 g/L.; d) Long-term stability of **A-pBuOzi-A/ATV** formulations. Formulations were stored in Eppendorf-tubes containing the initial precipitate at ambient conditions ($T \approx 25$ °C) under the exclusion of light. All formulations were prepared in triplicates and results are presented as means \pm SD; e) particle size distribution determined by dynamic light scattering of **A-pBuOzi-A/ATV** formulations in dependence of the solubilized ATV concentration at room temperature (≈ 25 °C) at 173° with a Zetasizer Nano ZS. The samples (**A-pBuOzi-A** = 10 g/L) were diluted with H₂O 1/5 (v/v) and measured unfiltered; f) mean hydrodynamic diameter D_h (intensity weighted) of the ATV-loaded **A-pBuOzi-A** micelles. Each formulation was prepared three times and data is given as mean \pm SD ($n = 3$). Inset in figure f) shows visual appearance of undiluted **A-pBuOzi-A/ATV** = 10/0.5; 10/0.8 and 10/2.8 g/L formulations.

Particle sizes of the **A-pBuOzi-A/ATV** formulations were highly dependent on the ATV-loading. At rather low loadings of 0.5 and 0.9 g/L (polymer = 10 g/L), micelles with average hydrodynamic diameters D_h of 15 nm and 26 nm were found, respectively (Figure 1e). The size distributions were monomodal with corresponding PDIs of 0.22 (Figure 1f). Increasing the ATV-loading to 2.8 and 4.0 g/L resulted in a dramatic increase in particle size to 609 nm and 847

nm, respectively, accompanied by an increase in PDI to 0.31 – 0.32. The increase in size was also apparent by visual inspection of the formulations (inset Figure 1f). Whereas up to **A-pBuOzi-A/ATV** = 10/0.8 g/L the formulations were completely clear, the sample containing 2.8 g/L ATV was opaque and emulsion-like (however samples for DLS were diluted 1/5 (v/v) to suppress artefacts due to multiple scattering etc.). Although being opaque, the samples did not show precipitation over extended periods of time (determined by visual inspection as well as relatively constant ATV loading up to 30 d (ATV feed = 5 & 8 g/L) or 10 d (ATV feed = 10 g/L) storage (Figure 1d)). A more detailed analysis of these aggregates using, *inter alia*, small angle neutron scattering is ongoing. However, such large aggregates, irrespective of their nature or structure are probably not ideal for the envisioned application *i.v.* for which smaller and better-defined micelles are preferred.

To get more insights into the ATV formulations on a molecular level^[59], ¹H-NMR spectra of neat ATV, neat polymer or ATV formulations at varying **A-pBuOzi-A/ATV** ratio were recorded. In DMSO-*d*₆, all signals related to ATV were clearly visible with expected intensities (Figure 2; black spectrum; for enlarged ATV and **A-pBuOzi-A** spectra, the reader is referred to Figure S4 and S5, respectively). In contrast, when solubilized with **A-pBuOzi-A**, ¹H-NMR signals of ATV were either strongly attenuated and broadened (**A-pBuOzi-A/ATV** $\leq 10/0.9$) or could not be detected anymore (**A-pBuOzi-A/ATV** $> 10/0.9$) in D₂O (Figure 2; enlarged spectra). A similar disappearance of ¹H-NMR signals was already observed for **A-pPrOzi-A/CUR** formulations.^[63] Systems which are hindered in their mobility are predestinated for short transverse relaxation times T_2 causing a broadening or complete disappearance of certain signals. Therefore, the disappearance of the ¹H-NMR signals indicates a strong decrease in molecular mobility of ATV incorporated into the hydrophobic core of **A-pBuOzi-A** even at low loading. Furthermore, the signals of the butyl sidechain of the hydrophobic block are clearly affected (Figure 2 III-V). Notably, the signal attributed to the methyl group in the sidechain of pBuOzi (signal V) splits up. Besides the initial triplet, a second, much broader signal was observed at lower chemical shift. Similarly, but somewhat less pronounced, signals III and IV shift and became increasingly attenuated with increasing ATV loading. This decrease again is intuitive for a hindered mobility due to interactions of ATV with the hydrophobic block of **A-pBuOzi-A**. In contrast, the signals related to the hydrophilic shell (Figure 2 I,II) appear entirely unaffected even at the highest investigated drug loading. This results in a decreased ratio of the integrals of the methyl group of pBuOzi (core, signal V) with respect to the methyl sidechain of pMeOx (shell, signal II) with increasing ATV-loading (Figure S6). The more or less linear decrease of the ratio as well as the largely unaffected signals related to the hydrophilic shell are somehow surprising considering the large change in particle size at higher ATV-loadings observed by DLS (Figure 1e,f). Also, we previously investigated **A-pPrOzi-A/CUR** formulations by solution and solid state NMR^[59] and found clear evidence for drug-polymer interactions in the hydrophilic pMeOx block. The lack of interaction of ATV with the pMeOx may therefore be responsible for the limited LC compared to CUR^[63] or PTX^[51] nanoformulations which exhibit LC of ≥ 50 wt.%. For reference, interactions between encapsulated ATV and the hydrophobic part of the polymeric drug carrier were observed previously for PLA-PEG-PLA-loaded ATV by FT-IR analysis.^[39]

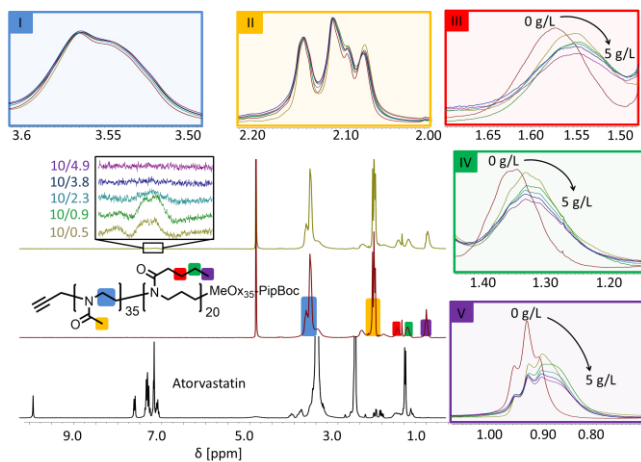


Figure 2: $^1\text{H-NMR}$ spectra (300 MHz, 298 K) of ATV (bottom black spectrum; DMSO-d_6), neat **A-pBuOzi-A** (middle red spectrum; D_2O) as well as **A-pBuOzi-A/ATV** = 10/0.5 g/L (top golden spectrum; D_2O). Inset shows enlarged region corresponding to aromatic ATV signals (700-fold increased signal intensity) with increasing ATV-loading (bottom to top; labelling is referred to **A-pBuOzi-A/ATV** = 10/y g/L). Enlarged sections of the signals corresponding to the hydrophilic shell of **A-pBuOzi-A** (I & II) as well as the hydrophobic core (III – V) in dependence of the ATV-loading. Intensities of spectra I-V were normalized to the methyl sidechain (II) of the hydrophilic shell. All formulations were prepared in H_2O , freeze-dried and subsequently redissolved in D_2O at $p(\text{polymer}) = 10 \text{ g/L}$.

Although stability of the aqueous **A-pBuOzi-A/ATV** formulations up to ATV feeds of 8 g/L was reasonably good, a minor loss in ATV content occurred in all formulations within 30 d storage (Figure 1d). Shelf-life of drug-loaded micelles can potentially be increased by freeze-drying the aqueous formulations and redispersing them right before usage. POx and POzi based formulations of PTX^[51] or CUR^[63] have already displayed excellent redispersibility without the need of cryoprotectants. Similar, freeze-dried **A-pBuOzi-A/ATV** = 10/2 g/L formulations could be conveniently redispersed in H_2O (Figure 3 blue), PBS (red) or PBS containing 40 g/L bovine serum albumin (BSA, green) after 7 d storage of the freeze-dried formulations at ambient conditions. Redispersion in PBS containing 40 g/L BSA corresponding to the albumin concentration in blood was performed as preliminary test for upcoming *in vitro* and potential *in vivo* studies, as initially stable formulations can precipitate in the presence of proteins. The excellent stability in the presence of serum protein suggests that this formulation may be safely injected *i.v.*

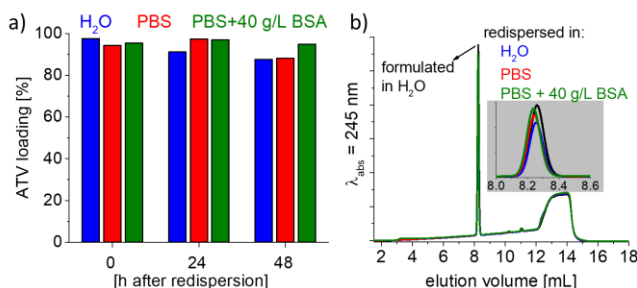


Figure 3: Residual aqueous ATV concentrations after redispersion of freeze-dried **A-pBuOzi-A/ATV** = 10/2 (g/L) formulations in H_2O (blue), PBS (red) or PBS containing 40 g/L bovine serum albumin (green). Loading [%] is referred to initial ATV concentration before freeze-drying. Prior to redispersion, the freeze-dried samples were stored for 7 d at ambient conditions ($T \approx 25 \text{ }^\circ\text{C}$) under the exclusion of light; b) corresponding HPLC elugrams at $\lambda_{\text{abs}} = 245 \text{ nm}$.

2D *in vitro* studies

Cytotoxicity of **A-pBuOzi-A/ATV** or ATV dissolved in DMSO against mouse glioma cells GL261 and CT-2A or human glioblastoma cells U87, U251 and U373 was evaluated after 24 h, 48 h and 72 h incubation (Figure 4). To the best of our knowledge, a potential growth inhibition or cytotoxicity of ATV against GL261, CT-2A and U373 has not previously been investigated. Except for CT-2A, cytotoxicity after 24 h incubation was moderate with half maximal inhibitory concentrations (IC_{50}) of 97 μM and higher. A similar low cytotoxicity of ATV after 24 h incubation (no decrease in proliferation up to $[\text{ATV}] = 50 \mu\text{M}$) compared to 48 h and 72 h was observed for human leukemic natural killer cells YT-INDY.^[64] Furthermore, absence of cytotoxicity against U87 after 24 h incubation at $[\text{ATV}] \leq 100 \mu\text{M}$ was also observed by Yongjun *et al.*^[23] In contrast, ATV exhibits a pronounced dose-dependent cytotoxicity after 48 h and 72 h incubation. The IC_{50} values for **A-pBuOzi-A/ATV** and DMSO/ATV were either comparable (U87 (72 h); U373 (48 and 72 h)) or slightly lower for **A-pBuOzi-A/ATV**. Generally, cytotoxicity increased from 48 h to 72 h incubation. Only for CT-2A, an unexpected increase in cell viability with IC_{50} values increasing from 33 μM (48 h) to 98 μM (72 h) occurred for DMSO/ATV . Furthermore, biphasic dose-response curves occurred in selected cases for DMSO/ATV (GL261) as well as **A-pBuOzi-A/ATV** (U251). Such multiphasic features are well known in cancer pharmacology^[65] due to the presence of combined agonist (stimulatory or hormetic^[66]) and antagonist effects as well as purely inhibitory features. Nevertheless, that with the same drug (ATV) both, sigmoidal and biphasic dose-responses occurred for a certain cell-line depending on the kind of formulation (DMSO or **A-pBuOzi-A**) is somehow surprising and needs to be evaluated further. Important to note, IC_{50} of DMSO/ATV for U87 ($\approx 8 \mu\text{M}$ (48 h)^[67] or $\approx 1.6 \mu\text{M}$ (48 h)^[68]) or U251 ($\approx 10 \mu\text{M}$; 48 h^[67]) cells reported in the literature were somewhat lower than the presently reported ones. However, different experimental setups (# cell passage, number of cells seeded, utilized assays) might have unintentionally caused such minor deviations. Important to note, inhibitory effects of ATV on growth and survival of U251 glioblastoma cells were attributed to decreased active Ras levels due to prenylation inhibition by ATV.^[67] In the same study, 5 μM ATV inhibited proliferation of four different glioblastoma cell lines slightly stronger than temozolomide at 10 μM . In combination with the presented cytotoxicity of ATV on various glioblastoma cell lines this strongly supports the rationale to use ATV for glioblastoma chemotherapy.

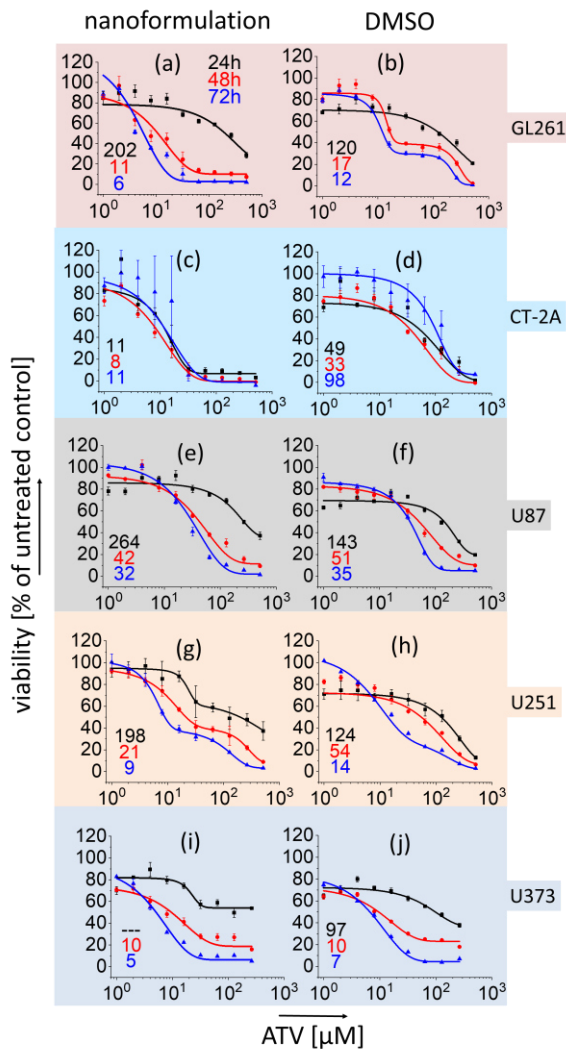


Figure 4: Concentration-dependent cell viability of **A-pBuOzi-A/ATV** (left column) or **DMSO/ATV** (right column) against mouse glioma cells GL261 (a,b) and CT-2A (c,d), or human glioblastoma cells U87 (e,f), U251 (g,h) and U373 (i,j). **DMSO/ATV** was prepared by dissolving 10 g/L (18 mM) ATV in **DMSO** upon dilution with PBS(-) to 1 g/L (1.8 mM) ATV and further dilution with cell specific medium to desired ATV concentrations. **ATV-loaded A-pBuOzi-A** micelles were prepared by thin-film method ($\rho(\text{A-pBuOzi-A/ATV}) = 10/1$ [g/L]) and diluted with cell-specific medium to desired ATV concentrations. Cell viability was determined (CCK-8 assay) after 24 h (black), 48 h (red) and 72 h (blue) ATV treatment. IC_{50} was determined per Boltzmann or biphasic dose-response fit using OriginPro 2019® and values for 24 h (black), 48 h (red) and 72 h (blue) are given in μM ATV in bottom left corner of each graph. Data are presented as mean \pm SD ($n = 3$ (individual 96 well-plates) \times 4 (wells per 96 plate)).

The dismal prognosis of glioblastomas is not only attributed to rapid tumor growth (and poor responses to chemo- and radiotherapy), but also to the diffuse intracerebral spread of migrating tumor cells.^[69, 70] We therefore examined the effects of ATV on the viability and cell migration of GBM6840 cells. This human cell line has been derived from a highly aggressive pediatric cerebellar glioblastoma multiforme^[71], and is characterized by rapid cell proliferation and –migration *in vitro* and *in vivo*^[72]. The GBM6840 cells were highly sensitive to ATV with an IC_{50} value of $\sim 8 \mu\text{M}$ after 48 h treatment, irrespective of whether ATV was dissolved in **DMSO** or formulated with **A-pBuOzi-A** (Figure 5a; for representative examples of the original FACS results, the reader is referred to Figure

S7). Importantly, neat **A-pBuOzi-A** did not cause cytotoxicity (viability > 80 %) up to high polymer concentrations of 10 g/L (Figure S8; for comparison: $[\text{A-pBuOzi-A}] = 50 \text{ mg/L}$ @ $IC_{50}(\text{A-pBuOzi-A/ATV})$, Figure 5a). We did not observe an effect of low ATV concentrations (2.5 or 5 μM) on the transwell-migration of GBM6840 cells towards epidermal growth factor (a prototypical chemoattractant for glioblastoma cells) even after 73 h of ATV treatment (Figure 5b). These ATV concentrations were chosen because they did not cause a substantial loss of cell viability (Figure S9). Thus, ATV appears to primarily affect GBM6840 cell viability, but not mobility.

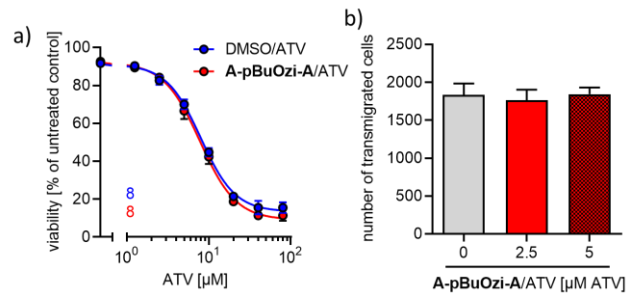


Figure 5: a) Concentration-dependent effect of **A-pBuOzi-A/ATV** (red) or **DMSO/ATV** (blue) on GBM6840 human glioblastoma cell viability after 48 h treatment. ATV was formulated or solubilized as described in the legend of Fig. 4. IC_{50} values were determined by non-linear regression (log(inhibitor) vs. response – variable slope (four parameters)) using GraphPad Prism v7.04. Data are means \pm SEM of $n=3$ independent experiments. b) Effect of **A-pBuOzi-A/ATV** on the epidermal growth factor-induced migration of GBM6840 cells through transwells. In total, eight (control and 2.5 μM ATV) or four (5 μM ATV) transwells were analyzed. Data are means \pm SEM of $n=2$ independent experiments.

Spheroid cell cultures

So far, we could show that ATV was able to efficiently decrease cell-viability of various glioblastoma cell-lines in conventional 2D cell culture. However, cancer cells grown in 3D cell-clusters such as spheroids can behave significantly different from their monolayer counterparts^[73] and we have recently reported differences in tumor spheroids depending whether the API was administered in polymer micelles or added as a ethanolic solution.^[57] The multicellular structures resemble actual tissues better in terms of structural and functional properties and often exhibit an enhanced resistance against therapeutic compounds.^[74] CT-2A cells were chosen due to their ability to form spheroids without the need of specialized devices or additives. Furthermore, the difference in cytotoxicity between **A-pBuOzi-A** (Figure 4c) and **DMSO/ATV** (Figure 4d) formulated ATV was most pronounced in this cell line. Spheroids were obtained by simply seeding the cells (5×10^3 cells/well) in U-bottom shaped 96 well-plates. Similar to conventional 2D-cell culture, both ATV formulations strongly decreased CT-2A cell viability in a concentration-dependent manner (Figure 6a,b). Here, **A-pBuOzi-A/ATV** again was clearly more effective than **DMSO/ATV**. Similar to conventional 2D cell culture (Figure 4d), cell viability in the spheroid model increased from 48 h (50 %) to 72 h (55 %) treatment with 8 μM **DMSO/ATV**. Unexpectedly, cytotoxicity of **A-pBuOzi-A/ATV** was higher in the spheroid model (Figure 6a,b) than in conventional 2D cell-culture (Figure 4c). A similarly high activity of ATV in 3D cell-culture was also observed for U87 glioma spheroids incorporated into a fibrin gel with IC_{50} (48 h) $\approx 10 \mu\text{M}$.^[73] Besides induction of apoptosis, migration and invasion of the U87 cells were inhibited in a dose-dependent manner in this case.

To further challenge ATV as potential chemotherapeutic agent against glioblastoma, its activity against spheroids composed of mouse-derived, glioblastoma cancer-stem cells (CSCs) was evaluated (Figure 6c,d). CSCs are cancer cells found within tumors with the ability of self-renewal, generation of daughter cells of various phenotypes and differentiation into phenotypically diverse populations of cells.^[75] Therefore, small populations of CSCs present after treatment can cause rapid cancer relapse as well as metastasis. Unfortunately this is favored by an increased resistance of CSCs to various otherwise unfavorable conditions^[76] including increased resistance against radiotherapy^[77] and chemotherapy^[78]. To the best of our knowledge, the cytotoxicity of ATV against glioblastoma stem cells or cancer stem cells in general has not been investigated before. However, for another statin, pitavastatin, autophagy induction in patient-derived stem cell-like primary GBM (as well as delayed U87 GBM tumor growth *in vivo*) was observed.^[21] Similar to CT-2A, the bRiTS-G2 brain tumor initiating cells rapidly formed spheroids when placed in U-bottom shaped 96 wells. Surprisingly, **A-pBuOzi-A/ATV** and to a lesser extent DMSO/ATV were highly active against the tumor spheres after 48 h and 72 h incubation (Figure 6c,d). Interestingly, a recently reported micellar mitotane nanoformulation of **A-pBuOx-A** was also slightly more active than mitotane simply dissolved in EtOH against adrenocortical NCI-H295R cells in a 3D tumor spheroid model ($IC_{50,48h} = 43 \mu M$ & $47 \mu M$ for nanoformulated & EtOH-dissolved mitotane, respectively).^[57] Important to note, the pronounced cytotoxicity of **A-pBuOzi-A/ATV** after 72 h treatment determined by CellTiterGlo®-3D luminescence assay was confirmed when quantifying the cell-viability by the intrinsic fluorescence of the GFP expressing bRiTS-G2 cells (inset Figure 6d). Although the absolute values slightly differed, both measurement techniques gave comparable results.

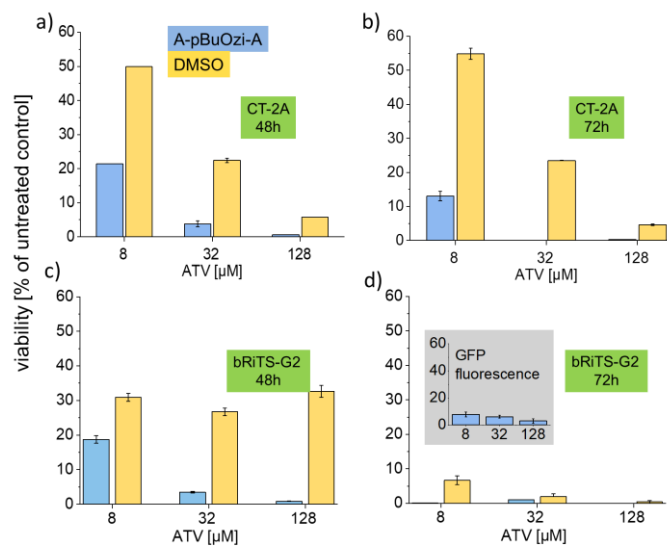


Figure 6: Concentration-dependent cytotoxicity of **A-pBuOzi-A/ATV** (blue) or DMSO/ATV (yellow) against spheroids of mouse glioma cells CT-2A after a) 48 h or b) 72 h treatment or against spheroids of mouse brain tumor initiating bRiTS-G2 cells after c) 48 h or d) 72 h treatment. DMSO/ATV was prepared by dissolving 10 g/L ATV in DMSO upon dilution with PBS(-) to 1 g/L ATV and further dilution with cell specific medium to desired ATV concentrations. ATV-loaded **A-pBuOzi-A** micelles were prepared by thin-film method ($p(\mathbf{A-pBuOzi-A}/\text{ATV}) = 10/1$ [g/L]) and diluted with cell-specific medium to desired ATV concentrations. Spheroids were obtained by seeding the cells in U-bottom shaped 96 well-plates at 5×10^3 cells/well. Cell viability was determined by CellTiter-Glo® 3D assay. Data are presented as mean \pm SD ($n = 3$ (individual 96 well-plates) \times 4 (wells per 96 plate)). As a

control, cell viability of bRiTS-G2 spheroids treated with **A-pBuOzi-A** formulated ATV was determined by intrinsic fluorescence of GFP-expressing bRiTS-G2 cells (inset Figure d). Data are presented as mean \pm SD ($n = 2$ (individual 96 well-plates) \times 4 (wells per 96 plate)).

ATV permeability through artificial blood-brain barrier

The pronounced cytotoxicity of ATV against glioblastoma in 2D cell culture (Figure 4, 5) as well as 3D spheroid models (Figure 6) suggests its potential for GBM chemotherapy. However, in order to unfold its therapeutic potential *in vivo*, ATV needs to reach tumor site first. This includes permeation through the BBB after e.g. parenteral administration.^[79] Several sophisticated *in vitro* BBB models were developed in recent years to resemble the situation *in vivo*.^[80, 81] One promising approach are models based on human induced pluripotent stem cells (hiPSCs) derived BBB endothelial cells.^[52, 82] Using such a hiPSC-derived model, physiological characteristics like high transendothelial electrical resistances (TEER) up to 2,500 $\Omega\text{-cm}^2$, distinct upregulation of typical BBB genes as well as the formation of an *in vivo*-like tight junction (TJ) network could be achieved.^[52] The hiPSC-derived BBB endothelial cells were seeded on top of a transwell insert and subsequently the permeability of ATV from the apical to the basolateral compartment was investigated (Figure 7a). A ratio of **A-pBuOzi-A/ATV** = 10/1 g/L was chosen due to the small size of the respective ATV-loaded micelles (Figure 1e,f) potentially facilitating transcellular permeability, assuming integrity of the drug loaded micelles. The latter is not necessarily given due to e.g. potential transfer of incorporated ATV to proteins^[83] present in solution as observed for **A-pBuOx-A/PTX** *in vitro* and *in vivo*.^[84] ATV was either solubilized with **A-pBuOzi-A** or dissolved in DMSO and applied at 90 μM (50 mg/L) as well as 150 μM (83 mg/L). For comparison, oral administration of 40 mg ATV in hypercholesterolaemic haemodialysis patients resulted in ATV peak plasma concentrations of $28.6 \pm 15.2 \mu g/L$ (51 nM; reached 1-2 hours after initial administration), together with the active metabolites o- and p-OH ATV (8.1 and 0.6 $\mu g/L$) as well as inactive 3-lactone metabolites (44.2 $\mu g/L$).^[85] This clearly shows the need of ATV-formulation to achieve necessary ATV concentrations potentially suitable for glioblastoma therapy. At both concentrations, no pronounced cytotoxic effects of ATV on the endothelial cells of the artificial BBB were observed after 4 h incubation, ensuring the integrity of the monolayer during the course of the experiment (Figure S10a). After 24 h incubation, again no cytotoxicity up to ATV = 90 μM occurred (Figure S10b). Only at ATV = 150 μM , cell viability decreased to 41 % and 49 % for DMSO/ATV and **A-pBuOzi-A/ATV**, respectively. ATV was quantified in the apical and basolateral chamber after 4 h and 24 h incubation. To ensure the permeability analysis of **A-pBuOzi-A/ATV** and DMSO/ATV through the BBB endothelial cell layer itself, transwells without cells were always included to correct the permeation values for the barrier formed by the membrane support. In all cases, a higher ATV concentration occurred on the basolateral side of the latter compared to wells containing cells (Figure S11). Furthermore, diffusion through the blank membrane was more or less the same for **A-pBuOzi-A/ATV** and DMSO/ATV therefore excluding variances due to different diffusion profiles. With respect to the wells without cells, the ATV transport through the BBB was less efficient at apical ATV feed of 150 μM , compared to 90 μM (Figure 7b). Nevertheless, absolute basolateral ATV concentrations increased from 4 h to 24 h incubation and from $[\text{ATV}]_{\text{feed}} = 90 \mu M$ to 150 μM in all samples (Figure S11). For both ATV concentrations and time-points, ATV permeability was slightly higher for **A-pBuOzi-A/ATV** than for DMSO/ATV, however, the dif-

ferences were within the standard deviations (Figure 7b). This suggests that our nanoformulation does not alter the permeation profile of ATV through this BBB *in vitro* model significantly. Whether this is due to a rapid release of ATV from the micelles to e.g. proteins present in medium or e.g. the disintegration of the ATV-loaded micelles at the cell-membrane – not further improving endocytosis or transcellular delivery – remains to be elucidated. However, rapid disintegration of drug-loaded micelles within the blood stream is not necessarily detrimental regarding therapeutic efficacy, as evidenced by POx/PTX nanoformulations, which exhibit an excellent therapeutic efficacy *in vivo*.^[84] Interestingly, the proportional basolateral ATV concentration with respect to the wells without cells increased from 4 h to 24 h incubation for both, DMSO/ATV and A-pBuOzi-A/ATV (Figure 7b). Taking a closer look at the TEER values showed a decrease in resistance after 24 h at both ATV feed concentrations of 90 and 150 μM (Figure 7c,d). Even though we observed no ATV cytotoxicity up to 90 μM (Figure S10), the integrity of the BBB is apparently affected, probably through a loosening of the tight junctions. This may be an early indication of cytotoxic effects. Although the transport across the BBB is not significantly improved, the presented novel POzi/ATV formulation may allow much higher ATV serum concentrations, compared to oral administration or alternative drug delivery systems, as much higher ATV concentrations can potentially be administered. Therefore, therapeutic doses may be reached, even without improved transport across the BBB. Furthermore, co-administration with agents temporarily permeabilizing the BBB could help to increase the ATV concentration across the BBB. Such agent could be SP1049C or small molecules known to permeabilize the BBB. Possibly, such agent could be coformulated with ATV and therefore improve co-delivery of both APIs.

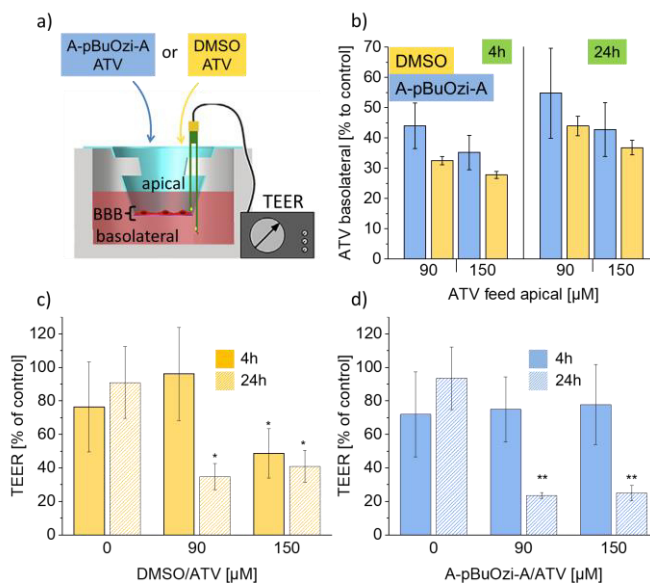


Figure 7: a) Setup to investigate the permeability of ATV through hiPSC-derived *in vitro* models of the human blood-brain barrier (BBB) in a transwell setup (image adapted from Appelt-Menzel *et al.*^[52]); b) A-pBuOzi-A/ATV = 10/1 [g/L] (blue) or DMSO/ATV (yellow) were diluted with cell specific medium to desired ATV concentrations of 90 μM or 150 μM and applied to the apical side of the transwells. Subsequently, basolateral ATV concentrations were quantified after 4 h and 24 h incubation with respect to the permeability through wells without cells (= control). Permeation was determined in three individual transwell-plates each containing the respective samples in duplicates. Data are presented as mean \pm SD; n = 3; TEER values of non-treated BBB as well as treatment with c) DMSO/ATV or d) A-pBuOzi-A/ATV for either 4 h (solid bars) or 24 h (dashed

bars). TEER values are presented with respect to TEER values measured prior to the transport assay (=control). TEER values were determined in three positions of three individual transwell-plates each containing the respective samples in duplicates. Data are presented as mean \pm SEM (n = 3, *p<0.05, **p<0.01, ***p<0.001).

CONCLUSION

We presented a novel nanoformulation of atorvastatin (ATV), a statin with potential in the treatment of various tumors, including glioblastoma. A moderate increase in the apparent aqueous solubility of ATV by a factor of 100 was achieved, but the sizes of the formed particles are too large for intravenous administration at the highest drug loading. Only at low drug loading < 10 wt.%, nanoformulations ($D_h < 50 \text{ nm}$) were obtained while at higher loading, large submicron particles were formed. The encapsulated ATV was fully bioactive and exhibited IC_{50} values in the low to medium micromolar range in a panel of different glioblastoma cell lines with no systematic difference between free, DMSO solubilized ATV and ATV solubilized using polymer micelles. In contrast, in tumor spheroids prepared from CT-2A mouse glioma and bRITS-G2 mouse glioma cancer stem cells, the micellar formulation was consistently more active. Very interestingly, we found particularly high activity against bRITS-G2 with minimal cell survival even at low micromolar ATV concentrations. Finally, transport through a blood-brain-barrier *in vitro* model based on differentiated human induced pluripotent stem cells was tested and revealed similar transport of micellar ATV and ATV dissolved by DMSO. However, as our novel micellar ATV formulations may enable much higher serum concentration of ATV, therapeutic doses may still be possible. Especially by combination with other active agents, micellar ATV may have potential for the treatment of glioblastoma.

ACKNOWLEDGEMENT

This work was supported by the Free State of Bavaria and the Deutsche Forschungsgemeinschaft (Project number 398461692, awarded to R.L.). Moreover, M.M.L. would like to thank the Evonik Foundation for providing a doctoral fellowship. We thank Christian May for technical support. Furthermore, we thank Dr. Tapia-Perez for inspiring this study.

REFERENCES

- [1] P. D. Delgado-López, E. M. Corrales-García, *Clin. Transl. Oncol.* **2016**, *18*, 1062-1071.
- [2] Q. T. Ostrom, H. Gittleman, P. Liao, C. Rouse, Y. Chen, J. Dowling, Y. Wolinsky, C. Kruchko, J. Barnholtz-Sloan, *Neuro-Oncol.* **2014**, *16 Suppl 4*, iv1-iv63.
- [3] R. Stupp, M. E. Hegi, W. P. Mason, M. J. van den Bent, M. J. B. Taphoorn, R. C. Janzer, S. K. Ludwin, A. Allgeier, B. Fisher, K. Belanger, P. Hau, A. A. Brandes, J. Gijtenbeek, C. Marosi, C. J. Vecht, K. Mokhtari, P. Wesseling, S. Villa, E. Eisenhauer, T. Gorlia, M. Weller, D. Lacombe, J. G. Cairncross, R.-O. Mirimanoff, *Lancet Oncol.* **2009**, *10*, 459-466.
- [4] Q. Xie, S. Mittal, M. E. Berens, *Neuro-Oncol.* **2014**, *16*, 1575-1584.
- [5] S. Osuka, E. G. Van Meir, *J. Clin. Investig.* **2017**, *127*, 415-426.
- [6] C. P. Haar, P. Hebbar, G. C. Wallace, A. Das, W. A. Vandergrift, J. A. Smith, P. Giglio, S. J. Patel, S. K. Ray, N. L. Banik, *Neurochem. Res.* **2012**, *37*, 1192-1200.
- [7] W. M. Pardridge, *J. Cereb. Blood Flow Metab.* **2012**, *32*, 1959-1972.

- [8] P. K. Pandey, A. K. Sharma, U. Gupta, *Tissue barriers* **2015**, *4*, e1129476-e1129476.
- [9] S. Y. Lee, *Genes & diseases* **2016**, *3*, 198-210.
- [10] M. Farnier, J. Davignon, *Am. J. Cardiol.* **1998**, *82*, 3J-10J.
- [11] J. K. Liao, *Am. J. Cardiol.* **2005**, *96*, 24F-33F.
- [12] K. Hindler, C. S. Cleeland, E. Rivera, C. D. Collard, *The Oncologist* **2006**, *11*, 306-315.
- [13] Y. G. Shellman, D. Ribble, L. Miller, J. Gendall, K. VanBuskirk, D. Kelly, D. A. Norris, R. P. Dellavalle, *Melanoma Res.* **2005**, *15*, 83-89.
- [14] M. Koyuturk, M. Ersoz, N. Altiok, *Neurosci. Lett.* **2004**, *370*, 212-217.
- [15] R. Girgert, Y. Vogt, D. Becke, G. Bruchelt, P. Schweizer, *Cancer Lett.* **1999**, *137*, 167-172.
- [16] A. Sassano, E. Katsoulidis, G. Antico, J. K. Altman, A. J. Redig, S. Minucci, M. S. Tallman, L. C. Platanius, *Cancer Res.* **2007**, *67*, 4524.
- [17] M. Yanae, M. Tsubaki, T. Satou, T. Itoh, M. Imano, Y. Yamazoe, S. Nishida, *J. Exp. Clin. Oncol. Res.* **2011**, *30*, 74.
- [18] S. Pisanti, P. Picardi, E. Ciaglia, A. D'Alessandro, M. Bifulco, *Pharmacol. Res.* **2014**, *88*, 84-98.
- [19] S. Gizzo, M. Quaranta, G. B. Nardelli, M. Noventa, *Curr. Drug Targets* **2015**, *16*, 1142-1159.
- [20] P. Prasanna, A. Thibault, L. Liu, D. Samid, *J. Neurochem.* **1996**, *66*, 710-716.
- [21] P. Jiang, R. Mukthavaram, Y. Chao, N. Nomura, I. S. Bharati, V. Fogal, S. Pastorino, D. Teng, X. Cong, S. C. Pingle, S. Kapoor, K. Shetty, A. Aggrawal, S. Vali, T. Abbasi, S. Chien, S. Kesari, *Br. J. Cancer* **2014**, *111*, 1562.
- [22] N. Bayat, S. Ebrahimi-Barough, A. Norouzi-Javidan, H. Saberi, R. Tajerian, M. M. M. Ardakan, S. Shirian, A. Ai, J. Ai, *Biomed. Pharmacother.* **2016**, *84*, 1959-1966.
- [23] Y. Yongjun, H. Shuyun, C. Lei, C. Xiangrong, Y. Zhilin, K. Yiquan, *J. Neuroimmunol.* **2013**, *260*, 1-8.
- [24] N. Bayat, S. Ebrahimi-Barough, A. Norouzi-Javidan, H. Saberi, M. M. M. Ardakan, A. Ai, M. Soleimannejad, J. Ai, *Mol. Neurobiol.* **2018**, *55*, 2102-2110.
- [25] F. Colotta, P. Allavena, A. Sica, C. Garlanda, A. Mantovani, *Carcinogenesis* **2009**, *30*, 1073-1081.
- [26] Y. T. Yeung, K. L. McDonald, T. Grewal, L. Munoz, *Br. J. Pharmacol.* **2013**, *168*, 591-606.
- [27] K. Shimada, R. Skouta, A. Kaplan, W. S. Yang, M. Hayano, S. J. Dixon, L. M. Brown, C. A. Valenzuela, A. J. Wolpaw, B. R. Stockwell, *Nat. Chem. Biol.* **2016**, *12*, 497.
- [28] A. K. Altwairgi, W. Alghareeb, F. Alnajjar, E. Alsaeed, A. Balbaid, H. Alhussain, S. Aldanan, Y. Orz, A. Lari, A. Alsharm, *Ann. Oncol.* **2016**, *27*.
- [29] T.-T. Tang, Y. Song, Y.-J. Ding, Y.-H. Liao, X. Yu, R. Du, H. Xiao, J. Yuan, Z.-H. Zhou, M.-Y. Liao, R. Yao, H. Jevallee, G.-P. Shi, X. Cheng, *J. Lipid Res.* **2011**, *52*, 1023-1032.
- [30] W. A. Banks, *BMC Neurol.* **2009**, *9 Suppl 1*, S3-S3.
- [31] J. B. David, *Curr. Pharm. Des.* **2004**, *10*, 1295-1312.
- [32] I. Tamai, A. Tsuji, *J. Pharm. Sci.* **2000**, *89*, 1371-1388.
- [33] A. Tsuji, A. Saheki, I. Tamai, T. Terasaki, *J. Pharmacol. Exp. Ther.* **1993**, *267*, 1085.
- [34] A. Saheki, T. Terasaki, I. Tamai, A. Tsuji, *Pharm. Res.* **1994**, *11*, 305-311.
- [35] B. G. Schultz, D. K. Patten, D. J. Berlau, *Transl. Neurodegener.* **2018**, *7*, 5-5.
- [36] F. M. Sahebzamani, C. L. Munro, O. C. Marroquin, D. M. Diamond, E. Keller, K. E. Kip, *J. Pharmacovigil.* **2014**, *2*, 1000141-1100015.
- [37] J. Shi, P. W. Kantoff, R. Wooster, O. C. Farokhzad, *Nat. Rev. Cancer* **2017**, *17*, 20-37.
- [38] H. Cabral, K. Miyata, K. Osada, K. Kataoka, *Chem. Rev.* **2018**, *118*, 6844-6892.
- [39] H. Danafar, K. Rostamizadeh, M. Hamidi, *J. Pharm. Investig.* **2017**, *48*, 381-391.
- [40] S. Andalib, P. Molhemazar, H. Danafar, *J. Biomater. Appl.* **2017**, *32*, 1127-1138.
- [41] P. Xu, H. Yu, Z. Zhang, Q. Meng, H. Sun, X. Chen, Q. Yin, Y. Li, *Biomaterials* **2014**, *35*, 7574-7587.
- [42] G. M. Mekhail, A. O. Kamel, G. A. S. Awad, N. D. Mortada, *Int. J. Biol. Macromol.* **2012**, *51*, 351-363.
- [43] S. S. A. C. H. G. P. D. C. R. B. A. Ravindran, *PLoS One* **2014**, *9*, e86317.
- [44] S. Şimşek, H. Eroğlu, B. Kurum, K. Ulubayram, *J. Microencapsul.* **2013**, *30*, 10-20.
- [45] E. V. Batrakova, S. Li, D. W. Miller, A. V. Kabanov, *Pharm. Res.* **1999**, *16*, 1366-1372.
- [46] T. O. Price, S. A. Farr, X. Yi, S. Vinogradov, E. V. Batrakova, W. A. Banks, A. V. Kabanov, *J. Pharmacol. Exp. Ther.* **2010**, jpet.109.158147.
- [47] J. Tong, X. Yi, R. Luxenhofer, W. A. Banks, R. Jordan, M. C. Zimmerman, A. V. Kabanov, *Mol. Pharm.* **2013**, *10*, 360-377.
- [48] W. A. Banks, A. Gertler, G. Solomon, L. Niv-Spector, M. Shpilman, X. Yi, E. Batrakova, S. Vinogradov, A. V. Kabanov, *Physiol. Behav.* **2011**, *105*, 145-149.
- [49] H. Witte, W. Seeliger, *Liebigs Ann. Chem.* **1974**, *1974*, 996-1009.
- [50] M. M. Lübtow, M. S. Haider, M. Kirsch, S. Klisch, R. Luxenhofer, *Biomacromolecules* **2019**, *20*, 3041-3056.
- [51] R. Luxenhofer, A. Schulz, C. Roques, S. Li, T. K. Bronich, E. V. Batrakova, R. Jordan, A. V. Kabanov, *Biomaterials* **2010**, *31*, 4972-4979.
- [52] A. Appelt-Menzel, A. Cubukova, K. Günther, F. Edenhofer, J. Piontek, G. Krause, T. Stüber, H. Walles, W. Neuhaus, M. Metzger, *Stem Cell Rep.* **2017**, *8*, 894-906.
- [53] M. M. Lübtow, L. Hahn, M. S. Haider, R. Luxenhofer, *J. Am. Chem. Soc.* **2017**, *139*, 10980-10983.
- [54] L. Hahn, M. M. Lübtow, T. Lorson, F. Schmitt, A. Appelt-Menzel, R. Schobert, R. Luxenhofer, *Biomacromolecules* **2018**, *19*, 3119-3128.
- [55] M. M. Lübtow, L. Keßler, A. Appelt-Menzel, T. Lorson, N. Gangloff, M. Kirsch, S. Dahms, R. Luxenhofer, *Macromol. Biosci.* **2018**, *18*, 1800155.
- [56] Y. Seo, A. Schulz, Y. Han, Z. He, H. Bludau, X. Wan, J. Tong, T. K. Bronich, M. Sokolsky, R. Luxenhofer, R. Jordan, A. V. Kabanov, *Polym. Adv. Technol.* **2015**, *26*, 837-850.
- [57] M. S. Haider, J. Schreiner, S. Kendl, M. Kroiß, R. Luxenhofer, *Macromol. Biosci.* **2019**, doi: 10.1002/mabi.201900178.
- [58] M. M. Lübtow, H. Marciniak, A. Schmiedel, M. Roos, C. Lambert, R. Luxenhofer, *Chem.: Eur. J.* **2019**, *25*, 12601-12610.
- [59] A.-C. Pöppler, M. M. Lübtow, J. Schlauersbach, J. Wiest, L. Meinel, R. Luxenhofer, *Angew. Chem. Int. Ed.* **2019**, doi:10.1002/anie.201908914.
- [60] S. Danson, D. Ferry, V. Alakhov, J. Margison, D. Kerr, D. Jowle, M. Brampton, G. Halbert, M. Ranson, *Br. J. Cancer* **2004**, *90*, 2085-2091.
- [61] A. V. Kabanov, E. V. Batrakova, D. W. Miller, *Adv. Drug Deliv. Rev.* **2003**, *55*, 151-164.
- [62] A. V. Kabanov, E. V. Batrakova, V. Y. Alakhov, *J. Control. Release* **2002**, *82*, 189-212.

- [63] M. M. Lübtow, L. C. Nelke, J. Seifert, J. Kühnemundt, G. Sahay, G. Dandekar, S. L. Nietzer, R. Luxenhofer, *J. Control. Release* **2019**, *303*, 162-180.
- [64] J. Crosbie, M. Magnussen, R. Dornbier, A. Iannone, T. A. Steele, *Biomark. Res.* **2013**, *1*, 33-33.
- [65] G. Y. Di Veroli, C. Fornari, I. Goldlust, G. Mills, S. B. Koh, J. L. Bramhall, F. M. Richards, D. I. Jodrell, *Sci. Rep.* **2015**, *5*, 14701.
- [66] E. J. Calabrese, *Environ. Pollut.* **2013**, *182*, 452-460.
- [67] P. Peng, W. Wei, C. Long, J. Li, *Biochem. Biophys. Res. Commun.* **2017**, *489*, 293-298.
- [68] J. H. Tapia-Pérez, E. Kirches, C. Mawrin, R. Firsching, T. Schneider, *Cancer Chemother. Pharmacol.* **2011**, *67*, 1193-1201.
- [69] S. K. Carlsson, S. P. Brothers, C. Wahlestedt, *EMBO Mol. Med.* **2014**, *6*, 1359-1370.
- [70] J. T. Huse, E. C. Holland, *Nat. Rev. Cancer* **2010**, *10*, 319.
- [71] E. Di Tomaso, J. C. S. Pang, H. K. Ng, P. Y. P. Lam, X. X. Tian, K. W. Suen, A. B. Y. Hui, N. M. Hjelm, *Neuropathol. Appl. Neurobiol.* **2000**, *26*, 22-30.
- [72] M. Schulze, O. Fedorchenko, T. G. Zink, C. B. Knobbe-Thomsen, S. Kraus, S. Schwinn, A. Beilhack, G. Reifenberger, C. M. Monoranu, A. L. Sirén, E. Jeanclos, A. Gohla, *Oncogene* **2015**, *35*, 3163.
- [73] R.-Z. Lin, H.-Y. Chang, *Biotechnol. J.* **2008**, *3*, 1172-1184.
- [74] B. Desoize, J.-C. Jardillier, *Crit. Rev. Oncol. Hematol.* **2000**, *36*, 193-207.
- [75] J. E. Visvader, G. J. Lindeman, *Nat. Rev. Cancer* **2008**, *8*, 755.
- [76] J. D. Lathia, S. C. Mack, E. E. Mulkearns-Hubert, C. L. L. Valentim, J. N. Rich, *Genes Dev.* **2015**, *29*, 1203-1217.
- [77] J. N. Rich, *Cancer Res.* **2007**, *67*, 8980.
- [78] D. Beier, J. B. Schulz, C. P. Beier, *Mol. Cancer* **2011**, *10*, 128.
- [79] F. Zhang, C.-L. Xu, C.-M. Liu, *Drug Des. Dev. Ther.* **2015**, *9*, 2089-2100.
- [80] A. Wolff, M. Antfolk, B. Brodin, M. Tenje, *J. Pharm. Sci.* **2015**, *104*, 2727-2746.
- [81] A. Avdeef, M. A. Deli, W. Neuhaus, in *Blood-Brain Barrier in Drug Discovery*, John Wiley, **2015**, pp. 188-237.
- [82] E. S. Lippmann, S. M. Azarin, J. E. Kay, R. A. Nessler, H. K. Wilson, A. Al-Ahmad, S. P. Palecek, E. V. Shusta, *Nat. Biotechnol.* **2012**, *30*, 783.
- [83] Q. Wang, C.-r. Huang, M. Jiang, Y.-y. Zhu, J. Wang, J. Chen, J.-h. Shi, *Spectrochim. Acta A* **2016**, *156*, 155-163.
- [84] Z. He, X. Wan, A. Schulz, H. Bludau, M. A. Dobrovolskaia, S. T. Stern, S. A. Montgomery, H. Yuan, Z. Li, D. Alakhova, M. Sokolsky, D. B. Darr, C. M. Perou, R. Jordan, R. Luxenhofer, A. V. Kabanov, *Biomaterials* **2016**, *101*, 296-309.
- [85] R. L. Lins, K. E. Matthys, G. A. Verpooten, P. C. Peeters, M. Dratwa, J. C. Stolear, N. H. Lameire, *Nephrol. Dial. Transplant.* **2003**, *18*, 967-976.
-

4.5 Drug-Loaded Hydrogels

To expand the way of administration, the drug-loaded micelles were incorporated into a hydrogel matrix possibly finding application as (sub)cutaneous drug depot from which the drug is released in a locally concentrated and sustained manner. Before incorporation of the micelles, the properties of the hydrogel itself will be discussed. Interestingly, the thermogelling diblock copolymer consists of the same POx and POzi building blocks as the triblock copolymer enabling one of the highest *LC* for CUR, however with higher degrees of polymerization. The thermally induced gelation was dependent on the individual block lengths, with gelation temperatures between room and body temperature associated with high mechanical strengths up to 4 kPa. SANS revealed a bicontinuous, sponge-like morphology, strongly deviating from e.g. widely used Pluronic gels. Due to its shear thinning properties and excellent recovery behavior, the hydrogel was 3D printed via extrusion-based bioprinting, possessing sufficient shape fidelity (shape integrity while printing multiple layers needs to be evaluated further). The diblock copolymer exhibited excellent cytocompatibility for murine NIH 3T3 fibroblasts even in the gel state (87 % metabolically active cells). Moreover, no sedimentation of the cells occurred, and printability was not influenced by the latter (1×10^6 cells/mL). Most interestingly, the printing process seemed to have no effect on the cell viability.

A Thermogelling Supramolecular Hydrogel with Sponge-Like Morphology as a Cytocompatible Bioink

Thomas Lorson,[†] Sebastian Jaksch,[§] Michael M. Lübtow,[†] Tomasz Jüngst,[‡] Jürgen Groll,[‡] Tessa Lühmann,^{||} and Robert Luxenhofer^{*,†,||}

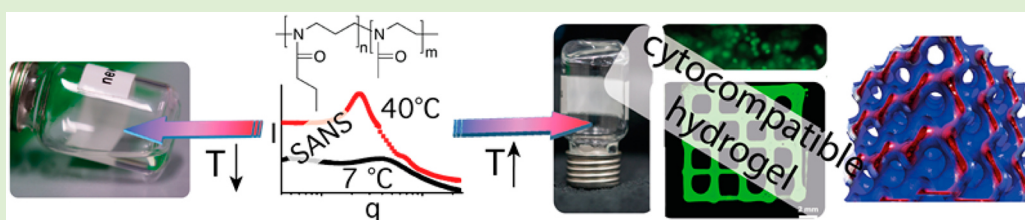
[†]Functional Polymer Materials, Chair for Advanced Materials Synthesis, Department of Chemistry and Pharmacy and Bavarian Polymer Institute, Julius-Maximilians-Universität Würzburg, Röntgenring 11, 97070 Würzburg, Germany

[§]Jülich Centre for Neutron Science JCNS, Forschungszentrum Jülich GmbH, Outstation at MLZ, Lichtenbergstraße 1, 85748 Garching, Germany

[‡]Chair for Functional Materials in Medicine and Dentistry and Bavarian Polymer Institute, Julius-Maximilians-Universität Würzburg, Pleicherwall 2, 97070 Würzburg, Germany

^{||}Institute of Pharmacy and Food Chemistry, Department of Chemistry and Pharmacy, Julius-Maximilians-Universität Würzburg, Am Hubland, 97074 Würzburg, Germany

S Supporting Information



ABSTRACT: Biocompatible polymers that form thermoreversible supramolecular hydrogels have gained great interest in biomaterials research and tissue engineering. When favorable rheological properties are achieved at the same time, they are particularly promising candidates as material that allow for the printing of cells, so-called bioinks. We synthesized a novel thermogelling block copolymer and investigated the rheological properties of its aqueous solution by viscosimetry and rheology. The polymers undergo thermogelation between room temperature and body temperature, form transparent hydrogels of surprisingly high strength ($G' > 1000$ Pa) and show rapid and complete shear recovery after stress. Small angle neutron scattering suggests an unusual bicontinuous sponge-like gel network. Excellent cytocompatibility was demonstrated with NIH 3T3 fibroblasts, which were incorporated and bioprinted into predefined 3D hydrogel structures without significant loss of viability. The developed materials fulfill all criteria for future use as bioink for biofabrication.

INTRODUCTION

Thermogelling polymers find application in food and pharmaceutical technology, biology and medicine.^{1,2} Apart from well-known biological polymers that show thermogelling properties, such as collagen,^{3–5} gelatin,^{3–5} agarose^{3–5} and others,^{4,6} also a few synthetic polymer systems exhibit this property. In this context, frequently used material include poly(*N*-isopropylacrylamide) (pNIPAAm)^{7–9} or two members of the family of Pluronics,¹⁰ F127 and P123. In recent years these systems have been investigated extensively for biomedical applications,¹¹ but limitations in respect to cytocompatibility have been reported.¹² The gelation mechanism of F127 was examined in detail by various techniques, including small angle neutron scattering (SANS).¹³ Increasing the temperature beyond the critical temperature (cloud point temperature, T_{cp}) leads to aggregation into spherical micelles. At concentrations of ≥ 5 wt %, those micelles arrange in a cubic lattice.¹³

Another important class of thermoresponsive polymers is based on cyclic imino ethers, particularly poly(2-substituted-2-oxazoline)s (POx) and poly(2-substituted-5,6-dihydro-4H-1,3-oxazine)s (in short, poly(2-oxazine)s; POzi). These polymers are accessible via living cationic ring-opening polymerization (Scheme S1)¹⁴ and can exhibit T_{cp} in aqueous solution where the transition temperature can be tuned over a large temperature range (0 to above 100 °C).^{15–18} In the past decade, POx were intensely investigated not only as thermoresponsive materials,^{19–22} but also in biomedical applications^{23–35} including covalently cross-linked hydrogels^{36–41} and as printable thermoplasts.⁴² While thermoresponsive POx are well-known, thermogelling polymers solely based on POx have so far hardly been explored. We have recently attempted to prepare thermogelling POx-based

Received: April 4, 2017

Revised: June 10, 2017

Published: June 27, 2017

triblock copolymers based on the hydrophilic poly(2-methyl-2-oxazoline) (PMeOx) and the thermoresponsive poly(2-n-propyl-2-oxazoline) (PnPrOx), but were unable to identify compositions that led to thermogelation.⁴³

In contrast to POx, POzi have received very little attention⁴⁴ with one report from Bloksma et al. referring to the thermoresponsive behavior of POzi homopolymers,¹⁸ but block copolymers of POx and POzi can only be found in a single report by Kobayashi et al. dealing with surfactants.^{44,45}

Thermogelling polymers have recently raised great interest as bioinks for three-dimensional (3D) cell culture and biofabrication.^{46–49} In this upcoming and rapidly growing research field, to date, the shortage of suitable and versatile bioinks represents a major limitation. Due to the diverse requirements, an ideal bioink must be available in a consistent quality, sufficient quantity, and with tunable physical and biological properties.^{4,50,51} In this study, we present the synthesis of a series of block copolymers comprising hydrophilic poly(2-methyl-2-oxazoline) and thermoresponsive poly(2-n-propyl-2-oxazine) (nPrOzi). The rheological properties of aqueous solutions were investigated in dependence of concentration and temperature. Small angle neutron scattering was used to study the gel network morphology at 20 wt %. Cytocompatibility was tested and finally, the thermoresponsive, shear-thinning and cell-laden hydrogels were printed.

■ EXPERIMENTAL SECTION

Materials and Methods. All substances for the preparation of monomers and polymers were purchased from Sigma-Aldrich (Steinheim, Germany), Acros (Geel, Belgium), or Fluka (Steinheim, Germany) and were used as received unless otherwise stated. Dulbecco's Modified Eagle Medium (DMEM), fluorescein diacetate (FDA), and propidium iodide (PI) were purchased from Sigma-Aldrich (Schnellendorf, Germany). Penicillin G and streptomycin solution were purchased from Biochrom AG (Berlin, Germany). Fetal bovine serum (FBS) was from Gibco (Darmstadt, Germany). 8-well LabTek chamber slides were from Nunc (Thermo Fisher Scientific, Schwerte, Germany). 96-well plates and 100 mm culture dishes were from Greiner Bio One (Frickenhausen, Germany). Water-soluble tetrazolium (WST-1) was from Roche (Basel, Switzerland). Methyl trifluoromethylsulfonate (MeOTf), 2-methyl-2-oxazoline (MeOx), 2-n-propyl-2-oxazine (nPrOzi), benzonitrile (PhCN) and other solvents were dried by refluxing over CaH₂ under dry argon atmosphere and subsequent distillation prior to use. Afterward, all chemicals were stored under dry and inert conditions in a MBRAUN (Garching, Germany) LABmaster130 glovebox.

NMR spectra were recorded on a Bruker Fourier 300 (¹H 300.12 MHz) at 298 K, Bruker BioSpin (Rheinstetten, Germany). The spectra were calibrated using the solvent signals (MeOD 3.31 ppm). Gel permeation chromatography (GPC) was performed on a Polymer Standard Service (PSS, Mainz, Germany) system (pump mod. 1260 infinity, RI-detector mod. 1260 infinity, precolumn GRAM 10 μm (50 × 8 mm), 30 Å PSS GRAM 10 μm (300 × 8 mm) and 1000 Å PSS GRAM 10 μm (300 × 8 mm)), with *N,N*-dimethylformamide (DMF) (1 g/L LiBr, 313 K, 1 mL/min) as eluent and calibrated against PEG standards. Prior to each measurement, the samples were filtered through a 0.2 μm Teflon filter (Thermo Scientific) to remove particles. IR spectra were recorded on a Jasco (Groß-Umstadt, Germany) FT/IR-4100 equipped with an ATR-unit. Rheology experiments were performed using an Anton Paar (Ostfildern, Germany) Physica MCR 301 utilizing a plate–plate geometry (diameter 25 mm). The rheometer was equipped with a Peltier element. All polymer solutions used for rheology were prepared just before the measurement and were kept in the fridge at approximately 8 °C. At the beginning of every measurement, the sample was allowed to equilibrate at 5 °C for 5 min. Then the temperature was raised linearly with 0.66 K/min from 5 °C up to 50 °C. The used frequency was 1 Hz and the strain 3%.

Dynamic viscosity was measured on an Anton Paar (Graz, Austria) Microviscometer LOVIS 2000 M using capillary LOVIS 1.8 equipped with a steel ball (Mat. No. 73109, diameter 1.5 mm, steel 1.4125). Prior to this, density was determined using an Anton Paar (Graz, Austria) Density Meter DMA 4100 M. Dialysis was performed using Spectra/Por membranes with a molecular weight cutoff (MWCO) of 1 and 4 kDa obtained from neoLab (Heidelberg, Germany).

The SANS measurements were performed at the KWS-1 instrument at the Jülich Centre for Neutron Science (JCNS) at Heinz Maier-Leibnitz Zentrum (MLZ) in Garching, Germany.⁵² In all cases, a wavelength of $\lambda = 7 \text{ \AA}$ was used. The sample detector distances (SDD) of 1.61, 7.61, and 19.61 m were used to cover the complete q range ($q = 4\pi \sin(\frac{\theta}{2})/\lambda$ is the momentum transfer with θ the scattering angle). The wavelength resolution was set to $\Delta\lambda/\lambda = 10\%$.

In KWS-1, the detector is a ⁶Li-glass detector with an active area of 60 × 60 cm². The exposure times were 5, 15, and 35 min for the SDDs of 1.61, 7.61, and 19.61 m, respectively. The sample was poured into a Hellma cuvette with a path length of 1 mm. This cuvette was placed into a temperature controlled oven. Dark current correction was carried out using boron carbide. The scattering of the empty cell was subtracted from the sample scattering, taking the transmissions into account. Poly(methyl methacrylate) was used to bring the data to absolute scale and to determine the detector sensitivity. The resulting intensities were azimuthally averaged. Good agreement was found in the overlap regions of the curves measured at different SDDs. All data reduction steps were performed with the software QtiKWS provided by JCNS. Subsequent data treatment was carried out with the NIST NCR SANS package for IGOR Pro⁵³ and procedures written by the authors.

Synthetic Procedures. Monomer Synthesis. The monomer nPrOzi was synthesized by an adapted standard procedure.⁵⁴ Zincacetate dihydrate (catalyst) was dissolved in butyronitrile and 3-amino-1-propanol was added dropwise at room temperature. The reaction mixture was stirred under reflux conditions for at least 24 h. Progression of the reaction was monitored by IR-spectroscopy. After total nitrile consumption, the monomer was purified by fractional distillation under inert argon atmosphere at 10 mbar and 40 °C to obtain a clear colorless liquid (yield: 303.09 g, 42.1%). ¹H NMR (300 MHz, δ in ppm, CDCl₃): 4.09 (t, $J = 5.5 \text{ Hz}$, 2H; CH₂O), 3.31 (t, $J = 5.9 \text{ Hz}$, 2H; CH₂N), 2.05 (t, $J = 7.8 \text{ Hz}$, 2H; OCCH₂–CH₂), 1.80 (quintet, $J = 5.7 \text{ Hz}$, 2H; OCH₂CH₂), 1.53 (sextet, $J = 7.4 \text{ Hz}$, 2H; CCH₂CH₂), 0.89 (t, $J = 7.4 \text{ Hz}$, 3H; CH₃).

Polymerizations. The polymerizations and workup procedures were carried out following a general procedure based on previous reports.^{29,55} Exemplarily, the preparation of methyl-P[nPrOzi₅₀-*b*-MeOx₅₀]-piperidine-4-carboxylic acid ethyl ester (50_A) was performed as follows. (Scheme S1) Under dry and inert conditions (glovebox), 276 mg (1.68 mmol, 1 equiv) MeOTf and 10.7 g (84.1 mmol, 50 equiv) of nPrOzi were added to 17.4 mL dry PhCN in a flame-dried flask at room temperature and polymerized at 120 °C for 4 h. The full monomer conversion was verified by IR-spectroscopy before addition of the monomer for the second block. The mixture was cooled to room temperature, and 7.15 g MeOx (84.0 mmol, 50 equiv) dissolved in 21 mL dry PhCN was added. After stirring at 100 °C for 4 h, the mixture was cooled to 0 °C and 850 mg (5.41 mmol, 3.2 equiv) ethyl isonipicotate were added and the mixture was stirred overnight at 40 °C. After cooling to room temperature, potassium carbonate (232 mg, 1.68 mmol, 1 equiv) were added and the mixture was stirred for 5 h. The solvent was removed at reduced pressure from the supernatant after centrifugation and the flask was placed in a vacuum drying oven at 40 °C and 20 mbar for 2 days. The product was dissolved in deionized water, dialyzed overnight using a membrane with a MWCO of 4kD and freeze-dried (yield: 14.3 g, 79%).

Cell Culture. Murine NIH 3T3 fibroblasts (ATCC-Number CRL-1658, ATCC, Manassas, VA) were maintained in 100 mm culture dishes in growth medium (DMEM containing 10% heat inactivated FBS, 100 U/mL penicillin G and 100 μg/μL streptomycin) at 37 °C and 5% CO₂.

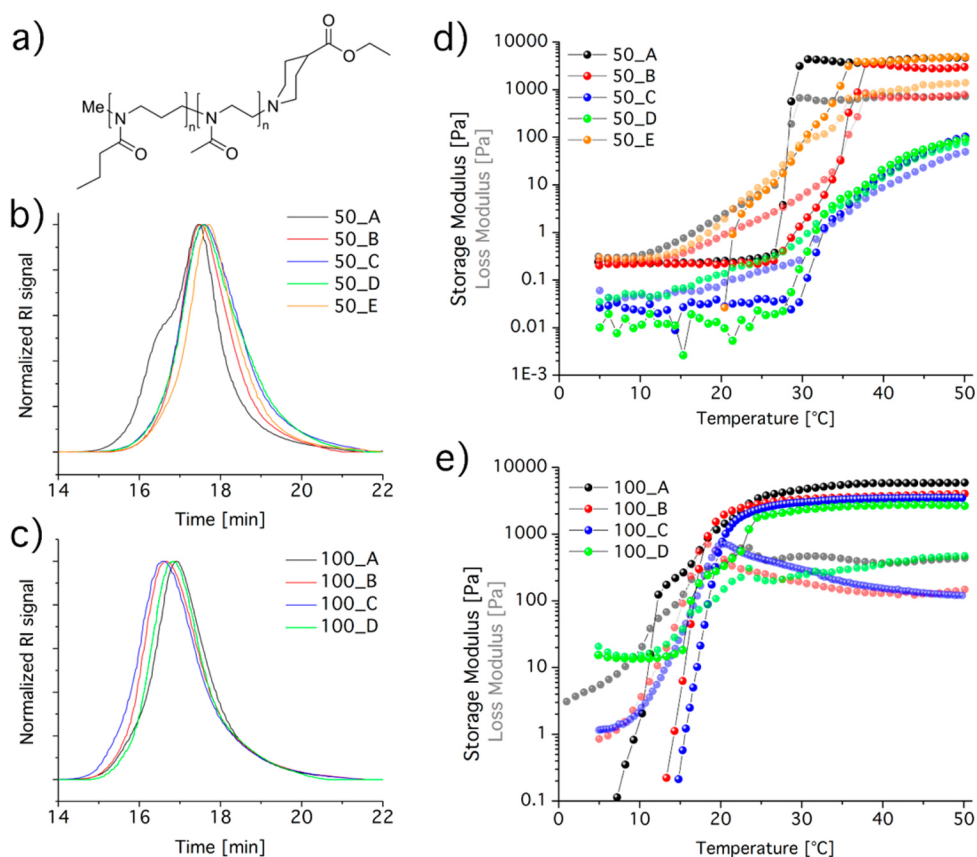


Figure 1. (a) Chemical structure of the investigated polymer, (b) GPC traces of the block copolymers with $n = 50$, (c) GPC traces of the block copolymers with $n = 100$, (d) temperature-dependent rheology of block copolymers with $n = 50$ with storage modulus (G') and loss modulus (G'') (20 wt %), and (e) temperature-dependent rheology of block copolymers with $n = 100$ with storage modulus (G') and loss modulus (G'') (20 wt %).

Cell Viability. The lyophilized polymer was dissolved in growth medium at 30 wt %. 20 000 NIH 3T3 fibroblasts dispersed in media were incorporated into the polymer stock-solution by gentle mixing with an Eppendorf pipet on ice to yield a 100 μ L solution, in which the final polymer concentration was 25 wt %. The solution was subsequently added to one well of a preheated (37 $^{\circ}$ C) 8-well LabTek chambers slide. After incubation for 24 h at 37 $^{\circ}$ C and 5% CO_2 , cells were suspended with ice-cold PBS and equally divided in two parts for staining with either 0.01 $\mu\text{g}/100$ cells FDA or 0.003 $\mu\text{g}/100$ cells PI dissolved in PBS for 3 min at room temperature as described before.⁵⁶ FDA as nonfluorescent substrate is a viability marker for enzymatic activity and cell-membrane integrity after active conversion to fluorescein ($\lambda_{\text{ex}} = 492$ nm $\lambda_{\text{em}} = 517$ nm) by intracellular esterases in living cells. By contrast, PI ($\lambda_{\text{ex}} = 540$ nm $\lambda_{\text{em}} = 608$ nm) does not penetrate intact membranes and intercalates stoichiometrically with nucleic acids in dead cells.^{57–59} The cells were subsequently analyzed by flow cytometry on a FACS Calibur system. For detection, a 488 nm laser was chosen with the emission channel FL2 (585 nm/ \pm 21 nm) for PI or the emission channel FL1 (530 nm/ \pm 15 nm) for FDA, respectively. A total number of 5000 events were counted with BD CellQuest Pro, and the geometric mean fluorescence intensity was determined for each condition using Flowing Software (version 2.5.1; Turku Bioimaging).

Distribution of NIH-3T3 Cells. To visualize cells within the thermoreversible gel, the cell pellet of NIH 3T3 fibroblasts was FDA-stained and 20000 cells were incorporated into a 25 wt % polymer solution and added into 37 $^{\circ}$ C preheated 8-well LabTek chambers slides as described above. FDA stained cells were subsequently analyzed with a Zeiss Observer Z1 epi-fluorescence microscope (Zeiss, Oberkochen, Germany) equipped with a 37 $^{\circ}$ C incubation chamber. 3D stacks with 1 μm z-stack intervals were taken. Acquired 3D stacks were analyzed with the ZEN Imaging Software (Zeiss, Oberkochen, Germany).

WST-1 Proliferation Assay. 2000 NIH 3T3 fibroblasts were seeded in growth medium in a 96-well-format and incubated overnight at 37 $^{\circ}$ C and 5% CO_2 . Dilution concentrations of the 30 wt % polymer stock solution were prepared (final polymer concentrations: 10, 5, 1, and 0.02 wt %) in growth medium on ice and added to the cells. Cell growth was stimulated for 48 h at 37 $^{\circ}$ C and 5% CO_2 . Before analysis, the cell medium was carefully exchanged and replaced by fresh growth medium. The cells were incubated with WST-1 for 3 h at 37 $^{\circ}$ C according to the manufacturer's instructions. The absorbance of the soluble formazan product was determined at 570 nm using a Spectramax 250 microplate reader from Molecular Devices (Sunnyvale, CA).

3D Bioprinting and Bioink Preparation. For printing a 3D bioprinter (3DDiscovery, regenHU, Switzerland) working on the principle of an extrusion-based printer was used. It was equipped with a pneumatic driven print head (syringe dispenser, DD-135N) and a 0.25 mm inner diameter precision needle (precision tip, Nordson EFD, Germany) was used as nozzle. The pressure was set to 1.2 bar and a print speed of 20 mm/min was applied for printing. Printing was performed at room temperature. In the case of cell-laden inks, the NIH 3T3 fibroblasts were stained with Hoechst and FDA (as described for the cell viability tests) and gently mixed with the cold 100_B 20 wt % gel at 4 $^{\circ}$ C. A final concentration of 1.0 million cells/mL was prepared and the ink was transferred to a 3 cm^3 barrel (Nordson EFD, Germany). The barrel was placed in an incubator at 37 $^{\circ}$ C to prevent sedimentation of cells. Before printing, the ink was cooled to room temperature and processed.

Confocal Laser Scanning Microscopy of Printed Constructs. The stained and printed cell-laden constructs were analyzed with a confocal laser scanning microscope (TCS SP8, Leica, Germany). The motorized stage in combination with the LASX software enabled 3D reconstruction of the constructs via tiles and z-stacks.

Quantification of Cell Survival. To quantify whether cells survive the printing process, cell-loaded bioinks were prepared, stained, and dispensed as described in the [3D Bioprinting and Bioink Preparation](#) section. Instead of printing constructs, the material leaving the nozzle was collected in 24-well plates. The same settings as for printing were applied (0.25 mm needle, 1.2 bar). Afterward, the polymer was dissolved, and the viability was analyzed by FACS as described above.

RESULTS AND DISCUSSION

We synthesized a POzi-*b*-POx block copolymer comprising a thermoresponsive POzi block (from nPrOzi, lower critical solution temperature (LCST) approximately 12 °C¹⁸) and a hydrophilic POx block (MeOx) ([Figure 1a](#)).

As we were preparing a highly concentrated aqueous polymer solution for freeze-drying, we noticed that this solution, while liquid at 4 °C, solidified at the elevated temperature (>25 °C) in our laboratory. To the best of our knowledge, this is the first case of thermogelling polymers comprising solely poly(cyclic imino ethers). During the course of this study, we synthesized several batches (50_A–50_E) of poly(nPrOzi)-*b*-poly(MeOx) with a degree of polymerization of 50 for each block. These polymers were analyzed using ¹H NMR and GPC ([Table 1](#)).

Table 1. Degree of Polymerization (DP) and Molar Masses (kg/mol) obtained by NMR and GPC of 50_A–50_E and 100_A–100_D

	DP theo	DP exp ^a	M _N theo	M _N ^a	M _N ^b	M _w ^b	Đ ^b
50_A	52/52	42/44	11.2	9.3	10.0	14.9	1.49
50_B	50/50	57/55	10.8	12.0	7.3	8.5	1.17
50_C	50/50	51/51	10.8	10.9	6.3	8.1	1.29
50_D	50/58	55/50	11.5	11.2	6.4	8.2	1.28
50_E	51/49	44/45	10.8	9.6	6.5	7.8	1.22
100_A	98/97	93/94*	20.9	20.0	9.3	12.2	1.31
100_B	99/100	94/94	21.3	20.1	10.1	13.4	1.34
100_C	100/99	88/98	21.3	20.1	10.4	14.3	1.38
100_D	75/97	77/105	18.9	20.1	9.9	12.2	1.24

^aDetermined by end-group analysis (¹H NMR spectroscopy in MeOD-d⁴ or CDCl₃* (300 MHz, 298 K)). ^bDetermined from GPC in DMF with LiBr (1 g/L) at 313 K.

The elugrams obtained by GPC ([Figure 1b](#)) appear, with the exception of the first batch, 50_A, essentially monomodal with only minor tailing to lower molar masses. Batch 50_A exhibits a significant shoulder at higher molar masses, and, accordingly, dispersity is highest in this sample (Đ = 1.49). NMR spectra were in good agreement with the targeted polymer composition ([Figure S1](#), [Table 1](#)).

Additionally, we wanted to investigate the influence of the chain length on the physicochemical properties of these novel block copolymers. Therefore, four batches (100_A–100_D) with a degree of polymerization of 100 for each block were synthesized and analyzed ([Figure S1](#), [Table 1](#)). GPC-elugrams ([Figure 1c](#)) also appear essentially monomodal with only minor tailing to lower molar masses.

Rheological properties of aqueous solutions were investigated of 50_A (20 wt %) in dependence of the temperature ([Figure 1d](#)) in the linear viscoelastic range ([Figure S2](#)). A relatively sharp sol–gel transition at approximately 27 °C was observed. It is noteworthy that *G'* increases by 4 orders of magnitude within a narrow temperature window. Notably, *G''* starts to increase at much lower temperature than *G'* (approximately 13 °C), which corresponds with the T_{CP} of

PnPrOzi as homopolymer.¹⁸ After gelation, *G'* reaches a plateau at about 4 kPa. Therefore, these gels are surprisingly strong compared to many other thermogelling polymers, for which values <1 kPa are more commonly found in the literature.^{60,61} A prominent exception are hydrogels of F127 at 20 wt % (approximately 10 kPa).⁶² Increasing the chain length to 100 monomer units for each block does not significantly influence the values of *G'*, which remain around 4 kPa in the gel condition ([Figure 1e](#)). However, *G''* with values around 0.2 kPa is lower compared to all samples comprising only 50 monomer units of each block (0.7 kPa–1.2 kPa). Consequently, the damping factor is lower, which indicates that the elastic character is more pronounced for polymers 100_A–100_D. Moreover, a distinct decrease of the gelation temperature to 17 °C for 100_D and 20 °C for 100_C is observed.

Comparing the different batches, we found that at 20 wt % only 50_A, 50_B, and 50_E formed gels with a more elastic character (*G''/G' = tan δ* ≈ 0.2). In contrast, even though 50_C and 50_D formed gels as evidenced by *G' > G''*, these are more viscous in character (*tan δ* ≈ 1; *G' < 0.1 kPa*). This was surprising as all batches, in particular 50_B–50_E, appeared very similar from NMR and GPC analysis. 50_C and 50_D only showed a somewhat more pronounced low-molecular tailing in the GPC elugrams ([Figure 1b](#)). Comparing all batches with respect to GPC elugrams and rheology, molar mass appeared to be a dominant factor for *G'* of the resulting gels. While a higher molar mass did not negatively influence *G'* (50_A), even a slightly higher content of lower molar mass components resulted in the formation of significantly weaker gels (50_C and 50_D). This data underlines the importance of studying batch-to-batch variations in the context of biomaterials research.⁶³

Based on this rheological characterization, we hypothesized polymers 50_A, 50_B, 50_E, and 100_A–100_D to appear suitable for bioprinting. Thus, we investigated shear thinning for 50_B and 100_B at 20 wt % and 37 °C, a crucial bioink parameter.⁶⁴ The viscosity decreased from 4 kPa*s and 12 kPa*s, respectively, to 1 Pa*s with increasing shear rate from 0.01 s⁻¹ to 100 s⁻¹ ([Figure 2a](#)).

Moreover, we measured temperature- and concentration-dependent viscosity of aqueous solutions of 50_B ([Figure 2b](#)). Below the T_{CP} of PnPrOzi, a transparent solution of relatively low viscosity was observed at all concentrations. Interestingly, at 5 wt % and above T_{CP} of nPrOzi, the solution became turbid, which was also observed for the longer block copolymers (100_series). The viscosity remained very low and decreased monotonously with temperature ([Figure 2b](#)). By contrast, in the case of 50_series, between approximately 10 and 20 wt %, the solutions remained clear and liquid over the entire temperature range investigated (5–50 °C), while the 100_series turned turbid ([Figure 2c](#)). The increase of viscosity started consistently around T_{CP} while the maximum of the viscosity goes through a plateau, the maximum of which shifts to higher temperatures with increasing polymer concentration. At concentrations of 20 wt % and above, the solutions of all presented polymers gel ([Figure 1d](#), [Figure 2c](#)). In this behavior these thermogelling polymers are quite distinct from F127 and P123, which also form gels at elevated temperature and/or concentration and are commonly used for gel plotting in biofabrication.⁶ Important for the prospective use as injectable hydrogel or as bioink, the viscosity of our material is relatively low at low temperature, in particular compared to the viscosity of Pluronic block copolymers (compare 700 mPa*s (F127) vs 7

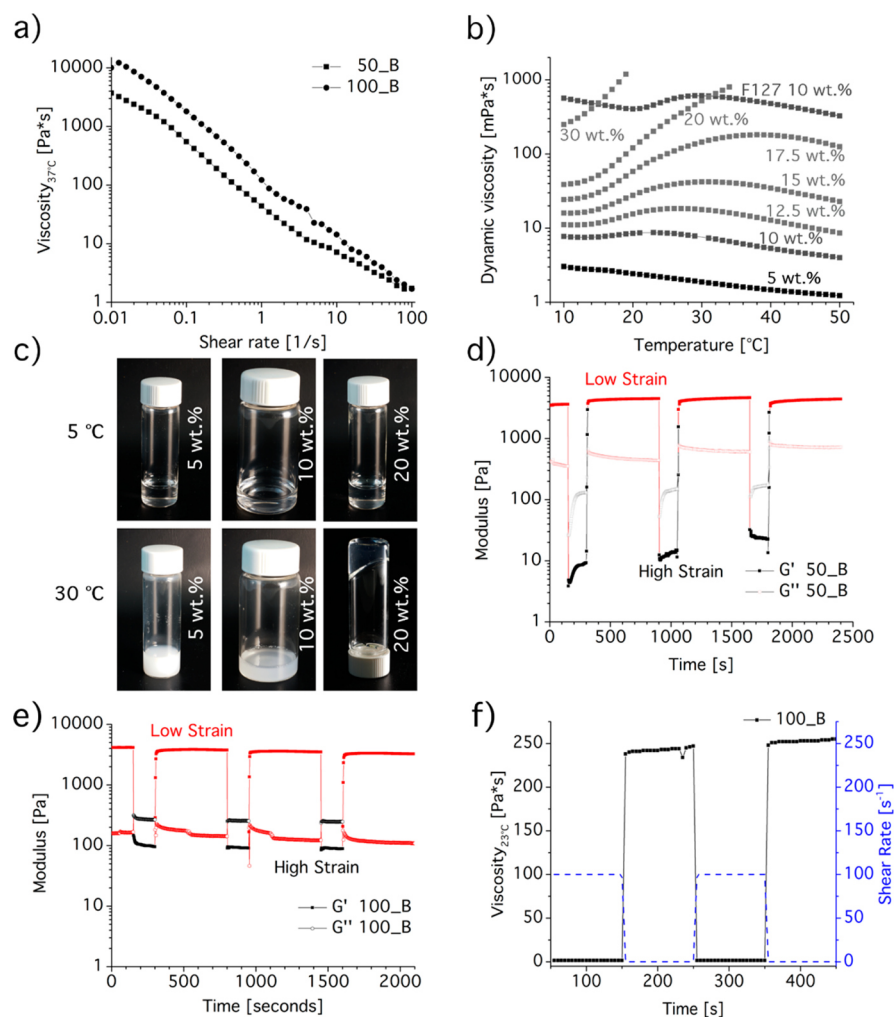


Figure 2. (a) Flow curve of 50_B and 100_B at 37 °C, (b) temperature- and concentration-dependent viscosity of 50_B at various concentrations compared with F127 at 10 wt %, (c) photographs of 100_B at different concentrations and temperature, (d,e) shear recovery at 37 °C and 10 rad/s (20 wt %) of 50_B and 100_B (low strain: 0.5%, high strain: 150%), and (f) structure recovery at 23 °C with viscosity (black curve) and applied shear rate (blue curve).

mPa*s (50_B) at 10 wt % and 10 °C). Even at 30 wt %, a solution of 50_B at 10 °C has a lower viscosity (approximately half) than a 10 wt % solution of F127 (Figure 2b), which does not form a gel at this concentration.

Trying to simulate the large shear deformation during the printing process, we investigated shear recovery of 50_B (Figure 2d) and 100_B (Figure 2e) at 37 °C using an oscillatory approach with an angular frequency of 10 rad/s. In detail, we first applied a low amplitude strain of 0.5% for 150 s followed by a large amplitude strain of 150% for 150 s. The storage modulus of 50_B (Figure 2d) drops from 3.6 kPa to 3.85 Pa. Upon returning to the low amplitude strain, the sample recovered immediately to essentially prestrain values. Subsequently, G' increased further to about 125% (within 600 s) of the initial value (4.5 kPa), which may indicate a ripening of the network over time. Similarly, the storage modulus of 100_B (Figure 2e) drops from 4.1 kPa to 147 Pa. Again, at low amplitude strain, G' recovered immediately to essentially initial values. In addition, structure-recovery of 100_B at 23 °C (Figure 2f) was examined using a rotational measurement. Applying a high shear rate of 100 s⁻¹ results in viscosity values of 1.5 Pa*s. Immediately after decreasing the shear rate to 0.5 s⁻¹, the viscosity increased within seconds to 240 Pa*s, which

shows rapid recovery of the investigated hydrogel after high shear. This result corroborates the results from the shear-thinning experiment conducted at 37 °C (Figure 2a). In summary, the rheological properties of the polymer show two aspects that are interesting for bioinks: pronounced isothermal shear-thinning and rapid recovery after shear stress.

As previously remarked, the viscosity profile of our polymers was different compared to Pluronic F127 and others as reported in the literature. This is likely to be linked to the structure of polymer self-assemblies in water. For many, if not most thermogelling polymers, the gelation is explained through an aggregation of spherical micelles into a cubic lattice. We studied one of our hydrogels (50_A, 20 wt %) using SANS (Figure 3a).

We chose to use SANS as it offers a good contrast between solvent and polymer (SLD polymer: $0.834 \times 10^{-6} \text{ \AA}^{-2}$; SLD D₂O: $6.393 \times 10^{-6} \text{ \AA}^{-2}$), while there is very little contrast in the case of X-ray scattering (SLD polymer $9.58 \times 10^{-6} \text{ \AA}^{-2}$; SLD H₂O: $9.46 \times 10^{-6} \text{ \AA}^{-2}$). Between the single blocks there is also insufficient contrast to allow a detailed analysis (SLD nPrOzi: $0.346 \times 10^{-6} \text{ \AA}^{-2}$; SLD MeOx: $0.757 \times 10^{-6} \text{ \AA}^{-2}$). This shortcoming may be alleviated in future experiments where one

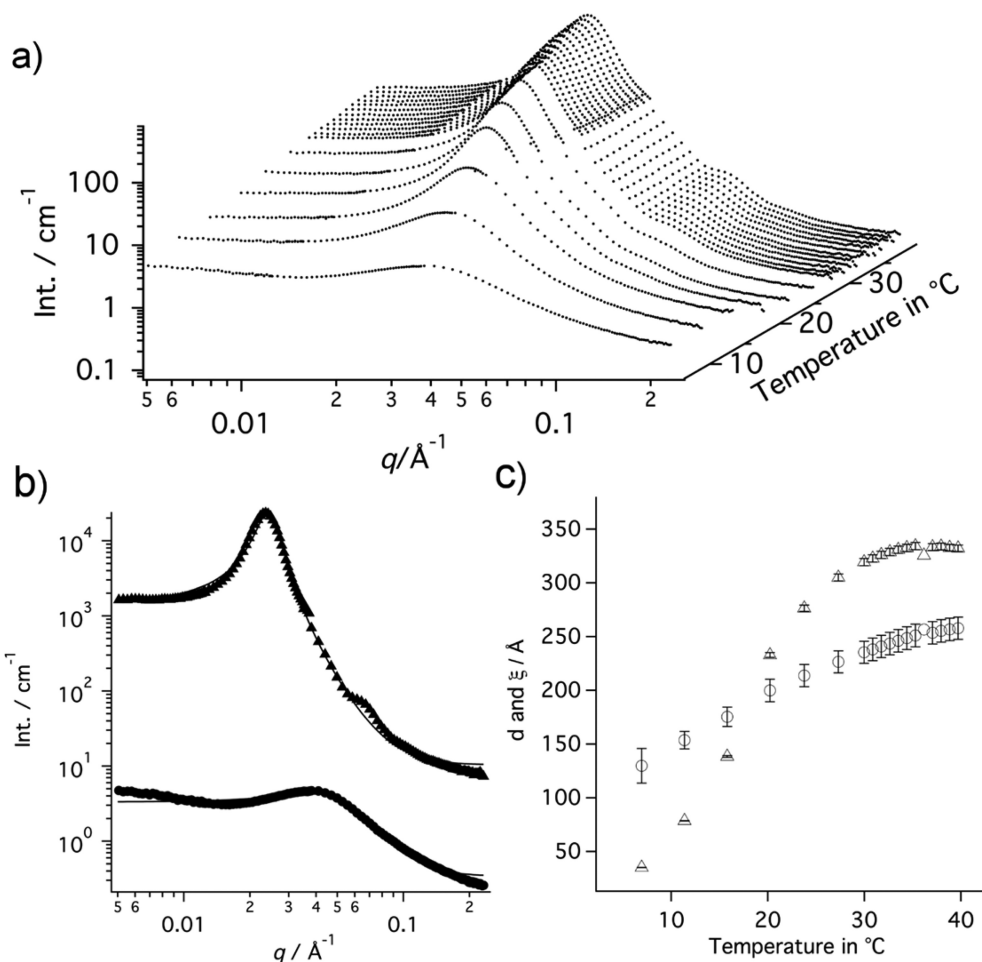


Figure 3. (a) SANS scattering data, (b) representative fits for a bicontinuous sponge-like structure for lowest (at 6.9 °C, dots) and highest (39.7 °C, triangles) temperature, and (c) resulting correlation length ξ (empty triangles) and characteristic domain size d (circles) of 50_B. Please note, the SANS scattering data at 39.7 °C and its respective fit was y -shifted using $\times 64$ for better visibility.

of the two blocks can be deuterated to improve contrast conditions.

For all temperatures, we observed a peak around $q = 0.03 \text{ \AA}^{-1}$ with a plateau before the peak and a sharp decay afterward. We were unable to fit this data assuming a cubic lattice of spherical micelles, unless employing a dispersity of 1, which appears to be physically nonsensical (Figure S4).¹³ Instead, we tested a model of a bicontinuous sponge-like structure as described by Teubner et al.⁶⁵ The expression they found is

$$I(q) = \frac{C}{a_2 + c_1 q^2 + c_2 q^4} \quad (1)$$

Here the proportionality constant $C = (8\pi)/\xi \langle \eta^2 \rangle c_2 V$ with $\langle \eta^2 \rangle$ being the mean square fluctuation of the scattering density ρ , and ξ is the correlation length. c_1 and c_2 are given by

$$\xi = \left[\frac{1}{2} \left(\frac{a_2}{c_2} \right)^{1/2} + \frac{1}{4} \frac{c_1}{c_2} \right]^{-1/2} \quad (2)$$

$$d = 2\pi \left[\frac{1}{2} \left(\frac{a_2}{c_2} \right)^{1/2} - \frac{1}{4} \frac{c_1}{c_2} \right]^{-1/2} \quad (3)$$

where d is the characteristic domain size (periodicity).

This model allowed us to fit the SANS data very well (Figure 3b, Figure S3) and yielded characteristic domain sizes and correlation lengths between 50 and 350 Å, depending on the temperature (Figure 3c). Important to note, the correlation length is a cutoff length, above which correlations are no longer noticeable in the system. At higher temperatures, an increase in the domain size as well as in the correlation length was observed, the latter eventually exceeding the former (at approximately 18 °C, Figure 3c). As this is well below the gelation temperature of this particular system, the correlation length apparently needs to exceed the characteristic distance considerably for a macroscopic rheological response from the system to occur. At temperatures just below 30 °C, the increase of the correlation length levels off, which coincides with macroscopic gelation observed at $\approx 27 \text{ °C}$ (Figure 1d). Both SANS and rheology confirmed that the structure of our hydrogels was very distinct from the commonly used Pluronic gels and may open up new avenues for their use as biomaterials, even though more detailed investigations seem warranted.

The shoulder that becomes visible at temperatures of 28 °C and above at approximately $q = 0.06 \text{ \AA}^{-1}$ is indicative of an additional phase besides the bicontinuous hydrogel in the sample. Unfortunately, as the features of that curve are hidden by the predominant scattering of the bicontinuous phase, only rough estimates concerning the properties of that phase are possible. Fits with a superposition of spherical particles together

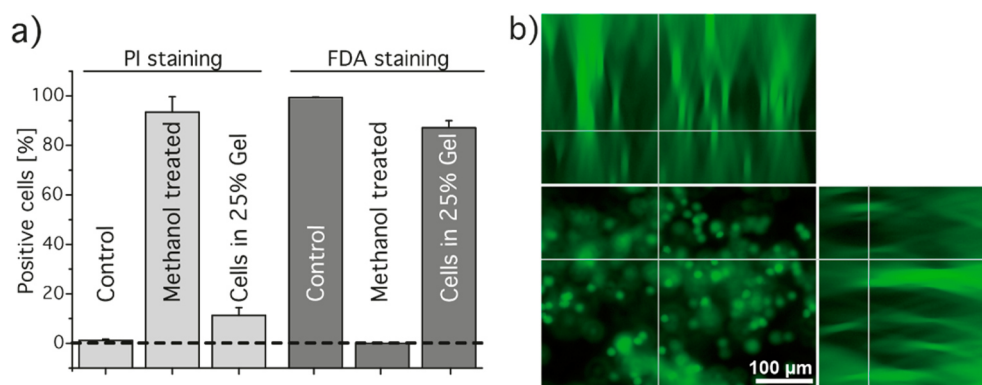


Figure 4. (a) Cell viability of NIH 3T3 fibroblasts and (b) z-stack image of FDA stained cells after incorporation into the bioink (25 wt %) after 24 h at 37 °C of 50_B. The total volume in panel b comprises 559.54 μm (x) × 419.25 (y) μm × 355 μm (z) with 1 μm z-interval.

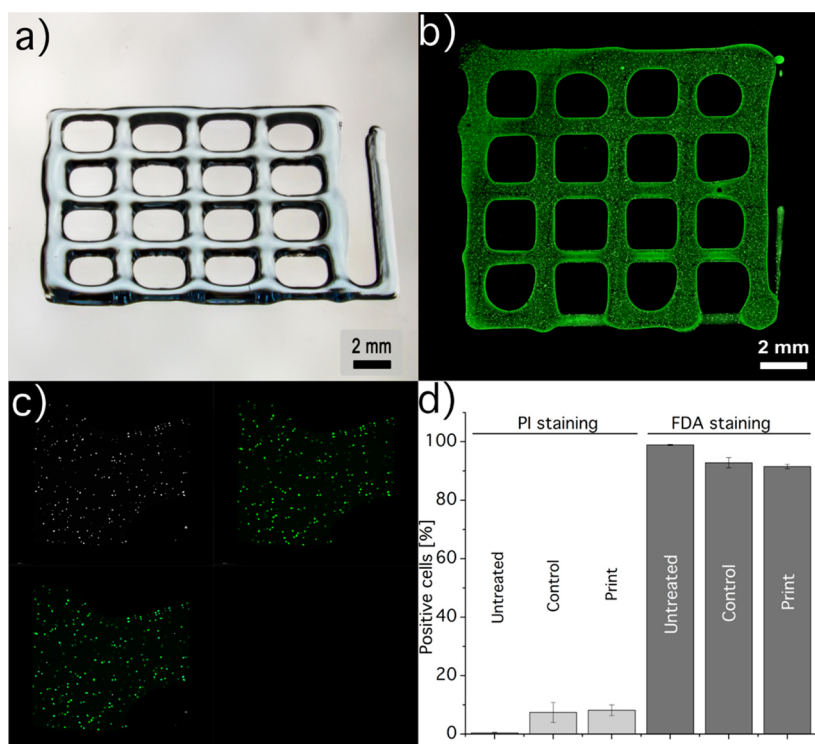


Figure 5. (a) Light microscope image of a printed constructs composed of orthogonal stacks of hydrogel strands with a base area of 12 × 12 mm² and a strand-center to strand-center distance of 3 mm, (b) cell-loaded constructs, (c) detailed view showing cell nucleus stained with Hoechst dye (top left), FDA stained cells (top right), and an overlay image (bottom left), and (d) results of FACS analysis on the influence of the printing process on the viability of NIH 3T3 fibroblasts. While the untreated control represents cells in medium, the control represents cells that were redispersed in the bioink but not printed.

with the form factor described in eq 1 were attempted but proved to be extremely unstable as probably the region of the primary maximum is dominated by the bicontinuous peak. Using the scaling constant C from eq 1, the volume fraction of the bicontinuous gel could be estimated to be $87.5 \pm 2\%$ at 42 °C. Assuming a spherical particle and supposing this maximum is the first maximum of a corresponding scattering curve the volume fraction of this secondary phase of particles is on the order of 1% (1% scattering contribution to the main maximum of the curve). A gauss fit to find the maximum of the shoulder rendered $q = 0.057 \text{ \AA}^{-1}$ at 42 °C, which, with the assumption of being the first maximum, renders a radius of approximately 100 Å. Due to the previously described limitations imposed by the low volume fraction, we did not perform a more detailed analysis of this phase, as any free running fit rendered

unphysical results. Also the position of the peak in the flank of the main peak makes the exact positioning a function of the respective intensities and therefore extremely imprecise, given the unequal distribution of relative intensity.

Comparing these data with previously published material of comparable systems, it is possible to hypothesize that the additional structure giving rise to the additional peak can actually be part of a larger lattice as described by Angelov et al.;⁶⁶ however, the experimental data are not conclusive in either direction as the scattering contribution is too weak for detailed analysis. The possibility of layer formation and thus the resulting Bragg peaks as described by Angelov et al.^{67,68} and Angelova et al.⁶⁹ was considered; however, the resulting fits did not describe the data as accurately as the bicontinuous model. Any further structure analysis of the present hydrogels will

require more experiments, which are currently being planned. However, such detailed SANS analysis, possibly in combination with small-angle X-ray scattering, is outside the scope of the present contribution.

POx have been often described as biocompatible,^{28–30,70–74} while corresponding reports regarding the cyto- or biocompatibility of poly(2-oxazine)s could not be found. We investigated nongelling concentrations of up to 100 g/L and found no marked dose-dependent cytotoxicity in murine NIH 3T3 fibroblasts (Figure S5). This is remarkable, as Schubert and co-workers found cytotoxicity well below this concentration for POx homopolymers.^{34,74} At even higher concentrations, the polymer solutions undergo gelation below 37 °C, also in cell culture media. Therefore, cells were suspended in cell culture media supplemented with 25 wt % 50_B and incubated for 24 h at 37 °C. Subsequently, the temperature was reduced, which resulted into gel liquefaction, and the cells were easily retrieved for analysis via flow cytometry. Also under these conditions, the polymers/gels exhibited very good cytocompatibility. Although a small fraction ($11.2 \pm 3.2\%$) was positive for PI staining (Figure 4a and Figure S6a), the vast majority ($87.1 \pm 2.9\%$) of cells were metabolically active (Figure 4a and Figure S6b). A particularly attractive feature of the new bioink is that cells did not sediment as evidenced by a z-stack analysis of the cell loaded hydrogel (Figure 4b). Important to note, at this point, the bioink does not contain bioinstructive cues such as peptide or sugar moieties or chemical cross-links; however, these can easily be introduced using the rich polymer analogue modifications available for POx and POzi.^{39,55,75,76}

Due to its shear thinning properties and its recovery behavior, our hydrogels seemed suitable for printing via extrusion-based bioprinting. To be able to work at room temperature without risking ink liquefaction, we conducted our first experiments using a 20 wt % concentration of batch 100_B. The pronounced shear thinning of the material enabled processing it at room temperature with a pressure of 1.2 bar using 0.25 mm inner diameter needles. With these settings, it was possible to generate defined constructs composed of orthogonal stacks of hydrogel strands with a base area of $12 \times 12 \text{ mm}^2$ and a strand-center to strand-center distance of 3 mm (Figure 5a).

Furthermore, by mixing 1.0 million/mL NIH-3T3 fibroblasts into this ink, cell-loaded constructs could be generated (Figure 5b). The cells did not influence the printability of the material, and the same setting as for cell-free inks could be applied to process the bioinks. The cell distribution within the constructs was homogeneous throughout the entire constructs (Figure 5c, Video S1 and Video S2). The homogeneous cell distribution was facilitated due to the thermoresponsive properties of the material. At low temperatures (ice bath), the ink has a very low viscosity and cells are readily distributed within the material via repeated mixing by pipetting. Once taken off the ice, the immediate, temperature-driven viscosity increase preserved the homogeneous cell distribution within the ink until the material was dispensed. As noted by Malda et al., it can be challenging to homogeneously distribute cells in highly viscous bioinks due to various issues (air bubbles, difficult pipetting/handling).⁷⁷ To analyze whether dispensing had a negative effect on cell viability, NIH-3T3 cells included in biofabricated scaffolds were further investigated via flow cytometry (Figure 5d). This revealed similar levels of cytocompatibility ($91.5\% \pm 0.8\%$) compared to cells incorporated into the material without further processing ($92.8\% \pm 1.7\%$) and untreated control cells

($98.9\% \pm 0.18\%$). Therefore, the printing process seems to have no effect on the cell viability when using our bioink.

CONCLUSION

In summary, we report on a series of thermogelling synthetic block copolymers comprising hydrophilic PMeOx and thermoresponsive PnPrOzi as excellent bioink candidates. The material is highly cytocompatible, and yields stable hydrogels with unusually high mechanical strength ($G' \approx 4 \text{ kPa}$) for a thermogelling material. At the same time, this material exhibits an unusual temperature–viscosity profile and pronounced shear thinning. SANS analysis revealed an unusual bicontinuous sponge-like structure. The formed hydrogels are optically clear, making them ideally accessible for light microscopy. In particular, in biofabrication, thermoresponsive gels are currently heavily investigated, but new materials that allow the tuning of the response temperature and the rheological properties are urgently needed. We found that our bioink was readily loaded with cells and subsequently printed with no negative effects upon the cell viability. Considering the rich chemistry available for POx and POzi, this contribution opens many new avenues for further basic and applied research.

ASSOCIATED CONTENT

Supporting Information

The Supporting Information is available free of charge on the ACS Publications website at DOI: 10.1021/acs.biomac.7b00481.

Schematic presentation of the copolymerization, ¹H NMR of polymers 50_A – 50_E and 100_A – 100_D, amplitude sweep for 50_B, additional SANS data and respective fits, SANS data with fits for polydisperse hard spheres, proliferation of NIH-3T3 cells, and flow cytometry analysis (PDF)

Homogenous cell distribution within the constructs (AVI)

Homogenous cell distribution within the constructs (AVI)

AUTHOR INFORMATION

Corresponding Author

*E-mail: robert.luxenhofer@uni-wuerzburg.de.

ORCID

Tessa Lühmann: 0000-0001-7552-6435

Robert Luxenhofer: 0000-0001-5567-7404

Notes

The authors declare the following competing financial interest(s): Thomas Lorson and Robert Luxenhofer are listed as co-inventors on a patent application pertinent to the materials described in the contribution.

ACKNOWLEDGMENTS

The authors would like to thank the Free State of Bavaria for start-up funding through the German Plastics Center SKZ and the University Würzburg. We thank André Muthig, Alexander Herrmann, Christian May, and Bernhard Brück for technical support.

■ REFERENCES

- (1) Kretlow, J. D.; Young, S.; Klouda, L.; Wong, M.; Mikos, A. G. Injectable Biomaterials for Regenerating Complex Craniofacial Tissues. *Adv. Mater.* **2009**, *21*, 3368–3393.
- (2) Peppas, N. A.; Hilt, J. Z.; Khademhosseini, A.; Langer, R. Hydrogels in Biology and Medicine: From Molecular Principles to Bionanotechnology. *Adv. Mater.* **2006**, *18*, 1345–1360.
- (3) Lee, K. Y.; Mooney, D. J. Hydrogels for Tissue Engineering. *Chem. Rev.* **2001**, *101*, 1869–1880.
- (4) Jüngst, T.; Smolan, W.; Schacht, K.; Scheibel, T.; Groll, J. Strategies and Molecular Design Criteria for 3D Printable Hydrogels. *Chem. Rev.* **2016**, *116*, 1496–1539.
- (5) Kirchmayer, D. M.; Gorkin, R., III; in het Panhuis, M. An overview of the suitability of hydrogel-forming polymers for extrusion-based 3D-printing. *J. Mater. Chem. B* **2015**, *3*, 4105–4117.
- (6) Fedorovich, N. E.; De Wijn, J. R.; Verbout, A. J.; Alblas, J.; Dhert, W. J. A. Three-dimensional fiber deposition of cell-laden, viable, patterned constructs for bone tissue printing. *Tissue Eng.* **2008**, *14*, 127–133.
- (7) Klouda, L. Thermoresponsive hydrogels in biomedical applications: A seven-year update. *Eur. J. Pharm. Biopharm.* **2015**, *97*, 338–349.
- (8) Schild, H. G. Poly(N-isopropylacrylamide): Experiment, theory and application. *Prog. Polym. Sci.* **1992**, *17*, 163–249.
- (9) Stile, R. A.; Burghardt, W. R.; Healy, K. E. Synthesis and Characterization of Injectable Poly(N-isopropylacrylamide)-Based Hydrogels That Support Tissue Formation in Vitro. *Macromolecules* **1999**, *32*, 7370–7379.
- (10) Alexandridis, P.; Alan Hatton, T. Poly(ethylene oxide)-poly(propylene oxide)-poly(ethylene oxide) block copolymer surfactants in aqueous solutions and at interfaces: Thermodynamics, structure, dynamics, and modeling. *Colloids Surf., A* **1995**, *96*, 1–46.
- (11) Kabanov, A. V.; Batrakova, E. V.; Sriadibhatla, S.; Yang, Z.; Kelly, D. L.; Alakov, V. Y. Polymer genomics: Shifting the gene and drug delivery paradigms. *J. Controlled Release* **2005**, *101*, 259–271.
- (12) Thonhoff, J. R.; Lou, D. I.; Jordan, P. M.; Zhao, X.; Wu, P. Compatibility of human fetal neural stem cells with hydrogel biomaterials in vitro. *Brain Res.* **2008**, *1187*, 42–51.
- (13) Mortensen, K.; Talmon, Y. Cryo-TEM and SANS Microstructural Study of Pluronic Polymer Solutions. *Macromolecules* **1995**, *28*, 8829–8834.
- (14) Aoi, K.; Okada, M. Polymerization of oxazolines. *Prog. Polym. Sci.* **1996**, *21*, 151–208.
- (15) Huber, S.; Jordan, R. Modulation of the lower critical solution temperature of 2-Alkyl-2-oxazoline copolymers. *Colloid Polym. Sci.* **2008**, *286*, 395–402.
- (16) Park, J.-S.; Kataoka, K. Precise Control of Lower Critical Solution Temperature of Thermosensitive Poly(2-isopropyl-2-oxazoline) via Gradient Copolymerization with 2-Ethyl-2-oxazoline as a Hydrophilic Comonomer. *Macromolecules* **2006**, *39*, 6622–6630.
- (17) Lin, P.; Clash, C.; Pearce, E. M.; Kwei, T. K.; Aponte, M. A. Solubility and miscibility of poly(ethyl oxazoline). *J. Polym. Sci., Part B: Polym. Phys.* **1988**, *26*, 603–619.
- (18) Bloksma, M. M.; Paulus, R. M.; van Kuringen, H. P. C.; van der Woerd, F.; Lambermont-Thijs, H. M. L.; Schubert, U. S.; Hoogenboom, R. Thermoresponsive poly(2-oxazine)s. *Macromol. Rapid Commun.* **2012**, *33*, 92–96.
- (19) Weber, C.; Hoogenboom, R.; Schubert, U. S. Temperature responsive bio-compatible polymers based on poly(ethylene oxide) and poly(2-oxazoline)s. *Prog. Polym. Sci.* **2012**, *37*, 686–714.
- (20) Hoogenboom, R.; Schlaad, H. Bioinspired Poly(2-oxazoline)s. *Polymers* **2011**, *3*, 467–488.
- (21) Hoogenboom, R.; Schlaad, H. Thermoresponsive poly(2-oxazoline)s, polypeptoids, and polypeptides. *Polym. Chem.* **2017**, *8*, 24–40.
- (22) Kim, J.-H.; Jung, Y.; Lee, D.; Jang, W.-D. Thermoresponsive Polymer and Fluorescent Dye Hybrids for Tunable Multicolor Emission. *Adv. Mater.* **2016**, *28*, 3499–3503.
- (23) Rinkenauer, A. C.; Tauhardt, L.; Wendler, F.; Kempe, K.; Gottschaldt, M.; Traeger, A.; Schubert, U. S. A Cationic Poly(2-oxazoline) with High In Vitro Transfection Efficiency Identified by a Library Approach. *Macromol. Biosci.* **2015**, *15*, 414–425.
- (24) He, Z.; Miao, L.; Jordan, R.; S-Manickam, D.; Luxenhofer, R.; Kabanov, A. V. A Low Protein Binding Cationic Poly(2-oxazoline) as Non-Viral Vector. *Macromol. Biosci.* **2015**, *15*, 1004–1020.
- (25) von Erlach, T.; Zwicker, S.; Pidhatika, B.; Konradi, R.; Textor, M.; Hall, H.; Lühmann, T. Formation and characterization of DNA-polymer-condensates based on poly(2-methyl-2-oxazoline) grafted poly(l-lysine) for non-viral delivery of therapeutic DNA. *Biomaterials* **2011**, *32*, S291–S303.
- (26) Tong, J.; Luxenhofer, R.; Yi, X.; Jordan, R.; Kabanov, A. V. Protein Modification with Amphiphilic Block Copoly(2-oxazoline)s as a New Platform for Enhanced Cellular Delivery. *Mol. Pharmaceutics* **2010**, *7*, 984–992.
- (27) Eskow Jaunarajs, K. L.; Standaert, D. G.; Viegas, T. X.; Bentley, M. D.; Fang, Z.; Dizman, B.; Yoon, K.; Weimer, R.; Ravenscroft, P.; Johnston, T. H.; Hill, M. P.; Brotchie, J. M.; Moreadith, R. W. Rotigotine polyoxazoline conjugate SER-214 provides robust and sustained antiparkinsonian benefit. *Mov. Disord.* **2013**, *28*, 1675–1682.
- (28) He, Z.; Schulz, A.; Wan, X.; Seitz, J.; Bludau, H.; Alakhova, D. Y.; Darr, D. B.; Perou, C. M.; Jordan, R.; Ojima, I.; Kabanov, A. V.; Luxenhofer, R. Poly(2-oxazoline) based micelles with high capacity for 3rd generation taxoids: Preparation, in vitro and in vivo evaluation. *J. Controlled Release* **2015**, *208*, 67–75.
- (29) Luxenhofer, R.; Schulz, A.; Roques, C.; Li, S.; Bronich, T. K.; Batrakova, E. V.; Jordan, R.; Kabanov, A. V. Doubly amphiphilic poly(2-oxazoline)s as high-capacity delivery systems for hydrophobic drugs. *Biomaterials* **2010**, *31*, 4972–4979.
- (30) Luxenhofer, R.; Han, Y.; Schulz, A.; Tong, J.; He, Z.; Kabanov, A. V.; Jordan, R. Poly(2-oxazoline)s as polymer therapeutics. *Macromol. Rapid Commun.* **2012**, *33*, 1613–1631.
- (31) Lühmann, T.; Schmidt, M.; Leiske, M. N.; Spieler, V.; Majdanski, T. C.; Grube, M.; Hartlieb, M.; Nischang, I.; Schubert, S.; Schubert, U. S.; Meinel, L. Site-Specific POxylation of Interleukin-4. *ACS Biomater. Sci. Eng.* **2017**, *3*, 304–312.
- (32) Raveendran, R.; Mullen, K. M.; Wellard, R. M.; Sharma, C. P.; Hoogenboom, R.; Dargaville, T. R. Poly(2-oxazoline) block copolymer nanoparticles for curcumin loading and delivery to cancer cells. *Eur. Polym. J.* **2017**, DOI: 10.1016/j.eurpolymj.2017.02.043.
- (33) Moreadith, R. W.; Viegas, T. X.; Bentley, M. D.; Harris, J. M.; Fang, Z.; Yoon, K.; Dizman, B.; Weimer, R.; Rae, B. P.; Li, X.; Rader, C.; Standaert, D.; Olanow, W. Clinical development of a poly(2-oxazoline) (POZ) polymer therapeutic for the treatment of Parkinson's disease – Proof of concept of POZ as a versatile polymer platform for drug development in multiple therapeutic indications. *Eur. Polym. J.* **2017**, *88*, 524–552.
- (34) Bauer, M.; Lautenschlaeger, C.; Kempe, K.; Tauhardt, L.; Schubert, U. S.; Fischer, D. Poly(2-ethyl-2-oxazoline) as Alternative for the Stealth Polymer Poly(ethylene glycol): Comparison of in vitro Cytotoxicity and Hemocompatibility. *Macromol. Biosci.* **2012**, *12*, 986–998.
- (35) He, Z.; Wan, X.; Schulz, A.; Bludau, H.; Dobrovolskaia, M. A.; Stern, S. T.; Montgomery, S. A.; Yuan, H.; Li, Z.; Alakhova, D.; Sokolsky, M.; Darr, D. B.; Perou, C. M.; Jordan, R.; Luxenhofer, R.; Kabanov, A. V. A high capacity polymeric micelle of paclitaxel: Implication of high dose drug therapy to safety and in vivo anti-cancer activity. *Biomaterials* **2016**, *101*, 296–309.
- (36) Dargaville, T. R.; Forster, R.; Farrugia, B. L.; Kempe, K.; Voorhaar, L.; Schubert, U. S.; Hoogenboom, R. Poly(2-oxazoline) hydrogel monoliths via thiol-ene coupling. *Macromol. Rapid Commun.* **2012**, *33*, 1695–1700.
- (37) Haigh, J. N.; Chuang, Y.-M.; Farrugia, B.; Hoogenboom, R.; Dalton, P. D.; Dargaville, T. R. Hierarchically Structured Porous Poly(2-oxazoline) Hydrogels. *Macromol. Rapid Commun.* **2016**, *37*, 93–99.

- (38) Kelly, A. M.; Wiesbrock, F. Strategies for the synthesis of poly(2-oxazoline)-based hydrogels. *Macromol. Rapid Commun.* **2012**, *33*, 1632–1647.
- (39) Chujo, Y.; Sada, K.; Saegusa, T. Reversible gelation of polyoxazoline by means of Diels-Alder reaction. *Macromolecules* **1990**, *23*, 2636–2641.
- (40) Zahoranová, A.; Kroneková, Z.; Zahoran, M.; Chorvát, D.; Janigová, I.; Kronek, J. Poly(2-oxazoline) hydrogels crosslinked with aliphatic bis(2-oxazoline)s: Properties, cytotoxicity, and cell cultivation. *J. Polym. Sci., Part A: Polym. Chem.* **2016**, *54*, 1548–1559.
- (41) Zahoranová, A.; Kronek, J. Hydrogels Based on Poly(2-oxazoline)s for Pharmaceutical Applications. In *Handbook of Polymers for Pharmaceutical Technologies: Bioactive and Compatible Synthetic/Hybrid Polymers*; Thakur, V. K., Thakur, M. K., Ed.; Scrivener Publishing, LLC: Salem, MA, 2016; Vol. 4, pp 231–258.
- (42) Hochleitner, G.; Hümmel, J. F.; Luxenhofer, R.; Groll, J. High definition fibrous poly(2-ethyl-2-oxazoline) scaffolds through melt electrospinning writing. *Polymer* **2014**, *55*, 5017–5023.
- (43) Zahoranová, A.; Mrlík, M.; Tomanová, K.; Kronek, J.; Luxenhofer, R. ABA and BAB triblock copolymers based on 2-methyl-2-oxazoline and 2-n-propyl-2-oxazoline: Synthesis and thermoresponsive behavior in water. *Macromol. Chem. Phys.* **2017**, DOI: 10.1002/macp.201700031.
- (44) Levy, A.; Litt, M. Polymerization of cyclic imino ethers. II. Oxazines. *J. Polym. Sci., Part B: Polym. Lett.* **1967**, *5*, 881–886.
- (45) Kobayashi, S.; Igarashi, T.; Moriuchi, Y.; Saegusa, T. Block copolymers from cyclic imino ethers: A new class of nonionic polymer surfactant. *Macromolecules* **1986**, *19*, 535–541.
- (46) Censi, R.; Schuurman, W.; Malda, J.; Di Dato, G.; Burgisser, P. E.; Dhert, W. J. A.; van Nostrum, C. F.; Di Martino, P.; Vermonden, T.; Hennink, W. E. A Printable Photopolymerizable Thermosensitive p(HPMAm-lactate)-PEG Hydrogel for Tissue Engineering. *Adv. Funct. Mater.* **2011**, *21*, 1833–1842.
- (47) Groll, J.; Boland, T.; Blunk, T.; Burdick, J. A.; Cho, D.-W.; Dalton, P. D.; Derby, B.; Forgacs, G.; Li, Q.; Mironov, V. A.; Moroni, L.; Nakamura, M.; Shu, W.; Takeuchi, S.; Vozzi, G.; Woodfield, T. B. F.; Xu, T.; Yoo, J. J.; Malda, J. Biofabrication: reappraising the definition of an evolving field. *Biofabrication* **2016**, *8*, 013001.
- (48) Shi, K.; Wang, Y.-L.; Qu, Y.; Liao, J.-F.; Chu, B.-Y.; Zhang, H.-P.; Luo, F.; Qian, Z.-Y. Synthesis, characterization, and application of reversible PDLLA-PEG-PDLLA copolymer thermogels in vitro and in vivo. *Sci. Rep.* **2016**, *6*, 19077.
- (49) Malda, J.; Visser, J.; Melchels, F. P.; Jüngst, T.; Hennink, W. E.; Dhert, W. J. A.; Groll, J.; Hutmacher, D. W. 25th anniversary article: Engineering hydrogels for biofabrication. *Adv. Mater.* **2013**, *25*, 5011–5028.
- (50) Wang, S.; Lee, J. M.; Yeong, W. Y. Smart hydrogels for 3D bioprinting. *Int. J. Bioprinting* **2015**, *1*, 3–14.
- (51) Murphy, S. V.; Atala, A. 3D bioprinting of tissues and organs. *Nat. Biotechnol.* **2014**, *32*, 773–785.
- (52) Feoktystov, A. V.; Frielinghaus, H.; Di, Z.; Jaksch, S.; Pipich, V.; Appavou, M.-S.; Babcock, E.; Hanslik, R.; Engels, R.; Kemmerling, G.; Kleines, H.; Ioffe, A.; Richter, D.; Brückel, T. KWS-1 high-resolution small-angle neutron scattering instrument at JCNS: Current state. *J. Appl. Crystallogr.* **2015**, *48*, 61–70.
- (53) Kline, S. R. Reduction and analysis of SANS and USANS data using IGOR Pro. *J. Appl. Crystallogr.* **2006**, *39*, 895–900.
- (54) Sinnwell, S.; Ritter, H. Microwave Accelerated Polymerization of 2-Phenyl-5,6-dihydro-4H-1,3-oxazine: Kinetics and Influence of End-Groups on Glass Transition Temperature. *Macromol. Rapid Commun.* **2006**, *27*, 1335–1340.
- (55) Luxenhofer, R.; Jordan, R. Click Chemistry with Poly(2-oxazoline)s. *Macromolecules* **2006**, *39*, 3509–3516.
- (56) Gutmann, M.; Memmel, E.; Braun, A.; Seibel, J.; Meinel, L.; Lühmann, T. Biocompatible azide alkyne "click" reactions for surface decoration of glyco-engineered cells. *ChemBioChem* **2016**, *17*, 886–875.
- (57) Ross, D. D.; Joneckis, C. C.; Ordóñez, J. V.; Sisk, A. M.; Wu, R. K.; Hamburger, A. W.; Nora, R. E. Estimation of Cell Survival by Flow Cytometric Quantification of Fluorescein Diacetate/Propidium Iodide Viable Cell Number. *Cancer Res.* **1989**, *49*, 3776–3782.
- (58) Jones, K. H.; Senft, J. A. An improved method to determine cell viability by simultaneous staining with fluorescein diacetate-propidium iodide. *J. Histochem. Cytochem.* **1985**, *33*, 77–79.
- (59) Clarke, J. M.; Gillings, M. R.; Altavilla, N.; Beattie, A. J. Potential problems with fluorescein diacetate assays of cell viability when testing natural products for antimicrobial activity. *J. Microbiol. Methods* **2001**, *46*, 261–267.
- (60) Li, C.; Buurma, N. J.; Haq, I.; Turner, C.; Armes, S. P.; Castelletto, V.; Hamley, I. W.; Lewis, A. L. Synthesis and Characterization of Biocompatible, Thermoresponsive ABC and ABA Triblock Copolymer Gelators. *Langmuir* **2005**, *21*, 11026–11033.
- (61) Xuan, S.; Lee, C.-U.; Chen, C.; Doyle, A. B.; Zhang, Y.; Guo, L.; John, V. T.; Hayes, D.; Zhang, D. Thermoreversible and Injectable ABC Polypeptoid Hydrogels: Controlling the Hydrogel Properties through Molecular Design. *Chem. Mater.* **2016**, *28*, 727–737.
- (62) Grassi, G.; Crevatin, A.; Farra, R.; Guarnieri, G.; Pascotto, A.; Rehmers, B.; Lapasin, R.; Grassi, M. Rheological properties of aqueous Pluronic–alginate systems containing liposomes. *J. Colloid Interface Sci.* **2006**, *301*, 282–290.
- (63) Luxenhofer, R. Polymers and nanomedicine: considerations on variability and reproducibility when combining complex systems. *Nanomedicine* **2015**, *10*, 3109–3119.
- (64) Kolesky, D. B.; Truby, R. L.; Gladman, A. S.; Busbee, T. A.; Homan, K. A.; Lewis, J. A. 3D Bioprinting of Vascularized, Heterogeneous Cell-Laden Tissue Constructs. *Adv. Mater.* **2014**, *26*, 3124–3130.
- (65) Teubner, M.; Strey, R. Origin of the scattering peak in microemulsions. *J. Chem. Phys.* **1987**, *87*, 3195–3200.
- (66) Angelov, B.; Angelova, A.; Mutafchieva, R.; Lesieur, S.; Vainio, U.; Garamus, V. M.; Jensen, G. V.; Pedersen, J. S. SAXS investigation of a cubic to a sponge (L3) phase transition in self-assembled lipid nanocarriers. *Phys. Chem. Chem. Phys.* **2011**, *13*, 3073–3081.
- (67) Angelov, B.; Angelova, A.; Filippov, S. K.; Narayanan, T.; Drechsler, M.; Štěpánek, P.; Couvreur, P.; Lesieur, S. DNA/Fusogenic Lipid Nanocarrier Assembly: Millisecond Structural Dynamics. *J. Phys. Chem. Lett.* **2013**, *4*, 1959–1964.
- (68) Angelov, B.; Angelova, A.; Filippov, S. K.; Drechsler, M.; Štěpánek, P.; Lesieur, S. Multicompartment lipid cubic nanoparticles with high protein upload: millisecond dynamics of formation. *ACS Nano* **2014**, *8*, 5216–5226.
- (69) Angelova, A.; Angelov, B.; Garamus, V. M.; Couvreur, P.; Lesieur, S. Small-Angle X-ray Scattering Investigations of Biomolecular Confinement, Loading, and Release from Liquid-Crystalline Nanochannel Assemblies. *J. Phys. Chem. Lett.* **2012**, *3*, 445–457.
- (70) Luxenhofer, R.; Sahay, G.; Schulz, A.; Alakhova, D.; Bronich, T. K.; Jordan, R.; Kabanov, A. V. Structure-property relationship in cytotoxicity and cell uptake of poly(2-oxazoline) amphiphiles. *J. Controlled Release* **2011**, *153*, 73–82.
- (71) Gaertner, F. C.; Luxenhofer, R.; Blechert, B.; Jordan, R.; Essler, M. Synthesis, biodistribution and excretion of radiolabeled poly(2-alkyl-2-oxazoline)s. *J. Controlled Release* **2007**, *119*, 291–300.
- (72) Kronek, J.; Lustoň, J.; Kroneková, Z.; Paulovičová, E.; Farkaš, P.; Petrenčíková, N.; Paulovičová, L.; Janigová, I. Synthesis and immunological efficiency of poly(2-oxazolines) containing a free amino group. *J. Mater. Sci.: Mater. Med.* **2010**, *21*, 879–886.
- (73) Chen, Y.; Pidhatika, B.; von Erlach, T.; Konradi, R.; Textor, M.; Hall, H.; Lühmann, T. Comparative assessment of the stability of nonfouling poly(2-methyl-2-oxazoline) and poly(ethylene glycol) surface films: An in vitro cell culture study. *Biointerphases* **2014**, *9*, 031003.
- (74) Bauer, M.; Schroeder, S.; Tauhardt, L.; Kempe, K.; Schubert, U. S.; Fischer, D. In vitro hemocompatibility and cytotoxicity study of poly(2-methyl-2-oxazoline) for biomedical applications. *J. Polym. Sci., Part A: Polym. Chem.* **2013**, *51*, 1816–1821.

(75) Gress, A.; Völkel, A.; Schlaad, H. Thio-Click Modification of Poly[2-(3-butenyl)-2-oxazoline]. *Macromolecules* **2007**, *40*, 7928–7933.

(76) Schmitz, M.; Kuhlmann, M.; Reimann, O.; Hackenberger, C. P. R.; Groll, J. Side-chain cysteine-functionalized poly(2-oxazoline)s for multiple peptide conjugation by native chemical ligation. *Biomacromolecules* **2015**, *16*, 1088–1094.

(77) Mouser, V. H. M.; Melchels, F. P. W.; Visser, J.; Dhert, W. J. A.; Gawlitta, D.; Malda, J. Yield stress determines bioprintability of hydrogels based on gelatin-methacryloyl and gellan gum for cartilage bioprinting. *Biofabrication* **2016**, *8*, 035003.

Although not further discussed in the context of drug-loaded hydrogels, another thermogelling polymer was discovered during the formulation studies using 18 different triblock copolymers. Interestingly, the copolymer with a modestly hydrophobic poly(2-*iso*-butyl-2-oxazoline) core was (by visual inspection) the only triblock copolymer exhibiting pronounced thermogelling properties. In contrast to the above discussed diblock copolymer, mechanical strength after gelation was lower with maximum 1 kPa and shear recovery from high strain deformations (shear thinning) to full strength took approximately 2 min, even though return to the gel state appeared immediate. Again, cytocompatibility for Calu-3 human lung adenocarcinoma and human embryonic kidney HEK293 cells was excellent even at highest investigated polymer concentrations of 10 wt.% (liquid state). Preliminary printing experiments showed reasonably good shape integrity up to strand distances of 1 mm (smaller distances caused merging of the individual strands). Although shape fidelity of a two-layer printed construct was reasonably good, merging of the construct occurred at 4-layers, inhibiting 3D printing at that point. Nevertheless, it is interesting how minute changes in the chemical structure of the hydrophobic block not only affect formulation, but also gelation properties. This becomes evident by the negligible-thermogelling behavior of the structural isomers comprising a poly(2-*n*-butyl-2-oxazoline) or a poly(2-*n*-propyl-2-oxazine) core, as discussed in the following publication.

Article

Temperature-Dependent Rheological and Viscoelastic Investigation of a Poly(2-methyl-2-oxazoline)-*b*-poly(2-*iso*-butyl-2-oxazoline)-*b*-poly(2-methyl-2-oxazoline)-Based Thermogelling Hydrogel

Michael M. Lübtow¹, Miroslav Mrlik^{1,2} , Lukas Hahn¹, Alexander Altmann¹, Matthias Beudert³, Tessa Lühmann³ and Robert Luxenhofer^{1,*} 

¹ Polymer Functional Materials, Chair for Advanced Materials Synthesis, Department of Chemistry and Pharmacy and Bavarian Polymer Institute, Julius-Maximilians-University Würzburg, 97084 Würzburg, Germany

² Centre of Polymer Systems, University Institute, Tomas Bata University in Zlin, Trida T. Bati 5678, 760 01 Zlin, Czech Republic

³ Institute of Pharmacy and Food Chemistry, Julius-Maximilians-University Würzburg, Am Hubland, 97074 Würzburg, Germany

* Correspondence: robert.luxenhofer@uni-wuerzburg.de

Received: 14 May 2019; Accepted: 30 July 2019; Published: 7 August 2019



Abstract: The synthesis and characterization of an ABA triblock copolymer based on hydrophilic poly(2-methyl-2-oxazoline) (pMeOx) blocks A and a modestly hydrophobic poly(2-*iso*-butyl-2-oxazoline) (p*i*BuOx) block B is described. Aqueous polymer solutions were prepared at different concentrations (1–20 wt %) and their thermogelling capability using visual observation was investigated at different temperatures ranging from 5 to 80 °C. As only a 20 wt % solution was found to undergo thermogelation, this concentration was investigated in more detail regarding its temperature-dependent viscoelastic profile utilizing various modes (strain or temperature sweep). The prepared hydrogels from this particular ABA triblock copolymer have interesting rheological and viscoelastic properties, such as reversible thermogelling and shear thinning, and may be used as bioink, which was supported by its very low cytotoxicity and initial printing experiments using the hydrogels. However, the soft character and low yield stress of the gels do not allow real 3D printing at this point.

Keywords: amphiphilic block copolymer; poly(2-oxazoline); viscoelasticity; thermoresponsive hydrogel; cytocompatibility

1. Introduction

Thermoresponsive polymers are a type of “smart” material which change their appearance and physical properties upon a change in temperature [1]. Such materials can serve as functional biomaterials, for example, as bioinks [2]. The thermoresponsive character can manifest in various manners. First and most commonly, at a critical temperature, a clear polymer solution may become turbid as the polymer forms mesoglobules with strongly increased light scattering. This temperature is called the “cloud point”, and it may depend on the solvent quality and polymer concentration. The lowest cloud point with respect to the polymer concentration is called the lower critical solution temperature (LCST) and is often accompanied by a decrease in viscosity. This phenomenon is typically reversible but may show some hysteresis [3–6]. Second, thermoresponsive polymer solutions may undergo thermogelling, which can be described as a

significant change in agglomeration/aggregation and which significantly increases the viscosity upon thermal stimulation [7–9]. In most cases, the transition from solution to gel takes place when the temperature increases [10–12]; however, there are also materials which show a gel-to-solution transition with increasing temperature, called “inverse gelation” [13]. One very prominent thermogelling polymer is Pluronic®F127, an ABA triblock copolymer bearing hydrophilic poly(ethylene glycol) as the A blocks and thermoresponsive poly(propylene glycol) as the B block. Another family of polymers which has a rich and versatile thermoresponsive profile and has received a lot of attention in recent years due to their applicability in various biomedical contexts are poly(2-oxazoline)s (POx) [3,14–17]. These structural isomers of polypeptides are accessible via living cationic ring-opening polymerization (LCROP) of 5-membered cyclic imino ethers, the 2-oxazolines [18]. Besides the use of POx in, e.g., protein/drug conjugates [14,19–25], non-covalent drug delivery systems [26–35], and anti-fouling modifications/surfaces [36–42], a plethora of POx-based hydrogels as soft biomaterials have been developed [43–46]. The emergence of the latter was supported by the low cytotoxicity/high biocompatibility of POx-based hydrogels [43], enabling their application as, e.g., bioink [46].

In a recent study [47], a small library of POx-based ABA triblock copolymers were synthesized based on 2-*n*-propyl-2-oxazoline and 2-methyl-2-oxazoline with the aim to mimic the behavior of Pluronic®F127. However, these polymers did not show any gelation, even at higher concentration (20–30 wt %) even though the materials exhibit cloud points depending on the ratio between individual blocks. In contrast, Monnery and Hoogenboom very recently reported that a BAB triblock copolymer with an inner block of poly(2-ethyl-2-oxazoline) and outer blocks of poly(2-*n*-propyl-2-oxazoline) showed irreversible thermal gelation at 20 wt % upon heating if the central block showed an extremely high degree of polymerization of 900 [48]. Contrary to this, diblock copolymers bearing poly(2-*n*-propyl-2-oxazoline) and poly(2-methyl-2-oxazoline) blocks showed reproducible thermal gelation at concentrations above 20 wt % at much lower total degrees of polymerization [46]. The obtained storage modulus for this system, containing 100 monomeric units of each block, was found to be 4 kPa.

Here, we investigated the viscoelastic properties of aqueous solutions of a POx-based, amphiphilic ABA triblock copolymer comprising two hydrophilic poly(2-methyl-2-oxazoline) (pMeOx) blocks A and a modestly hydrophobic poly(2-*iso*-butyl-2-oxazoline) (*i*BuOx) block B (A-*i*BuOx-A). A copolymer with the same structure (but with slightly different chain lengths and a different end group) was previously investigated as a drug-delivery system for non-water-soluble drugs such as taxanes [49], curcumin, efavirenz, and others [50]. However, in this study, thermogelling behavior was not observed.

2. Materials and Methods

2.1. Materials

All substances for the preparation of the polymer were purchased from Sigma-Aldrich (Steinheim, Germany) or Acros (Geel, Belgium) and were used as received unless otherwise stated. The monomer 2-*iso*-butyl-2-oxazoline (*i*BuOx) was prepared as previously described [49]. Deuterated chloroform for NMR analysis was obtained from Deutero GmbH (Kastellaun, Germany). The substances used for polymerization, specifically methyl trifluoromethylsulfonate (MeOTf), 2-methyl-2-oxazoline (MeOx), and 2-*iso*-butyl-2-oxazoline (*i*BuOx), were refluxed over CaH₂, distilled, and stored under argon. Benzonitrile (PhCN) was refluxed over phosphorus pentoxide, distilled, and stored under argon. For a detailed description of *i*BuOx synthesis and characterization, the reader is referred to Figure S1 in the supporting information.

2.2. Polymer Synthesis

The polymerization and work-up procedures were carried out as described previously [26]. For polymer synthesis and characterization, see Figures S2 and S3. Briefly, initiator was added to a dried and nitrogen-flushed flask and dissolved in PhCN. The monomer 2-methyl-2-oxazoline

(MeOx) was added, and the reaction mixture was heated to 100 °C for approximately 4 h. Reaction progress and monomer consumption was controlled by FTIR and ¹H-NMR spectroscopy. After complete consumption of MeOx, the mixture was cooled to RT, and 2-*iso*-butyl-2-oxazoline was added. The reaction mixture was heated to 100 °C overnight. The procedure was repeated for the third block, MeOx, and after monomer consumption was confirmed, termination was carried out by addition of 1-*tert*-butyl piperazine 1-carboxylate (PipBoc) at 50 °C for 4 h. Subsequently, K₂CO₃ was added and the mixture was stirred at 50 °C for 4 h. Precipitates were removed by centrifugation and the solvent removed under reduced pressure. The supernatant was transferred into a dialysis bag (molecular weight cut-off (MWCO) 1 kDa, cellulose acetate) and dialyzed against deionized water overnight. The solution was recovered from the bag and lyophilized.

3. Methods

3.1. Nuclear Magnetic Resonance Spectroscopy (NMR)

NMR spectra were recorded on a Fourier 300 (¹H: 300.12 MHz), Bruker Biospin (Rheinstetten, Germany) at 298 K. The spectra were calibrated to the signal of residual protonated solvent (CDCl₃ at 7.26 ppm).

3.2. Gel Permeation Chromatography (GPC)

Gel permeation chromatography (GPC) was performed on an Agilent 1260 Infinity System (Polymer Standards Service (PSS), Mainz, Germany) with hexafluoroisopropanol (HFIP) containing 3 g/L potassium trifluoroacetate as eluent; precolumn: 50 × 8 mm PSS PFG linear M; two columns: 300 × 8 mm PSS PFG linear M (particle size 7 μm; pore size 0.1–1000 kg/mol). The columns were kept at 40 °C and the flow rate was 0.7 mL/min. Prior to each measurement, samples were filtered through 0.2 μm PTFE filters (Roth, Karlsruhe, Germany). Conventional calibration was performed with PEG standards (0.1–1000 kg/mol), and data were processed using WinGPC software.

3.3. Characterization of the Hydrogel

The polymer solution was prepared by dissolving A-*pi*BuOx-A at 20 wt % in deionized water. For complete dissolution, the solution was shaken at 4 °C overnight.

3.4. Rheological Investigations

Rheological and viscoelastic properties were investigated using the Rheometer Physica MCR-301 (Anton Paar, Graz, Austria). Measurements were performed using a stainless steel parallel plate geometry with 25 mm (PP 25) in diameter and a 300 μm gap between the upper and lower plates in all investigations. For steady shear experiments, the control shear rate mode was used to investigate the rheological behavior from 1 s⁻¹ to 500 s⁻¹, and 6 points per decade were used with a logarithmic increase and at various temperatures (5 °C, 25 °C, and 37 °C). In order to investigate the reversibility of the gelation created in the system upon elevated temperatures, the viscosity data were obtained at a shear rate of 1 s⁻¹, and a discrete, stepwise increase of temperatures from 5 °C to 25 °C to 37 °C and back was performed three times. For equilibration, the system was given a one-minute waiting time to reach the desired temperature for both the heating and cooling regimes. The steady shear rheological data, namely, the dependence of the shear stress on the shear rate, were plotted using the Vocadlo model shown in Equation (1) [51], and parameters of the model were calculated using a least square method:

$$\tau = \left[K \frac{1}{n} |\dot{\gamma}|^{\frac{n-1}{n}} + \left(\frac{\tau_0}{|\dot{\gamma}|} \right)^{\frac{1}{n}} \right]^n \dot{\gamma} \quad (1)$$

where τ is the shear stress, K is the consistency index, n is the power law index [51] or flow index [52], $\dot{\gamma}$ is the shear rate, and τ_0 is the yield stress as a measure of the internal structural integrity developed upon elevated temperature.

According to the literature, the Herschel–Bulkley (H-B) model is recommended for investigation of the yield stress for hydrogel structures [52]. The H-B model is described in Equation (2), and the parameters have the same meaning as was described for the Vocadlo model previously:

$$\tau = \tau_0 + K \cdot \dot{\gamma}^n \quad (2)$$

For the investigation of the viscoelastic properties, all measurements were performed in the linear viscoelastic range (LVR). This range was obtained from the amplitude sweep where the storage G' and loss moduli G'' were measured against the strain deformation from 0.01% to 10% for A-*p*iBuOx-A at 5 °C and from 0.01% to 100% at 25 °C and 37 °C. From these experiments, the yield stress was also determined by plotting the dependency of storage G' and loss moduli G'' on the applied shear stress. The onset of G' decrease was defined as the yield point. Then, the frequency sweep from 0.1 Hz up to 100 Hz was measured at the obtained deformation from LVR, namely 2% for 5 °C, 0.2% for 25 °C, and 0.3% for 37 °C. Moreover, the viscoelastic behavior was investigated at 25 °C and 37 °C at a frequency of 1 Hz, and deformations were alternated from 0.1% to 10%. Here, five cycles were measured. This measurement was not performed at 5 °C due to the liquid-like behaviour of the sample; thus, just small differences would be expected due to the nearly Newtonian behavior. Finally, the temperature sweep from 5 °C to 45 °C was measured at a strain of 1% and a frequency of 1 Hz in order to prove the reversible sol-gel transition upon temperature sweep measurement.

3.5. Microscopic Investigations

Microscopic examination was performed on a Crossbeam 340 scanning electron microscope (Zeiss, Oberkochen, Germany). Aqueous polymer solution (20 wt %) was heated to 40 °C (gel state), shock frozen in liquid nitrogen, and freeze-dried. Prior to the measurement, the freeze-dried sample was sputter coated with 20 Å of platinum using an EM ACE 600 sputter coater (Leica, Wetzlar, Germany).

3.6. Printing

Hydrogel scaffolds of a 20 wt % aqueous solution were printed at 30 °C using a compact bench-top 3D bioprinter (Incredible, Cellink, Gothenburg, Sweden) working on the principle of a pneumatic extrusion-based printer. The printing speed was set to 600 mm/min, and a pressure of 50 kPa was applied using a 0.2 mm (27 GA) diameter nozzle (8 mm length) (Nordson EFD, Oberhaching, Germany). First, the printability was established by printing one layer with different strand distances varying over 0.75 mm, 1 mm, 1.25 mm, and 1.5 mm. Two- and four-layered constructs of 12 × 12 mm with four strands and a layer height of 0.3 mm were printed.

3.7. Cell Culture

Human embryonic kidney HEK293 cells (HEK-Blue™ IFN- α/β , Invivogen) were cultured in growth medium (DMEM 10% fetal calf serum (FCS), 100 U/mL penicillin G, and 100 μ g/mL streptomycin) on 25 cm² culture flasks at 37 °C and 5% CO₂. Calu-3 cells (human lung adenocarcinoma, ATCC HTB-55) were maintained in growth medium (MEM 10% FCS, 100 U/mL penicillin G, 100 μ g/mL streptomycin, 1% non-essential amino acids (NEA), 1 mM pyruvate, 2 mM glutamine, and 2.88 g/L glucose) at 37 °C and 5% CO₂.

3.8. WST-1 Proliferation Assay

For the measurement of the cytotoxicity of the polymer, 5000 cells/well of both Calu-3 and HEK cells were seeded in 96-well plates in growth medium and incubated at 37 °C and 5% CO₂ for 24 h and 48 h, respectively. Final polymer concentrations of 10%, 5%, 1%, and 0.1% were prepared from a

stock solution (20 wt %) in growth medium on ice and added to the cells. After 24 h of cell growth, the medium was removed and replaced by fresh cell culture medium. Cells were incubated with WST-1 reagent for 1–4 h at 37 °C according to the manufacturer's manual. The formation of formazan was monitored at 450 and 630 nm using a Spectramax 250 microplate reader (Molecular Devices, San Jose, CA, USA). Results were normalized using cells incubated with polymer-free cell culture medium.

4. Results and Discussions

Previously, A-*pi*BuOx-A was utilized for the solubilization of hydrophobic molecules at a concentration of 10 g/L. Its critical micelle concentration, however, lies much lower, at around 12 mg/L [50]. Inspired by the ongoing search for novel bioinks for utilization in biofabrication [53] and by our previous work on thermoresponsive di- and triblocks based on poly(2-oxazoline)s and poly(2-oxazine)s [46,47], we tested the visual appearance of higher concentrations of aqueous solutions of A-*pi*BuOx-A up to 20 wt % (Figure 1) at different temperatures ranging from 5 °C to 80 °C. At all concentrations and temperatures, the solutions were turbid, more so with increasing concentration, indicating the presence of larger self-assemblies or mesoglobules scattering light. At 5 °C, all samples were clearly liquids of rather low viscosity that flowed freely. At higher temperatures, the viscosity of the 20 wt % solution visibly increased until a turbid gel was formed at 20 °C. The visual impression remained unchanged for all samples up to 80 °C. It is important to note that neither of the blocks of the triblock copolymer exhibited an LCST at around 20 °C. While *pi*BuOx is essentially water-insoluble even at around 0 °C, *p*MeOx is excellently water-soluble even at temperatures approaching 100 °C. Therefore, the gelation cannot be attributed to an LCST of either block, but is a property of the triblock, similar to the situations observed for other thermogelling triblock copolymers [54].

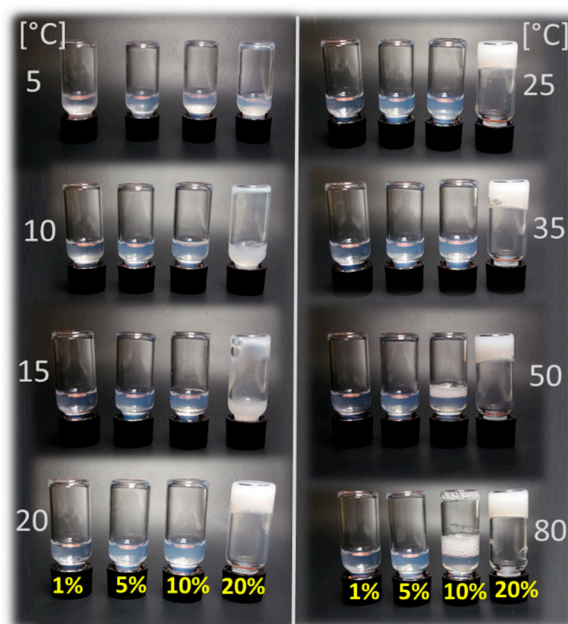


Figure 1. Visual appearance and flow properties of A-*pi*BuOx-A dissolved in H₂O at 1, 5, 10, and 20 wt % (left to right vials) at 5–80 °C. Only at 20 wt %, a turbid, non-flowing gel was formed at T > 20 °C (highly viscous sol at T = 15 °C).

A first impression of the microscopic structure of the hydrogel was obtained by scanning electron microscopy of freeze-dried samples. The structure of the prepared hydrogel is crucial from the point of view of its potential applicability, since the porosity and network structure of the hydrogel influence its mechanical properties. It can be seen that the sample exhibited a porous structure with open pores and a pore size in the range of several micrometers (Figure 2). Such big pores are not necessarily expected for physical hydrogels at such high concentrations, and we cannot rule out at this point that

the observed structure may in part be an artefact from sample preparation (freeze-drying). In particular, some features such as the sharp, teeth-like protrusions (Figure 2, right-hand image) are likely to have originated from sample preparation.

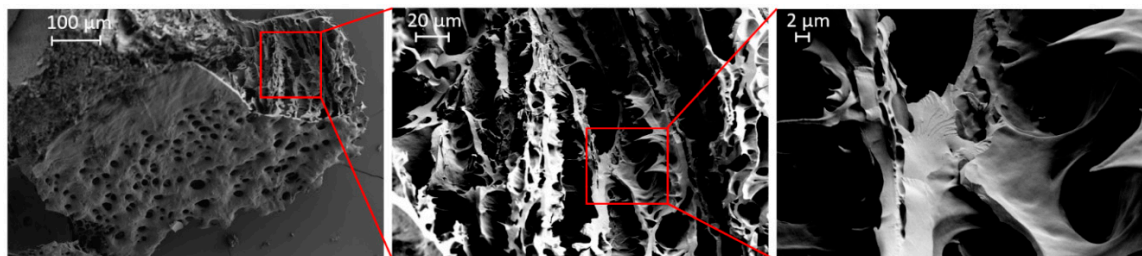


Figure 2. SEM images of the freeze-dried hydrogel (20 wt %) at different magnifications displaying a porous surface and a 3D-interconnected interior.

In order to investigate the reversibility and repeatability of the internal structure formation due to physical cross-linking, the viscosity profiles of the 20 wt % sample were repeatedly recorded during three heating and cooling cycles at 5 °C, 25 °C, and 37 °C (Figure 3a). At 5 °C, viscosities of only 2 Pa·s were obtained. Changing the temperature to 25 °C, a rapid increase in viscosity to 35 Pa·s occurred, further increasing to 60 Pa·s at 37 °C. This pronounced increase in viscosity highlights the material's tunable properties upon various temperature profiles. Most importantly, this behavior was reversible, as cooling down the samples from 37 °C to 25 °C decreased the viscosity again. However, a small hysteresis was observed for the cooling step to 25 °C, as slightly higher viscosities were obtained than at the initial heating stage at 25 °C. In contrast, the initial values of 2 Pa·s were immediately reached upon cooling to 5 °C. During the three cycles, the viscosity profiles upon temperature change were essentially identical.

To determine the reproducibility of the liquefaction and gelation upon continuous temperature change, the viscoelastic properties of the polymer gel were investigated in eight heating/cooling cycles between 5 °C and 45 °C (Figure 3b) in oscillation mode. Again, the results were highly reproducible. The gel points determined as the crossover point of the storage and loss moduli always occurred at approximately 22 °C. Furthermore, the liquefaction process was also very similar during all cycles. Only a minor increase in the storage moduli at low temperatures occurred with progressing cycles, which might be due to minor dehydration of the samples at higher temperatures (45 °C). However, such an increase in G' was not observed at higher temperatures, which does not corroborate significant dehydration. Clearly, the gelation and liquefaction process was highly reproducible and reversible for this hydrogel; this is in contrast to recently published hydrogels based on POx BAB triblock copolymers, which exhibited higher values of the storage modulus but showed irreversible crosslinking (gelation) in consecutive heating/cooling cycles [48].

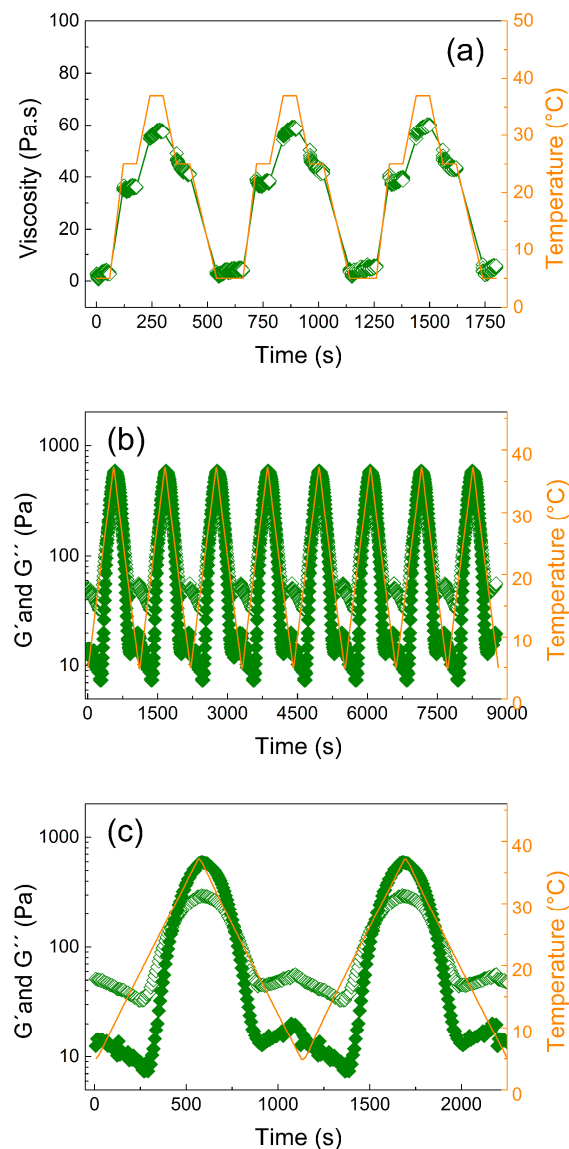


Figure 3. (a) Viscosity measurement under steady shear conditions over time for 20 wt % polymer solution at different temperatures (5 °C, 25 °C, and 37 °C) and a constant shear rate, $\dot{\gamma}$, of 1 s^{-1} . (b) Dependence of the storage, G' , (solid symbols) and loss modulus, G'' , (open symbols) on time at simultaneously increasing and decreasing temperature (5 °C and 37 °C) using eight heating/cooling cycles with a rate of 3 °C min^{-1} at 1% strain deformation and frequency 1 Hz. (c) First two cycles from Figure 3b to more clearly show the difference between the storage and loss moduli during cycling.

In order to investigate the gelation process in more detail, the viscoelastic properties were determined. At 5 °C, no relevant data at low strain deformations of $<0.4\%$ could be obtained due to the low viscosity (Figure 4a). At strain deformations between 0.4% and 10%, the liquid-like behavior of the polymer solution was confirmed, as the loss modulus G'' exceeded the storage modulus G' . Increasing the temperature to 25 °C led to markedly altered viscoelastic properties. At low deformations, the storage modulus dominated, indicating that physical cross-linking was already present. With increasing strain deformation, shear thinning occurred, resulting in liquid-like properties above 1% deformation. A further increase in temperature to 37 °C strengthened the physical cross-links. This was represented by higher initial G' -values as well as longer-lasting solid-like behavior up to deformations of 3%. Similarly, as for 25 °C, significant recovery upon deformation was observed, which will be investigated in more detail below.

The frequency dependence of the viscoelastic moduli exhibited a marked temperature dependence, as the initial liquid-like behavior of the sample at 5 °C vanished with increasing frequency, resulting in solid-like properties at frequencies of >2.5 Hz (Figure 4b). Such behavior is common for similar types of polymer solutions [54]. However, at 25 °C and 37 °C, the frequency had only a minor effect on the viscoelastic properties of the gel. The solid-like behavior remained during the whole frequency range up to 100 Hz. At 25 °C, the underlying physical cross-linking network was still affected by the frequency, as noticeable fluctuation of the storage modulus occurred. At 37 °C, it appears that well-developed physical cross-links with storage moduli around 700 Pa were stable in the whole frequency range.

To obtain the values of the yield stress, the viscoelastic moduli were plotted against the shear stress (Figure 4c). The yield stress was evaluated by tangent analysis of the drop of the storage modulus from the linear region. It can be seen that the sample measured at 5 °C had quite scattered data due to the low viscosity, similar to that seen in Figure 4a, and was not evaluated. Increasing the temperature to 25 °C yielded somewhat better data; however, the storage modulus was not entirely constant at low shear stress and decreased more gradually. Nevertheless, a tentative yield stress of 2 Pa could be obtained. The more pronounced physical cross-linking at 37 °C allowed better analysis and resulted in an enhanced value for the yield stress of 20 Pa. These findings are in good agreement with investigations of the yield stress from steady shear measurements, which are described in the following.

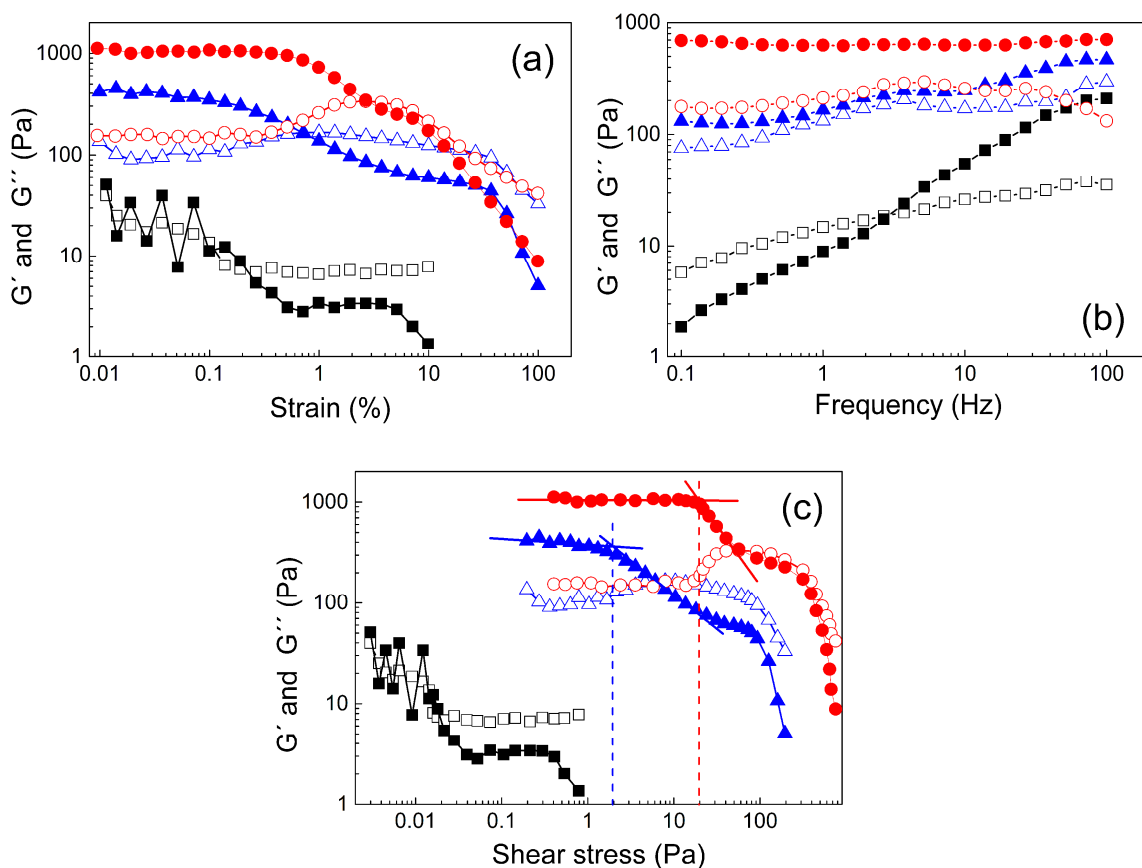


Figure 4. Dependence of the storage G' (solid symbols) and loss modulus G'' (open symbols) on the strain deformation (a), frequency (b), and shear stress (c) for 20 wt % polymer solution at various temperatures (■, 5 °C; ▲, 25 °C; ●, 37 °C).

For an alternative determination of the yield point, steady shear measurements were performed. At 5 °C, the viscosity decreased very slowly with increasing shear rate indicating mostly Newtonian or slightly pseudo-plastic behavior (Figure 5a). Increasing the temperature to 25 °C increased the

viscosity by over one order of magnitude, again indicating internal structure formation. Furthermore, more pseudo-plastic behavior was observed, as the decrease in viscosity with increasing shear rate was more pronounced at elevated temperature. Finally, increasing the temperature to 37 °C further increased the viscosity, corroborating intensified physical cross-linking and strengthening of the gel structure while retaining a pronounced shear thinning character.

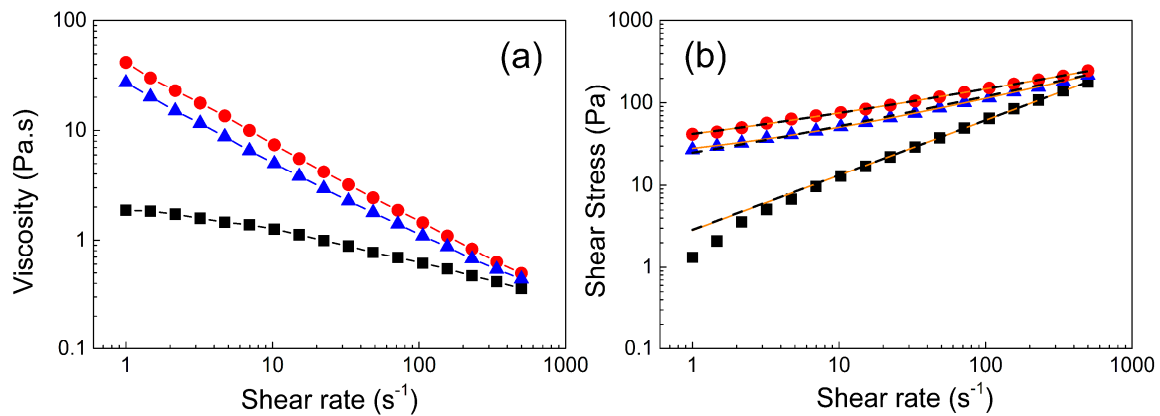


Figure 5. Dependence of the viscosity (a) and shear stress (b) on the shear rate at various temperatures (black square ■, 5 °C; blue triangle ▲, 25 °C; and red circle ●, 37 °C). Orange solid lines in Figure 5b represent the Vocadlo model fit and black dashed lines represent the Herschel–Bulkley (H-B) model fit.

The viscosity decreased by more than two orders of magnitude at high shear rates. Such behavior can be advantageous from a practical point of view, as the material can be, e.g., injected quite easily, but it might provide sufficiently high viscosity for local embolization.

In order to quantify the yield stress of the polymer gel formed at elevated temperatures, the experimental data (Figure 5b) were fitted according to the Vocadlo Equation (1) and Herschel–Bulkley model to calculate the yield stress, consistency index, and index of non-Newtonian behavior (Table 1).

Table 1. Summarized parameters obtained from the calculation of the Vocadlo and Herschel–Bulkley models.

Temperature [°C]	τ_0 , Yield Stress [Pa]	K, Consistency [Pa·s]	n , Non-NEWTONIAN Index [-]
Vocadlo model parameters			
5 °C	0.05	0.16	0.89
25 °C	70	0.20	0.70
37 °C	117	0.22	0.69
Herschel–Bulkley model parameters			
5 °C	0.05	2.8	0.77
25 °C	22	18	0.39
37 °C	36	28	0.34

At 5 °C, both fits provided a very low yield stress and a power law index n close to 1, indicating only slightly pseudo-plastic behavior of the polymer solution. In contrast, much higher yield stresses were obtained at 25 °C and 37 °C. The fit using the Vocadlo model did not provide reasonable values for the power law indices and consistency indices for samples measured at 25 °C and 37 °C. In contrast, the Herschel–Bulkley model provided values for the consistency index, power law index, and yield stress that appear more reasonable. The power law index decreased with increasing temperatures, confirming the transition from liquid-like to solid-like state and pronounced shear thinning behavior. Moreover, the consistency index increased, as did the yield stress, as a result of the created physical cross-links in the material at elevated temperature, which is in agreement with the evaluated values

during the dynamic oscillation stress/strain sweeps. The obtained yield stress of 36 Pa at 37 °C is rather low in comparison to common hydrogels mentioned in a review article by Townsend et al. [52]; however, it is still higher than values reported for other materials elsewhere [55–57].

The experimentally determined value of the yield stress for the hydrogel measured at 37 °C (Figure 4c) is in the same order of magnitude but slightly lower compared to the calculated yield stress from the H-B model. This difference is tentatively attributed to wall slippage present between the hydrogel and stainless steel geometry.

In order to investigate the shear thinning and structure recovery properties in more depth, the viscoelastic moduli were collected over time at two regimes with either 0.1% or 10% strain deformation (Figure 6). For this, the sample at 5 °C was omitted due to the negligible change between these two strain deformations. At low deformation, both samples measured at 25 °C and 37 °C exhibited strong, solid-like behavior, as the storage modulus significantly dominated over the loss modulus.

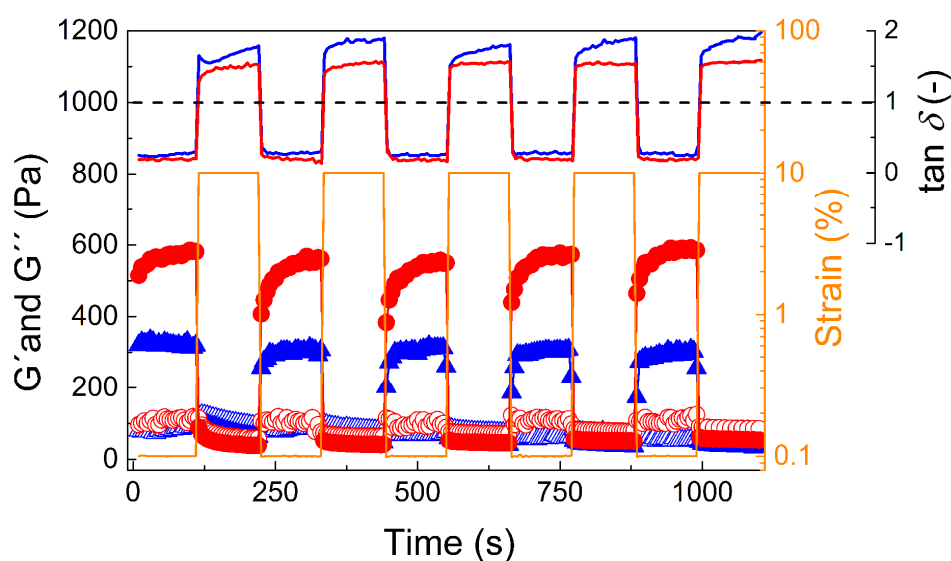


Figure 6. Dependence of the storage, G' (solid symbols), and loss modulus, G'' (open symbols), on time at various strain deformation regimes (0.1% and 10%) for 20 wt % polymer solution. Samples were measured at 25 °C (blue triangles) and 37 °C (red circles) and at frequency 1 Hz. Solid lines represent the values of $\tan \delta$ for hydrogel samples measured at 25 °C (blue solid line) and 37 °C (red solid line). The black dashed line represents $\tan \delta = 1$ as a guide for the eye to differentiate between the solid-like and liquid-like states at various strain deformations.

However, at 10% strain deformation, both samples dramatically changed to liquid-like behavior with a dominating loss modulus, similarly to what was observed for a hydrogel based on hyaluronic acid, albeit at much higher strain deformation (500%) [58]. This change was also confirmed by $\tan \delta$ visualization at various deformation regimes: at low deformations (0.1%) the samples exhibited $\tan \delta = 0.25$ and 0.18, while for high deformations (10%) they exhibited $\tan \delta = 1.5$ and 1.8 (for 25 °C and 37 °C, respectively). Moreover, this change in viscoelastic properties was fully reversible during five deformation cycles. However, after the high strain regime, the return to full strength took a significant amount of time (approximately 2 min) even though return to the gel state appeared to be immediate. This observation stands in stark contrast to the rapid recovery to full strength of a previously described POx-based bioink [44]. This again is a good foundation for possible injection of the polymer gel into the body as, e.g., an embolization agent or drug depot, since upon small deformations, solid-like behavior occurred. However, the slow recovery of the gel strength in combination with the low yield stress might prove problematic with respect to shape fidelity in 3D printing.

Cytocompatibility is an important property regarding applications, e.g., as bioink [46] or drug depots. Therefore, we investigated the cytotoxicity of different non-gelling concentrations ranging

from 0.1 to 10 wt % and observed no dose-dependent cytotoxicity in either HEK293 and human Calu-3 cells after 24 h of incubation (Figure 7). However, we did see an increase in the apparent cell viability. This has been observed before for POx-based polymers in select cases but not as pronounced in the case of Calu-3 cells observed here [35]. This phenomenon requires further and detailed investigations; these are, however, outside the scope of the present contribution.

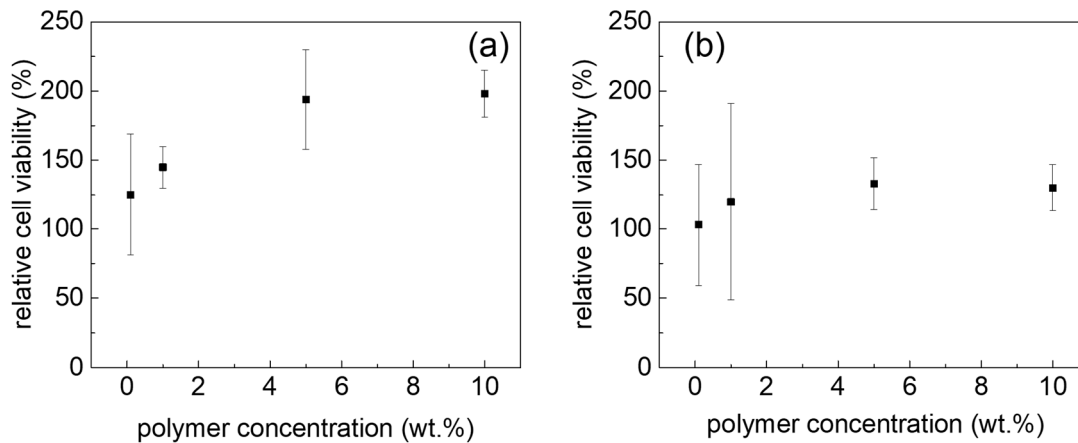


Figure 7. Relative cell viability of Calu-3 (a) and HEK cells (b) at different block copolymer concentrations after 24 h incubation at 37 °C, normalized to the cell viability of Calu-3 and HEK cells cultured without polymer. Values are presented as means \pm standard deviations ($n = 3$).

For the presented physically cross-linked hydrogel, one potential application could be as a functional printable ink. Therefore, hydrogel scaffolds of a 20 wt % aqueous solution were printed at 30 °C using a compact extrusion-based bench-top 3D bioprinter with a printing speed of 600 mm/min utilizing 50 kPa constant pressure. First, the printability was tested by printing one layer with different strand distances (Figure 8a). It is apparent that at the largest distance tested (1.5 mm), some strand separation can be observed, while at the lowest distance (0.75 mm), the printed strands merged into one homogenous layer. However, the layer deposition is rather exact and deposited strands remained well in position (Figure 8b). Subsequently, two- and four-layered constructs of 12 \times 12 mm with four strands (3 mm layer distances) and a layer height of 0.3 mm were printed. It is clearly evident that layers printed on top of each other merge, so real 3D printing is not possible at this point with this material. This can also readily be explained by the comparably low viscosity and storage moduli values in the gel state in conjunction with the low yield stress of the material. While in the case of the two-layered print, the overall 4 \times 4 grid remains reasonably well resolved (Figure 8c), the strands fuse significantly when four strands are printed on top of each other, showing that the material is obviously not able to hold its own weight—a fundamental prerequisite for real 3D printing. However, future work will address whether modifications in the polymer structure or additives such as laponite may be useful to improve the printing properties of the presented hydrogel, as has been previously reported by Peak et al. [59] and others. It is important to note that if the shape fidelity can be improved, cytocompatibility must again be assessed and conditions relevant for printing will also have to be tested.

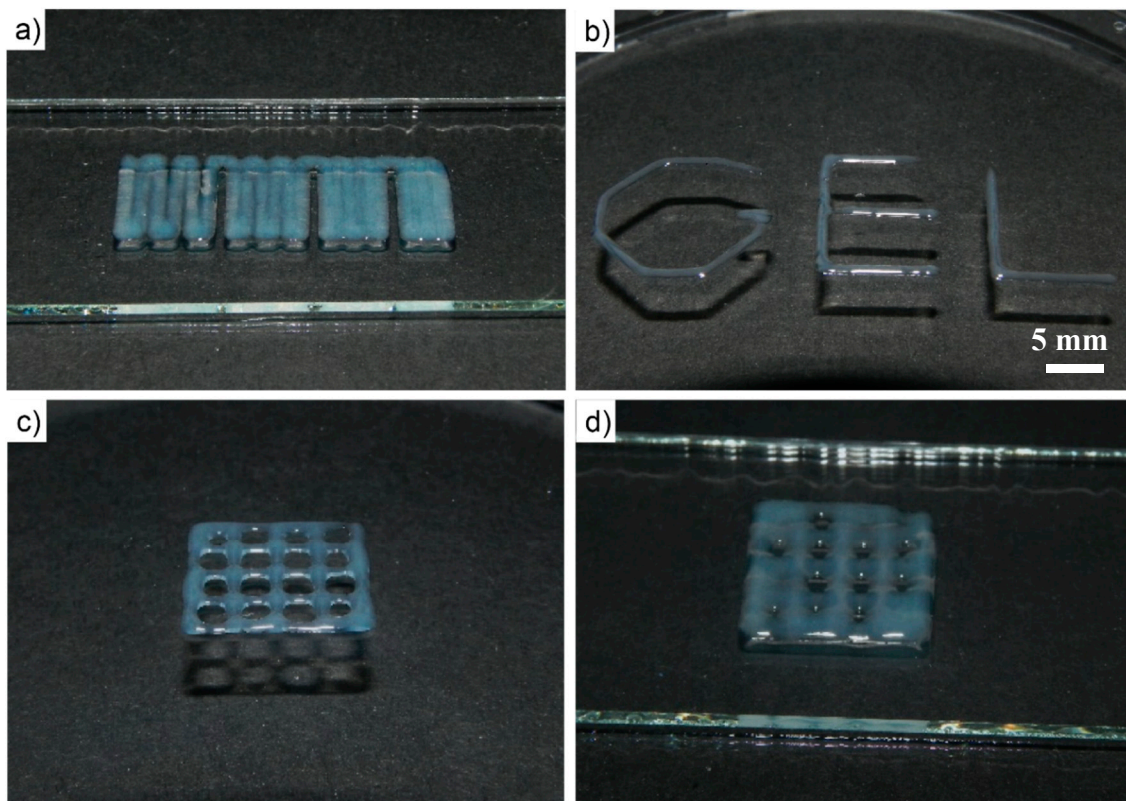


Figure 8. Photographic images of printing experiments using 20 wt % A-*p*BuOx-A aqueous solution. (a) Using variable strand distances (0.75 mm–1.5 mm in 0.25 mm steps), merging of adjacent strands can be assessed. (b) Strand placement is reasonably exact and placed strands stay in place well. Photographic images of (c) two- and (d) four-layered printed constructs of 12 × 12 mm with four strands and a layer height of 0.3 mm.

5. Conclusions

In this study, an ABA triblock copolymer based on poly(2-methyl-2-oxazoline) and poly(2-*iso*-butyl-2-oxazoline) was synthesized and characterized by $^1\text{H-NMR}$ and GPC. Visual inspection of polymer solutions at various concentrations and temperatures revealed thermal gelation at concentrations of at least 20 wt % of the ABA triblock copolymer in water. Steady shear experiments at various temperatures confirmed the transition from solution to a gel-like structure. The viscoelastic investigation showed a soft hydrogel forming above 25 °C exhibiting an elastic modulus of 150 Pa, while at 37 °C it showed an elastic modulus of almost 600 Pa. Furthermore, shear thinning behavior was confirmed to be highly reversible, as the elastic moduli measured at 37 °C changed from 600 Pa to 20 Pa for 0.1% and 10% strain deformation, respectively. Finally, the reproducibility of the thermal gelation was confirmed using eight cycles with transition from 5 °C to 37 °C. The material exhibited low cytotoxicity in both Calu-3 and HEK cells at all investigated polymer concentrations after 24 h at 37 °C. The results of the presented rheological, viscoelastic, and printing investigations suggest that the fabricated hydrogel may be used as a functional printable bioink, but further modifications will be necessary to improve shape fidelity. This could include light-induced curing of polymers modified with cross-linking functionalities, addition of viscoelastic modifiers such as laponite or further tuning of the polymer structure.

Supplementary Materials: The following are available online at <http://www.mdpi.com/2079-4983/10/3/36/s1>. Synthetic procedures for monomer and polymer preparation; Figure S1: $^1\text{H-NMR}$ characterization of the monomer 2-*iso*-butyl-2-oxazoline; Figure S2: $^1\text{H-NMR}$ characterization of the polymer A-*p*BuOx-A; Figure S3: GPC elugrams of A-*p*BuOx-A and its intermediate products.

Author Contributions: M.M.L. was responsible for the synthesis and characterization of the investigated material; L.H. and A.A. performed the printing experiments; M.M. conducted rheological and viscoelastic investigations; M.B. conducted cell viability experiments; R.L. supervised the entire study. The manuscript was written through contributions by M.M.L., M.M., L.H., T.L., and R.L.

Funding: This research was funded by the Deutsche Forschungsgemeinschaft (DFG, German Research Foundation) project number 326998133-TRR 225 (subproject A03) and project number 398461692 (awarded to R.L.). Moreover, M.M.L. would like to thank the Evonik Foundation for providing a doctoral fellowship. M.M. also gratefully acknowledges the Ministry of Education, Youth and Sports of the Czech Republic—program NPU I (LO1504). We thank the Deutsche Forschungsgemeinschaft for funding the Zeiss CB 340 crossbeam scanning electron microscope (INST 105022/58-1 FUGG) within the DFG State Major Instrumentation Programme.

Acknowledgments: We thank Judith Friedlein (Department for Functional Materials in Medicine and Dentistry, University Hospital Würzburg) for technical support.

Conflicts of Interest: There are no conflicts of interest for any of the authors.

References

1. Peng, H.Y.; Wang, W.; Gao, F.H.; Lin, S.; Liu, L.Y.; Pu, X.Q.; Liu, Z.; Ju, X.J.; Xie, R.; Chu, L.Y. Ultrasensitive diffraction gratings based on smart hydrogels for highly selective and rapid detection of trace heavy metal ions. *J. Mater. Chem. C* **2018**, *6*, 11356–11367. [[CrossRef](#)]
2. Ho, L.; Hsu, S.H. Cell reprogramming by 3D bioprinting of human fibroblasts in polyurethane hydrogel for fabrication of neural-like constructs. *Acta Biomater.* **2018**, *70*, 57–70. [[CrossRef](#)] [[PubMed](#)]
3. Hoogenboom, R.; Thijs, H.M.L.; Jochems, M.; van Lankvelt, B.M.; Fijten, M.W.M.; Schubert, U.S. Tuning the LCST of poly(2-oxazoline)s by varying composition and molecular weight: alternatives to poly(N-isopropylacrylamide)? *Chem. Commun.* **2008**, 5758–5760. [[CrossRef](#)] [[PubMed](#)]
4. Hruby, M.; Filippov, S.K.; Panek, J.; Novakova, M.; Mackova, H.; Kucka, J.; Vetvicka, D.; Ulbrich, K. Polyoxazoline Thermoresponsive Micelles as Radionuclide Delivery Systems. *Macromol. Biosci.* **2010**, *10*, 916–924. [[CrossRef](#)]
5. Salzinger, S.; Huber, S.; Jaksch, S.; Busch, P.; Jordan, R.; Papadakis, C.M. Aggregation behavior of thermo-responsive poly(2-oxazoline)s at the cloud point investigated by FCS and SANS. *Colloid Polym. Sci.* **2012**, *290*, 385–400. [[CrossRef](#)]
6. Aseyev, V.; Hietala, S.; Laukkanen, A.; Nuopponen, M.; Confortini, O.; Du Prez, F.E.; Tenhu, H. Mesoglobules of thermoresponsive polymers in dilute aqueous solutions above the LCST. *Polymer* **2005**, *46*, 7118–7131. [[CrossRef](#)]
7. Navarro, S.; Shkilnyy, A.; Tiersch, B.; Taubert, A.; Menzel, H. Preparation, Characterization, and Thermal Gelation of Amphiphilic Alkyl-poly(ethyleneimine). *Langmuir* **2009**, *25*, 10558–10566. [[CrossRef](#)]
8. Foreman, M.B.; Coffman, J.P.; Murcia, M.J.; Cesana, S.; Jordan, R.; Smith, G.S.; Naumann, C.A. Gelation of amphiphilic lipopolymers at the air-water interface: 2D analogue to 3D gelation of colloidal systems with grafted polymer chains? *Langmuir* **2003**, *19*, 326–332. [[CrossRef](#)]
9. Oroojalian, F.; Babaei, M.; Taghdisi, S.M.; Abnous, K.; Ramezani, M.; Alibolandi, M. Encapsulation of Thermo-responsive Gel in pH-sensitive Polymersomes as Dual-Responsive Smart carriers for Controlled Release of Doxorubicin. *J. Control. Release* **2018**, *288*, 45–61. [[CrossRef](#)]
10. Osaka, N.; Hamamoto, K. Simultaneous stiffening, strengthening and toughening of poly(vinylidene fluoride)/propylene carbonate gels by thermal annealing near peak melting temperature. *Polymer* **2018**, *141*, 132–142. [[CrossRef](#)]
11. Al Khateb, K.; Ozhmukhametova, E.K.; Mussin, M.N.; Seilkhanov, S.K.; Rakhypbekov, T.K.; Lau, W.M.; Khutoryanskiy, V.V. In situ gelling systems based on Pluronic F127/Pluronic F68 formulations for ocular drug delivery. *Int. J. Pharm.* **2016**, *502*, 70–79. [[CrossRef](#)] [[PubMed](#)]
12. Liu, S.J.; Bao, H.Q.; Li, L. Role of PPO-PEO-PPO triblock copolymers in phase transitions of a PEO-PPO-PEO triblock copolymer in aqueous solution. *Eur. Polym. J.* **2015**, *71*, 423–439. [[CrossRef](#)]
13. Costanzo, S.; Pasquino, R.; Donato, R.; Grizzuti, N. Effect of polymer concentration and thermal history on the inverse thermogelation of hydroxypropylcellulose aqueous solutions. *Polymer* **2017**, *132*, 157–163. [[CrossRef](#)]
14. Luxenhofer, R.; Han, Y.; Schulz, A.; Tong, J.; He, Z.; Kabanov, A.V.; Jordan, R. Poly(2-oxazoline)s as Polymer Therapeutics. *Macromol. Rapid Commun.* **2012**, *33*, 1613–1631. [[CrossRef](#)] [[PubMed](#)]

15. Lorson, T.; Lübtow, M.M.; Wegener, E.; Haider, M.S.; Borova, S.; Nahm, D.; Jordan, R.; Sokolski-Papkov, M.; Kabanov, A.V.; Luxenhofer, R. Poly(2-oxazoline)s based biomaterials: A comprehensive and critical update. *Biomaterials* **2018**, *178*, 204–280. [[CrossRef](#)] [[PubMed](#)]
16. Viegas, T.X.; Bentley, M.D.; Harris, J.M.; Fang, Z.; Yoon, K.; Dizman, B.; Weimer, R.; Mero, A.; Pasut, G.; Veronese, F.M. Polyoxazoline: Chemistry, Properties, and Applications in Drug Delivery. *Bioconjugate Chem.* **2011**, *22*, 976–986. [[CrossRef](#)] [[PubMed](#)]
17. Weber, C.; Hoogenboom, R.; Schubert, U.S. Temperature responsive bio-compatible polymers based on poly(ethylene oxide) and poly(2-oxazoline)s. *Prog. Polym. Sci.* **2012**, *37*, 686–714. [[CrossRef](#)]
18. Monnery, B.D.; Jerca, V.V.; Sedlacek, O.; Verbraeken, B.; Cavill, R.; Hoogenboom, R. Defined High Molar Mass Poly(2-Oxazoline)s. *Angew. Chem. Int. Ed.* **2018**, *57*, 15400–15404. [[CrossRef](#)]
19. Sedlacek, O.; Monnery, B.D.; Mattova, J.; Kucka, J.; Panek, J.; Janouskova, O.; Hocherl, A.; Verbraeken, B.; Vergaelen, M.; Zadinova, M.; et al. Poly(2-ethyl-2-oxazoline) conjugates with doxorubicin for cancer therapy: In vitro and in vivo evaluation and direct comparison to poly[N-(2-hydroxypropyl)methacrylamide] analogues. *Biomaterials* **2017**, *146*, 1–12. [[CrossRef](#)]
20. Nawroth, J.F.; McDaniel, J.R.; Chilkoti, A.; Jordan, R.; Luxenhofer, R. Maleimide-Functionalized Poly(2-Oxazoline)s and Their Conjugation to Elastin-Like Polypeptides. *Macromol. Biosci.* **2016**, *16*, 322–333. [[CrossRef](#)]
21. Moreadith, R.W.; Viegas, T.X.; Bentley, M.D.; Harris, J.M.; Fang, Z.; Yoon, K.; Dizman, B.; Weimer, R.; Rae, B.P.; Li, X.; et al. Clinical development of a poly(2-oxazoline) (POZ) polymer therapeutic for the treatment of Parkinson’s disease—Proof of concept of POZ as a versatile polymer platform for drug development in multiple therapeutic indications. *Eur. Polym. J.* **2017**, *88*, 524–552. [[CrossRef](#)]
22. Yi, X.A.; Zimmerman, M.C.; Yang, R.F.; Tong, J.; Vinogradov, S.; Kabanov, A.V. Pluronic-modified superoxide dismutase 1 attenuates angiotensin II-induced increase in intracellular superoxide in neurons. *Free Radic. Biol. Med.* **2010**, *49*, 548–558. [[CrossRef](#)] [[PubMed](#)]
23. Tong, J.; Zimmerman, M.C.; Li, S.M.; Yi, X.; Luxenhofer, R.; Jordan, R.; Kabanov, A.V. Neuronal uptake and intracellular superoxide scavenging of a fullerene (C-60)-poly(2-oxazoline)s nanoformulation. *Biomaterials* **2011**, *32*, 3654–3665. [[CrossRef](#)] [[PubMed](#)]
24. Mero, A.; Fang, Z.H.; Pasut, G.; Veronese, F.M.; Viegas, T.X. Selective conjugation of poly(2-ethyl 2-oxazoline) to granulocyte colony stimulating factor. *J. Control. Release* **2012**, *159*, 353–361. [[CrossRef](#)] [[PubMed](#)]
25. Li, J.W.; Zhou, Y.X.; Li, C.W.; Wang, D.S.; Gao, Y.J.; Zhang, C.; Zhao, L.; Li, Y.S.; Liu, Y.; Li, X.R. Poly(2-ethyl-2-oxazoline)-Doxorubicin Conjugate-Based Dual Endosomal pH-Sensitive Micelles with Enhanced Antitumor Efficacy. *Bioconjugate Chem.* **2015**, *26*, 110–119. [[CrossRef](#)]
26. Lübtow, M.M.; Hahn, L.; Haider, M.S.; Luxenhofer, R. Drug Specificity, Synergy and Antagonism in Ultrahigh Capacity Poly(2-oxazoline)/Poly(2-oxazine) based Formulations. *J. Am. Chem. Soc.* **2017**, *139*, 10980–10983. [[CrossRef](#)]
27. He, Z.; Wan, X.; Schulz, A.; Bludau, H.; Dobrovolskaia, M.A.; Stern, S.T.; Montgomery, S.A.; Yuan, H.; Li, Z.; Alakhova, D.; et al. A high capacity polymeric micelle of paclitaxel: Implication of high dose drug therapy to safety and in vivo anti-cancer activity. *Biomaterials* **2016**, *101*, 296–309. [[CrossRef](#)]
28. Hwang, D.; Zhao, Y.L.; Liu, H.D.; Kabanov, A.; Gershon, T.; Sokolsky, M. Enhanced efficacy of nano-formulated vismosdegib shows the potential for polyoxazoline micelles to improve drug delivery to brain tumors. *Neuro-Oncology* **2018**, *20*, 139–140. [[CrossRef](#)]
29. Wan, X.M.; Min, Y.Z.; Bludau, H.; Keith, A.; Sheiko, S.S.; Jordan, R.; Wang, A.Z.; Sokolsky-Papkov, M.; Kabanov, A.V. Drug Combination Synergy in Worm-like Polymeric Micelles Improves Treatment Outcome for Small Cell and Non-Small Cell Lung Cancer. *ACS Nano* **2018**, *12*, 2426–2439. [[CrossRef](#)]
30. He, Z.J.; Schulz, A.; Wan, X.M.; Seitz, J.; Bludau, H.; Alakhova, D.Y.; Darr, D.B.; Perou, C.M.; Jordan, R.; Ojima, I.; et al. Poly(2-oxazoline) based micelles with high capacity for 3rd generation taxoids: Preparation, in vitro and in vivo evaluation. *J. Control. Release* **2015**, *208*, 67–75. [[CrossRef](#)]
31. Hahn, L.; Lübtow, M.M.; Lorson, T.; Schmitt, F.; Appelt-Menzel, A.; Schobert, R.; Luxenhofer, R. Investigating the Influence of Aromatic Moieties on the Formulation of Hydrophobic Natural Products and Drugs in Poly(2-oxazoline)-Based Amphiphiles. *Biomacromolecules* **2018**, *19*, 3119–3128. [[CrossRef](#)] [[PubMed](#)]

32. Lübtow, M.M.; Kessler, L.; Appelt-Menzel, A.; Lorson, T.; Gangloff, N.; Kirsch, M.; Dahms, S.; Luxenhofer, R. More Is Sometimes Less: Curcumin and Paclitaxel Formulations Using Poly(2-oxazoline) and Poly(2-oxazine)-Based Amphiphiles Bearing Linear and Branched C9 Side Chains. *Macromol. Biosci.* **2018**, *18*, 17. [[CrossRef](#)] [[PubMed](#)]
33. Datta, S.; Jutkova, A.; Sramkova, P.; Lenkayska, L.; Huntosova, V.; Chorvat, D.; Miskovsky, P.; Jancura, D.; Kronek, J. Unravelling the Excellent Chemical Stability and Bioavailability of Solvent Responsive Curcumin-Loaded 2-Ethyl-2-oxazoline-graft-(4-dodecyloxyphenyl)-2-oxazoline Copolymer Nanoparticles for Drug Delivery. *Biomacromolecules* **2018**, *19*, 2459–2471. [[CrossRef](#)] [[PubMed](#)]
34. Raveendran, R.; Mullen, K.M.; Wellard, R.M.; Sharma, C.P.; Hoogenboom, R.; Dargaville, T.R. Poly(2-oxazoline) block copolymer nanoparticles for curcumin loading and delivery to cancer cells. *Eur. Polym. J.* **2017**, *93*, 682–694. [[CrossRef](#)]
35. Lübtow, M.M.; Nelke, L.C.; Seifert, J.; Kühnemundt, J.; Sahay, G.; Dandekar, G.; Nietzer, S.; Luxenhofer, R. Drug induced micellization into ultra-high capacity and stable curcumin nanoformulations: Physico-chemical characterization and evaluation in 2D and 3D in vitro models. *J. Control. Release* **2019**, *303*, 162–180. [[CrossRef](#)] [[PubMed](#)]
36. He, Z.J.; Miao, L.; Jordan, R.; S-Manickam, D.; Luxenhofer, R.; Kabanov, A.V. A Low Protein Binding Cationic Poly(2-oxazoline) as Non-Viral Vector. *Macromol. Biosci.* **2015**, *15*, 1004–1020. [[CrossRef](#)] [[PubMed](#)]
37. Konradi, R.; Acikgoz, C.; Textor, M. Polyoxazolines for Nonfouling Surface Coatings — A Direct Comparison to the Gold Standard PEG. *Macromol. Rapid Commun.* **2012**, *33*, 1663–1676. [[CrossRef](#)]
38. Zhang, N.; Pompe, T.; Amin, I.; Luxenhofer, R.; Werner, C.; Jordan, R. Tailored Poly(2-oxazoline) Polymer Brushes to Control Protein Adsorption and Cell Adhesion. *Macromol. Biosci.* **2012**, *12*, 926–936. [[CrossRef](#)]
39. Bludau, H.; Czapar, A.E.; Pitek, A.S.; Shukla, S.; Jordan, R.; Steinmetz, N.F. POxylation as an alternative stealth coating for biomedical applications. *Eur. Polym. J.* **2017**, *88*, 679–688. [[CrossRef](#)]
40. Mansfield, E.D.H.; de la Rosa, V.R.; Kowalczyk, R.M.; Grillo, I.; Hoogenboom, R.; Sillence, K.; Hole, P.; Williams, A.C.; Khutoryanskiy, V.V. Side chain variations radically alter the diffusion of poly(2-alkyl-2-oxazoline) functionalised nanoparticles through a mucosal barrier. *Biomater. Sci.* **2016**, *4*, 1318–1327. [[CrossRef](#)]
41. Schulz, A.; Stocco, A.; Bethry, A.; Lavigne, J.P.; Coudane, J.; Nottelet, B. Direct Photomodification of Polymer Surfaces: Unleashing the Potential of Aryl-Azide Copolymers. *Adv. Funct. Mater.* **2018**, *28*, 7. [[CrossRef](#)]
42. Dargaville, T.R.; Park, J.-R.; Hoogenboom, R. Poly(2-oxazoline) Hydrogels: State-of-the-Art and Emerging Applications. *Macromol. Biosci.* **2018**, *18*, 1800070. [[CrossRef](#)] [[PubMed](#)]
43. Hartlieb, M.; Kempe, K.; Schubert, U.S. Covalently cross-linked poly(2-oxazoline) materials for biomedical applications – from hydrogels to self-assembled and templated structures. *J. Mater. Chem. B* **2015**, *3*, 526–538. [[CrossRef](#)]
44. Kelly, A.M.; Wiesbrock, F. Strategies for the Synthesis of Poly(2-Oxazoline)-Based Hydrogels. *Macromol. Rapid Commun.* **2012**, *33*, 1632–1647. [[CrossRef](#)] [[PubMed](#)]
45. Zahoranová, A.; Kroneková, Z.; Zahoran, M.; Chorvát, D.; Janigová, I.; Kronek, J. Poly(2-oxazoline) hydrogels crosslinked with aliphatic bis(2-oxazoline)s: Properties, cytotoxicity, and cell cultivation. *J. Polym. Sci., Part A: Polym. Chem.* **2015**, *54*, 1548–1559. [[CrossRef](#)]
46. Lorson, T.; Jaksch, S.; Lübtow, M.M.; Jüngst, T.; Groll, J.; Lühmann, T.; Luxenhofer, R. A Thermogelling Supramolecular Hydrogel with Sponge-Like Morphology as a Cytocompatible Bioink. *Biomacromolecules* **2017**, *18*, 2161–2171. [[CrossRef](#)] [[PubMed](#)]
47. Zahoranova, A.; Mrlik, M.; Tomanova, K.; Kronek, J.; Luxenhofer, R. ABA and BAB Triblock Copolymers Based on 2-Methyl-2-oxazoline and 2-n-Propyl-2-oxazoline: Synthesis and Thermoresponsive Behavior in Water. *Macromol. Chem. Phys.* **2017**, *218*, 12. [[CrossRef](#)]
48. Monnery, B.D.; Hoogenboom, R. Thermoresponsive hydrogels formed by poly(2-oxazoline) triblock copolymers. *Polym. Chem.* **2019**. in print. [[CrossRef](#)]
49. Seo, Y.; Schulz, A.; Han, Y.; He, Z.; Bludau, H.; Wan, X.; Tong, J.; Bronich, T.K.; Sokolsky, M.; Luxenhofer, R.; et al. Poly(2-oxazoline) block copolymer based formulations of taxanes: effect of copolymer and drug structure, concentration, and environmental factors. *Polym. Adv. Technol.* **2015**, *26*, 837–850. [[CrossRef](#)]
50. Lübtow, M.M.; Haider, M.S.; Kirsch, M.; Klisch, S.; Luxenhofer, R. Like Dissolves Like? A Comprehensive Evaluation of Partial Solubility Parameters to Predict Polymer-Drug Compatibility in Ultra-High Drug Loaded Polymer Micelles. *Biomacromolecules* **2019**, in print. [[CrossRef](#)]

51. Cvek, M.; Mrlik, M.; Pavlinek, V. A rheological evaluation of steady shear magnetorheological flow behavior using three-parameter viscoplastic models. *J. Rheol.* **2016**, *60*, 687–694. [[CrossRef](#)]
52. Townsend, J.M.; Beck, E.C.; Gehrke, S.H.; Berkland, C.J.; Detamore, M.S. Flow behavior prior to crosslinking: The need for precursor rheology for placement of hydrogels in medical applications and for 3D bioprinting. *Prog. Polym. Sci.* **2019**, *91*, 126–140. [[CrossRef](#)]
53. Moroni, L.; Boland, T.; Burdick, J.A.; De Maria, C.; Derby, B.; Forgacs, G.; Groll, J.; Li, Q.; Malda, J.; Mironov, V.A.; et al. Biofabrication: A Guide to Technology and Terminology. *Trends Biotechnol.* **2018**, *36*, 384–402. [[CrossRef](#)] [[PubMed](#)]
54. Ruel-Gariepy, E.; Leroux, J.C. In situ-forming hydrogels—review of temperature-sensitive systems. *Eur. J. Pharm. Biopharm.* **2004**, *58*, 409–426. [[CrossRef](#)] [[PubMed](#)]
55. Gaharwar, A.K.; Avery, R.K.; Assmann, A.; Paul, A.; McKinley, G.H.; Khademhosseini, A.; Olsen, B.D. Shear-thinning nanocomposite hydrogels for the treatment of hemorrhage. *ACS nano* **2014**, *8*, 9833–9842. [[CrossRef](#)]
56. Dumas, J.E.; BrownBaer, P.B.; Prieto, E.M.; Guda, T.; Hale, R.G.; Wenke, J.C.; Guelcher, S.A. Injectable reactive biocomposites for bone healing in critical-size rabbit calvarial defects. *Biomed. Mater.* **2012**, *7*, 024112. [[CrossRef](#)]
57. Abbadessa, A.; Blokzijl, M.; Mouser, V.; Marica, P.; Malda, J.; Hennink, W.; Vermonden, T. A thermo-responsive and photo-polymerizable chondroitin sulfate-based hydrogel for 3D printing applications. *Carbohydr. Polym.* **2016**, *149*, 163–174. [[CrossRef](#)]
58. Chen, M.H.; Wang, L.L.; Chung, J.J.; Kim, Y.H.; Atluri, P.; Burdick, J.A. Methods To Assess Shear-Thinning Hydrogels for Application As Injectable Biomaterials. *ACS Biomater. Sci. Eng.* **2017**, *3*, 3146–3160. [[CrossRef](#)]
59. Peak, C.W.; Stein, J.; Gold, K.A.; Gaharwar, A.K. Nanoengineered Colloidal Inks for 3D Bioprinting. *Langmuir* **2018**, *34*, 917–925. [[CrossRef](#)]



© 2019 by the authors. Licensee MDPI, Basel, Switzerland. This article is an open access article distributed under the terms and conditions of the Creative Commons Attribution (CC BY) license (<http://creativecommons.org/licenses/by/4.0/>).

Although the extraordinary high loading capacities and pronounced cytotoxicity in conventional 2D cell culture as well as 3D bioreactor systems against various cancer cell lines of POx/POzi based CUR-formulation are promising, its IV administration might be strongly hampered due to limited stability *in vivo* and therefore low concentration at site of action. For certain diseases, the administration of hydrogel-based drug depot formulations circumvents the latter problems, due to a locally concentrated drug release over prolonged periods of time. The incorporation of CUR into the thermogelling POx/POzi diblock copolymer can be realized directly, or in the form of CUR-loaded micelles. To investigate this systematically, either neat CUR or one of three different polymer amphiphiles incorporating CUR at various polymer/CUR ratios were incorporated at different overall CUR concentrations. Although bearing the same building blocks as a triblock copolymer exhibiting LCs up to 54 wt.%, the maximum CUR loading of the thermogelling diblock-copolymer was much lower with LC = 10 wt.%. The CUR-loaded micelles could be conveniently solubilized with the hydrogel matrix in the form of freeze-dried powder. Interestingly, the presence of neat CUR strongly decreased mechanical strength of the hydrogel, which could be somehow reversed by the pre-formulation of CUR with the triblock-copolymers. Important to note, the incorporation of the empty triblock copolymers affected thermogelling properties very differently, depending on the polymer structure. These deviations were much less pronounced in the case of the CUR-loaded micelles, suggesting the integrity of the latter after incorporation into the hydrogel. Apart from that, all CUR-loaded hydrogels (w/ or w/o pre-incorporation into polymer amphiphiles) exhibited excellent shelf-life with no sign of CUR-degradation or precipitation even after 22 months storage in aqueous solution at 5 °C. In accordance with the lower mechanical strength of the hydrogel directly incorporating CUR, the CUR-release of the latter after injection in a collagen matrix was faster compared to the hydrogels incorporating the CUR-loaded micelles at same CUR concentration. With the latter, a sustained and essentially quantitative CUR-release up to 70 days could be realized. Most interestingly, injecting micellar CUR at same CUR concentration into the collagen matrix without incorporation into the hydrogel caused premature CUR precipitation strongly decreasing maximum released CUR to 36% and 72%. Therefore, the incorporation of CUR into the hydrogel matrix not only prolonged cargo-release but might also provide sufficient stability after e.g. subcutaneous injections.

The following publication was reprinted with permission from *Macromol. Chem. Phys.* **2019**, *221*, 1900341

<https://doi.org/10.1002/macp.201900341>; © 2019 The Authors, Published by Wiley-VCH Verlag GmbH & Co. KGaA



Combining Ultra-High Drug-Loaded Micelles and Injectable Hydrogel Drug Depots for Prolonged Drug Release

Michael M. Lübtow, Thomas Lorson, Tamara Finger, Florian-Kai Gröber-Becker, and Robert Luxenhofer*

Hydrogel-based drug depot formulations are of great interest for therapeutic applications. While the biological activity of such drug depots is often characterized well, the influence of incorporated drug or drug-loaded micelles on the gelation properties of the hydrogel matrix is less investigated. However, the latter is of great importance from fundamental and application points of view as it informs on the physicochemical interactions of drugs and water-swollen polymer networks and it determines injectability, depot stability, as well as drug-release kinetics. Here, the impact of incorporated drug, neat polymer micelles, and drug-loaded micelles on the viscoelastic properties of a cyto-compatible hydrogel is investigated systematically. To challenge the hydrogel with regard to the desired application as injectable drug depot, curcumin (CUR) is chosen as a model compound due to its very low-water solubility and limited stability. CUR is either directly solubilized by the hydrogel or pre-incorporated into polymer micelles. Interference of CUR with the temperature-induced gelation process can be suppressed by pre-incorporation into polymer micelles forming a binary drug delivery system. Drug release from a collagen matrix is studied in a trans-well setup. Compared to direct injection of drug formulations, the hydrogel-based systems show improved and extended drug release over 10 weeks.

1. Introduction

Once administered into the human body, a drug faces various challenges before reaching its target location. Drug delivery systems such as liposomes or polymer nanoparticles/micelles are utilized to protect the drug but any circulating system is also challenged to a certain degree by excretion and/or biotransformation in the human body.^[1] Control of pharmacokinetics and pharmacodynamics is particularly important and challenging when administering readily metabolized compounds. Another important aspect for drug delivery systems is the drug release kinetics. As intrinsically dynamic systems, drug-loaded polymer micelles often face the challenge of rapid drug release, which then associates with proteins present in the blood stream^[2,3]; is excreted, or taken up in tissue other than desired one, which may be detrimental for the therapeutic efficacy.^[4] To enable a more sustained release, active pharmaceutical ingredients (API) can be embedded in drug depots from

which the drug is released continuously, maintaining a high local drug concentration in the surrounding tissue over an extended period of time.^[5–7] Ideally, the depot formulation not only prolongs drug release, but also protects the incorporated compound from premature degradation. Besides microfabricated devices,^[8] metallic implants,^[9] organogels^[10] or electrospun fibers,^[11] hydrogels^[12] are considered promising drug depot matrices. Hydrogels are three-dimensionally cross-linked networks of water-soluble polymers.^[13,14] Due to their high water content, hydrogels are generally regarded as highly biocompatible.^[15,16] Drug-loaded hydrogels as depot formulations showed great therapeutic potential in various scenarios *in vitro*^[17–21] as well as *in vivo*.^[22–29] *In situ* forming or injectable hydrogels are of particular interest due to their ease of application without surgical needs.^[30–33] In this context, physically crosslinked thermogelling hydrogels based on hydrophobic interactions are advantageous, as they can be injected in the cold, liquid state to solidify at body temperature without the addition of crosslinkers or any other external trigger.^[34,35] Various compounds including PTX,^[36] interleukin-2,^[37] topotecan,^[38] doxorubicin,^[25] or fluorouracil^[39] have been incorporated into thermogelling hydrogels to prolong drug release as well as enhance retention at tumor site.

M. M. Lübtow, Dr. T. Lorson,^[†] Prof. R. Luxenhofer
 Functional Polymer Materials
 Chair for Advanced Materials Synthesis
 Department of Chemistry and Pharmacy and Bavarian Polymer Institute
 University of Würzburg
 Röntgenring 11, 97070 Würzburg, Germany
 E-mail: robert.luxenhofer@uni-wuerzburg.de
 T. Finger, Dr. F.-K. Gröber-Becker
 Translational Center 'Regenerative Therapies' (TLC-RT) Fraunhofer
 Institute for Silicate Research (ISC)
 Neunerplatz 2, 97082 Würzburg, Germany
 Dr. F.-K. Gröber-Becker
 Chair of Tissue Engineering and Regenerative Medicine
 University Hospital Würzburg
 Röntgenring 11, 97070 Würzburg, Germany

The ORCID identification number(s) for the author(s) of this article can be found under <https://doi.org/10.1002/macp.201900341>.

^[†]Present address: Institute of Pharmacy and Food Chemistry, Julius-Maximilians-University Würzburg, Am Hubland, 97074 Würzburg, Germany

© 2019 The Authors. Published by WILEY-VCH Verlag GmbH & Co. KGaA, Weinheim. This is an open access article under the terms of the Creative Commons Attribution License, which permits use, distribution and reproduction in any medium, provided the original work is properly cited.

DOI: 10.1002/macp.201900341

A compound which is particularly challenging to formulate—in form of hydrogels or otherwise—is curcumin (CUR). A plethora of preclinical studies pointed out the antioxidative,^[40] cardioprotective,^[41] or antitumor^[42] activities of the “generally recognized as safe” (GRAS; evaluated by United States Food and Drug Administration (FDA))^[43] compound. Despite a large number of clinical trials, it has not been approved as drug for human use. Besides potentially troublesome evaluation of preclinical data,^[44–47] this is most likely associated with the extremely low water solubility of 0.6 mg L⁻¹ (1.6 μM)^[48] of CUR as well as the molecules’ high susceptibility to degradation, not only in water,^[49,50] but also to biomedical transformations such as carbon chain cleavage, reduction, conjugation with glucuronic acid or sulfate in biological media in vitro^[51] and in vivo.^[52] These issues make CUR an interesting model compound to challenge hydrogels with respect to their desired application as injectable drug depot. Previously, poly(2-oxazoline) (POx) and poly(2-oxazine) (POzi)-based drug-delivery vehicles with interesting structure–property relationships with respect to drug loading and potential for parenteral administration of CUR were reported.^[53–58] The loading capacities (LCs) for CUR in ABA triblock-copolymers comprising the same hydrophilic poly(2-methyl-2-oxazoline) (PMeOx) corona (= A) and either poly(2-*n*-butyl-2-oxazoline) (PBuOx) (= A-BuOx-A) or poly(2-*n*-propyl-2-oxazine) (PPrOzi) (= A-PrOzi-A) as hydrophobic blocks ranged from 21.6 wt% to 54.5 wt%.^[53] Although benefits with respect to therapeutic efficacy of intravenously administered, ultra-high loaded A-BuOx-A/paclitaxel formulations (LC = 45 wt%) and combination formulations of hydrophobic cis-platin prodrug and etoposide or PTX have been observed in vivo,^[59–63] this might not be true for CUR due to its susceptibility to degradation or toxicity at high concentrations (not achievable orally). Inspired by CUR-loaded hydrogels for cutaneous wound repair^[28] or intranasal drug delivery to the brain,^[64] we wondered, if we could incorporate CUR in a recently reported, cytocompatible PMeOx-*b*-PPrOzi copolymer-based hydrogel,^[65] for subcutaneous or intratumoral injection in order to avoid systemic circulation and/or allow prolonged release. From a more fundamental and practical point of view, it was also interesting to investigate the influence of hydrophobic CUR on the viscoelastic properties of a hydrogel that is formed based on dynamic hydrophobic interactions. Furthermore, the effect of nanoformulated CUR incorporated into the hydrogel matrix is of interest. Although drug-loaded polymer micelles incorporated into hydrogel matrices are readily found in the literature,^[17,28,29,66] such systematic investigations of the viscoelastic properties of hydrogels containing nanoformulated hydrophobic drugs are rare. In addition, to assess the potential as an injectable thermogelling drug depot, the CUR-loaded hydrogels were injected into a collagen matrix and CUR release quantified.

2. Experimental Section

2.1. Reagents and Solvents

All substances used for the preparation of polymers were purchased from Sigma-Aldrich (Steinheim, Germany) or Acros (Geel, Belgium) and were used as received unless otherwise stated. Curcumin powder from *Curcuma longa* (turmeric)

was purchased from Sigma-Aldrich and analyzed in-house (curcumin = 79%; demethoxycurcumin = 17%, bisdemethoxycurcumin = 4%; determined by HPLC analysis; Figure S18, Supporting Information). Deuterated chloroform (CDCl₃) or methanol (MeOD) for NMR analysis was obtained from Deutero GmbH (Kastellaun, Germany).

The monomers 2-*n*-propyl-2-oxazine (*n*PrOzi), 2-*n*-butyl-2-oxazoline (*n*BuOx) and 2-*n*-butyl-2-oxazine (*n*BuOzi) were synthesized according to Seeliger et al.^[67] (Figures S1–S4, Supporting Information). All substances used for polymerization, namely methyl trifluoromethylsulfonate (MeOTf), propargyl *p*-toluenesulfonate, benzonitrile (PhCN), sulfolane and all monomers were refluxed over CaH₂ (PhCN was refluxed over P₂O₅) and distilled under argon.

2.2. Polymer Synthesis

The polymerizations and work-up procedures of the ABA triblock-copolymers^[54] as well as the AB diblock-copolymers^[65] were described recently and can be found in Figures S5–S16, Supporting Information. Briefly, the preparation of block-copolymers was performed as follows: initiator was added to a dried and nitrogen flushed flask and dissolved in the respective amount of solvent. The monomer for the first block was added and the reaction mixture was heated to 100 °C (2-*R*-2-oxazoline) or 120 °C (2-*R*-2-oxazine). Reaction progress was controlled by FTIR- and ¹H-NMR-spectroscopy. After complete monomer consumption, the mixture was cooled to RT and the monomer for the second block was added. After complete monomer consumption, the procedure was repeated for the third block in the case of ABA triblock-copolymers. After monomer consumption was confirmed for the last block, termination was carried out by addition of a secondary amine at 50 °C for 4 h. Subsequently, K₂CO₃ was added and the mixture was stirred at 50 °C for 4 h. Precipitates were removed by centrifugation and the solvent was removed under reduced pressure. The supernatant was transferred into a dialysis bag and dialyzed against Millipore water overnight. The solution was recovered from the bag and lyophilized.

2.3. Nuclear Magnetic Resonance Spectroscopy

¹H-NMR spectra were recorded on a Fourier 300 (300 MHz), Bruker Biospin (Rheinstetten, Germany) at 298 K. The spectra were calibrated to the signal of residual protonated solvent signal (CDCl₃; 7.26 ppm). Multiplicities of signals are depicted as follows: s, singlet; d, doublet; t, triplet; q, quartet; quin, quintet; dt; doublet of triplets; m, multiplet; b, broad.

2.4. Dialysis

Dialysis was performed using Spectra/Por membranes with a molecular weight cutoff of 1 kDa (ABA-triblock copolymers) or 8 kD (AB-diblock copolymers) (material: cellulose acetate) obtained from neoLab (Heidelberg, Germany). Water (Millipore) was renewed after 1 and 4 h, and every 12 h subsequently, until end of dialysis.

2.5. Gel Permeation Chromatography

Gel permeation chromatography (GPC) was performed on an Agilent 1260 Infinity System, Polymer Standard Service (Mainz, Germany) with either HFIP containing 3 g L⁻¹ potassium trifluoroacetate; precolumn: 50 × 8 mm PSS PFG linear M; 2 columns: 300 × 8 mm PSS PFG linear M (particle size 7 μm) or DMF containing 1 g L⁻¹ LiBr; precolumn: 50 × 8 mm PSS GRAM; columns: 30 and 1000 Å 300 × 8 mm PSS GRAM (particle size 10 μm) as eluent. The columns were kept at 40 °C and flow rates were 1.0 mL min⁻¹ (DMF) or 0.7 mL min⁻¹ (HFIP). Prior to each measurement, samples were filtered through 0.2 μm PTFE filters, Roth (Karlsruhe, Germany). Conventional calibration was performed with PEG standards (0.1–1000 kg mol⁻¹) and data were processed with WinGPC software.

2.6. CUR-Loaded Polymer Micelles

CUR-loaded polymer micelles were prepared by thin film method.^[59] Ethanolic polymer (20 g L⁻¹) and CUR (5.0 g L⁻¹) stock solutions were mixed in desired ratio. After complete removal of the solvent at 50 °C under a mild stream of argon, the films were dried in vacuo (≤ 0.2 mbar) for 20 min. Subsequently, preheated (37 °C) H₂O was added. Complete solubilization was facilitated by shaking the solutions at 1250 rpm at 55 °C for 12 min with a Thermomixer comfort, Eppendorf AG (Hamburg, Germany). Non-solubilized drug (if any) was removed by centrifugation for 5 min at 9.000 rpm with a MIKRO 185 (Hettich, Tuttlingen, Germany). Solubilization experiments were performed with three individually prepared samples and results are presented as mean ± standard deviation (SD).

CUR quantification was performed by UV–vis absorption on a BioTek Eon Microplate Spectrophotometer, Thermo Fisher Scientific (MA, USA) using a calibration curve obtained with known amounts of CUR (Figure S19, Supporting Information). Samples were prepared in Rotilabo F-Type 96 well plates, Carl Roth GmbH & Co. KG (Karlsruhe, Germany) at a constant volume of 100 μL. Spectra were recorded from 300–600 nm at 25 °C and CUR was quantified at 428 nm. Prior to UV–vis absorption measurements, the aqueous formulations were appropriately diluted with ethanol. The following equations were used to calculate LC and loading efficiency (LE):

$$LE = \frac{m_{\text{drug}}}{m_{\text{drug, added}}} \quad (1)$$

$$LC = \frac{m_{\text{drug}}}{m_{\text{drug}} + m_{\text{polymer}}} \quad (2)$$

where m_{drug} and m_{polymer} are the weight amounts of solubilized drug and polymer excipient in solution and $m_{\text{drug, added}}$ is the weight amount of drug initially added to the dispersion. No loss of polymer during micelles preparation was assumed.

2.7. CUR-Loaded Hydrogels

CUR-loaded hydrogels were prepared using a modified thin film method. Dried CUR/polymer films were dissolved in pre-cooled (5 °C) H₂O (Millipore) and shaken at 1200 rpm at 8 °C with a Thermomixer comfort, Eppendorf AG (Hamburg, Germany) until no solids were detectable anymore by visual inspection (≈6 h). The clear, viscous solutions were used without further purification. For CUR quantification, small amounts of CUR-loaded hydrogels were sampled and dissolved in ethanol. Drug content was determined by UV–vis absorption according to Equation (3):

$$\text{CUR}(\text{mg/g}) = \frac{m_{\text{drug}}}{m_{\text{hydrogel, wet}}} \quad (3)$$

where m_{drug} is the weight amount of solubilized drug and $m_{\text{hydrogel, wet}}$ is the weight of CUR-loaded hydrogel in the wet state. Loading capacity LC was determined according to Equation (2). For the determination, three samples were taken from the respective hydrogel and measured individually. However, each hydrogel was prepared once.

2.8. Incorporation of CUR-Loaded Polymer Micelles into Hydrogel

Respective amounts of freeze-dried, CUR-loaded polymeric micelles were added to a pre-cooled (≈8 °C) aqueous solution of the respective hydrogel (20 wt%). The dispersion was gently shaken at ≈8 °C until the freeze-dried micelles were completely dissolved in the hydrogel solution (≈2 days). The drug contents of the clear, highly viscous solutions were determined according to Equation (8) and LC was determined according to Equation (2).

2.9. Rheology

Rheological analysis was performed on a Physica MCR 301, Anton Paar (Ostfildern, Germany) utilizing a plate–plate geometry (diameter 25 mm). The rheometer was equipped with a Peltier element. Prior to temperature-sweep measurements, the samples were allowed to equilibrate on the rheometer at 5 °C for 3 min. Following this, the temperature was raised linearly from 5 to 60 °C at 5 °C min⁻¹. Frequency was 1 Hz and the amplitude was 0.5% at 0.5 mm plate–plate distance. Within these conditions, the hydrogels (20 wt% in deionized H₂O) were within their linear viscoelastic region^[65] and CUR-loaded hydrogels were assumed to be as well.

2.10. HPLC Measurements

CUR-loaded hydrogels were analyzed on a LC-20A Prominence HPLC, Shimadzu (Duisburg, Germany) equipped with a system controller CBM-20A, a solvent delivery unit LC-20 AT (double plunger), an online degassing unit DGU-20A, an auto-sampler SIL-20AC, and a SPD-20A UV–vis detector. As stationary phase, a ZORBAX Eclipse Plus, Agilent (Santa Clara,



CA, USA) C18 column (4.6 × 100 mm; 3.5 μm) was used. The mobile phase was a gradient of H₂O/ACN (Figure S18a, Supporting Information) at 40 °C and a flow rate of 1 mL min⁻¹. CUR was quantified at 427 nm. Possible degradation products were investigated at 220 nm.

2.11. Long-Term Stability Studies

For long-term stability studies, CUR-loaded hydrogels were stored in the freezer (≈8 °C). For CUR quantification, small amounts of CUR-loaded hydrogels were sampled and dissolved in ethanol. Drug content was determined by UV–vis absorption at 428 nm. To confirm CUR integrity, small amounts of CUR-loaded hydrogels were sampled and diluted with ACN/H₂O = 60/40 (v/v) and characterized by HPLC analysis at 220 and 427 nm.

2.12. CUR-Release Studies

For CUR-release studies, CUR-loaded hydrogels were injected into trans-well inserts (24-well plate, BRANDplates insert system, BRAND GmbH & Co. KG, Wertheim, Germany) filled with collagen hydrogels at a final concentration of 6 g L⁻¹ as reported previously^[68] with a Hamilton syringe (injection volume: 10 μL). For every sample, three injection of the same batch of formulation were placed in individual wells. To ensure constant injection depth and position, a 3D-printed scaffold was utilized as guidance for the syringe. Prior to injection, the CUR-loaded hydrogel filled Hamilton syringe was cooled in the freezer (≈8 °C) to ensure liquidity of respective hydrogels. Basolateral chamber was filled with 1500 μL PBS and collagen matrix in the apical side was covered with 100 μL PBS. At specific time-points mentioned in main text, the solution of the basolateral side was removed, freeze-dried and dissolved in ethanol. Ethanolic solutions were centrifuged for 10 min at 9000 rpm in order to avoid scattering from undissolved salts from PBS. CUR content of the supernatant was quantified by UV–vis absorption at 428 nm and CUR integrity confirmed by HPLC analysis at 220 and 427 nm.

3. Results and Discussion

3.1. CUR Solubilization

Whereas A-BuOx-A nanoformulations exhibit CUR LCs comparable to those found in the literature for other polymer amphiphiles (LC ≈20 wt%^[69]), its structural isomer A-PrOzi-A enables very high CUR-loadings >50 wt%^[54]. The drug formulations with these ABA-triblock copolymers are designed for intravenous (IV) administration; however, rapid clearance of APIs in highly dynamic polymer micelles has been observed.^[60] In contrast, steady serum concentrations, which can be crucial in many applications, could be achieved through the use of subcutaneous depots.^[70] In 2017, Lorson et al. reported a POx/POzi-based reversibly thermogelling hydrogel as cytocompatible bioink.^[65] As this polymer comprises the same building

Table 1. Analytical data of investigated block copolymers including the yield, molar mass M_n and dispersity \bar{D} .

Composition ^{a)}	Polymer ID	Yield [%]	$M_n^a)$	$M_n^b)$	$M_n^c)$	$\bar{D}^d)$
			[kg mol ⁻¹]			
PMeOx ₃₅ - <i>b</i> -PPrOzi ₂₀ - <i>b</i> -PMeOx ₃₅	A-PrOzi-A	67	8.7	9.8*	6.1	1.16
PMeOx ₃₅ - <i>b</i> -PBuOx ₂₀ - <i>b</i> -PMeOx ₃₅	A-BuOx-A	82	8.6	7.0*	7.2	1.18
PMeOx ₃₅ - <i>b</i> -PBuOzi ₂₀ - <i>b</i> -PMeOx ₃₅	A-BuOzi-A	67	9.0	9.4*	5.6	1.20
PPrOzi ₅₀ - <i>b</i> -PMeOx ₅₀	H50	75	10.8	10.4**	7.3	1.17
PPrOzi ₁₀₀ - <i>b</i> -PMeOx ₉₉	H100	89	21.3	20.2**	10.4	1.38

^{a)}According to $[M]_0/[I]_0$; ^{b)}Obtained by ¹H-NMR (*CDCl₃; **MeOD); evaluated as mean of all relevant signals; ^{c)}Obtained by GPC (eluent: DMF, calibrated with PEG standards); deviations in molar mass determination between NMR end-group analysis and GPC standard calibration can be attributed to the use of PEG-standards for calibration.^[55] Synthesis and characterization of the triblock-^[54] as well as diblock-copolymers^[65] was previously reported.

blocks as A-PrOzi-A but has a different architecture (AB diblock vs ABA triblock) and monomer ratio, the effects of solubilized CUR on the hydrogel properties (gel temperature, storage/loss modulus) are of interest. Hence, CUR was incorporated into aqueous solutions of PPrOzi₅₀-*b*-PMeOx₅₀ (H50) and PPrOzi₁₀₀-*b*-PMeOx₉₉ (H100) (Table 1; for polymer synthesis and characterization, the reader is referred to Figures S12–S16, Supporting Information). Such, the influence of the degree of polymerization (DP) of both blocks on the solubilization capacity for CUR can be assessed.

Although exhibiting the same building blocks as A-PrOzi-A, both diblocks exhibited much lower LCs for CUR than the former as well as compared to A-BuOzi-A and A-BuOx-A. At 10 g L⁻¹ polymer, only 0.87 g L⁻¹ (LC = 8 wt%) or 0.91 g L⁻¹ (8.4 wt%) CUR could be solubilized using H50 or H100, respectively (Figure 1a). Increasing the polymer concentration to 50 g L⁻¹ somehow increased CUR loadings up to 15 wt% (CUR = 8.8 g L⁻¹) in the case of H50. Similar shortcoming of AB diblock-copolymers compared to the corresponding ABA triblock-copolymers with respect to their solubilization capacity has been observed before. Whereas A-BuOx-A exhibits LCs up to 49 wt% for the water-insoluble drug paclitaxel (PTX), the corresponding diblock only enabled PTX-loadings of 17 wt%.^[71] However, in this case, the DP of the respective blocks were similar while in the present case the thermoresponsive block has a much higher DP in the diblocks compared to the triblock. At ≤50 g L⁻¹, neither H50 nor H100 forms a gel, but apparently, the self-assemblies formed -presumably polymersomes-^[72] are not well suited for CUR solubilization.^[65]

The polymer concentrations of 10 and 50 g L⁻¹ were chosen to compare the solubilization behavior of H50 or H100 with those of the previously reported A-BuOx-A, A-PrOzi-A, and A-BuOzi-A. The latter were designed as drug vehicles for intravenous administration, for which those moderate polymer concentrations are most suitable. In contrast, drug-loaded hydrogels find applications often at much higher polymer concentrations. Therefore, LC of H100 was also investigated at polymer concentrations of 20 wt% at which gelation occurs. As H100 already forms a gel <20 °C at this concentration the dried drug/polymer films were re-dispersed with water at 5 °C until no solid particles were detectable anymore by visual

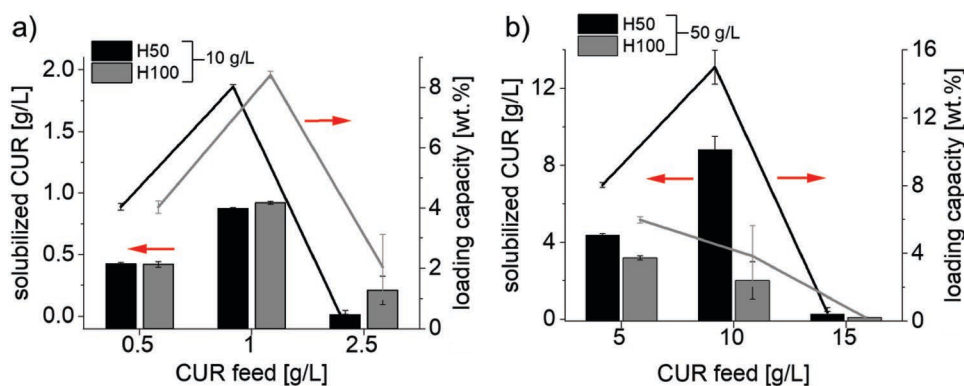


Figure 1. Solubilized aqueous CUR concentrations (bars, left axis) and corresponding loading capacities (lines, right axis) in dependence of the CUR feed by H50 (black) or H100 (gray) at polymer concentrations of a) 10 or b) 50 g L⁻¹. Data are given as means ± SD (n = 3).

inspection (≈6 h). The obtained clear solutions were moderately viscous at $T \leq 5 \text{ }^\circ\text{C}$ and showed an increasing viscosity with increasing CUR loading, as per visual inspection. As defined volumes could not be easily sampled from the viscous solutions even at $T \leq 5 \text{ }^\circ\text{C}$, small amounts of the CUR-loaded hydrogels were weighed, and the CUR loading will be defined as the ratio of solubilized CUR (mg) with respect to the total weight of the hydrogel in the hydrated state (g) (Equation (3)). Loading

efficiencies (LE) between 75% and 83% and rather high aqueous CUR concentrations of up to $23.6 \pm 0.5 \text{ mg/g}$ (LC = 10.6 wt%) at mass concentration of $\rho(\text{H100}) = 20 \text{ wt\%}$ (Figure 2a) could be obtained. The fact that those high CUR concentrations were feasible using H100 and because H50 only gelled at elevated temperature with ($T_{\text{gel}} > 57 \text{ }^\circ\text{C}$) or without ($T_{\text{gel}} = 40 \text{ }^\circ\text{C}$) the addition of triblock copolymers (Figure S20, Supporting Information), H50 was not investigated further in the present work. It should

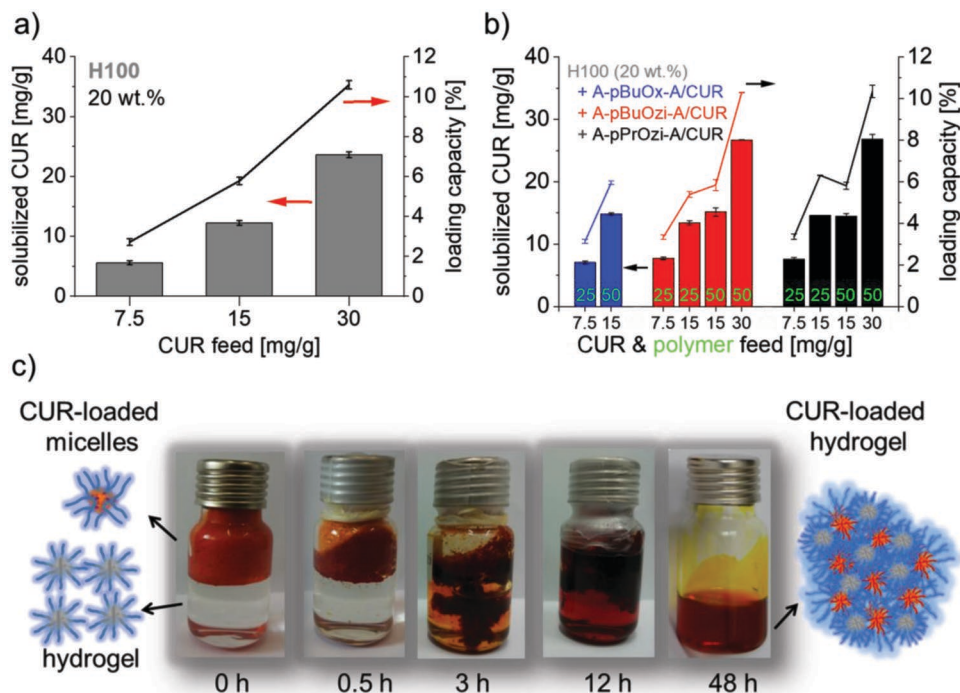


Figure 2. a) Solubilized aqueous CUR concentrations (bars, left axis) and corresponding loading capacities (line, right axis) in dependence of the CUR feed by H100 at 20 wt% in H₂O. Data are given as means ± SD (n = 3); b) solubilized aqueous CUR concentrations (bars, left axis) and corresponding loading capacities (lines, right axis) in dependence of the CUR feed by H100 (20 wt% in H₂O) after incorporation of freeze-dried, CUR-loaded micelles of either A-BuOx-A (blue), A-BuOzi-A (red), or A-PrOzi-A (black). Amount of polymer within the CUR-loaded micelles was either 25 mg/g_{hydrogel,wet} or 50 mg/g_{hydrogel,wet} (green). Each hydrogel was prepared once; however, CUR concentration was quantified with three withdrawn samples each to confirm homogeneous CUR distribution and absence of precipitation; c) images of the incorporation of freeze-dried, CUR-loaded micelles (A-PrOzi-A/CUR = 50/30 g/g) into H100 (20 wt% in H₂O). The amounts of A-PrOzi-A and CUR were 50 and 15 mg/g, respectively. Samples were gently shaken at 5 °C for 2 days. Illustration of CUR-loaded micelles and (CUR-loaded) gels, are given as a very rough visualization and should not be confused with the actual structure of the respective solutions.

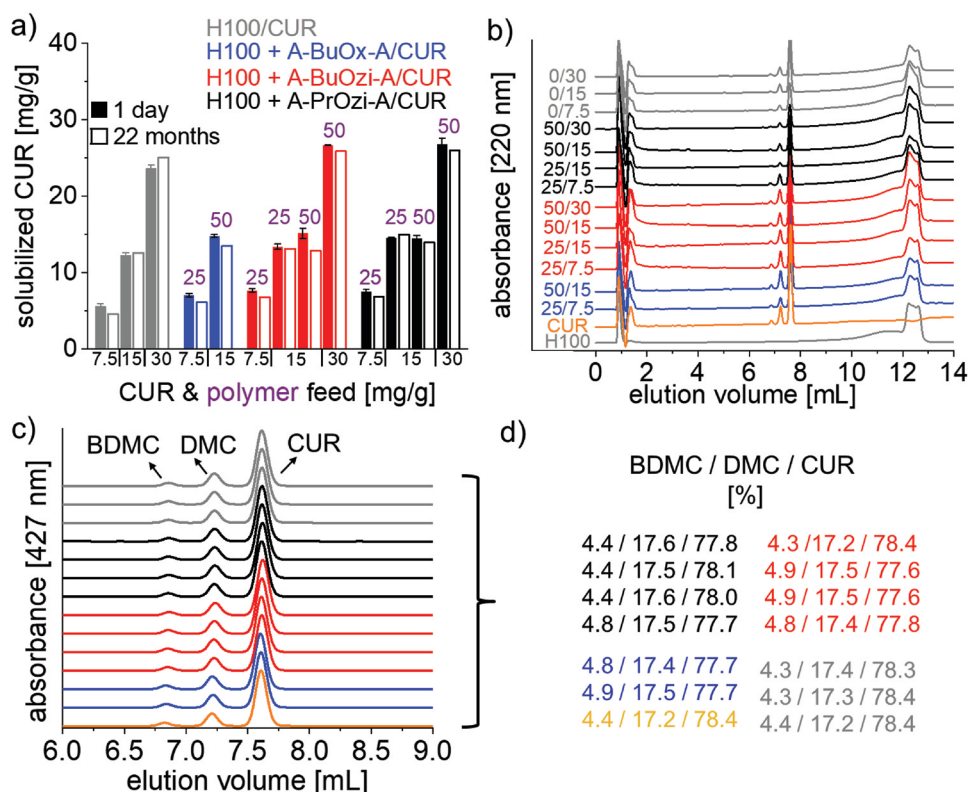


Figure 3. a) Solubilized aqueous CUR concentrations in dependence of the CUR feed (*x*-axis) by H100 (20 wt% in H₂O) after preparation (full bars) or 22 months storage at 8 °C under the exclusion of light (hollow bars). CUR was either directly solubilized by H100 (gray) or pre-incorporated into polymer micelles of A-BuOx-A (blue), A-BuOzi-A (red), or A-PrOzi-A (black). Concentration of the ABA triblock-copolymers is given by purple numbers (mg/g_{hydrogel,wet}); b) corresponding HPLC elugrams after 22 months storage at λ_{abs} = 220 nm to exclude CUR degradation. Elugrams of neat H100 (bottom, gray) and CUR (2nd bottom, orange) are given for comparison. Numbers left of the elugrams correspond to amount of ABA triblock-copolymer/CUR (mg/g_{hydrogel,wet}); c) detailed view of the HPLC elugrams at λ_{abs} = 427 nm as well as d) corresponding ratio of BDMC, DMC, and CUR.

be noted that reproducibility of T_{gel} of H50 is generally more susceptible to batch-to-batch variations compared to H100.^[65]

In addition to direct solubilization of CUR with H100, freeze-dried CUR nanoformulation of either A-BuOx-A (Figure 2b, blue), A-BuOzi-A (red) or A-PrOzi-A (black) were incorporated at same CUR feed concentrations of 7.5, 15, and 30 mg/g. To obtain more detailed insights into the influence of the ABA-triblock copolymers, two different triblock concentrations (25 and 50 mg/g) were investigated. Due to the limited LC of A-BuOx-A for CUR, highly loaded micelles were only feasible using A-BuOzi-A or A-PrOzi-A. The aqueous solutions of H100 (20 wt% in H₂O) were precooled to 5 °C and the respective amount of lyophilized, CUR nanoformulation was added. The mixture was shaken at 5 °C for 2–4 days (depending on the used polymer and CUR concentration) until a completely clear and viscous solution was formed (Figure 2c). Similar to the solubilization of neat CUR (Figure 2a), the hydrogels incorporating CUR-loaded micelles exhibited excellent LEs >95% (Figure 2b) with no visible sign of precipitation.

The CUR-loaded hydrogels showed even higher stability than the CUR nanoformulations of, for example, A-PrOzi-A^[54] and drastically prolonged shelf-life with no apparent loss of CUR-content even after 22 months of storage in the sol-state at 8 °C under the exclusion of light (Figure 3a).

This is remarkable, as 90% of CUR was reported elsewhere to be degraded in water (pH = 7.2; 37 °C) after 30 min.^[49,50] Although exhibiting high polymer concentrations up to 25 wt% (H100 = 20 wt% + ABA triblock copolymer = 5 wt%), the major component of the CUR-loaded hydrogels remains water. Important to note, the prolongation of the aqueous CUR solubility was observed irrespective whether CUR was directly solubilized by H100 (Figure 3a, gray bars) or incorporated as nanoformulation (blue, red, black bars). Furthermore, this remarkable long-term stability was found irrespective of the chemical structure of the triblock copolymers. Similarly, an extraordinary suppression of crystallization was previously observed in nanoformulations of paclitaxel using A-BuOx-A.^[71] HPLC analysis suggests that no CUR degradation occurred as the ratio between the curcuminoids bisdemethoxycurcumin (BDMC), demethoxycurcumin (DMC) and CUR remained constant during 22 months storage (Figure 3b,c) which reportedly shifts during degradation processes.^[73] Hennink and co-workers previously reported that polymer micelles can stabilize CUR in water by several orders of magnitude, but they still clearly observed degradation within a few days.^[69] As all samples showed comparable loading and long-term stabilities, the rheological properties of all CUR loaded hydrogels were determined as described in the following.

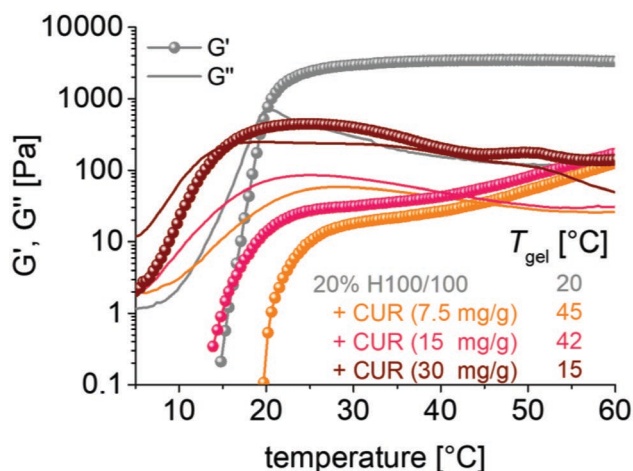


Figure 4. Temperature dependent rheological analysis of H100 (20 wt%) before (gray) and after solubilization of 7.5 (orange), 15 (pink) or 30 (brown) mg/g CUR. Samples were heated from 5 to 60 °C at 5 °C min⁻¹. Frequency was 1 Hz at 0.5% amplitude. T_{gel} is defined as the crossover of storage G' (lines with symbols) and loss modulus G'' (lines without symbols).

3.2. Rheological Properties

3.2.1. CUR-Loaded Hydrogels

Addition of hydrophobic CUR strongly affected the thermoresponsive and viscoelastic properties of H100-based hydrogels (Figure 4). Especially at low CUR feed concentrations of 7.5 or 15 mg/g, T_{gel} significantly increased from 20 °C (neat H100; 20 wt%) to 45 and 42 °C, respectively. Accordingly, the storage modulus (G') at 37 °C strongly decreased several magnitudes from 3.4 kPa (0 mg/g CUR) to 24 Pa (7.5 mg/g) and 39 Pa (15 mg/g). Clearly, incorporation of CUR significantly weakened the gel structure at same strain. Arguably, both trends are disadvantageous for the intended use as injectable drug depot, as T_{gel} should be below body temperature forming a gel with sufficient strength to prevent rapid dissolution/dispersion of the depot. A decrease in G' to 253 Pa (37 °C) was also observed at 30 mg/g CUR feed, whereas T_{gel} decreased to 16 °C. However, this gel remained rather weak with pronounced viscous character as the loss factor ($\tan \delta = G''/G'$) remained close to unity. In any case, CUR clearly interferes significantly with the formation of a physically crosslinked polymer network necessary for gelation.

Similar trends of decreasing gel stiffness with increasing drug-content were also observed for other hydrogels such as poly(D,L-lactic acid-co-glycolic acid) (PLGA)-polyethylene glycol (PEG)-PLGA.^[27] In this report, G'_{max} ($T \approx 35$ °C) decreased from 520 to 280 and 250 Pa by incorporation of 0, 4, and 8 g L⁻¹ docetaxel (DTX), respectively. It should be mentioned that a dramatic decrease of G' to essentially 0 Pa at $T > 37$ °C occurred for both, the neat as well as the DTX-loaded hydrogel. Nevertheless, a single intratumoral injection of DTX-containing hydrogel was as efficient as three IV injections of DTX. In a different report, a decrease in maximum viscosity (η_{max} , 37 °C) with increasing drug content for

doxorubicin (0.6 g L⁻¹ DOX)^[25] as well as PTX (2 g L⁻¹ PTX)^[26] loaded PEG-*b*-polycaprolactone (PEG-PCL)-based hydrogels was observed. In another report, the gelation of PLGA-PEG-PLGA was completely prevented by the incorporation of 1.6 g L⁻¹ rapamycin. Interestingly, this strong interference could be suppressed by co-solubilization of two other hydrophobic drugs, paclitaxel and tanespimycin (17-AAG).^[22] While the incorporation of hydrophobic drugs in various hydrogels consistently decreased gel stiffness, the influence on T_{gel} appeared to be rather small without a trend, as T_{gel} sometimes slightly increased,^[19,25,26] and sometimes slightly decreased.^[27]

However, we wondered if CUR addition in form of CUR nanoformulations^[54] could prevent the detrimental interference with the gel, retaining the initial viscoelastic properties of H100.

3.2.2. Incorporation of ABA Triblock Copolymers into Hydrogel Matrix

Prior to the incorporation of CUR nanoformulations, the influence of the ABA triblock copolymers alone on the gelation properties of H100 is of interest. At low polymer concentrations of 25 mg/g hydrogel, only minor changes of the thermogelling properties of H100 occurred (Figure 5a). In the case of A-BuOzi-A and A-PrOzi-A, T_{gel} slightly increased to 23 and 25 °C respectively, whereas it remained constant in the case of A-BuOx-A. In case of A-PrOzi-A, the storage modulus (G') was reduced somewhat throughout the investigated temperature range ($G' = 2.2$ kPa (37 °C)), whereas it increased slightly through the incorporation of polymers bearing butyl side chains. The increase was most pronounced for A-BuOx-A with $G' = 4.7$ kPa (37 °C). The trend of decreasing T_{gel} and increasing gel stiffness became more prominent with increasing A-BuOx-A concentration. At A-BuOx-A = 50 mg/g, G' increased by a factor of two to 6.8 kPa (37 °C) (Figure 5b). T_{gel} decreased further to 17 °C, whereas G' kept increasing to 7.8 kPa (37 °C) when 100 mg/g A-BuOx-A were added (Figure 5c). At this point, the total polymer concentration was 27 wt%. However, the decrease in T_{gel} and increase of G' was not simply due to an increase in solids content, as shown in the case of A-BuOzi-A and A-PrOzi-A. At both, 50 and 100 mg/g triblock copolymer concentration, A-BuOzi-A as well as A-PrOzi-A increased T_{gel} and decreased gel stiffness (Figure 5b,c). This was most pronounced for A-PrOzi-A. As the latter comprises the same building blocks as H100, it seems reasonable that A-PrOzi-A interfered most with the gelation of H100. As both, hydrophilic and hydrophobic block are identical and the degree of polymerization does not differ very much, these two polymers should be expected to mix freely. Since the self-assembly of block copolymers does strongly depend on the block volume ratio, this must be expected to affect the self-assembly and thus, thermogelation of H100. A-BuOzi-A, sharing the same backbone but bearing a more hydrophobic central B block still interferes significantly, albeit somewhat less with the gelation of H100. Even though being intermediate with respect to hydrophobicity, A-BuOx-A exhibits an entirely different influence on the thermogelation of H100. At this point, we can only assume that the different backbone (POx vs POzi) of the hydrophobic block reduces mixing,

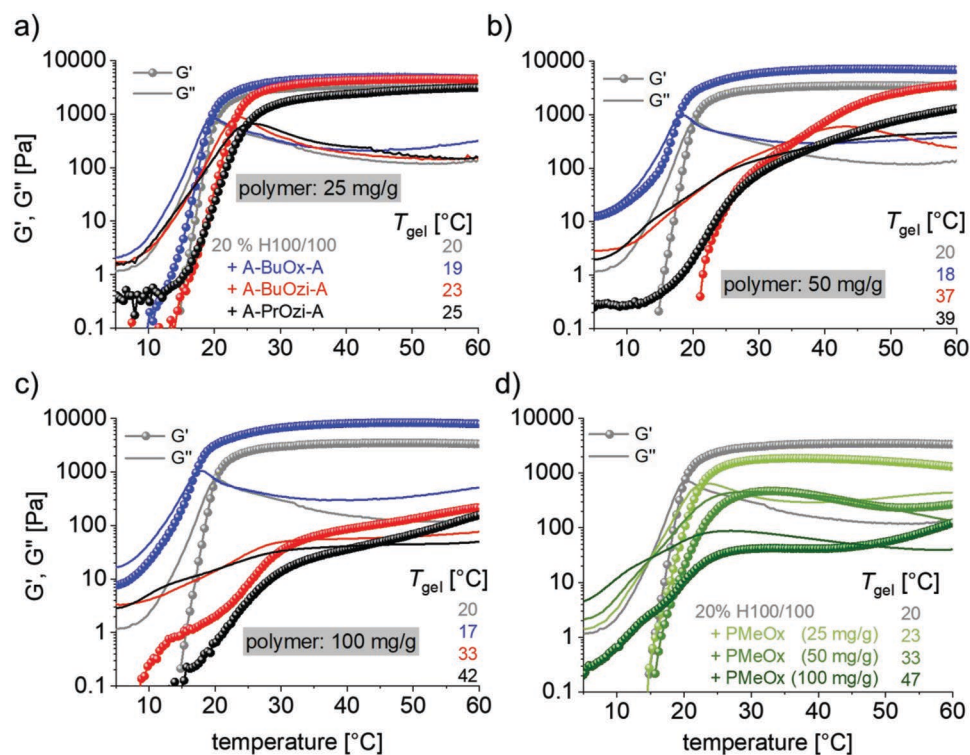


Figure 5. Temperature dependent rheological analysis of H100 (20 wt%) before (gray) and after addition of a) 25; b) 50; or c) 100 mg/g of A-BuOx-A (blue), A-BuOzi-A (red), or A-PrOzi-A (black); d) incorporation of PMeOx homopolymer (DP = 30) at the same polymer concentration as it would be present by the incorporation of ABA triblock-copolymers at 25, 50, and 100 mg/g. Samples were heated from 5 to 60 °C at 5 °C min⁻¹. Frequency was 1 Hz at 0.5% amplitude. T_{gel} is defined as the intersection of storage G' (lines with symbols) and loss modulus G'' (lines without symbols).

and therefore, does not influence network formation of H100 as much. The lower T_{gel} and higher G' may be explained by macromolecular crowding and competition for water molecules for hydration. Similarly, T_{gel} of thermoresponsive Pluronic F127 gel (18 wt%) also decreased from 27.4 to 25.8 and 23.1 °C when incorporating 0.21%, 0.42%, and 1.24% w/v phospholipid-based liposomes, respectively.^[17] This was attributed to dehydration of F127 micellar cores due to entrapment of water in the inner hydrophilic core of the liposomes leading to a greater extend of dehydration and lower T_{gel} .

Important to note, A-BuOx-A, being the only polymer to decrease T_{gel} and increase G' , was also the only ABA triblock copolymer exhibiting a thermogelling behavior on its own, albeit only at 20 wt%, and rather high temperatures $T_{gel} = 41$ °C. Also, the resulting gel was very weak with a low G' ($G'_{50\text{ °C}} = 180$ Pa) (Figure S21, Supporting Information). As a control to test the macromolecular crowding hypothesis, we also investigated the influence of PMeOx homopolymer with a DP of 100, approximately corresponding to the overall length of the ABA block copolymers. PMeOx was incorporated into H100 at the same concentrations as it is present incorporating the respective triblock copolymers at 25, 50, and 100 mg/g (Figure 5d). Interestingly, the PMeOx exhibited a weakening effect very similar to the one of A-PrOzi-A, yielding comparable temperature-dependent rheological profiles, sol–gel transition temperatures as well as gel stiffnesses. This, in combination with the difference between PMeOx and, for example, A-BuOx-A once more highlights the influence of the hydrophobic block

of the respective triblock copolymers. Next, it was interesting to investigate how the incorporation of CUR nanoformulations of the different triblock copolymers affect the thermoresponsive behavior of H100.

3.2.3. Incorporation of CUR Nanoformulations of ABA Triblock Copolymers into Hydrogel Matrix

In contrast to neat CUR or neat polymers, the incorporation of CUR and polymer in form of nanoformulations of A-BuOx-A, A-BuOzi-A, or A-PrOzi-A affected the viscoelastic properties to a lesser extent (Figure 6). Overall, T_{gel} was either comparable or lower than that of neat H100 (20 wt%). This suggests that the CUR nanoformulations remain largely intact during their dissolution in H100. Having a distinct core–shell structure in mind, all CUR loaded micelles present the same hydrophilic PMeOx corona, somehow masking the influence of the different hydrophobic cores (Figure 5a–c).

That such core–shell structure is probably not a fully accurate representation of the actual micellar morphology becomes evident when considering the remaining small differences between the hydrogels incorporating different CUR nanoformulations suggesting a small but noticeable effect of the hydrophobic block on the hydrogel properties. We recently reported that in fact the hydrophilic corona is involved in the binding of CUR in this system.^[74] Similar to the incorporation of the neat triblock copolymers, A-BuOx-A/CUR exhibited the highest gel

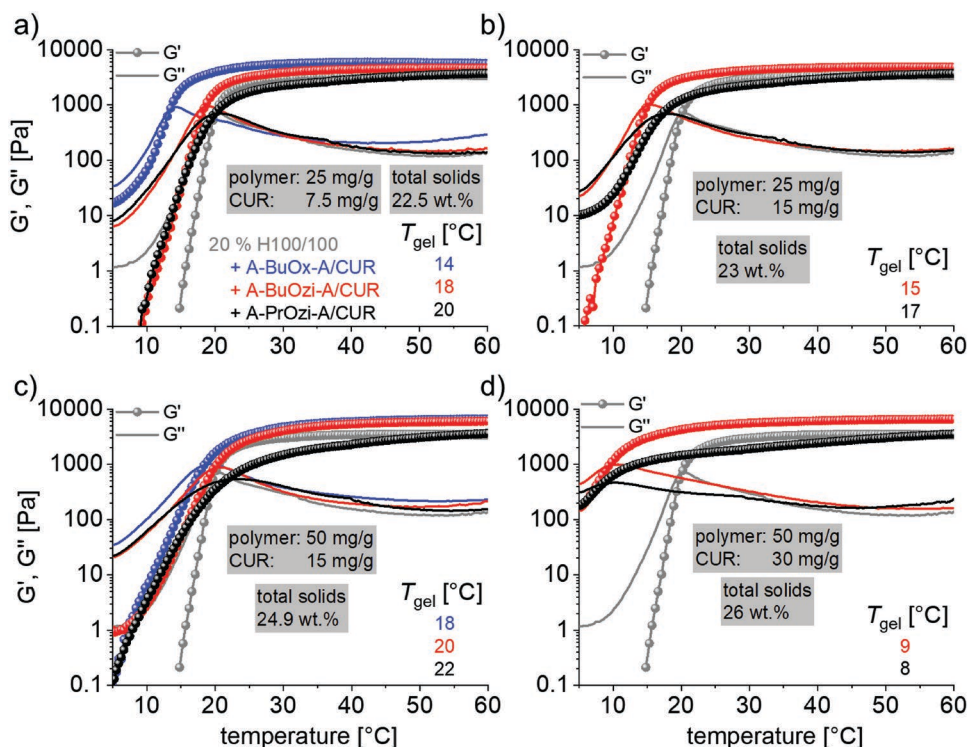


Figure 6. Temperature dependent rheological analysis of H100 (20 wt%) before (gray) and after incorporation of CUR-loaded polymer micelles of A-BuOx-A (blue), A-BuOzi-A (red), or A-PrOzi-A (black). Concentration of polymer/CUR added was either a) 25/7.5; b) 25/15; c) 50/15; or d) 50/30 mg/g_{H100,wet}. Samples were heated from 5 to 60 °C at 5 °C min⁻¹. Frequency was 1 Hz at 0.5% amplitude. T_{gel} is defined as the intersection of storage G' (lines with symbols) and loss modulus G'' (lines without symbols).

stiffness at a given temperature, whereas G' of A-PrOzi-A/CUR was still below that of neat H100.

To verify the reproducibility of our observations, we synthesized a second batch of H100 and investigated its rheological properties (Figure S22a, Supporting Information). More importantly, also the influence of A-PrOzi-A/CUR at both, the lowest (25/7.5 mg/g_{H100,wet}; Figure S22b, Supporting Information) and highest solids content (50/30 mg/g_{H100,wet}; Figure S22c, Supporting Information), was highly reproducible using the different batch of H100. A-PrOzi-A/CUR was either added as dry powder to 20 wt% H100 (as employed above) or added as highly concentrated aqueous solution (A-PrOzi-A/CUR = 150/90 or 75/22.5 g/L) to 30 wt% H100 to yield the same final polymer, CUR and hydrogel concentrations. Although the latter preparation method is faster, aqueous polymer/drug concentrations of 150/90 g/L may not be generally feasible with most systems.

The differences between the various nanoformulations were also apparent by the flow properties of the respective hydrogels, as H100 + A-BuOx-A/CUR exhibited shape integrity already at 15 °C, whereas A-BuOzi-A/CUR or A-PrOzi-A/CUR were free-flowing sols under the same conditions (Figure 7a), despite rheological analysis might suggest otherwise ($G' < G''$ for all samples at 15 °C, Figure 7b). Nevertheless, all hydrogels incorporating CUR nanoformulations exhibited sol-gel transitions well below body temperature as well as sufficient stability at 37 °C, making them promising candidates as injectable drug depots. Therefore, the CUR release of selected hydrogels was investigated in the next step.

3.2.4. CUR Release from Hydrogels Embedded in Collagen

To investigate the CUR release under conditions related to the desired application as injectable, subcutaneous drug depot, the CUR-loaded hydrogels were injected into a collagen matrix embedded on the apical side of trans-well inserts and subsequently the CUR release determined on the basolateral side. Collagen was chosen since it reflects the composition and structure of human connective tissue to which drug-loaded hydrogels might be applied in a future clinical setting. In preliminary experiments, we noticed major variabilities in the drug release profile, which we attributed to variation of the positioning of the hydrogel depot within the collagen matrix. To reduce such variations, the syringes containing the CUR-loaded hydrogels were guided using a 3D-printed scaffold to ensure reproducible injection depth (0.25 cm at 0.5 cm height of collagen) as well as injection position (Figure 8a). Before injection, the syringes loaded with the respective hydrogels were cooled for 20 min at 8 °C to ensure liquidity of the respective sols. CUR was either neatly incorporated into the hydrogel (20 wt% H100 + 15 mg/g CUR) or in the form of A-PrOzi-A (polymer/CUR = 50/30 mg/g) or A-BuOx-A (polymer/CUR = 50/15 mg/g) nanoformulations, both at maximum CUR-loadings. These hydrogels were selected due to their different gel properties. Whereas H100 directly incorporating CUR exhibited a sol-gel transition above body-temperature ($T_{gel} = 42$ °C; $G'_{37°C} = 37$ Pa; Figure 4), both hydrogels incorporating triblock-copolymers are solid gels at the investigated 37 °C (Figure 6c,d). Interestingly,

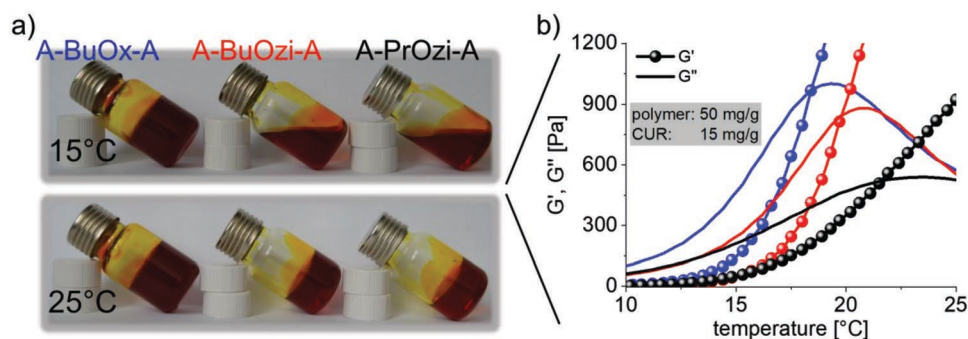


Figure 7. a) Flow properties of H100 (20 wt% in H₂O) incorporating CUR-loaded polymeric micelles (polymer/CUR = 50/15 mg/g) at either 15 (top) or 25 °C (bottom); b) corresponding rheological properties of respective hydrogels.

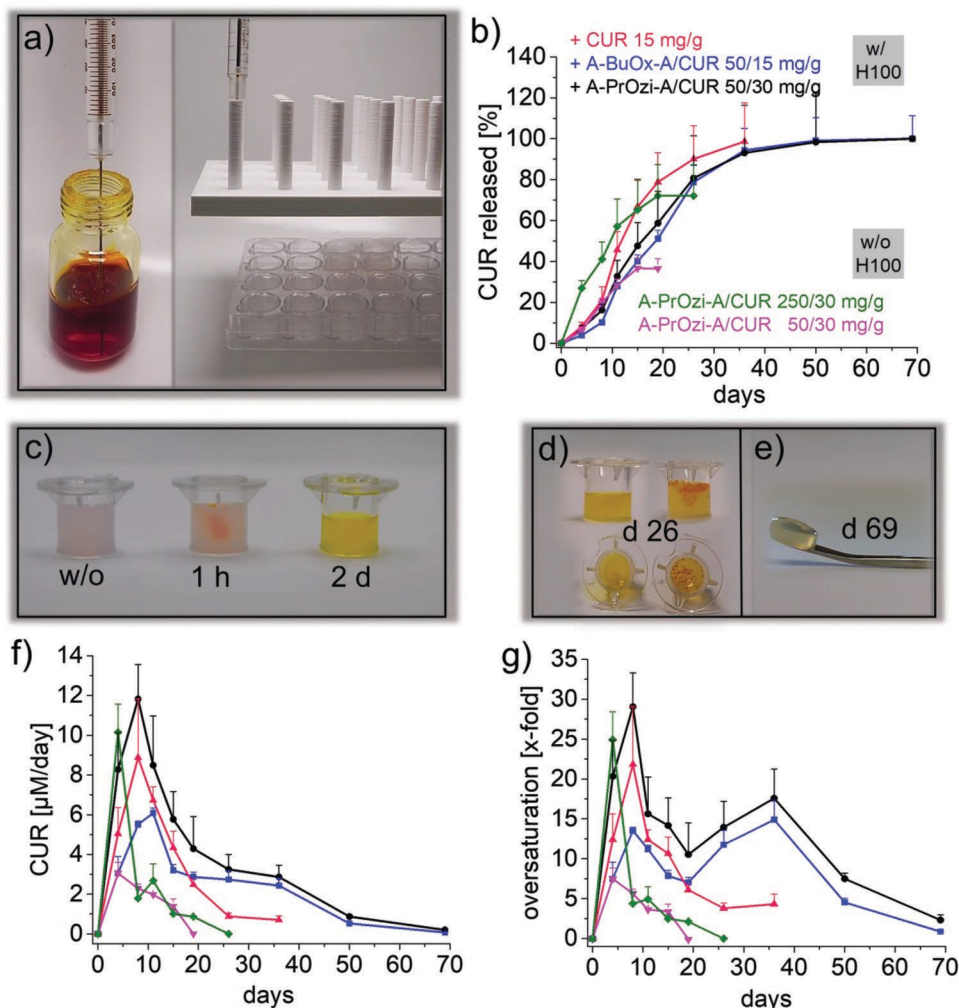


Figure 8. a) Setup for CUR release studies from CUR-loaded hydrogels or CUR-loaded polymer micelles injected into a collagen matrix. Hydrogel was added in a Hamilton syringe, cooled to 8 °C and subsequently injected (10 µL) into a transwell containing collagen. To ensure same injection depths and positions within the collagen matrix, the syringe was guided with a 3D printed scaffold (right picture); b) long-term CUR release of CUR directly incorporated into H100 (20 wt%; red curve) or pre-incorporated into either A-BuOx-A (polymer/CUR = 50/15 mg/g; blue curve) or A-PrOzi-A (polymer/CUR = 50/30 mg/g, black curve). A-PrOzi-A/CUR at either polymer/CUR = 250/30 mg/g (green) or 50/30 mg/g (pink) without H100 for comparison; c) appearance of collagen matrix before (left) and 2 h (middle) or 2 days (right) after injection of H100/A-PrOzi-A/CUR (representative for all hydrogel containing samples); d) appearance of collagen containing H100/A-PrOzi-A/CUR (left) or A-PrOzi-A/CUR = 250/30 mg/g (right) after 26 days incubation in PBS; e) collagen matrix initially containing H100/A-PrOzi-A/CUR after release experiment (d 69); f) aqueous CUR concentration in basolateral chamber released per day; g) concentration of released CUR with respect to CUR aqueous solubility (= oversaturation) at day of quantification. All CUR-loaded samples were prepared once and injected in three individual trans-wells containing collagen. Results are presented as mean ± SD ($n = 3$).

H100/CUR exhibited the fastest CUR-release of all samples (Figure 8b, red curve). Nevertheless, a sustained release was obtained with 50% CUR release after approximately 15 days ($t_{50\%}$). H100 incorporating A-BuOx-A/CUR at the same CUR concentration of 15 mg/g (blue curve) exhibited a slower release profile, with $t_{50\%} = 19$ days. This may be attributed to the much stronger network, as evidenced by their rheological properties ($G'_{37^\circ\text{C}}(\text{H100/CUR}) = 37$ Pa; $G'_{37^\circ\text{C}}(\text{H100/A-BuOx-A/CUR}) = 5.7$ kPa). The slower release in the presence of A-BuOx-A could also be due to altered pore sizes of the respective hydrogel which might to some extent correlate with the gel stiffness. To investigate this hypothesis, more detailed investigations utilizing, for example, fluorescence recovery after photobleaching would be necessary, which are outside the scope of the current contribution.

A more sustained release of acetylsalicylic acid (AS) pre-incorporated into lipid nanoparticles compared to directly solubilized AS also occurred for κ -carrageenan-based hydrogels within the first 2 h after immersing the respective hydrogels in water.^[66] However in contrast to the presently reported findings, the cumulative release within 40 h of directly solubilized AS was much lower than that of formulated one reaching a plateau already after 15 h (= incomplete overall drug release). Unfortunately, the influence of the nanoformulation on gelation properties was not further investigated in this report. Similarly, Nie et al.^[17] observed a prolonged release of PTX pre-incorporated into liposomes compared to solubilization of neat PTX with Pluronic F127 at both, the dialysis method (20% vs 40% release after 8 h) as well as when immersing the gels in water (60% vs 90% release after 8 h).

H100 incorporating A-PrOzi-A/CUR (Figure 8b, black curve) exhibited the longest release profile with 50% release after approximately 23 days and 80% release after 36 days. As the differences between H100 incorporating either A-PrOzi-A/CUR or A-BuOx-A/CUR became evident only at later stage of 19 days and after, the longer release of the former is probably due to the higher CUR concentration in the case of A-PrOzi-A/CUR rather than the viscoelastic properties of the hydrogel ($G'_{37^\circ\text{C}}(\text{H100/A-PrOzi-A/CUR}) = 2.0$ kPa). A similar faster cumulative release at lower drug-loading was also observed for PEG-PCL-PEG-based hydrogels when immersed at 37 °C in PBS.^[75] At 1 g L⁻¹ honokiol, 45% drug was released after 8 days, whereas only 35% were released at 2 g L⁻¹ in the same time period. Cumulative release of honokiol reached a plateau already at day 8 with little less than 50% overall release after 14 days, hinting toward drug crystallization/precipitation preventing further release. However, the release studies in this report were only performed once and conclusions should be regarded with great care. In accordance with the previous observations, a slower drug release also occurred for PLGA-PEG-PLGA-based hydrogels incorporating increasing amounts of DTX.^[27] Cumulative drug release after 3 weeks at 37 °C were 92% and 85% at 2 and 8 g L⁻¹ DTX, respectively. Similarly, cumulative release from PEG-PCL hydrogel was slower at 2 g L⁻¹ PTX (30% after 30 days) than at 1 g L⁻¹ (40% after 30 days).^[26]

Important to note, the CUR release from the drug-loaded hydrogels was essentially quantitative with overall CUR releases of $\geq 98\%$. In contrast, when injecting neat A-PrOzi-A/CUR nanoformulations into collagen without incorporation

into H100 at either the same nanoformulation concentration as present in H100 hydrogel (50/30 mg/g; pink curve) or at the same total polymer concentration (hydrogel + nanoformulation, 250/30 mg/g; green curve), a strikingly different release profile occurred. At the latter, CUR release was fastest with half-life of 10 days. The slower CUR release at lower A-PrOzi-A concentration of 50 mg/g (pink curve) may be attributed to a non-homogenous distribution in the collagen matrix or a smaller excess of polymer carrier. Whereas A-PrOzi-A/CUR = 250/30 mg/g enabled a decent overall release of 72%, only 36% of total added CUR was released from A-PrOzi-A/CUR = 50/30 mg/g. Visual inspection of the respective collagen samples revealed the reason for this incomplete release in the absence of H100. Immediately after injection, a more or less spherical depot is discernable at the injection site (Figure 8c, 1 h). After day 1, the yellow color of CUR distributed homogeneously throughout the whole collagen matrix (Figure 8c, 2 days). This homogeneity remained throughout the whole release experiment in all samples containing H100. In contrast, without H100, precipitation of CUR occurred at a later stage (Figure 8d, right sample) correlating with the incomplete CUR release (Figure 8b, green and pink curves). This is quite interesting, as the nanoformulation A-PrOzi-A/CUR itself exhibits excellent stability in aqueous media.^[54] This suggests that the collagen matrix somehow destabilizes the nanoformulations while this was apparently not the case when using H100/CUR depots. This is of great importance regarding the desired application as injectable drug depot, as it enables sustained and complete release over long periods of time. Important to note, after the release experiments, as suggested by the quantitative analysis, all collagen matrices initially containing H100 were completely colorless showing no sign of retained CUR (Figure 8e).

Important to note, only the CUR release of A-pPrOzi-A/CUR directly incorporated into collagen without H100 showed a linear release profile at early timepoints (followed by plateau region) when plotted against square root of time (Figure S23b, Supporting Information). A linear trend is typical of the Fickian diffusion mechanism.^[76] In contrast, when incorporated into H100, a sigmoidal CUR release was observed (Figure S23a, Supporting Information). The deviation from the often observed linear square root release kinetic of small compounds incorporated into hydrogel matrices might be due to the dual hydrogel system, that is, incorporation of drug-loaded hydrogel (H100) into another hydrogel (collagen). In case of the neat nanoformulations, the maximum CUR concentrations released per day were already reached at day 4 (Figure 8f). In contrast, employing H100 depots, released CUR concentration gradually increased up to day 8 (H100/CUR; H100/A-PrOzi-A/CUR) or day 11 (H100/A-BuOx-A/CUR), respectively, before they started to decrease. This can be attributed to the reduced diffusivity in H100, prolonging the homogenous distribution of the respective gels in the collagen matrix. CUR concentrations well above CUR aqueous solubility of 1.6 μM (0.6 mg L⁻¹)^[48] were reached in all samples in the recipient chamber. Therefore, we must assume that CUR was not released as free drug, but in solubilized form, presumably in the form of drug-loaded polymer micelles. In the case of the hydrogel incorporating A-PrOzi-A/CUR, a pronounced oversaturation with respect to

CUR aqueous solubility was achieved at day 11 ($[CUR] = 47 \mu\text{M}$, 29-fold, Figure 8g, black curve) and the oversaturation extended for several weeks (e.g., 18-fold at day 36) suggesting the long-term integrity of CUR nanoformulations in the collagen matrix. Important to note, the increase in CUR oversaturation from day 19 to day 36 is due to longer time intervals between sampling of the basolateral solution (Figure 8g, black and blue curves). In terms of controlled release, the drug depot featuring the A-BuOx-A/CUR showed arguably the most promising performance. The early-time concentration spike was less pronounced and quite steady release was observed over the course of 30 days.

4. Conclusion

CUR was incorporated into a cytocompatible hydrogel either directly or in form of a nanoformulation for a prospective injectable drug depot. Solubilization of neat CUR strongly interfered with the gelation of the hydrogel while incorporation of neat polymer used in nanoformulations resulted in two opposing trends. The purely POx-based triblock copolymer increased gel stiffness as well as decreased T_{gel} , whereas polymers bearing POzi-based hydrophobic cores similar or same to the one present in the hydrogel impeded the gelation process. Interestingly the influence of both, CUR and the neat polymers, was strongly attenuated by incorporating both into the hydrogel matrix in form of CUR nanoformulations suggesting that the drug-loaded polymer micelles remain largely intact within the POx-based hydrogel. After injection into a collagen matrix used as a simple model for subcutaneous administration, all POx-based systems exhibited essentially quantitative CUR-release. Interestingly, CUR directly incorporated into the hydrogel showed the fastest cumulative release, whereas the CUR nanoformulations exhibit markedly prolonged drug release. This is in accordance with their viscoelastic properties. Even after 50 days, the concentration of released CUR was above the inherent CUR water solubility, illustrating the release of CUR in a solubilized form from this novel combined drug depot and delivery systems. Most interestingly, CUR-loaded polymer micelles injected without hydrogel showed CUR precipitation in the collagen matrix. In contrast, collagen containing CUR-loaded POx hydrogels showed no sign of CUR precipitation during 69 days of release experiment. These findings together with the extraordinary shelf life of the CUR-loaded hydrogels with no loss of CUR-content even after 22 months make them an interesting platform as a combined drug depot and delivery system for, for example, subcutaneous or intraocular injections. As the presently investigated hydrogel has been demonstrated to be suitable as a bioink for 3D cell printing, we envision the combination of 3D cell bioprinting with 3D printed drug depots with extended release as potential future development.

Supporting Information

Supporting Information is available from the Wiley Online Library or from the author.

Acknowledgements

This work was supported by the Free State of Bavaria and the Deutsche Forschungsgemeinschaft (Project numbers 398461692 and 326998133—TRR 225 (subproject A03) awarded to R.L.). Moreover, M.M.L. would like to thank the Evonik Foundation for providing a doctoral fellowship. The authors would also like to thank Christian May, Lisa Holz, and Maria Krebs for technical support in monomer and polymer synthesis, respectively.

Conflict of Interest

M.M.L., T.L., and R.L. are listed as inventors on patent applications pertinent to materials discussed in this contribution.

Keywords

curcumin, drug depots, drug-loaded hydrogels, poly(2-oxazine), poly(2-oxazoline), sustained release

Received: August 8, 2019

Revised: October 1, 2019

Published online:

- [1] D. E. Owens, N. A. Peppas, *Int. J. Pharm.* **2006**, *307*, 93.
- [2] T. Kar, P. Basak, S. Sen, R. K. Ghosh, M. Bhattacharyya, *Front. Biol.* **2017**, *12*, 199.
- [3] X. Yang, Z. Ye, Y. Yuan, Z. Zheng, J. Shi, Y. Ying, P. Huang, *Luminescence* **2013**, *28*, 427.
- [4] S. Behzadi, V. Serpooshan, R. Sakhtianchi, B. Müller, K. Landfester, D. Crespy, M. Mahmoudi, *Colloids Surf., B* **2014**, *123*, 143.
- [5] J. Li, D. J. Mooney, *Nat. Rev. Mater.* **2016**, *1*, 16071.
- [6] N. A. Peppas, *Curr. Opin. Colloid Interface Sci.* **1997**, *2*, 531.
- [7] P. I. Lee, C.-J. Kim, *J. Control. Release* **1991**, *16*, 229.
- [8] C. L. Stevenson, J. T. Santini, R. Langer, *Adv. Drug Delivery Rev.* **2012**, *64*, 1590.
- [9] J. A. Lyndon, B. J. Boyd, N. Birbilis, *J. Control. Release* **2014**, *179*, 63.
- [10] A. Vintiliou, J.-C. Leroux, *J. Control. Release* **2008**, *125*, 179.
- [11] M. Chen, Y.-F. Li, F. Besenbacher, *Adv. Healthcare Mater.* **2014**, *3*, 1721.
- [12] G. W. Ashley, J. Henise, R. Reid, D. V. Santi, *Proc. Natl. Acad. Sci. USA* **2013**, *110*, 2318.
- [13] E. M. Ahmed, *J. Adv. Res.* **2015**, *6*, 105.
- [14] M. Calderera-Moore, N. A. Peppas, *Adv. Drug Delivery Rev.* **2009**, *61*, 1391.
- [15] A. S. Hoffman, *Adv. Drug Delivery Rev.* **2012**, *64*, 18.
- [16] M. K. Nguyen, D. S. Lee, *Macromol. Biosci.* **2010**, *10*, 563.
- [17] S. Nie, W. L. W. Hsiao, W. Pan, Z. Yang, *Int. J. Nanomed.* **2011**, *6*, 151.
- [18] X. J. Loh, B. J. H. Yee, F. S. Chia, *J. Biomed. Mater. Res., Part A* **2012**, *100A*, 2686.
- [19] G. D. Kang, S. H. Cheon, S.-C. Song, *Int. J. Pharm.* **2006**, *319*, 29.
- [20] A. Altunbas, S. J. Lee, S. A. Rajasekaran, J. P. Schneider, D. J. Pochan, *Biomaterials* **2011**, *32*, 5906.
- [21] A. Almomen, S. Cho, C.-H. Yang, Z. Li, E. A. Jarboe, C. M. Peterson, K. M. Huh, M. M. Janát-Amsbury, *Pharm. Res.* **2015**, *32*, 2266.
- [22] H. Cho, G. S. Kwon, *J. Drug Targeting* **2014**, *22*, 669.
- [23] J.-J. Xuan, Y.-D. Yan, D. H. Oh, Y. K. Choi, C. S. Yong, H.-G. Choi, *Drug Delivery* **2011**, *18*, 305.
- [24] J. Y. Lee, K. S. Kim, Y. M. Kang, E. S. Kim, S.-J. Hwang, H. B. Lee, B. H. Min, J. H. Kim, M. S. Kim, *Int. J. Pharm.* **2010**, *392*, 51.



- [25] Y. M. Kang, G. H. Kim, J. I. Kim, D. Y. Kim, B. N. Lee, S. M. Yoon, J. H. Kim, M. S. Kim, *Biomaterials* **2011**, *32*, 4556.
- [26] S. Xu, W. Wang, X. Li, J. Liu, A. Dong, L. Deng, *Eur. J. Pharm. Sci.* **2014**, *62*, 267.
- [27] Y. Gao, F. Ren, B. Ding, N. Sun, X. Liu, X. Ding, S. Gao, *J. Drug Targeting* **2011**, *19*, 516.
- [28] C. Gong, Q. Wu, Y. Wang, D. Zhang, F. Luo, X. Zhao, Y. Wei, Z. Qian, *Biomaterials* **2013**, *34*, 6377.
- [29] C. Ju, J. Sun, P. Zi, X. Jin, C. Zhang, *J. Pharm. Sci.* **2013**, *102*, 2707.
- [30] A. Hatefi, B. Amsden, *J. Control. Release* **2002**, *80*, 9.
- [31] A. Fakhari, J. Anand Subramony, *J. Control. Release* **2015**, *220*, 465.
- [32] X. J. Loh, J. Li, *Expert Opin. Ther. Pat.* **2007**, *17*, 965.
- [33] S. Kempe, K. Mäder, *J. Control. Release* **2012**, *161*, 668.
- [34] M. A. Ward, T. K. Georgiou, *Polymers* **2011**, *3*, 1215.
- [35] C. Gong, T. Qi, X. Wei, Y. Qu, Q. Wu, F. Luo, Z. Qian, *Curr. Med. Chem.* **2013**, *20*, 79.
- [36] C. Ju, J. Sun, P. Zi, X. Jin, C. Zhang, *J. Pharm. Sci.* **2013**, *102*, 2707.
- [37] W. E. Samlowski, J. R. McGregor, M. Jurek, M. Baudys, G. M. Zentner, K. D. Fowers, *J. Immunother.* **2006**, *29*, 524.
- [38] G. Chang, T. Ci, L. Yu, J. Ding, *J. Control. Release* **2011**, *156*, 21.
- [39] C. Gong, C. Wang, Y. Wang, Q. Wu, D. Zhang, F. Luo, Z. Qian, *Nanoscale* **2012**, *4*, 3095.
- [40] T. Ak, İ. Gülçin, *Chem.-Biol. Interact.* **2008**, *174*, 27.
- [41] S. Miriyala, M. Panchatcharam, P. Rengarajulu, in *The Molecular Targets and Therapeutic Uses of Curcumin in Health and Disease*, Springer, Berlin **2007**, pp. 359–377.
- [42] X. Yang, Z. Li, N. Wang, L. Li, L. Song, T. He, L. Sun, Z. Wang, Q. Wu, N. Luo, C. Yi, C. Gong, *Sci. Rep.* **2015**, *5*, 10322.
- [43] S. C. Gupta, S. Patchva, B. B. Aggarwal, *AAPS J.* **2013**, *15*, 195.
- [44] M. A. W. Jonathan Baell, *Nature* **2014**, *513*, 481.
- [45] M. Heger, *Nature* **2017**, *543*, 40.
- [46] E. Burgos-Morón, J. M. Calderón-Montaño, J. Salvador, A. Robles, M. López-Lázaro, *Int. J. Cancer* **2010**, *126*, 1771.
- [47] B. T. Kurien, S. P. Dillon, Y. Dorri, A. D'Souza, R. H. Scofield, *Int. J. Cancer* **2011**, *128*, 242.
- [48] B. T. Kurien, A. Singh, H. Matsumoto, R. H. Scofield, *Assay Drug Dev. Technol.* **2007**, *5*, 567.
- [49] Y.-J. Wang, M.-H. Pan, A.-L. Cheng, L.-I. Lin, Y.-S. Ho, C.-Y. Hsieh, J.-K. Lin, *J. Pharm. Biomed. Anal.* **1997**, *15*, 1867.
- [50] M. Kharat, Z. Du, G. Zhang, D. J. McClements, *J. Agric. Food Chem.* **2017**, *65*, 1525.
- [51] C. Schneider, O. N. Gordon, R. L. Edwards, P. B. Luis, *J. Agric. Food Chem.* **2015**, *63*, 7606.
- [52] G. M. Holder, J. L. Plummer, A. J. Ryan, *Xenobiotica* **1978**, *8*, 761.
- [53] M. M. Lübtow, L. Hahn, M. S. Haider, R. Luxenhofer, *J. Am. Chem. Soc.* **2017**, *139*, 10980.
- [54] M. M. Lübtow, L. C. Nelke, J. Seifert, J. Kühnemundt, G. Sahay, G. Dandekar, S. L. Nietzer, R. Luxenhofer, *J. Control. Release* **2019**, *303*, 162.
- [55] M. M. Lübtow, L. Keßler, A. Appelt-Menzel, T. Lorson, N. Gangloff, M. Kirsch, S. Dahms, R. Luxenhofer, *Macromol. Biosci.* **2018**, *18*, 1800155.
- [56] E. Vlassi, A. Papagiannopoulos, S. Pispas, *Eur. Polym. J.* **2017**, *88*, 516.
- [57] T. Lorson, M. M. Lübtow, E. Wegener, M. S. Haider, S. Borova, D. Nahm, R. Jordan, M. Sokolski-Papkov, A. V. Kabanov, R. Luxenhofer, *Biomaterials* **2018**, *178*, 204.
- [58] Y. Milonaki, E. Kaditi, S. Pispas, C. Demetzos, *J. Polym. Sci., Part A: Polym. Chem.* **2012**, *50*, 1226.
- [59] R. Luxenhofer, A. Schulz, C. Roques, S. Li, T. K. Bronich, E. V. Batrakova, R. Jordan, A. V. Kabanov, *Biomaterials* **2010**, *31*, 4972.
- [60] Z. He, X. Wan, A. Schulz, H. Bludau, M. A. Dobrovolskaia, S. T. Stern, S. A. Montgomery, H. Yuan, Z. Li, D. Alakhova, M. Sokolsky, D. B. Darr, C. M. Perou, R. Jordan, R. Luxenhofer, A. V. Kabanov, *Biomaterials* **2016**, *101*, 296.
- [61] X. Wan, Y. Min, H. Bludau, A. Keith, S. S. Sheiko, R. Jordan, A. Z. Wang, M. Sokolsky-Papkov, A. V. Kabanov, *ACS Nano* **2018**, *12*, 2426.
- [62] X. Wan, J. J. Beaudoin, N. Vinod, Y. Min, N. Makita, H. Bludau, R. Jordan, A. Wang, M. Sokolsky, A. V. Kabanov, *Biomaterials* **2019**, *192*, 1.
- [63] A. Zinger, L. Koren, O. Adir, M. Poley, M. Alyan, Z. Yaari, N. Noor, N. Krinsky, A. Simon, H. Gibori, M. Krayem, Y. Mumblat, S. Kasten, S. Ofir, E. Fridman, N. Milman, M. M. Lübtow, L. Liba, J. Shklover, J. Shainsky-Roitman, Y. Binenbaum, D. Hershkovitz, Z. Gil, T. Dvir, R. Luxenhofer, R. Satchi-Fainaro, A. Schroeder, *ACS Nano* **2019**, *13*, 11008.
- [64] X. Chen, F. Zhi, X. Jia, X. Zhang, R. Ambardekar, Z. Meng, A. R. Paradkar, Y. Hu, Y. Yang, *J. Pharm. Pharmacol.* **2013**, *65*, 807.
- [65] T. Lorson, S. Jaksch, M. M. Lübtow, T. Jüngst, J. Groll, T. Lühmann, R. Luxenhofer, *Biomacromolecules* **2017**, *18*, 2161.
- [66] C. V. Kulkarni, Z. Moinuddin, Y. Patil-Sen, R. Littlefield, M. Hood, *Int. J. Pharm.* **2015**, *479*, 416.
- [67] H. Witte, W. Seeliger, *Justus Liebigs Ann. Chem.* **1974**, *1974*, 996.
- [68] C. Reuter, H. Walles, F. Groeber, in *3D Cell Culture, Methods in Molecular Biology*, Vol. 1612 (Ed: Z. Koledova), Humana Press, New York **2017**, p. 191.
- [69] O. Naksuriya, S. Okonogi, R. M. Schifflers, W. E. Hennink, *Biomaterials* **2014**, *35*, 3365.
- [70] R. W. Moreadith, T. X. Viegas, M. D. Bentley, J. M. Harris, Z. Fang, K. Yoon, B. Dizman, R. Weimer, B. P. Rae, X. Li, C. Rader, D. Standaert, W. Olanow, *Eur. Polym. J.* **2017**, *88*, 524.
- [71] Y. Seo, A. Schulz, Y. Han, Z. He, H. Bludau, X. Wan, J. Tong, T. K. Bronich, M. Sokolsky, R. Luxenhofer, R. Jordan, A. V. Kabanov, *Polym. Adv. Technol.* **2015**, *26*, 837.
- [72] T. Lorson, *Ph.D. Thesis*, University of Würzburg **2019**.
- [73] O. Naksuriya, M. J. van Steenberg, J. S. Torano, S. Okonogi, W. E. Hennink, *AAPS J.* **2016**, *18*, 777.
- [74] A.-C. Pöppler, M. M. Lübtow, J. Schlauersbach, J. Wiest, L. Meinel, R. Luxenhofer, *Angew. Chem.* **2019**, <https://doi.org/10.1002/ange.201908914>.
- [75] C. Gong, S. Shi, P. Dong, B. Kan, M. Gou, X. Wang, X. Li, F. Luo, X. Zhao, Y. Wei, Z. Qian, *Int. J. Pharm.* **2009**, *365*, 89.
- [76] E. Mauri, A. Negri, E. Rebellato, M. Masi, G. Perale, F. Rossi, *Gels* **2018**, *4*, 74.

5 Summary and Outlook

Although poly(2-oxazoline) (POx) based drug carriers enabled extraordinary high *LC*s for non-water soluble drugs in selected cases, the formulation of other hydrophobic compounds has failed. However, due to their chemical versatility, drug loading of the latter could be increased by some extent by alterations in the hydrophilic/lipophilic balance induced by sidechain variation within the hydrophobic core of triblock copolymers.

Within this thesis, the chemical versatility of the drug carriers was further expanded by introducing an additional methylene unit in the polymer mainchain to obtain the so far scarcely investigated polymer class of poly(2-oxazine)s (POzi). Emphasize was put on the impact of the hydrophobic core of ABA triblock copolymers on solubilization properties. Therefore, unless otherwise stated, the hydrophilic A blocks will be kept constant (A = poly(2-methyl-2-oxazoline), whereas the hydrophobic block B will be varied. Backbone modification was already expected to have a stronger influence on polymer properties, as shown in the generally stronger dependency of POx/POzi water solubility as well as flexibility (in solid state) on mainchain, than on sidechain variation. In accordance with the latter, *LC* for hydrophobic CUR was more strongly dependent on the polymer backbone within the hydrophobic core of the polymer amphiphile than on the polymer sidechain. Generally, *LC* for CUR was higher for POzi based hydrophobic cores than for corresponding POx with either the same, or structurally similar alkyl sidechains enabling extremely high CUR loadings up to 54 wt.% as well as unrivalled high aqueous CUR solubilities of 55 g/L (90,000-fold increase in water-solubility) with 50 g/L polymer. However, a generalization of this trend is not possible, as *LC* for PTX was more dependent on the polymer sidechain, than the polymer mainchain, whereas *LC* for efavirenz was more or less independent of both. Similar to POx, sidechain alterations also strongly influenced formulation properties of POzi as observed for barely hydrophobic C₃ and C₄, strongly hydrophobic C₉ as well as aromatic phenyl and benzyl sidechains. Important to note, solubilization properties of the amphiphiles cannot be derived from the stability of the empty polymer micelles, as the presence of hydrophobic compounds can induce micellization in triblock copolymers with an amphiphilic contrast not pronounced enough

to form micelles on their own (up to polymer = 10 g/L; room temperature) resulting in excellent LCs and shelf-life of the latter combinations in selected cases.

Although the drug loading of POzi based amphiphiles was almost in all cases superior to their POx counterparts (except for PTX), the formulation of dexamethasone or tanshinone IIa (T2A) failed for both with aqueous drug concentrations < 1 g/L. Interestingly this was in accordance with the solubility profile of T2A, being soluble only in solvents without hydrogen-bond acceptors (31 solvents tested). Conversely, POx and POzi being polyamides comprise a high density of H-bond acceptors. Unfortunately, the polymer-drug compatibilities of 18 different polymer amphiphiles and five hydrophobic, structurally versatile drugs could not be predicted with widely applied group contribution methods such as Hildebrand or Hansen solubility parameters. Although certain trends regarding good and poor solubilizers could be estimated, the influence of small changes in the chemical structure such as branching or cyclization in the polymer sidechain was out of range. This was true for purely calculated as well as empirically determined solubility parameters.

The unpredictable nature of polymer-drug compatibility can be partly explained by the observation that stronger polymer-drug interactions not necessarily correlate with higher drug loadings. Although polymer-CUR interactions were more pronounced for a POx based amphiphile than for its structural POzi isomer, the latter (POzi) enabled LCs surpassing 50 wt.%, whereas the former (POx) already collapsed at CUR loadings > 25 wt.%. The stronger host-guest interactions were expressed in more closely embedded CUR molecules in the POx matrix causing a decrease in CUR molecular mobility as well as suppression of conformational changes, observed by (temperature dependent) steady state spectroscopy as well as fluorescence upconversion.

The highly unusual LCs > 50 wt.% were further investigated using solid state NMR. In accordance with fluorescence upconversion, increasing CUR loading (17, 38 and 52 wt.%) led to an increasing resemblance with the NMR spectrum of non-formulated, quench-cooled amorphous CUR. This corresponds to a more diverse, *i.e.* less ordered molecular microenvironment for CUR. Mainly the aromatic OCH₃ and OH moieties of CUR interacted with the polymer amphiphile, whereas CUR enol moiety seemed to be mostly involved in intramolecular interactions. Most interestingly, with increasing CUR content, the occurrence of additional carbonyl signals indicated that not only the amide groups of the hydrophobic core, but also of the hydrophilic shell interacted with CUR. Therefore, as the interaction sites within the core become saturated with increasing CUR loading, an increasing proportion of the hydrophilic block stabilized the solubilized cargo. Conversely, the hydrophilic corona gets more and more physically crosslinked, finally causing colloidal instabilities and precipitation.

The latter was confirmed by small angle neutron scattering (SANS), showing a transition of the drug-loaded micelles from a core-shell, to a core-shell-shell morphology at $CUR \geq 3$ g/L (polymer = 10 g/L). The second, inner shell is in good agreement with the participation of the hydrophilic polymer block in the stabilization of solubilized CUR at higher CUR loadings, investigated by solid state NMR.

Furthermore, increasing CUR loading caused a dehydration of the initially hydrated core, as well as inner shell due to increasing amounts of CUR in the respective layers. The ever more parts of CUR in the hydrophilic shell causes a dehydration of the micelle as a whole, finally causing agglomeration and precipitation. This is in accordance with the precipitation of not only CUR, but polymer/CUR at high CUR loading observed by liquid NMR. Furthermore, physical crosslinking of the hydrophilic shell was also expressed in decreasing dissolution rates of the freeze-dried CUR-loaded micelles with increasing CUR loading. The influence of the hydrophilic shell on formulation properties was further elucidated by replacing the hydrophilic poly(2-methyl-2-oxazoline) (PMeOx) shell of the ABA triblock copolymers (A = hydrophilic block; B = hydrophobic block) either partly (A-B-A*) or completely (A*-B-A*) with similarly water-soluble poly(2-ethyl-2-oxazoline) (PEtOx). A significant drop in the *LC* of all amphiphiles comprising PEtOx occurred, although the specificity pattern with respect to the hydrophobic core was largely preserved. Interestingly, the interaction between the PEtOx shell and the incorporated hydrophobic small molecules was more pronounced than for its PMeOx counterparts, reducing colloidal stability of the respective drug-loaded micelles at much lower drug loading. These findings once more demonstrate that a simple core-shell architecture, in which the core incorporates the hydrophobic drug and the corona facilitates micellar water solubility, is an oversimplification. Although main emphasize of this thesis was put on the impact of the micellar hydrophobic core on polymer-drug compatibility, the influence of the hydrophilic shell should be investigated further. This becomes clear, when considering the generally limited *LC* of polymer micelles of 20 wt.% and below, in which the hydrophilic corona of the vast majority of described systems is composed of polyethylene glycol.

From a more pharmaceutical point of view, the CUR-loaded micelles exhibited pronounced cytotoxicity in conventional 2D cell culture against human dermal fibroblasts ($IC_{50,72h} = 45 \mu M$), Caco-2 ($IC_{50,24h} = 60 \mu M$) as well as MDA-MB231 triple negative breast cancer cells ($IC_{50,72h} = 19 \mu M$). Those IC_{50} values were comparable to those of CUR simply dissolved in DMSO, showing that polymer solubilized CUR was completely active even at very high drug loadings of polymer/CUR = 10/11 g/L. Interestingly, CUR-loaded micelles also inhibited tumor growth in a more sophisticated 3D tissue model composed of MDA-MB231 cells seeded onto a decellularized porcine intestine. As the tumor cells exhibited an increased resistance against CUR therapy in the 3D model and as

serum stability of polymer/CUR was higher than for DMSO/CUR, the former might be able to allow high dose *in vivo* therapy necessary to reach sufficient CUR concentrations at the site of action. However, this is highly challenging due to the chemical instability of CUR and needs to be evaluated further. Apart from that, nanoformulated CUR also suppressed the adherence of malignant SW480 cells to a collagen scaffold in a flow bioreactor, suggesting anti-metastatic potential of CUR.

The pharmaceutical potential of drug-loaded POzi based micelles was further evaluated in the treatment of very aggressive and up to date incurable glioblastoma. Water solubility of the statin atorvastatin (ATV) could be strongly increased by solubilization with an POzi based amphiphile up to $ATV = 7 \text{ g/L}$ (polymer = 10 g/L). However, in contrast to polymer/CUR, large aggregates with hydrodynamic diameters $> 600 \text{ nm}$ were formed at ATV concentrations $\geq 3 \text{ g/L}$. The nanosized ATV-loaded micelles (polymer/ATV = $10/1 \text{ g/L}$; $D_h = 26 \text{ nm}$) exhibited pronounced cytotoxicity against various mouse and human glioblastoma cells in 2D cell culture (IC_{50} values between 5 and $32 \mu\text{M}$). This was also true for 3D spheroid models of highly aggressive and rapidly proliferating mouse brain tumor initiating bRiTS-G2 cells. Permeability of the POzi formulated ATV through an artificial blood-brain-barrier (BBB) derived from human induced pluripotent stem cells was not enhanced compared to DMSO/ATV.

To expand the way of administration, the drug-loaded micelles were incorporated into a cytocompatible POx/POzi based hydrogel matrix possibly finding application as (sub)cutaneous drug depot from which the drug is released in a locally concentrated and sustained manner. Interestingly, the presence of neat CUR strongly decreased mechanical strength of the hydrogel, which could be somehow reversed by incorporation of triblock copolymer-formulated CUR at same CUR concentrations. Important to note, the incorporation of the empty triblock copolymers affected thermogelling properties very differently, depending on their chemical structure. These deviations were much less pronounced in the case of the CUR-loaded micelles, suggesting the integrity of the latter after incorporation into the hydrogel. Apart from that, all CUR-loaded hydrogels (w/ or w/o pre-incorporation into polymer amphiphiles) exhibited excellent shelf-life with no sign of CUR-degradation or precipitation even after 22 months storage in the sol state at $5 \text{ }^\circ\text{C}$. In accordance with the lower mechanical strength of the hydrogel solubilizing neat CUR, the CUR-release of the latter after injection in a collagen matrix (to simulate subcutaneous injection) was faster compared to the hydrogels incorporating the CUR-loaded micelles at same CUR concentration. With the latter, a sustained and essentially quantitative CUR-release up to 70 days could be realized. Most interestingly, injecting micellar CUR at same CUR concentration into the collagen matrix without incorporation into the hydrogel caused premature CUR precipitation

strongly decreasing maximum released CUR to 36% and 72%. Therefore, the incorporation of CUR into the hydrogel matrix not only prolonged cargo-release but might also provide sufficient stability after e.g. subcutaneous injections.

The here reported findings strongly encourage the use and further evaluation of POzi based drug-formulations for various pharmaceutical applications. Furthermore, it became evident how small changes in the chemical structure of the individual components, or their concentrations can have a large impact on crucial formulation characteristics. Although polymer-drug interactions seem to be unpredictable to a certain extent, extensive research effort including thorough characterization of the (nano)materials will help to further optimize formulation characteristics and therefore increase patient convenience as well as maximize treatment outcomes.

Especially cheminformatics driven simulations will help more and more to precisely adjust medical properties in a targeted manner. This was already demonstrated by Kabanov and coworkers [*Sci. Adv.* **2019**, *5*, eaav9784], being able to predict the *LE* and *LC* for 6 out of 8 drugs reasonably good, by taking into account formulation conditions such as the drug-feed concentration. The scope of such computer assisted approaches is further illustrated in the predictive power of artificial intelligence (AI) driven retrosynthetic analysis, optimization of reaction conditions and even the identification of new chemistry in synthetic organic chemistry [*Nat. Rev. Chem.* **2019**, *3*, 589-604]. To generate such productive AI, access to high-quality data in generous amounts is necessary. Advantageously, large data collections are not only available for synthetic chemistry (e.g. via SciFinder or Reaxys), but also for polymer based drug formulations. For the latter, the biggest challenge might be the extraction of relevant information from the plethora of publications due to non-standardized formulation descriptions and characterizations, not to mention uncertainties regarding the characterization of the polymeric drug carriers themselves.

From a more pharmaceutical point of view, the treatment of up to date incurable pancreatic ductal adenocarcinoma is of greatest interest. Due to an overexpressed extracellular matrix, the drug penetration into the tumor is strongly hampered associated with poor survival prognosis. Very recently, we and cooperation partners demonstrated that a pretreatment based on a proteolytic-enzyme nanoparticle disassembles the dense collagen matrix. This led to an increased penetration of a POx based PTX formulation into the pancreatic tumor *in vivo*, strongly increasing anti-tumor efficacy compared to non-pretreatment [*ACS Nano* **2019**, *13*, 11008-11021]. In this study, the proteolytic enzyme and chemotherapeutic PTX were in different nanoparticulate systems. However, co-formulating the latter in the same micellar system might even increase

treatment efficacy, due to the immediate entry of PTX into the tumor site as soon as the integrity of the tumor stroma is not given anymore.

Such immediate treatment is especially important for pancreatic cancer, as the degradation of the extracellular matrix can cause an increase of circulating tumor cells or metastasis [*Cancers* **2018**, *10*, 316]. A “fast” treatment might not be possible by separately administered formulations due to different pharmaco-dynamics and -kinetics of the individual systems. Non-covalent protein delivery strategies, in which the cargo is delivered as part of a supramolecular complex, are often based on the interaction of a protein with short, mostly cationic peptide structures (so called protein transduction domains (PTDs)) of a polymeric carrier system. Tew and coworkers developed amphiphilic block copolymers composed of synthetic PTD mimics with cationic as well as hydrophobic domains for the delivery of various enzymes [*Polym. Chem.* **2016**, *7*, 7514-7521]. The hydrophobic domains have been employed to improve cell penetration. Although only investigated for protein delivery, such amphiphilic polymers might also be able to solubilize and deliver both, enzymes as well as hydrophobic drugs. Due to their chemical and structural versatility, POx and POzi based drug carriers are ideal candidates to adjust individual block lengths as well as overall composition (e.g. gradient copolymer vs. block copolymer) in order to maximize cargo loading, particle stability, as well as cellular uptake.

6 Zusammenfassung und Ausblick

Obwohl Poly(2-Oxazolin) (POx) basierte Wirkstoffträgersysteme außergewöhnlich hohe Beladungskapazitäten (*BK*) für wasserunlösliche Wirkstoffe in bestimmten Fällen aufwiesen, schlug die Formulierung anderer hydrophober Verbindungen fehl. Aufgrund ihrer chemischen Vielseitigkeit konnte die Wirkstoffbeladung mit letzteren Verbindungen jedoch erhöht werden indem die hydrophile/lipophile Balance durch Variationen in der Polymerseitenkette innerhalb des hydrophoben Kerns von Triblockcopolymeren optimiert wurde.

Innerhalb dieser Dissertation wurde die chemische Vielseitigkeit der Wirkstoffträger weiter erhöht, indem eine zusätzliche Methylengruppe in die Polymerhauptkette eingeführt wurde. Dadurch erhält man die bisher kaum untersuchte Polymerklasse der Poly(2-Oxazin)e (POzi). Hauptaugenmerk wurde auf den Einfluss des hydrophoben Blocks von ABA Triblockcopolymeren auf Solubilisierungseigenschaften gelegt. Falls nicht anders erwähnt, basierten die hydrophilen A Blöcke auf Poly(2-methyl-2-oxazolin), wohingegen der hydrophobe Block B variiert wurde. Es wurde bereits vermutet, dass Änderungen in der Polymerhauptkette einen starken Einfluss auf die Polymereigenschaften haben, da die Wasserlöslichkeit als auch die Flexibilität (im Festkörper) von POx und POzi stärker durch Veränderungen in der Polymerhauptkette, als in der Seitenkette beeinflusst werden. Damit übereinstimmend war die *BK* für das hydrophobe Molekül Curcumin (CUR) stärker von der Struktur der Polymerhaupt-, als der Polymerseitenkette beeinflusst. Generell war die *BK* für CUR höher für POzi basierte hydrophobe Kerne, als für die entsprechenden POx basierten Systeme sowohl mit derselben, als auch strukturell ähnlichen, Alkyl-basierten Seitenketten. Erstere ermöglichten extrem hohe CUR-Beladungen von bis zu 54 Gew.% wie auch unübertroffen hohe CUR Konzentrationen in Wasser von bis zu 55 g/L (90.000-fache Erhöhung der Wasserlöslichkeit) bei einer Polymerkonzentration von 50 g/L. Eine Verallgemeinerung dieses Trends ist jedoch nicht möglich, da die *BK* für Paclitaxel (PTX) stärker von der Polymerseiten-, als der Hauptkette abhing. Im Gegensatz dazu war die *BK* für Efavirenz mehr oder weniger unbeeinflusst von beidem. Davon abgesehen waren in den meisten Fällen die Formulierungseigenschaften von POzi stark abhängig von der Polymerseitenkette, wie etwa kaum hydrophober C₃ und C₄, stark hydrophober C₉ wie auch aromatischer Phenyl oder Benzyl Seitenketten.

Die Solubilisierungseigenschaften besagter Amphiphile konnten nicht von der Stabilität der unbeladenen Polymermizellen abgeleitet werden, da die Hinzugabe hydrophober Moleküle eine Mizellarisierung in Triblockcopolymeren hervorrufen kann, dessen amphiphiler Kontrast ansonsten nicht stark genug ist um selbst Mizellen zu bilden (bis zu Polymerkonzentrationen von 10 g/L bei Raumtemperatur). In ausgewählten Fällen ermöglichte die Kombination von letzteren Polymeren mit bestimmten hydrophoben Wirkstoffen sogar ausgesprochen hohe *BK* sowie Lagerbeständigkeit in wässriger Lösung.

Obwohl die Wirkstoffbeladung von POzi basierten Amphiphilen in fast allen Fällen höher war als für die entsprechenden POx mit ähnlicher Seitenkette (außer für PTX), konnte mit keinem der besagten Wirkstoffträgersysteme Dexamethason oder Tanshinon IIa (T2A) erfolgreich formuliert werden (wässrige Wirkstoffkonzentrationen < 1 g/L). Interessanterweise stimmte das mit dem Löslichkeitsprofil von T2A überein, da dieses nur in Lösungsmitteln ohne Wasserstoffbrückenakzeptoren löslich war (insgesamt 31 getestete Lösungsmittel). POx und POzi als Polyamide weisen hingegen eine sehr hohe Dichte an H-Brücken Akzeptoren auf. Die Kompatibilität zwischen Polymer und Wirkstoff von 18 verschiedenen amphiphilen Polymeren und 5 hydrophoben, strukturell unterschiedlichen Wirkstoffen konnte nicht mit den oftmals verwendeten Gruppenbeitragsmethoden wie Hildebrand oder Hansen Löslichkeitsparametern hervorgesagt werden. Obwohl bestimmte Trends in Bezug auf guter oder schlechter Löslichkeitsvermittler abgeschätzt werden konnten, konnte der Einfluss kleiner Änderungen in der chemischen Struktur der polymeren Trägerstoffe wie etwa Verzweigungen oder Zyklisierungen in der Seitenkette nicht bestimmt werden. Dies war sowohl für rein berechnete als auch empirisch bestimmte Löslichkeitsparameter der Fall.

Die Unvorhersagbarkeit der Polymer-Wirkstoff Kompatibilität kann zum Teil dadurch erklärt werden, dass stärkere Polymer-Wirkstoff Wechselwirkungen nicht immer mit höheren Wirkstoffbeladungen korrelieren. Obwohl Polymer-CUR Wechselwirkungen stärker für ein POx basiertes Amphiphil als für dessen POzi Strukturisomer ausgeprägt waren, wies letzteres (POzi) *BK* über 50 Gew.% auf, wohingegen ersteres (POx) bereits bei *BK* > 25 Gew.% begann auszufallen. Die stärkeren Wirt-Gast Wechselwirkungen zeigten sich durch stärker eingebettete CUR Moleküle in der POx Matrix, was zu einer Reduktion der molekularen Mobilität wie auch der Unterdrückung von Änderungen in der Konformation von CUR führte (beobachtet durch (Temperatur abhängige) Steady-State Spektroskopie wie auch Fluoreszenz-Hochkonversion).

Die ungewöhnlich hohen $BK > 50$ Gew.% wurden des Weiteren mit Festkörper-NMR untersucht. In Übereinstimmung mit Fluoreszenz-Hochkonversion, näherten sich die NMR Spektren mit Erhöhung der CUR-Beladung (17, 38 und 52 Gew.%) denen von nicht-formuliertem, schockgefrorenen amorphen CUR an. Dies entspricht einer weniger geordneten, molekularen Mikroumgebung von CUR. Interessanterweise wechselwirkten vor allem die aromatischen OCH_3 und OH Gruppen von CUR mit dem polymeren Amphiphil, wohingegen die zentrale Enol-Gruppe hauptsächlich intramolekular interagiert. Mit zunehmendem CUR-Anteil tauchten zusätzliche Carbonyl-Signale im NMR-Spektrum auf, welche auf die Wechselwirkung von nicht nur den Amid-Gruppen des hydrophoben Kerns, sondern auch den der hydrophilen Schale mit CUR hindeuteten. Dies bedeutet, dass mit zunehmender CUR-Beladung die Bindungsstellen innerhalb des Kerns immer stärker abgesättigt werden, wodurch ein immer größerer Anteil des hydrophilen Blocks die gelösten, hydrophoben Moleküle stabilisiert. Im Gegenzug wird dadurch die hydrophile Korona immer stärker physikalisch-quervernetzt, was zu kolloidalen Instabilitäten und somit zum Ausfall (Niederschlag) der Formulierung führt.

Letzteres wurde mithilfe von Kleinwinkelneutronenstreuung (SANS; *engl.*: small angle neutron scattering) bestätigt, bei dem ein Übergang der wirkstoffbeladenen Mizellen von einer Kern-Schale, zu einer Kern-Schale-Schale Morphologie bei CUR Konzentrationen über 3 g/L (Polymer = 10 g/L) beobachtet wurde. Die zweite, innere Schale stimmt gut mit der Beteiligung des hydrophilen Polymerblocks in der Stabilisierung von solubilisiertem CUR bei höheren CUR-Beladungen (beobachtet mit Festkörper-NMR) überein. Des Weiteren führte eine Erhöhung der CUR-Beladung zu einer Dehydratisierung des Kerns wie auch der inneren Schale, was eine Dehydratisierung der gesamten Mizelle bewirkt, und letzten Endes zur Agglomeration und zum Ausfall führt. Dies stimmt mit der Beobachtung von Flüssig-NMR überein, dass nicht nur CUR, sondern Polymer/CUR bei hohen CUR-Beladungen ausfällt. Die zunehmende physikalische-Quervernetzung der hydrophilen Schale zeigte sich ebenfalls in geringeren Auflösungsraten von gefriergetrockneten, CUR-beladenen Mizellen mit steigender CUR-Beladung.

Der Einfluss der hydrophilen Schale auf Formulierungseigenschaften wurde ebenfalls deutlich indem der hydrophile Poly(2-Methyl-2-Oxazolin) (PMeOx) Block der ABA Triblock Copolymere (A = hydrophiler Block; B = hydrophober Block) entweder teilweise (A-B-A*) oder komplett (A*-B-A*) mit ähnlich wasserlöslichem Poly(2-Ethyl-2-Oxazolin) (PEtOx) ausgetauscht wurde. Die BK von allen Amphiphilen mit PEtOx war deutlich geringer als für die entsprechenden Polymere mit PMeOx. Abgesehen von der geringeren BK blieben die Polymer-Wirkstoff Spezifitäten in Bezug auf den hydrophoben Kern jedoch weitestgehend erhalten. Interessanterweise waren die Wechselwirkungen zwischen der PEtOx Schale und den eingelagerten, hydrophoben Wirkstoffen

laut Flüssig-NMR stärker ausgeprägt als für die PMeOx Schale, was zu einer Verringerung der kolloidalen Stabilität der wirkstoffbeladenen Mizellen bereits bei geringen Wirkstoffbeladungen führte. Dies zeigt erneut, dass eine ausgeprägte Kern-Schale Morphologie, in welcher der hydrophobe Kern den hydrophoben Wirkstoff und die hydrophile Korona die Wasserlöslichkeit gewährleistet, eine starke Vereinfachung darstellt. Obwohl Hauptaugenmerk dieser Dissertation auf den Einfluss des hydrophoben Kerns auf die Polymer-Wirkstoff Kompatibilität gelegt wurde, sollte der Einfluss der hydrophilen Schale weiter untersucht werden. Dies wird insbesondere deutlich, wenn man bedenkt dass die meisten Polymer basierten Mizellen eine begrenzte BK von unter 20 Gew.% aufweisen, und die verschiedenen polymeren Systeme meist eine hydrophile Korona aus Polyethylenglycol besitzen.

Aus pharmazeutischer Sicht wiesen die CUR-beladenen Polymermizellen eine ausgeprägte Zytotoxizität in konventioneller 2D Zellkultur gegen human-dermale Fibroblasten ($IC_{50,72h} = 45 \mu M$), Caco-2 ($IC_{50,24h} = 60 \mu M$) wie auch MDA-MB231 Brustkrebszellen ($IC_{50,72h} = 19 \mu M$) auf. Die IC_{50} Werte waren vergleichbar mit denen von in DMSO gelöstem CUR, was verdeutlichte, dass Polymer-formuliertes CUR selbst bei sehr hohen Wirkstoffbeladungen von Polymer/CUR = 10/11 g/L vollständig aktiv und verfügbar war. Interessanterweise unterdrückten die CUR-beladenen Mizellen das Tumorwachstum ebenfalls in anspruchsvolleren 3D Gewebemodellen, in welchen die MDA-MB231 Zellen auf einem dezellularisierten Schweinedarm angesiedelt wurden. Da die Tumorzellen resistenter in dem 3D Model waren und die Serum Stabilität von Polymer/CUR höher war als für DMSO/CUR, könnte erstere hochdosierte *in vivo* Therapien ermöglichen, in welchen die nötigen CUR Konzentrationen am Tumor erreicht werden könnten. Trotz der positiven *in vitro* Ergebnisse ist dies jedoch aufgrund der chemischen Instabilität von CUR hochfragwürdig. Abgesehen davon unterdrückte nanoformuliertes CUR die Anlagerung von malignen SW480 kolorektalen Karzinomen an eine Kollagenmatrix in einem Durchfluss-Bioreaktor, was auf ein anti-metastatisches Potential von CUR hinweist.

Das pharmazeutische Anwendungspotential von wirkstoffbeladenen POzi Mizellen wurde des Weiteren in der Behandlung von aggressiven und bis zum jetzigen Zeitpunkt unheilbaren Glioblastomen getestet. Die Wasserlöslichkeit des Statins Atorvastatin (ATV) konnte durch die Formulierung mit POzi basierten Amphiphilen bis zu ATV = 7 g/L (Polymer = 10 g/L) stark erhöht werden. Jedoch im Gegensatz zu POzi/CUR bildeten sich bei ATV Konzentrationen über 3 g/L größere Aggregate mit hydrodynamischen Durchmessern über 600 nm. Nanoformuliertes ATV (Polymer/ATV = 10/1 g/L; $D_h = 26 \text{ nm}$) wies eine ausgeprägte Zytotoxizität gegen verschiedene Maus wie auch humane Glioblastom Zelllinien in 2D Zellkulturen auf (IC_{50} Werte zwischen 5 und 32 μM) . Polymer/ATV war ebenfalls zytotoxisch in 3D Spheroid Modellen von hochaggressiven

und schnell proliferierenden Maus-Gehirntumor initiierenden bRiTS-G2 Zellen. Die Permeabilität von POzi formuliertem ATV über eine künstliche Blut-Hirn-Schranke basierend auf human-induzierten, pluripotenten Stammzellen war jedoch nicht höher als für DMSO/ATV.

Um das Einsatzgebiet von den Polymer-basierten Formulierungen zu erweitern, wurden die wirkstoffbeladenen Mizellen in ein zellkompatibles, POx/POzi basiertes Hydrogel eingearbeitet, um so als (sub)kutan verabreichtes Wirkstoffdepot, von welchem der Wirkstoff in lokal konzentrierter und länger anhaltenden Weise freigesetzt wird, Anwendung finden zu können. Wohingegen die direkte Einlagerung von CUR die mechanische Festigkeit des Hydrogels stark herabsetzte, wirkte sich die Einlagerung von CUR-beladenen Triblockcopolymeren weit weniger auf die rheologischen Eigenschaften aus (bei gleichen CUR Konzentrationen im Hydrogel). Interessanterweise wurden die thermogellierenden Eigenschaften des Gels bei Einlagerung der reinen Blockcopolymeren (ohne CUR) in Abhängigkeit deren chemischen Struktur stark unterschiedlich beeinflusst. Für die verschiedenen CUR-beladenen Mizellen waren diese Unterschiede weitaus weniger ausgeprägt, was auf die Integrität der Mizellen bei Einlagerung in das Hydrogel hindeutete (alle Mizellen präsentieren nach außen die gleiche hydrophile Corona). Abgesehen davon wiesen alle CUR-beladenen Hydrogele (mit oder ohne vorherige Formulierung von CUR mit Triblockcopolymeren) eine exzellente Lagerstabilität auf, so dass selbst nach 22-monatiger Lagerung im Sol Zustand bei 5 °C keine Anzeichen einer Zersetzung von CUR zu erkennen waren. In Übereinstimmung mit der geringeren mechanischen Festigkeit der Hydrogele in welche CUR direkt aufgenommen wurde, erfolgte die Wirkstofffreisetzung aus letzteren nach Injektion in eine Kollagenmatrix (als Modell für eine subkutane Injektion) schneller als für die entsprechenden Hydrogele mit Triblockcopolymer-formuliertem CUR (bei gleichen CUR Konzentrationen im Gel). Mit letzteren konnte eine langanhaltende und im wesentlichen quantitative CUR-Freisetzung über 70 Tage lang realisiert werden. Interessanterweise führte die Injektion von mizellarem CUR bei gleichen CUR Konzentrationen in die Kollagenmatrix ohne vorherige Einlagerung in das POx/POzi Hydrogel zu einem vorzeitigen Ausfall von CUR, wodurch die maximale Menge an freigesetztem CUR auf 36 % und 72 % stark reduziert wurde. Aus diesem Grund verlängerte die Einlagerung von CUR in die Hydrogelmatrix nicht nur die Wirkstofffreisetzung, sondern könnte möglicherweise auch die nötige Stabilität nach subkutaner Injektion ermöglichen.

Die hier beschriebenen Ergebnisse bestärken die Verwendung und weitere Untersuchung von POzi basierten Wirkstoffformulierungen für diverse pharmazeutische Anwendungen. Des Weiteren wurde deutlich wie kleine Änderungen in der chemischen Struktur der unterschiedlichen Bestandteile oder deren Konzentrationen sich stark auf entscheidende

Formulierungscharakteristika auswirken können. Obwohl Polymer-Wirkstoff Wechselwirkungen und Kompatibilitäten zu einem bestimmten Teil unvorhersehbar erscheinen, wird die ausführliche Untersuchung und Charakterisierung derartiger (Nano)Materialien helfen um Formulierungseigenschaften weiter zu optimieren um dadurch die Patientenverträglichkeit sowie die Wirksamkeit der Therapien verbessern zu können.

Besonders Chemoinformatik basierte Simulationen werden in Zukunft immer stärker dazu beitragen bestimmte medizinische Eigenschaften präzise und vor allem gezielt einstellen zu können. Dies wurde bereits teilweise von Kabanov und Mitarbeitern demonstriert [*Sci. Adv.* **2019**, *5*, eaav9784], in dem Sie die BK von 6 von insgesamt 8 Wirkstoffen unter Einbezug bestimmter Formulierungsparameter wie etwa der Menge an hinzugegebenem Wirkstoff zuverlässig vorhersagten. Die Möglichkeiten derartiger, Informatik basierter Techniken zeigt sich des Weiteren in der Vorhersagekraft von künstlicher Intelligenz (KI) für die retrosynthetische Analyse, der Optimierung von Reaktionsbedingungen wie auch der Identifizierung von gänzlich neuer Chemie in synthetischer, organischer Chemie [*Nat. Rev. Chem.* **2019**, *3*, 589-604]. Um derartige KI basierte Vorhersagen treffen zu können, ist der Zugang zu qualitativ hochwertigen Datensammlungen in großen Mengen erforderlich. Vorteilhafterweise sind derartige Datenmengen nicht nur für die synthetische Chemie (bspw. via SciFinder oder Reaxys), sondern auch für Polymer-basierte Wirkstoffformulierungen zugänglich. Das größte Problem hierbei könnte jedoch die Gewinnung relevanter Information aus der Vielzahl an Publikationen sein aufgrund von nicht-standardisierten Durchführungsprotokollen und Charakterisierungen von Formulierungen, ganz abgesehen von der Ungewissheit in Bezug auf die Charakterisierung der polymeren Wirkstoffträger selbst.

Aus pharmazeutischer Sicht ist die Behandlung von bis zum jetzigen Zeitpunkt unheilbaren Bauchspeicheldrüsenkrebs von größtem Interesse. Aufgrund einer überexprimierten extrazellulären Matrix ist die Wirkstoffpenetration in den Tumor stark behindert was zu einer niedrigen Überlebensrate beiträgt. Vor kurzem haben wir in Zusammenarbeit mit Kooperationspartnern zeigen können, dass eine Vorbehandlung mit Nanopartikeln, welche ein proteolytisches Enzym in sich tragen, die dichte Kollagenmatrix abbauen kann. Dies führte zu einer erhöhten Penetration einer POx basierten PTX Formulierung in den Tumor *in vivo*, was zu einer stark erhöhten anti-tumor Effektivität verglichen zu nicht-vorbehandelten Tiermodellen führte [*ACS Nano* **2019**, *13*, 11008-11021]. In dieser Studie waren das proteolytische Enzym und das Chemotherapeutikum PTX in verschiedenen, nanopartikulären Systemen eingekapselt. Eine Koformulierung in einer Mizelle könnte die Behandlungseffektivität jedoch weiter steigern, aufgrund des sofortigen Eintritts von PTX in den Krebsherd sobald die Integrität des umgebenden

Tumorstroma nicht mehr gewährleistet ist. Solch eine unmittelbare Behandlung ist insbesondere für Bauchspeicheldrüsenkrebs von Bedeutung, da der Abbau der extrazellulären Matrix zu einer Erhöhung der zirkulierenden Tumorzellen, bzw. Metastasen führen kann [Cancers **2018**, 10, 316]. Eine derartige „schnelle“ Behandlung könnte bei separat verabreichten Formulierungen (für Enzym und PTX) aufgrund unterschiedlicher Pharmakodynamiken, wie auch Kinetiken der einzelnen Systeme nicht möglich sein. Nicht-kovalente Proteintransportstrategien basieren häufig auf den Wechselwirkungen eines Enzyms mit kurzen, meist kationischen Peptidstrukturen (sogenannte protein transduction domains (PTDs)) eines polymeren Trägersystems. Tew und Mitarbeiter entwickelten amphiphile Blockcopolymere für den Transport von Enzymen, welche aus synthetischen PTDs mit kationischen als auch hydrophoben Domänen aufgebaut sind [Polym. Chem. **2016**, 7, 7514-7521]. Die hydrophoben Domänen führten zu einer Erhöhung der zellulären Aufnahme. Obwohl nur im Kontext von Proteinsolubilisierung und Transport diskutiert, könnten derartige amphiphile Polymere in der Lage sein beides einzukapseln – Enzyme als auch hydrophobe Wirkstoffe. Aufgrund ihrer chemischen sowie strukturellen Vielfältigkeit sind POx und POzi basierte Wirkstoffträger ideal um bspw. die einzelnen Blocklängen sowie die insgesamt Zusammensetzung (Gradientcopolymer vs. Blockcopolymer) gezielt einzustellen, um die Beladungskapazität, Partikelstabilität, wie auch zelluläre Aufnahme zu maximieren.

Erklärung

Die vorliegende Arbeit wurde unter der wissenschaftlichen Betreuung von Prof. Dr. Robert Luxenhofer von August 2016 bis September 2019 an der Fakultät für Chemie und Pharmazie der Julius-Maximilians-Universität Würzburg angefertigt.

Hiermit versichere ich, dass ich die vorliegende Arbeit ohne unzulässige Hilfe Dritter und ohne Benutzung anderer als der angegebenen Hilfsmittel angefertigt habe. Die aus fremden Quellen direkt oder indirekt übernommenen Gedanken sind als solche kenntlich gemacht. Die Arbeit wurde bisher weder im Inland noch im Ausland in gleicher oder ähnlicher Form einer anderen Prüfungsbehörde vorgelegt.

Würzburg, den 19.11.2019



Michael M. Lübtow

Eigenanteil

“Drug induced micellization into ultra-high capacity and stable curcumin nanoformulations: Physico-chemical characterization and evaluation in 2D and 3D *in vitro* models”

M. M. Lübtow*, L. C. Nelke, J. Seifert, J. Kühnemundt, G. Sahay, G. Dandekar, S. L. Nietzer, R. Luxenhofer[†]

Journal of Controlled Release **2019**, 303, 162-180

Autor 1 (M. M. L), Autor 2 (L. C. N), Autor 3 (J. S.), Autor 4 (J. K.), Autor 5 (G. S.), Autor 6 (G. D.), Autor 7 (S. L.N.), Autor 8 (R. L.)									
Autor	A1	A2	A3	A4	A5	A6	A7	A8	Σ in Prozent
Monomer- & Polymersynthese	8								8
Kritische Mizellbildungskonzentration	3								3
Wirkstoffformulierung	12								12
Dynamische Lichtstreuung	3								3
NMR Studien	6								6
Cryo-Transmissionselektronenmikroskopie					6				6
Dynamische Differenzkalorimetrie	3								3
Röntgendiffraktometrie	3								3
2D Zellstudien	1.5	3	0.5						5
3D Zellkronen		9							9
3D Umlaufreaktor			5.4	3.6					9
Verfassen der Veröffentlichung	8					1.5	1.5	4	15
Korrektur der Veröffentlichung	2					0.5	0.5	2	5
Koordination der Veröffentlichung	3.8					0.65	0.65	7.9	13
Summe	53.3	12	5.9	3.6	6	2.65	2.65	13.9	100%

“More Is Sometimes Less: Curcumin and Paclitaxel Formulations Using Poly(2-oxazoline) and Poly(2-oxazine)-Based Amphiphiles Bearing Linear and Branched C9 Side Chains”

M. M. Lübtow*, L. Keßler, A. Appelt-Menzel, T. Lorson, N. Gangloff, M. Kirsch, S. Dahms, R. Luxenhofer[†]
Macromolecular Bioscience **2018**, *18*, 1800155

Autor 1 (M. M. L.), Autor 2 (L. K.), Autor 3 (A. A.-M.), Autor 4 (T. L.), Autor 5 (N. G.), Autor 6 (M. K.), Autor 7 (S. D.), Autor 8 (R. L.)									
Autor	A1	A2	A3	A4	A5	A6	A7	A8	Σ in Prozent
Monomer- & Polymersynthese	4.5	4.5				3	3		15
MALDI	0.6				2.4				3
Wirkstoffformulierung	6	14							20
Kritische Mizellbildungskonzentration	0.4	1.6							2
Dynamische Lichtstreuung		2.1		0.9					3
Zellstudien & Hämolyse	0.6		2.4						3
IR Studien	0.6	2.4							3
NMR Studien	2.1	0.9							3
Thermogravimetrie	0.4	1.6							2
Dynamische Differenzkalorimetrie	2.1	0.9							3
Verfassen der Veröffentlichung	11	3						6	20
Korrektur der Veröffentlichung	2.5							2.5	5
Koordination der Veröffentlichung	10							8	18
Summe	40.8	31	2.4	0.9	2.4	3	3	16.5	100%

“Drug Specificity, Synergy and Antagonism in Ultrahigh Capacity Poly(2-oxazoline)/Poly(2-oxazine) based Formulations”

M. M. Lübtow*, L. Hahn, M. S. Haider, R. Luxenhofer[†]
Journal of American Chemical Society **2017**, *139*, 10980-10983

Autor 1 (M. M. L.), Autor 2 (L. H.), Autor 3 (M. S. H.), Autor 4 (R. L.)					
Autor	A1	A2	A3	A4	Σ in Prozent
Monomer- & Polymersynthese	18	2			20
Wirkstoffformulierung	18	2			20
Studien mit Reichardt's Farbstoff	2		3		5
Dynamische Lichtstreuung	5				5
Verfassen der Veröffentlichung	17			13	30
Korrektur der Veröffentlichung	2.5			2.5	5
Koordination der Veröffentlichung	6			9	15
Summe	68.5	4	3	24.5	100%

“Like Dissolves Like? A Comprehensive Evaluation of Partial Solubility Parameters to Predict Polymer–Drug Compatibility in Ultrahigh Drug-Loaded Polymer Micelles”

M. M. Lübtow*, M. S. Haider, M. Kirsch, S. Klisch, R. Luxenhofer[†]
Biomacromolecules **2019**, *20*, 3041-3056

Autor 1 (M. M. L.), Autor 2 (M. S. H.), Autor 3 (M. K.), Autor 4 (S. K.), Autor 5 (R. L.)						
Autor	A1	A2	A3	A4	A5	Σ in Prozent
Monomer- & Polymersynthese	18		2			20
Kritische Mizellbildungskonzentration	5					5
Wirkstoffformulierung	18			2		20
Dynamische Differenzkalorimetrie	5					5
Berechnung Löslichkeitsparameter	6	3	1			10
Bestimmung Löslichkeiten	10					10
Verfassen der Veröffentlichung	10.5	0.75		0.75	3	15
Korrektur der Veröffentlichung	2.5				2.5	5
Koordination der Veröffentlichung	3				7	10
Summe	82	3.75	3	2.75	8.5	100%

“Ultra-high to ultra-low drug loaded micelles: Probing host-guest interactions by fluorescence spectroscopy”

M. M. Lübtow*, H. Marciniak, A. Schmiedel, M. Roos, C. Lambert, R. Luxenhofer[†]
Chemistry: A European Journal **2019**, *25*, 12601-12610

Autor 1 (M. M. L.), Autor 2 (H. M.), Autor 3 (A. S.), Autor 4 (M. R.), Autor 5 (C. L.), Autor 6 (R. L.)							
Autor	A1	A2	A3	A4	A5	A6	Σ in Prozent
Dynamische Lichtstreuung	10						10
Steady State Absorption & Fluoreszenz	30						30
Fluoreszenz Upconversion		7	3				10
Temperaturabhängige Spektroskopie	10						10
Anisotropie	0.6			2.4			3
Verfassen der Veröffentlichung	8				4	6	18
Korrektur der Veröffentlichung	2.5				2.5	2	7
Koordination der Veröffentlichung	3.4				1.2	7.4	12
Summe	64.5	7	3	2.4	7.7	15.4	100%

“Investigating the Influence of Aromatic Moieties on the Formulation of Hydrophobic Natural Products and Drugs in Poly(2-oxazoline)-Based Amphiphiles”

L. Hahn*, M. M. Lübtow, T. Lorson, F. Schmitt, A. Appelt-Menzel, R. Schobert, R. Luxenhofer[†]
Biomacromolecules **2018**, *19*, 3119-3128

Autor 1 (L. H.), Autor 2 (M. M. L.), Autor 3 (T. L.), Autor 4 (F. S.), Autor 5 (A. A.-M.), Autor 6 (R. S.), Autor 7 (R. L.)								
Autor	A1	A2	A3	A4	A5	A6	A7	Σ in Prozent
Monomer- & Polymersynthese	13	2						15
Wirkstoffextraktion	15							15
Wirkstoffformulierung	13.5	1.5						15
Zellkultur				2.5	2.5			5
Dynamische Lichtstreuung	3.5		1.5					5
Dynamische Differenzkalorimetrie	5							5
Kritische Mizellbildungskonzentration	5							5
Verfassen der Veröffentlichung	7	4.2				2.5	6.3	20
Korrektur der Veröffentlichung	2	1					2	5
Koordination der Veröffentlichung	2	2					6	10
Summe	66	10.7	1.5	2.5	2.5	2.5	14.3	100%

“Poly(2-oxazoline)s based biomaterials: A comprehensive and critical update”

T. Lorson*, M. M. Lübtow*, E. Wegener, M. S. Haider, S. Borova, D. Nahm, R. Jordan, M. Sokolski-Papkov, A. V. Kabanov, R. Luxenhofer[†]
Biomaterials **2018**, *178*, 204-280

Autor 1 (T. L.), Autor 2 (M. M. L.), Autor 3 (E. W.), Autor 4 (M. S. H.), Autor 5 (S. B.), Autor 6 (D. N.), Autor 7 (R. J.), Autor 8 (M. S.-P.), Autor 9 (A. V. K.) Autor 10 (R. L.)											
Autor	A1	A2	A3	A4	A5	A6	A7	A8	A9	A10	Σ in Prozent
Verfassen der Veröffentlichung	11	11	6	4	4	4	4	6	6	24	80
Korrektur der Veröffentlichung	1.2	1.2								2.6	5
Koordination der Veröffentlichung	1	1								13	15
Summe	13.2	13.2	6	4	4	4	4	6	6	39.6	100%

“Loading dependent Structural Model of Polymeric Micelles Encapsulating Curcumin by Solid-State NMR Spectroscopy”

A.-C. Pöppler*, M. M. Lübtow, J. Schlauersbach, J. Wiest, L. Meinel, R. Luxenhofer[†]
Angewandte Chemie **2019**, doi:org/10.1002/anie.201908914

Autor 1 (A.-C. P.), Autor 2 (M. M. L.), Autor 3 (J. S.), Autor 4 (J. W.), Autor 5 (L. M.), Autor 6 (R. L.)							
Autor	A1	A2	A3	A4	A5	A6	Σ in Prozent
Röntgendiffraktometrie	2						2
Flüssig NMR	15						15
Festkörper NMR	30						30
Wirkstoffformulierung		5					5
Auflösungsstudien			2.5	0.5			3
Verfassen der Veröffentlichung	16	1	0.25	0.25	0.5	2	20
Korrektur der Veröffentlichung	9.5				0.5		10
Koordination der Veröffentlichung	10.5	0.8			0.7	3	15
Summe	83	6.8	2.75	0.75	1.7	5	100%

“Temperature-Dependent Rheological and Viscoelastic Investigation of a Poly(2-methyl-2-oxazoline)-b-poly(2-iso-butyl-2-oxazoline)-b-poly(2-methyl-2-oxazoline)-Based Thermogelling Hydrogel”

M. M. Lübtow*, M. Mrlik*, L. Hahn, A. Altmann, M. Beudert, T. Lühmann, R. Luxenhofer[†]
Journal of Functional Biomaterials **2019**, 10, 36

Autor 1 (M. M. L.), Autor 2 (M. M.), Autor 3 (L. H.), Autor 4 (A. A.), Autor 5 (M. B.), Autor 6 (T. L.), Autor 7 (R. L.)								
Autor	A1	A2	A3	A4	A5	A6	A7	Σ in Prozent
Monomer- & Polymersynthese	8							8
Rheologie	2	24	4					30
Rasterelektronenmikroskopie	5							5
Zellstudien					5			5
Drucken			3	2				5
Verfassen der Veröffentlichung	2.5	12	1		0.5	0.5	3.5	20
Korrektur der Veröffentlichung	2.4	4.8					4.8	12
Koordination der Veröffentlichung	2.3	3.5				0.7	8.5	15
Summe	22.2	44.3	8	2	5.5	1.2	16.8	100%

“A Thermogelling Supramolecular Hydrogel with Sponge-Like Morphology as a Cytocompatible Bioink”

T. Lorson*, S. Jaksch, M. M. Lübtow, T. Jüngst, J. Groll, T. Lühmann, R. Luxenhofer[†]
Biomacromolecules **2017**, *18*, 2161-2171

Autor 1 (T. L.), Autor 2 (S. J.), Autor 3 (M. M. L.), Autor 4 (T. J.), Autor 5 (J. G.), Autor 6 (T. L.), Autor 7 (R. L.)								
Autor	A1	A2	A3	A4	A5	A6	A7	Σ in Prozent
Monomer- & Polymersynthese	17		1					18
Rheologie	24		1					25
Neutronenstreuung	2	8						10
Zellstudien						4		4
Drucken	2			6		2		10
Verfassen der Veröffentlichung	6	1.5			0.5	0.5	6.5	15
Korrektur der Veröffentlichung	2.5						2.5	5
Koordination der Veröffentlichung	3				0.5	0.5	9	13
Summe	56.5	9.5	2	6	1	7	18	100%

“Combining ultra-high drug loaded micelles and injectable hydrogel drug depots for prolonged drug release”

M. M. Lübtow*, T. Lorson, T. Finger, F.-K. Gröber-Becker, R. Luxenhofer[†]
Macromolecular Chemistry and Physics **2019**, <https://doi.org/10.1002/macp.201900341>

Autor 1 (M. M. L.), Autor 2 (T. L.), Autor 3 (T. F.), Autor 4 (F.-K. G.-B.), Autor 5 (R. L.)						
Autor	A1	A2	A3	A4	A5	Σ in Prozent
Monomer- & Polymersynthese	4.8	0.2				5
Wirkstoffformulierung	15					15
Rheologie	16	4				20
Wirkstofffreisetzung	13		2			15
Verfassen der Veröffentlichung	17			1	7	25
Korrektur der Veröffentlichung	2.5				2.5	5
Koordination der Veröffentlichung	7			1.5	6.5	15
Summe	75.3	4.2	2	2.5	16	100%

“Probing the complex loading dependent structural changes in ultra-high drug loaded polymer micelles by small angle neutron scattering”

B. Sochor*, Ö. Düdükçü*, M. M. Lübtow, S. Jaksch, B. Schummer, R. Luxenhofer[†]
ChemRxiv 2019, doi.org/10.26434/chemrxiv.10259552

Autor 1 (B. S.), Autor 2 (Ö. D.), Autor 3 (M. M. L.), Autor 4 (S. J.), Autor 5 (B. S.), Autor 6 (R. L.)							
Autor	A1	A2	A3	A4	A5	A6	Σ in Prozent
Wirkstoffformulierung			5				5
Dichtemessungen		10					10
Messung Neutronenstreuung			5	10			15
Auswertung Neutronenstreuung	10	8	2	6	2	2	30
Verfassen der Veröffentlichung	5	3	3	2		7	20
Koordination der Veröffentlichung	4	3	3	2		8	15
Summe	19	24	18	20	2	17	100%

“*In vitro* blood-brain-barrier permeability and cytotoxicity of atorvastatin-loaded nanoformulation against glioblastoma in 2D and 3D models”

M. M. Lübtow*, S. Oerter, S. Quader, E. Jeanclos, A. Cubukova, M. Krafft, C. Schulte, L. Meier, M. Rist, O. Sampetean, H. Kinoh, A. Gohla, K. Kataoka, A. Appelt-Menzel, R. Luxenhofer[†]
ChemRxiv 2019, doi.org/10.26434/chemrxiv.10067993.v1

Autor 1 (M. M. L.), Autor 2 (S. O.), Autor 3 (S. Q.), Autor 4 (E. J.), Autor 5 (A. C.), Autor 6 (M. K.), Autor 7 (C. S.), Autor 8 (L. M.), Autor 9 (M. R.), Autor 10 (O. S.), Autor 11 (H. K.), Autor 12 (A. G.), Autor 13 (K. K.), Autor 14 (A. A.-M.), Autor 15 (R. L.)																
Autor	A1	A2	A3	A4	A5	A6	A7	A8	A9	A10	A11	A12	A13	A14	A15	Σ in Prozent
Wirkstoffformulierung	1						2	1								4
Dynamische Lichtstreuung	2															2
NMR Studien	4															4
2D Zellstudien	11		3								1					15
Zellmigration				5								3				8
3D Zellstudien	5		2							1	2					10
Permeabilität Blut-Hirn-Schranke	2	3			3	2			1					4		15
Verfassen der Veröffentlichung	9	2		1								1		1	6	20
Koordination der Veröffentlichung	6	1										1	1	2	11	22
Summe	40	6	5	6	3	2	2	1	1	1	3	5	1	7	17	100%

“Think beyond the core: The impact of the hydrophilic corona on the drug solubilization using polymer micelles”

M. S. Haider*, M. M. Lübtow, V. Aseyev, A.-C. Pöppler, R. Luxenhofer[†]
ChemRxiv 2019, doi.org/10.26434/chemrxiv.9710579.v1

Autor 1 (M. S. H.), Autor 2 (M. M. L.), Autor 3 (V. A.), Autor 4 (A.-C. P.), Autor 5 (R. L.)						
Autor	A1	A2	A3	A4	A5	Σ in Prozent
Monomer- & Polymersynthese	12	3				15
Wirkstoffformulierung	13.5	1.5				15
Reichardt's Farbstoff	5					5
Flüssig NMR	4.5	0.5				5
Dynamische Lichtstreuung	3					3
Dynamische Differenzkalorimetrie	2.7	0.3				3
Thermogravimetrie	3					3
Kritische Mizellbildungskonzentration	3					3
Mikrokalorimetrie			3			3
Diffusion NMR & NOESY				5		5
Verfassen der Veröffentlichung	7	2		2	11	22
Koordination der Veröffentlichung	6.5	2.5			9	18
Summe	60.2	9.8	3	7	20	100%